Symbolic Derivation of Spectral Green's Functions for Anisotropic Multilayer Structures

I. Bianchi and J. C. da S. Lacava
Laboratório de Antenas e Propagação, Instituto Tecnológico de Aeronáutica, Brazil

Abstract— A new systematic procedure for calculating the electromagnetic fields in anisotropic multilayer microstrip structures is presented. Working in the Fourier domain and using symbolic computation, expressions for the spectral Green's functions are derived in compact, closed form. A flat dipole fed by electromagnetic coupling printed on a *biaxial* multilayer structure is analyzed and its input impedance is evaluated by the Method of Moments (MoM). For validation purposes, our results are compared to those simulated with commercial software such as *HFSS*.

1. INTRODUCTION

Electromagnetic fields created by sources embedded in stratified media are currently used in the analysis of phenomena in optoelectronics, microwave circuits, military surveillance and antenna theory. For accurate results, the analysis requires numerical methods such as the MoM, Finite Elements or Finite Differences [1]. It is presently widely accepted that MoM-based algorithms are suitable for rigorous numerical analysis of printed structures of small to medium sizes (in terms of wavelength) stacked up in layers [2]. However, for the application of this method, the corresponding dyadic Green's functions need be derived. Although rigorous and elegant, these calculations are usually tedious and error-prone when done by hand, what is especially true in the analysis of structures with bi-isotropic [3] or anisotropic materials [4].

To overcome this limitation, this paper presents a new, systematic procedure for calculating the spectral fields in multilayer structures. Working in the Fourier domain and utilizing the symbolic computation capability of the *Mathematica*® package, closed-form expressions for the transformed electromagnetic fields are derived in a straightforward, error-free way. Consequently, the spectral Green's functions can be determined in compact, closed form, with considerable reduction of the calculation time. Using this new procedure, spectral Green's functions for microstrip structures with *biaxial* anisotropy are derived. Based on these functions, a method-of-moments algorithm is implemented in *FORTRAN* for the analysis of a printed dipole fed by electromagnetic coupling. For validation purposes, results obtained with this algorithm are compared to those simulated with commercial software such as *HFSS*, which makes use of the finite elements technique.

2. THEORY

The structure under consideration is depicted in Figure 1. The microstrip feed line of length L_F and width w is printed on the lower substrate. The flat dipole of length b and width a is printed on the upper superstrate. In the current formulation, each layer is considered as a linear homogeneous medium with *biaxial* anisotropy, i.e., characterized by permittivity $[\varepsilon]^{(\nu)}$ and permeability $[\mu]^{(\nu)}$ tensors (the index $\nu = 1$ or 2 identifies each anisotropic layer). The planar interface $z = \ell_2$ separates the superstrate from free space region ($z > \ell_2$, permittivity ε_0, and permeability μ_0). A perfectly conducting ground is located at $z = 0$.

The radiation structure is considered as a boundary value problem where the surface electric current densities on the microstrip feed line $\boldsymbol{J}_1(x, y)$ and on the flat dipole $\boldsymbol{J}_2(x, y)$ (boldface letters represent vectors) are the virtual sources of the electromagnetic fields. As the three layers of the structure are free of sources, the electric field in the spatial domain of a monochromatic wave can be written, according to the spectral techniques, as a superposition of plane waves, as follows [5].

$$\boldsymbol{E}(x, y, z) = \frac{1}{4\pi^2} \int_{-\infty}^{\infty} \int_{-\infty}^{\infty} \boldsymbol{E}(k_x, k_y, z)\, e^{-i(k_x x + k_y y)} dk_x dk_y \tag{1}$$

where the function $\boldsymbol{E}(k_x, k_y, z)$ is the spectral electric field, and k_x and k_y are the spectral variables.

Since the substrate and the superstrate are confined layers, the spectral fields $\boldsymbol{E}^{(\nu)}(k_x, k_y, z)$ and $\boldsymbol{H}^{(\nu)}(k_x, k_y, z)$ can be written as the superposition of four plane waves traveling in the $\pm z$

$$[\varepsilon]^{(\nu)} = \begin{bmatrix} \varepsilon_1^{(\nu)} & 0 & 0 \\ 0 & \varepsilon_5^{(\nu)} & 0 \\ 0 & 0 & \varepsilon_9^{(\nu)} \end{bmatrix}$$

The *biaxial* permittivity tensor.

$$[\mu]^{(\nu)} = \begin{bmatrix} \mu_1^{(\nu)} & 0 & 0 \\ 0 & \mu_5^{(\nu)} & 0 \\ 0 & 0 & \mu_9^{(\nu)} \end{bmatrix}$$

The *biaxial* permeability tensor.

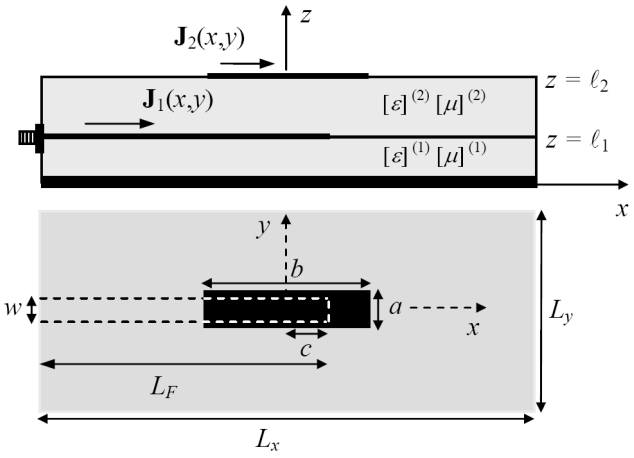

Figure 1: *Biaxial* tensors and geometry of printed dipoles fed by electromagnetic coupling.

directions, that is

$$\boldsymbol{E}^{(\nu)}(k_x,\, k_y,\, z) \,=\, \sum_{\tau=1}^{4} \boldsymbol{e}_\tau^{(\nu)}(k_x,\, k_y)\, e^{\,i\,\gamma_\tau^{(\nu)}\, z} \tag{2}$$

$$\boldsymbol{H}^{(\nu)}(k_x,\, k_y,\, z) \,=\, \sum_{\tau=1}^{4} \boldsymbol{h}_\tau^{(\nu)}(k_x,\, k_y)\, e^{\,i\,\gamma_\tau^{(\nu)}\, z} \tag{3}$$

where $\boldsymbol{e}_\tau^{(\nu)}(k_x, k_y)$ and $\boldsymbol{h}_\tau^{(\nu)}(k_x, k_y)$ are the amplitudes of the transformed fields, and the propagation constants $\gamma_\tau^{(\nu)}$ are obtained by solving the following equation.

$$\left\{ \boldsymbol{k}^{(\nu)} \times \left\{ \left([\mu]^{(\nu)} \right)^{-1} \cdot \boldsymbol{k}^{(\nu)} \times [I] \right\} + \omega^2 [\varepsilon]^{(\nu)} \right\} \cdot \boldsymbol{e}^{(\nu)}(k_x,\, k_y) = 0 \tag{4}$$

where $[I]$ is the idemfactor and $\boldsymbol{k}^{(\nu)} = k_x \boldsymbol{x} + k_y \boldsymbol{y} - \gamma^{(\nu)} \boldsymbol{z}$.

On the other hand, the transformed fields in free space are

$$\boldsymbol{E}_0(k_x,\, k_y,\, z) \,=\, \boldsymbol{e}_0(k_x,\, k_y)\, e^{\,-i\,k_{z0}\, z} \tag{5}$$

$$\boldsymbol{H}_0(k_x,\, k_y,\, z) \,=\, \boldsymbol{h}_0(k_x,\, k_y)\, e^{\,-i\,k_{z0}\, z} \tag{6}$$

where $k_{z0} = [\omega^2 \mu_0 \varepsilon_0 - k_x^2 - k_y^2]^{1/2}$.

Application of the boundary conditions for the electromagnetic fields at the interfaces $z = 0$, $z = \ell_1$ and $z = \ell_2$ produces a set of equations in the spectral domain in terms of the components of $\boldsymbol{e}_\tau^{(\nu)}(k_x, k_y)$, $\boldsymbol{h}_\tau^{(\nu)}(k_x, k_y)$, $\boldsymbol{e}_0(k_x, k_y)$, and $\boldsymbol{h}_0(k_x, k_y)$, and of the components of $\boldsymbol{j}_1(k_x, k_y)$ and $\boldsymbol{j}_2(k_x, k_y)$ the Fourier transforms of $\boldsymbol{J}_1(x, y)$ and $\boldsymbol{J}_2(x, y)$ respectively. Solving this set of equations, closed-form expressions for the transformed electromagnetic fields can be derived in a straightforward, error-free way.

3. GREEN'S FUNCTION COMPUTATION

Utilizing the symbolic computational capability of the *Mathematica*®, expressions for the spectral fields are calculated in four simple steps. Then, the spectral Green's functions for the microstrip structure under consideration are derived in a fifth step.

Step 1: from Maxwell's equations the amplitudes of the spectral fields in the x and y directions $-e_{x\tau}^{(\nu)}$, $e_{y\tau}^{(\nu)}$, $h_{x\tau}^{(\nu)}$, $h_{y\tau}^{(\nu)}$, with $\nu = 1$ or 2 and $\tau = 1$, 2, 3 or 4 — can be expressed in terms of the field amplitudes in the z direction, $e_{z\tau}^{(\nu)}$, and $h_{z\tau}^{(\nu)}$, according to [4].

Step 2: following a similar procedure, expressions for e_{x0}, e_{y0}, h_{x0}, and h_{y0} can be obtained in terms of e_{z0} and h_{z0}.

Step 3: application of the appropriate boundary conditions at the interfaces $z = 0$, $z = \ell_1$ and $z = \ell_2$ to the expressions determined in Steps 1 and 2 produce a set of ten equations in the unknown variables $e_{z\tau}^{(\nu)}$, e_{z0} and h_{z0}. After eliminating the two latter variables, Figure 2 shows the final system of eight equations derived through the symbolic computation capability of *Mathematica*®, where $d_1 = \ell_1$, $d_2 = \ell_2 - \ell_1$, and to make the nomenclature simple, the components of the spectral fields were written as $\xi = \xi(k_x, k_y)$. Expressions for $\gamma_\tau^{(\nu)}$, $W_\tau^{(\nu)}$, $U_\tau^{(\nu)}$ and $Y_\tau^{(\nu)}$ are given in [6].

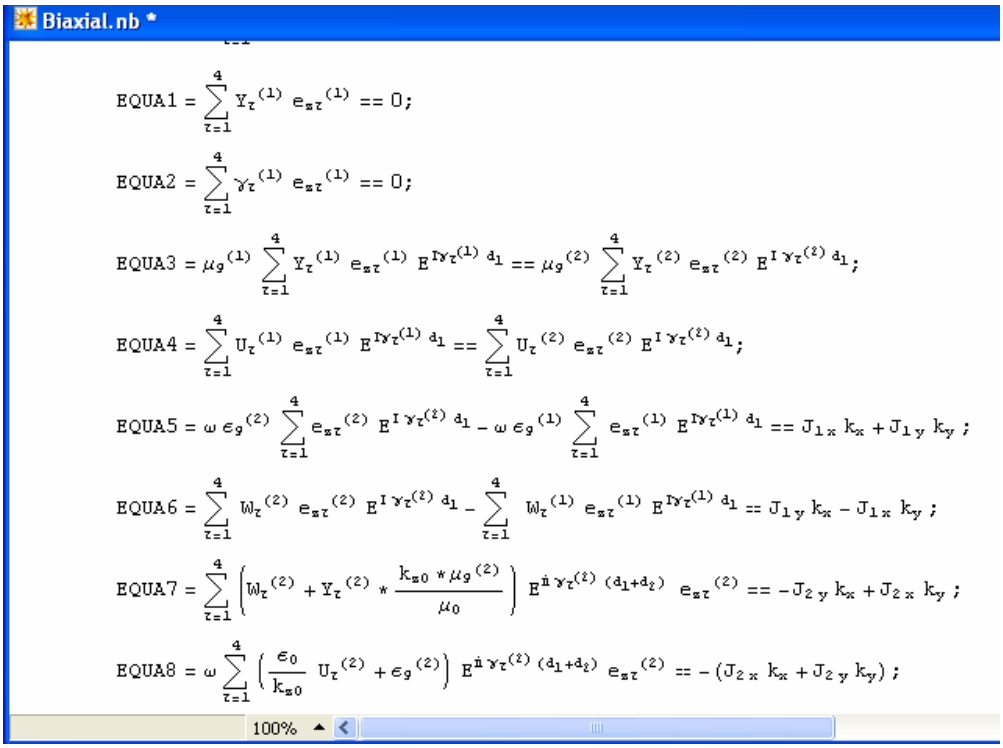

Figure 2: Window of *Mathematica*® showing the final system of equations.

Step 4: the system of equations determined in the previous step can now be solved in terms of $e_{z\tau}^{(\nu)}$, resulting in the following relation

$$e_{z\tau}^{(\nu)} = \frac{\Delta e_{z\tau}^{(\nu)}}{\Delta bi} \tag{7}$$

where the expressions for Δbi and $\Delta e_{z\tau}^{(\nu)}$ are also given in [6].

Step 5: once the expressions for the amplitudes of the spectral fields $e_{p\tau}^{(2)}$, are introduced into Equation (2), the components of the spectral fields can then be written as follows

$$\begin{aligned} E_p^{(2)}(k_x, k_y, z) =& G_{px1}^{(2)}(k_x, k_y, z)\, j_{x1}(k_x, k_y) + G_{px2}^{(2)}(k_x, k_y, z)\, j_{x2}(k_x, k_y) \\ &+ G_{py1}^{(2)}(k_x, k_y, z)\, j_{y1}(k_x, k_y) + G_{py2}^{(2)}(k_x, k_y, z)\, j_{y2}(k_x, k_y) \end{aligned} \tag{8}$$

where $G_{pq\nu}^{(2)}(k_x, k_y, z)$, for $p = x$, y or z and $q = x$ or y are the desired electric Green's functions for the superstrate region [6]. Expressions for the Green's functions for the substrate region and for free space can be similarly generated.

4. GREEN'S FUNCTION ANALYSIS

Once the Green's functions are determined, *Mathematica*® can also be used for their analysis in a straightforward way. As an illustration, the analysis of $G_{xx1}^{(2)}(k_x, k_y, z)$ at the interface $z = d_1$ is presented. The 3-D graphics for the imaginary part of $G_{xx1}^{(2)}(k_x, k_y, d_1)$, denoted as $\mathrm{Im}[G_{xx}]$, is shown in Figure 3, at $f = 2.0\,\mathrm{GHz}$ for a microstrip structure with $d_1 = 3.0\,\mathrm{mm}$, $d_2 = 1.5\,\mathrm{mm}$,

$\varepsilon_{r1}^{(1)} = 2.5$, $\varepsilon_{r5}^{(1)} = 3.0$, $\varepsilon_{r9}^{(1)} = 5.0$, $\varepsilon_{r1}^{(2)} = 2.0$, $\varepsilon_{r5}^{(2)} = 3.0$, and $\varepsilon_{r9}^{(2)} = 6.0$, both layers with loss tangent = 0.0018 and magnetically isotropic (μ_0). Its 2-D graphics on the $k_y = 30\,\text{rad/m}$ plane is presented in Figure 4. As seen from these figures, the function $G_{xx1}^{(2)}(k_x, k_y, z)$ is discontinuous at its poles and divergent when $k_x \to \infty$. Knowledge of the Green's function behavior is key for subsequent applications of the Method of Moments.

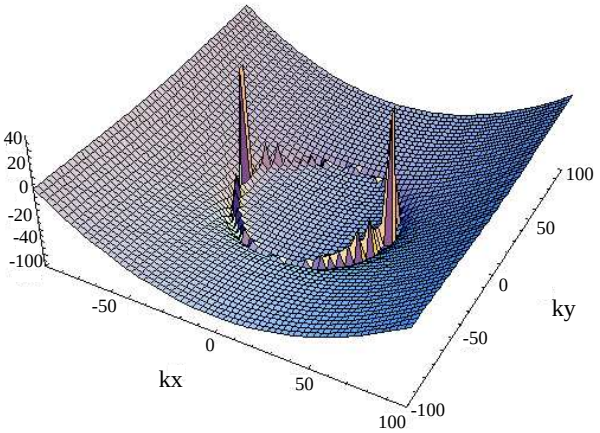

Figure 3: 3-D graphics for Im$[G_{xx}]$.

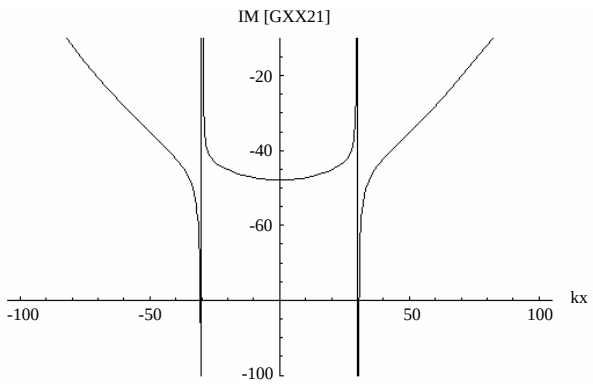

Figure 4: 2-D graphics for Im$[G_{xx}]$ on the $k_y = 30\,\text{rad/m}$ plane.

5. PRINTED DIPOLE ANALYSIS

Using this new procedure, a method-of-moments algorithm is implemented in *FORTRAN* for the analysis of a printed dipole fed by electromagnetic coupling. MoM is the most widely utilized numerical techniques for rigorous analysis of printed geometries on multilayer planar media. It is based upon the transformation of a system of integral equations into a linear matrix equation. In this application of the MoM, triangular sub-domain basis function with edge condition are employed along with Galerkin's procedure for the estimation of the current densities flowing the dipole.

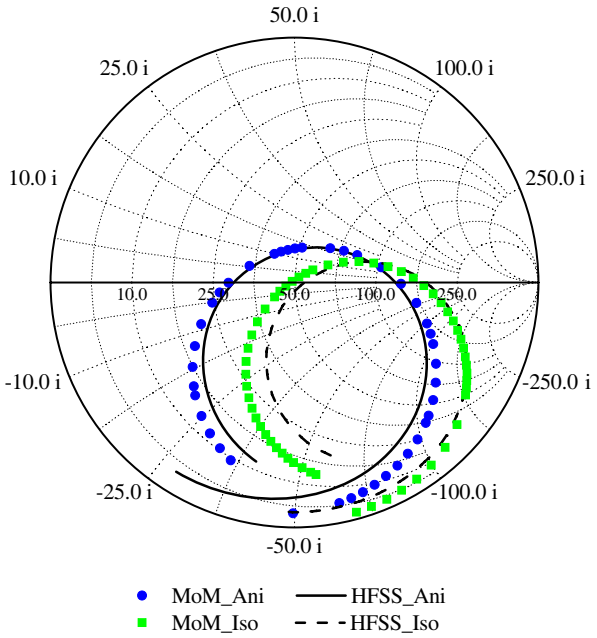

Figure 5: Dipole input impedance.

Results for the input impedance of a printed dipole (with $L_F = 78.0\,\text{mm}$, $c = 12.6\,\text{mm}$, $w = 3.0\,\text{mm}$, $a = 3.0\,\text{mm}$, $b = 39.0\,\text{mm}$, $d_1 = 3.048\,\text{mm}$, and $d_2 = 1.524\,\text{mm}$) are shown in Figure 5

for both *biaxial* and isotropic configurations. For the *biaxial* case, the dipole input impedance was calculated for a substrate with $\varepsilon_{r1}^{(1)} = 2.5$, $\varepsilon_{r5}^{(1)} = 2.6$, and $\varepsilon_{r9}^{(1)} = 2.8$, and for a superstrate with $\varepsilon_{r1}^{(2)} = 2.2$, $\varepsilon_{r5}^{(2)} = 2.0$, and $\varepsilon_{r9}^{(2)} = 2.4$, the loss tangent of both being 0.0022. On the other hand, the isotropic case was computed for $\varepsilon_{r1}^{(1)} = \varepsilon_{r5}^{(1)} = \varepsilon_{r9}^{(1)} = \varepsilon_{r1}^{(2)} = \varepsilon_{r5}^{(2)} = \varepsilon_{r9}^{(2)} = 2.55$.

As seen from this figure, there is good agreement between the results obtained with the implemented algorithm and those simulated with commercial software *HFSS* (in which case, the following dimensions were utilized for the ground plane and dielectric layers: $L_x = 120.0\,\text{mm}$ and $L_y = 42.0\,\text{mm}$) thus validating our procedure. Calculations were performed around 2.73 GHz for the *biaxial* case and close to 2.66 GHz for the isotropic one.

6. CONCLUSIONS

A new procedure is presenting for the calculation of the electromagnetic fields of anisotropic multilayer microstrip structures. Using the symbolic computation capability of *Mathematica*®, expressions for the spectral fields are obtained in a straightforward way. Consequently, the corresponding Green's functions are determined in compact, closed form, with considerable reduction of the calculation time. As an application, a flat dipole fed by electromagnetic coupling, printed on a *biaxial* multilayer structure is analyzed. Results for its input impedance are compared to those simulated with commercial software such as *HFSS*, which makes use of the finite elements technique. Good agreement is observed, thus validating this procedure.

ACKNOWLEDGMENT

This work was partially supported by FAPESP, CAPES and FINEP.

REFERENCES

1. Aksun, M. I. and G. Dural, "Clarification of issues on the closed-form Green's functions in stratified media," *IEEE Trans. Antennas Propagat.*, Vol. 53, No. 11, 3644–3653, 2005.
2. Mesa, F., R. Marqués, and M. Horno, "On the computation of the complete spectral Green's dyadic for layered bianisotropic structures," *IEEE Trans. Microwave Theory Tech.*, Vol. 46, No. 8, 1158–1164, 1998.
3. Lumini, F. and J. C. S. Lacava, "A full-wave analysis method for chirostrip structures," *Eighth International Conference on Antennas and Propagation*, 37–40, Edinburgh, UK, 1993.
4. Lacava, J. C. S., A. V. Proaño De la Torre, and L. Cividanes, "A dynamic model for printed apertures in anisotropic stripline structures," *IEEE Trans. Microwave Theory Tech.*, Vol. 50, No. 1, 22–26, 2002.
5. Balanis, C. A., *Antenna Theory: Analysis and Design*, 3rd ed., John Wiley, New York, 2005.
6. Bianchi, I., "Analysis of anisotropic multilayer microstrip antennas by symbolic computation and the method of moments," (in Portuguese), Ph.D. Thesis, ITA, 2006.

Design Optimization of an Inverted V-dipole

Johanna M. LoTempio[1], **Jose A. Martinez-Lorenzo**[2]
Carey M. Rappaport[2], **and Herbert Aumann**[1]

[1]MIT Lincoln Laboratory, Lexington, MA, USA
[2]The Gordon CenSSIS, Northeastern University, Boston, MA, USA

Abstract— A design optimization technique that addresses the impedance mismatch problem of inverted V-dipoles is proposed. The antenna-modeling tool CST Microwave Studio was used to analyze the impedance and radiation characteristics of a V-dipole. The analysis shows that increasing the distance of the dipole's arms from the ground plane, which is typically a quarter-wavelength, reduces the coupling between them and greatly improves the impedance match. The analysis results show an improved impedance match for a maximum arm height ranging from 0.30λ to 0.40λ. This range is dependent on the desired bandwidth. In addition, analysis results show that an adjustment to the balun feedline length is needed to maintain the impedance match and achieve a large bandwidth. This adjustment can be achieved by making the balun feedlines shorter than the maximum height of the dipole. The analysis results are verified with antenna impedance measurements.

1. INTRODUCTION

Previous research and measurements [1–5] have shown the existence of nulls or "blind spots" in the pattern of balun-fed straight-arm dipole phased arrays. This "blindness" effect has been associated with the coupling between the dipole balun feedlines. It can be eliminated by bending the dipole arms 45° toward the ground plane forming an inverted V-dipole. This variation to a dipole's shape does address the pattern null problem. However, it also changes the dipole's impedance characteristics, providing a poor impedance match over the operating frequency band. Several analytical and computational theories [3, 6–8] have been proposed to model the behavior of an inverted V-dipole. Nonetheless, all of these models fail to predict the observed impedance mismatch.

The purpose of this communication is to provide a simple understanding of the behavior of a V-dipole and to present an optimization technique to improve its response over the frequency band of interest.

2. IMPEDANCE OPTIMIZATION OF V-DIPOLES

The impedance of an inverted V-dipole, as shown in Figure 1, is dependent on parameters like the arm length and thickness, the arm incline angle, α, the distance of the arms from the ground plane, h, and other dipole dimension not explicitly mentioned in this communication. The dipole impedance is also influenced by its balun matching network, which matches the balanced dipole to an unbalanced feedline. The balun consists of a pair of metal tubes of length h that are electrically connected to the dipole arms and to the ground plane. A conductor is inserted in one of the tubes forming a coaxial transmission line that is electrically connected to the second tube.

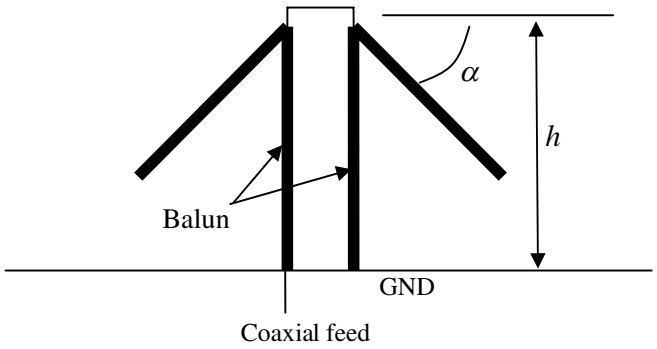

Figure 1: V-dipole geometry.

Research [1] has shown that an increase in the arm incline angle changes the dipole radiation pattern and impedance characteristics. An increase in arm incline heightens the mutual coupling

between the dipole arms, the coupling between the arms and the balun feedline, and the coupling between the arms and the ground plane. These interactions make the nominal dipole arm height of $h = 0.25\lambda$ not the optimal value for the design of a V-dipole, providing a poor impedance match in the frequency band of interest. The response of the V-dipole can be significantly improved by increasing the arm height. However, increasing h reduces the coupling between the arms and the ground plane, shifting the operating frequency and increasing the dipole's bandwidth.

A V-dipole antenna was modeled for arm heights varying from $0.25\lambda \leq h \leq 0.40\lambda$. The antenna-modeling tool Microwave Studio [9] was used to analyze the V-dipole. The dipole was designed to operate at a center frequency of 650 MHz with a bandwidth of approximately 300 MHz ($S_{11} \leq -10$ dB). The simulation results, plotted in Figure 2, show that for $h = 0.25\lambda$ the dipole does not meet its bandwidth specification. As h was increased, the response improved over the frequency band of interest.

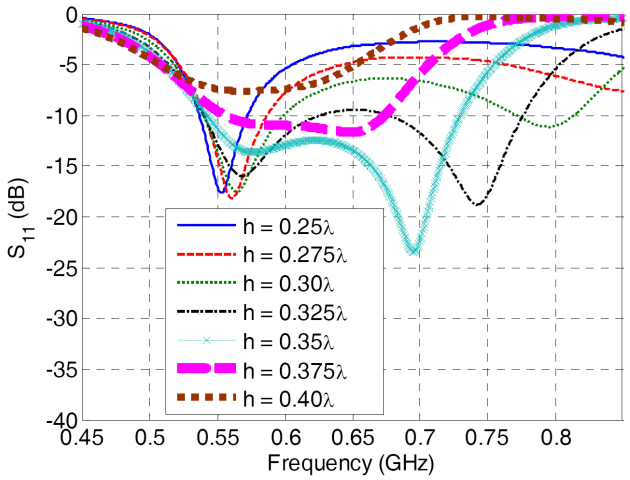

Figure 2: CST simulation results: V-dipole return loss vs. frequency and arm maximum height.

The results plotted in Figure 2 show a practical range for the arm height $0.30\lambda \leq h \leq 0.35\lambda$. For arm heights $h > 0.35\lambda$ the dipole response starts to deteriorate. This is due to the balun's length, which is the same as the dipole height, h, becoming now too long. For these values, a readjustment of the balun's length is required. This is achieved by inserting a shorting stub a distance h'' from the maximum height of the arms, as shown in Figure 3.

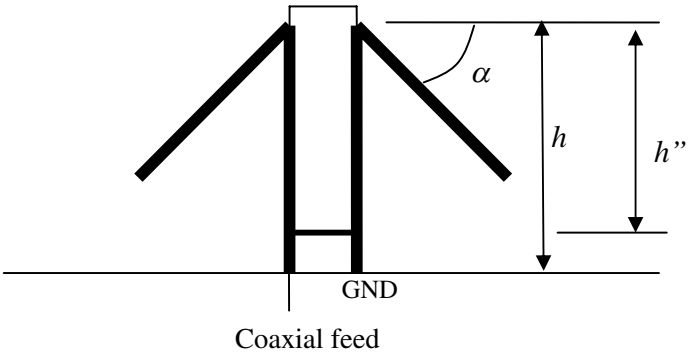

Figure 3: Modified V-dipole.

Once more, the V-dipole was modeled using CST Microwave Studio. This time the shorting stub was added to the model. The value of h was set to 0.37λ. The stub position h'' was varied from 0.305λ to 0.331λ. Figure 4 plots the simulation results. A significant improvement in the response is observed for all values of $h'' < h$. For this V-dipole geometry, the arm height and stub position that provide the largest bandwidth are $h = 0.375\lambda$ and $h'' = 0.317\lambda$.

In addition to the impedance, the dipole's pattern is also affected by h. As h increases, the maximum gain decreases and the number and magnitude of sidelobes increases. These effects on

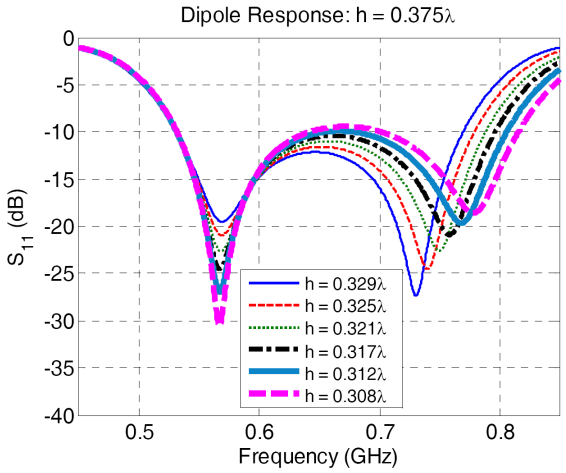

Figure 4: CST simulation results: V-dipole return loss vs. frequency and stub position.

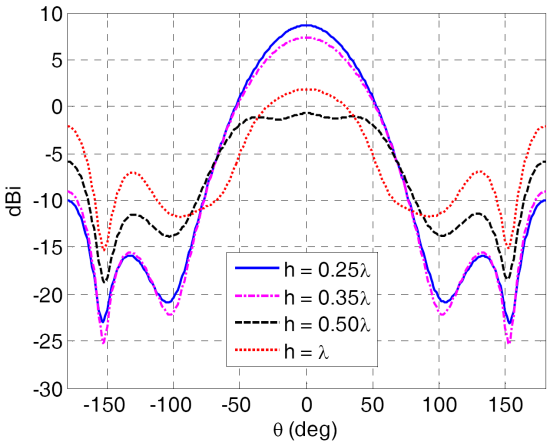

Figure 5: V-dipole gain as a function of arm distance from the ground plane.

the radiation pattern set a limit to how high the dipole arms can be. Figure 5 plots a wire dipole's gain pattern for various heights h and assuming a $1.5\lambda \times 1.5\lambda$ ground plane.

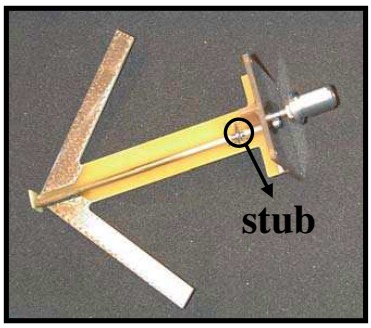

Figure 6: Fabricated V-dipole.

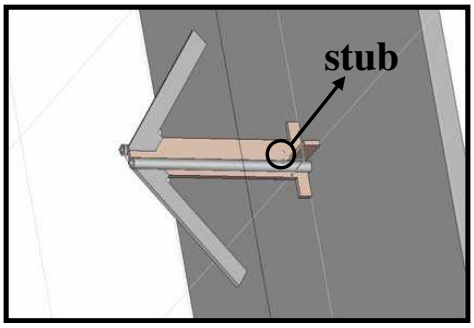

Figure 7: CST model.

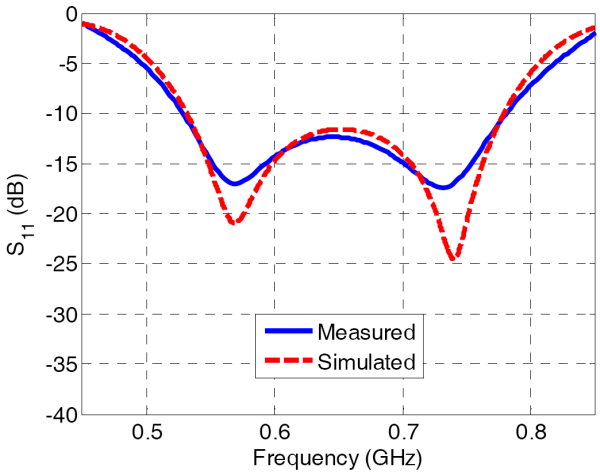

Figure 8: V-dipole return loss.

3. SIMULATION AND MEASUREMENT COMPARISON

A V-dipole antenna as described in the previous section was fabricated from FR-4 printed circuit material, copper and semirigid coaxial cable. The antenna had a maximum arm height of $h =$

0.375λ. The shorting stub was placed at approximately $h'' = 0.32\lambda$. Figure 6 shows a photo of the fabricated antenna. The fabricated dipole's performance was then measured. The antenna measurements, frequency response and radiation pattern, were then compared to the CST model ($h = 0.375\lambda$, $h'' = 0.325\lambda$). Figure 7 shows the CST model.

Figure 8 plots the measured and simulated frequency responses. The center frequency is 650 MHz and the bandwidth is approximately 275 MHz. The bandwidth is 25 MHz short of the required bandwidth but it still acceptable for the application. Figure 9 plots the radiation pattern of a dipole in an anechoic chamber and the simulated radiation pattern. The plots show good agreement between the CST model and the fabricated antenna performance.

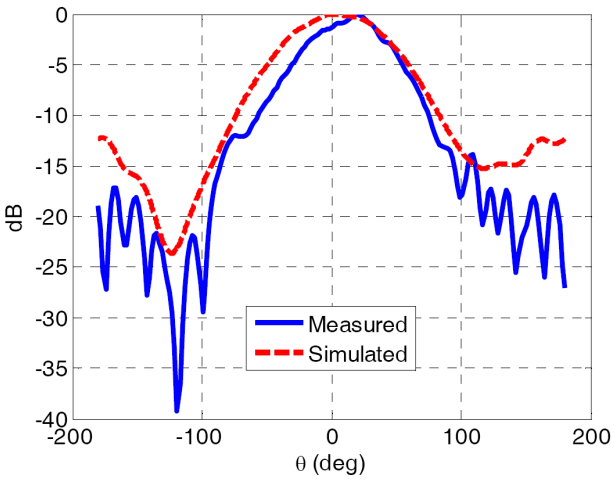

Figure 9: V-dipole radiation pattern.

4. CONCLUSIONS

A design optimization method for improving the impedance match of an inverted V-dipole has been presented. This optimization technique consists of increasing the distance between the arms and the ground plane and readjusting the balun length as needed. A practical range for the maximum dipole height, h, was found to be 0.30λ to 0.40λ. For $h > 0.35\lambda$, an adjustment to the balun feedline length is needed. An antenna was designed and fabricated using this optimization method. The antenna measurements and the CST model were in good agreement.

ACKNOWLEDGMENT

This work was sponsored by the United States Air Force under Air Force Contract ESC-XPQ. Opinions, interpretations, conclusions, and recommendations are those of the authors and are not necessarily endorsed by the United States Government.

REFERENCES

1. LoTempio, J. M., "Impedance and radiation characterization if inverted V-dipoles antennas and arrays," Masters Thesis, Northeastern University, 2007.
2. Mailloux, R. J., "Phased array theory and technology," *Proc. IEEE*, Vol. 70, No. 3, 246–291, 1982.
3. Schuman, H. K., D. R. Pflug, and L. D. Thompson, "Infinite planar arrays of arbitrarily bent thin wire radiators," *IEEE Trans. on Antennas. and Propagat.*, Vol. 32, No. 4, 1984.
4. Knittel, G. H., A. Hessel, and A. A. Oliner, "Element pattern nulls in phased arrays and their relation to guides waves," *Proc. IEEE*, Vol. 56, No. 11, 1968.
5. Mayer, E. and A. Hassel, "Feed region modes in dipole phased arrays," *IEEE Trans. on Antennas and Propagat.*, Vol. 30, No. 1, 1982.
6. Fenn, A. J., "Element gain pattern prediction for finite arrays of V-dipole antennas over ground plane," *IEEE Trans. Antennas and Propagat.*, Vol. 36, No. 11, 1629–1633, 1988.
7. Jones, J. E., "Analysis of center-fed V-dipole antenna," *IEEE Trans. Antennas and Propagat.*, Vol. 24, 316–322, 1976.

8. Nakamura, T. and T. Honjo, "Single-fed crossed V-dipoles with four masts for circular polarization," *Electronics and Communications in Japan*, Vol. 85, No. 11, 44–51, 2002.
9. *CST Microwave Studio Version 2006b Getting Started*, CST Computer Simulation Technology, 2006.

Design of Beam Steering Antenna Array for RFID Reader Using Fully Controlled RF Switches

D. Zhou, **R. A. Abd-Alhameed**, **P. S. Excell**, **C. H. See**
M. M. Abusitta, **Y. F. Hu**, **S. M. R. Jones**, **and N. J. McEwan**
Mobile and Satellite Communications Research Centre
University of Bradford, Bradford, West Yorkshire, BD7 1DP, UK

Abstract— An approach of using beam steering antenna array for RFID reader is applied as an effective strategy to improve performance of an RFID system under the constraint that the tag, reader and protocol design cannot be modified. The antenna beam steering was achieved by implementing RF switches with ON or OFF mode functions to excite the radiating elements of the antenna array. The switching control process is implemented using genetic algorithm method subject to scalar and binary genes. Anti-phase feeding of radiating elements is also considered and investigated. Ring antenna array with reflectors is modeled and analyzed. In addition, a novel RF switch circuit, used to control the RF signal fed to the dipole antenna and placed directly before the dipole, was presented and implemented.

1. INTRODUCTION

In recent years Radio Frequency Identification (RFID) has become very popular in many commercial applications such as access control, animal tracking, security, and toll collection, because of its ability to track moving objects and its low-cost implementation [1–4]. A typical RFID system is always made up of two components, including the tags (transponders) and readers (interrogators). The antennas, as a key part of the system, enable the tag or reader to send and receive the signals. A tag comprises an antenna and an application-specific integrated circuit (ASIC, or microchip) that is given a unique electronic product code [1]. Readers are devices that read tags, and they equipped with antennas, a transceiver, and a processor (server with software system).

There are two types of tags: active and passive. An active tag contains a small power source (e.g., a battery), whereas a passive tag does not contain any power source and uses the power generated by a reader. Most tags are passive due to the cost efficiency of mass production. In a passive RFID system, the reader sends a signal using the reader antenna to excite the tag antenna. Once the tag is powered on, then it will send the stored data back to the reader. The data are then passed to a server for processing.

Operating frequency determines the capability of an RFID system, and several frequency bands have been assigned to RFID applications examples include: low frequency at 125 Hz, high frequency at 13.56 MHz, UHF frequency at 868–915 MHz, and microwave at 2.45 and 5.8 GHz [5]. The design of RFID antenna becomes more complicated and critical when the operating frequency rises into the microwave region. A tag antenna should be considered low profile and compact size, for reducing the cost and for convenience in use. However, reader antenna should be characterized as compact, directional with high gain, circular polarization, easily to be integrated and low cost. Recently, many kinds of RFID antenna have been proposed for the tags and the readers [6–14].

With the recent developments of the modern supply chain management (SCM), RFID systems have been paid more and more attention, and have a huge potential market. In this paper, problems encountered in practice associated with RFID reading systems in multi-portal implementation were identified. As a consequence, a solution on reader antenna design with enhanced performance was then developed by using beam steering antenna array approach.

2. RFID READER ANTENNA PROBLEMS

Tag antennas placed in close proximity to one another or close to the highly variable content of the crates will suffer from coupling effects that modify their gain, radiation pattern and polarization properties, thus reducing their performance. The mounting and location of the reader antennas will affect how effectively they illuminate their target. Backscatter and sidelobe patterns may influence mutual interference between readers.

In the RFID reading systems in multi-portal implementation, the reading systems are configured as portals, each of which supports a reader, several antennas and sensing devices. There are three

problems associated with the deployment of RFID technology in SCM applications have been identified:

- Passive RFID tags are mounted on plastic crates, which are stacked on a pallet. Although two RFID labels are tagged to each crate, the RFID reader is sometimes unable to read the tags. This may be because, for example, both RFID labels are blocked by adjacent crates.
- The RFID reader has to capture information from some more than one hundred RFID labels within a short time period. Techniques may be required to prolong the reading duration to ensure that tags are being read.
- A most common problem for multi-portal implementation is the 'dense reader' problem whereby the performance of the RFID system will be limited by the interference between RFID readers. Although RFID readers use different channels to minimise collision, the limitation in radio resource implies that in-channel collision will also happen.

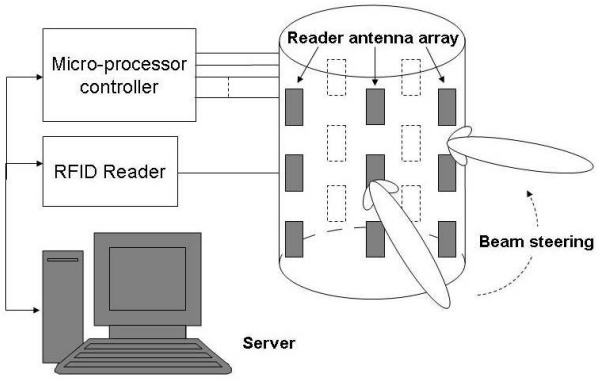

Figure 1: Reader system with beam steering antenna array applied as the reader antenna.

A constraint in identifying possible solutions is that RFID tags are proprietary and no modifications should be made; intelligence of the reader is also proprietary. This leaves the options of modifying antenna locations and design, possibly introducing automated control of the radiation pattern and direction and changing the way in which the antenna diversity is operated. Careful antenna design to improve target illumination whilst reducing interference, the use of sophisticated array antennas with adaptively controlled patterns and optimum use of antenna diversity options permitted by the reader architecture will all need to be considered.

3. A NOVEL READER ANTENNA DESIGN

3.1. Design Principle of Proposed Beam Steering Antenna Array

The use of adaptive array antennas [15–18] for cellular base station application has recently become an active area of research and development. According to the capability to transmit and receive or steer the beam, adaptive antennas can be placed into three categories [19], Switched Beam array, Phased array, and Adaptive array.

In author's previous work [20], a set of simple design procedures for beam steering single circular and concentric circular ring antenna arrays were presented. The proposed designs were used to achieve 360° coverage area for increasing the capacity of wireless communication networks without increasing the number of sites. This was realised by exciting only a certain number of elements of the array antenna. This was done by implementing an ON/OFF system concept to excite only specific elements of the array antenna and thus achieve beam steering. In this study, a similar design principle for beam steering was applied in designing antenna array for RFID reader applications but with applying genetic algorithms that will update the direction and width of the steering beams subject to multi-constraints. The proposed RFID reader antenna system is illustrated in Fig. 1. As can be seen, a cylindrical antenna array for the reader antenna was proposed; a micro-processor controller, used to control the excitation of the antenna elements so as to steer the antenna beam, was subsequently employed. Moreover, a novel RF switch of the RF power fed to the antenna element was described and discussed theoretically and practically, which will be presented in the following section.

3.2. Antenna Model and Design Specification Using Genetic Algorithms

Ring antenna array with its specified reflectors elements was considered for our Reader model as shown in Fig. 2. For this model, the beam steered and controlled over azimuth angle only. The beam control over elevation was neglected, however, can also be considered in a similar way. The direction and width of single and multi beams constraints are achieved by using appropriate genetic algorithms. Initially the GA was run to adjust several parameters such as the radius of the radiating ring array, reflectors elements and also the height of the reflector element. Then a binary gene variable is introduced in which its maximum value is equivalent to the number of the radiating elements ring array. A half wavelength radiating element on outer ring was considered for all possible outcomes of the method applied. The fitness function of the design problem can be illustrated by the following:

$$F = W_1 \times G_1 + W_2 \times G_2$$

where

$$G_1 = \frac{1}{K_v} \sum_{i=1}^{Ni} \sum_{k=1}^{N_b} \frac{w_i}{VSWR_k(f_i)}$$

$$K_v = \frac{1}{\sum_{1}^{N_i} w_i}, \quad G_2 = \frac{1}{1+\sqrt{e_2}}$$

$$e_2 = \frac{1}{M} \sum_{k=1}^{M} \left| \frac{R_{\theta k} - P_{\theta g}}{R_{\theta k}} \right|^2$$

$$R_{\theta k} = E_{\theta ref}(\phi_k, \theta_k), \quad P_{\theta k} = E_{\theta}(\phi_k, \theta_k)$$

$$VSWR_k(f_i) = \frac{1 + |\Gamma_k(f_i)|}{1 - |\Gamma_k(f_i)|}$$

$$\Gamma_k(f_i) = \frac{Z_k(f_i) - Z_o}{Z_k(f_i) + Z_o}$$

W_1 and W_2 are the weighting coefficients for the cost function. N_i, N_b and M are numbers of operating frequencies, number of the excited radiating elements and number of the far field desired points. $\Gamma_k(f_i)$, $\mathrm{VSWR}_k(f_i)$ and $Z_k(f_i)$ are the reflection coefficient, voltage standing wave ratio and input impedance at the kth input port of the excited radiating element k respectively. Z_o is the reference matched load.

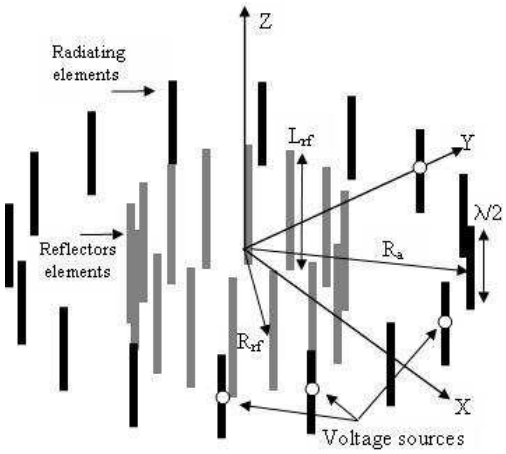

Figure 2: Antenna model used for GA method.

Table 1 presents the optimum values that specify the most required antenna geometry. Three antenna arrays were considered for which the number of radiating elements at the outer ring are 8, 16 and 32 elements. The antenna parameters were found subject to all possible binary sequences

set by the GA method. The length of the binary genes used is equivalent to the number of the radiating elements. Fig. 3 shows the radiation pattern when beam steering angle was set at 0° azimuth for 10 dB power gain to all three ring arrays. For this example the total number of the radiating elements switched on for all arrays was found between two to five elements. In spite the power beam width for 8, 16 and 32 elements were not considered in the cost function, however it was found to be 64°, 56° and 38° respectively. Fig. 4 shows the movements of the steered beam for −10°, 0°, and 10° azimuth angles using 32 ring array, for which the minimum excited number of the radiating elements considered was three. It is clear to be noted that the beams provide a minimum 10 dB power gain for most steered angle over azimuth angle ±10°.

Table 1: Properties of the applied Genetic Algorithms and its optimum parameters values (N is the number of the radiating elements at the outer ring).

GA parameters		Parameters cm	Min. $N = 8$, 16 and 32	Max. $N = 8$, 16 and 32	Optimum $N = 8$, 16 and 32
Population size	4	R_a	(10), (18), (40)	(12), (23), (42)	(10.4), (21.2), (41.8)
Number of parameters	4	R_{rf}	(3.8), (8), (28)	(4.2), (12), (32)	(4.0), (10.4), (31.1)
Probability of mutation	0.02	L_{rf}	(8), (8), (8)	(12), (12), (12)	(9.2), (9.4), (10.5)
Maximum generation	100				
Number of possibilities	2^8–2^{32}				

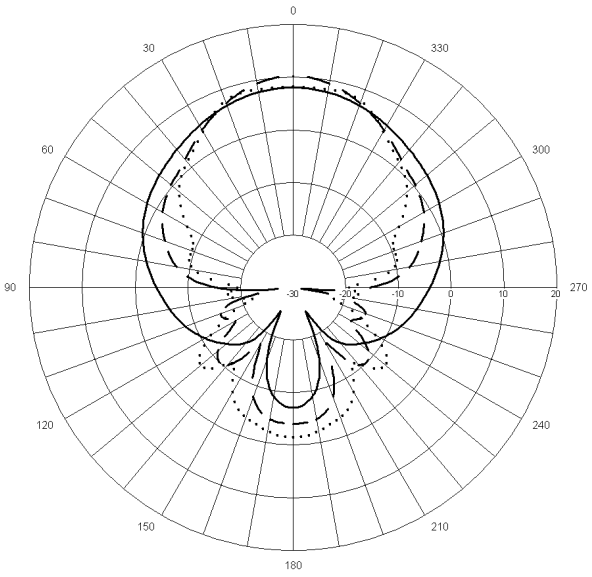

Figure 3: The radiation patterns of 8, 16 and 32 ring arrays obtained at the maximum generation of GA method at steered angle 0° azimuth ('—': 8 elements, '. . . . . ': 16 elements, '- - - -': 32 elements).

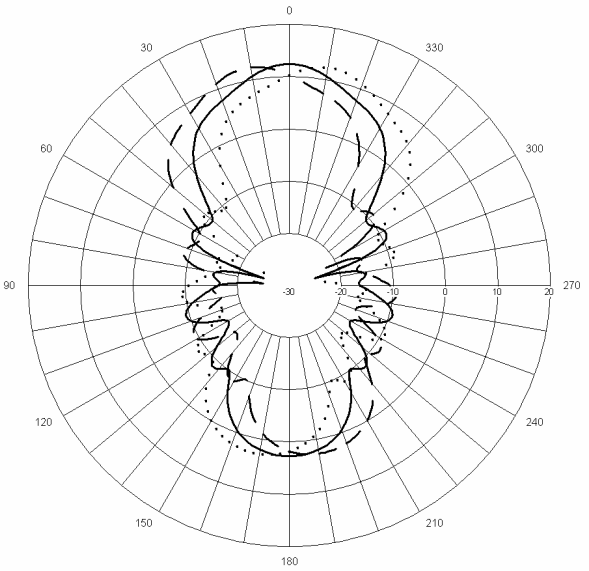

Figure 4: The radiation patterns of 32 ring arrays obtained at the maximum generation of GA method at azimuth steered angles 10°: '- - - -', 0°: '—' and −10°: '. . . . . '.

Figure 5 introduces another binary gene of equivalent length of the switched control gene used in Figs. 3 and 4, which controls anti phase excitations sources of the radiating elements that are switched on. This is included to control the width of the HPBW required in the desired beam steered direction in which the far field nulls can be considered. This is valid when the number of the degree of freedoms allows this for a minimum excitation number. The results clearly show the 32 ring array performed better on reducing the HPBW and preserve the 10 dB power gain. Basically this technique introduces side lobe levels next to the main beam for all ring antenna arrays that was found around 10 to 15 dBs.

3.3. Printed Dipole and RF Switch for Beam Steering Antenna Array for RFID Reader

In this section, a printed dipole antenna integrated with a duplex RF switch to support the function of the RFID reader ring array antenna is presented. A coplanar waveguide (CPW) to coplanar

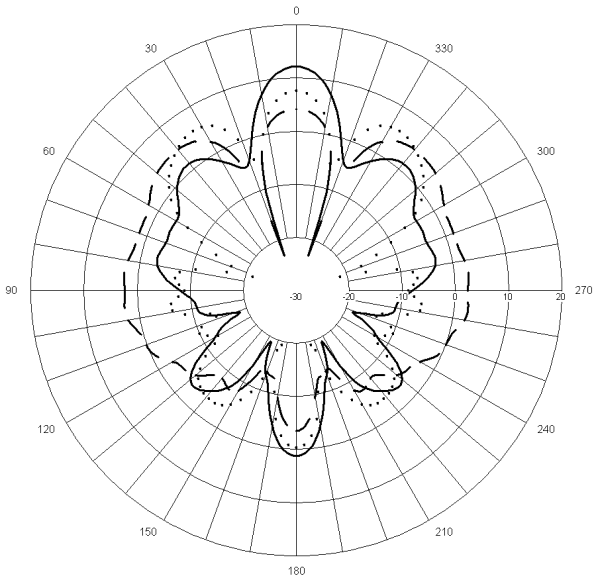

Figure 5: The radiation patterns of 8, 16 and 32 ring arrays obtained at the maximum generation of GA method at steered angle 0° azimuth with reduced HPBW ('- - - -': 8 elements, '. . . . . ': 16 elements, '—': 32 elements).

strip (CPS) transition was adopted from [21, 22] to feed the printed dipole, and examined using ADS package [23]. The measured data for the CPW-to-CPS balun and the associated practical performance of the RF switch were well addressed in [24].

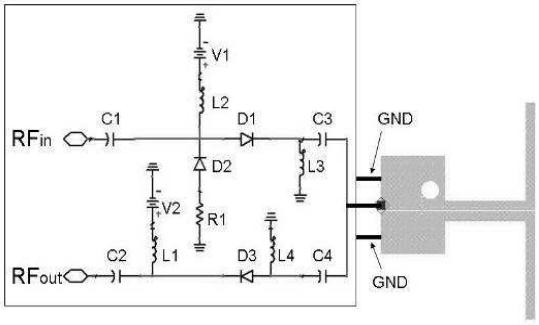

Figure 6: Overall circuit diagram of the RF switch integrated with balun and dipole.

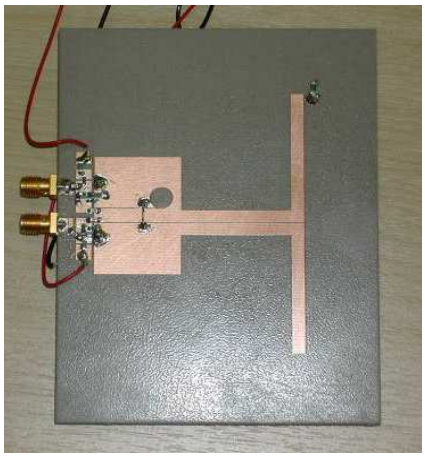

Figure 7: Photograph of the fabricated prototypes of the RF switch integrated with balun and dipole.

The proposed switch used for duplex operation is illustrated in Fig. 6. As can be seen, capacitors C1, C2, C3 and C4 are for dc blocking, and three diodes in the circuit with appropriate biasing voltage was used to provide a function as RF switch. When both V1 and V2 are supplied with positive voltage, RF signal passes through forward biased diode D1 and transmit power to the antenna. There is no signal returned to the path through diode D3 since it is reverse biased. Therefore, the switch is ON and in RF transmission mode. On the contrary, when the power supply is given negative voltage both V1 and V2, diode D1 is in reverse biasing which can be effectively used for blocking the RF signal transmits to the antenna and the reflected RF signal can be eliminated through the diode D2 due to the fact that RF signal is shorted via a 50 ohm resistor (R1) to the ground. In this way, the switch is apparently OFF and in the RF reception mode since only RF signal path through diode D3 is turned on. Thus, a dual mode operation is realized. Prototypes of the RF switch integrated with balun and dipole is shown in Fig. 7.

From the forgoing practical investigation of the proposed RF switch that exhibits a relatively

good performance at 'ON' and 'OFF' mode to control beam in the design of beam steering antenna array for RFID reader antenna applications. Therefore, a follow-up study on practical realisation to the RFID reader antenna with enhanced performance using build in GA process of the beam steering principle in cooperation with the novel RF switch proposed will be carried out in the future work.

4. CONCLUSIONS

A simple process of beam steering ring arrays using genetic algorithms for RFID reader application has been presented and discussed. The GA process using an 'On' and 'OFF' switchable modes for each radiating element through generating a binary gene for maximum fitness. Anti – phase switchable mode was also considered using another binary gene whose length is equivalent to the number of the radiating elements. A good control margin of the HPBW can be achieved using this gene. The design of the CPW-fed CPS balanced dipole antenna integrated with a RF switching circuit for antenna beam steering application used for RFID reader, was presented. The integration of the RF switch with the GA process for various array antenna configurations to RFID applications as a real time system will be considered in the future work.

REFERENCES

1. Finkenzeller, K., *RFID Handbook*, 2nd ed., John Wiley & Sons, Ltd., Chichester, 2004.
2. Bhatt, H. and B. Glover, *RFID Essentials*, O'Reilly, January 2006.
3. Sweeney, P. J., *RFID for Dummies*, Wiley, 2005.
4. Want, R., "An introduction to RFID technology," *Pervasive Computing*, Vol. 5, 25–33, 2006.
5. Chen, Z. N., *Antenna for Portable Devices*, Chapter 3, Wiley, 2007.
6. Rao, K. V. S., P. V. Nikitin, and S. F. Lam, "Antenna design for UHF RFID tags: A review and a practical application," *IEEE Transactions on Antennas and Propagation*, Vol. 53, 3870–3876, 2005.
7. Subramanian, V., J. M. J. Frechet, P. C. Chang, D. C. Huang, J. B. Lee, S. E. Molesa, A. R. Murphy, D. R. Redinger, and S. K. Volkman, "Progress toward development of all-printed RFID tags — Materials, processes, and devices 2," *Proceedings of the IEEE*, Vol. 93, 1330–1338, 2005.
8. Qing, X. M. and N. Yang, "A folded dipole antenna for RFID," *Proceedings of the IEEE Antennas and Propagation Society International Symposium*, Vol. 1, 97–100, June 2004.
9. Ukkonen, L., M. Schaffrath, J. Kataja, L. Sydänheimo, and M. Kivikoski, "Evolutionary RFID tag antenna design for paper industry applications," *Int. J. Radio Frequency Identification Technology and Applications*, Vol. 1, No. 1, 107–122, 2006.
10. Marrocco, G., "RFID antennas for the UHF remote monitoring of human subjects," *IEEE Transactions on Antennas and Propagation*, Vol. 53, 1862–1870, 2007.
11. Ma, D. and W. X. Zhang, "Broadband CPW-fed RFID antenna at 5.8 GHz," *Electronics Letters*, Vol. 42, No. 22, October 2006.
12. Choo, J., H. Choo, I. Park, and Y. Oh, "Design of multi-layered polygonal helix antennas for RFID readers in UHF band," *IEEE AP-S symposium*, 283–286, 2005.
13. Qing, X. and N. Yang, "2.45 GHz circularly polarized RFID reader antenna," *The Ninth International Conference on Communications Systems*, 612–615, Sept. 6–8, 2004.
14. Leong, K. S., M. L. Ng, and P. H. Cole, "Positioning analysis of multiple antennas in a dense RFID reader environment," *Proceedings of the International Symposium on Applications and the Internet Workshops (SAINTW'06)*, 4, 2006.
15. Irie, Y., S. Hara, Y. Nakaya, T. Toda, and Y. Oishi, "A beamforming method for a reactively steered adaptive array antenna with RF-MEMS device," *IEEE Topical Conference on Wireless Communication Technology*, 396–397, Oct. 2003.
16. Imamura, K. and H. Morishita, "Analysis of the mobile terminal adaptive array antenna in consideration of a case and elements," *IEEE Antennas and Propagation Society Symposium*, Vol. 3, 3195–3198, June 2004.
17. Chiba, I., R. Yonezawa, and K. Kihira, "Adaptive array antenna for mobile communication," *IEEE International Conference on Phased Array Systems and Technology*, 109–112, May 2000.
18. Nakaya, Y., T. Toda, S. Hara, and Y. Oishi, "MIMO receiver using an RF-adaptive array antenna with a novel control method," *IEEE International Conference on Communication*, Vol. 5, 2568–2572, June 2004.

19. Holter, B., "Adaptive antennas — An introduction," *SINTEF Telecom and Informatics*, 7465 Trondheim, Norway, 1999.
20. Abd-Alhameed, R. A., N. T. Ali, P. S. Excell, M. K. Atiya, and C. H. See, "Beam steering antenna array for mobile base stations," *3rd IEEE International Conference on Systems, Signals & Devices SSD'05*, Paper Ref. SSD05-CSP-118, Sousse, Tunisia, March 2005.
21. Tilley, K., X.-D. Wu, and K. Chang, "Coplanar waveguide fed coplanar strip dipole antenna," *Electronics Letters*, Vol. 30, No. 3, 176–177, 1994.
22. Kolsrud, A. T., M.-Y. Li. and K. Chang, "Dual-frequency electronically tunable CPW-fed CPS dipole antenna," *Electronics Letters*, Vol. 34, No. 7, 609–610, 1998.
23. Advanced Design System, Agilent Technologies, version 2005A.
24. Abusitta, M. M., D. Zhou, R. A. Abd-Alhamed, and P. S. Excell, "Simulation and measurement of controlled RF switch for beam steering antenna array," *National URSI Symposium*, paper No. 5, Portsmouth, UK, 2007.

The Design and Optimization of Planar LPDAs

A. A. Gheethan and D. E. Anagnostou
ECE Department, South Dakota School of Mines & Technology, Rapid City, SD 57701, USA

Abstract— A significant space reduction of a Planar Log-Periodic Dipole Array (LPDA) is achieved in this work. This reduction was performed by utilizing the first order iteration meander shape dipole in the design of a planar LPDA. The minimization procedure is illustrated in this work by presenting two designs for a Euclidean LPDA with linear dipoles and a meander LPDA operating over the entire S frequency band. Both designs are compared through the main common characteristics of an antenna: return loss response, radiation pattern and the maximum gain. The agreement between the results of both designs was very good and the properties of the meander LPDA were identical to those of the Euclidean LPDA.

1. INTRODUCTION

As the numerous demands and applications that require the use of large sections of the EM spectrum appeared in the 1950's, antenna designers attempted to create antennas that do not depend on the operating frequency of the application needed to be used with. This type of antennas was later named "frequency independent antennas" [1]. A type of antenna which closely parallels the frequency independent concept is the wire log-periodic structure, found by DuHamel and Isbell [2] and studied by Carrel [3]. In the design of wire LPDAs, half wavelength dipoles of different dimensions are connected and fed by a transmission line through a boom. The lengths of the largest and the smallest elements in a wire LPDA are controlled by the operating frequency limits, while the remaining elements lengths are related to each other by the geometry constant (τ) and the spacing factor (σ), which define the log-periodic performance. However, as the operating frequency exceeds the UHF range, wire dipoles and conventional feeding transmission lines become inadequate for LPDA design. In addition, wire dipoles can be bent, damaged or truncated which affects LPDA's performance by producing side lobes and reducing the F/B ratio [4]. For these reasons, planar LPDAs were studied [5–7].

For applications where space and size are constrained; size reduction of a planar LPDA is preferable. Different attempts were performed to reduce the size of planar LPDA by using Koch dipoles and quasi-fractal geometries [8, 9]. In this work, the size of a planar LPDA was reduced by the design of a planar LPDA with a first order iteration meander line as a basic element of the array. Two identical designs of planar meander and Euclidean LPDA are illustrated and compared in this paper LPDA. The selection of the first order meander dipole shape is justified. The measured results for both designs show that the miniaturized meander LPDA characteristics are very similar to the characteristics of the Euclidean LPDA.

2. LPDA DESIGN DESCRIPTION

A schematic and photo for both designs is shown in Figures 1(a)–(c). The planar LPDAs consist of N flat dipoles fabricated on a substrate of thickness t. The dipoles are placed on the top layer of the substrate and on the bottom layer, alternatively. A single coaxial cable was used to feed the antenna. The cable's outer metallic cylinder, which represents the ground, is filled with Teflon® while the center conductor is embedded through the Teflon®. To ensure a balanced feeding, the cylinder of the coaxial was soldered to the bottom layer of the LPDA while the center conductor (RF) was connected to the top layer at the smallest element of the LPDA using a small via through the substrate. In this way, the need of using a balun is fulfilled, and thus, the antenna design is simplified. The two designs were fabricated on RO4003C Roger substrate with a thickness of 32 mil and dielectric constant $\varepsilon_r = 3.38$.

For both designs, the geometry constant (τ) was adjusted to be 0.9 and the spacing factor (σ) was equal to 0.16. The resultant apex angle (α) was 8.88° and 12 elements were needed to cover the entire S band according to the design equations for LPDA. The relation between the design

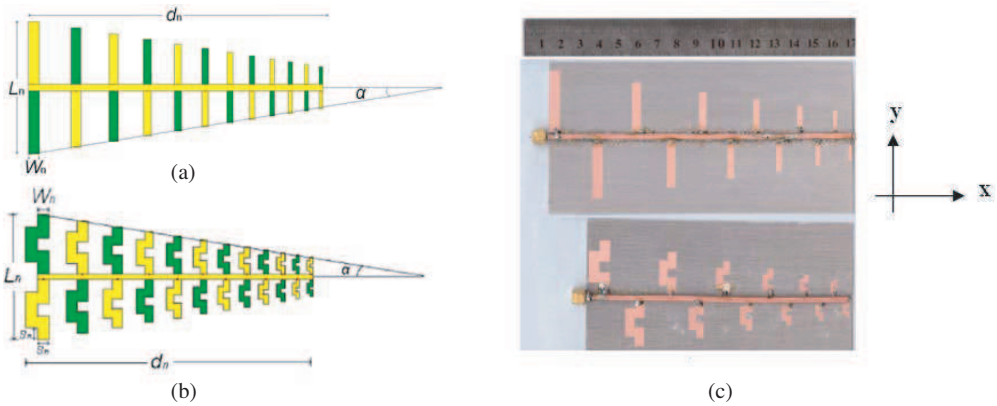

Figure 1: (a) Schematic of the Euclidean log-periodic antenna design, (b) schematic of the meander log-periodic antenna design, and (c) photo of the fabricated prototypes.

parameters are given by:

$$\tau = \frac{W_n}{W_{n-1}} = \frac{L_n}{L_{n-1}} = \frac{d_n}{d_{n-1}} \tag{1}$$

$$\alpha = \tan^{-1}\left[\frac{1-\tau}{4\sigma}\right], \tag{2}$$

where the subscript (n) represents the nth element starting from the largest dipole.

The design of the largest element in both radiators was the first step for the design of the array. The largest element was designed so it resonates at $f = 2\,\text{GHz}$. It was shown in [10] that the meander line resonates at the same resonance frequency of the Euclidean line when the total length of the meander line is larger than the total length of the Euclidean line. However, the vertical length of the meander line (L_n) should be less than the vertical length of the Euclidean line, which is the key of reducing the size of a planar LPDA.

The largest element of the Euclidean LPDA, including the width of the boom, is 70.8 mm length, while the total length for the same element in the meander LPDA is 62 mm. The width for both elements is 5.844 mm, which was obtained to achieve an equal width among the total length of the meander line. The dimensions for the other elements then found depending on Equation (1).

The total trapezoidal occupied area was $7528.7\,\text{mm}^2$ and $5714.72\,\text{mm}^2$ for the Euclidean and the meander LPDA respectively. This results show 24% space reduction, which is a considered a significant size reduction compared to previous works in minimization of planar LPDAs.

It should be noticed that using more iterations for the meander line design would result to a more miniaturized LPDA; meanwhile, the addition of iterations to the meander line will reduce its radiation resistance and its bandwidth [10]. This degrading in the basic element performance of the meander dipoles as the iteration order increases will be reflected on the total array.

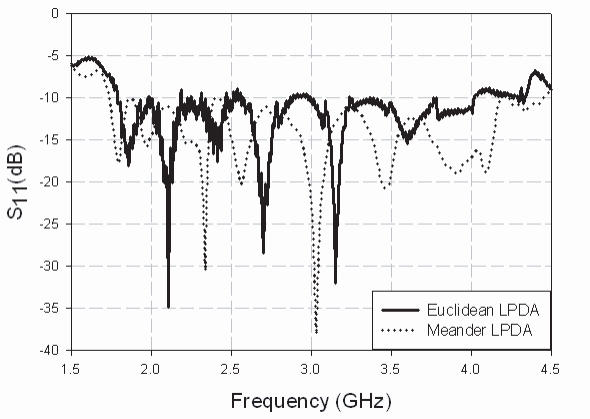

Figure 2: Measured return loss response for meander and Euclidean LPDAs.

3. DESIGN RESULTS

The full wave commercial software Zeland IE3D® based on MoM algorithm was used to simulate the designs. The simulation results were compared with the measurements, which have been carried out using an 8510C Agilent VNA, at the custom-built antenna chamber at SDSM&T. The measured return loss response is shown in Figure 2. Both designs exhibit a similar and very good return loss response with $|S_{11}|$ less than -10 dB over the 2–4 GHz design frequency range.

The measured normalized co-polarized and cross-polarized E-plane radiation patterns at different frequencies for both designs are depicted in Figure 3, while Figure 4 show the measured maximum gain. The co-polarized E-plane radiation pattern for both meander and Euclidean LPDAs exhibits symmetry around $\varphi = 0$. This symmetry is achieved because of using a balanced feeding method where the current distributes equally on the dipoles parts.

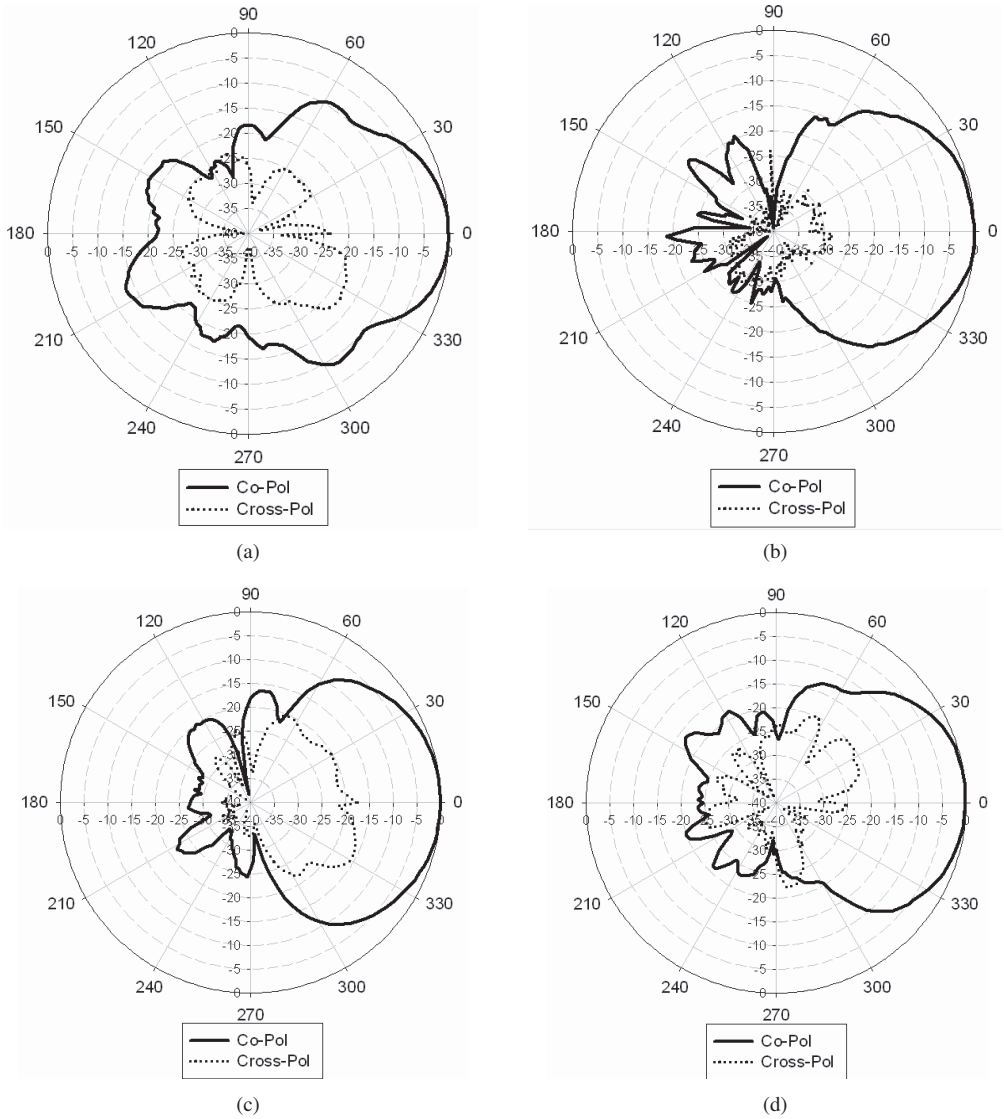

Figure 3: The normalized radiation pattern for: (a) Euclidean LPDA at $f = 3$ GHz, (b) Euclidean LPDA at $f = 4$ GHz, (c) Meander LPDA at $f = 3$ GHz and (d) Meander LPDA at $f = 4$ GHz.

The cross-polarized pattern in Figure 3 shows very low values and decreases as the frequency increases. However, the meander LPDA has higher cross-polarized radiation pattern, which still has very low values. A maximum gain of 7.5 dBi has been achieved for both designs over the design frequency.

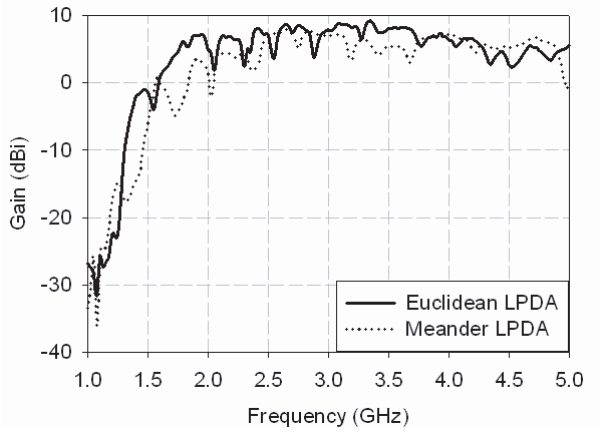

Figure 4: Maximum measured gain for Euclidean and meander LPDAs.

4. CONCLUSION

A size reduction for planar LPDA was shown in this work. The reduction in the occupied space for a planar LPDA was achieved by using the meander line instead of using the Euclidean line in the design. Both of the prototypes were shown and expressed. The comparison between the designs showed that reducing the size of the planar LPDA doesn't affect the main characteristics of the conventional LPDA.

REFERENCES

1. Rumsey, V., "Frequency independent antennas," *IRE National Convention Record*, Vol. 5, 114–118, 1957.
2. DuHamel, R. H. and D. E. Isbell, "Broadband logarithmically periodic antenna structures," *IRE International Convention Record*, Pt. 1, 119–128, 1957.
3. Carrel, R., "The design of log-periodic dipole antennas," *IRE National Conventional Record*, 61–75, 1961.
4. Balmain, K. G. and J. N. Kent, "Asymmetry phenomena of log periodic dipole antenna," *IEEE Transaction on Antenna & Propagation*, Vol. 24, No. 4, 1976.
5. Paul. A. and I. Gupta, "An analysis of log periodic antenna with printed dipoles," *IEEE Transaction on MTT*, Vol. 29, No. 2, Feb. 1981.
6. Campbell, I., M. S. Tranboulay, and K. Kneve, "Design of a stripline log-periodic dipole antenna," *IEEE Transaction on Antenna & Propagation*, Vol. 25, No. 5, Sept. 1977.
7. Pantoja, R. R. and F. C. M. Filho, "A microwave printed planar log-periodic dipole array antenna," *IEEE Transaction on Antenna & Propagation*, Vol. 35, No. 10, Oct. 1987.
8. Anagnostou, D. E., C. G. Papapolymerou, C. G. Christodoulou, and M. Tentzeris, "A small planar log-periodic kock-dipole antenna (LPKDA)," *IEEE APS/URSI International Symposium*, 3685–3688, 2006.
9. Sharma, S. K. and L. Shafai, "Investigations on minimized endfire vertically polarized quasi-fractal log-periodic zigzag antenna," *IEEE Transaction on Antenna & Propagation*, Vol. 52, No. 8, 1957–1962, 2004.
10. Best, S. R., "On the performance properties of the Koch fractal and other bent wire monopoles," *IEEE Transaction on Antenna & Propagation*, Vol. 51, No. 6, Jun. 2003.

Radiation Efficiency of the Metamaterial Zero-order Resonator Antenna

David Vrba and Milan Polívka
Department of Electromagnetic Field, Czech Technical University
Technická 2, Praha 166 27, Czech Republic

Abstract— In this paper a technique for improvement of radiation efficiency of metamaterial zero order antenna based on increasing of vertical antenna height is presented. Comparison of the two microstrip line implementation of the zero order resonator (ZOR) antennas with different height over ground plane is demonstrated. Improved ZOR antenna exhibit 75% efficiency compared to 10% of the reference antenna.

1. INTRODUCTION

Zeroth order mode resonator (ZOR) as a basic element of metamaterial (MTM) antenna has been used by several researchers, e.g., [1, 2]. Radiation efficiency has not been often studied or the presented or relatively low values are presented, between approx. 5 to 50%. In Fig. 1(a) we can see the case of four ZORs used to create the antenna. For corresponding relation of our antenna to its equivalent circuit model (Fig. 1(b)) we are using interdigital capacitors that create a series capacity. As a parallel inductance an inductive stub connected by viaholes to the ground metallic plane has been used. In some literature described antennas [1] a meander line is being used, but in such case the contribution to radiated EM field from current elements flowing in the opposed direction is being eliminated, also the current flowing in the ground plane in opposite direction compared to current in inductive meander lines and so it decreases radiation efficiency of mentioned antennas. That's why we prepared an experiment with increased height ZOR MTM antenna, where this elimination of radiation is suppressed. Physical dimensions of further presented antenna structure are 120×49 mm. Antenna was excited by coaxial feeder.

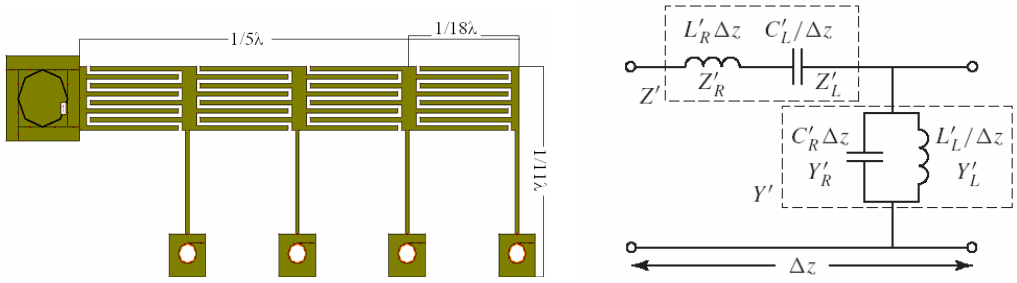

Figure 1: (a) Model of 4 unit cells ZOR MTM antenna. (b) Equivalent circuit model for one unit cell.

Our antenna was designed to work at frequency $f = 5.64$ GHz. In this case overall length of one basic cell $p = 3$ mm, length of fingers in interdigital capacitors is $l = 2.5$ mm and the width of finger is w and its the same as width of the gap s, i.e., $w = s = 0.1$ mm. Equivalent circuit model of this structure correspond to schema according to Fig. 1(b) with value of its single elements $L_R = 0.92$ nH, $C_L = 0.29$ pF, $C_R = 0.51$ nH, $L_L = 1.32$ pF.

From the current density distribution (see Fig. 2(a)) we can see, that inductive stubs contribute significantly to antenna radiation. These inductive stubs can be also used as very suitable elements for tuning of discussed antenna to required working frequency. Dependence of resonance frequency on the length of the inductive stub is depicted in Fig. 2(b). Generally we can discuss, that the longer will be the length of the inductive stub, the lower will be the resonant frequency of ZORs.

According to literature [1] the value of radiation efficiency for MTM antennas realized on a thin dielectric substrate is at working frequency typically about 10%. In our experiments we used dielectric substrate with following parameters: $h = 0.5$ mm, $\varepsilon_r = 3.05$, $\mathrm{tg}\delta = 0.003$. The way how

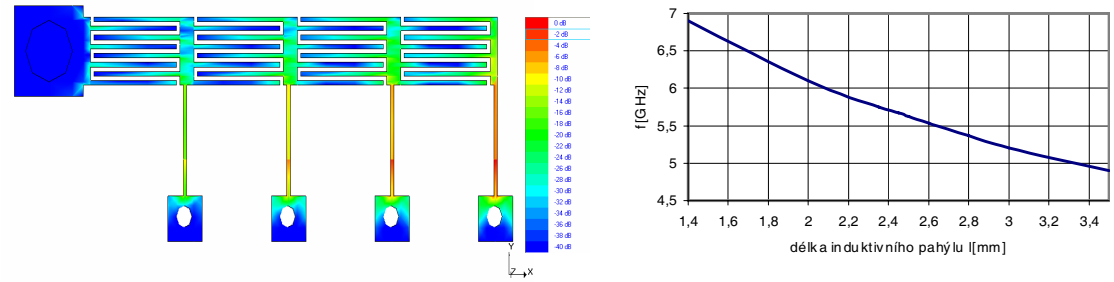

(a) (b)

Figure 2: (a) Current distribution for resonating frequency $f = 5.64\,\text{GHz}$ on mode $m = 0$. (b) Dependence of resonance frequency on the length of the inductive stub.

to improve radiating efficiency has been looked for. In Fig. 3, dependence of the antenna efficiency on frequency is shown, where:

$$\begin{aligned}\text{Radiation efficiency} &= \text{Radiated Power/Input Power and Antenna efficiency} \\ &= \text{Radiated Power/Incident Power}\end{aligned}$$

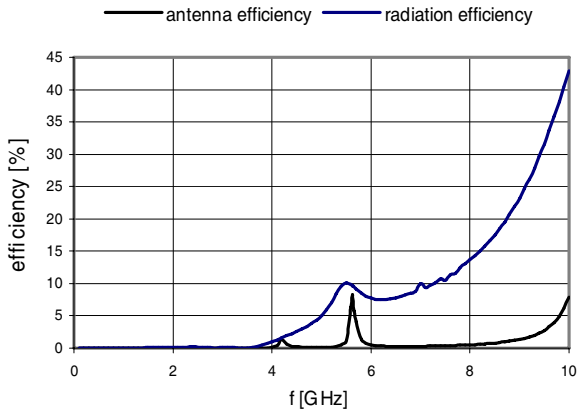

Figure 3: Radiating and antenna efficiency for resonant frequency of ZORs: $f = 5.64\,\text{GHz}$.

The described antenna was designed for higher radiation efficiency. The topology for new antenna is modified (Fig. 4(a)). The difference between original antenna and the modified one is that additional air layer is being placed between the ground plane and the dielectric substrate. The height of the air layer is increased to $h = 6.4\,\text{mm}$ $(1/9\lambda)$.

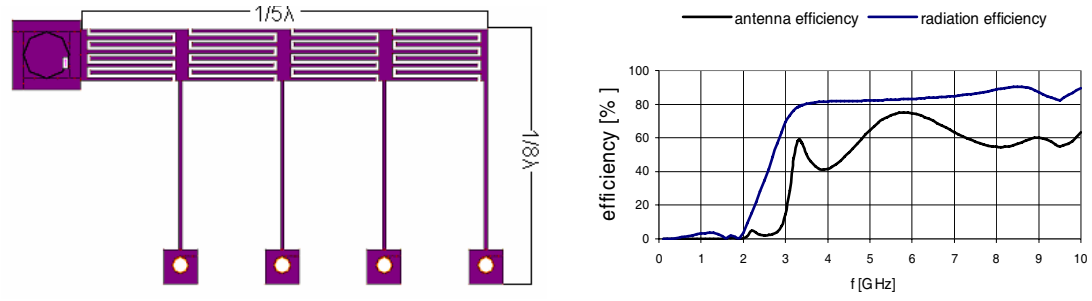

(a) (b)

Figure 4: (a) Design of antenna with higher radiating efficiency. (b) Radiating and antenna efficiency for resonating frequency $f = 5.64\,\text{GHz}$ on mode $m = 0$.

The reason why radiation efficiency is dependent on the height of the air layer will be explained based on definition of quality factor Q.

The quality factor of an antenna tuned at a frequency ω_0 is defined by the ratio of reactive energy W to accepted power P_A as

$$Q(\omega_0) = \frac{\omega_0 W}{P_A} \tag{1}$$

Thus Q is a measure of the loss in a resonant circuit; the lower loss implies a higher Q.

As a consequence of increasing height of an air layer the effective permittivity will decrease and thus the resonating frequency will be increased. The easiest way how to tune frequency to required frequency is to extend inductive stub.

2. ANTENNA REALIZATION

For comparison of the two discussed antennas with different height of dielectric substrate were realized. From measured and simulated frequency behavior of reflection coefficient S_{11} (see Fig. 5(a) and 5(b)) it can be seen, that for antenna without air substrate the shapes of these curves are almost identical (case in Fig. 5(a)).

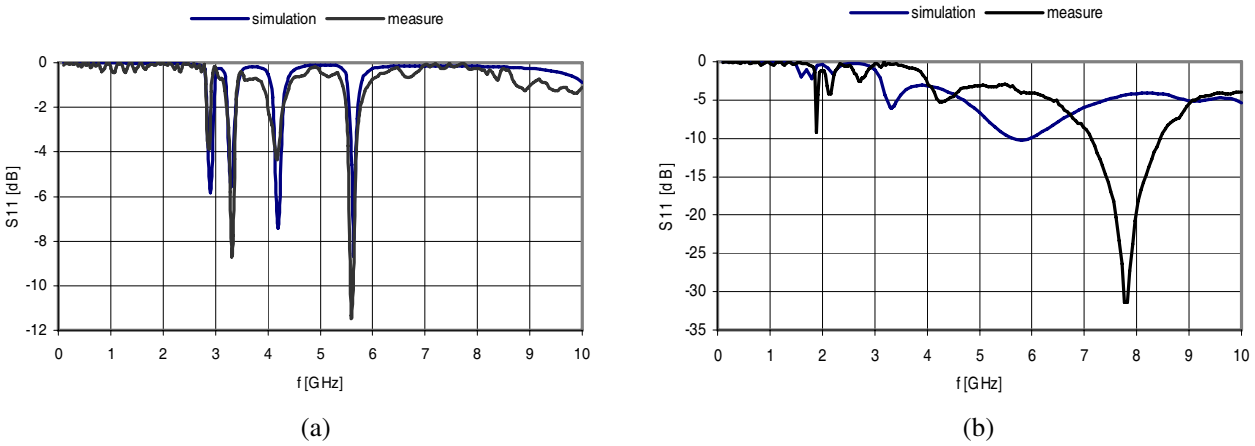

Figure 5: Measured and simulated reflection coefficient of realized prototype (a) for antenna from Fig. 1(a). (b) for antenna from Fig. 4(a).

On the contrary, for the modified antenna separated by air layer such that the top of the upper plate and the top of the bottom plate are 6.4 mm apart each from other, then the calculated and measured curves (S_{11} vs. frequency) are different (case in Fig. 5(b)). This effect can be caused by several reasons, e.g., by two layers of dielectric media and so more complicated way of propagation of EM wave along the antenna structure, further by not the best accuracy of fabrication, etc.

Measured values of gain G and calculated value of efficiency η (for resonant frequencies with $m = \{0, -1, -2, -3\}$) are presented in Tables 1 and 2.

Table 1: Measured values of gain G and calculated value of efficiency η for antenna from Fig. 1(a).

f [GHz]	2.88	3.30	4.18	5.58
G [dBi]	−39.25	−31.51	−15.98	−6.89
η [%]	0.0	0.0	1	6

Table 2: Measured values of gain G and calculated value of efficiency η antenna from Fig. 4(a).

f [GHz]	1.88	2.14	2.71	4.28	7.79
G [dBi]	−23.67	−19.57	−10.47	−4.56	−0.52
η [%]	0.1	0.4	1.9	9.3	25.0

3. CONCLUSION

Dependence of radiation efficiency of ZOR antenna implemented in microstrip line technology on the vertical height of the antenna structure has been demonstrated in this paper. Radiation efficiency of improved antenna of the height 6.4 mm has been increased to 75% compared with 10% of reference antenna with the height 0.5 mm. It can be stated that radiation efficiency dominantly depends on the vertical size of the antenna structure.

ACKNOWLEDGMENT

This work has been conducted at the Department of Electromagnetic Field of the Czech Technical University in Prague and supported and by the two projects of the Grant Agency of the Czech Republic No. 102/08/1282 "Artificial electromagnetic structures for miniaturization of high-frequency and microwave radiation and circuit elements", and doctoral project No. 102/08/H018, further by the Czech Ministry of Education, Youth and Sports in the frame of the Research Project in the Area of the Prospective Information and Navigation Technologies MSM 6840770014, and by the COST project IC0603 "Antenna Systems & Sensors for Information Society Technologies".

REFERENCES

1. Caloz, C. and T. Itoh, *Electromagnetic Metamaterials: Transmition Line Theory and Microwave Applications*, John Wiley & Sons, 2006.
2. Lai, A., C. Caloz, and T. Itoh, "Composite right/left-handed transmission line metamaterials," *IEEE Microwave Magazine*, Vol. 5, No. 3, 34–50, September 2004.
3. Vrba, D., "Electrically small antenna with lumped LC elements," Master thesis, CVUT FEL, 2008.
4. Schaler, M., J. Freese, and R. Jakoby, "Design of compact planar antennas using LH-transmission lines," *Microwave Symposium Digest, 2004 IEEE MTT-S International*, Vol. 1, 209–212, 2004.

The Magnetic Manipulation of Surface Plasmons — Consideration of Possible Technologies

Dave M. Newman, **M. Lesley Wears**, **and Raphael J. Matelon**
School of Engineering, Computing & Mathematics, University of Exeter, Exeter EX4 4QF, UK

Abstract— An as yet unexploited mechanism for producing controlled shifts in the frequency of lightwaves via their temporary conversion to surface plasmons propagating on a ferromagnetic surface or under the action of applied magnetic fields is introduced. Indirect evidence of the observation of this phenomena is presented and the technological possibilities it might offer are explored and discussed.

Interfaces between dielectric and metallic media possessing negative permittivity (ε) can support electromagnetic waves propagating as longitudinal density oscillations in the free-electron plasma at the metallic surface. Like photons, the quanta of these collective excitations remain bosons and are known as surface plasmons. Moreover, under conditions satisfying the relevant conservation laws, photons and plasmons are mutually transformable. Photons incident on a metallic surface may for example be temporarily induced to convert to plasmons that propagate on the surface for a while before their subsequent recovery as photons emitted back into the incident medium. The most exciting and complete confirmation of the nature of this process is evidenced in the work of Altewischer et al. [1] which demonstrated that a photon, having followed a path that includes its conversion to a plasmon and back to a photon, retains entanglement with the twin with which it was originally created in a down-conversion process. The objective here is to draw attention to the potential to exploit this two way conversion process to operate on photons in ways not previously considered.

More than 30 years ago Chiu and Quinn [2] and Nakamura and Paranjape [3] first described theoretically how propagating plasmons undergo frequency shifts when subject to influence by appropriately orientated dc magnetic fields (H) applied orthogonal to the plasmon flux. In more recent times Smolyaninov et al. [4] have interpreted the equations of Chiu and Quinn [2] and Nakamura and Paranjape [3] as describing a second-order mixing process between the ac plasmon field (E_p) and any applied dc magnetic field (H). If $\chi^{(2)}$ is a generalised susceptibility then such mixing processes generate terms of the form $\chi^{(2)}E_p^2H$ in the plasmon field energy density and the breaking of inversion symmetry at the interfaces requisite for the very existence of surface plasmons determines that terms such as $\chi^{(2)}E_p^2$ will always be present.

The plasmon energy and hence frequency consequently acquire a contribution linear in the applied field H which is real and in light of the results of Altewischer et al. [1] transposable to a photon emission field when the plasmon is intercepted by a grating out-coupler. We have obtained strong indirect evidence of the reality of this position by studying plasmon propagation on a nickel surface on which a linear grating with a period of 1.13 µm and depth of 0.7 µm is modulated, as shown schematically in Figure 1, by a shallower structure with an order of magnitude greater periodicity of about 12.5 µm [5].

When this structured surface is illuminated at an angle of incidence (θ_i) of exactly 19.85° by optical radiation with a wavelength of 800 nm and conservation of wavevector is satisfied by the addition of that associated with the 1.13 µm structural periodicity to that of the incident photons, a deep absorption trough is observed as shown on the left of Figure 1 indicating the resonant generation of a flux of forward propagating surface plasmons. Because of the finite spectral width of the incident optical beam, its residual divergence and the inherent error in the periodicity of the 1.13 µm coupling structure this flux consists of plasmons with a narrow spectrum of wavevectors rather than a single identical wavevector and the population of this spectrum is primarily determined by the Gaussian intensity profile of the incident beam. The width of the plasmon spectrum at full width half maximum ΔK_{sp}(FWHM) may be estimated by examination and analysis of the form of the reflectivity trough in Figure 1 to be of the order of $0.35 \times 10^{-3}\,\mathrm{nm}^{-1}$. This plasmon flux subsequently interacts in a much weaker fashion with the longer and shallower periodic structure which re-couples it back to an emissive optical field emerging from the surface at an angle of 77° as shown on the right of Figure 1. Full Fourier analysis of the surface structure and the diffractive orders and other phenomena it supports shows that the optical beam emerging from the surface

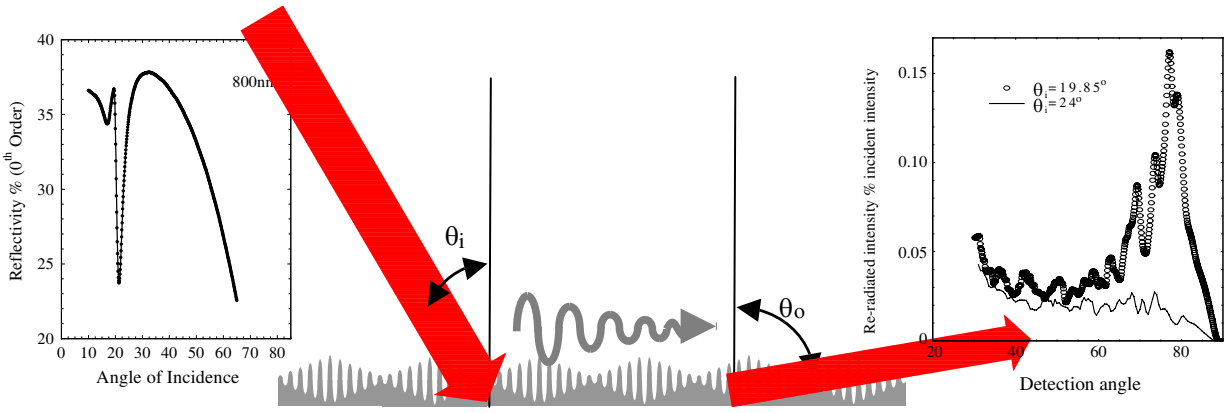

Figure 1: Bi-periodic nickel grating interaction with incident radiation.

at 77° arises solely from plasmons created by the beam incident at 19.85° which having travelled a short distance across the surface are re-coupled out. Fourier analysis of the surface periodicities also yields the width ΔK_{st}(FWHM) of the wavevector spectrum associated with imperfections in the periodicity of the output coupling structure as of the order of $0.24 \times 10^{-3}\,\mathrm{nm}^{-1}$. Any plasmon in the spectrum ΔK_{sp} can re-transform to form part of the well directed, low (∼85 mrad half angle) divergence beam of the optical radiation observed emanating from the surface at 77° if it can make an appropriate exchange of wave-vector with surface structure to satisfy conservation criteria.

Under the action of a magnetic field applied in the plane of the surface and transverse to the plasmon flux the intensity of the optical radiation emitted at 77° is recorded as a linear function of applied magnetic field. This is because as illustrated in Figure 2, the recorded output intensity arises from all possible combinations of wave-vectors in and between the spectra of the plasmons and output coupling structure subject to the constraint of wave-vector conservation $k_{sp}^{i} - k_{st}^{j} = k_{p}^{ij}\sin(\theta_o)$ where k_{sp}^{i} and k_{st}^{j} are respectively specific surface plasmon and structure wave-vectors within the corresponding spectra ΔK_{sp} and ΔK_{st} and $k_{p}^{ij}\sin(\theta_o)$ is the wave-vector of a re-emitted photon.

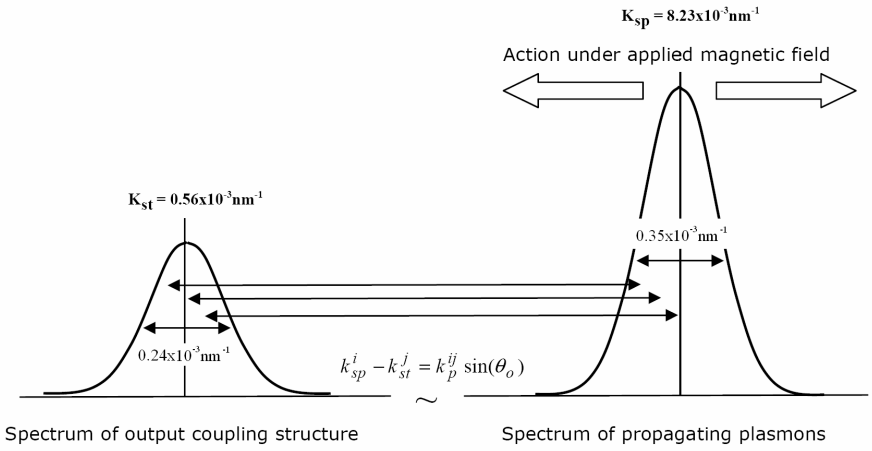

Figure 2: Origin of emission from grating and its magnetic dependency.

Therefore as the applied magnetic field reverses the magnetization of the nickel surface the frequency of the plasmons varies as determined by Nakamura and Paranjape [3] shifting the plasmon spectrum ΔK_{sp} first one way and then the other about its mean position in the absence of an applied field. This effectively "scans" states in the plasmon spectrum across those in the spectrum ΔK_{st} of wavevector states associated with the surface structure, which of course remain unchanged under magnetization reversal, producing the change in emitted intensity as the combinations of k_{sp}^{i} with k_{st}^{j} possible under the conservation constraints vary.

Significantly no similar variation in emitted output is recorded when the applied field and hence

the nickel magnetization is reversed along a direction collinear with the plasmon flux. A negative result in this configuration also precludes the effects observed in the transverse configuration arising from any conventional magneto-optic effect or resulting from changes in the coupling efficiencies of the input and out couplers as a consequence of magnetization induces changes in permittivity.

In principle we have an as yet unexploited mechanism for the frequency shifting or frequency modulation of optical radiation offering the prospect of new devices and technologies. Theory indicates that frequency shifts of an order relevant to wavelength division multiplexing in optical communications, frequency selection in spectral domain data storage technologies or the novel readout of conventionally recorded magnetic data may all be achievable. Practical realisation of these concepts is however somewhat constrained by the materials available and the strength of the magnetic fields required. Whilst silver and aluminium are the surfaces of choice for the efficient generation and propagation of plasmons the production of frequency shifts significantly greater than about ± 2.6 GHz in plasmons propagating on either silver or aluminium is predicted to require the application of localised magnetic fields of magnitudes not easily attainable. However, much greater frequency shifts are predicted for magnetized ferromagnetic surfaces but at the expense of greatly reduced creation and propagation efficiencies. In Nickel the plasmon frequency shift under the action of the internal induction field is calculated to be about ± 56 GHz. We have shown that not only do the surfaces of all three of the principle ferromagnetic elements support plasmon creation and propagation but that it is also possible to combine both metallic systems to optimise desired behaviour. Figure 3 for example, shows experimentally that the fields associated with plasmons propagating on thin silver layers deposited on top of a Nickel grating penetrate the Nickel surface to produce enhancement in the magneto-optic behaviour.

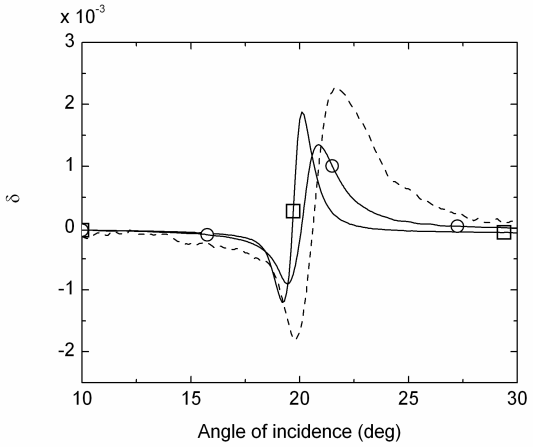

Figure 3: Transverse Kerr effect (δ) measurements *versus* angle of incidence at an optical frequency of 3.66×10^{14} Hz (819 nm) on silver films of different thicknesses ($\square$ 16 nm and $\circ$ 9 nm) supported on a 1200 nm period Ni grating, data for the bare Ni grating is shown for comparison (dotted line).

We explore the potential to create practical and useful devices based on the magnetic manipulation of propagating plasmons by considering the efficiencies of simple structures such as shown in Figure 4 and using the material data in Table 1.

Table 1.

	Wavelength nm	n	k	Propagation length μm	Penetration depth nm
Silver	1442	0.431	8.7	117	26
Nickel	1442	3.25	6.47	5	40

If the structure in Figure 4 is fabricated in silver, the plasmon path between input and output couplers is 30 μm and the angles of incidence, emission and the depths of the grating couplers are

chosen to optimize the coupling efficiencies then the frequency of incident radiation can be easily shifted by ±2.6 GHz with an overall efficiency of 65%. This drops to 10% for nickel and requires the path length be reduced to 5 μm but should produce a frequency shift of the order of ±56 GHz, well within the range useful to the telecommunications industry.

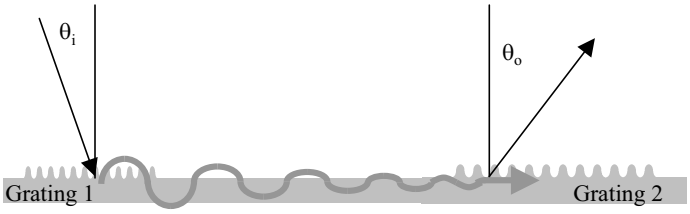

Figure 4: Schematic of simplest possible technologically relevant device.

At first sight it might appear that a similar sort of efficiency (11%) and frequency shift (13 GHz) should also be obtained by passing radiation back and forwards five times through the device fabricated in silver. Unfortunately the effect is reciprocal in nature in the transverse configuration. This concept should however be possible in the configuration in which the magnetic field is applied normal to the surface on which the plasmons propagate when the non reciprocal nature of the predicted interaction also offers the possibility of building novel optical- isolators.

Further calculations indicate that the overall input-output efficiency of devices fabricated in nickel can be dramatically improved whilst retaining much of the frequency shifting power of the ferromagnetic. This is achieved by overcoating them with very thin layers of silver. Plasmon generation efficiencies between 88% and 99.9% are obtained on optimally structured nickel profiles when overcoated with silver films between 5 nm and 15 nm in thickness. Under these circumstances the plasmon continue to interact with the field produced by the nickel since the plasmon penetration depth in silver is considerably less than the thickness of the silver films.

It would appear that devices based on this principle and of real relevance to the telecoms and other optical industries may be possible and certainly at the tens' of micron scale devices such as illustrated schematically below, where the arrows indicate reversible localized fields realized via current elements, could already be fabricated.

Figure 5: Schematics of other possible simple devices. (Left) Separation of information on to two frequency separated channels — depending on direction of field applied to individual arms their output frequency can be up-shifted, down shifted or unchanged with respect to the input. (Right) A device such as might be used to explore plasmon interferometers.

REFERENCES

1. Altewischer, E., M. P. van Exter, and J. P. Woerdman, "Plasmon-assisted transmission of entangled photons," *Nature*, Vol. 418, 304–306, 2002.
2. Chiu, K. W. and J. J. Quinn, "Magnetoplasma surface waves in metals," *Phys. Rev. B*, Vol. 5, No. 12, 4707–4709, 1972.
3. Oi Nakamura, Y. and B. V. Paranjape, "Surface plasmon in a parallel magnetic field," *Solid State Commun.*, Vol. 16, 467–470, 1975.
4. Smolyaninov, I. I., et al., "Plasmon-induced magnetization of metallic nanostructures," *Phys. Rev. B*, Vol. 71, 035425, 2005.
5. Newman, D. M., M. L. Wears, and R. J. Matelon, "Plasmon transport phenomena on a continuous fermagnetic surface," *Europhys. Lett.*, Vol. 68, No. 5, 692–698, 2004.

Application of the General Theory of Exact Relations to Fiber-reinforced Conducting Composites with Hall Effect

Yury Grabovsky
Temple University, USA

Abstract— In this paper we present all microstructure-independent relations for effective conductivity of fiber-reinforced composites with Hall effect. We also present all possible links between effective conductivities of two composites that have the same microstructure but are built using different materials. Our results use general theory of exact relations for composite materials and are valid for composites made with an arbitrary number of constituents.

1. INTRODUCTION

The effective conductivity of a composite material depends non only on the conductivities and volume fractions of its constituents but also on its microstructure. The dependence is so strong that generically the set of all possible conductivities will occupy a set with non-empty interior in the space of all possible tensors. In special situations, for instance when constituent satisfy certain relations, some combination of components of the effective conductivity will be independent of the microstructure. A typical example is given by the Keller-Dykhne relation [3, 11]. If the anisotropic conductivities $\boldsymbol{\sigma}_i$, $i = 1, \ldots, N$ of the N crystalline constituents of a polycrystal satisfy $\det \boldsymbol{\sigma}_1 = \ldots = \det \boldsymbol{\sigma}_N = d_0$, then the effective conductivity $\boldsymbol{\sigma}^*$ will also satisfy $\det \boldsymbol{\sigma}^* = d_0$. Examples like these, though rare in any one physical situation, abound in the literature on composite materials (see e.g., [9] and references therein). In a series of papers [4, 5, 8–10] we have developed a general theory that can produce a complete, exhaustive list of all microstructure-independent relations in a wide variety of physical contexts (see also Milton's book [14, Chapter 17]).

In [5, 9] we show that in order to compute all microstructure-independent relations, one needs to solve a linear algebra problem, corresponding to the physics at hand. This linear algebra problem can be stated as the problem of complete characterization of a class of special Jordan algebras. Any such Jordan algebra gives rise to an exact relation for the effective tensor of a composite. In this paper we describe this linear algebra problem and all of its solutions corresponding to fiber reinforced composites exhibiting Hall effect.

In addition to microstructure-independent relations, our theory is also capable of identifying relations involving volume averages of functions of the local tensor. Of highest importance, however, is an extension of our theory to links between uncoupled composites that share the same microstructure. This is because a link is capable of mapping a complicated exact relation to a simpler one. This allows us to list only the simplest and most transparent exact relations together with the links to describe the entirety of exact relations.

2. PRELIMINARIES AND NOTATIONS

The fiber-reinforced periodic composite material with fibers along the x_3 direction can be described in terms of tensors and fields that depend only on the transversal variables $\boldsymbol{x} = (x_1, x_2)$. However, the tensorial nature of the fields is three-dimensional. To utilize the simplifications afforded by the cylindrical symmetry of our problem we write both the local conductivity $\boldsymbol{L} = \boldsymbol{L}(\boldsymbol{x})$ and the effective conductivity $\boldsymbol{L}^*$ in the block form

$$\boldsymbol{L}(\boldsymbol{x}) = \begin{bmatrix} \boldsymbol{\Lambda}(\boldsymbol{x}) & \boldsymbol{p}(\boldsymbol{x}) \\ \boldsymbol{q}(\boldsymbol{x}) & \alpha(\boldsymbol{x}) \end{bmatrix}, \qquad \boldsymbol{L}^* = \begin{bmatrix} \boldsymbol{\Lambda}^* & \boldsymbol{p}^* \\ \boldsymbol{q}^* & \alpha^* \end{bmatrix},$$

where $\boldsymbol{\Lambda}$-block is the 2×2 positive definite matrix of the transversal conductivity; $\alpha > 0$ is the conductivity along the fibers and $\boldsymbol{p}$ and $\boldsymbol{q}$-blocks are $\mathbb{R}^2$ vectors linking fields along and across the fibers. The possible lack of symmetry of the matrices $\boldsymbol{L}$ and $\boldsymbol{\Lambda}$ is due to the Hall effect.

The effective tensor $\boldsymbol{L}^*$ of the fiber-reinforced conductor can be given in terms of the non-local operator $\Gamma_{\boldsymbol{\Lambda}}$ on $L^2(Q; \mathbb{R}^2)$ (see [6]), given by $\Gamma_{\boldsymbol{\Lambda}} \boldsymbol{p} = \nabla \psi$, where $\psi(\boldsymbol{x})$ is the unique (up to an additive constant) Q-periodic solution of $-\nabla \cdot \boldsymbol{\Lambda}(\boldsymbol{x}) \nabla \psi = \nabla \cdot \boldsymbol{p}(\boldsymbol{x})$. The operator $\Gamma_{\boldsymbol{\Lambda}}$ is a generalization of

the Helmholtz projection operator $\Gamma = \Gamma_{\boldsymbol{I}}$, where $\boldsymbol{I}$ is the identity matrix.

$$\begin{aligned} \boldsymbol{\Lambda}^* &= \langle \boldsymbol{\Lambda} \rangle + \langle \boldsymbol{\Lambda} \Gamma_{\boldsymbol{\Lambda}} \boldsymbol{\Lambda} \rangle, \qquad & \boldsymbol{p}^* &= \langle \boldsymbol{p} \rangle + \langle \boldsymbol{\Lambda} \Gamma_{\boldsymbol{\Lambda}} \boldsymbol{p} \rangle, \\ \alpha^* &= \langle \alpha \rangle + \langle (\Gamma_{\boldsymbol{\Lambda}} \boldsymbol{p}, \boldsymbol{q}) \rangle, \qquad & \boldsymbol{q}^* &= \langle \boldsymbol{q} \rangle + \langle (\Gamma_{\boldsymbol{\Lambda}} \boldsymbol{\Lambda})^T \boldsymbol{q} \rangle, \end{aligned} \tag{1}$$

where the operator $\Gamma_{\boldsymbol{\Lambda}}$ is extended to $L^2(Q; \mathrm{End}(\mathbb{R}^2))$ by $(\Gamma_{\boldsymbol{\Lambda}} \boldsymbol{P})\boldsymbol{e} = \Gamma_{\boldsymbol{\Lambda}}(\boldsymbol{P}\boldsymbol{e})$ for any $\boldsymbol{e} \in \mathbb{R}^2$.

3. JORDAN ALGEBRAS

There is an analog of the periodic Helmholtz operator that is appropriate in a wide variety of situations in physics. As in the standard case, the Helmholtz operator $\mathcal{H}$ is local in Fourier space and is defined by its action on a arbitrary Q-perodic field $\boldsymbol{f}$ by $\widehat{\mathcal{H}\boldsymbol{f}}(\boldsymbol{k}) = \widehat{\Gamma}(\boldsymbol{k})\widehat{\boldsymbol{f}}(\boldsymbol{k})$, where $\widehat{\Gamma}(\boldsymbol{k})$ is the Fourier multiplier determined by the physical context. In our case

$$\widehat{\Gamma}(\boldsymbol{k}) = \frac{\boldsymbol{L}_0 \boldsymbol{k} \otimes \boldsymbol{k}}{(\boldsymbol{L}_0 \boldsymbol{k}, \boldsymbol{k})}.$$

We define $\mathcal{A} = \mathrm{Span}\{\widehat{\Gamma}(\boldsymbol{k}) - \widehat{\Gamma}(\boldsymbol{k}_0) : |\boldsymbol{k}| = 1\}$ (which is independent of the choice of $\boldsymbol{k}_0$). The linear algebra problem alluded to in the introduction is stated as follows. Find all subspaces $\Pi \subset \mathrm{End}(\mathbb{R}^3)$, such that

$$\boldsymbol{P}_1 *_{\boldsymbol{A}} \boldsymbol{P}_2 = \frac{1}{2}(\boldsymbol{P}_1 \boldsymbol{A} \boldsymbol{P}_2 + \boldsymbol{P}_2 \boldsymbol{A} \boldsymbol{P}_1) \in \Pi \tag{2}$$

for all $\{\boldsymbol{P}_1, \boldsymbol{P}_2\} \subset \Pi$ and all $\boldsymbol{A} \in \mathcal{A}$. The Equation (2) can be simplified by applying the transformation $\boldsymbol{P} \mapsto \boldsymbol{C}_1 \boldsymbol{P} \boldsymbol{C}_2$. In [7] we show how to choose the invertible matrices $\boldsymbol{C}_1$ and $\boldsymbol{C}_2$ such that the subspace $\mathcal{A}$ simplifies to

$$\mathcal{A} = \left\{ \begin{bmatrix} a & b & 0 \\ b & -a & 0 \\ 0 & 0 & 0 \end{bmatrix} : \{a, b\} \subset \mathbb{R} \right\}.$$

We begin by solving (2) for the case of two-dimensional conductivity, where all matrices are 2×2 and the subspace $\mathcal{A}$ is $\mathcal{A}_{2d} = \{\boldsymbol{A} \in \mathrm{End}(\mathbb{R}^2) : \boldsymbol{A}^T = \boldsymbol{A},\ \mathrm{Tr}\, \boldsymbol{A} = 0\}$. By the $2d$ Cayley-Hamilton theorem $(\boldsymbol{P}\boldsymbol{A})^2 = \mathrm{Tr}\,(\boldsymbol{P}\boldsymbol{A})\boldsymbol{P}\boldsymbol{A} - \det(\boldsymbol{P}\boldsymbol{A})\boldsymbol{I}$. Therefore,

$$\boldsymbol{P}\boldsymbol{A}\boldsymbol{P} = \mathrm{Tr}\,(\boldsymbol{P}\boldsymbol{A})\boldsymbol{P} - \det(\boldsymbol{P}\boldsymbol{A})\boldsymbol{A}^{-1}.$$

This implies that Π is a solution of the $2d$ version of (2) if and only if either $\mathcal{A}_{2d}$ is a subspace of Π or Π consists entirely of rank-one matrices and zero. Using this observation as a starting point, we were able to make a complete list of solutions of (2), corresponding to the $3d$ fiber-reinforced composites. The description of this list can be considerably simplified using the idea of symmetry. We will say that the invertible linear map $\boldsymbol{\Psi} : \mathrm{End}(\mathbb{R}^3) \to \mathrm{End}(\mathbb{R}^3)$ is a symmetry of (2) if $\boldsymbol{\Psi}(\boldsymbol{P}_1 *_{\boldsymbol{A}} \boldsymbol{P}_2) = \boldsymbol{\Psi}(\boldsymbol{P}_1) *_{\boldsymbol{A}} \boldsymbol{\Psi}(\boldsymbol{P}_2)$. We can show that $\boldsymbol{\Psi}$ is a symmetry if and only if it has the form

$$\boldsymbol{\Psi}(\boldsymbol{P}) = \boldsymbol{X}\boldsymbol{P}\boldsymbol{Y} \text{ or } \boldsymbol{X}\boldsymbol{P}^T\boldsymbol{Y},\ \boldsymbol{X} = \begin{bmatrix} \cos\theta & -\sin\theta & 0 \\ \sin\theta & \cos\theta & 0 \\ a_1 & a_2 & a_3 \end{bmatrix},\ \boldsymbol{Y} = \begin{bmatrix} \cos\theta & -\sin\theta & b_1 \\ \sin\theta & \cos\theta & b_2 \\ 0 & 0 & b_3 \end{bmatrix}, \tag{3}$$

where θ and $\boldsymbol{a}, \boldsymbol{b} \in \mathbb{R}^3$ are parameters.

Now, instead of listing all solutions of (2) we need to list only those that cannot be transformed into one another by a symmetry (3). The same idea can also be used in the $2d$ case discussed above. The set of non-symmetry related solutions Π_{2d} is given by the following simplified list: $\{\boldsymbol{0}\}$; $\Pi_{\boldsymbol{a},\boldsymbol{a}} = \mathbb{R}(\boldsymbol{a} \otimes \boldsymbol{a})$, $|\boldsymbol{a}| = 1$; $\Pi_{\boldsymbol{a}} = \{\boldsymbol{u} \otimes \boldsymbol{a} : \boldsymbol{u} \in \mathbb{R}^2\}$, $|\boldsymbol{a}| = 1$; $\mathcal{A}_{2d}$; $\mathrm{Sym}(\mathbb{R}^2)$; $\mathrm{End}(\mathbb{R}^2)$. All the solutions of (2) can then be listed as follows

1. $\left\{ \begin{bmatrix} \boldsymbol{K} & \boldsymbol{u} \\ \boldsymbol{v} & \rho \end{bmatrix} : \boldsymbol{K} \in \Pi_{2d},\ \boldsymbol{u}, \boldsymbol{v} \in \mathbb{R}^2,\ \rho \in \mathbb{R} \right\}$
2. $\left\{ \begin{bmatrix} \boldsymbol{K} & \boldsymbol{0} \\ \boldsymbol{v} & \rho \end{bmatrix} : \boldsymbol{K} \in \Pi_{2d},\ \boldsymbol{v} \in \mathbb{R}^2,\ \rho \in \mathbb{R} \right\}$

3. $\left\{\begin{bmatrix} \boldsymbol{K} & \boldsymbol{0} \\ \boldsymbol{v} & 0 \end{bmatrix} : \boldsymbol{K} \in \Pi_{2d},\ \boldsymbol{v} \in \mathbb{R}^2 \right\}$

4. $\left\{\begin{bmatrix} \boldsymbol{K} & \boldsymbol{0} \\ \boldsymbol{0} & \rho \end{bmatrix} : \boldsymbol{K} \in \Pi_{2d},\ \rho \in \mathbb{R} \right\}$

5. $\left\{\begin{bmatrix} \boldsymbol{K} & \boldsymbol{0} \\ \boldsymbol{0} & 0 \end{bmatrix} : \boldsymbol{K} \in \Pi_{2d} \right\}$

6. $\left\{\begin{bmatrix} \boldsymbol{K} & \boldsymbol{u} \\ \boldsymbol{u} & \rho \end{bmatrix} : \boldsymbol{K} \in \Pi_{2d},\ \boldsymbol{u} \in \mathbb{R}^2,\ \rho \in \mathbb{R} \right\}$, $\Pi_{2d} = \mathrm{Sym}(\mathbb{R}^2)$, $\mathcal{A}_{2d}$, $\Pi_{\boldsymbol{a},\boldsymbol{a}}$, $\{\boldsymbol{0}\}$.

7. $\left\{\begin{bmatrix} \boldsymbol{K} & \boldsymbol{0} \\ t\boldsymbol{a} & \rho \end{bmatrix} : \boldsymbol{K} \in \Pi_{2d},\ t \in \mathbb{R},\ \rho \in \mathbb{R} \right\}$, $\Pi_{2d} = \Pi_{\boldsymbol{a}}$, $\Pi_{\boldsymbol{a},\boldsymbol{a}}$, $\{\boldsymbol{0}\}$

8. $\left\{\begin{bmatrix} \boldsymbol{K} & \boldsymbol{u} \\ t\boldsymbol{a} & \rho \end{bmatrix} : \boldsymbol{K} \in \Pi_{2d},\ \boldsymbol{u} \in \mathbb{R}^2,\ t \in \mathbb{R}, \rho \in \mathbb{R} \right\}$, $\Pi_{2d} = \Pi_{\boldsymbol{a}}$, $\Pi_{\boldsymbol{a},\boldsymbol{a}}$, $\{\boldsymbol{0}\}$

9. $\left\{\begin{bmatrix} \boldsymbol{K} & \boldsymbol{0} \\ t\boldsymbol{a} & 0 \end{bmatrix} : \boldsymbol{K} \in \Pi_{2d},\ t \in \mathbb{R} \right\}$, $\Pi_{2d} = \Pi_{\boldsymbol{a}}$, $\Pi_{\boldsymbol{a},\boldsymbol{a}}$, $\{\boldsymbol{0}\}$

10. $\left\{\begin{bmatrix} \boldsymbol{K} & t\boldsymbol{a} \\ t\boldsymbol{a} & \rho \end{bmatrix} : \boldsymbol{K} \in \Pi_{2d},\ t \in \mathbb{R},\ \rho \in \mathbb{R} \right\}$, $\Pi_{2d} = \Pi_{\boldsymbol{a},\boldsymbol{a}}$, $\{\boldsymbol{0}\}$

11. $\left\{\begin{bmatrix} \boldsymbol{K} & s\boldsymbol{a} \\ t\boldsymbol{a} & \rho \end{bmatrix} : \boldsymbol{K} \in \Pi_{2d},\ t \in \mathbb{R},\ \rho \in \mathbb{R} \right\}$, $\Pi_{2d} = \Pi_{\boldsymbol{a},\boldsymbol{a}}$, $\{\boldsymbol{0}\}$

12. $\left\{\begin{bmatrix} \boldsymbol{K} & \boldsymbol{u} \\ \boldsymbol{u} + t\boldsymbol{a} & \rho \end{bmatrix} : \boldsymbol{K} \in \Pi_{2d},\ \boldsymbol{u} \in \mathbb{R}^2,\ t \in \mathbb{R},\ \rho \in \mathbb{R} \right\}$, $\Pi_{2d} = \Pi_{\boldsymbol{a},\boldsymbol{a}}$, $\{\boldsymbol{0}\}$

13. $\left\{\begin{bmatrix} \boldsymbol{0} & \boldsymbol{u} \\ \boldsymbol{M}\boldsymbol{u} & \rho \end{bmatrix} : \boldsymbol{u} \in \mathbb{R}^2,\ \rho \in \mathbb{R} \right\}$.

Each of the above solutions (together with solutions of the form $\boldsymbol{\Psi}(\Pi)$) corresponds to a microstructure-independent relation for effective conductivity of fiber-reinforced conducting composites. Some of these relations could be augmented by additional relations involving volume averages. The number of additional relations, according to our theory, is equal to the codimension of the derived ideal Π^2 in Π, where $\Pi^2 = \mathrm{Span}\{\boldsymbol{PAP} : \boldsymbol{P} \in \Pi,\ \boldsymbol{A} \in \mathcal{A}\}$. The derived ideals, the volume fraction relations and the actual exact relations corresponding to the complete list of Jordan algebras above have been computed. We will describe these results after we discuss the simplifications afforded by the links.

The links between effective tensors of two composites with the same microstructure are described by the subspaces $\widehat{\Pi} \subset V = \mathrm{End}(\mathbb{R}^3) \oplus \mathrm{End}(\mathbb{R}^3)$ satisfying

$$\widehat{\boldsymbol{P}}' *_{\widehat{\boldsymbol{A}}} \widehat{\boldsymbol{P}}'' \in \widehat{\Pi} \tag{4}$$

for all $\{\widehat{\boldsymbol{P}}', \widehat{\boldsymbol{P}}''\} \subset \widehat{\Pi}$ and all $\widehat{\boldsymbol{A}} \in \widehat{\mathcal{A}} = \{[\boldsymbol{A}, \boldsymbol{A}] : \boldsymbol{A} \in \mathcal{A}\}$. In other words, $\widehat{\Pi}$ consists of pairs $\widehat{\boldsymbol{P}} = [\boldsymbol{P}_1, \boldsymbol{P}_2]$ forming a Jordan algebra with respect to the multiplication

$$\widehat{\boldsymbol{P}}' *_{\widehat{\boldsymbol{A}}} \widehat{\boldsymbol{P}}'' = \left[\boldsymbol{P}_1' *_{\boldsymbol{A}} \boldsymbol{P}_1'', \boldsymbol{P}_2' *_{\boldsymbol{A}} \boldsymbol{P}_2''\right].$$

All the subspaces $\widehat{\Pi}$, corresponding to links can be described in terms of the algebraic structure of the solutions Π of (2) (see [9] for more details). If $\widehat{\Pi}$ satisfies (4) then the canonical projections

$$\Pi_1 = \left\{\boldsymbol{P}_1 : [\boldsymbol{P}_1, \boldsymbol{P}_2] \in \widehat{\Pi},\ \text{for some } \boldsymbol{P}_2\right\}, \quad \Pi_2 = \left\{\boldsymbol{P}_2 : [\boldsymbol{P}_1, \boldsymbol{P}_2] \in \widehat{\Pi},\ \text{for some } \boldsymbol{P}_1\right\}.$$

are solutions of (2). The kernels of these canonical projections

$$\mathcal{I}_1 = \left\{ \boldsymbol{P}_1 \in \Pi_1 : [\boldsymbol{P}_1, \boldsymbol{0}] \in \widehat{\Pi} \right\}, \quad \mathcal{I}_2 = \left\{ \boldsymbol{P}_2 \in \Pi_2 : [\boldsymbol{0}, \boldsymbol{P}_2] \in \widehat{\Pi} \right\}$$

are Jordan ideals in Π_1 and Π_2 respectively. Moreover, the subspace $\widehat{\Pi}$ induces the Jordan algebra isomorphism between factor-algebras $\Pi_1/\mathcal{I}_1$ and $\Pi_2/\mathcal{I}_2$. This isomorphism maps an equivalence class $[\![\boldsymbol{P}_1]\!] \in \Pi_1/\mathcal{I}_1$ into an equivalence class $[\![\boldsymbol{P}_2]\!]$, where $[\boldsymbol{P}_1, \boldsymbol{P}_2] \in \widehat{\Pi}$. Therefore, we can describe all solutions $\widehat{\Pi}$ of (4) if we can find all the isomorphic pairs $\Pi_1/\mathcal{I}_1$ and $\Pi_2/\mathcal{I}_2$ and all of their isomorphisms. This task has been accomplished (see [7]).

In order to formulate the final and complete list of all exact relations and links for fiber-reinforced conducting composites in a concise form, we eliminate those relations and links that can be obtained by combining several other relations. The following is a complete non-redundant list of all microstructure-independent relations.

4. EXACT RELATIONS AND LINKS

1.

$$\begin{aligned} &\boldsymbol{\Lambda}' = \tau_0 \boldsymbol{\Psi}(\boldsymbol{\Lambda}) + r_0' \boldsymbol{S}, \ \boldsymbol{p}' = \boldsymbol{p}_0' + \mu_0 \boldsymbol{\Psi}(\boldsymbol{\Lambda})(\boldsymbol{p} - \boldsymbol{p}_0)^\perp, \ \boldsymbol{q}' = \boldsymbol{q}_0' + \nu_0 \boldsymbol{\Psi}(\boldsymbol{\Lambda})^T (\boldsymbol{q} - \boldsymbol{q}_0)^\perp, \\ &\alpha' = \alpha_0 + \tfrac{\mu_0 \nu_0}{\tau_0} \left\{ (\boldsymbol{\Psi}(\boldsymbol{\Lambda})(\boldsymbol{p} - \boldsymbol{p}_0)^\perp, (\boldsymbol{q} - \boldsymbol{q}_0)^\perp) - \alpha \right\}, \quad \boldsymbol{\Psi}(\boldsymbol{\Lambda}) = \tfrac{(\boldsymbol{\Lambda} - r_0 \boldsymbol{S})^T}{\det(\boldsymbol{\Lambda} - r_0 \boldsymbol{S})}, \end{aligned} \tag{5}$$

where $\boldsymbol{S} = \begin{bmatrix} 0 & -1 \\ 1 & 0 \end{bmatrix}$ and $\boldsymbol{a}^\perp = \boldsymbol{S}\boldsymbol{a} = (-a_2, a_1)$. Here r_0, r_0', τ_0, μ_0, ν_0, α_0 are arbitrary constants and $\boldsymbol{p}_0$, $\boldsymbol{q}_0$, $\boldsymbol{p}_0'$, $\boldsymbol{q}_0'$ are arbitrary vectors in $\mathbb{R}^2$.

2.

$$\begin{aligned} &\boldsymbol{\Lambda}' = \tau_0 \boldsymbol{\Lambda} + r_0' \boldsymbol{S}, \quad \boldsymbol{p}' = \boldsymbol{\Lambda}\boldsymbol{p}_0 + \mu_0 \boldsymbol{p} + \boldsymbol{p}_0', \quad \boldsymbol{q}' = \boldsymbol{\Lambda}^T \boldsymbol{q}_0 + \nu_0 \boldsymbol{q} + \boldsymbol{q}_0', \\ &\alpha' = \tau_0^{-1} \left\{ \mu_0 \nu_0 \alpha + \mu_0 (\boldsymbol{p}, \boldsymbol{q}_0) + \nu_0 (\boldsymbol{q}, \boldsymbol{p}_0) + (\boldsymbol{\Lambda}\boldsymbol{p}_0, \boldsymbol{q}_0) \right\} + \alpha_0, \end{aligned} \tag{6}$$

The link (6) is a limiting case of the link (5), when some of the parameters in (5) go to infinity.

3. The effective tensor $\boldsymbol{L}^*$ enjoys the "transpose symmetry", [15, Proposition 2], $(\boldsymbol{L}^T)^* = (\boldsymbol{L}^*)^T$.

4. $\boldsymbol{\Lambda}^*$ depends only on $\boldsymbol{\Lambda}(\boldsymbol{x})$ and not $\boldsymbol{p}$, $\boldsymbol{q}$ or α. It is computed as an effective conductivity of the 2D periodic composite with local conductivity $\boldsymbol{\Lambda}(\boldsymbol{x})$. Also, $\boldsymbol{p}^*$ depends only on $\boldsymbol{\Lambda}(\boldsymbol{x})$ and $\boldsymbol{p}(\boldsymbol{x})$.

5. If the constituents of the fiber-reinforced composite do not exhibit transversal Hall effect, i.e., $\boldsymbol{\Lambda}(\boldsymbol{x}) = \boldsymbol{\sigma}(\boldsymbol{x})$ is symmetric, then

$$\begin{bmatrix} \boldsymbol{\sigma} & \boldsymbol{p} + \boldsymbol{q} \\ \boldsymbol{q} & \alpha \end{bmatrix}^* = \begin{bmatrix} \boldsymbol{\sigma}^* & \boldsymbol{p}^* + \boldsymbol{q}^* \\ \boldsymbol{q}^* & \alpha^* \end{bmatrix}, \text{ where } \begin{bmatrix} \boldsymbol{\sigma} & \boldsymbol{p} \\ \boldsymbol{q} & \alpha \end{bmatrix}^* = \begin{bmatrix} \boldsymbol{\sigma}^* & \boldsymbol{p}^* \\ \boldsymbol{q}^* & \alpha^* \end{bmatrix}. \tag{7}$$

6. If $\boldsymbol{p}(\boldsymbol{x}) = \boldsymbol{p}_0$ then $\boldsymbol{p}^* = \boldsymbol{p}_0$ and $\alpha^* = \langle \alpha \rangle$.

7. If $\boldsymbol{\Lambda}(\boldsymbol{x})\boldsymbol{e}_0 = \boldsymbol{j}_0$ then $\boldsymbol{\Lambda}^*\boldsymbol{e}_0 = \boldsymbol{j}_0$ and $(\boldsymbol{q}^*, \boldsymbol{e}_0) = (\langle \boldsymbol{q} \rangle, \boldsymbol{e}_0)$.

8. If $\boldsymbol{\Lambda}(\boldsymbol{x}) = \boldsymbol{\Lambda}_0$ then $\boldsymbol{\Lambda}^* = \boldsymbol{\Lambda}_0$, $\boldsymbol{p}^* = \langle \boldsymbol{p} \rangle$ and $\boldsymbol{q}^* = \langle \boldsymbol{q} \rangle$.

The properties (5) and (6) are not immediately readable off the formulas (1), even though (6) can be proved by substituting the expressions for $\boldsymbol{\Lambda}'$, $\boldsymbol{p}'$, $\boldsymbol{q}'$ and α' into (1). The remaining microstructure-independent relations are easy to prove using formulas (1). However, it is not clear how starting with (1) one can *generate* all items on our list.

In this connection we must mention the work of Bergman and Strelniker [1, 2, 16, 17], who extended ideas of duality of Dykhne [3], Keller [11], Mendelson [12] and Milton [13] and obtained many exact reactions in the present context, at least for the case of two and three-component composites.

ACKNOWLEDGMENT

The author is grateful for the efforts of fourteen talented undergraduates, who have participated in the REU program under his direction in 2002–2004. They are (in alphabetical order) Erin R. Blew, David Carchedi, Edward Corcoran, Ryan Fuoss, Joseph Galante, Jerome Hodges IV, Russell Howes, Matthew Jacobs, Matthew Macauley, John Quah, Austin Roberts, Elianna Ruppin, Steven Stewart, Peter Tom-Wolverton. This material is based upon work supported by the National Science Foundation under Grants NSF-0138991 (REU), NSF-0094089 and NSF-0707582.

REFERENCES

1. Bergman, D. J. and Y. M. Strelniker, "Duality transformation in a three dimensional conducting medium with two dimensional heterogeneity and an in-plane magnetic field," *Phys. Rev. Lett.*, Vol. 80, No. 15, 3356–3359, Apr. 1998.
2. Bergman, D. J. and Y. M. Strelniker, "Magnetotransport in conducting composite films with a disordered columnar microstructure and an in-plane magnetic field," *Phys. Rev. B*, Vol. 60, No. 18, 13016–13027, Nov. 1999.
3. Dykhne, A. M., "Conductivity of a two-dimensional two-phase system," *Sov. Phys. JETP*, Vol. 32, 63–65, 1971. [Zh. Eksp. Teor. Fiz, 59, 110–115, 1970.].
4. Grabovsky, Y., "Exact relations for effective tensors of polycrystals I: Necessary conditions," *Arch. Ration. Mech. Anal.*, Vol. 143, No. 4, 309–330, 1998.
5. Grabovsky, Y., "Algebra, geometry and computations of exact relations for effective moduli of composites," In G. Capriz and P. M. Mariano, editors, *Advances in Multifield Theories of Continua with Substructure (Modeling and Simulation in Science, Engineering and Technology)*, 167–197, Birkhäuser, Boston, 2004.
6. Grabovsky, Y., "An application of the general theory of exact relations to fiber reinforced conducting composites with Hall effect," *Mechanics of Materials*, To appear.
7. Grabovsky, Y., "Exact relations for effective conductivity of fiber-reinforced conducting composites with Hall effect via a general theory," submitted.
8. Grabovsky, Y. and G. W. Milton, "Exact relations for composites: Towards a complete solution," *Doc. Math. J. DMV*, Extra Volume ICM III, 623–632, 1998.
9. Grabovsky, Y., G. W. Milton, and D. S. Sage, "Exact relations for effective tensors of polycrystals: Necessary conditions and sufficient conditions," *Comm. Pure. Appl. Math.*, Vol. 53, No. 3, 300–353, 2000.
10. Grabovsky, Y. and D. S. Sage, "Exact relations for effective tensors of polycrystals. II: Applications to elasticity and piezoelectricity," *Arch. Ration. Mech. Anal.*, Vol. 143, No. 4, 331–356, 1998.
11. Keller, J. B., "A theorem on the conductivity of a composite medium," *J. Math. Phys.*, Vol. 5, 548–549, 1964.
12. Mendelson, K. S., "A theorem on the conductivity of two-dimensional heterogeneous medium," *J. Appl. Phys.*, Vol. 46, 4740–4741, 1975.
13. Milton, G. W., "Classical hall effect in two-dimensional composites: A characterization of the set of realizable effective conductivity tensors," *Physical Review B*, Vol. 38, No. 16, 11296–11303, Dec. 1988.
14. Milton, G. W., "The theory of composites," *Cambridge Monographs on Applied and Computational Mathematics*, Vol. 6, Cambridge University Press, Cambridge, 2002.
15. Murat, F. and L. Tartar, "H-convergence," *Topics in the Mathematical Modelling of Composite Materials*, 21–43, Birkhäuser Boston, Boston, MA, 1997.
16. Strelniker, Y. M. and D. J. Bergman, "Exact relations between magnetoresistivity tensor components of conducting composites with a columnar microstructure," *Phys. Rev. B*, Vol. 61, No. 9, 6288–6297, Mar. 2000.
17. Strelniker, Y. M. and D. J. Bergman, "Exact relations between macroscopic moduli of composite media in three dimensions: Application to magnetoconductivity and magneto-optics of three-dimensional composites with related columnar microstructures," *Phys. Rev. B*, Vol. 67, No. 18, 184416, May 2003.

Models and Devices Based on Thin-layer Metamaterials

A. N. Lagarkov and V. N. Kisel
Institute for Theoretical and Applied Electromagnetics
Izhorskaya 13, Moscow 125412, Russia

Abstract— The review paper highlights some of the results of the ITAE studies into the theory and application of the thin-layer metamaterials, including structures that reveal the phenomenon of superresolution. It is noted that in many cases the rigorous electromagnetic models are much more suitable to investigate electromagnetic phenomena in metamaterials as compared to the homogenization theories, especially when considering the fields of the filamentary sources located nearby a thin-layer composite plate, the inclusion dimensions of which are close to the plate thickness. The superresolution is shown to emerge here due to the selective response of the composite cell to the different (propagating and evanescent) components of the incident field. The similarity and differences in the performance of realistic composite and hypothetic homogeneous metasubstance are outlined. Several conclusions are made with regards to the possibilities to compensate the metamaterial losses by means of incorporating active portions into a metasubstance or installing active devices into inclusions of a realistic composite; as was shown, these possibilities are quite different. The discussed theoretical and experimental results show numerous fields to utilize thin-layer metamaterials as a low-profile broad-angle absorbers, thin open resonators etc, which may be used to engineer advanced microwave devices and solve the electromagnetic compatibility and security problems.

1. INTRODUCTION

Suitability of Some Simulation Techniques

In recent years, the attention of numerous research groups working in physics and electromagnetics has been focused on studying metamaterials, i.e., materials with specific properties which are rarely or neither observable in nature, for example, the substances with negative permittivity ε and permeability μ. This paper discusses some of the results of the ITAE studies into the theory and application of the thin-layer shaped metamaterials.

A wide variety of techniques can be applied to analyze electromagnetic excitation of metamaterials, e.g., eigenfunction expansions (EE), volume integral equations (VIE) etc. Investigations revealed that no specific restrictions arise when using methods based on integral equation or EEs to study electromagnetic phenomena in the presence of a matter with negative real parts of ε and μ. Care should be taken only in calculating multi-valued functions of complex arguments. In this connection let's note that one can readily choose the proper Riemann sheet provided the complex wavenumber is evaluated as $k = \sqrt{\varepsilon}\sqrt{\mu}$ (instead of a conventional formula $k = \sqrt{\varepsilon\mu}$), the terms like $\sqrt{k^2 - \nu^2}$ which enter the integral expansions of the fields should be calculated as a product $\sqrt{k-\nu}\sqrt{k+\nu}$ and so on. To our mind, the method of VIEs can yield in highly reliable results. This is because the fields of polarization currents can always be expressed via Green's function of the free space, and in this case ε and μ appear in the VIE only as factors like $(\varepsilon - 1)$ and $(\mu - 1)$, not in the arguments of multi-valued functions. Likewise, no additional (derived) properties of the medium, e.g., wavenumber or intrinsic impedance, are entered into the problem. However, the wide application of VIEs is restricted by their high demands to the computer resources (memory, calculation time); therefore after mutual verification of the test results we carried out the investigations of the flat or cylindrical structures mainly by means of the efficient analytical or EEs-based techniques. Sometimes we had to use more cumbersome rigorous methods, particularly, to study in details the excitation of a complicated electromagnetic system (composite) taking into account all mutual interaction between its inclusions.

2. FOCUSING SYSTEMS AND DEVICES WITH SUPERRESOLUTION

A lot of important applications make use of the thin-layer shaped metamaterials, the focusing device based on a flat plate made of metasubstance ("Veselago's lens") [1] being one of the most exciting examples of such kind. Not long ago several options were proposed to create composites with the suitable effective properties [2–7]. At the same time a great idea was expressed by Prof. J. B. Pendry [8] about the possibility of overcoming so called "diffraction limit" (image detailing of order half a wavelength) by the use of the Veselago's lens which was shown to exhibit a

growth of the evanescent components of a point source radiation with the result of restoring the fine details of an image. It is important to note that the required magnitudes of evanescent modes are achieved there due to the phenomenon of the reactive energy accumulation nearby a flat interface between the outer space and the metasubstance. Shortly after that several research groups [9–14] almost simultaneously elucidated the crucial role of the material losses in the possibility of imaging with superresolution. However, in [13, 14] an important detail was noted and explored, namely, the analysis of obtained expressions indicated that the use of electrically thin metamaterial plates brings about a drastic reduction of loss requirements. Mostly thanks to that conclusion the requirements to the experimental setup have been established and registration of superresolution effect has turned possible to be achieved in laboratory conditions [15, 16], where distinct imaging of the filamentary sources spaced by one sixth of a wavelength was reported.

3. METASUBSTANCE AND METAMATERIAL

Note, however, that regardless of potential efficiency, the use of effective parameters is hardly self-evident as a correct tool for studying the wave propagation in thin-layer metamaterials. For example, it was shown in [17] that, in the case of composites containing extended resonant inclusions, one can introduce the effective permittivity only for sheet materials whose thickness exceeds some critical value and, generally speaking, the value of permittivity may differ depending on the experimental conditions (see also the discussion in [18]). To demonstrate some characteristic features of electromagnetic wave propagation in a real composite and expose the aspects which turn out to be hidden when the effective parameters are used in Maxwell equations we applied a rigorous approach (integral equation method) to obtain a full-wave solution for the electromagnetic fields [19, 20]. We started from the results of numerical simulation obtained for a composite plate with a finite number of elements which corresponds to that of a real experimental sample [16]. There the experimental "superlens" was provided by a plate of a composite material filled with resonant elements as spirals with a small pitch and linear half-wave segments of copper wire, excited by the magnetic and electric components, respectively, of a field generated by two linear wire radiators.

Thus, some theoretical predictions based on the concept of the uniform plate made of hypothetical metasubstance have led us to the design of a passive device which, indeed, revealed the expected phenomenon of superresolution. However, it would be rather doubtful to identify the electromagnetic processes occurring in an experimental composite plate with the electromagnetic wave transmission through a layer of homogeneous (perfect) metasubstance with $\varepsilon < 0$ and $\mu < 0$. One of the obvious reasons for this is the discrete structure of the composite. It is known [15] that, in regular structures, the value of the lattice spacing constrains the limiting resolution of the system. In this case, however, one more fact is worthy of note. As was mentioned above, one can count on the manifestation of the effect of superresolution only when thin plates with low loss are employed; therefore, in the setup described above, the plate consisted of only one layer of resonators. It is hard to set up a correspondence between this structure and a plate of homogeneous material, even if because of the absence of clearly defined boundaries of the composite in the transverse direction. One can assume that the location of these (conventional) boundaries must depend on the characteristic features of distribution of the electromagnetic field in the vicinity of inclusions. Then, one must not rule out the possibility that the electromagnetic process in a thin-layer composite plate differs significantly from phenomena occurring in a homogeneous material; as a result, the usage of the effective parameters of the medium ε and μ will turn out to be invalid. In any case, a traditional Fresnel coefficients or a ray-based approaches seem to be really inadequate when we consider the interaction of the field of a point-like source with a thin composite plate consisting of one layer of resonators.

In order to construct the computational model, an equation of the Pocklington type was used, which is based on a thin-wire approximation with regard for the finite conductivity of the wire metal including the skin effect. Because of using integral equation approach, we were able to take into account all mutual interactions between the composite cells. In the course of numerical simulation it was demonstrated that a plate of a composite exhibits some properties typical of a plate of metasubstance. For example, a frequency band exists (as predicted by theory, it is located in the vicinity of and a little higher than the resonance frequency of inclusions) in which the effect of superresolution shows up. The composite plate proper may be by and large characterized as a device, in which a backward wave exists, i.e., there is a zone of space in the vicinity of resonators in which the phase and group velocities are opposite to each other.

However, one could easily note the differences in the field distribution between a thin composite plate and a plate of metasubstance. For example, in a system with a homogeneous plate with $\varepsilon = \mu = -1$, the phase and group velocities bear different signs only within the plate, and a strong excitation of the linear wires of the composite plate leads to the emergence of a zone with negative phase velocity outside of the geometric bounds of the structure (the results of calculations are given in [19, 20]). It is further known (e.g., [16, 21]) that, when a plane-parallel plate of metasubstance is excited, the reactive energy of evanescent modes accumulates in the vicinity of the interfaces (first of all, in the neighborhood of the unilluminated face of the plate), owing to which the superresolution may be realized. No such interfaces exist in the experimental plate; however, resonance phenomena are present, and the field energy accumulates within and in the vicinity of individual resonators (a maximum of the accumulated reactive energy is attained in the central part of the composite plate in the vicinity of the axial lines of inclusions).

Suggested in [19] explanation of the imaging with superresolution by a realistic metamaterial plate is based on the selective response of the composite cell (coupled linear wire and ring) to the propagating and evanescent modes of the incident field. Emphasizing the evanescent components appears possible due to the specific phase shift of 90 degrees between E and H vectors and corresponding peculiarities of the electromagnetic interference in the system (details are given in [19, 20]). Of course, the resonant properties of the inclusions (at sufficiently low losses) facilitate their magnitude to get raised.

Thus, the main differences in the pictures of the field distribution, which are registered in composite materials and in plates of homogeneous metasubstance, are defined by the characteristic features of the employed resonators, in particular, by the degree of their electromagnetic coupling with the environment, by the number of layers in the transverse direction of the plate, and (to a lesser extent) by the discrete structure of the composite. Because the field of resonators extends significantly beyond the geometric bounds of the sample (including the zone of location of radiators and the zone of measurements), there is no point in using the effective values of the parameters ε and μ in the considered case; investigation of the fields nearby and inside the composite metamaterial should be carried out by means of the full-wave solution of the electromagnetic boundary problem.

4. COMPENSATION OF THE LOSSES IN A METAMATERIAL

The difference between metamaterial and metasubstance may be important when studying the possibilities to compensate the metamaterial losses by means of incorporating active portions into a metasubstance or switching active devices in the inclusions of a realistic composite; as was clarified, these possibilities are considerably different. Let's discuss this issue in more details.

Typically, metamaterial inclusions are made of metals, and their imperfectness becomes especially significant at extreme high frequencies thus making the problem to reduce absorption even more important. There are suggestions [22, 23] to offset the losses in metamaterial inclusions by using an active medium in order to reach the superresolution in an optical regime, however, it remains unclear how the composite structure discontinuity would affect the attainable degree of the compensation of losses, what are the features of unavoidable distortions of the electromagnetic field inside the metamaterial and whether it is possible to reach the optical superresolution eventually through that way.

We made an attempt to evaluate the compensating and distorting effects of the active inclusions distributed over the metamaterial plate. This was done by means of numerical simulation of the imaging of two closely spaced sources with the Veselago-Pendry lens. Two different arrangements were considered, first, a lens made of a hypothetic absorptive metasubstance with, e.g., $\varepsilon = \mu = -1 - i0.2$, and, second, a flat lens made of realistic composite filled with resonant rings and linear wires (similar device was used earlier to achieve superresolution in a microwave experiment [16]). To simulate active inclusions immersed into metasubstance we used small local insets of an "amplifying" dielectric with negative losses, e.g., $\varepsilon = \mu = -1 + i0.05$. Active devices of the realistic composite were simulated via capacitors switched in the resonant rings and linear wires, the losses of capacitors also being taken negative.

Our numerical investigations demonstrated that provided sufficiently small (e.g., about $\lambda/150$) active inclusions are packed densely in an absorptive metasubstance, one should be able to compensate losses with a great success; the quality of an image developed by a "thick" Veselago-Pendry lens would be enhanced significantly. Unfortunately, it is not the case when active devices are switched in much bigger inclusions of a realistic composite which are necessarily distributed so that the distance between them is only few times less than the separation of the sources to be imaged.

Serious corruption of the field picture inside the composite plate occurs, and the lower the metal conductivity, the bigger distortions are observed. Finally, accounting for the constitutive properties of metals under optical illumination and for the realistic dimensions of inclusions (approximately tenths of a wavelength) we quite hardly foresee the possibilities for the active compensation of losses to achieve a distant superresoltion in an optical regime, as far as about few wavelengths from the source.

5. THIN-LAYER METAMATERIALS AS ABSORBERS AND OPEN RESONATORS

At the same time there are numerous applications where the losses inherent to the metamaterials can be successfully utilized. As early as in [24, 25] we noted that metamaterials can demonstrate superiority over the ordinary materials when being used as electromagnetic absorbers. This can be possible because artificial materials can be engineered in such a way as to impart them some special properties, neither observed in the nature. For example, one can hope to obtain a considerable electromagnetic energy absorption in a coating without its strong mismatching to the outer space. At the same time, such an absorber can be thin, lightweight while offering good service performance. Unfortunately, the unique properties of metamaterials are observed in a rather narrow frequency band, but many of the coatings made of ordinary materials are also relatively narrow-band [26].

However, there are numerous applications (e.g., solution of the electromagnetic compatibility problems) where a wide angular range of the effective operation of the coating is of primary importance. And this is the case when one can greatly benefit from using metamaterials.

Let's consider a simple model problem of investigating the radiation of a point-like (or filamentary) source placed above an infinite conducting plane coated with an absorbing layer. Evidently, at the absence of the coating the energy radiated by the source is totally transmitted into the outer (free) half-space. As to the other extreme case, when a "perfect" non-reflecting coating is applied, the considered omnidirectional source radiates equal portions of electromagnetic energy into upper and lower half-spaces; the same is true when no coated plane is located in the lower half-space at all. Here exactly one half of a radiated power is transmitted into the upper half-space. In contrary, we shown recently [27, 28] that a metamaterial-based coating can be created in such a way that it will secure the *total* suppression of the field emitted by the source in the upper half-space, correspondingly, all radiated power will be transferred into the lower half-space and absorbed therein. Thus, no outgoing radiation will be observed in the outer region from an omnidirectional source placed above a conducting plane with a properly designed metamaterial coating.

Along with the field cancellation in the outer half-space, the regions with a high field concentration due to accumulating reactive energy come into being nearby the metamaterial layer. Due to this particular feature one can design novel open resonators without usual restrictions on the thickness of the system in terms of a wavelength [27]. Besides it, a set of novel absorbers of the energy of a plane electromagnetic wave can be engineered making use of the thin-layer metamaterials. Special absorption properties of these coatings can be achieved by means of arranging a wave path so as to cross the metamaterial structure with the result of suitable phase compensation. Particularly, the total phase advance of the wave going through the coating can be made equal to zero irrespectively of the incident angle, therefore, it is possible to achieve a very broad angular range in which such an absorber should operate efficiently, in contrast to classical designs. Finally, as there are no fundamental physical restrictions on the thickness of the described absorber, it can be made electrically thin (at least, in principle). Our experimental investigations [28] supported these theoretical suggestions and revealed the expected outstanding angular properties of the metamaterial-based absorbers.

REFERENCES

1. Veselago, V. G., "The electrodynamics of substances with simultaneously negative values of ε and μ," *Sov. Phys. Usp.*, Vol. 10, 509, 1968.

2. Smith, D. R., W. J. Padilla, D. C. Vier, S. C. Nemat-Nasser, and S. Schultz, "Composite medium with simultaneously negative permeability and permittivity," *Phys. Rev. Lett.*, Vol. 84, 4184, 2000.

3. Lagarkov, A. N., V. N. Semenenko, V. A. Chistyaev, D. E. Ryabov, S. A. Tretyakov, and C. R. Simovski, "Resonance properties of bi-helix media at microwaves," *Electromagnetics*, Vol. 17, 213, 1997.

4. Lagarkov, A. N., V. N. Semenenko, V. N. Kisel, and V. A. Chistyaev, "Development and simulation of microwave artificial magnetic composites utilizing nonmagnetic inclusions," *Journ. Magnetism Magn. Materials*, Vol. 258–259, 161, 2003.
5. Antonov, A. S., V. M. Batenin, A. P. Vinogradov, et al., *Electrophysical Properties of Percolation Systems*, Ed. by A. N. Lagarkov, Institute for High Temperatures, Academy of Sciences, USSR, Moscow, 1990, (in Russian).
6. Lagarkov, A. N., A. K. Sarychev, Y. R. Smychkovich, and A. P. Vinogradov, "Effective medium theory for microwave dielectric constant and magnetic permeability of conducting stick composites," *Journal of Electromagnetic Waves and Applications*, Vol. 6, No. 9, 1159, 1992.
7. Eleftheriades, G. V., A. K. Iyer, and P. C. Kremer, "Planar negative refractive index media using periodically L-C loaded transmission lines," *IEEE Trans. Microwave Theory and Techniques*, Vol. 50, 2702, 2002.
8. Pendry, J. B., "Negative refraction makes a perfect lens," *Phys. Rev. Lett.*, Vol. 85, 3966, 2000.
9. Fang, N. and X. Zhang, "Imaging properties of a metamaterial superlens," *Appl. Phys. Lett.*, Vol. 82, No. 2, 161, 2003.
10. Smith, D. R., D. Schurig, M. Rosenbluth, S. Schultz, S. A. Ramakrishna, and J. B. Pendry, "Limitations on sub-diffraction imaging with a negative refractive index slab," *Appl. Phys. Lett.*, Vol. 82, No. 10, 1506, 2003.
11. Ong, C. K. and X. S. Rao, "Resolution enhancement of a left-handed material superlens," *Electromagnetic Materials. Proc. of the Symp. F, ICMAT 2003*, 123, World Scientific Publishing Co, Singapore, 2003.
12. Rao, X. S. and C. K. Ong, "Subwavelength imaging by a left-handed material superlens," *Phys. Rev. E*, Vol. 68, 067601, 2003.
13. Kissel, V. N. and A. N. Lagarkov, "A study into the possibility of field focusing using 'left-handed' materials," *Electromagnetic Materials. Proc. of the Symp. F. ICMAT 2003*, 145, World Scientific Publishing Co, 2003.
14. Lagar'kov, A. N. and V. N. Kisel', "Quality of focusing electromagnetic radiation by a plane-parallel slab with a negative index of refraction," *Doklady Physics*, Vol. 49, No. 1, 5–10, 2004.
15. Lagarkov, A. N. and V. N. Kissel, "Numerical and experimental investigation of the superresolution in a focusing system based on a plate of "left-handed" material," *Electromagnetic Materials. Proc. of the Symp. F. ICMAT 2003*, 157, World Scientific Publishing Co, 2003.
16. Lagarkov, A. N. and V. N. Kissel, "Near-perfect imaging in a focusing system based on a left-handed-material plate," *Phys. Rev. Lett.*, Vol. 92, 077401, 2004.
17. Vinogradov, A. P., D. P. Makhnovskii, and K. N. Rozanov, "Effective boundary layer in composite materials," *J. Communications Technology and Electronics*, Vol. 44, 317, 1999.
18. Liu, L., S. M. Matitsine, Y. B. Gan, and K. N. Rozanov, "The thickness dependence of resonance frequency in anisotropic composites with long conductive fibers," *Electromagnetics*, Vol. 25, 69, 2005.
19. Kissel, V. N. and A. N. Lagarkov, "Superresolution in left-handed composite structures: From homogenization to a detailed electrodynamic description," *Phys. Rev. B*, Vol. 72, 085111, 2005.
20. Lagarkov, A. N. and V. N. Kisel, "Metamaterials and superresolution: From homogenization to rigorous approach," *Physica B*, Vol. 394, No. 2, 163, 2007.
21. Cui, T. J., Z.-C. Hao, X. Yin, X. Hong, and J. A. Kong, "Study of lossy effects on the propagation of propagating and evanescent waves in left-handed materials," *Physics Letters A*, Vol. 323, 484, 2004.
22. Caloz, C. and T. Itoh, *Electromagnetic Metamaterials: Transmission Line Theory and Microwave Applications. The Engineering Approach*, Wiley-Interscience, New York, 2006.
23. Sarychev, A. K. and V. M. Shalaev, *Electrodynamics of Metamaterials*, World Scientific, Singapore, 2007.
24. Lagarkov, A. N. and V. N. Kisel, "Electrodynamic properties of simple bodies made of materials with negative permeability and negative permittivity," *Doklady Physics*, Vol. 46, No. 3, 163–165, 2001.
25. Kisel, V. N. and A. N. Lagarkov, "Electromagnetic wave scattering from bodies made of materials with negative index of refraction," *Electromagnetic Waves and Electronic Systems*, Vol. 7, No. 7, 62, Russian, 2002.
26. Vinoy, K. J. and R. M. Jha, *Radar Absorbing Materials: From Theory to Design and Characterization*, Kluwer Academic, Boston, 1996.

27. Kisel, V. N. and A. N. Lagarkov, "Near perfect absorption by a flat metamaterial plate," *Phys. Rev. E*, Vol. 76, 065601, 2007.
28. Lagarkov, A. N., V. N. Kisel, and V. N. Semenenko, "Wide-angle absorption by the use of a metamaterial plate," *Progress In Electromagnetics Research Letters*, Vol. 1, 35, 2008.

Simultaneous Switching Noise Mitigation in High-speed Circuits Using Ring-type High-impedance Surface Structures

Chin-Sheng Chang[1], **Ding-Bing Lin**[2], **Kuo-Chiang Hung**[2]
I-Tseng Tang[3], **and Mau-Phon Houng**[1]

[1]Institute of Microelectronics, Department of Electrical Engineering
Advanced Optoelectronic Technology Center, National Cheng-Kung University
Tainan 701, Taiwan
[2]Institute of Computer and Communication Engineering
National Taipei University of Technology, Taipei, Taiwan
[3]Department of Environment and Energy, Nation University of Tainan, Tainan, Taiwan

Abstract— In this work, we presents a novel design for ring-type high-impedance surface structures (R-HIS) embedded in printed circuit boards. It is capable of selectively suppressing the simultaneously switching noise (SSN) at several desired frequencies. The suppression range of proposed structures is from dc to 1.56 GHz. The proposed structure is effective to reduce EMI, as well as to ensure signal integrity (SI) issues.

1. INTRODUCTION

With fast edge rates, high clock frequencies, and low voltage levels, one of the major concerns for the high-speed circuits is simultaneous switching noise (SSN) also known as ground bounce noise (GBN) or Delta-I noise on the power and ground planes. The resonance modes of the parallel-plate waveguide can be excited by SSN. This resonance noise propagating between the power and ground planes will induce serious signal integrity (SI) or electromagnetic interference (EMI) problems.

Several researchers have contributed to suppress the SSN. Isolation moat is a typical method to eliminate SSN from dc to several hundred megahertz. A bridge electrically connecting the power planes of the isolated region and the rest area is necessary to eliminate the EMI problem by supplying the RF return current for signal traces crossing the moat [1]. But the SSN could be transferred to outside of the slits through the connecting bridges. Adding decoupling capacitors between power and ground planes is another efficiently method to suppress the noise. This method provides a low impedance path leading noise to ground. However, the wideband suppression behavior needs about one hundred capacitors to obtain [2, 3] and decoupling capacitors are not effective above several megahertz, due to the effective series inductance of the capacitors. In recent years, high-impedance surface (HIS) structures have been extensively studied in the high-speed circuits. Although the HIS structure provides wide stopband to eliminate the SSN in gigahertz [4]. But limited by low-period design, this structure could not be used in the frequency below 1 GHz.

In this work, we proposed the R-HIS which embedded high impedance surface in the substrate. The surface impedance of ring-type HIS structure is frequency sensitive since the HIS structure actually constructs a LC network with specific resonant frequencies. The electromagnetic properties of the HIS unit cells can be described using lump-circuit elementscapacitors and inductors. In it resonator frequency range, the surface impedance is very low. It does not only provide SSN suppression behavior, but also keep the power and ground integrities.

2. STRUCTURE DESIGN AND SSN SUPPRESSION

Figure 1 shows the proposed structure. The power and ground plane are kept continuous and structures for ensuring the good signal integrity. The dimension of three-layer PCB is 100 mm × 100 mm. The dielectric constant of the substrate is 4.4 with a thickness of h_1 and h_2 are 0.8 and 0.4 mm, respectively. The top view HIS structure embedded in ground plane, which consists of a rectangular path with four vias each posted in the centers of each side of the ring-type HIS structure.

In this model, a simple LC series resonance equivalent circuit as shown in Figure 2, could be represented of the ring-type HIS structure. Hence, the impedance of the ring-type HIS is given as

$$Z_0 = j\left(\frac{1}{\omega C_1}\right) + j\left(\frac{1}{\omega L_v - \frac{1}{\omega L_v}}\right) = j\left(\frac{C_1}{\omega C_1}\right) + j\left(\frac{\omega L_v}{\omega^2 L_v C_2 - 1}\right) = j\left[\frac{\omega^2 L_v (C_1 + C_2) - 1}{(\omega C_1)(\omega^2 L_v C_2 - 1)}\right] \quad (1)$$

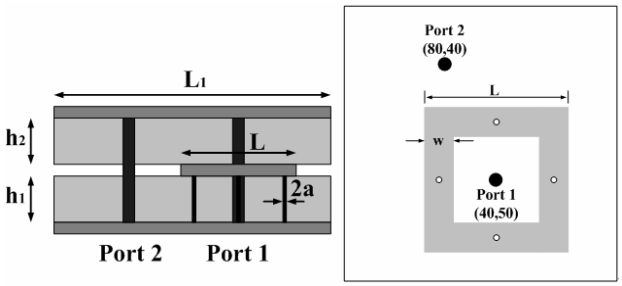

(a) (b)

Figure 1: The proposes testing board. (a) side view. (b) top view.

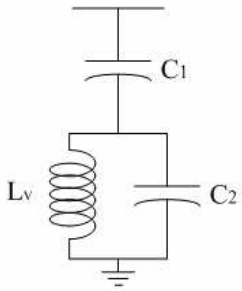

Figure 2: Compact model of the ring-type HIS.

where C_1 and C_2 represent the parallel-plate to patch capacitance and L_v is the inductance of vias. The self-resonance frequency of the ring-type is given as

$$\omega = \frac{1}{\sqrt{L_v\,(C_1 + C_2)}} \tag{2}$$

Table 1 lists the center frequency of ring-type HIS with difference patch size ($L \times W$). In first case, we varied patch length L with the patch width W fixed at 13 mm to observe the SSN suppression behavior. It is clearly seen that when the patch length is increased, the center frequency will be decreased. Because of the both effective inductance and capacitance are increased as the patch length increased. The second case, we focused on difference top layer thickness. Figure 3 shows the magnitude of S_{21} versus frequency with various substrate thicknesses. It is observed that the center frequency would be moved to lower frequency as the thickness decreased. When the top layer thickness is 0.2 mm, the center frequency is 0.71 GHz. The center frequency is closed to 1.1 GHz while the thickness is increased to 1 mm.

Table 1: Center frequency analysis of ring-type high-impedance surface.

Patch Size $L \times W$ (mm^2)	46×13	50×13	54×13	58×13	62×13
Center Frequency (GHz)	0.87	0.8	0.74	0.7	0.66

Figure 4 shows the measurement results of proposed structures with corresponding parameters of each side of the ring-type HIS are $a = 0.25$ mm, $W = 13$ mm, and $L = 54$ mm. The bandwidth is defined by $|S_{21}|$ lower than -20 dB. Comparison the SSN suppression capability with reference board, it is clearly seen that ring-type HIS structure significantly provided suppression of resonances in PCB boards. The power plane resonance noise on the reference board at 750 MHz was separated to two peaks that magnitudes were less than -20 dB at 690 MHz and 860 MHz by ring-type HIS structure. The measured result of proposed structure is from about 140 MHz to 1.56 GHz with

suppression bandwidth is 1.42 GHz. Although the SSN could be eliminated by isolation moat structure, a bridge electrically connecting the power planes of the isolated region and the rest area is necessary to eliminate the EMI problem. It can be shown that the ground bounce noise can be transferred to outside of the slits through the connecting bridges at the frequency about 470 MHz, as shown in Figure 4.

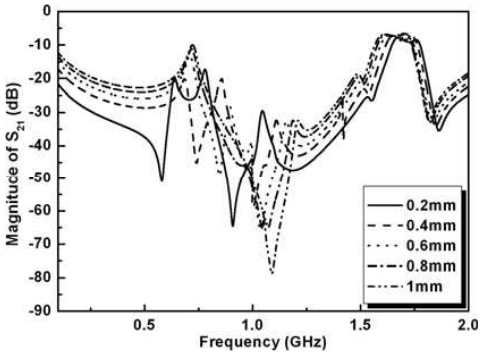

Figure 3: The magnitude of S_{21} versus frequency with varied h_2.

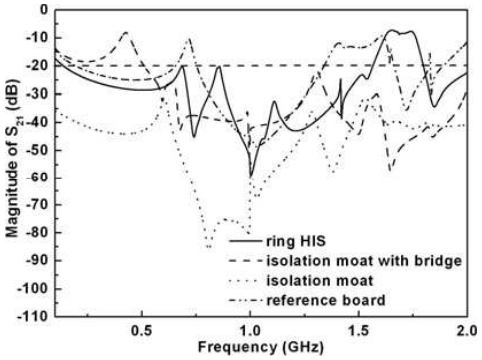

Figure 4: Comparison of the measured results between reference board, isolation moat, and ring-type HIS structure.

3. CONCLUSIONS

New types of embedded isolation moat structures for suppression of simultaneous switching noise in high-speed circuit have been proposed. Using the concept of ring-type HIS structures, the noise between power and ground planes can be significantly reduced. Compared with conventional isolation moat structure, proposed structure is effective to reduce EMI, as well as to ensure SI issues.

ACKNOWLEDGMENT

This work was supported by the National Science Council under the contracts NSC 96-2221-E-006-353-MY2.

REFERENCES

1. Hwang, J. N. and T. L. Wu, "The bridging effect of the isolation moat on the EMI caused by ground bounce noise between power/ground planes of PCB," *2001 IEEE EMC Symposium*, Vol. 1, 471–474, Montreal, Canada, Aug. 2001.
2. Archambeault, B. and A. E. Ruehli, "Analysis of power/ground-plane EMI decoupling performance using the partial-element equivalent circuit technique," *IEEE Transactions on Electromagnetic Compatibility*, Vol. 43, No. 4, 437–445, Nov. 2001.
3. Archambeault, B., "Analyzing power/ground plane decoupling performance using the partial element equivalent circuit (PEEC) simulation technique," *IEEE International Symposium on Electromagnetic Compatibility Symposium Record*, Vol. 2, 779–784, Washington, D.C., Aug. 21–25, 2000.
4. Sievenpiper, D., L. Zhang, R. F. J. Broas, N. G. Alexopolous, and E. Yablonovitch, "High-impedance electromagnetic surfaces with a forbidden frequency band," *IEEE Trans. Microw. Theory Tech.*, Vol. 47, No. 11, 2059–2074, Nov. 1999.

Design of High Performance FPGA Based Face Recognition System

I. Sajid, **M. M. Ahmed**, **I. Taj**, **M. Humayun**, **and F. Hameed**
Department of Electronic Engineering
Mohammad Ali Jinnah University, Islamabad, Pakistan

Abstract— A number of defense, security and commercial applications demand real time face recognition systems, especially when other biometric techniques are not feasible. Eigen values are widely used in engineering problems and particularly in face recognition algorithms. Floating point operations are used in Eigen values algorithms because Eigen values are highly sensitive for precision. Floating point operations are costly and complex in terms of hardware. Whereas fixed point technique with software hardware co-design (SHcoD) methodology reduces machine cycles and provides the flexibility in face recognition systems. It has been demonstrated that SHcoD concept can be used with dynamic partial reconfigurability to improve the conventional face recognition systems. An FPGA based novel design has been developed for efficient face recognition system which provides SHcoD, customization of algorithm and adaptability in the system. It has been shown that the proposed system is reasonably power efficient than floating point architecture and can be employed for portable applications.

1. INTRODUCTION

A number of defense, security and commercial applications demand real time face recognition systems [1], especially when other biometric techniques are not feasible. Finding a face from a video frame is one of the situations where face recognition may help reasonably. Human can easily and quickly identify this variance while machine is slower and error prone.

Now-a-days research has been focused the design and development of machine face recognition algorithms and their embedded implementation.

Mapping of matlab or C algorithm without modification in the software code on hardware, results may not be efficient or expected. Most of engineering applications uses Eigen values for projection of input data. Usually floating point operations are used in Eigen values algorithms, but they are costly and complex in terms of hardware [2]. Fixed-point implementation of floating-point operations is one of the classical techniques which may speed up the algorithm [3] with marginally lose in precision. Eigen values are highly depending upon precision of intermediate values. Trade-off between precision and efficiency would be analyzed for better use.

In the proposed system, RISC μ-processor decides of downloading the intellectual property IPs/functional units (FUs) at run time by observing instructions level demand. Downloading the memory FUs will enhance the on-chip memory, while arithmetic operation units may boost up the computing power.

Therefore a novel technique is being proposed which provides software-hardware co-design partitioning, customization of algorithm and adaptability in the system. In this technique energy, FPGA resources would be saved. The high level view of proposed system is presented in Fig. 2.

2. BACKGROUND

Biometric techniques/algorithms are not new methods for verification. Babylonian kings used clay finger prints for authenticity several year ago [4]. Egyptian used anatomical features like length of hand or half arm for biometric identification. Algorithm for face recognition can be broadly divided into holistic, feature base, and hybrid types. Holistic algorithms of face recognition address the global structure because it computes only the co-relation within the images [5]. Principal component analysis (PCA) is one of the holistic algorithm performs unsatisfactory when local details of images are vital [6].

Real time adaptive face recognition needs efficient software implementation of algorithms which would be designed as per the target reconfigurable hardware (FPGA) structure. Earlier designed systems [7, 8] did not produced acceptable results because they lacked customization of algorithms according to the target hardware resources. Therefore a decade earlier, conventional face recognition systems were not answering the real life challenges because they have limitation like producing power dissipation, poor response time and lack of adaptability.

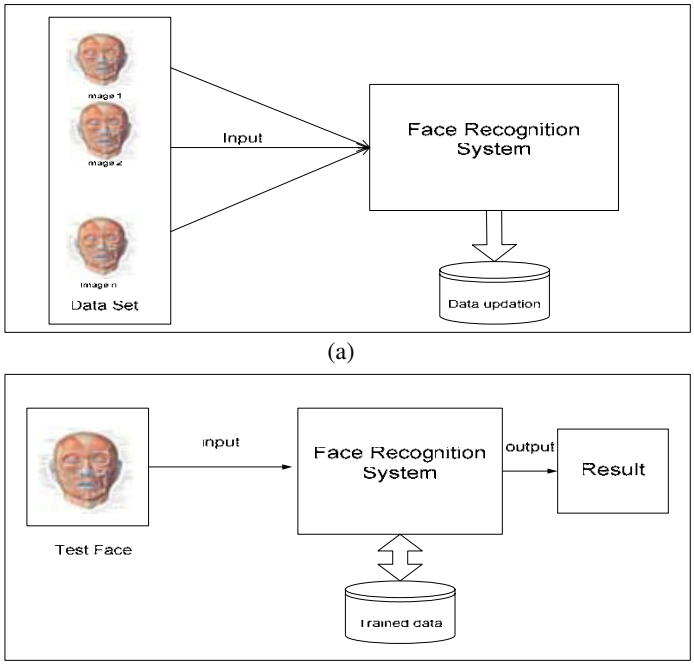

Figure 1: Overview of a general face recognition system (a) Training Phase (b) After the completion of training.

3. MOTIVATION

Intrusive and non-intrusive are main categorization of biometric techniques. Researcher are more seriously thinking about facial recognition as one of the suitable non-intrusive biometric especially after 9/11 accident.

Face recognition is one of the non-intrusive biometric techniques. Most of the face recognition algorithms produce burst of data flow between processor and memory [9, 10]. To run these algorithms

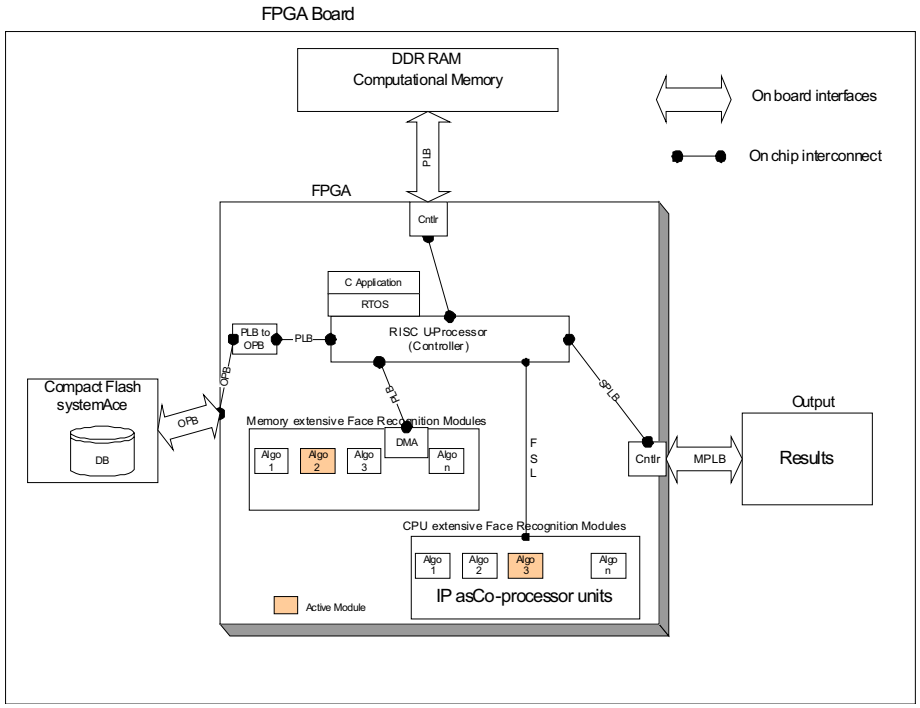

Figure 2: High level description Proposed system.

in general purpose machine will choke the processor performance because processor architecture may not be designed for such type of image processing algorithms. Specialized general processor based systems give acceptable performance however they are not flexible.

The design of hardware system in field programmable devices (FPDs) has many benefits over application specific integrated circuits (ASIC), like low cost rapid prototyping (LCRP) [11]. During the development cycle of new algorithms in hardware, LCRP has the key advantage. High logic capacity of field programmable gate array (FPGA) among FPDs makes possible designing of complex system on-chip (SoC). The application is slower and power hunger when algorithm is implemented in FPGAs as compared with the same applications implemented in custom ASICs [12]. To address with these two issues while maintaining LCRP and flexibility. Customization, software hardware co-designs (SHcoD), and dynamic partial reconfigurability (DPR) are introduced in face recognition algorithms.

4. CUSTOMIZATION/PARTITIONING OF ALGORITHM

Mapping of matlab or C algorithm without modification in the software code according to reconfigurable hardware, results may not be efficient or expected [12]. SHcoD means some part of the system works like hardware and other runs as software over the hardware. Manual partitioning of code according to the devices is not only laborious but also error prone. Single tool from any vendors does not provide efficient and full automatic partitioning for SHcoD [13], but integration of more than one tool may facilitate some process of SHcoD [12].

Few chunks of code in the algorithm should be identified, which are computational extensive and they can work independently. These codes are designed as hardware units while remaining algorithm works as high level C code. Few new tools facilitate to convert user defined high level code to HDL [12], however advanced architectural techniques like loop unrolling are necessary to optimization or efficient performance.

These converted HDL code is treated as intellectual property (IPs) soft-cores and necessary to integrate with high speed bus like FSL in the proposed architecture. The limitation of power, size and time would be addressed in embedded system with SHcoD methodology [14].

4.1. Precision Vs Efficiency

Most of the face recognition algorithm need for Eigen values. Eigen values and vectors are highly sensitive to precision of intermediate calculations. Software algorithms use double or float data type to avoid precision errors. Floating point computations in hardware are very expensive in terms of machine cycles. Therefore most of the real time systems do not like float operations.

Floating point supported u-processor PPC 405D5 or PPC 405F6 [15] core would be simpler solution which is efficient but not energy saver. Float point instructions are also consuming more micro-processor machine cycles.

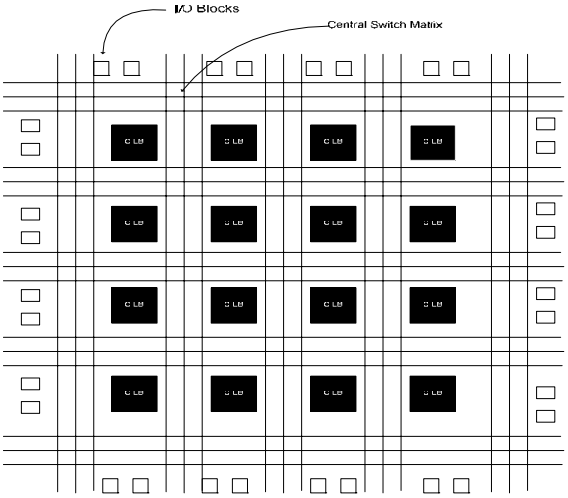

Figure 3: Basic architecture of an FPGA.

Fix-point arithmetic is a programmatic technique which preserves real values within certain limits depending upon fractional bits [3], while saves tremendously machine cycles for same oper-

ation. Fix-point is attractive for efficient and energy conscious hardware system, but it can not work such algorithm whose minimum and maximum value ranges fluctuate widely. To achieve acceptable accuracy of Eigen values by using fix format technique is a challenging task because simple fix format can not calculate numerically convergent Eigen values. Adaptive fix-point format is designed which adjust itself during the intermediate values. The Section 7 depicts the successful effort in this regard.

5. ADAPTABILITY

Various areas like control and automobile have taken the benefits of dynamic partial reconfigurability [16, 17]. Automated dynamic partial reconfiguration has achieved with the help of ROCCC compiler and partial bitstream (PARBIT) tool [24]. Dynamic reconfiguration is proposed for the face recognition in the context as shown in Fig. 3.

Adaptive systems may reduce the size, space and power of the system, because in this pattern physical resources of FPGA use same while system may have more computing power. Dynamic reconfiguration or adaptable system [10] may adjust itself at run time according to the requirement.

In dynamic reconfiguration or reconfigurable computing (RC), certain area of the device can be reconfigured while system is running on FPGA device [18]. RC is a technique through which the free part of FPGA can be reconfigured/converted into computing units or on-chip cache [9, 10] as per demand, while considering inter-communication constrains [19]. Basic architecture of FPGA illustrates that huge logic gates and registers may be configured by programmatically. Configurable logic block (CLB) contains four slices which are responsible for combinational, sequential logic and storage elements in FPGA as shown in Fig. 3 [20]. By considering FPGA architectural aspects, the proposed system may use optimal number of CLBs for the required functionality. This means less hardware resources are required to implement the algorithm as compare to implement the same algorithm without proposed technique. This will reduce power dissipation and other related VLSI issues in the system.

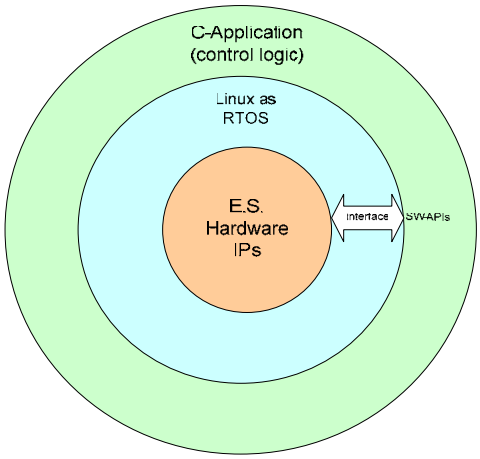

Figure 4: Layer view of system.

6. DESIGN OF PROPOSED SYSTEM

Assembly view in Fig. 5 gives hardware integration view of system. Peripheral local bus (PLB), peripheral on chip bus (OPB), fast simplest link (FSL) and fabric core bus FCB interfaces are proposed in system. PLB is high speed 64-bits address and 128-bits data bus. Processor core and bus controller are integrated with on-chip PLB. PLB masters are attached to PLB through separate address bus, while PLB slaves are connected to PLB through shared bus [21]. Master driven operation is achieved by central arbitration mechanism. High speed devices are connected with direct PLB, like DDR memory. OPB is designed for common devices. Processor core communicates with TFT controller and UART through OPB bus. OPB is 64-bits address and 32 or 64 bits data bus [22]. Intellectual Property Interface (IPIF) is used as sandwich between IP and selected bus [23].

Power PC is used as controlling unit in the proposed architecture. Like processing elements in the architecture of Hau T. Ngo [7], we proposed IPs or patch of algorithm. Layer view (Fig. 4)

of HW/SW design methodology indicates that some computation is part of hardware and other is part of software application.

CPU extensive parts like matrix multiplication or calculation of covariance matrix are implemented as IP core. Thses IPs are implemented as co-processing units [24]. These co-processing units are connected to auxiliary processing unit (APU) through FSL/FCB channels. This hierarchy may distribute/balance the load of embedded system (ES) in reconfigurable media.

The calculation of distance vectors based on neighboring pixel value is used frequently in face recognition algorithms. Such memory extensive modules is proposed to connect with PLB, co-processing unit is proposed to connect with FLS in virtex II or FCB in virtex4 devices. DMA controller drives PLB for rapid memory access.

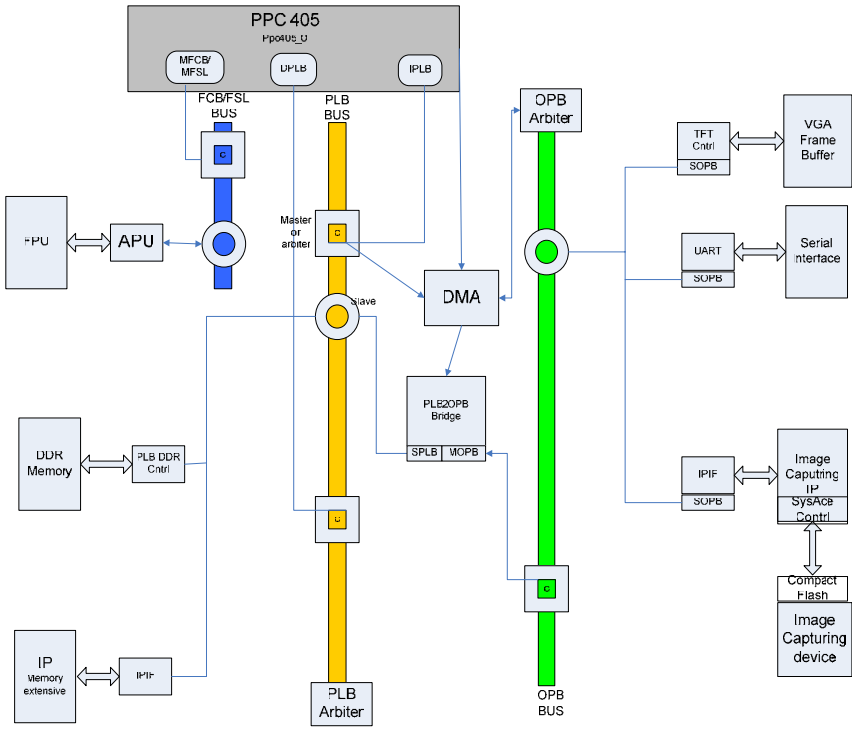

Figure 5: Hardware component integration of the connected to PLB.

Face images are treated as matrices in image processing. Matrices are store on non-volatile media Compact flash (CF). Processing of images explode burst of data. Streaming model is proposed for image processing applications due to high speed data rate transfer between cpu and memory. These matrices are used for features extraction in the training process. OPB has sufficient speed for CF disk and it is synchronous with processor core [22]. On board CF is controlled by sysace controller (hardware). Through C level APIs this data is read from CF and would be loaded into DDR memory for further face recognition computation, for example to calculate eigen faces. DDR is fast memory storage device; therefore it is connected to PLB.

Native PPC 405 core does not support floating point instruction [25]. Face recognition algorithms badly need real number arithmetic. PPC 405F6 core is closely interface by auxiliary processor unit (APU) controller [25]. Floating point instructions are executed by FCM. This architecture of PPC 405F6 can only be supported by Virtex-4-Fx family. Matrices multiplication of real numbers is used for precision comparison. In this regard floating point unit (FPU) is connected to micro-processor through fabric co-processor module (FCM).

With this motivation and SHcoD of face recognition algorithm imparts the designing detail of IPs/function units. This design is part of my PhD work. These units will be coded in C/HDL languages. Partial bit-streams are created after synthesis, routing and mapping steps. These bitstreams is used for adaptive nature of the system. In this way an efficient, low power system is designed without compromising on the functionality.

7. RESULTS

PCA needs weighted vector for recognition. First three values contribute 99.43195583 percent of the whole weight, while 99.42413122 percent in case of fixed point implementation. Therefore recognition or reconstruction result does not affect more than 0.0079 percent. On the other hand fixed point operations on vertex device are supported by native hard core. Floating point unit (APU) can be connected through APU in vertex4 FX devices. Fixed point computations are fully compliant with user instruction set architecture of Power PC 405 hard core instance. Floating point MAC operation in PPC 405 instance of vertex4 consume 15 times more cycles. FPU takes 1600 slices, 2 block ram and 4 dsp blocks. This novel implementation of HH algorithm saves power in the cost of losing precision no more than .008 percent in the diagonal values of computed matrix.

Data set images 20

resolution 292x376

Table 1. Simulation results of house holder algorithm

H.H.Floating	H.H Fixed point	Diff(FLP-FP)	% Diff
33547739136	33550653440	-2914304	-0.008687035
1800899968	1800899840	128	7.10756E-06
255354944	250970624	4384320	1.716951288
31969308	22567680	9401628	29.40829373
22742982	22560000	182982	0.804564878
20840046	19640064	1199982	5.758058308
19436386	19608320	-171934	-0.884598608
17626140	19313920	-1687780	-9.57543739
12864361	19285760	-6421399	-49.91619094
12475056	12296448	178608	1.431721028
9660825	10238976	-578151	-5.984488902
8189179.5	8933632	-744452.5	-9.090684848
7029789	7297536	-267747	-3.808748741
6516366	7192320	-675954	-10.37317425
6399316.5	6599680	-200363.5	-3.13101407
6343345.5	6355712	-12366.5	-0.194952332
6315585.5	6252032	63553.5	1.006296249
5948435.5	6220288	-271852.5	-4.570151261
5650524.5	6145536	-495011.5	-8.760452238
3394177.5	5703424	-2309246.5	-68.03552554

Eigen values weight		
	FLP	FP
Total	35807395872	35808735232
First 3	35603994048	35602523904
diff	203401823.5	206211328
%	99.43195583	99.42413122
% diff	0.007825	

8. CONCLUSION/FUTURE WORK

1 FPGA based high level design and component integration view has been demonstrated.

2 Minimum and maximum ranges of intermediates values have been found during iterative part of householder (HH) and QL decomposition algorithms.

3 Fixed point implementation HH algorithm saves thousands of machine cycles in the cost of losing 008% weight in highest three Eigen values.

The following steps would be required for efficient and low power implementation of HH on FPGA. In fact the following steps have been proposed in my PhD synopsis.

a Fix-point dynamic macros that accommodate the step (3) requirement would be designed.

b Modified code which uses dynamic macros would be run on hardware (without floating point unit) and total machine cycles used for such a scenario would be calculated. Time of execution of HH algorithm in terms of nano second and power consumed in term of pico watts would be calculated.

c Convert householder and QL algorithmic part into HDL and then compare the machine cycles and power factor.

d Acceptable results in terms of efficiency and accuracy in step (d) with the floating point co-processor would be appreciable academic contribution in the face recognition particularly and other engineering fields specially.

REFERENCES

1. Zhao, W., R. Chellappa, P. J. Phillips, and A. Rosenfeld, "Face recognition: A literature survey," *ACM Computing Surveys*, Vol. 35, No. 4, Dec. 2003.
2. Kang, J. and W. Sung, "Fixed-point C compiler for Tms320c50 digital signal processor," *IEEE International Conference on Acoustics, Speech, and Signal Processing*, Vol. 1, 707–710, Apr. 1997.
3. Kum, K.-I., J. Kang, and W. Sung, "A floating-point to fixed-point C converter for fixed-point digital signal processors," *Proc. 2nd SUIF Compiler Workshop*, August 1997.
4. Ashbourn, J., *Biometrics: Advanced Identity Veri_cation*, Springer, 2002.
5. He, X., S. Yan, Y. Hu, P. Niyogi, and H. Zhang, "Face recognition using laplacianfaces," *IEEE Transactions on Pattern Analysis and Machine Intelligence*, Vol. 27, No. 3, 328–340, Mar. 2005.
6. Belhumeur, P. N., J. P. Hespanha, and D. J. Kriegman, "Eigenfaces vs. fisherfaces: Recognition using class specific linear projection," *IEEE Transactions on Pattern Analysis and Machine Intelligence*, Vol. 19, No. 7, 711–720, Jul. 1997.
7. Ngo, H. T., R. Gottumukkal, and V. K. Asari, "A flexible and efficient hardware architecture for real-time face recognition based on eigenface," *IEEE Computer Society Annual Symposium on VLSI: New Frontiers in VLSI Design (ISVLSI'05)*, 280–281, 2005.
8. Zaki, G. F., R. A. Girgis, W. W. Moussa, and W. R. Gobran, "Using HW/SW Co-design to implement an embedded face recognition/verification system on an FPGA".
9. Sangireddy, R., H. Kim, and A. K. Somani, "Low-power high-performance reconfigurable computing cache architectures," *IEEE Transactions on Computers*, Vol. 53, No. 10, 1274–1290, Oct. 2004.
10. Kim, H., "Towards adaptive balanced computing (ABC) using reconfigurable functional caches (Rfcs)," PhD Thesis at Lowa State University, 2001.
11. Brown, S. and J. Rose, "Architecture of FPGAs and CPLDs: A tutorial," *IEEE Computer Society Press*, Vol 13, Issue 2, Los Alamitos, CA, USA, Jun. 1996.
12. Pellerin, D. and S. Thibault, *Practical FPGA programming in C*, Prentice Hall PTR, ISBN: 0-13-154318-0.
13. Saha, P., "Automatic software hardware co-design for reconfigurable computing systems," *17th International Conference on Field Programmable Logic and Applications*, 27–29, Amsterdam, Netherlands, Aug. 2000.
14. Cox, J., J. Ghosn, and P. N. Yianilos, "Feature-based face recognition using mixture-distance," *IEEE Computer Society Conference on Computer Vision and Pattern Recognition (CVPR'96)*, 209, 1996.
15. PowerPC 405 Processor Block Reference Guide, Embedded Development Kit, UG018 (v2.1), Jul. 20, 2005.
16. Toscher, S., T. Reinemann, and R. Kasper, "An adaptive FPGA mechatronic control system supporting partial reconfiguration of controller functionalities," *Nas/Esa Conference on Adaptive Hardware and Systems*, 2006.
17. Uiimann, M. and M. Hubner, "An FPGA run-time system for dynamical on-demand reconfiguration," *18th International Parallel and Distributed Processing Symposium IEEE*, 2004.
18. Two Flows for Partial Reconfiguration: Module Based or Difference Based, Xilinx, Sep. 2004.
19. Robertson, J. I., "A design flow for partially reconfigurable hardware," *ACM Transactions on Embedded Computing Systems*, Vol. 3, No. 2, 257–283, May 2004.
20. Virtex-II Pro and Virtex-II Pro X Platform FPGAs: Complete Data Sheet DS083, Xilinx, Oct.
21. Virtex-II Pro and Virtex-II Pro X Platform FPGAs: Complete Data Sheet DS083, Xilinx, Oct. 2005.
22. IBM On-Chip Peripheral Bus Architecture Specifications Version 2.1, Apr. 2001.
23. OPB IPIF architecture, Xilinx, DS414, Aug. 2004.
24. Mitra, Z. G., A. Baner, and W. Najjar, "Dynamic co-processor architecture for software acceleration on csoCs," *IEE Int. Conf. on Computer Design (ICCD)*, Oct. 2006.
25. UG018 (v2.1), PowerPC 405 Processor Block Reference Guide, July 20, 2005.

High Sensitivity of Phase-based Surface Plasmon Resonance in Nano-cylinder Array

Bing-Hung Chen, Yih-Chau Wang, and Jia-Hung Lin
Institute of Electronic Engineering, National Dong Hwa University
Hualien 97401, Taiwan, R. O. C.

Abstract— Surface plasmon resonance sensor is used to measure the variation of dielectric constant sample, but its sensitivity is limited to surrounding temperature fluctuation. We present a high sensitivity phase-based surface plasmon resonance sensor made by gold nano-cylinder array. This structure is not only to reduce thermal conduction by the non-continuous gold array, but also to enhance surface plasma by these nano-size surfaces. This device consists of 160 nm diameter, 400 nm height gold cylinders on 47 nm gold film coated on Corning 1737 glass, and match with BK7 prism by NuSil LS-5252 optical matching liquid. Surface plasma wave was excited by a 632.8 nm HeNe laser irradiating on this prism at a particular angle. The phase variation between the signal light and reference light are collected by a pair of photo-detectors and recorded by a lock-in amplifier (Stanford Research 830). By considering heterodyne interference optical path, the sensitivity of this tool can reach 10^{-7} RIU.

1. INTRODUCTION

The purpose of sensing technology is qualitative and quantitative analysis the physic phenomenon around environment. Due to nano-scale device manufacturing technologies are increasingly fine and delicate, the accompanied sensing approach also become more important for detecting the tiny variations of physic parameters in the industrial applications and biochemical area. In recent years, surface plasmon resonance (SPR) sensing technology has been proposed and applied in many fields because of its various advantages such as real time, label free, high sensitivity, high throughput screening and qualitative and quantitative analysis interaction between bio-molecules.

SPR sensing approach using a thin metal film to couple incident light and plasmon wave is very sensitive to slight changes of surface film thickness and surrounding medium refractive index. However, this kind of SPR based on intensity interrogation has relative low sensitivity compared with phase-based SPR. It has been found that the phase can change much more abruptly than the intensity as the change of thickness of metal thin film or refractive index of media on the sensor surface, and therefore becomes an attractive sensing technology [1]. The theoretical prediction has shown that the phase measurement gives the sensitivity of about 10^2 to 10^3 times higher than the conventional one [2, 3]. Several experimental configurations have been proposed to measure the phase variation of the SPR excitation, for example phase shifting interferometry (PSI) [3], and heterodyne interferometry (HI) [4] etc. PSI has the drawback that is easily disturbed by environmental noise, like temperature and mechanical vibration, and then sensitivity is limited. HI is an optical modulation technique which can suppress the noise caused by environmental disturbance, thus it can offers much higher sensitivity than PSI. In the HI configuration, the reflective light contains a pair of correlated and orthogonal linear polarized p and s light wave with different phase caused by SPR are collected by photodetector and then amplified by lock-in amplifier.

On the other hand, the field enhancement or plasmon wave confinement is another critical factor for high sensitivity SPR device. To excite localized surface plasmons (LSP) has been demonstrated and presented high localized electric and magnetic field nearby sensing surface [5]. Compared with conventional SPR sensor, LSP has localized and highly enhanced plasmon can interact with biomolecule binding events close to sensor surface and cause a larger shift of resonant LSP modes [6]. Nano-wire SPR is a kind of LSP, and has been numerically calculated the sensitivity to be more than order than the conventional one [7].

In this paper, we proposed a nano-cylinder array based sensor accompanying heterodyne interferometry configuration to develop a high sensitivity LSP sensor. In which, on the one hand pair of cylinders can be regard as in parallel wires with symmetry electrical resonance mode, on the other hand pair of cylinders with bottom connection with asymmetry magnetic resonance mode. Both of these two modes can enhance light interaction with plasmonic nanowire system [11]. This gold nano-cylinder array is not only to reduce thermal conduction fluctuation, but also to increase the resonance effect by array pattern interference. We expect the sensitivity can reached to 10^{-7} refractive index unit (RIU).

2. EXPERIMENTAL SETUP

In this section, we will present the sensor's fabrication procedure and the optical experimental setup. BK7 prism was chosen as coupler of incident light with LSP mode.

2.1. Gold Nano-cylinder Array Fabrication

Figure 1 shows the gold nano-cylinder array fabrication process. With the assistance of lithography, molding and UV forming, photo-patterned features of the gold nano-cylinder array were constructed on a glass and mounted on the BK7 prism via optical match liquid.

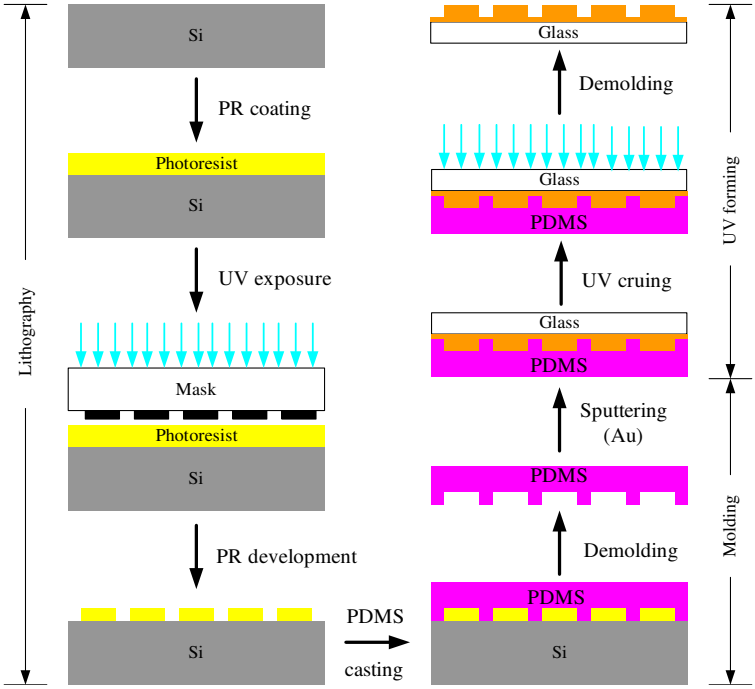

Figure 1: Gold nano-cylinder array fabrication process.

The pattern features was outlined with design software and printed out to be a photo mask. Photo-resist (PR) layer then was spin-coated on the silicon substrate surface. After UV exposure and PR development, the desired pattern was transferred to the PR layer. The follow up step was to cove transparency film (PDMS) to PR layer. Then removed PR and sputtered gold onto PDMS. Finally, de-mode and bond pattern gold film on the Corning 1737 glass as shown in Fig. 2(a).

The gold nano-cylinder has 160 nm diameter, 400 nm height and with 160 nm space on a 47 nm thickness gold film. Kreschmann prism coupler was chosen to excite surface plasmon wave [10]. In which, gold cylinder array is the active metal material and glass slide mounted on the prism by using optical matching liquid as shown in Fig. 2(b). The morphological profile of the array can be seen in SEM picture in Fig. 2(c).

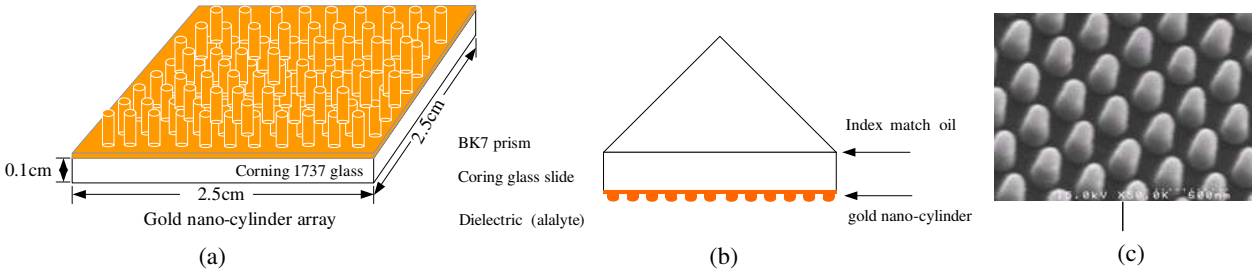

Figure 2: (a) The gold nano-cylinder array on a glass substrate. (b) The prism coupler used in our experiment. (c) The SEM of thenano-cyliner array structure.

2.2. Experimental Setup

The proposed optical path structure of heterodyne interferometry with phase-based LSP sensor is shown in Fig. 3. The proposed optical path structure of heterodyne interferometry with phase-based LSP sensor is shown in Fig. 3. The light source is a frequency stabilized He-Ne laser operating at the wavelength of 632.8 nm having output power 15 mW. The chopper, mirror (2 and 3) and beam splitter (1 and 4) is used for obtaining a linear polarized sensing beam with difference frequency shift. The sensing beam is then split into a reference and a signal beam by beam splitter (6). The reference beam go through a polarizer (polarizer 7, oriented at 45° relative to the horizontal direction) and is receive by photo-detector (8). None the less, the signal beam was used for surface plasmon excitation in the Kreschmann configuration at an incidence angle having maximum SPW coupling efficiency. The reflected beam then go through a polarizer (polarizer 10, oriented at 45° relative to the horizontal direction) and is receive by photo-detector (11).

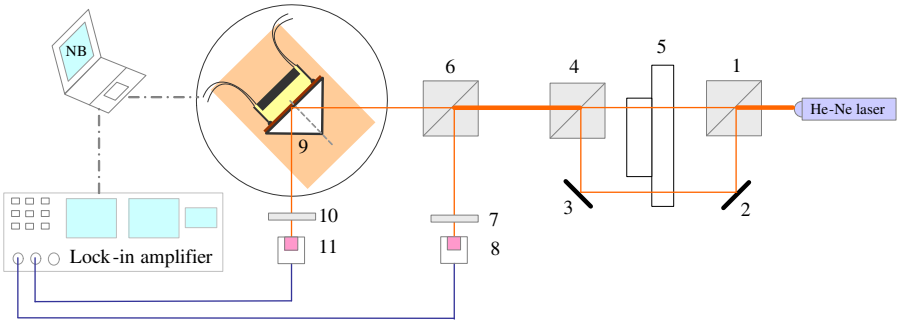

Figure 3: The optical path structure of heterodyne interferometry with phase based LSP sensor. In which, (1, 4 and 6) are beam splitters, (2 and 3) are mirrors, (5) is chopper, (7 and 10) are polarizers, (8 and 11) are photo-detectors, (9) is Kreschmann coupler.

Finally, compare signal and reference beam to obtain phase difference by lock-in amplifier. The advantage of this sensor system is that any unwanted phase drift by mechanical and temperature can be eliminated through nano-cylinder array and heterodyne interfermetry.

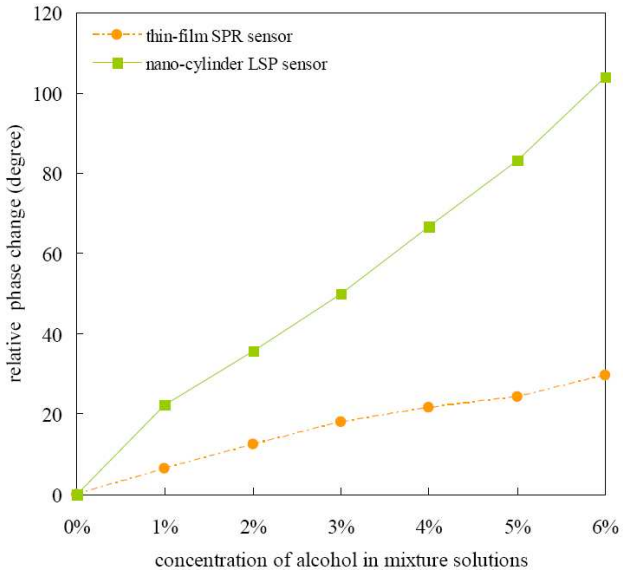

Figure 4: Experimentally relative phase changes versus different alcohol concentrations. The dash and solid line represent experimental results of a thin-film SPR sensor and a nano-cylinder LSP sensor, respectively.

3. RESULTS AND DISCUSSION

To demonstrate the high sensitivity of this nano-cylinder array LSP sensor we prepared two distinguish structure devices, one is the conventional thin-film SPR with film thickness 47 nm and the

other is the novel one sensor, both having the same optical circumstances.

We chose the alcohol-water mixtures with different alcohol concentrations as our testing samples. These seven samples have alcohol concentration range of 0% to 6% at the same room temperature. According to the literature which describes the mixtures solution concentration following up the rule of weight percentage [8], the refractive index would theoretically variate in the range of 1.3330 to 1.3367.

Results of relative phase changes with respect to the alcohol concentration variation are shown in Fig. 4. The sensitivity, σ_n, is a criterion to evaluate a SPR measurement system to resolve the smallest change of refractive index in an ambient medium. According to the definition [9], sensitivity should be $\sigma_n = (\Delta n/\Delta\delta)\,\sigma_\delta$, where Δn is the change of refractive index and $\Delta\delta$ is the corresponding phase variation, and σ_δ is the instrument smallest resolution. Analyzing from measured dada, Δn, is 3.7×10^{-3} RIU, σ_δ is 0.01° of our lock-in amplifier and $\Delta\delta$ are 29.71°, 103.96° for thin-film SPR sensor and nano-cylinder LSP sensor, respectively. The overall system sensitivity of thin-film SPR sensor can reach to 1.25×10^{-6} RIU, but the nano-cylinder LSP sensor can reach to 3.55×10^{-7} RIU.

4. CONCLUSION

In this paper, we have present a high sensitivity phase based surface plasmon resonance sensor structure and the accompanying optical path configuration. This structure is not only effectively to reduce thermal fluctuation by the gold array, but also to enhance localized surface plasma by symmetry electrical field resonance mode. Phase measurement between p and s polarized light can eliminate any unwanted phase shift caused by mechanical and temperature by using heterodyne interferometry. From experimental results we have demonstrated that nano-cylinder array LSP sensor has higher sensitivity than thin-film-based SPR sensor, and the sensitivity can reach to 10^{-7} RIU. We expected that use of nano-cyliner array can further enhance the sensitivity of sensor by adjusting the diameter and space between cylinders to observe the localized magnetic resonance.

ACKNOWLEDGMENT

This work was supported by the National Science Council of Taiwan under Grant NSC96-2120-M-002-017.

REFERENCES

1. Yu, X., D. Wang, X. Wei, X. Ding, W. Liao, and X. Zhao, "A surface plasmon resonance imaging interferometry for protein micro-array detection," *Sensors and Actuators B*, Vol. 108, 765–771, 2005.
2. Markowicz, P. P., W. C. Law, A. Baev, P. N. Prasad, S. Patskovsky, and A. Kabashin, "Phase-sensitive time-modulated surface plasmon resonance polarimetry for wide dynamic range biosensing," *Opt. Express*, Vol. 15, 1745–1754, 2007.
3. Wu, S. Y., H. P. Ho, W. C. Law, and C. L. Lin, "Highly sensitive differential phase-sensitive surface plasmon resonance biosensor based on the mach-Zehnder configuration," *Opt. Lett.*, Vol. 29, 2378–2380, 2004.
4. Chiang, H.-P., H.-T. Yeh, C.-M. Chen, J.-C. Wu, S.-Y. Su, R. Chang, Y.-J. Wu, D. P. Tsai, S. U. Jen, and P. T. Leung, "Surface plasmon resonance monitoring of temperature via phase measurement," *Optics Communications*, Vol. 241, No. 4–6, 409–418, November 16, 2004.
5. Prasad, P. N., *Nanophotonics*, Wiley-Interscience, 2004.
6. Byun, K. M., S. J. Yoon, D. Kim, and S. J. Kim, "Experimental study of sensitivity enhancement in surface plasmon resonance biosensors by use of periodic metallic nanowires," *Opt. Lett.*, Vol. 32, 1902–1904, 2007.
7. Kim, K., S. J. Yoon, and D. Kim, "Nanowire-based enhancement of localized surface plasmon resonance for highly sensitive detection: A theoretical study," *Opt. Express*, Vol. 14, 12419–12431, 2006.
8. Lide, D. R., *Handbook of Chemistry and Physics*, 82nd ed., CRC Press, Boca Raton, FL, 2001.
9. Nelson, S. G., K. S. Johnston, and S. S. Yee, "High sensitivity surface plasmon resonance sensor based on phase detection," *Sensors and Actuators B*, 35–36, 187–191, 1996.
10. Kretschmann, E. and H. Raether, "Radiative decay of nonradiative surface plasmons excited by light," *Z. Naturforsch. A*, Vol. 23, 2135–2136, 1968.
11. Podolskiy, V. A., "Resonant light interaction with plasmonic nanowire systems," *J. of Optics A: Pure Appl. Opt.*, Vol. 7, S32–S3, 2005.

Similarity between Two Targets and Its Application to Polarimetric Target Detection for Sea Area

Wentao An[1, 2], **Weijie Zhang**[1], **Jian Yang**[1], **and Wen Hong**[2]

[1]Dept. of Electronic Eng., Tsinghua University, Beijing 100084, China
[2]National Key Lab of Microwave Imaging Technology
Institute of Electronics, CAS, Beijing 100080, China

Abstract— A similarity parameter between two polarimetric covariance matrices is proposed in this paper. This parameter can be applied not only to the data case of one-look polarimetric synthetic aperture radar (SAR), but also to the case of multi-look polarimetric SAR. Six properties of the similarity parameter are presented and analyzed. As an application, this parameter is used to target detection for multi-look polarimetric SAR case. Two kinds of improved power maximization synthesis detector are proposed. Finally, the experimental result of different detectors for sear area are presented and analyzed.

1. INTRODUCTION

For target classification and recognition in radar polarimetry, one important problem is how to analyze the similarity between two radar targets. Yang [1] proposed the similarity parameter between two scattering matrices, which is independent of the span of the scattering matrices and the target orientation angle. It also contains many other useful properties, and has been applied for feature extraction [2] and classification [3] of polarimetric SAR images. The similarity parameter is only applied to the case of one-look polarimetric radar. However, nowadays, most data of a polarimetic synthetic aperture radar (SAR) are multi-look and the scattering matrix can not be obtained directly. So the application scope of similarity parameter is restricted. To solve this problem, the similarity parameter is extended in this paper, so that it could be applied to both one-look and multi-look polarimetric SAR data. Then it is employed for polarimetric target detection.

2. SIMILARITY PARAMETER [1]

A target scattering matrix in a linear horizontal and vertical polarization base is expressed as

$$\boldsymbol{S} = \begin{bmatrix} S_{HH} & S_{HV} \\ S_{VH} & S_{VV} \end{bmatrix} \tag{1}$$

According to Huynen's theory [4], Let ψ denote the orientation angle of the target, the scattering matrix $\boldsymbol{S}$ could be rotated to a special position, where the orientation angle of the target is zero, as follows

$$\boldsymbol{S}^0 = [\boldsymbol{J}(-\psi)][\boldsymbol{S}][\boldsymbol{J}(\psi)] = \begin{bmatrix} S^0_{HH} & S^0_{HV} \\ S^0_{VH} & S^0_{VV} \end{bmatrix} \tag{2}$$

where

$$\boldsymbol{J}(\psi) = \begin{bmatrix} \cos(\psi) & -\sin(\psi) \\ \sin(\psi) & \cos(\psi) \end{bmatrix} \tag{3}$$

For the monostatic radar, if the reciprocity holds, then $S^0_{HV} = S^0_{VH}$, so the scattering matrix is equivalent to

$$\boldsymbol{k} = \frac{1}{\sqrt{2}} \left[S^0_{HH} + S^0_{VV},\, S^0_{HH} - S^0_{VV},\, 2S^0_{HV} \right]^t \tag{4}$$

which is called the modified Pauli-scattering vector, where the superscript t denotes transpose.

The similarity parameter between two scattering matrices $\boldsymbol{S}_1$ and $\boldsymbol{S}_2$ was defined by Yang [1] as

$$r(\boldsymbol{S}_1,\, \boldsymbol{S}_2) = \frac{\left| (\boldsymbol{k}_1)^H \boldsymbol{k}_2 \right|^2}{\|\boldsymbol{k}_1\|_2^2 \, \|\boldsymbol{k}_2\|_2^2} \tag{5}$$

where the superscript H denotes conjugate transpose; $\boldsymbol{k}_1$ and $\boldsymbol{k}_2$ corresponds to $\boldsymbol{S}_1$ and $\boldsymbol{S}_2$ respectively, after having been rotated to zero orientation angle; $\|\cdot\|_2^2$ denotes the square sum of the absolute values of the three elements of the vector.

3. GENERALIZED SIMILARITY PARAMETER

For multi-look poloarimetric SAR data, a pixel is corresponding to a 4×4 Kennaugh matrix, or a polarimetric covariance matrix. The scattering matrix can not be obtained directly. As mentioned, the similarity parameter is only applied to one-look case. To solve this problem, the generalized similarity parameter (GSP) between two polarimetric covariance matrices is defined in this section, which can also be used to multi-look polarimetric SAR data. We use the following vector to express a target for the one-look case

$$\boldsymbol{x} = \left[S_{HH},\, \sqrt{2}S_{HV},\, S_{VV}\right]^T \tag{6}$$

If the orientation angle of the target is ψ, then

$$\boldsymbol{x}^0 = \boldsymbol{P}_\psi \boldsymbol{x} = \left[S^0_{HH} \quad \sqrt{2}S^0_{HV} \quad S^0_{VV}\right]^T \tag{7}$$

where

$$\boldsymbol{P}_\psi = \begin{bmatrix} \dfrac{\cos(2\psi)+1}{2} & \dfrac{\sin(2\psi)}{\sqrt{2}} & \dfrac{1-\cos(2\psi)}{2} \\ -\dfrac{\sin(2\psi)}{\sqrt{2}} & \cos(2\psi) & \dfrac{\sin(2\psi)}{\sqrt{2}} \\ \dfrac{1-\cos(2\psi)}{2} & -\dfrac{\sin(2\psi)}{\sqrt{2}} & \dfrac{\cos(2\psi)+1}{2} \end{bmatrix} \tag{8}$$

$\boldsymbol{P}_\psi$ is an unitary matrix.

For N-look polarimetric data, the polarimetric covariance matrix $\boldsymbol{C} = \frac{1}{N}\sum\limits_{i=1}^{N} \boldsymbol{x}\boldsymbol{x}^H$ can be obtained from the Kennaugh matrix. Similar to the one-look data processing, the orientation angle ψ of $\boldsymbol{C}$ also can be obtained from Kennaugh matrix, so the covariance matrix $\boldsymbol{C}$ is rotated to zero orientation angle by the following formula.

$$\boldsymbol{C}^0 = \boldsymbol{P}_\psi \boldsymbol{C} \boldsymbol{P}_\psi^H \tag{9}$$

If there are two covariance matrices $\boldsymbol{C}_1$ and $\boldsymbol{C}_2$, rotate both of them to zero orientation angle and denote both the covariance matrices in zero orientation angle by $\boldsymbol{A}$ and $\boldsymbol{B}$, respectively

$$\boldsymbol{A} = \boldsymbol{P}_{\psi 1}\boldsymbol{C}_1\boldsymbol{P}_{\psi 1}^H, \quad \boldsymbol{B} = \boldsymbol{P}_{\psi 2}\boldsymbol{C}_2\boldsymbol{P}_{\psi 2}^H \tag{10}$$

where ψ_1 and ψ_2 are the orientation angles of $\boldsymbol{C}_1$ and $\boldsymbol{C}_2$, respectively. The generalized similarity parameter between the covariance matrices $\boldsymbol{C}_1$ and $\boldsymbol{C}_2$ is defined as

$$\begin{aligned} R(\boldsymbol{C}_1, \boldsymbol{C}_2) =& \frac{|\langle \boldsymbol{A}, \boldsymbol{B}\rangle|}{\|\boldsymbol{A}\|_F \|\boldsymbol{B}\|_F} \\ =& \frac{\left|tr(\boldsymbol{A}^H\boldsymbol{B})\right|}{\sqrt{tr(\boldsymbol{A}^H\boldsymbol{A})\cdot tr(\boldsymbol{B}^H\boldsymbol{B})}} \end{aligned} \tag{11}$$

where $tr(\cdot)$ is the trace of a matrix, $\langle\cdot\rangle$ is the inner product of two matrices, defined as $\langle \boldsymbol{A}, \boldsymbol{B}\rangle = tr(\boldsymbol{A}^H\boldsymbol{B})$; $\|\cdot\|_F$ is the Frobenius norm of a matrix, which is defined as:

$$\|\boldsymbol{A}\|_F = \left(\sum_{i=1}^{M}\sum_{j=1}^{N}|a_{ij}|^2\right)^{\frac{1}{2}} = \left(tr(\boldsymbol{A}^H\boldsymbol{A})\right)^{\frac{1}{2}} \tag{12}$$

Generally, for N-look polarimetric data, $\boldsymbol{C}_1$, $\boldsymbol{C}_2$, $\boldsymbol{A}$ and $\boldsymbol{B}$ are Hermitian matrices, then

$$R(\boldsymbol{C}_1, \boldsymbol{C}_2) = \frac{|tr(\boldsymbol{A}\boldsymbol{B})|}{\sqrt{tr(\boldsymbol{A}^2)\cdot tr(\boldsymbol{B}^2)}} \tag{13}$$

4. PROPERTIES OF THE GSP

The generalized similarity parameter has the following properties:

1. $R(\boldsymbol{C}_1, \boldsymbol{C}_2) = R(\boldsymbol{C}_2, \boldsymbol{C}_1)$;
2. $R(\boldsymbol{P}_{\theta 1}^H \boldsymbol{C}_1 \boldsymbol{P}_{\theta 1}, \boldsymbol{P}_{\theta 2}^H \boldsymbol{C}_2 \boldsymbol{P}_{\theta 2}) = R(\boldsymbol{C}_1, \boldsymbol{C}_2)$, where θ_1 and θ_2 are two arbitrary angles;
3. $R(\alpha_1 \cdot \boldsymbol{C}_1, \alpha_2 \cdot \boldsymbol{C}_2) = R(\boldsymbol{C}_1, \boldsymbol{C}_2)$, where α_1 and α_2 are two arbitrary positive numbers;
4. $0 \leq R(\boldsymbol{C}_1, \boldsymbol{C}_2) \leq 1$, where $R(\boldsymbol{C}_1, \boldsymbol{C}_2) = 1$ if and only if $\boldsymbol{C}_2 = \alpha \boldsymbol{P}_\theta^H \boldsymbol{C}_1 \boldsymbol{P}_\theta$; and where α is an arbitrary positive number, θ is an arbitrary angle;
5. $R(\boldsymbol{U}^H \boldsymbol{C}_1 \boldsymbol{U}, \boldsymbol{U}^H \boldsymbol{C}_2 \boldsymbol{U}) = R(\boldsymbol{C}_1, \boldsymbol{C}_2)$, where $\boldsymbol{U}$ is an arbitrary unitary matrix, $\boldsymbol{U}^H \boldsymbol{U} = \boldsymbol{U}\boldsymbol{U}^H = \boldsymbol{I}$, $\boldsymbol{I}$ is a 3×3 identity matrix, and the rotation matrix P_ψ should be changed to $\boldsymbol{U}^H \boldsymbol{P}_\psi \boldsymbol{U}$ when calculating $R(\boldsymbol{U}^H \boldsymbol{C}_1 \boldsymbol{U}, \boldsymbol{U}^H \boldsymbol{C}_2 \boldsymbol{U})$.

Some interpretations of the fifth property are presented as follows. As we know, besides a covariance matrix $\boldsymbol{C}$, the polarimetric data of multi-look case can also be expressed by a coherency matrix $\boldsymbol{T}$. $\boldsymbol{C}$ and $\boldsymbol{T}$ can be transformed to each other as follows

$$\boldsymbol{C} = \boldsymbol{Q}^H \cdot \boldsymbol{T} \cdot \boldsymbol{Q}, \quad \boldsymbol{T} = \boldsymbol{Q} \cdot \boldsymbol{C} \cdot \boldsymbol{Q}^H \tag{14}$$

where $\boldsymbol{Q}$ is an orthogonal matrix given by

$$\boldsymbol{Q} = \frac{1}{\sqrt{2}} \begin{bmatrix} 1 & 0 & -1 \\ 1 & 0 & -1 \\ 0 & \sqrt{2} & 0 \end{bmatrix} \tag{15}$$

According to the fifth property we know that $R(\boldsymbol{C}_1, \boldsymbol{C}_2) = R(\boldsymbol{T}_1, \boldsymbol{T}_2)$. So the fifth property means that the GSP remains the same with arbitrary unitary similarity transformation of $\boldsymbol{C}$ and $\boldsymbol{T}$.

Let's consider the case of one-look polarimetric SAR data. The rank of covariance matrix of one-look data is one. So if there are two covariance matrices $\boldsymbol{C}_1$ and $\boldsymbol{C}_2$ for one-look data case, $\boldsymbol{A}$ and $\boldsymbol{B}$ are the matrices that have been rotated to zero orientation angle from $\boldsymbol{C}_1$ and $\boldsymbol{C}_2$, respectively. According to eigenvalue decomposition [5], $\boldsymbol{A}$ and $\boldsymbol{B}$ can be expressed as follows

$$\boldsymbol{A} = \lambda_A \cdot \boldsymbol{v} \cdot \boldsymbol{v}^H, \quad \boldsymbol{B} = \lambda_B \cdot \boldsymbol{u} \cdot \boldsymbol{u}^H \tag{16}$$

where $\boldsymbol{u}$ and $\boldsymbol{v}$ are unitary eigenvectors. From (13) and (16) we can obtain

$$R(\boldsymbol{C}_1, \boldsymbol{C}_2) = \left| \boldsymbol{v}^H \boldsymbol{u} \right|^2 \tag{17}$$

According to (5), (17) and the fifth property of the GSP, if the rank of $\boldsymbol{C}_1$ and $\boldsymbol{C}_2$ are one, $\boldsymbol{S}_1$ and $\boldsymbol{S}_2$ are the corresponding scattering matrices of $\boldsymbol{C}_1$ and $\boldsymbol{C}_2$, respectively, then

$$R(\boldsymbol{C}_1, \boldsymbol{C}_2) = r(\boldsymbol{S}_1, \boldsymbol{S}_2) \tag{18}$$

(20) shows that the GSP and the similarity parameter are the same in one-look data case. So the similarity parameter can be regarded as the GSP for the case of one-look polarimetric data.

Similar to the similarity parameter, the GSP also has the property as follows. If $\boldsymbol{C}_1$, $\boldsymbol{C}_2$, $\boldsymbol{C}_3$ are three nonzero covariance matrices which satisfy

$$R(\boldsymbol{C}_1, \boldsymbol{C}_2) = R(\boldsymbol{C}_2, \boldsymbol{C}_3) = R(\boldsymbol{C}_1, \boldsymbol{C}_3) = 0 \tag{19}$$

then for an arbitrary covariance matrix $\boldsymbol{C}$, with the rank of one, we have

$$R(\boldsymbol{C}, \boldsymbol{C}_1) + R(\boldsymbol{C}, \boldsymbol{C}_2) + R(\boldsymbol{C}, \boldsymbol{C}_3) = 1 \tag{20}$$

5. POLARIMETRIC TARGET DETECTION

In this section, the application of GSP on multi-look polarimetric SAR data for target detection is presented. According to [6], the Power Maximization Synthesis (PMS) detector does not require the prior knowledge of a target and the statistical characteristic of clutter. Moreover, for multi-look case, every pixel's scattering matrix is unnecessary, which means the PMS detector is proper for the target detection of multi-look polarimetric SAR data. So in the next, we will mainly analyze the PMS detector using multi-look polarimetric SAR data.

The PMS detector is specified by

$$\frac{1}{2}\left[Span + \sqrt{(|S_{HH}|^2 - |S_{VV}|^2) + 4|S_{HH}^* S_{HV} + S_{VV} S_{HV}^*|^2}\right] > Z \tag{21}$$

where the superscript $*$ denotes complex conjugate, and Z is the detection threshold. For the multi-look polarimetric data case, (33) can be rewritten as follows

$$P_{PMS} = k_{11} + \sqrt{k_{12}^2 + k_{13}^2 + k_{14}^2} > Z \tag{22}$$

where k_{11}, k_{12}, k_{13}, k_{14} are the elements of the first line of a Kennaugh matrix. P_{PMS} is the maximal power that can be received in the matched-polarized channel of each pixel.

In a sea area, the plate scattering is usually dominant. If there is a ship, a very strong diplane scattering will occur. Let $\boldsymbol{B}_1$ and $\boldsymbol{B}_2$ denote the polarimetric covariance matrices of a plate and a diplane, respectively, and

$$\boldsymbol{B}_1 = a_1 \begin{bmatrix} 1 & 0 & 1 \\ 0 & 0 & 0 \\ 1 & 0 & 1 \end{bmatrix}, \quad \boldsymbol{B}_2 = a_2 \begin{bmatrix} 1 & 0 & -1 \\ 0 & 0 & 0 \\ -1 & 0 & 1 \end{bmatrix} \tag{23}$$

where a_1 and a_2 are two positive numbers.

According to Section 3, the GSP between a plate and each pixel of polarimetric SAR image is $R(\boldsymbol{C}, \boldsymbol{B}_1)$, where $\boldsymbol{C}$ is the covariance matrix of each pixel. As $\boldsymbol{C}$ can also be expressed as

$$\boldsymbol{C} = P_{PMS} \cdot \frac{\mathbf{C}}{P_{PMS}} \tag{24}$$

According to the third property of the GSP, we know that

$$R(\boldsymbol{C}, \boldsymbol{B}_1) = R\left(\frac{\boldsymbol{C}}{P_{PMS}}, \boldsymbol{B}_1\right) \tag{25}$$

So the PMS detector (22) can be improved as

$$Y = (1 - R(\boldsymbol{C}, \boldsymbol{B}_1)) \cdot \left(k_{11} + \sqrt{k_{12}^2 + k_{13}^2 + k_{14}^2}\right) > Z \tag{26}$$

where Z is the detection threshold, P_{PMS} is the power, and $1 - R(\boldsymbol{C}, \boldsymbol{B}_1)$ represents the difference between the pixel and plate. For a pixel in sea area, the more different it is from a plate, the more probable it is a desired target. According to (25) and the third property of the GSP, it is easy to check that $1 - R(\boldsymbol{C}, \boldsymbol{B}_1)$ and P_{PMS} are independent. So Y in (26) includes more information of the real data than P_{PMS}.

Similarly, the GSP between each pixel and a diplane $R(\boldsymbol{C}, \boldsymbol{B}_2)$ can also be applied to improve the PMS detector as follows

$$Y = R(\boldsymbol{C}, \boldsymbol{B}_2) \cdot \left(k_{11} + \sqrt{k_{12}^2 + k_{13}^2 + k_{14}^2}\right) > Z \tag{27}$$

where $R(\boldsymbol{C},\boldsymbol{B}_2)$ and P_{PMS} are independent, too. (27) implies that for sea area, the more the scattering is similar to a diplane, the more probable it is a desired target.

6. EXPERIMENT RESULT

A part of the NASA/JPL AIRSAR 4-look L-band data of San Francisco is used for the experiment of PMS detector and improved PMS detectors. The experimental procedure is as follows:

1) Calculate the $1 - R(\boldsymbol{C}, \boldsymbol{B}_1)$ and $R(\boldsymbol{C}, \boldsymbol{B}_2)$ for each pixel using (26) and (27), respectively.

2) In order to eliminate the influence of noise, average the data of $1 - R(\boldsymbol{C}, \boldsymbol{B}_1)$ and $R(\boldsymbol{C}, \boldsymbol{B}_2)$ by a 3×3 mean filter.

3) Calculate the P_{PMS} and Y of the whole image using (22), (26) and (27), respectively.

4) Obtain the detection threshold Z for each detector and compute the final results.

The approach to obtain the detection threshold Z is as follows: observing the area around the Golden Gate from Google Earth, we can find out that there is a platform or a marina in the quadrate area A of Figs. 1–3. Find out the maximal P_{PMS} and Y in this area. For each algorithm, Z is equal to the maximal P_{PMS} or Y, respectively. This approach implies that we consider a pixel as a target, only when its P_{PMS} or Y is larger than the marina's.

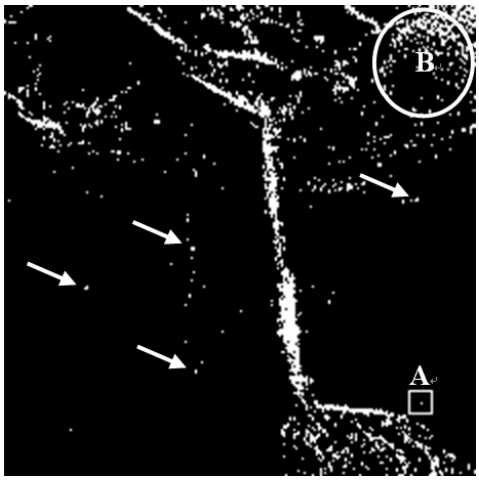

Figure 1: PMS detecor output.

Figure 1 shows the result of the PMS Detector. As shown, there are lots of false alarms, so the performance of the PMS Detector is not very good.

Figure 2 and Fig. 3 are the detection results of the two improved PMS detectors (26) and (27), respectively. It is easy to find out that the number of false alarms has been sharply eliminated.

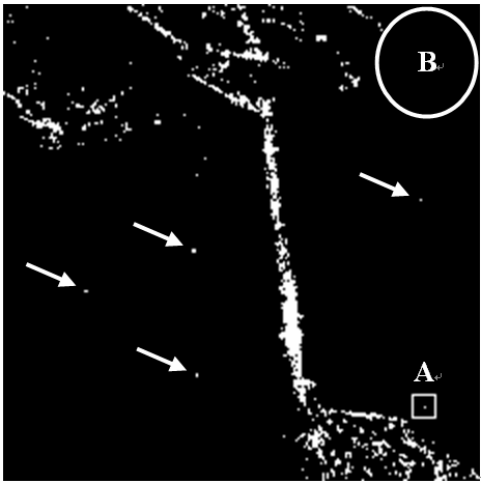

Figure 2: PMS with GSP of plate output.

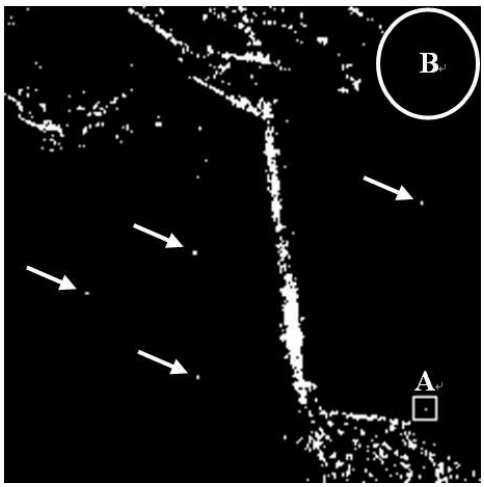

Figure 3: PMS with GSP of diplane output.

As we know, there is something wrong in the data of circular area B in the image of NASA/JPL AIRSAR San Francisco. So by the contrast of circular area B in Fig. 1 and Figs. 2–3 it is easy to find out that the counter-noise performance can be extremely enhanced by the application of the GSP information.

According to the output of all three detectors, the pixels pointed by the arrows in Figs. 1–3 are considered as the final results of target detection which most probably are ships.

7. CONCLUSIONS

The generalized similarity parameter between two polarimetric covariance matrices has been proposed in this paper for describing the similarity of the polarizations of two targets. This parameter is independent of the spans of the covariance matrices and the orientation of the targets and can be used to not only one-look but also multi-look polarimetric SAR data. Six properties of this parameter and the analysis were presented.

As an application, the target detection of multi-look polarimetric SAR data has been discussed. Two kinds of improved power maximization synthesis detectors were proposed. According to the experiment result and analysis in this paper, we find out that the generalized similarity parameter can be used to analyze the similarity between the polarizations of two targets and it is helpful to polarimetric target detection.

ACKNOWLEDGMENT

This work was supported in part by the National Natural Science Foundation of China (40571099) and in part by the Research Fund of National Key Lab of Microwave Imaging Technology, Institute of Electronics, Chinese Academy of Sciences (9140c1903020803).

REFERENCES

1. Yang, J., Y. N. Peng, and S. M. Lin, "Similarity between two scattering matrices," *Electronics Letters*, Vol. 37, No. 3, 193–194, 2001.
2. Xu, J., J. Yang, and Y. Peng, "New method of feature extraction in polarimetric SAR image classification," *Proceedings of SPIE 4741, Battlespace Digitization and Network-Centric Warfare II*, 337–344, Orlando, FL., USA, Apr. 2002.
3. Xu, J., J. Yang, Y. Peng, C. Wang, and Y.-A. Liou, "Using similarity parameters for supervised polarimetric SAR image classification," *IEICE Trans. on Communication*, Vol. E85-B, No. 12, 2934–2942, 2002.
4. Huynen, J. R., "Phenomenological theory of radar target," PhD Dissertation, Technical University, Delft, The Netherlands, 1970.
5. Cloude, S. R. and E. Pottier, "A review of target decomposition theorems in radar polarimetry," *IEEE Trans. Geosci. Remote Sensing*, Vol. 35, No. 1, 68–78, 1997.
6. Chaney, R. D., M. C. Burl, and L. M. Novak, "On the performance of polarimetric target detection algorithms," *Aerospace and Electronic Systems Magazine, IEEE*, Vol. 5, No. 11, 10–15, 1990.

The Effect of Reflectivity Dispersion on Gap Solitons in a Bragg Grating

D. Royston Neill[1], **Javid Atai**[1], **and Boris A. Malomed**[2]

[1]School of Information and Electrical Engineering
University of Sydney, Australia
[2]Department of Interdisciplinary Studies, Faculty of Engineering
Tel Aviv University, Israel

Abstract— Moving gap solitons (GSs) in a model of Bragg grating with dispersive reflectivity are considered. It is found that the dispersive reflectivity expands the solitons' stability region. Collisions between moving solitons are studied too.

1. INTRODUCTION AND THE MODEL

Fiber Bragg gratings (FBGs) are produced by a periodic variation of the refractive index along an optical fiber. The resulting coupling between counter-propagating waves results in a strong effective dispersion [1, 2]. When combined with the Kerr nonlinearity, the FBG can give rise to gap solitons (GSs). Standard equations governing the nonlinear pulse propagation in the uniform FBG within the framework of the coupled-mode theory (CMT) are [2].

$$\begin{aligned} iu_t + iu_x + \left(\frac{1}{2}|u|^2 + |v|^2\right)u + v = 0 \\ iv_t - iv_x + \left(\frac{1}{2}|v|^2 + |u|^2\right)v + u = 0 \end{aligned} \tag{1}$$

A nonuniform modulation of the refractive index, $n(x) = n_0 + \delta n(x)\cos((4\pi/\lambda_0)x + \theta(x)))$, gives rise to the FBG subject to the apodization $\delta n(x)$ and spatial chirp $\theta(x)$. A simple phenomenological generalization of (1) to include effects of the apodization adds to the model spatial dispersion of the Bragg reflectivity, accounted for by coefficient m [3],

$$\begin{aligned} iu_t + iu_x + \left(\frac{1}{2}|u|^2 + |v|^2\right)u + v + mv_{xx} = 0 \\ iv_t - iv_x + \left(\frac{1}{2}|v|^2 + |u|^2\right)v + u + mu_{xx} = 0 \end{aligned} \tag{2}$$

Soliton solutions to the modified equations can be obtained by the substitution of ansatz $\{u, v\} = \{U(x), V(x)\}e^{-i\omega t}$ and solving the resulting equations for U and V numerically. In Ref. [3], it was found that quiescent GSs completely fill the bandgap in the modified model. The dispersive reflectivity was also observed to have a stabilizing effect on the GSs, expanding the stability region previously found in the standard model [4, 5]. However, moving solitons, which are objects of the primary interest to the experiment [6], were not yet studied in the modified model, which is the subject of the present work.

2. STABILITY OF MOVING SOLITONS AND COLLISIONS

For the study of moving solitons, Eqs. (2) were transformed into a moving reference frame, and then solved by means of a numerical relaxation algorithm. A modified split-step Fourier method was used to propagate the pulses.

Figure 1 demonstrates the effect of the velocity on the stability of the pulses. It is seen that the reflectivity dispersion stabilizes the moving pulses, although the stabilizing effect becomes weaker with the increase of the velocity. The increased stability may be qualitatively explained as follows [3]: the soliton creates for itself a spot with a reduced effective reflectivity, which is tantamount to a local FBG defect with partially suppressed reflectivity. Such defects are known to attract and stabilize GSs [7, 8]. A moving soliton effectively induces a mobile defect, which plays a similar role. For unstable solitons, various outcomes of the evolution were observed, including splitting of the pulse, or its rearrangement into to a "lighter" one through emission of radiation.

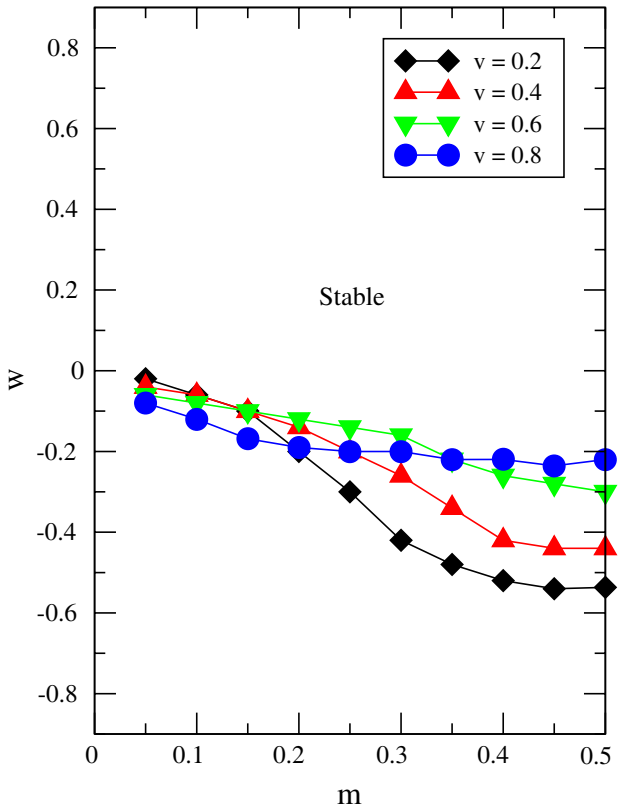

Figure 1: Stability region for the gap solitons described by the modified coupled mode system 2.

An example of collisions between the solitons in the model with the dispersive reflectivity is displayed in Figure 2. As a result of the collision, the solitons merge and a quiescent soliton, representing "standing light", emerges. Similar outcomes of collisions have been reported in the standard FBG model [9].

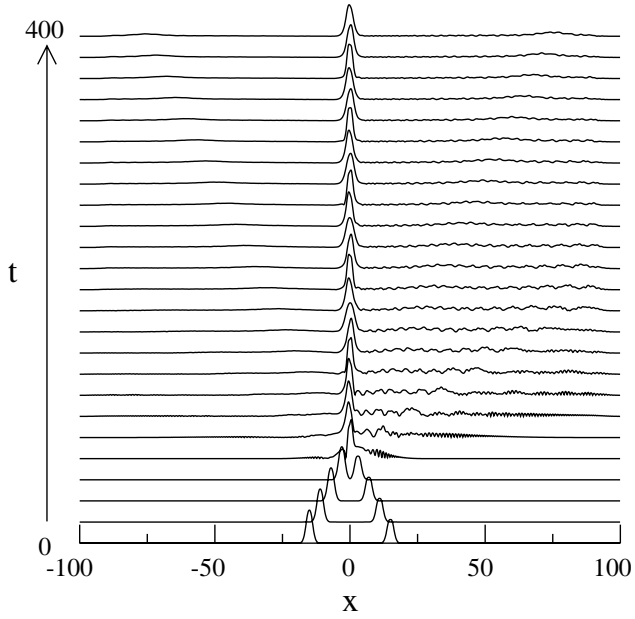

Figure 2: Collision of two solitons for the parameters $m = 0.3$, $v = \pm 0.25$ and $\omega = -0.2$.

3. CONCLUSION

The properties of moving solitons in the generalization to the coupled-mode equations describing fiber Bragg gratings were investigated. The generalization includes the reflectivity dispersion, which models effects induced by apodization or a weak disorder of the grating. It is demonstrated that the dispersion stabilizes the pulses, both quiescent and moving ones. Collisions between the solitons result in various outcomes, including the merger into a standing pulse.

REFERENCES

1. Russell, P. S. J., "Bloch wave anaylsis of dispersion and pulse propagation in pure distributed feedback," *J. Mod. Opt.*, Vol. 38, 1599, 1991.
2. De Sterke, C. M. and J. E. Sipe, "Gap solitons," *Prog. Opt.*, Vol. 33, 203, 1994.
3. Atai, J. and B. A. Malomed, "Gap solitons in Bragg gratings with dispersive reflectivity," *Phys. Lett. A*, Vol. 342, 404, 2005.
4. Malomed, B. A. and R. S. Tasgal, "Vibration modes of gap soliton in a nonlinear optical medium," *Phys. Rev. E*, Vol. 49, 5787, 1994.
5. Barashenkov, I. V., D. E. Pelinovsky, and E. V. Zemlyanaya, "Vibrations and oscillatory instabilities of gap solitons," *Phys. Rev. Lett.*, Vol. 80, 5117, 1998.
6. Mok, J. T., C. M. de Sterke, I. C. M. Littler, and B. J. Eggleton, "Dispersionless slow light using gap solitons," *Nature Phys.*, Vol. 2, 775, 2006.
7. Goodman, R. H., R. E. Slusher, and M. I. Weinstien, "Stopping light on a defect," *J. Opt. Soc. Am. B*, Vol. 19, 1635, 2002.
8. Mak, W. C. K., B. A. Malomed, and P. L. Chu, "Interaction of a soliton with a local defect in a fiber Bragg grating," *J. Opt. Soc. Am. B*, Vol. 20, 725, 2003.
9. Mak, W. C. K., B. A. Malomed, and P. L. Chu, "Formation of standing light pulse through collision of gap solitons," *Phys. Rev. E*, Vol. 68, 026609, 2003.

Application of a Modified Broyden's Method in the Finite Difference Method for Electromagnetic Field Solutions

Boguslaw Oleksiejuk[1] **and Andrew Nafalski**[1,2]

[1]Lublin University of Technology, Lublin, Poland
[2]University of South Australia, Adelaide, Australia

Abstract— The method outlined in the paper is a modified Broyden's method that offers an efficient approach to solve the nonlinear equation set obtained as a result of application of the Finite Difference Method (FDM) and is applicable for an anisotropic and nonlinear electromagnetic environment. As the classical Broyden's method, the new method does not require the determination of the Jacobi matrix elements. An example presented in the paper illustrates the application of the proposed method to nonlinear magnetic circuit configurations described by FDM.

1. INTRODUCTION

The fundamental approach to solving nonlinear equation sets is the Newton-Raphson (Newton's) matrix method. It requires time-consuming computations of the Jacobi matrix with evaluations of partial derivative functions. In order to avoid this computational expense, the Broyden's method [1] is used that does not require the evaluation of the Jacobi matrix of partial derivatives. In general the Broyden's method and its derivatives such as [2] are classified as an extension of the secant method of root finding to higher dimensions.

In the case of nonlinear and/or anisotropic materials, the basic Broyden's method does not guarantee a successful solution. An alternative method could be the direct application of the simple iterative method that in the case of non-linear magnetic circuits also often fails to converge.

The method outlined in the paper is a modified Broyden's method that offers an efficient approach to solve the nonlinear equation set obtained as a result of application of the Finite Difference Method (FDM) and is applicable for an anisotropic and/or nonlinear electromagnetic environment [3].

2. THE PROBLEM

The example used to illustrate the application of the modified Broyden's method as applied to an anisotropic nonlinear magnetic environment is a solenoid consisting of a coil with a ferromagnetic core. There are three different magnetic permeability values in the system: that of the winding, the surrounding air and the ferromagnetic core (nonlinear field dependent function). The nonlinear equation system was created using the Finite Difference Method (FDM). The investigated solenoid's volume was discretised using a rectangular non-uniform mesh of points. Mixed boundary conditions were used for this case, which were boundary conditions of Neumann and Dirichlet types specified on different subsets of the boundary. Neumann boundary conditions, that assume the continuity of the normal component of the magnetic flux density vector, were used for points situated on the border between environments with different material parameters. For the points far away from the magnetic field source, where the magnetic field is close to zero, Dirichlet boundary conditions were used. The object's symmetry simplified the analysed configuration to a quarter of the complete system. The simplifying assumptions and resulting equations for the solenoid are presented in [3, 4].

3. THE ALGORITHM

The solution of nonlinear equation sets relies on the calculation of the update $\boldsymbol{s}$ in consecutive iterations until a condition to terminate the calculation is met. In the quoted example, calculations have been also conducted by a simplified Newton's method and by the simple iterative method. In the Broyden's approach the update s_i for the i-th iteration is calculated from Equation (1) [1, 2].

$$D \cdot s_i = -f\left(A^{(i)}\right) \tag{1}$$

where f is the function describing the magnetic field in a point of a given discretisation mesh of the considered area, and A denotes the magnetic vector potential.

The next iteration value is calculated from the formula:

$$A^{(i+1)} = A^{(i)} + s_i \tag{2}$$

The matrix $\boldsymbol{D}$ is a matrix that approximates the Jacobi matrix; initially it can be the unity matrix and its next values are calculated from the formula:

$$D_{i+1} = D_i + \frac{f\left(A^{(i+1)}\right) s_i^T}{s_i^T s_i} \tag{3}$$

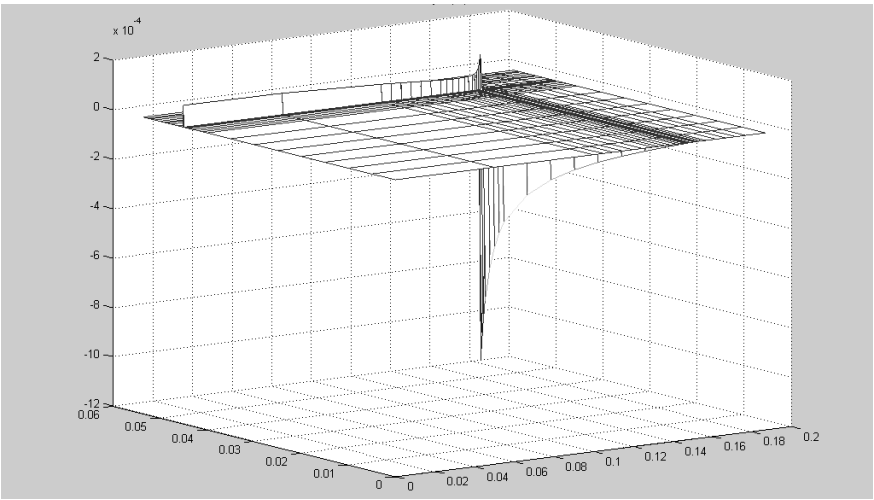

Figure 1: The update distribution over the object mesh (one quarter of the object).

The update in Fig. 1 illustrates the behaviour of the Broyden's method in solving a nonlinear equation set. In this case, the solution is not convergent, but the Broyden's update can be used to obtain, what we define here as a **useful update** $\boldsymbol{u}$, which is calculated by solving the equation set below.

$$\boldsymbol{E}\left(\boldsymbol{A^{(i)}}\right) \cdot u_i = s_i \tag{4}$$

where $\boldsymbol{E(A^{(i)})}$ is the matrix of arguments, with elements calculated from the last approximation of $\boldsymbol{A^{(i)}}$. The knowledge of the last solution enables us to calculate the respective function values of magnetic reluctivity $\boldsymbol{\rho(A)}$, necessary to evaluate the matrix $\boldsymbol{E(A^{(i)})}$ in the area of the ferromagnetic core. The next approximation of $\boldsymbol{A^{(i)}}$ is calculated from:

$$A^{(i+1)} = A^{(i)} + u_i \tag{5}$$

The proposed new algorithm of the modification of the Broyden's method can be described as follows.

Step 1: Evaluation of the reluctivity vector $\boldsymbol{\rho_0}$, most frequently the same starting value is set for all vector elements.

Step 2: Calculation of $\boldsymbol{E_0}$ elements for a given $\boldsymbol{\rho_0}$.

Step 3: The equation system below is solved in order to determine the starting iteration point in the form of a vector $\boldsymbol{A^{(0)}}$.

$$E_0 \cdot A^{(0)} = j \tag{6}$$

where $\boldsymbol{j}$ is the current density in the mesh points (different than zero if in the area of the winding)

Step 4: The function value for the current density approximation is calculated.

$$f^{(i)} = f\left(A^{(i)}\right) \tag{7}$$

Step 5: The initial matrix $\boldsymbol{D}$ is set to the unity.

Step 6: The Broyden's update is calculated from the equation system below.

$$D \cdot s_i = -f^{(i)} \tag{8}$$

Step 7: The reluctance vector $\boldsymbol{\rho_i}$ is calculated from the current approximation.

$$\rho_i = \rho\left(A^{(i)}\right) \tag{9}$$

Step 8: Values of the matrix $\boldsymbol{E_i}$ are calculated for the given approximation and the calculated vector $\boldsymbol{\rho_i}$.

$$E_i = E\left(A^{(i)}, \rho_i\right) \tag{10}$$

Step 9: The **useful update** values $\boldsymbol{u_i}$ are calculated using the equation system:

$$E_i \cdot u_i = s_i \tag{11}$$

Step 10: The next approximation is calculated.

$$A^{(i+1)} = A^{(i)} + u_i \tag{12}$$

Step 11: The function values are calculated for a given approximation.

$$f^{(i+1)} = f\left(A^{(i+1)}\right) \tag{13}$$

Step 12: The condition of the termination of iterations is checked using the square norm (the norm) below.

$$\sum_{j=1}^{w} f_j\left(A^{(i+1)}\right)^2 < \varepsilon \tag{14}$$

Step 13: If the condition (14) is met, the calculation process is terminated; if not a new matrix $\boldsymbol{D}$ is calculated.

$$D = D + \frac{f^{(i)} s_i^T}{s_i^T s_i} \tag{15}$$

we set:

$$f^{(i)} = f^{(i+1)} \quad \text{and} \quad A^{(i)} = A^{(i+1)} \tag{16}$$

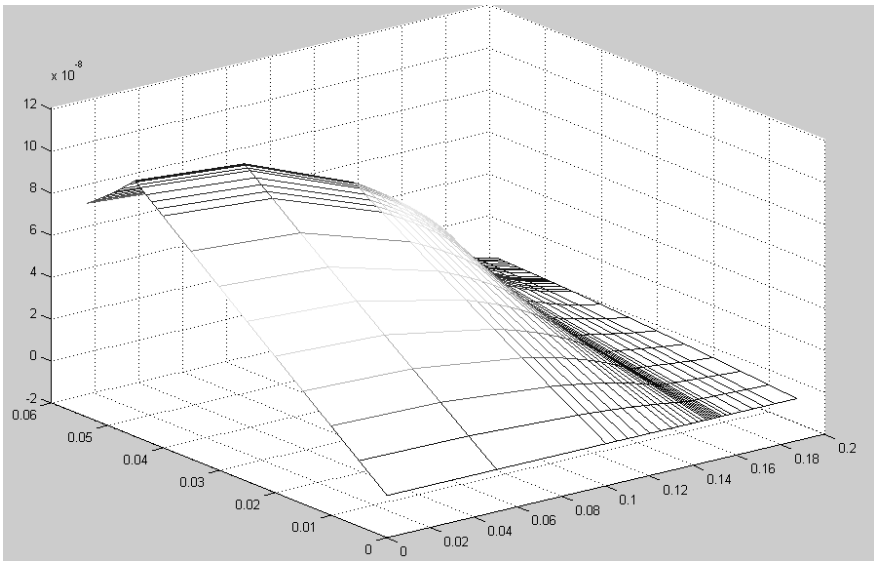

Figure 2: Distribution of the useful update (the proposed modification) in the first iteration step.

and return to the step 6.

In the considered example, calculating the update using the original Broyden's method does not lead to the convergence. It is necessary to convert the Broyden's update into the useful update (11). An example of a useful update distribution over the discretisation mesh is shown in Fig. 2. The process is convergent.

4. PARTIAL DERIVATIVES

In order to compare the proposed method with the Newton's method, the simplified partial derivative formulae of Jacobi matrix have been introduced as shown below.

$$\frac{\partial f_i}{\partial A_i} = e,\ \frac{\partial f_i}{\partial A_{i+m}} = epm,\ \frac{\partial f_i}{\partial A_{i-m}} = emm,\ \frac{\partial f_i}{\partial A_{i+1}} = ep1,\ \frac{\partial f_i}{\partial A_{i-1}} = em1 \tag{17}$$

In (17) ***e, epm, emm, ep1 and em1*** are calculated for air, core and the horizontal and vertical boundary between the core and air, respectively [3, 4].

5. COMPARISON OF RESULTS

Calculations for the given magnetic configuration have been conducted using the simple iteration method, the Newton's method, with the derivative values calculated from (17), and the proposed modification to the Broyden's method, for low and high saturation conditions of the magnetic core [4, 5].

As expected, for low core flux densities — basically a linear magnetisation case — all three methods deliver solutions at comparable iteration numbers. In the case of the nonlinear magnetisation core conditions the norm values are diversified for the three methods (an example is shown in Table 1).

Table 1: Comparison of the norm for the three methods after 20 iterations

Method	The value of the norm (14) after the last iteration
Simple iteration	$5,3931 * 10^{9}$
Newton's method	$8,3102 * 10^{10}$
The proposed modified Broyden's method	$3,6472 * 10^{-9}$

The starting point for A_{s1} was calculated for all mesh points and all methods under the assumption that the initial reluctivity of the core is the same as that of air. The simple iteration method and the Newton' method are non-convergent in this case. In other analysed cases the Newton's method is convergent but requires more iteration steps that the proposed Broyden's modified method.

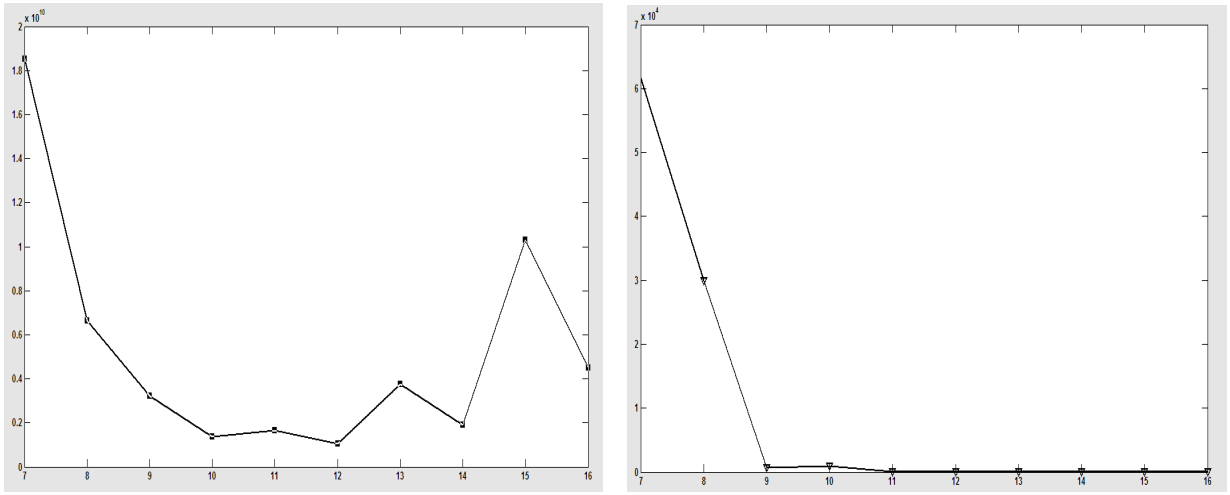

Figure 3: Norm values in consecutive iterations. On the left the Newton's method, on the right the proposed Broyden's modification.

The Fig. 3 and the Table 1 illustrate the convergence process for the same core high saturation case. Both Newton's and the simple iteration methods (not shown in Fig. 3) fail to convergence and oscillate away from the solution. On the other hand the proposed modified Broyden's method is convergent after several iterations.

6. CONCLUSIONS

A modification to a classical Broyden's method that deals efficiently in solving the equations of electromagnetic configurations with material discontinuities (singular points) has been proposed. The proposed method was compared with the simple iteration and the Newton's methods and demonstrated its superiority in terms of the existing convergence and the required iteration time. Calculations using the modified Broyden's method for the solenoid were verified by means of the Final Element Method package Opera 3D by VECTOR FIELDS, with comparable results obtained.

REFERENCES

1. Broyden, C. G., "A class of methods for solving nonlinear simultaneous equations," *Mathematics of Computation*, Vol. 19, No. 92, 577–593, 1965.
2. Martinez, J. M., "A family of quasi-Newton methods for nonlinear equations with direct secant updates of matrix factorizations," *SIAM Journal on Numerical Analysis*, Vol. 27, No. 4, 1034–1049, 1990.
3. Oleksiejuk, B., "Equation systems describing nonlinear magnetic field of a nonlinear magnetic circuit," (in Polish), *Proceedings of Lublin Academic IT Forum, Varia Informatica, Algorithms and Programs*, 145–152, Lublin, Poland, 2006.
4. Oleksiejuk, B., "Application of Newton-like methods for modelling of static magnetic fields of a nonlinear magnetic circuit," (in Polish), *Materials of the 4th PhD Seminar of the Faculty of Electrical Engineering, Lublin University of Technology*, 121–129, Lublin, 2004.
5. Marciniak, A., D. Gregulec, and J. Kaczmarek, *Basic Numerical Procedures*, (in Polish), Nakom, Poznan, Poland, 2000.

The Complex Faraday Tensor for Relativistic Evolution of a Charged Particle in a Constant Field

Y. Friedman and M. M. Danziger
Jerusalem College of Technology, Israel

Abstract— In this paper, we define the complex Faraday tensor $\mathcal{F}_{\mathcal{C}}$ as an operator representation of the electromagnetic field. The electromagnetic stress-energy tensor can be expressed as $T = \frac{\bar{\mathcal{F}}_{\mathcal{C}}\mathcal{F}_{\mathcal{C}}}{2\mu_0}$. We obtain the general solution of the relativistic evolution of a charged particle in a constant field by use of $\mathcal{F}_{\mathcal{C}}$ and its properties. The method of the derivation of this solution is significantly simpler than the ones which appear in the literature. All of the commonly solved special cases can easily be derived from it.

We discuss possible interpretation of the complexification of the electromagnetic tensor. We indicate that $\mathcal{F}_{\mathcal{C}}$ may express the action of the electromagnetic field not only upon the charge of an electron but also upon its spin. We conjecture that this representation is more accurate than the standard representation and that a complex 4D space can be defined to include a description of the evolution of the magnetic moment.

1. INTRODUCTION

In general, the electromagnetic field tensor F, expressed by a four-by-four matrix, is used to describe the electromagnetic field intensity. This tensor provides a convenient expression for the Lorentz force and therefore can describe the evolution of a charged particle. In addition to this representation, the complex Faraday vector $\mathbf{F} = \mathbf{E} + i\mathbf{B}$ has been used widely in the literature to obtain the Lorentz field invariants [7]. Silberstein first combined both concepts in 1907 to define a complex Faraday tensor $F + iF^*$ [8, 9]. He used a quaternion based formalism and did not apply the tensor to describe any kinematic phenomena. It was later shown that Maxwell's equations can be derived from such a tensor [10].

The relativistic motion of a charge in constant, uniform, and mutually perpendicular electric and magnetic fields is treated in a number of classic texts [4, 7]. The solution of the relativistic motion of a charge in a constant, uniform field by use of Clifford algebra techniques is given in [1]. A solution for mutually perpendicular electric and magnetic fields as viewed in the laboratory frame is given in [3] by use of the notion of symmetric velocity. A covariant solution of the problem is given in [6].

We propose here to apply the operator representing the complex Faraday tensor to solve the evolution problem. The square of this operator is a scalar multiple of the identity matrix, which is not the case for the standard electromagnetic tensor. This property is critical for obtaining explicit solutions in an easy way.

2. OPERATOR REPRESENTATION OF THE FARADAY VECTOR

Given the electric field intensity $\mathbf{E}(\mathbf{r}, t)$ and the magnetic field intensity $\mathbf{B}(\mathbf{r}, t)$ one can define a complex 3D-vector, called the Faraday vector as

$$\mathbf{F} = \mathbf{E} + ic\mathbf{B}. \tag{1}$$

For the rest of the paper we will use units in which $c = 1$ and we will thus omit it from further equations. The Faraday vector is used to describe the Lorentz invariant field constants [7]. The electromagnetic tensor $F_{\mu\nu}$ [4, 5] is used to show the covariance of electromagnetism. The Lorentz force $\mathbf{F} = q(\mathbf{E} + \mathbf{v} \times \mathbf{B})$ on a charged particle with charge q acts on the four-velocity U^μ of this particle as a linear operator. This operator is described by q times the mixed tensor $F = F^\nu_\mu$ with the matrix

$$F^\nu_\mu = \begin{pmatrix} 0 & E_1 & E_2 & E_3 \\ E_1 & 0 & B_3 & -B_2 \\ E_2 & -B_3 & 0 & B_1 \\ E_3 & B_2 & -B_1 & 0 \end{pmatrix}. \tag{2}$$

It is known (see [5]) that the four-velocity $U(\tau)$ of a charged particle of mass m and charge q is the solution of the relativistic dynamic equation

$$\frac{dU^\nu}{d\tau} = \frac{q}{m} F^\nu_\mu U^\mu \tag{3}$$

with the initial condition $U(0) = U_0$ — the initial four-velocity. If the field is constant we get a first order system of differential equations with constant coefficients. From a known theorem of differential equations, such an initial value problem has a solution

$$U(\tau) = \exp\left(\frac{q}{m}\tau F\right) U_0. \tag{4}$$

but it is not so easy to obtain an explicit form of this operator exponent.

To obtain an easy explicit solution we define an operator representation of the Faraday vector via a complex matrix

$$\mathcal{F}_\mathcal{C} = \begin{pmatrix} 0 & F_1 & F_2 & F_3 \\ F_1 & 0 & -iF_3 & iF_2 \\ F_2 & iF_3 & 0 & -iF_1 \\ F_3 & -iF_2 & iF_1 & 0 \end{pmatrix} \tag{5}$$

in which $F_j = E_j + iB_j$. We will call this matrix *the complex Faraday tensor.*

The electromagnetic stress energy tensor T is related to $\mathcal{F}_\mathcal{C}$ via

$$\frac{1}{2}\mathcal{F}_\mathcal{C}\bar{\mathcal{F}}_\mathcal{C} = \mu_0 T, \tag{6}$$

where μ_0 is the magnetic permeability of a vacuum.

The real part of this tensor is the mixed electromagnetic tensor:

$$F = Re(\mathcal{F}_\mathcal{C}) = \frac{1}{2}(\mathcal{F}_\mathcal{C} + \bar{\mathcal{F}}_\mathcal{C}), \tag{7}$$

where $\bar{\mathcal{F}}_\mathcal{C}$ denotes the complex conjugate of the matrix $\mathcal{F}_\mathcal{C}$. In the evolution equation (3) and its solution (4) we can replace the mixed electromagnetic tensor with with $Re(\mathcal{F}_\mathcal{C})$. To do this efficiently we have to study the properties of the complex Faraday tensor.

3. PROPERTIES OF THE COMPLEX FARADAY TENSOR

It is natural to decompose $\mathcal{F}_\mathcal{C}$ as a linear combination of the following basis of matrices:

$$\mathcal{F}_\mathcal{C} = F_1 K_1 + F_2 K_2 + F_3 K_3 \tag{8}$$

in which

$$K_1 = \begin{pmatrix} 0 & 1 & 0 & 0 \\ 1 & 0 & 0 & 0 \\ 0 & 0 & 0 & -i \\ 0 & 0 & i & 0 \end{pmatrix}, \; sK_2 = \begin{pmatrix} 0 & 0 & 1 & 0 \\ 0 & 0 & 0 & i \\ 1 & 0 & 0 & 0 \\ 0 & -i & 0 & 0 \end{pmatrix}, \; K_3 = \begin{pmatrix} 0 & 0 & 0 & 1 \\ 0 & 0 & -i & 0 \\ 0 & i & 0 & 0 \\ 1 & 0 & 0 & 0 \end{pmatrix}. \tag{9}$$

These matrices have the following multiplication properties:

$$K_k K_l = i\epsilon^m{}_{kl} K_m + \delta_{kl} I, \quad \bar{K}_k \bar{K}_l = -i\epsilon^m{}_{kl} \bar{K}_m + \delta_{kl} I \tag{10}$$

$$\bar{K}_k K_l = K_l \bar{K}_k = R_k(i\epsilon^m{}_{kl} K_m + \delta_{kl} I), \tag{11}$$

where ϵ^{klm} denotes the Levi-Civita tensor, δ_{jk} denotes the Kronecker delta and R_k denotes the space reversal about the k spacial axis. From (10) it follows that $\{K_k\}$ fulfill the canonical anti-commutation relations (CAR):

$$\frac{1}{2}(K_k K_l + K_l K_k) = \delta_{kl} I. \tag{12}$$

The commutators of these matrices are

$$[K_k, K_l] = 2i\epsilon^m{}_{kl} K_m, \tag{13}$$

which shows that the $J_k = iK_k/2$ matrices fulfill the angular momentum commutation relations, while $K_k/2$ fulfill the commutation relations of generators of boosts. Moreover

$$[K_k, \bar{K}_l] = 0. \tag{14}$$

Table 1: $-iK_kK_l$ — The table shows the row matrix multiplied by the column matrix and multiplied by $-i$. R_k indicates a matrix of space reflection about the k axis and without a time reversal.

$k\backslash l$	K_1	K_2	K_3	$\bar{K}_1$	$\bar{K}_2$	$\bar{K}_3$
K_1	iI	K_3	$-K_2$	iR_x	R_yK_3	R_zK_2
K_2	$-K_3$	iI	K_1	R_xK_3	iR_y	$-R_zK_1$
K_3	K_2	$-K_1$	iI	R_xK_2	R_yK_1	iR_z
$\bar{K}_1$	iR_x	R_xK_3	$-R_xK_2$	iI	$-\bar{K}_3$	$\bar{K}_2$
$\bar{K}_2$	$-R_yK_3$	iR_y	R_yK_1	$\bar{K}_3$	iI	$-\bar{K}_1$
$\bar{K}_3$	R_zK_2	$-R_zK_1$	iR_z	$-\bar{K}_2$	$\bar{K}_1$	iI

Using (12), we can state that

$$\mathcal{F_C}^2 = (F_1^2 + F_2^2 + F_3^2)I = z^2 I \tag{15}$$

for a complex constant scalar z. Plugging in $F_k = E_k + iB_k$ we find that $z^2 = \mathbf{E}^2 - \mathbf{B}^2 + i2\mathbf{E}\cdot\mathbf{B}$. The real and imaginary parts of z^2 are the two Lorentz invariants of the electromagnetic field. Thus, also z is a Lorentz invariant.

4. RELATIVISTIC EVOLUTION OF A CHARGE IN A CONSTANT UNIFORM FIELD

We consider now the relativistic evolution of the four-velocity of a charge in a constant field. Restating its solution (4) with $\mathcal{F_C}$ we obtain

$$U(\tau) = \exp[(\mathcal{F_C} + \bar{\mathcal{F}}_\mathcal{C})\omega\tau]U_0 \tag{16}$$

in which $\omega = \frac{q}{2m}$. From (14) we can see that $[\mathcal{F_C}, \bar{\mathcal{F}}_\mathcal{C}] = 0$. From a known theorem in mathematics, if two operators A and B commute, ie $[A, B] = 0$, then $\exp(A + B) = \exp(A)\exp(B)$. Hence

$$\exp[(\mathcal{F_C} + \bar{\mathcal{F}}_\mathcal{C})\omega\tau] = \exp(\mathcal{F_C}\omega\tau)\cdot\exp(\bar{\mathcal{F}}_\mathcal{C}\omega\tau) \tag{17}$$

Since $\exp(\bar{\mathcal{F}}_\mathcal{C}\omega\tau)$ is the complex conjugate of $\exp(\mathcal{F_C}\omega\tau)$, it remains only to solve for $\exp(\mathcal{F_C}\omega\tau)$.

By expanding the exponent as a Taylor series and using (15), we can break down the series into its even and odd terms. For every even term, $\mathcal{F_C}^{2n} = z^{2n}I$ and for every odd term $\mathcal{F_C}^{2n+1} = z^{2n}\mathcal{F_C} = z^{2n+1}\frac{\mathcal{F_C}}{z}$. Assuming that $z \neq 0$, we get:

$$\exp(\mathcal{F_C}\omega\tau) = \sum_{n=0}^{\infty}\frac{(\mathcal{F_C}\omega\tau)^n}{(n)!} = \sum_{n=0}^{\infty}\frac{(z\omega\tau)^{2n}}{(2n)!}I + \frac{\mathcal{F_C}}{z}\sum_{n=0}^{\infty}\frac{(z\omega\tau)^{2n+1}}{(2n+1)!} = \cosh(z\omega\tau)I + \frac{\mathcal{F_C}}{z}\sinh(z\omega\tau) \tag{18}$$

We will examine the case where $z = 0$ below.

As we established in (17), the full solution is the product of (18) and its conjugate:

$$U(\tau) = \big(\cosh(z\omega\tau)I + \frac{\mathcal{F_C}}{z}\sinh(z\omega\tau)\big)\big(\cosh(\bar{z}\omega\tau)I + \frac{\bar{\mathcal{F}}_\mathcal{C}}{\bar{z}}\sinh(\bar{z}\omega\tau)\big)U_0 \tag{19}$$

Using basic hyperbolic trigonometric identities, Equation (6) and writing $z = a + ib$, we obtain:

$$U(\tau) = \cosh(2a\omega\tau)A_0 + \sinh(2a\omega\tau)A_1 + \cos(2b\omega\tau)A_2 - \sin(2b\omega\tau)A_3 \tag{20}$$

in which

$$A_0 = \left(\frac{1}{2} + \frac{\mu_0}{|z|^2}T\right)U_0, \quad A_1 = \Re\left[\frac{\mathcal{F_C}}{z}\right]U_0, \quad A_2 = \left(\frac{1}{2} - \frac{\mu_0}{|z|^2}T\right)U_0, \quad A_3 = \Im\left[\frac{\mathcal{F_C}}{z}\right]U_0 \tag{21}$$

and $\Re[\mathcal{F_C}/z]$ and $\Im[\mathcal{F_C}/z]$ denote the real and imaginary parts of the complex matrix $\mathcal{F_C}/z$, respectively.

In other words, the evolved four-velocity is expressed as a linear combination of four constant four-velocities. All of the four vectors are Lorentz orthogonal. The vector A_0 is time-like, A_1 is

space-like and they are both of the same magnitude. Together they define uniform acceleration in the $\mathbf{E}\times\mathbf{B}$ direction. The vectors A_2 and A_3 are space-like, of the same magnitude and together they define a rotation about the $\mathbf{E}\times\mathbf{B}$ axis. To find the world line of the charge, we need only integrate $\int_0^t U(\tau)d\tau$. Since the vectors are constant, the integral is only on the magnitude coefficients, which are simple integrals.

5. SPECIAL CASES

The three commonly solved [4, 5] cases ($\mathbf{E}=0, \mathbf{B}=0$ and $\mathbf{E}\cdot\mathbf{B}=0$) are easily obtained special cases of (20).

Case 1: $\mathbf{B}=0$, $\mathbf{F}=\mathbf{E}$. According to (15), $z^2=\mathbf{E}^2$ and $z=|\mathbf{E}|=a$ is real. Since $b=0$, solution (20) simplifies to

$$U(\tau)=\left(\frac{1}{2}-\frac{\mu_0}{a^2}T\right)U_0+\sinh(2a\omega\tau)\frac{F}{a}U_0+\cosh(2a\omega\tau)\left(\frac{1}{2}+\frac{\mu_0}{a^2}T\right)U_0. \tag{22}$$

If we assume $\mathbf{E}=(E,0,0)$, we get:

$$U(\tau)=\begin{pmatrix}\cosh((Eq/m)\tau) & \sinh((Eq/m)\tau) & 0 & 0\\ \sinh((Eq/m)\tau) & \cosh((Eq/m)\tau) & 0 & 0\\ 0 & 0 & 1 & 0\\ 0 & 0 & 0 & 1\end{pmatrix}U_0 \tag{23}$$

Case 2: $\mathbf{E}=0$, $\mathbf{F}=i\mathbf{B}$ and $\mathbf{F^2}=-\mathbf{B^2}$. According to (15), $z^2=-\mathbf{B}^2$ and $z=i|\mathbf{B}|=ib$ is purely imaginary. Since $a=0$, solution (20) simplifies to

$$U(\tau)=\left(\frac{1}{2}+\frac{\mu_0}{b^2}T\right)U_0+\sin(2b\omega\tau)\frac{F}{b}U_0+\cos(2b\omega\tau)\left(\frac{1}{2}-\frac{\mu_0}{b^2}T\right)U_0 \tag{24}$$

Once again, if we assume $\mathbf{B}=(B,0,0)$, we get:

$$U(\tau)=\begin{pmatrix}1 & 0 & 0 & 0\\ 0 & 1 & 0 & 0\\ 0 & 0 & \cos((Bq/m)\tau) & \sin((Bq/m)\tau)\\ 0 & 0 & -\sin((Bq/m)\tau) & \cos((Bq/m)\tau)\end{pmatrix}U_0. \tag{25}$$

Case 3: $\mathbf{E}\cdot\mathbf{B}=0$. From (15) $z^2=\mathbf{E}^2-\mathbf{B}^2$. This implies three different possible behaviors for $z=a$, $z=ib$ or $z=0$.

- $\mathbf{E^2}-\mathbf{B^2}>0$: In this case, $z=\sqrt{\mathbf{E^2}-\mathbf{B^2}}=a$ and the evolution is according to (22). The only difference is the following. The constant term in Case 1 depends only on the initial condition, as we can see from (23). Now, this term depends on the field as well and when the initial velocity is zero it becomes equal to the known drift velocity.

- $\mathbf{E^2}-\mathbf{B^2}<0$:In this case, $z=i\sqrt{\mathbf{B^2}-\mathbf{E^2}}=ib$ and the evolution is according to (24). The only difference is the following. The constant term in Case 2 depends only on the initial condition, as we can see from (25). Now, this term depends on the field as well and when the initial velocity is zero it becomes equal to the known drift velocity.

- $\mathbf{E^2}-\mathbf{B^2}=0$: In this case, $z=0$. This case demands that we use (17) before we divided by z in (18). Since ${\mathcal{F}_{\mathcal{C}}}^2=0$, the Taylor series is finite and the general solution is

$$U(\tau)=(1+\mathcal{F}_{\mathcal{C}}\omega\tau)(1+\bar{\mathcal{F}}_{\mathcal{C}}\omega\tau)U_0=U_0+2\omega\tau FU_0+2\omega^2\tau^2\mu_0TU_0. \tag{26}$$

  In this case for large τ the velocity will be defined by the last term which is in the $\mathbf{E}\times\mathbf{B}$ direction.

6. DISCUSSION AND CONCLUSION

The Lorentz force of an electromagnetic field on a charge is usually described by the action of a linear operator F, associated with the electro-magnetic tensor, on the four-velocity of the charge. We have shown that by introducing a complex matrix $\mathcal{F}_{\mathcal{C}}$, for which F is its real part, we can significantly simplify the solution for the relativistic dynamics of a charge in a constant field. We have also found (6) that $\mathcal{F}_{\mathcal{C}}$ is some kind of matrix square root of the electromagnetic stress tensor. It seems that $\mathcal{F}_{\mathcal{C}}$ is not simply a technical tool to help solve problems, but rather a more accurate description of the electromagnetic field.

As we have seen, the components $\frac{1}{2}K_j$ and $\frac{i}{2}K_j$ of this tensor satisfy the same commutation relations as the relativistic boost and angular momentum generators in the Lorentz group, respectively. In [2], it was shown that these operators represent the angular momentum of a spin 1/2 representation. Moreover, if on the complexified space of representations, we choose the Newman-Penrose basis, the coordinates in this basis are the Dirac bi-spinors. This indicates that the complex tensor $\mathcal{F}_{\mathcal{C}}$ is somehow related to the description of the action of the electromagnetic field on the electron.

The standard electromagnetic tensor acts on the real 4D space of four-velocities. It is natural to assume that the complex Faraday tensor $\mathcal{F}_{\mathcal{C}}$ would act upon a complex 4D space for which the real part would be the four-velocity of a test charge. We conjecture that the imaginary part of this space will have information on the angular velocity of the test charged particle. In this case we expect to obtain the action of the electromagnetic field not only on the position of the charge but also upon its angular momentum. Since most charged particles in nature have a magnetic moment, a full description of the action of the field upon them must also involve information about the evolution of their magnetic moment.

REFERENCES

1. Baylis, W. E., *Electrodynamics, A Modern Geometric Approach, Progress in Physics*, Vol. 17, Birkhäuser, Boston, 1999.
2. Friedman, Y., "Representations of the Poincaré group on relativistic phase space," arXiv:0802.0070v1, 2008.
3. Friedman, Y. and M. Semon, "Relativistic acceleration of charged particles in uniform and mutually perpendicular electric and magnetic fields as viewed in the laboratory frame," *Phys. Rev. E*, Vol. 72, No. 2, 026603, 2005.
4. Jackson, J. D., *Classical Electrodynamics*, Wiley & Sons, New York, 1999.
5. Rindler, W., *Relativity: Special, General, and Cosmological*, Oxford University Press, New York, 2001.
6. Muñoz, G., "Charged particle in a constant electromagnetic field: Covariant solution," *American Journal of Physics*, Vol. 65, No. 5, 429–433, 1997.
7. Landau, L. D. and E. M. Lifschitz, *The Classical Theory of Fields*, Pergamon, Oxford, 1962.
8. Silberstein, L., "Nachtrag zur abhandlung über electromagnetische grundgleichungen in bivektorieller behandlung," *Ann. Phys. Lpz.*, Vol. 24, 783–784, 1907.
9. Silberstein, L., *The Theory of Relativity*, Macmillan and Co., London, 1927.
10. Schrödinger, E., "Contributions to Born's new theory of the electromagnetic field," *Proc. Roy. Soc. London A*, Vol. 120, 465–477, 1935.

Electromagnetic Information Theory for Wireless and Antenna Systems

F. K. Gruber and E. A. Marengo
Department of Electrical and Computer Engineering, Northeastern University
360 Huntington Ave., Boston, MA 02115, USA

Abstract— This paper investigates certain fundamental aspects not fully covered by previous work on information-theoretic characterization, via Shannon's information capacity and number of degrees of freedom, of wave radiation (antenna) and wireless propagation systems. Specifically, the paper derives, from the fundamental physical point of view of Maxwell's equations, the information capacity of space-time wireless channels formed by electromagnetic sources and receivers in a known background medium. The theory is developed for the two cases of essentially bandlimited and time-limited systems and of purely bandlimited systems. Connections to the strictly spatial case (time-harmonic or narrowband sources) are also mentioned. The developments take into account the physical radiated power constraint in addition to the more usual constraint in the source L^2 norm. Based on such radiated power and/or current L^2 norm constraints we derive the information capacity of canonical wireless and antenna systems in free space, for a given additive Gaussian noise level, as well as an associated number of degrees of freedom resulting from such capacity calculations. This approach constitutes a rigorous, information-theoretic method to define under given noise the dimensionality of the field.

1. ELECTROMAGNETIC INFORMATION CHANNELS IN A SPHERICAL SCANNING GEOMETRY

Consider an electromagnetic source $\mathcal{J}(\mathbf{r},t)$ (a current density) confined to the spherical volume $V_T = \{\mathbf{r} \in R^3 : r \equiv |\mathbf{r}| \leq a\}$. The frequency domain representation of this source is obtained by taking the temporal Fourier transform of $\mathcal{J}(\mathbf{r},t)$, which gives the spectral current density $\mathbf{J}(\mathbf{r},f) = \int \mathcal{J}(\mathbf{r},t)e^{-\imath 2\pi ft}dt$ where $\imath = \sqrt{-1}$. For notational simplicity in this section we will suppress the f dependence, e.g., we will use $\mathbf{J}(\mathbf{r})$ in place of $\mathbf{J}(\mathbf{r},f)$, with the understanding that all quantities depend on the frequency f. This source $\mathbf{J}(\mathbf{r})$ is assumed to belong to the Hilbert space $\mathcal{X} = L^2(V_T)$ of square integrable functions of support V_T with inner product defined by $\langle \mathbf{J}|\mathbf{J}'\rangle_{\mathcal{X}} \equiv \int_{V_T} \mathbf{J}^*(\mathbf{r}) \cdot \mathbf{J}'(\mathbf{r})d^3r$ where $*$ over a quantity means its complex conjugate.

The electric field $\mathbf{E}(\mathbf{r})$ is measured in a spherical scanning surface $V_R = \{\mathbf{r} \in R^3 : r = b\}$ of radius b concentric to the source. This *measured* field belongs to the Hilbert space $\mathcal{Y} = L^2(V_R)$ with inner product defined by $\langle \mathbf{E}|\mathbf{E}'\rangle_{\mathcal{Y}} \equiv \int_{V_R} \mathbf{E}^*(\mathbf{r}) \cdot \mathbf{E}'(\mathbf{r})d^3r$ and is given by

$$\mathbf{E}(\mathbf{r}) = (P\mathbf{J})(\mathbf{r}) = I_{V_R}(\mathbf{r}) \int_{V_T} \mathbf{G}(\mathbf{r},\mathbf{r}') \cdot \mathbf{J}(\mathbf{r}')d^3r' \tag{1}$$

where we have introduced the radiation operator $P : \mathcal{X} \to \mathcal{Y}$, $I_{V_R}(\mathbf{r})$ is an indicator function parameterized by V_R with value 1 if $\mathbf{r} \in V_R$ or 0 if $\mathbf{r} \notin V_R$, and $\mathbf{G}(\mathbf{r},\mathbf{r}')$ represents the dyadic Green function satisfying

$$\nabla \times \nabla \times \mathbf{G}(\mathbf{r},\mathbf{r}') - k^2\mathbf{G}(\mathbf{r},\mathbf{r}') = \imath 2\pi f\mu_0 \mathbf{I}\delta(\mathbf{r}-\mathbf{r}')$$

where $\mathbf{I}$ is the identity dyadic, δ is Dirac's delta function, and $k = 2\pi f\sqrt{\mu_0\varepsilon_0}$ is the wavenumber where ε_0 is the free-space permittivity and μ_0 is the free-space permeability. In particular, if the transmission and reception volumes are finite and disjoint, the Green function kernel in (1) is square integrable [1–3] so that the operator P is compact and can be represented via the SVD [2–4].

It is possible to show by means of the multipole expansion [5, 6] of $\mathbf{E}(\mathbf{r})$ that the singular system of P is given by $(\mathbf{u}_{j,l,m}(\mathbf{r}),\ \mathbf{v}_{j,l,m}(\mathbf{r}),\ \sigma_l^{(j)};\ j = 1,2;\ l = 1,2,\ldots;\ m = -l,-l+1,\ldots,l-1,l)$ where

$$\mathbf{u}_{j,l,m}(\mathbf{r}) = I_{V_R}(\mathbf{r})\frac{\mathbf{A}_{j,l,m}(\mathbf{r})}{\|\mathbf{A}_{j,l,m}\|_{\mathcal{Y}}}, \tag{2}$$

$$\mathbf{v}_{j,l,m}(\mathbf{r}) = I_{V_T}(\mathbf{r})\frac{\mathbf{B}_{j,l,m}(\mathbf{r})}{\|\mathbf{B}_{j,l,m}\|_{\mathcal{X}}}, \tag{3}$$

and

$$\sigma_l^{(j)} = \|\mathbf{B}_{j,l,m}\|_{\mathcal{X}}\|\mathbf{A}_{j,l,m}\|_{\mathcal{Y}}, \tag{4}$$

where here and henceforth $\|\cdot\|$ denotes Euclidean norm (so that $\|\mathbf{B}_{j,l,m}\|_{\mathcal{X}}^2 = \langle\mathbf{B}_{j,l,m}|\mathbf{B}_{j,l,m}\rangle_{\mathcal{X}}$).

The electric and magnetic multipole fields, $\mathbf{A}_{1,l,m}(\mathbf{r})$ and $\mathbf{A}_{2,l,m}(\mathbf{r})$, in (2)–(4) are given by

$$\mathbf{A}_{1,l,m}(\mathbf{r}) = \nabla \times \left[h_l^+(kr)\mathbf{Y}_{l,m}(\hat{\mathbf{r}})\right] \tag{5}$$

and

$$\mathbf{A}_{2,l,m}(\mathbf{r}) = \imath k h_l^+(kr)\mathbf{Y}_{l,m}(\hat{\mathbf{r}}) \tag{6}$$

where h_l^+ is the spherical Hankel function of the first kind (corresponding to outgoing waves) and order l, and $\mathbf{Y}_{l,m}$ is the vector spherical harmonic of degree l and order m defined by [7, 8] $\mathbf{Y}_{l,m}(\hat{\mathbf{r}}) = \mathbf{L}Y_{l,m}(\hat{\mathbf{r}})$ where $\mathbf{L} = -\imath\mathbf{r}\times\nabla$ (the angular momentum operator), $\hat{\mathbf{r}} = (\theta, \phi)$ represents the direction of $\mathbf{r}$, and $Y_{l,m}(\hat{\mathbf{r}}$ represents the spherical harmonics [9, p. 787]. The spherical wavefunctions $\mathbf{B}_{j,l,m}$ are defined by

$$\mathbf{B}_{1,l,m}(\mathbf{r}) = -\frac{\eta}{l(l+1)}I_{V_T}(\mathbf{r})\nabla \times [j_l(kr)\mathbf{Y}_{l,m}(\hat{\mathbf{r}})] \tag{7}$$

and

$$\mathbf{B}_{2,l,m}(\mathbf{r}) = -\frac{ik\eta}{l(l+1)}I_{V_T}(\mathbf{r})j_l(kr)\mathbf{Y}_{l,m}(\hat{\mathbf{r}}) \tag{8}$$

where η is the free-space impedance ($\approx 377\,\Omega$), and j_l is the spherical Bessel function of order l.

Expanding the field $\mathbf{E}(\mathbf{r})$ and the source $\mathbf{J}(\mathbf{r})$ in terms of the singular functions (2) and (3) yields the alternative (singular system or diagonalizing) representation of (1)

$$a_{i,l,m} = \sigma_l^{(j)} b_{i,l,m} \tag{9}$$

where $a_{j,l,m} = \langle\mathbf{u}_{j,l,m}|\mathbf{E}\rangle_{\mathcal{Y}}$ and $b_{j,l,m} = \langle\mathbf{v}_{j,l,m}|\mathbf{J}\rangle_{\mathcal{X}}$.

2. SPACE-TIME CAPACITY OF BANDLIMITED CHANNELS

As shown in (9), for each frequency f the source $\mathbf{J}(\mathbf{r}, f)$ can be represented in terms of a set of equivalent independent circuits corresponding to each of the spherical modes in the multipole expansion of the electric field. Applying the inverse Fourier transform so that, for example, $\tilde{a}_{j,l,m}(t) = \int_{-\infty}^{\infty} a_{j,l,m}(f)e^{\imath 2\pi ft}df$ and considering the presence of white Gaussian noise at the receiver we find the model:

$$\tilde{a}_{j,l,m}(t) = \int \tilde{b}_{j,l,m}(\tau)\tilde{\sigma}_{W,l}^{(j)}(t-\tau)d\tau + \tilde{n}_{j,l,m}(t) \tag{10}$$

where $\sigma_{W,l}^{(j)}(f) = \sigma_l^{(j)}(f)I_W(f)$, $\sigma_l^{(j)}(f)$ is given by (4), $I_W(f) = 1$, if $f_c - W/2 \le |f| \le f_c + W/2$ and 0 otherwise, and f_c is the central frequency. Each spatial mode j, l, m represents a continuoustime random process that is assumed wide-sense stationary so that, e.g., the autocorrelation of the input signal $\tilde{b}_{j,l,m}(t)$ is $R_{\tilde{b}_{j,l,m}}(\tau) = E[\tilde{b}_{j,l,m}(t)\tilde{b}_{j,l,m}^*(t-\tau)]$. It is also assumed that the noise signals corresponding to different spatial modes are independent so that $E[\tilde{n}_{j,l,m}(t)\tilde{n}_{j',l',m'}^*(t-\tau)] = N_0\delta(\tau)\delta_{j,j'}\delta_{l,l'}\delta_{m,m'}$.

Consider first the case when the source radiates only during a finite time period $-T/2 \le \tau \le T/2$ while the received signal is measured at all times. The transmission and reception functions can be represented in terms of the singular functions of the integral operator with kernel given by

$$h_{j,l}(t,\tau) = \tilde{\sigma}_{W,l}^{(j)}(t-\tau)I_{-\frac{T}{2},\frac{T}{2}}(\tau) \tag{11}$$

where $I_{-\frac{T}{2},\frac{T}{2}}(\tau) = 1$ if $-\frac{T}{2} \le \tau \le \frac{T}{2}$ and 0 otherwise, so that

$$\int \phi_{j,l,m,k}(\tau)h_{j,l}(t,\tau)d\tau = \lambda_{j,l,m,k}\theta_{j,l,m,k}(t) \tag{12}$$

where $\phi_{j,l,m,k}(t)$ and $\theta_{j,l,m,k}(t)$ are the singular functions, and $\lambda_{j,l,m,k}$ are the singular values.

The expansion in terms of the singular functions $\phi_{j,l,m}$ and $\theta_{j,l,m}$ yields the discrete independent parallel Gaussian channels

$$a_{j,l,m,k} = \lambda_{j,l,m,k} b_{j,l,m,k} + n_{j,l,m,k} \;\; \forall j = 1,2; l = 1,2,\ldots; m = -l, -l+1, \ldots, l-1; k = 1,2,\ldots \quad (13)$$

where $a_{j,l,m,k} = (\theta_{j,l,m,k}, \tilde{a}_{j,l,m})$, $b_{j,l,m,k} = (\phi_{j,l,m,k}, \tilde{b}_{j,l,m})$, and $n_{j,l,m,k} = (\theta_{j,l,m,k}, \tilde{n}_{j,l,m})$ and where $(f,g) = \int f^*(t) g(t) dt$.

The L^2 norm constraint of the source $\mathcal{J}(\mathbf{r}, t)$ is given by

$$\sum_{j,l,m} \sum_{k=1}^{\infty} \varepsilon_{j,l,m,k} \leq T\varepsilon \quad (14)$$

while the radiated power (calculated from Poynting's theorem) is given by

$$\frac{1}{2\eta} \sum_{j,l,m} \sum_{k=1}^{\infty} \left[\hat{\lambda}_{j,l,m,k}\right]^2 \varepsilon_{j,l,m,k} \leq TP \quad (15)$$

where $\varepsilon_{j,l,m,k} = E[|b_{j,l,m,k}|^2]$, E represents the expected value, and $\hat{\lambda}_{j,l,m,k}$ are the singular values in (12) corresponding to a receiver located in the far zone.

Letting the capacity for a transmission time interval T be denoted by C_T then applying the Lagrange multipliers technique it is found that the space-limited and time-limited capacity is given by

$$C_T = \sum_{j,l,m} \sum_{k=1}^{\infty} \left[\log_2 \frac{[\lambda_{j,l,m}]^2}{N_0} \left(\frac{1}{\lambda_1 + \lambda_2 \frac{1}{2\eta} \left[\hat{\lambda}_{j,l,m}\right]^2} \right) \right]^+ \left[\frac{\text{bits}}{\text{use}}\right] \quad (16)$$

where λ_1 and λ_2 are two non-negative constants chosen to satisfy the two constraints in (14) and (15) with the replacement $\varepsilon_{j,l,m,k} \to \hat{\varepsilon}_{j,l,m,k}$ and the two equations

$$\lambda_1 \left(\sum_{j,l,m} \sum_{k=1}^{\infty} \hat{\varepsilon}_{j,l,m,k} - T\varepsilon \right) = 0 \quad (17)$$

$$\lambda_2 \left(\frac{1}{2\eta} \sum_{j,l,m} \sum_{k=1}^{\infty} \left[\hat{\lambda}_{j,l,m,k}\right]^2 \hat{\varepsilon}_{j,l,m,k} - TP \right) = 0 \quad (18)$$

where $\hat{\varepsilon}_{j,l,m,k}$ is given in terms of λ_1 and λ_2 by

$$\hat{\varepsilon}_{j,l,m,k} = \left(\frac{1}{\lambda_1 + \lambda_2 \frac{1}{2\eta} \left[\hat{\lambda}_{j,l,m,k}\right]^2} - \frac{N_0}{[\lambda_{j,l,m,k}]^2} \right)^+ . \quad (19)$$

The capacity in (16) represents the space-time capacity of a source of finite volume and transmission time constrained in L^2 norm and radiated power. The NDF is obtained from the number of channels with nonzero functional energy $\hat{\varepsilon}_{j,l,m,k}$ in (19) and represents the number of discrete spatio-temporal modes that are relevant for the current geometry, constraint levels, and noise.

Figure 1 shows the capacity in (16) and the NDF as a function of the noise variance N_0 parameterized by the parameter $c_p = \pi WT/2$ for a source with $ka = 0.38$ operating at a central frequency $f = 900\,\text{MHz}$ and a bandwidth of $W = 25\,\text{KHz}$. As expected, increasing the time-bandwidth product (WT) increases the number of spatio-temporal degrees of freedom and the capacity.

Letting $T \to \infty$ and defining the capacity as $C = \lim_{T\to\infty} \frac{1}{T} C_T$ [10] then by applying the Toeplitz distribution theorem for continuous processes ([11, Lemma 8.5.7] or [12, Theorem C.3]) the bandlimited and space-limited capacity is given by

$$C = \sum_{j,l,m} \int_W \left[\log_2 \frac{\left[\sigma_l^{(j)}(f)\right]^2}{N_0} \left(\frac{1}{\lambda_1 + \lambda_2 \frac{1}{2\eta} \left[\hat{\sigma}_l^{(j)}(f)\right]^2} \right) \right]^+ df \left[\frac{\text{bits}}{\text{s}}\right] \quad (20)$$

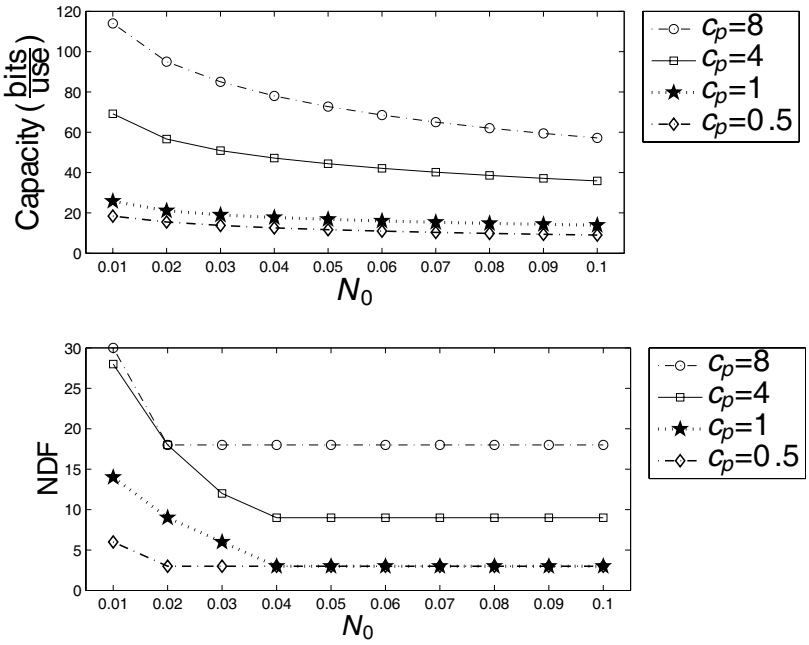

Figure 1: Capacity and NDF vs. noise variance N_0 for different values of the parameter $c_p = \pi WT/2$ for a source with $ka = 0.38$, a constraint in source L^2 norm $\varepsilon = 0.25$, and a reception sphere of radius $b = 2\,\mathrm{m}$.

where λ_1 and λ_2 are chosen to agree with

$$\sum_{j,l,m} \hat{\varepsilon}_{j,l,m} \leq \varepsilon, \tag{21}$$

$$\frac{1}{2\eta} \sum_{j,l,m} \left[\hat{\sigma}_l^{(j)}\right]^2 \hat{\varepsilon}_{j,l,m} \leq P, \tag{22}$$

$$\lambda_1 \left(\sum_{j,l,m} \hat{\varepsilon}_{j,l,m} - \varepsilon \right) = 0, \tag{23}$$

and

$$\lambda_2 \left(\frac{1}{2\eta} \sum_{j,l,m} \left[\hat{\sigma}_l^{(j)}\right]^2 \hat{\varepsilon}_{j,l,m} - P \right) = 0, \tag{24}$$

where

$$\hat{\varepsilon}_{j,l,m} = \int_W \left(\frac{1}{\lambda_1 + \lambda_2 \frac{1}{2\eta} \left[\hat{\sigma}_l^{(j)}(f)\right]^2} - \frac{N_0}{\left[\sigma_l^{(j)}(f)\right]^2} \right)^+ df. \tag{25}$$

Figure 2 shows, for the same source, the spectral efficiency (defined by $\mathcal{C} = C/W$) vs. the noise variance N_0.

If the bandwidth is sufficiently small so that $\sigma_l^{(j)}(f)$ is constant with respect to the frequency f then the spectral efficiency is given by

$$\mathcal{C} = \sum_{j,l,m} \left[\log_2 \frac{\left[\sigma_l^{(j)}(f)\right]^2}{N_0} \left(\frac{1}{\lambda_1 + \lambda_2 \frac{1}{2\eta} \left[\hat{\sigma}_l^{(j)}(f)\right]^2} \right) \right]^+ df \left[\frac{\text{bits}}{\text{use}}\right] \tag{26}$$

which is the strictly spatial capacity with constraints in the source L^2 norm and radiated power.

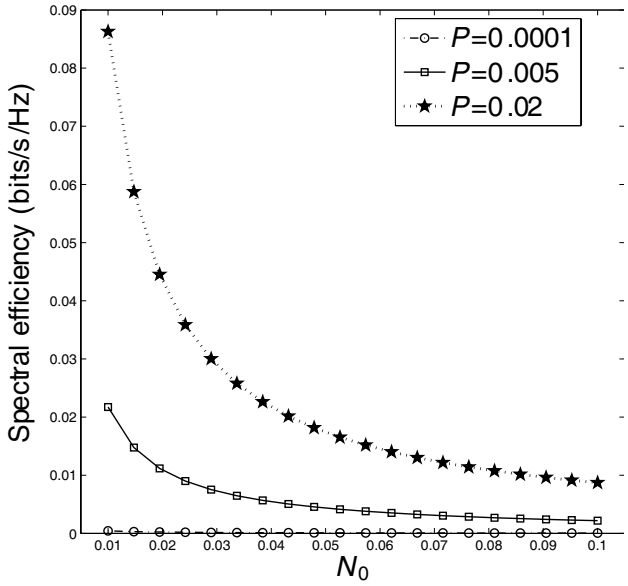

Figure 2: Spectral efficiency vs. noise variance N_0 for a source with $ka = 0.38$, a bandwidth of 25 KHz, a receiver radius $b = 2\,\mathrm{m}$, a source L^2 norm constraint $\varepsilon = 0.25$, and several power constraint levels P.

On the other hand, if the radiated power constraint P is unbounded then the optimal λ_2 is 0 and (20) reduces to the spatio-temporal version of the well known expressions for the capacity of temporal channels with a constraint in source L^2 norm (compare, e.g., with [11, eqs. (8.5.72), (8.5.73)] involving temporal channels):

$$C = \sum_{j,l,m} \int_W \left[\log_2 \left(\frac{\left[\sigma_l^{(j)}(f)\right]^2}{\lambda_1 N_0} \right) \right]^+ df \left[\frac{\text{bits}}{\text{s}} \right]. \tag{27}$$

ACKNOWLEDGMENT

Support by AFOSR (Grant No. FA9550-06-01-0013), and NSF (Grant No. 0746310).

REFERENCES

1. Piestun, R. and D. A. B. Miller, "Electromagnetic degrees of freedom of an optical system," *J. Opt. Soc. Am. A.*, Vol. 17, No. 5, 892–902, May 2000.
2. Hanson, G. W. and A. B. Yakovlev, *Operator Theory for Electromagnetics*, Springer, New York, 2001.
3. Bertero, M. and P. Boccacci, *Introduction to Inverse Problems in Imaging*, IOP Publishing, London, UK, 1998.
4. Bertero, M., "Linear inverse and ill-posed problems," *Advances in Electronics and Electron Physics*, Vol. 75, 1–120, Academic Press, New York, 1989.
5. Collin, R. E., *Field Theory of Guided Waves*, IEEE Press, Piscataway, NJ, second edition, 1990.
6. Marengo, E. A. and A. J. Devaney, "The inverse source problem of electromagnetics: Linear inversion formulation and minimum energy solution," *IEEE T. Antenn. Propag.*, Vol. 47, No. 2, 410–412, February 1999.
7. Jackson, J. D., *Classical Electrodynamics*, Wiley, third edition, 1998.
8. Devaney, A. J. and E. Wolf, "Multipole expansions and plane wave representations of the electromagnetic field," *J. Math. Phys.*, Vol. 15, No. 2, 234–244, February 1974.
9. Arfken, G. B. and H. J. Weber, *Mathematical Methods For Physicists*, Academic Press, San Diego, CA, fifth edition, 2001.
10. Shannon, C. E., *A Mathematical Theory of Communication*, CSLI Publications, 1948.
11. Gallager, R. G., *Information Theory and Reliable Communication*, Wiley, 1968.
12. Blahut, R. E., *Principles and Practice of Information Theory*, Electrical and Computer Engineering, Addison-Wesley, 1987.

Spatial Filtering Characteristics of Scattered Fields by Inhomogeneous Waveguide Grids for X-ray Image Diagnosis

Yasumitsu Miyazaki
Department of Media Informatics, Aichi University of Technology
50-2 Manori, Nishihazama-cho, Gamagori 443-0047, Japan

Abstract— Image characteristics of computer aided diagnosis in X-ray medical examination systems depend on absorption properties and scattering phenomena in human bodies. Image information of received X-rays through human bodies given by X-ray absorption properties of atoms constructing biological organizations, is disturbed by scattering characteristics of X-rays due to atomic structures. Stochastic scattering fields in random biological media for medical image diagnosis are studied by statistical electromagnetic theory. Spatial filtering characteristics of scattered fields by lossy waveguide grid arrays are shown by waveguide mode expansion method. Spatial filterings for scattered fields of large scattering angle are discussed in inhomogeneous waveguide grids with lossy claddings.

1. INTRODUCTION

Medical image diagnosis and computer aided diagnosis using nano-meter electromagnetic waves and X-ray are very important medical techniques. Medical image diagnosis using X-ray is very important technical tool for physiological examination of human body and biological tissues. Image responses of X-ray transmitted wave projection include X-ray absorption effects and also X-ray scattering effects, depending on atomic characteristics of biological tissues and molecules of a few KeV energy levels. Received image signals of receiving plates that contain important information of absorption characteristics in biological interior structures are disturbed by noises of scattered fields due to biological inhomogeneous media. By spatial filtering of scattered fields at output of biological tissues, fine image information containing only absorption characteristics of biological tissues may be obtained [1, 2].

Spatial filters can be constructed by X-ray inhomogeneous waveguide grids. Each periodic section of grid array is inhomogeneous X-ray waveguide with the graded index distribution. Core region has parabolic index distribution of no absorption characteristics and clad region has parabolic and higher order index distribution of the fourth and sixth of complex absorption characteristics. Electromagnetic fields of X-ray in inhomogeneous waveguide with complex graded index distribution can be expressed by the Hermite or Laguerre functions with complex arguments [3].

X-ray is incident to biological media and propagates through biological media. After propagation in random biological media, transmitted and scattered X-rays are incident to input of the inhomogeneous graded index type waveguide. On-axial transmitted X-rays are coupled to low modes of inhomogeneous waveguides with low losses. Off-axial scattered X-rays are coupled to higher modes with higher losses. Scattered fields are coupled to higher modes of inhomogeneous waveguides of the grid and filtered in the grid array. These grid arrays consisting of inhomogeneous X-ray waveguides can operate as spatial filters in X-ray image diagnosis.

2. X-RAY SCATTERING FIELD IN BIOLOGICAL RANDOM MEDIA

In the biological body region, X-ray transmitted and scattered waves through random biomedical media are studied. X-rays, nanometer electromagnetic waves are incident on random media (I) $(0 \leq z \leq \ell)$ from left side in Fig. 1 [4, 5]. Incident X-ray has y-direction linearly polarization $\mathbf{E} = \phi(x\,z)\mathbf{i}_y$. Biological random media in the region (I) have dielectric constants as

$$\varepsilon_t = \varepsilon + \varepsilon\Delta\eta(\mathbf{r}_t) \tag{1}$$

where $\Delta\eta$ is random function and $\varepsilon = \varepsilon' - j\varepsilon''$. Here, $\mathbf{r}_t = x\mathbf{i}_x + z\mathbf{i}_z$, and we consider two dimensional scattering fields. The field function $E(x,\, z)$ concerned with electric field of y polarization satisfies the following wave equations, using $k^2 = \omega^2\varepsilon\mu = (k_r - jk_i)^2$

$$\nabla_{xy}^2 E(\mathbf{r}_t) + k^2 E(\mathbf{r}_t) = -\omega^2\varepsilon\Delta\eta E(\mathbf{r}_t) \tag{2}$$

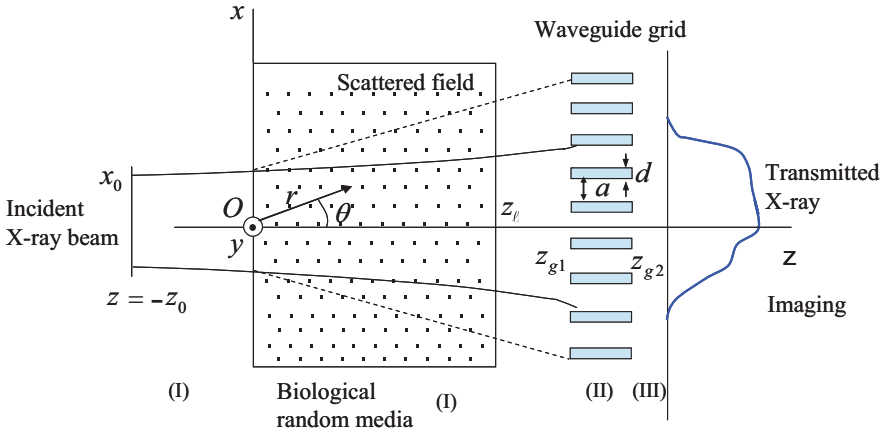

Figure 1: X-ray scattering and X-ray grid.

For incident Gaussian X-ray of y polarization, $\mathbf{E}^{inc} = E_{inc}(\mathbf{r}_t)\mathbf{i}_y$ is written as

$$\mathbf{E}_{inc}\left(\mathbf{r}_t\right) = \mathbf{i}_y \frac{A}{\sqrt{1-j\zeta}} e^{-jk(z+z_0)} e^{\frac{x^2}{x_0^2(1-j\zeta)}} \tag{3}$$

where beam parameter is $\zeta = \frac{2(z+z_0)}{kx_0^2}$, beam waist is $z = -z_0$, and beam spot size is x_0.

Applying Green's formula in random biological media (I), we have total fields as when $\underline{\Gamma} = G\mathbf{I}$, using unit dyad $\mathbf{I}$, and Green's function $G(\mathbf{r}_t, \mathbf{r}'_t)$ for free space

$$\begin{aligned} G(\mathbf{r}_t, \mathbf{r}'_t) &= -\frac{j}{4} H_0^{(2)}\left(k\left|\mathbf{r}_t - \mathbf{r}'_t\right|\right) \\ \mathbf{E}_{totl} &= \mathbf{E}_{inc} + \int k^2 \Delta\eta \underline{\Gamma}\left(\mathbf{r}_t, \mathbf{r}'_t\right) \cdot \mathbf{E}_{totl}\left(\mathbf{r}'_t\right) dS' \end{aligned} \tag{4}$$

From Maxwell's equation, magnetic field is derived as,

$$\mathbf{H}_{totl} = \mathbf{H}_{inc} - \frac{1}{j\omega\mu} \int k^2 \Delta\eta \nabla \times \underline{\Gamma} \cdot \mathbf{E}_{totl} dS' \tag{5}$$

If we define vectors $\mathbf{E}_0$ and $\mathbf{E}$ in functional space for the vectors $\mathbf{E}_{inc}$ and $\mathbf{E}_{totl}$, and integral operator K_E for the integral $\int k^2 \Delta\eta \underline{\Gamma} \cdot dS'$, we obtain the field as follows:

$$\mathbf{E} = (\mathbf{I} - K_E)^{-1}\mathbf{E}_0 = \mathbf{E}_0 + K_E\mathbf{E}_0 + K_E K_E \mathbf{E}_0 + \ldots \tag{6}$$

Using the similar definition for the magnetic field and Equation (5), we have

$$\mathbf{H} = \mathbf{H}_0 + K_H\mathbf{E} = \mathbf{H}_0 + K_H\mathbf{E}_0 + K_H K_E \mathbf{E}_0 + K_H K_E K_E \mathbf{E}_0 + \ldots \tag{7}$$

The optical intensity, i.e., the mean intensity of the energy flow in the harmonic electromagnetic field is given by

$$\mathbf{I} = \mathrm{Re}\bar{\mathbf{S}} = \frac{1}{2}\mathrm{Re}\left(\mathbf{E} \times \mathbf{H}^*\right) \tag{8}$$

We assume that the statistical average $\langle \Delta\eta \rangle$ of fluctuations in the sample is equal to zero, and the correlation function is defined by

$$\langle \Delta\eta\left(\mathbf{r}'_t\right) \Delta\eta\left(\mathbf{r}''_t\right) \rangle = B_\eta\left(\mathbf{r}'_t - \mathbf{r}''_t\right) \tag{9}$$

The statistical average of the total field is expressed as

$$\langle \mathbf{I} \rangle = \mathbf{I}_0 + \frac{1}{2}\mathrm{Re}\left\langle \{K_E\mathbf{E}_0 \times (K_H\mathbf{E}_0)^* + \mathbf{E}_0 \times (K_H K_E \mathbf{E}_0)^* + (K_E K_E \mathbf{E}_0) \times \mathbf{H}_0^* + \ldots\} \right\rangle + \ldots \tag{10}$$

We study here the dominant term of the X-ray scattering. In this case, we can write approximately the scattered field as follows:

$$\langle \mathbf{I}_s \rangle = \frac{k}{\omega\mu}\left(\frac{k^2}{4}\right)^2 \frac{2}{\pi k}\mathrm{Re}\iint \frac{e^{-jk_r|\mathbf{r}_t-\mathbf{r}'_t|+jk_r|\mathbf{r}'_t-\mathbf{r}''_t|}}{\sqrt{|\mathbf{r}_{t'}-\mathbf{r}'_t|\,|\mathbf{r}_t-\mathbf{r}''_t|}} e^{-k_i|\mathbf{r}_t-\mathbf{r}'_t|}e^{-k_i|\mathbf{r}_t-\mathbf{r}''_t|}B_\eta\left(\mathbf{r}'_t,\,\mathbf{r}''_t\right)\mathbf{n}''E'_{inc}E''^{*}_{inc}dS'dS'' \tag{11}$$

The incident X-ray beam is assumed to be the Gaussian TEM_{00} mode. Here, we define $g(k_i|\mathbf{r}_t - \mathbf{r}'_t|) = e^{-2k_i|\mathbf{r}_t-\mathbf{r}'_t|}$ inside random media, $\zeta_0 = 2z_0/kx_0^2$ and the correlation function $B_\eta(\rho_t) = \overline{\Delta\eta^2}e^{-\rho^2/\rho_0^2}$ where parameters $\overline{\Delta\eta^2}$ and ρ_0 give the variances and correlation lengths of fluctuations.

For length of random media ℓ, we have for the cylindrical coordinate $(r,\,\theta)$ assuming $g(k_i|\mathbf{r}_t - \mathbf{r}'_t|) = e^{-2k_\ell|z_\ell-z'|}$ in random media of $0 \le z \le z_\ell$,

$$\langle \mathbf{I}_s \rangle = \mathbf{i}_r \frac{k}{\omega\mu}\frac{\sqrt{2\pi}}{16}\overline{\Delta\eta^2}A^2k^3x_0\rho_0^2\frac{1}{|\mathbf{r}|}e^{-k^2\rho_0^2\sin^2\frac{\theta}{2}}e^{-2k_i(z_\ell+z_0)}z_\ell \tag{12}$$

Figure 2 shows angular distribution of Thomson scattering with $k = 2\pi/\lambda$. For large $k\rho_0$, forward scattering is large and small $k\rho_0$, scattering is homogeneous.

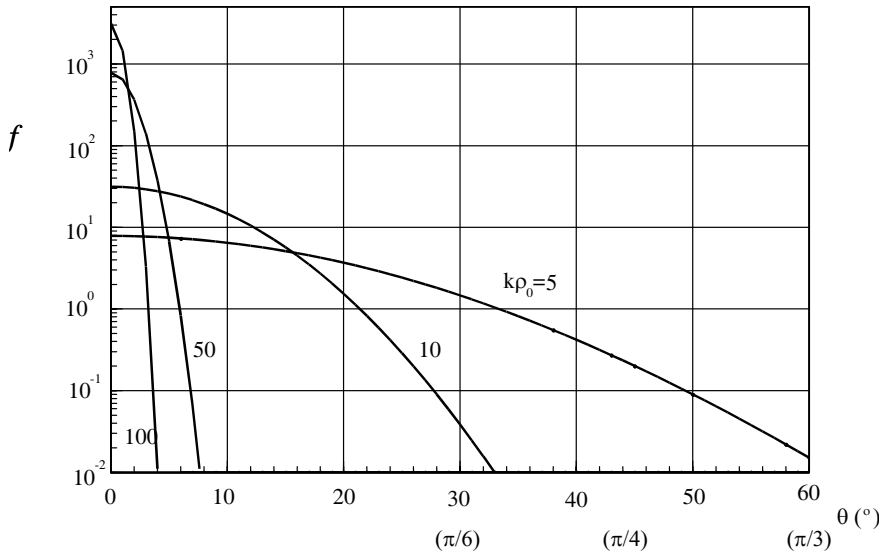

Figure 2: Angular distribution of Thomson scattering. $\frac{|\mathbf{I}_s|}{|\mathbf{I}_0|} = \overline{\Delta\eta^2}(kx_0)\left(\frac{z_\ell}{|\mathbf{r}|}\right)f,\;\; f = \frac{\sqrt{2\pi}}{8}(k\rho_0)^2e^{-(k\rho_0)\sin^2\frac{\vartheta}{2}}$.

3-dimensional Thomson scattering is shown similarly, for incident Gaussian beam with beam waist $z = -z_0$, beam spot size r_0, and polarization of τ direction,

$$\langle \mathbf{I}_s \rangle = \mathbf{i}_R\frac{k^4\pi^{1/2}}{32}I_0\sum_i r_{0z}^2\rho_{0i}^3\overline{\Delta\eta_i^2}\sin^2(\mathbf{i}_R,\,\tau)\,\frac{\ell}{R^2}\cdot e^{-k^2\rho_{0i}^2\sin^2\frac{\vartheta}{2}} \tag{13}$$

Based on these fundamental scattering characteristics, long distance propagation properties with diffusion characteristics can be discussed.

3. FILTERING CHARACTERISTICS OF LOSSY WAVEGUIDE GRID

Lossy waveguides with absorption clad layers have large propagation losses for higher modes and may have filtering characteristics of incident waves of large incident angles. Lossy waveguide grids with period of $a + d$ for the x direction of core width a and clad width $d/2$ are shown in Fig. 2. These waveguides have mode characteristics for the E_y component as

$$\Phi_m(x,\,z) = \Psi_m(x)e^{-j\beta_m z} \tag{14}$$

$$\int_{-\frac{a+d}{2}}^{\frac{a+d}{2}}\Psi_m(x)\Psi_n^*(x)dx = \delta_{mn} \tag{15}$$

where propagation constants $\beta_m = \beta_m^{(r)} - j\beta_m^{(i)}$ have large attenuation characteristics of $\beta_m^{(i)}$. When scattered waves with scattered angles θ are incident to lossy waveguide (II) at the input $z = z_{g1}$ from region (I), fields in the waveguide region (II) can be expressed as, for one grid section,

$$\begin{aligned} E_y^{(II)}(x,\, z) &= \sum_m a_m \Psi_m(x) e^{-j\beta(z-z_{g1})} \\ a_m &= \int_{-\frac{a+d}{2}}^{\frac{a+d}{2}} E_{scatt}\,(x,\, z_{g1})\, \Psi_m^*(x) dx \end{aligned} \tag{16}$$

Mode coefficients a_m show filtering characteristics. At the output of waveguide grids, $z = z_{g2}$, only lower modes propagate through lossy waveguides that couple with incident fields of small scattering angles and higher modes that couple with high angle scattered fields can not pass through the waveguides.

Filtered fields in the region (III) are derived by, using Green's function, for one grid section,

$$\begin{aligned} E_{fil}^{(III)}(x,\, z) &= \int_{-\frac{a+d}{2}}^{\frac{a+d}{2}} \left\{ -G\frac{\partial E_y^{(II)}}{\partial z} + E_y^{(II)} \frac{\partial G}{\partial z} \right\} dx \\ &= \left(-\frac{j}{4}\right) \sum_m (jk + j\beta_m) \sqrt{\frac{2}{\pi k z'}} e^{-jkz' + j\frac{\pi}{4}} a_m e^{-j\beta_m z'} \int_{-\frac{a+d}{2}}^{\frac{a+d}{2}} e^{-j\frac{k}{2z}(x-x')^2} \Psi_m(x') dx' \end{aligned} \tag{17}$$

where $z' = z - z_{g2}$ and a_m for large m is very small.

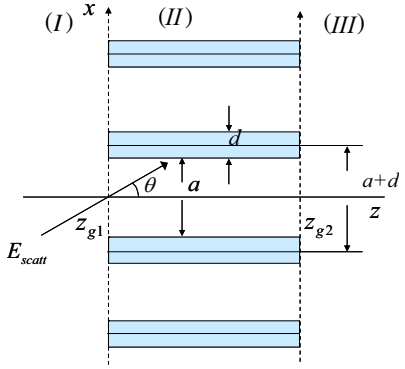

Figure 3: Lossy waveguide grid for scattering filter.

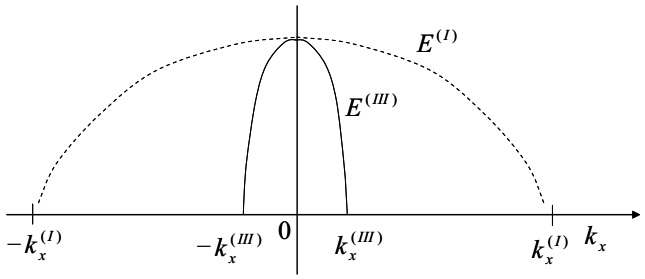

Figure 4: Spatial frequency and filtering characteristics.

If we describe filtering characteristics using spatial frequencies $k_x = \sqrt{k^2 - k_z^2}$, in these three regions, for $t = I, II, III$, Fourier components are

$$E^{(t)}(k_x) = \int_{-\infty}^{\infty} E^{(t)}(x) e^{+jk_x x} dx \tag{18}$$

Filtering characteristics of lossy waveguide grids $\hat{F}(k_x^{(II)})$ are defined as

$$\hat{E}^{(I)}\left(k_x^{(I)}\right) \hat{F}\left(k_x^{(II)}\right) = \hat{E}^{(III)}\left(k_x^{(III)}\right) \tag{19}$$

Spatial frequency $k_x^{(II)}$ of lossy waveguide grid filter is proportional to mode number m.

4. FILTERING CHARACTERISTICS IN LOSSY INHOMOGENEOUS GRID WAVEGUIDES

Electromagnetic characteristics of X-rays in lossy waveguide arrays consisting of grid structures are expressed by mode expansions of lossy modes. In the region (II) of grid arrays in Fig. 4, propagation spaces in the core with lossy metal clad are $z_{g1} \le z \le z_{g2}$, $\frac{(2s-1)}{2}(a+d) \le x \le \frac{(2s+1)}{2}(a+d)$,

$s = -m, -(m-1), \ldots, -1, 0, 1, \ldots, m-1, m$. Lossy inhonmogeneous waveguides are consisting of graded index waveguides with lossy clads of dielectric constants

$$\begin{aligned} \varepsilon(x_s) &= \varepsilon^{(r)}(x_s) - j\varepsilon^{(i)}(x_s) = \varepsilon' \left[1 - (\ell_x x_s)^2 + (D_{IV}\ell_x x_s)^4 + D_{VI}(\ell_x x_s)^6\right] \\ x_s &= x - s(a+d), \ \frac{(2s-1)}{2}(a+d) \le x \le \frac{(2s+1)}{2}(a+d) \end{aligned} \tag{20}$$

where complex focusing parameters D_{IV}, D_{VI} are

$$D_{\substack{IV \\ VI}} = D^{(r)}_{\substack{IV \\ VI}} - jD^{(i)}_{\substack{IV \\ VI}}$$

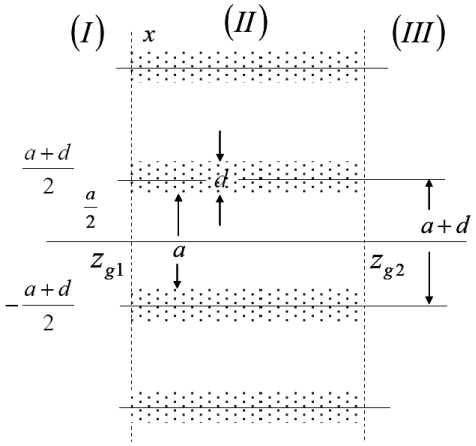

Figure 5: Waveguide type grid structure for scattering filtering.

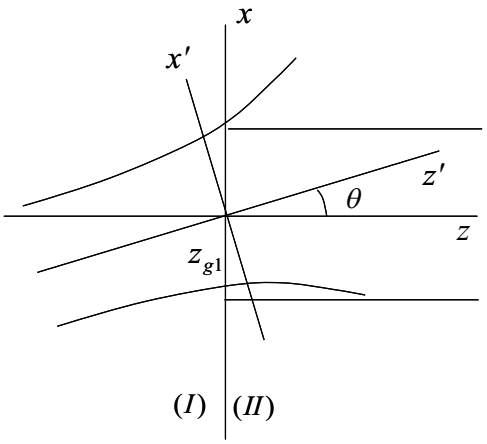

Figure 6: Mode couplings of scattered fields.

Electromagnetic eigen fields in section $s = 0$ of self-focusing optical waveguide with inhomogeneous lossy cladding are derived from inhomogeneous wave equation for the y polarization

$$\left[\frac{\partial^2}{\partial x^2} + \frac{\partial^2}{\partial z^2} + \omega^2\varepsilon(x)\mu\right] E_y + \nabla\left(\frac{\nabla\varepsilon}{\varepsilon} \cdot E_y \mathbf{i}_y\right) = 0 \tag{21}$$

Electric field can be expressed as

$$E_y(x,\, z) \int \hat{E}_y(x,\, \gamma) e^{-j\gamma z} d\gamma \tag{22}$$

Using scalar function $\Phi = \Psi(x)e^{-j\beta_\Phi z}$ satisfying scalar wave equation

$$\left[\frac{\partial^2}{\partial x^2} + \frac{\partial^2}{\partial z^2} + \varepsilon_1\omega^2\mu\right] \Phi = 0 \tag{23}$$

where eigen functions $\Phi_m = \Psi_m(x)e^{-j\beta_\Phi(m)z}$ have complete orthogonality characteristics. Eigen functions Φ_m are given for $\varepsilon_1 = \varepsilon'(1 - (\ell_x x)^2)$

$$\Phi_m(x,\, z) = \Psi_m(x)e^{-j\beta_\Phi(m)z}, \ \Psi_m(x) = b_m e^{-\frac{a_x^2 x^2}{2}} H_m(a_x x), \ a_x = \sqrt{\beta_1 \ell_x}, \ \beta_1^2 = \omega^2\varepsilon'\mu, \ b_m^2 = \frac{a_z}{2^m m!\sqrt{\pi}} \tag{24}$$

Electric field component $\hat{E}_y$ can be expanded as

$$\hat{E}_y(x,\, \gamma) = \sum_m a_m(\gamma)\Psi_m(x) \tag{25}$$

Complex propagation constants γ_m are derived as

$$\gamma_m = \beta_m - j\alpha_m \tag{26}$$

where

$$\beta_m = \omega\sqrt{\varepsilon'\mu}\left[1-(2n+2m+2)\frac{\ell_x}{\beta_1}-\frac{\ell_x^2}{\beta_1^2}-\frac{\ell_x^2\left(1-2D_{IV}^{(r)}\right)}{\beta_1^3}(3m+2)+\frac{D_{IV}^{(r)}}{4}\frac{\ell_x^2}{\beta_1^2}A_m+\frac{D_{IV}^{(i)}\ell_x^3}{8\beta_1^3}B_m\right]$$

$$\alpha_m = \omega\sqrt{\varepsilon'\mu}\left[D_{IV}^{(i)}\left\{\frac{\ell_x^2}{\beta_1^2}\frac{A_m}{4}+\frac{\ell_x^3}{\beta_1^3}(3m+2)\right\}+\frac{D_{VI}^{(i)}\ell_x^3}{8\beta_1^3}B_{mn}\right],$$

$$A_m = 3(m+1)^2+3m^2+3+2(2m+1)$$

$$B_m = 6\left[(m+1)^2+m^2\right](m+2)+6(3m+2)+(m+1)(4m+6)+m(m-1)(4m-2)+6$$

Using large attenuation characteristics of higher modes in inhomogeneous waveguide of graded index distribution with lossy cladding, spatial filtering of scattered X-rays that are coupled with higher modes in grid filter is accomplished through grid array of inhomogeneous waveguides.

Filtering characteristics of lossy waveguide arrays are shown by coupling mode coefficients. Fig. 6 shows coordinate transformation between incident beams of scattered fields and lossy waveguides

$$\begin{bmatrix} x' \\ z' \end{bmatrix} = \begin{bmatrix} \cos\theta & -\sin\theta \\ \sin\theta & \cos\theta \end{bmatrix}\begin{bmatrix} x \\ z \end{bmatrix} \tag{27}$$

Parts of scattered fields can be expressed as

$$E_{scatt} = E_s e^{-jk_s z'} e^{-\frac{x'^2}{x_0^2(1-j\zeta)}} e^{-jk_s z_0'} \tag{28}$$

where $\zeta = \frac{2(z'+z_0')}{k_s x_0^2}$.

When x_0 is larger than core width, coupling coefficients a_m are given by, using $C_2 = e^{-jk_s z_0'}e^{-j\beta_m z_{g1}}$, $\beta' = k_s\sin\theta$

$$\begin{aligned} a_m &= \int_{-\infty}^{\infty} E_{scatt}(x,\, z_{g1})\Phi_m(x,\, z)dx = b_m C_2\int_{-\infty}^{\infty} e^{-jk_s z'}\Psi_m(x)dx \\ a_{2m'} &= \sqrt{2\pi}(-1)^{m'}e^{-\frac{1}{2}\left(\frac{\beta'}{a_x}\right)^2}\frac{1}{a_x}H_{2m'}\left(\frac{\beta'}{a_x}\right), \\ a_{2m'+1} &= -j\sqrt{2\pi}(-1)^{m'}e^{\frac{1}{2}\left(\frac{\beta'}{a_x}\right)^2}\frac{1}{a_x}H_{2m'+1}\left(\frac{\beta'}{a_x}\right) \end{aligned} \tag{29}$$

Coupling coefficients a_m show small mode coupling for large scattered angles and for large incident angle θ, corresponding higher modes with large attenuation constants are coupled and filtered.

5. CONCLUSIONS

Scattering characteristics of X-rays in random bio-medical media consisting of bio-molecules, are studied by statistical theory of electromagnetic field. For X-ray CT in medical diagnosis using X-ray, nano-meter electromagnetic waves, spatial filtering of scattered waves by lossy waveguide grids is discussed. Inhomogeneous waveguide grids of graded index distribution with lossy cladding are very useful to obtain precise image processing. Attenuation properties of higher modes that are excited by scattered fields of large scattering angles are investigated and based on higher mode characteristics, spatial filtering characteristics of scattered fields are discussed for improvement of precise diagnosis.

REFERENCES

1. Miyazaki, Y., "Electromagnetic characteristics of grid structures for scattering fields of nanometer electromagnetic waves and X-rays," *PIERS Proceedings*, 643–647, Tokyo, Aug. 2006.
2. Miyazaki, Y., "Electromagnetic characteristics of waveguide-type grid filters for scattered nanometer waves in transmitted X-ray diagnostic images," *Proc. of EMTS 2007*, EMTS128, Ottawa, ON, Canada, Jul. 2007.
3. Miyazaki, Y., "Partially coherent optical waves in random gradient fibers," *Optical and Quantum Electronics*, Vol. 9, 153–165, 1977.

4. Miyazaki, Y., "Beam propagation and radiation fields in a uniformly curved X ray dielectric gradient waveguides," *Trans. IEE of Japan*, Vol. 120-C, No. 1, 68–73, Jan. 2000.
5. Miyazaki, Y., "Light scattering of laser beams by random micro-inhomogeneities in glasses and polymers," *Jpn. Jour. Appl. Phys.*, Vol. 13, No. 8, 1238–1248, 1974.

Propagation and Scattering Characteristics of Microwaves over Forests in WiMAX Wireless Communications Using FDTD Method

Yasumitsu Miyazaki, **Takuya Takada**, **and Koichi Takahashi**
Department of Media Informatics, Aichi University of Technology
50-2 Manori, Nishihasama-cho, Gamagori 443-0047, Japan

Abstract— WiMAX wireless communication has been rapidly developed for broadband mobile communication. To design excellent high performance mobile communication systems, accurate evaluation of communication systems is indispensable. In the past, building and street effects on high speed signal propagation were studied by FDTD method. However, wave propagation and scattering characteristics by presence of forest and trees are not so much studied. In this paper, the effects of multiple scattering and attenuation of microwaves over forests in WiMAX wireless communications are analyzed numerically using FDTD method. These results may yield important factors for design of high performance and reliable WiMAX communication systems.

1. INTRODUCTION

In recent years, WiMAX wireless communication has been rapidly developed for broadband mobile communication. Mobile WiMAX communication system uses microwave carrier of 2.5 GHz frequency band and modulation system is mainly OFDM for transmission of signals. By using OFDM technique, WiMAX provides high speed and reliable communication against the multi pass interference due to the presence of obstacles in communication channels. To design excellent high performance wireless communication systems, accurate evaluation of communication channels is indispensable. By using parallel FDTD, we studied fundamental microwave propagation and scattering characteristics in urban area [1]. In these analyses, building and street effects on high speed signal propagation have been investigated by computer simulation of FDTD method. However, wave propagation and scattering characteristics by presence of forest and trees are not so much studied. The effects of multiple scattering and attenuation of microwave by forest is severe factors of high speed wireless communications. Size of branches and leaves of trees are comparable with microwave wavelength and yield strong interaction phenomena of broadband propagation.

In this paper, propagation and scattering characteristics of microwave over forests in WiMAX wireless communication is numerically analyzed using FDTD method. FDTD method can be applied for signal and noise analysis about several different complex models and inhomogeneous materials such as forests in communication channels. By applying FDTD method for the analysis of communication channels of propagation over trees and forests, numerical simulations of signal and noise propagation for various tree structures at different frequencies and digital signal bit rates are demonstrated. In FDTD simulations, the incident wave is assumed to be a traveling wave from transmission antenna station at a far distance. Numerical results in this paper show and analyze the effects of various structures of forests and beam spot size of incident waves. The shape of forest is assumed to be constructed by random surface and distribution of branches of trees are inhomogeneous. Forest and trees in radio communication channel is considered to be as random surface and inhomogeneous materials. Fig. 1 shows the situation for microwave propagation in mobile WiMAX wireless communiction over forests.

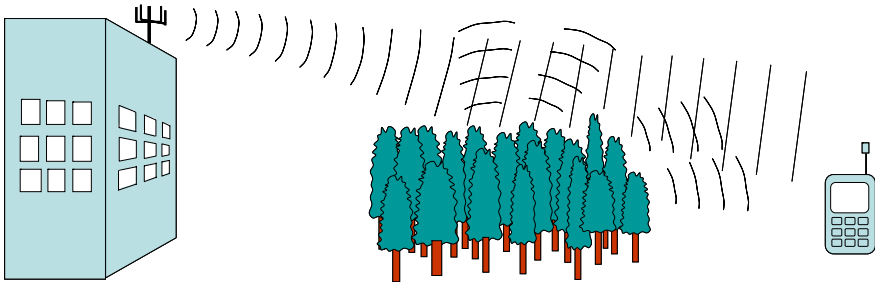

Figure 1: Microwave propagation in mobile WiMAX wireless communication.

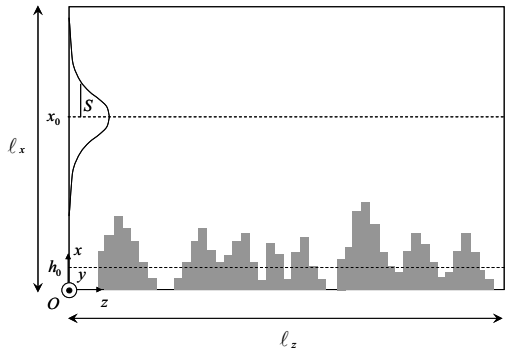

Figure 2: Two dimensional analysis model of FDTD method.

2. FDTD ANALYSIS OF MICROWAVE PROPAGATION AND SCATTERING

Microwave propagation and scattering by forests are very important phenomena for wireless broadband communication such as mobile WiMAX communication. Computer simulation using FDTD method is very useful to evaluate these characteristics numerically. Two-dimensional analysis model for microwave propagation and scattering characteristics over forests is shown in Fig. 2. Analysis region is defined as $\ell_x \times \ell_z$. In FDTD simulations, the incident wave is assumed to be a traveling wave from transmission antenna station at a far distance. The incident wave is y-polarized Gaussian beam wave with angular frequency $\omega = 2\pi f$, beam waist $z = z_0$ and beam spot size S.

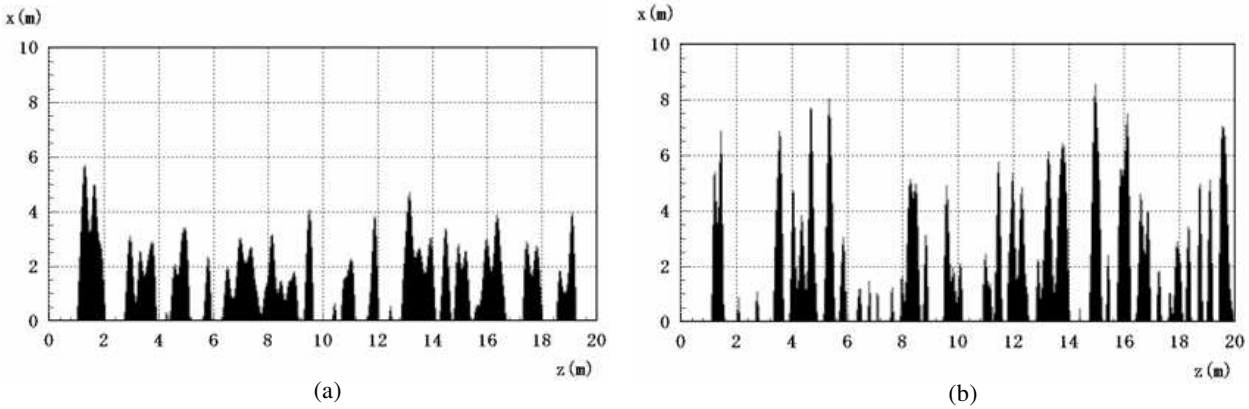

Figure 3: Forest models by random surface, (a) Case 1, $h = 2\,(\mathrm{m})$, $\ell = 0.2\,(\mathrm{m})$, (b) Case 2, $h = 3.4\,(\mathrm{m})$, $\ell = 0.15\,(\mathrm{m})$.

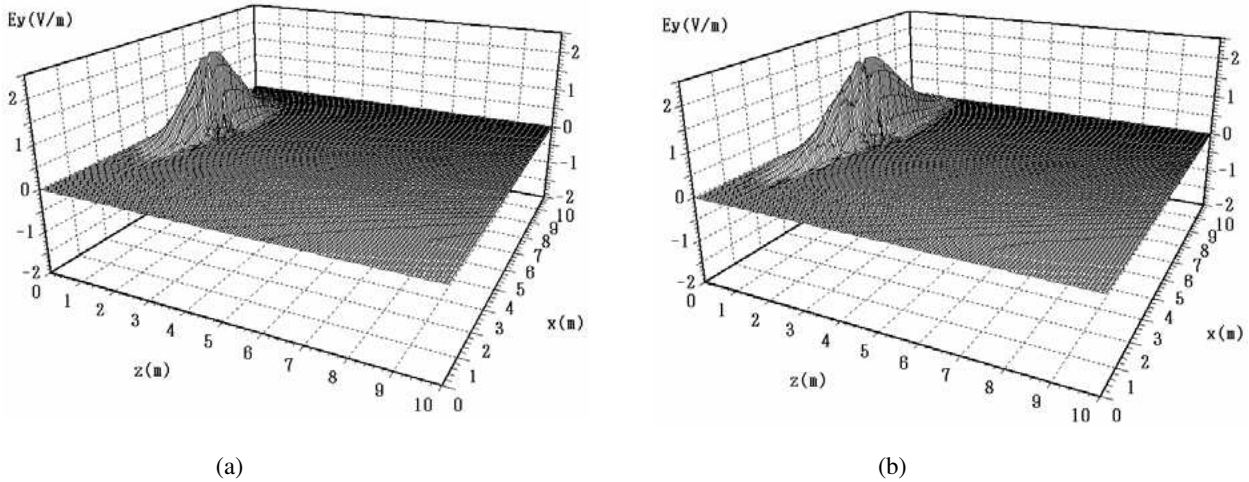

Figure 4: Electric field of the incident wave at $t = 400\Delta t = 8\,(\mathrm{ns})$ in Case 1, (a) $S = 1.6\,(\mathrm{m})$, (b) $S = 2.2\,(\mathrm{m})$.

In the simulation model, the electromagnetic fields are point (i, j) at time $n\Delta t$ are calculated by difference equations,

$$\begin{aligned} E_y^n(i,\,j) &= c_1 E_y^{n-1}(i,\,j) + c_2 J_y^{n-1}(i,\,j) + c_3\left\{H_x^{n-1}(i,\,j) - H_x^{n-1}(i,\,j-1) - H_z^{n-1}(i,\,j) + H_z^{n-1}(i-1,\,j)\right\} \\ H_x^n(i,\,j) &= H_x^{n-1}(i,\,j) + c_4\left\{E_y^n(i,\,j+1) - E_y^n(i,\,j)\right\},\ H_z^n(i,\,j) = H_z^{n-1}(i,\,j) - c_4\left\{E_y^n(i+1,\,j) - E_y^n(i,\,j)\right\} \\ J_y^n(i,\,j) &= \begin{cases} \neq 0 & (j=1) \\ = 0 & (j\neq 1) \end{cases},\ c_1 = \frac{1-\sigma\Delta t/(2\varepsilon)}{1+\sigma\Delta t/(2\varepsilon)},\ c_2 = \frac{\Delta t/\varepsilon}{1+\sigma\Delta t/(2\varepsilon)},\ c_3 = \frac{c_2}{\Delta s},\ c_4 = \frac{\Delta t}{\mu_0\Delta s} \end{aligned} \tag{1}$$

Here, x, z and t are discretized by $x = i\Delta s$, $z = j\Delta s$ and $t = n\Delta t$ and $0 \le i \le N_x$, $0 \le j \le N_z$.

The incident wave is generated by current density

$$J_y^n(i,\,1) = J_0 \exp\left\{-\left(\frac{i\Delta s - x_0}{S}\right)^2\right\} \exp\left\{-\left(\frac{n\Delta t - t_0}{T}\right)^2\right\} \sin(2\pi f n\Delta t) \tag{2}$$

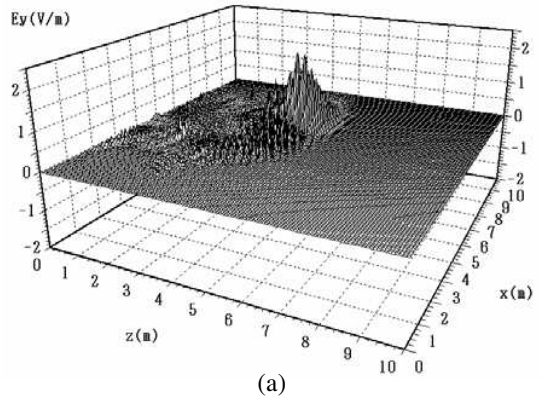

Figure 5: Electric field E_y in Case 1, $S = 1.6$(m), (a) $t = 1000\Delta t = 20$ (ns), (b) $t = 2000\Delta t = 40$ (ns), (c) $t = 3000\Delta t = 60$ (ns).

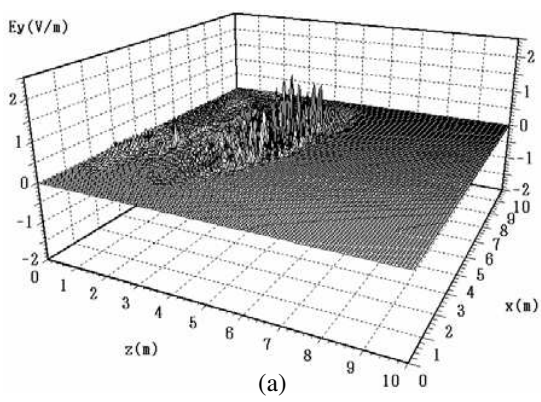

Figure 6: Electric field E_y in Case 2, $S = 1.6$(m), (a) $t = 1000\Delta t = 20$ (ns), (b) $t = 2000\Delta t = 40$ (ns), (c) $t = 3000\Delta t = 60$ (ns).

where f is the frequency of incident wave, x_0 is the center point of incident beam, S is the beam spot size at $z = z_0(j = 1)$, T is the parameter for transmission pulse width. Mur's boundary condition applied to obtain the electromagnetic fields at the boundary of analysis space.

In the analysis model, the shape of trees and forests are realized by random surfaces. Random surface is generated by giving rms height h and correlation length ℓ. In Fig. 2, h_0 is the average height of random surfaces.

3. PROPAGATION AND SCATTERING CHARACTERISTICS OF MICOWAVES OVER FORESTS

Propagation and scattering characteristics of Gaussian beam waves with microwave frequency are evaluated using FDTD method. In FDTD simulation, $\ell_x = 1000\Delta s = 10\,(\mathrm{m})$, $\ell_z = 2000\Delta s = 20\,(\mathrm{m})$, $= 6\,(\mathrm{m})$ and h_0=0.1 (m) are used. For incident wave, $f = 2.5\,\mathrm{GHz}$, $T = 2\,(\mathrm{ns})$, $t_0 = 5\,(\mathrm{ns})$ and $J_0 = 1\,(\mathrm{A/m^2})$ are used. Here, wavelength λ is 0.12 (m) and size of analysis space ℓ_x and ℓ_z become 83.3λ and 166.7λ, respectively. Numerical parameters for FDTD analysis are shown in Table 1. Fig. 3 shows the forest model generated by giving rms height h and correlation length ℓ of random surface. Here, correlation length of random surface is defined as

$$\ell = \{x | R(x) = 1/e\} \tag{3}$$

where $R(x)$ is the auto correlation function of random surface, $R(x) = \int h(x')h(x'+x)dx'$.

Table 1: Numerical parameters for FDTD analysis.

Parameters	Values
f: Frequency of incident wave	2.5 GHz
λ: Wavelength of incident wave	0.12 m
ℓ_x: Length of analysis space (x)	10 m(83.3λ)
ℓ_z: Length of analysis space (z)	20 m(166.7λ)
x_0: Center point of the beam	0.6 m
S: Beam spot size	1.6 m(13.3 λ), 2.2 m(18.3 λ)
t_0: Peak time of incident pulse	5 ns
T: Parameter for pulse width	2 ns
Δs: Length of a cell	0.01 m
Δt: Time increment	0.02 ns
ε_r: Relative dielectric constant of surfaces	4.0
σ: Conductivity of surfaces	10^{-7} S/m
h_0: Average height of surfaces	0.1 m
h: rms height of surfaces	2.0 m (Case 1)
	3.4 m (Case 2)
ℓ: Correlation length of surfaces	0.20 m (Case 1)
	0.15 m (Case 2)

In Case 1, the transmitted signal keeps strong intensity above the height of 6 (m). However, the transmitted signal in Case 2 is highly attenuated due to the scattering by forests. Particularly, Fig. 6 shows the strong multiple scattering because the correlation length of forest model is comparable to the incident wavelength. Figs. 7 and 8 are the results with different beam spot size of the incident wave. In Fig. 8(b) shows that the attenuation of transmitted signal is still strong and the field distribution is disturbed due to the presence of tall trees. Therefore, in this case, it seems difficult to accomplish reliable communication between the transmitter and receivers. By using statistical function, such as average, variance and correlation of random surface and time waveform of received electric field at receiving point, signal and noise characteristics in broadband mobile communication can be evaluated.

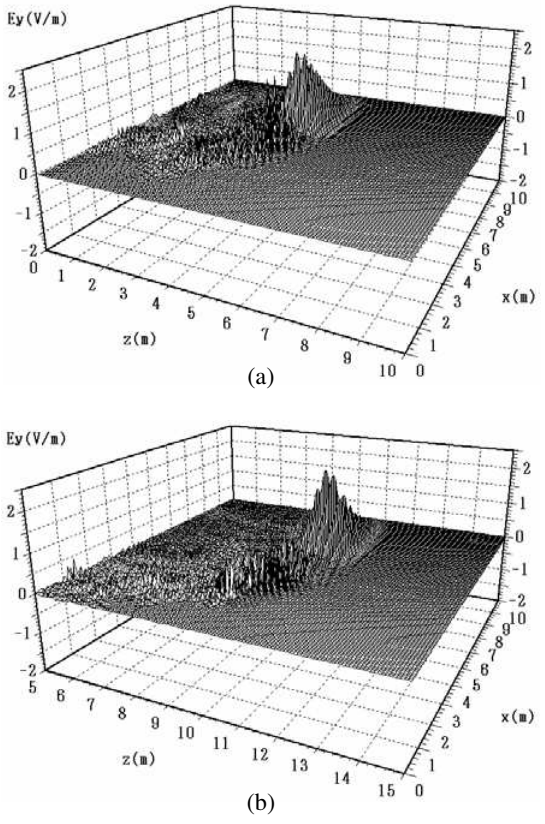

Figure 7: Electric field E_y in Case 1, $S = 2.2\,(\mathrm{m})$, (a) $t = 1000\Delta t = 20\,(\mathrm{ns})$, (b) $t = 2000\Delta t = 40\,(\mathrm{ns})$.

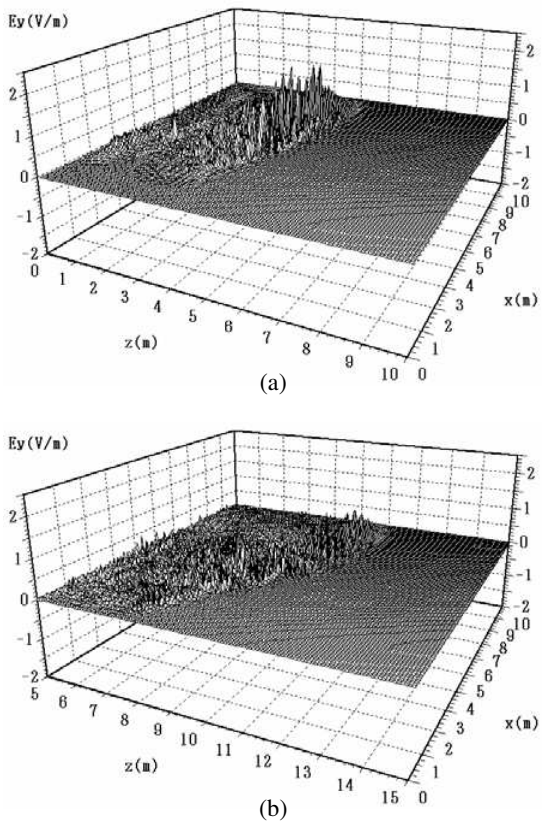

Figure 8: Electric field E_y in Case 2, $S = 2.2\,(\mathrm{m})$, (a) $t = 1000\Delta t = 20\,(\mathrm{ns})$, (b) $t = 2000\Delta t = 40\,(\mathrm{ns})$.

4. CONCLUSIONS

Microwave propagation and scattering by forests are very important phenomena for wireless broadband communication. In this paper, propagation and scattering characteristics of microwave over forests in WiMAX wireless communication is numerically analyzed using FDTD method. FDTD method can be applied for signal and noise analysis about several different complex models and inhomogeneous materials such as forests in communication channels. By applying FDTD method for the analysis of communication channels of propagation over trees and forests, numerical simulations of signal and noise propagation for various tree structures at different frequencies and digital signal bit rates can be considered.

REFERENCES

1. Selormey, P. and Y. Miyazaki, "Electromagnetic compativility characteristics of buildings in mobile radio waves propagation channel," *Trans. IEE Japan*, Vol. 119-C, No. 1, 97–104, 1999.
2. Rodriguez, G., Y. Miyazaki, and N. Goto, "Matrix-based FDTD parallel algorithm for big areas and its applications to high-speed wireless communications," *IEEE Trans. Antennas & Propagat.*, Vol. 54, No. 3, 785–796, 2006.
3. Masuda, T., Y. Miyazaki, and Y. Kashiwagi, "Analysis of electromagnetic wave propagation in out-door active RFID system using FD-TD method," *PIERS Online*, Vol. 3, No. 6, 937–939, 2007.

Parallel Processing of Forward-backward Time-stepping Method for Time Domain Inverse Scattering

T. Moriyama[1], **Y. Yamaguchi**[2], **K. A. Hong Ping**[1], **T. Tanaka**[1], **and T. Takenaka**[1]

[1]Nagasaki University, Japan
[2]Nagasaki Broadcasting Company, Japan

Abstract— Parallel computing is applied to FBTS method, which is one of the solution methods of time domain inverse scattering problem, to shorten the calculation time. A cluster of 8 PCs is constructed and parallel processing is realized using MPI. A 3-D reconstruction of wooden hollow cylinder from the experimental data is examined by parallel FBTS algorithm. It is shown that the parallel processing reduces the calculation time and FBTS algorithm provides proper reconstructed profiles of target with respect to relative permittivity and conductivity.

1. INTRODUCTION

Electromagnetic wave inverse scattering problem are investigated in various fields such as medical imaging, geophysical exploration, nondestructive testing, and target identifications [1–6]. We have proposed a time-domain inverse scattering imaging technique, the forward-backward time-stepping (FBTS) method, to reconstruct the electrical parameter profiles of scattering objects. It was clarified that quite good reconstructed results were obtained using the FBTS method in several numerical simulations [7]. We also showed its usefulness in real situations by applying the FBTS method to experimental data [8]. Although the FBTS method is effective to inverse scattering problems, the computation time is quite long to get accurate results in dealing with three-dimensional (3-D) objects. Therefore reconstruction processing time in the FBTS method is required to be greatly reduced.

In this paper, we investigate the reduction of the computation time of the FBTS method by introducing parallel processing of the method. In the FBTS method, it is necessary that the same number of direct and adjoint scattering problems as that of transmitter points are calculated in order to obtain the gradient vector which is related to the update of the estimation for electrical parameters [1–4]. We construct a cluster of 8 personal computers and implement a parallel algorithm for FBTS method using Message Passing Interface (MPI) library. Since the calculation of direct and adjoint problems is conducted simultaneously by several computers, parallel FBTS algorithm is expected to reduce the computation time. The experiment to acquire the measured data of a wooden hollow cylinder by circular array antenna in cross sectional slices is carried out, and 3-D reconstruction of the target is examined by proposed parallel FBTS method. In the following sections, the FBTS algorithm, parallel method and reconstruction results are shown.

2. FBTS ALGORITHM

Maxwell's equations in the matrix form is given by

$$L\mathbf{v} = \mathbf{J} \tag{1}$$

where

$$\begin{aligned} \mathbf{v} &= [E_x(\mathbf{r},t)\ E_y(\mathbf{r},t)\ E_z(\mathbf{r},t)\ \eta H_x(\mathbf{r},t)\ \eta H_y(\mathbf{r},t)\ \eta H_z(\mathbf{r},t)]^T, \\ \mathbf{J} &= [\eta J_x(\mathbf{r},t)\ \eta J_y(\mathbf{r},t)\ \eta J_z(\mathbf{r},t)\ 0\ 0\ 0]^T. \end{aligned} \tag{2}$$

The differential operator L is defined as

$$L = \bar{A}\frac{\partial}{\partial x} + \bar{B}\frac{\partial}{\partial y} + \bar{C}\frac{\partial}{\partial z} - \bar{F}\frac{\partial}{\partial (ct)} - \bar{G} \tag{3}$$

where $\bar{A}$, $\bar{B}$ and $\bar{C}$ are constant matrices, $\bar{F}$ and $\bar{G}$ are matrices consisting of the tensor permittivity and tensor electric conductivity (These parameters are introduced in reference [8]). c and η are the speed of light and intrinsic impedance in free space. We assume that the transmitter is turned on at time $t = 0$ and before that time there are no fields, so that the direct scattering problem is solved

under the initial condition of zero fields $\mathbf{v}(\mathbf{r}, 0) = 0$. The inverse scattering problem considered here can be formulated as an optimization problem of finding the parameter distributions which minimize the following cost functional:

$$F(\mathbf{p}) = \int_0^{cT} \sum_{m=1}^{M} \sum_{n=1}^{N} K_m(\mathbf{r}_n^r, t) \left|\mathbf{v}_m(\mathbf{p}; \mathbf{r}_n^r, t) - \tilde{\mathbf{v}}_m(\mathbf{r}_n^r, t)\right|^2 d(ct) \tag{4}$$

where $\mathbf{p}$ is the parameter vector

$$\mathbf{p} = (\varepsilon_r(\mathbf{r}),\, \mu_r(\mathbf{r}),\, \delta(\mathbf{r}))^t = (p_1,\, p_2,\, p_3)^t \tag{5}$$

and ε_r, μ_r, σ are the relative permittivity, relative permeability, and conductivity, respectively. The vector $\tilde{\mathbf{v}}_m(\mathbf{r}_n^r,\, t)$ is the measured electromagnetic fields at $\mathbf{r}_n^r$ due to the source $\mathbf{j}_m$ located at the m-th point and the vector $\mathbf{v}_m(\mathbf{p};\, \mathbf{r}_n^r,\, t)$ is the calculated electromagnetic fields for an estimated parameter at the same receiver position under the same source excitation. The superscript 't' indicates transposition. M is the number of transmitters and N is the number of receivers. T is the time duration of the measurement. The function $K_m(\mathbf{r}_n^r,\, t)$ is a nonnegative weighting function which takes a value of zero at $t = T$.

We apply a gradient method to minimization of the cost functional. The gradient of the functional is given by

$$\mathbf{g}(\mathbf{r}) = (g_\varepsilon(\mathbf{r}),\, g_\mu(\mathbf{r}),\, g_\delta(\mathbf{r}))^t \tag{6}$$

where

$$\begin{aligned} g_\varepsilon &= 2 \int_0^{cT} \sum_{m=1}^{M} \sum_{i=1}^{3} w_{mi}(p; r, t) \frac{\partial}{\partial(ct)} v_{mi}(p : r, t) d(ct), \\ g_\mu &= 2 \int_0^{cT} \sum_{m=1}^{M} \sum_{i=4}^{6} w_{mi}(p; r, t) \frac{\partial}{\partial(ct)} v_{mi}(p : r, t) d(ct), \\ g_\sigma &= 2 \int_0^{cT} \sum_{m=1}^{M} \sum_{i=1}^{3} w_{mi}(p; r, t) v_{mi}(p : r, t) d(ct) \end{aligned} \tag{7}$$

and the adjoint field vector $\mathbf{w}_m = (w_{m1}, w_{m2}, w_{m3}, w_{m4}, w_{m5}, w_{m6})^t$ is the solution of the following adjoint equation

$$L^* \mathbf{w}_m = \sum_{n=1}^{N} \mathbf{u}_m \left(\mathbf{p}; \mathbf{r}_n^r, t\right) \delta \left(\mathbf{r} - \mathbf{r}_n^r\right), \tag{8}$$

$$L^* = -\bar{A} \frac{\partial}{\partial x} - \bar{B} \frac{\partial}{\partial y} - \bar{C} \frac{\partial}{\partial z} + \bar{F} \frac{\partial}{\partial(ct)} - \bar{G} \tag{9}$$

under the final condition $\mathbf{w}_m\left(\mathbf{p}; \mathbf{r}_n^r, T\right) = 0$. L^* is the adjoint operator and $\delta(\mathbf{r} - \mathbf{r}_n^r)$ is a Dirac delta function. $\mathbf{u}_m(\mathbf{p}; \mathbf{r}_n^r, t)$ is the weighted residual, that is the weighted difference of the calculated and measured field data:

$$\mathbf{u}_m(\mathbf{p}; \mathbf{r}_n^r, t) = K_m(\mathbf{r}_n^r, t) \{\mathbf{v}_m(\mathbf{p}; \mathbf{r}_n^r, t) - \tilde{\mathbf{v}}_m(\mathbf{r}_n^r, t)\} \tag{10}$$

The adjoint field vector $\mathbf{w}_m\left(\mathbf{p}; \mathbf{r}, t\right)$ is calculated by propagating the residuals $\mathbf{u}_m(\mathbf{p}; \mathbf{r}_n^r, t)$ backward in time. This is carried out using FDTD method with backward time stepping starting at time $t = T$.

The conjugate gradient method is applied to this minimization problem. The update formula for the unknown electric parameters is given by

$$p_i^{(k+1)}(\mathbf{r}) = p_i^{(k)}(\mathbf{r}) + \alpha_i^{(k)} d_i^{(k)}(\mathbf{r}) \quad i = 1, 2, 3 \tag{11}$$

where the superscript 'k' indicate the k-th iteration. The new search direction $\mathbf{d}^{(k+1)}$ whose i-th component $d_i^{(k+1)}$ is given by

$$\mathbf{d}^{(k+1)} = -\mathbf{g}^{(k+1)} + \frac{\left\langle \mathbf{g}^{(k+1)} - \mathbf{g}^{(k)},\, \mathbf{g}^{(k+1)} \right\rangle}{\left\langle \mathbf{g}^{(k)},\, \mathbf{g}^{(k)} \right\rangle} \mathbf{d}^{(k)} \quad i = 1, 2, 3 \tag{12}$$

where $< \bullet, \bullet >$ indicates inner product. The step size $\alpha_i^{(k)}$ is determined approximately by solving the system of linear equation as shown in [7].

3. PARALLEL FBTS METHOD

Measurements were taken in cross sectional "slices" through the object by utilizing a fixed circular array of 8 dipole antennas and recording the scattered data among the 7 remaining antennas at three different vertical positions at 1.5 cm interval, as shown in Fig. 1. The number of transmitter points are $8 \times 3 = 24$ and $24 \times 7 = 168$ scattered field data are obtained.

Taking it into account that the scattered field data due to one transmitted pulse is independent from those due to other transmitted pulse, we rewrite the functional as

$$F(\mathbf{p}) = \sum_{l=1}^{L} \left\{ \int_0^{cT} \sum_{m'=1}^{M'} \sum_{n=1}^{N} K_{m'l}(\mathbf{r}_n^r, t) \left| \mathbf{v}_{m'l}(\mathbf{p}; \mathbf{r}_n^r, t) - \tilde{\mathbf{v}}_{m'l}(\mathbf{r}_n^r, t) \right|^2 d(ct) \right\} \tag{13}$$

where L is the number of parallelization nodes (the number of processors), M' is the number of transmitter points assigned to a node. Therefore, the total number of transmitter points are given by $M = L \times M'$. The number m in Eq. (4) is related to the numbers m' and l in Eq. (4) by $m = M' \times (l-1) + m'$. The gradient vector $\mathbf{g(r)}$ is rewritten as

$$\begin{aligned}
g_\varepsilon &= \sum_{l=1}^{L} \left\{ 2 \int_0^{cT} \sum_{m'=1}^{M'} \sum_{i=1}^{3} w_{m'li}(p; r, t) \frac{\partial}{\partial(ct)} v_{m'li}(p : r, t) d(ct) \right\}, \\
g_\mu &= \sum_{l=1}^{L} \left\{ 2 \int_0^{cT} \sum_{m'=1}^{M'} \sum_{i=4}^{6} w_{m'li}(p; r, t) \frac{\partial}{\partial(ct)} v_{m'li}(p : r, t) d(ct) \right\}, \\
g_\sigma &= \sum_{l=1}^{L} \left\{ 2 \int_0^{cT} \sum_{m'=1}^{M'} \sum_{i=1}^{3} w_{m'li}(p; r, t) v_{m'li}(p : r, t) d(ct) \right\}
\end{aligned} \tag{14}$$

4. PARALLEL COMPUTING

There are two types of parallel computing: shared memory type and distributed memory type. A shared type parallel computing is performed by a computer with a number of processors and a shared memory. A distributed memory type parallel computing is performed by a number of computers each of which has a processor with own memory. The transmission and reception of data between the computers are made via the interconnection network. We selected the latter type. A cluster of 8 computers is constructed and parallel processing for FBTS is realized using Message Passing Interface (MPI).

5. RESULTS

The parallel FBTS algorithm was confirmed by a reconstruction of a target from experimental data. The target is a wooden hollow circular cylinder of 5 cm outer-diameter, 3 cm inner-diameter and 6 cm height, as shown in Fig. 2. The average relative permittivity and conductivity are 2.4

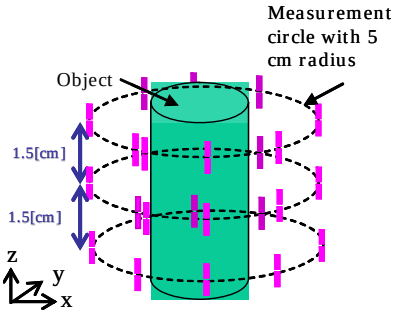

Figure 1: Configuration of the problem.

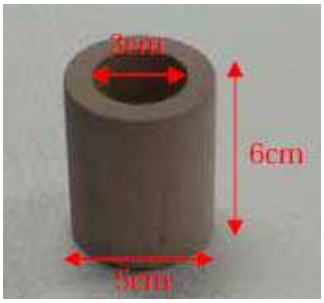

Figure 2: Wooden hollow cylinder.

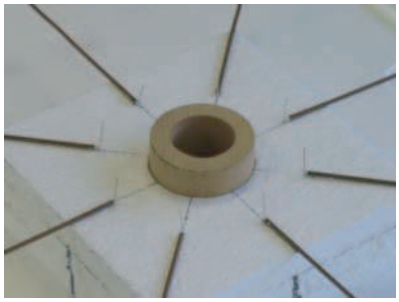

Figure 3: Measurement situation.

and 0.045 s/m over the used frequency range from 2 to 4 GHz. Fig. 3 shows a photograph of a measurement situation. The eight half-wavelength dipole antennas are circularly arranged at regular intervals. The FDTD grid parameters are shown in Table 1. For parallel computing, a PC cluster is made which consists of eight personal computers in which each computer has a CPU of AMD Athlon 64 4000+ and 4-GB memory. Since the transmitter points are 24, the number of computers used for parallel computing is the common divisor of 24, i.e., 2, 3, 4, 6, 8. The execution time is given by Table 2. This result is obtained for the reconstruction after two iterations of FBTS algorithm, and clearly shows the high performance of the parallelization. The total calculation time of eight computers is 6 times faster than that of one computer. Reconstructed relative permittivity and conductivity profiles after 10 iterations are shown in Figs. 4 and 5. Part (a) of both figures shows a cross sectional image in the xy plane (through the middle of cylinder along the z axis) and part (b) shows a slice in the xz plane (through the middle of cylinder along the y axis). The shape is stretched in xy plane and the distributions of electronic property are inhomogeneous. These errors arise from the measurement inaccuracies as well as a restriction due to imprecise alignment of wooden circular cylinder with the cubical FDTD lattice. In order to confirm the effects of measurement inaccuracies on experiment data, S-parameters measured without target (S_{41} and S_{61}) are indicated in Fig. 6. S_{pq} means a response at the antenna p due to a signal from the antenna q by using vector network analyzer. The fluctuation of S-parameter is caused by unwanted reflections (floor, etc). When the experimental data is applied to FBTS method, these reflections are removed by time-gating technique. After time-gating, there is still a difference between S_{41} and S_{61}. S_{41} should be equal to S_{61} due to the symmetric position of antenna 4 and 6 toward antenna 1, as shown in Fig. 7. The cause of this difference is the antenna position's misalignment. However, in spite of such measurement error, the FBTS method has successfully provided proper reconstructed profiles of target with respect to relative permittivity and conductivity.

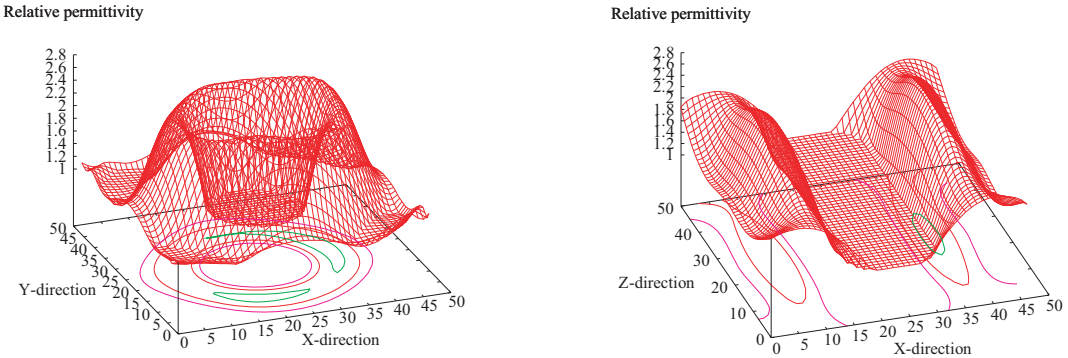

(a) xy plane (b) xz plane

Figure 4: Cross section profile of relative permittivity.

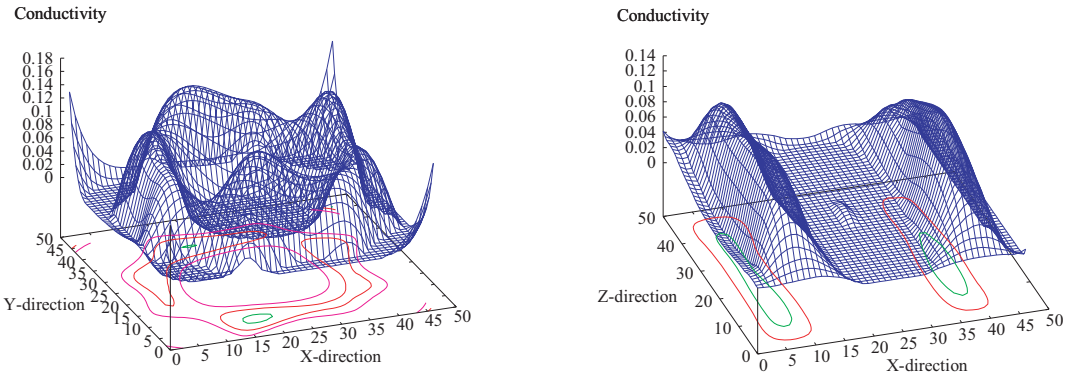

(a) xy plane (b) xz plane

Figure 5: Cross section profile of conductivity.

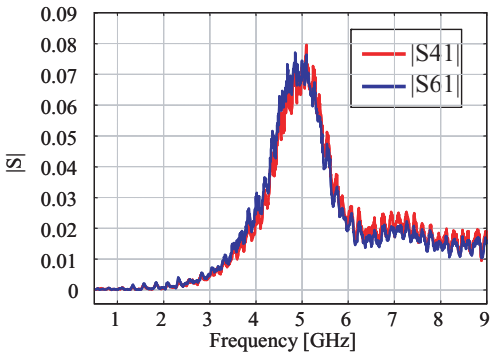

Figure 6: S-parameters, S_{41} and S_{61}, measured without target.

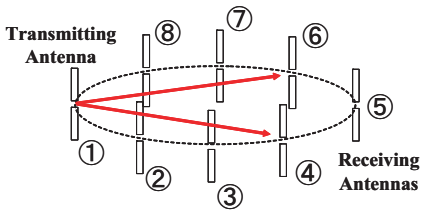

Figure 7: Measurement of S_{41} and S_{61}.

Table 1: The FDTD grid parameters.

Computation region	$111 \times 111 \times 81$ cells
Reconstruction area	$47 \times 47 \times 51$ cells
Space step size	1.3 mm
Time step size (Δt)	2.45 ps
Observation time	$600\,\Delta t$
Number of source points	24
Number of obsevation points per source	7

Table 2: The execution time and communication time.

No. of node	Total time	Communication time
1	10 h 47 m	
2	6 h 19 m	21 s
3	4 h 24 m	4 m 24 s
4	3 h 12 m	49 s
6	2 h 18 m	2 m 20 s
8	1 h 43 m	1 m 14 s

6. CONCLUSIONS

The parallel computation for FBTS method has been described. Evaluation test on reconstruction of the relative permittivity and conductivity of a wooden hollow cylindrical object from experimental data showed that the parallelization reduces the calculation time and FBTS method provides the electrical parameter profiles of the target. The parallelizing of FBTS method is done in only the part related to the independent calculation of the direct and adjoint problems due to each transmitting point. In order to get higher efficiency, further investigations are necessary into parallelization in FDTD computation by using GPU (Graphics Processing Unit) or FPGA (Field Programmable Gate Array). The possibilities of the future research efforts might also include a diagnosis of damaged wooden pole.

REFERENCES

1. Chew, W. C. and Y. M. Wang, "Reconstruction of two-dimensional permittivity distribution using the distorted Born iterative method," *IEEE Trans. Med. Imag.*, Vol. 9, No. 4, 218–225, Apr. 1990.
2. Franchois, A. and C. Pichot, "Microwave imaging — complex permittivity reconstruction with a Levenberg-Marquardt method," *IEEE Trans. Antennas Propagat.*, Vol. 45, No. 2, 203–214, Feb. 1997.

3. Isernia, T., V. Pascazio, and R. Pierri, "A nonlinear estimation method in tomographic imaging," *IEEE Trans. Geosci. Remote Sensing*, Vol. 35, No. 4, 910–923, Apr. 1997.
4. Van den Berg, P. M., A. L. van Broekhoven, and A. Abubakar, "Extended contrast source inversion," *Inverse Problems*, Vol. 15, No. 5, 1325–1344, May 1999.
5. Caorsi, S., A. Massa, and M. Pastorino, "Numerical assessment concerning a focused microwave diagnostic method for medical applications," *IEEE Trans. Microwave Theory Tech.*, Vol. 48, No. 11, 1815–1830, Nov. 2000.
6. Moghaddam, M. and W. C. Chew, "Study of some practical issues in inversion with the Born iterative method using time-domain data," *IEEE Trans. Antennas Propagat.*, Vol. 41, No. 2, 177–184, Feb. 1993.
7. Takenaka, T., H. Jia, and T. Tanaka, "Microwave imaging of electrical property distributions by a forward-backward time-stepping method," *Journal of Electromagnetic Waves and Applications*, Vol. 14, No. 12, 1611–1628, 2000.
8. Johnson, J., H. Zhou, and T. Takenaka, "Experimental three-dimensional time-domain reconstruction of dielectric objects for breast cancer detection," *Mediterranean Microwave Symposium*, 423–426, Sept. 2006.

On the Development of Tunable Microwave Devices for Frequency Agile Applications

Jia-Sheng Hong and Young-Hoon Chun

Department of Electrical, Electronic and Computer Engineering
Heriot Watt University, Edinburgh, EH14 4AS, United Kingdom

Abstract— This paper presents a recent development of electronically tunable microwave devices for frequency agile applications such as emerging cognitive radios and ultra-wide band (UWB) wireless systems.

1. INTRODUCTION

Since the demands for wireless communications increase and become complex, RF front-ends need multi-band or wideband circuits to satisfy several standards of wireless systems, which makes a tunable circuit essential [1, 2]. An adaptive controlled system which can enhance the performances of a wireless system also requires the tunable devices and circuits such as tunable phase shifters and tunable filters. In this paper, we review some our newly developed tunable microwave devices, which are based on new device structures and tuning elements [3–6]. For example, we have investigated new tunable device structures comprised of variable characteristic impedance (Z_C) transmission line which can be used as a distributed tuning circuit. Demonstrators for this type of tunable devices have been designed, fabricated and tested. Both simulated and experimental results are presented.

In addition to semiconductor tuning elements used, ferroelectric materials are of great interest for the development of electrically tuned microwave components and circuits. Rapid tuning speed, moderate insertion loss at microwave frequencies, high power handling capacity and simple fabrication process make them more attractive. In this paper, as a practical application of ferroelectric materials, we will present some newly developed bandstop filters based on variable capacitors on BST thin film. A tunable bandstop or band reject filter, which is considered as an application of BST varactors in this work, has become more essential for wideband wireless communication systems as it can reduce incoming or emitted unwanted signals effectively. The designs using defected ground structures or electromagnetic bandgap structures will be described.

2. TUNABLE PHASE SHIFTER

Figure 1(a) is a unit cell of conventional distributed phase shifter. Overall input impedance should be designed to vary around 50 Ω and its delay will be changed, while variable capacitance devices, such as varactor diodes (D_p), have different values of capacitance (C_{var1}). In this case, the return loss can be degraded due to varying C_{var1} while a transmission line, which is inductive, has a fixed value of Z_C. It usually limits the tuning range of phase shifters. If we are able to implement a device in Fig. 1(b), wider tuning range of phase shifters can be achievable. Fig. 1(c) illustrates how a tunable Z_C transmission line can be implemented with conventional devices such as CPW lines and lumped elements. Simulated results show that Z_C can be electronically varied from 55 to 100 Ω at the center frequency of 800 MHz, which has higher value of Z_C for impedance of a phase shifter. A fabricated tunable phase shifter of this type is photographed in Fig. 2(a). It consists of four tunable Z_C lines and five tuning varactor diodes, D_p, which are adjusted by dc bias, V_{C1}. Varactor diode, D_Z, with adjustable capacitance, C_{var2}, is controlled by co have better return losses with consistent phase differences. All the varactors used are Infenion BB833. Its differential phase shift is demonstrated in Fig. 2(b) which shows the differential phase shift as a function of frequency for several bias values for the condition that the return losses are less than −12 dB up to 850 MHz. It can be seen from this graph that, at 850 MHz, the differential phase shift is continuously variable from 0° to 90° by adjusting the bias. When V_{C2} is fixed, tuning range with the same return loss property shrinks to 85°. From the measured data the figure of merit (i.e., degree/dB) for the phase shifter can be extracted. Some typical data are given as follows. For a fixed V_{C2} of 20 V, when V_{C1} varies the figures of merit are 86 degree/dB, 104 degree/dB and 114 degree/dB for $V_{C1} = 6.5$, 8 and 10 V respectively. As can be seen the figure of merit increases against V_{C1}. This is because the capacitance of the varactors used is actually decreased when the bias voltage V_{C1} increases,

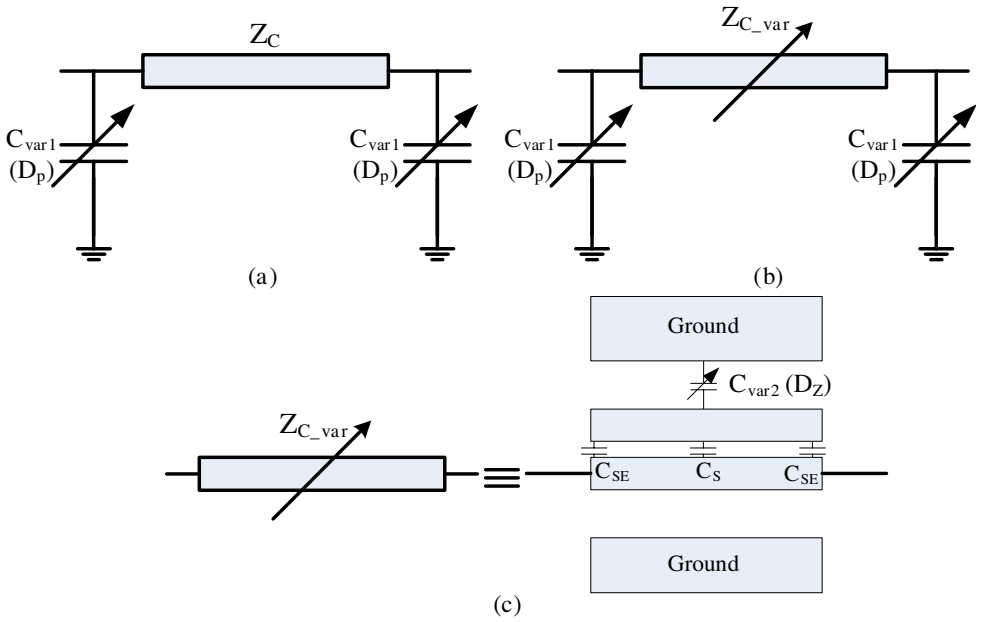

Figure 1: Schematic diagram of a phase shifter using novel tunable transmission line; (a) a unit cell of the conventional distributed phase shifter, (b) a unit cell of a proposed phase shifter, and (c) a detailed block diagram for the realization of a tunable transmission line.

resulting in a higher quality factor at a larger V_{C1}. Using high Q varactors can improve the figure of merit. Also, a higher figure of merit can be obtained if referring to another V_{C2}.

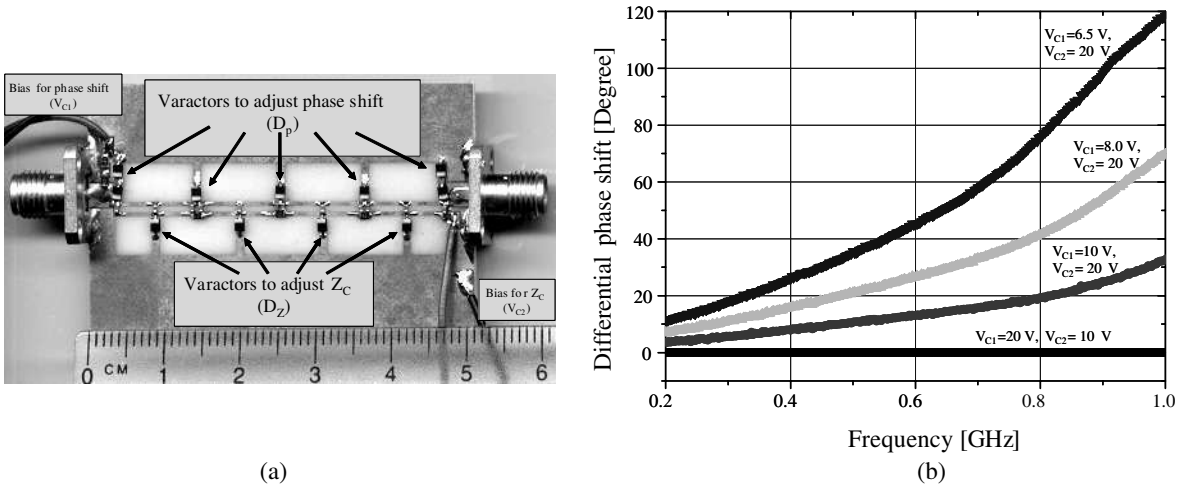

Figure 2: (a) Photograph of the fabricated tunable phase shifter. (b) Differential phase shift versus frequency for selected values of varactors bias. The phase shift is with respect to the transmitted phase at $V_{C1} = 20\,\mathrm{V}$ and $V_{C2} = 10\,\mathrm{V}$ bias.

3. TUNABLE FILTERS

3.1. Tunable Bandstop Filters

A bandstop filter (BSF) is designed at the center frequency of 1.5 GHz with the bandwidth of 20% which has a schematic diagram of Fig. 3(a). Its resonators can be easily replaced with stepped impedance line resonators of Fig. 3(b). Their frequency responses are identical at the center frequency. In order to make the circuit tunable, we modified it further as shown in Fig. 3(c) and (d). Whereas Fig. 3(c) can be straightforwardly realized by connecting varactor chips at the end of shunt stubs, the realization of Fig. 3(d) would be sophisticated. We can change either the electrical length or the characteristic impedance, or both of them as indicated in Fig. 4. The first method is

a capacitive loaded transmission line. It is quite frequently used to implement a phase shifter. The second method is a variable Z_C transmission line which could adjust the characteristic impedance of the transmission line with slight change of electrical length described above.

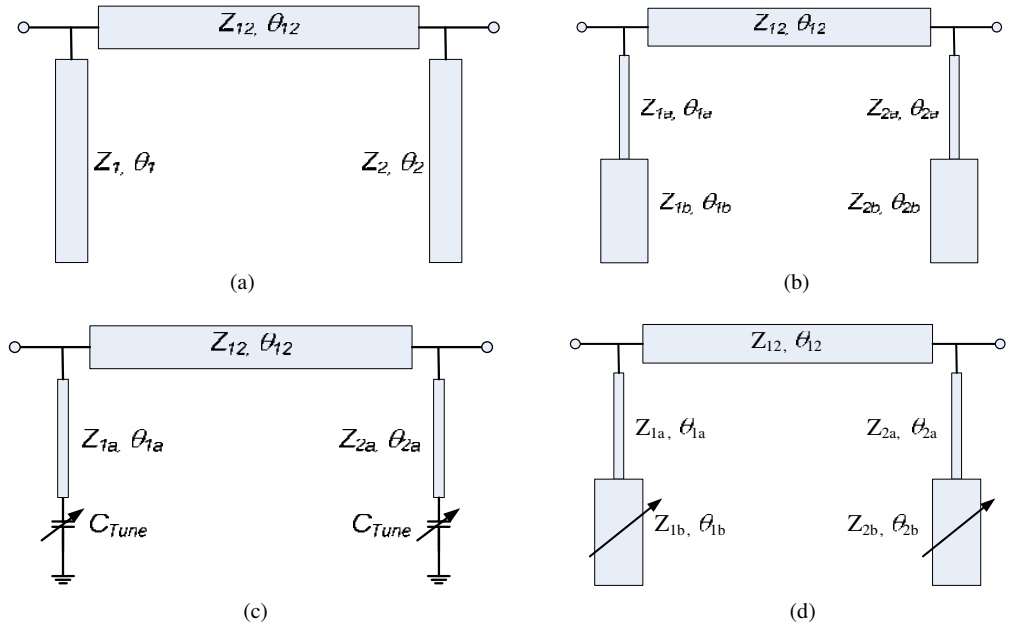

Figure 3: (a) Schematic of a bandstop filter, (b) its modified circuit with SIRs and tunable BSFs using a tunable SIR with lumped circuit (c) and distributed circuit (d).

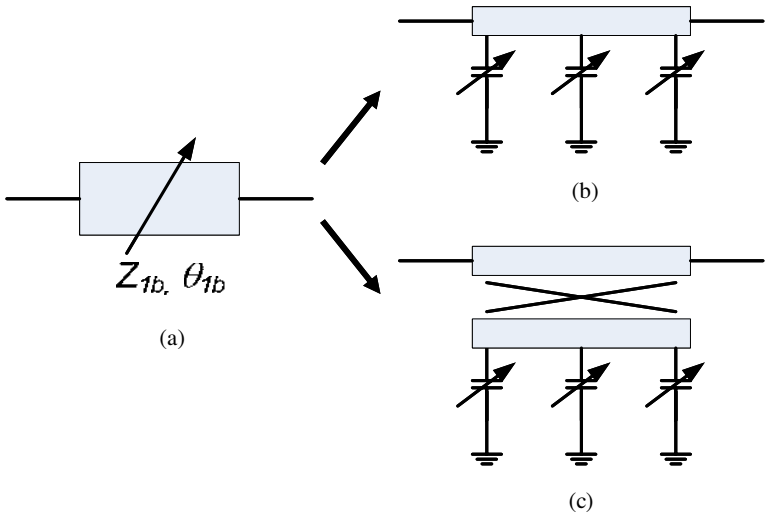

Figure 4: Realization methods of a tunable transmission line of (a): (b) capacitor loaded transmission line and (c) variable Z_C transmission line.

Figure 5(a) shows a physical realization of the proposed tunable BSF, where the Ferroelectric Barium-Strontium-Titanate (BST) film varactor chips are used as the tuning elements. The measured results are plotted in Fig. 5(b), showing a tuning range that is around 10%. This type of BSF has not only good rejection, but also has an advantage to implement a DC bias circuit. In this case, the DC voltage is applied to an additional coupled line instead of a transmission line which is connected with input or output, which reduces spurious response from bias circuitry.

Another newly developed BST-varactor tunable bandstop filter (BSF) is based on a defected or slotted ground structure as shown in Fig. 6(a). This structure can be explained as a kind of electromagnetic bandgap (EBG) structure. The BST varactor chips are attached onto the fabricated BSF as illustrated. The fabricated tunable BSF with slotted ground structure has overall dimensions

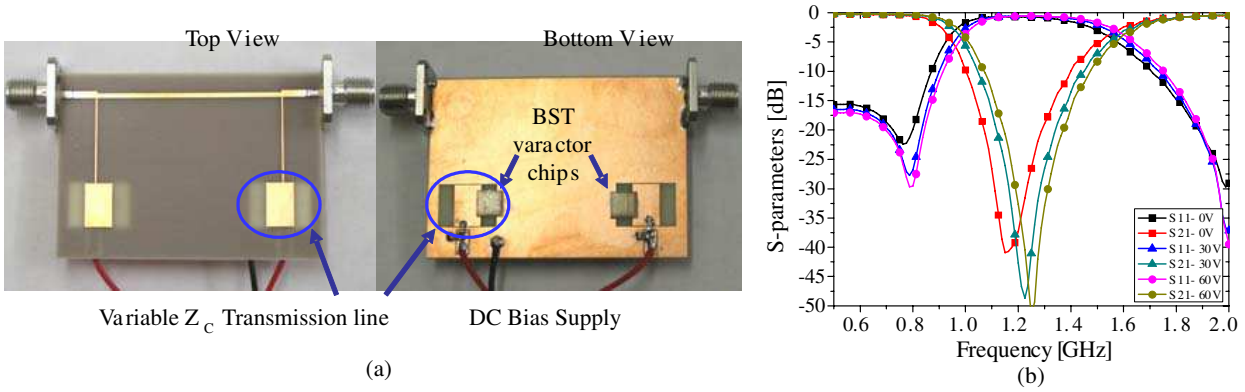

Figure 5: (a) Fabricated tunable BSF. (b) Measured results.

of 5.0 by 2.5 cm^2. Scattering parameter measurements are performed using Agilent 8510B network analyzer over the frequency range from 0.5 to 2.5 GHz. Fig. 6(b) gives the simulated and measured responses of the bandstop filter in which we can observe that it operates at the center frequency from 1.2 to 1.4 GHz and has the bandwidth 100 MHz. Hence, the measured tuning range is 14%.

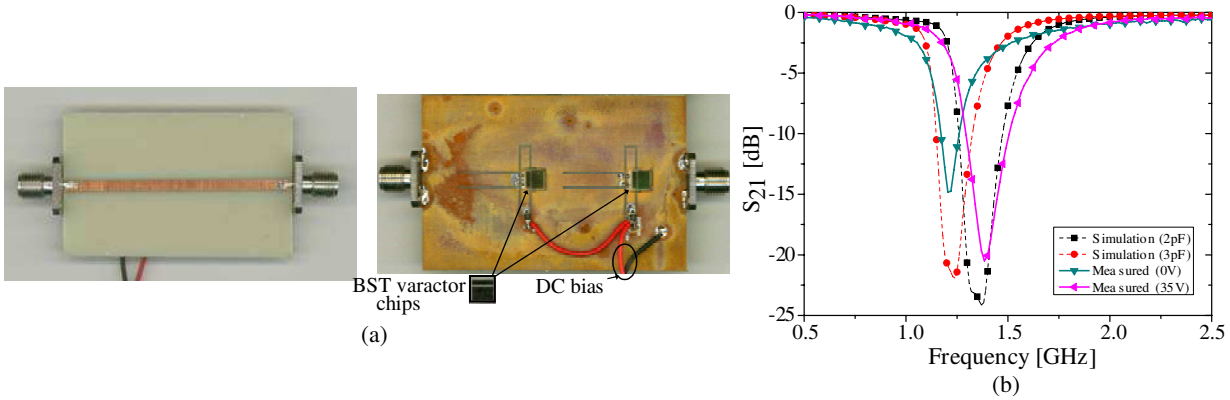

Figure 6: (a) Tunable microstrip BSF filter based on slotted ground structure. (b) Simulated and measured results.

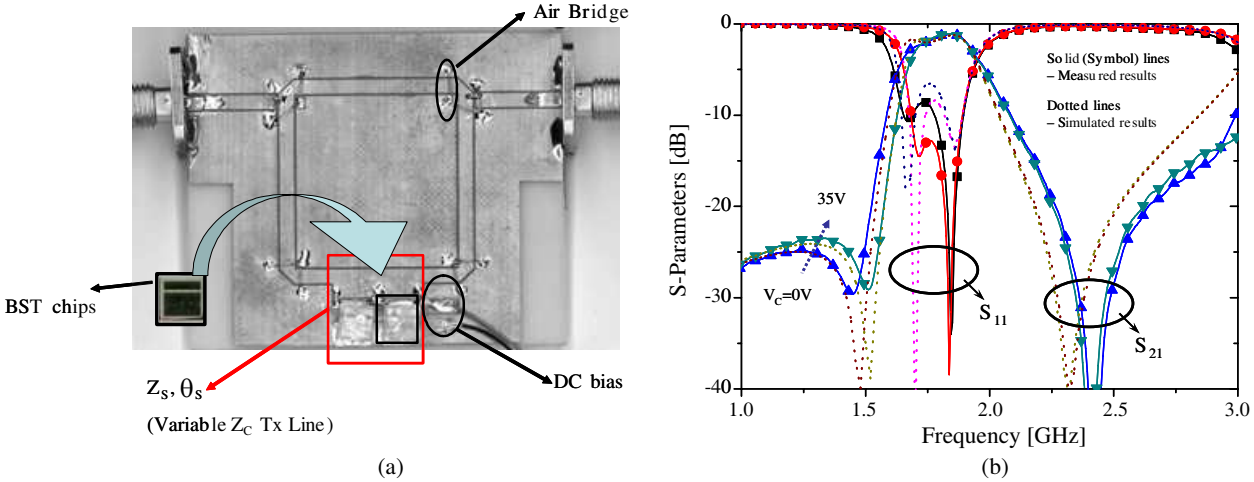

Figure 7: (a) BST-varactor tunable bandpass filter. (b) Simulated and measured results.

3.2. Tunable Bandpass Filters

Figure 7(a) shows a recently developed BST-varactor tunable bandpass filter (BPF). This is a bandwidth-tunable dual-mode ring-resonator bandpass filter, which is designed by adopting a novel tunable circuit based on variable Z_C or tunable impedance transmission line. The variable Z_C transmission line is used for the perturbation of two degenerate modes which makes the bandwidth of filter adjusted as the value of characteristic impedance of the transmission line. A demonstrator of thin-film BST-based tunable bandpass filter with dual mode ring resonator is fabricated on CPW substrate and measured. Fig. 7(b) gives the simulated and measured responses of the bandpass filter in which we can observe that it operates at the center frequency of around 1.8 GHz and has the adjustable 3-dB bandwidth from 276 MHz to 318 MHz. Hence, the tuning ratio of maximum to minimum bandwidth is 1.15:1 for the given DC bias range.

4. CONCLUSIONS

Several electronically tunable devices including tunable phase shifters, tunable bandstop and bandpass filters have been presented. It has been shown that the use of the variable Z_C transmission line in association with the semiconductor or ferroelectric BST varactors can make the electronic tuning effectively.

ACKNOWLEDGMENT

The support from the U.K. Engineering and Physical Research Council (EPSRC) is acknowledged. The authors would also like to thank their project partners at the University of Birmingham and Cranfield University for fabricating the BST thin film devices.

REFERENCES

1. Mitola III, J., "Cognitive radio for flexible mobile multimedia communications," *IEEE Int. Workshop on Mobile Multimedia Comm. Dig.*, 3–10, Nov. 1999.
2. "Revision of part 15 of the Commission's rules regarding ultra-wide-band transmission system," ET-Docket 98-153, First note and order, Federal Communication Commission, Feb. 14, 2002.
3. Chun, Y. H. and J.-S. Hong, "A novel tunable transmission line and its application to a phase shifter," *IEEE Microwave and Wireless Components Letters*, Vol. 15, No. 11, 784–786, Nov. 2005.
4. Chun, Y. H., J.-S. Hong, P. Bao, T. J. Jackson, and M. J. Lancaster, "Tunable bandstop filters using BST varactor chips," *37th European Microwave Conference Proceedings, EuMC2007*, 8–12, Oct. 2007.
5. Chun, Y. H., J.-S. Hong, P. Bao, T. J. Jackson, and M. J. Lancaster, "BST-varactor tunable dual-mode filter using variable Z_C transmission line," *IEEE Microwave and Wireless Components Letters*, Vol. 18, No. 3, 167–169, Mar. 2008.
6. Chun, Y. H., J.-S. Hong, P. Bao, T. J. Jackson, and M. J. Lancaster, "BST varactor tuned bandstop filter with slotted ground structure," *2008 IEEE MTT-S*, Jun. 2008.

A Compact Ultra-wideband Bandpass Filter with Low Insertion Loss Using Stub Circuits with Defected Ground Structure

Wen-Jeng Lin[1], **I-Tseng Tang**[2], **Ding-Bing Lin**[3]
Chi-Min Li[4], **Min-Yuan Chiu**[4], **and Mau-Phon Houng**[1]

[1]Institute of Microelectronics, Department of Electrical Engineering
Advanced Optoelectronic Technology Center, National Cheng-Kung University, Tainan, Taiwan
[2]Department of Environment and Energy, Nation University of Tainan, Tainan, Taiwan
[3]Institute of Computer and Communication Engineering
National Taipei University of Technology, Taipei, Taiwan
[4]Department of Communications and Guidance Engineering
Nation Taiwan Ocean University, Keelung, Taiwan

Abstract— A novel ultra-wideband (UWB) bandpass filter is proposed, designed and implemented. The UWB bandpass filter (BPF) is designed for short-circuited stubs with defected ground structure (DGS). The rectangular slot provides attenuation pole to suppress the spurious in the stopband. The quarter-wavelength short-circuited stubs are used to realize the lower stopband, and the etching on the ground plane with rectangular slots is employed to attenuate the upper stopband. Both simulated and measured results show that the filter has a good performance, including an ultra-wideband bandpass (3.1–10.6 GHz), a small insertion loss, a group delay variation of less than 0.12 ns.

1. INTRODUCTION

Since the U.S. Federal Communications Commission (FCC) relieved the unlicensed use of the ultra-wideband (UWB) (3.1–10.6 GHz) for indoor and hand-held systems in 2002 [1], an increasing interest has been aroused among both academic and industrial spheres on exploring various UWB components and systems [2]. As one of the key blocks, a few initial UWB bandpass filters have been reportedly studied with the aim of making up a UWB passband with 110% fractional bandwidth at 6.85 GHz. Recently the UWB has been developed and applied widely. It usually was used in short distance communication. Generally speaking, traditional parallel-coupled line structure, very strong coupling structure could be achieves a wide bandwidth [3].

Although the structure has a wide bandwidth, the spurious band will interest in the upper band. To solve the drawback, a wideband bandpass filter (BPF) can be constructed by a cascade of a low-pass filter (LPF) and a high-pass filter (HPF) [4]. To utilize step-impedance (SI) LPF structure that has a wide stopband upper the cut-off frequency. The HPF consisting of a cascade of shunt short-circuited stubs was adopted for the UWB filter design. The SI LPF has been connected a shunt short-circuited stub HPF, to become a UWB BPF that have a very wide stopband. A new concept UWB bandpass filter has been proposed. Etching pattern on the ground plane is called defected ground structure (DGS) [5]. DGS is a novel technique to improve the performance of filter, and it shows that DGS can enhance the attenuation of stopband and eliminate the parasitical passband in stopband.

Base on the DGS concept, the UWB bandpass filter uses shunt short-circuited stubs with DGS structure to achieve the ultra-wideband bandwidth. The structure has four shunt short-circuited stubs on the top layer, and four rectangular slots on the ground plane, as shown in Fig. 1. Three sections about the UWB filter are described as follows, design, experiment and conclusion, respectively.

2. PROPOSED UWB FILTER DESIGN

Figure 1 shows the layout of the proposed UWB BPF structure. The UWB BPF has four stubs that via hole in the ground, to design broadband high-pass filter, and attenuation lower than 3 GHz [6]. If the stubs are short circuited, the proposed technique may be used to design high-pass filters with wide bandwidths. Besides a good control of the band-pass characteristics, the filters provide also nearly constant group delay over the passband. Based on the theory and applications of transmission lines, the electrical length of the short-circuited stubs is determined as $\theta_S = 25.71^\circ$ and the sizes of physical stubs are shown in Table 1.

There is a problem at this structure of HPF that has periodic spurious on the upper transition band. But we will use DGS to solve this problem. Etching four rectangular slots on the ground plane, as shown in Fig. 1, the resonator interest the attenuation pole to suppress harmonic at 11.85 GHz, frequency response has a very wide stopband higher than 11.85 GHz. Four rectangular slots physical lengths and widths are shown in Table 1. The UWB bandpass filter, built on a FR4 substrate with relative permittivity $\varepsilon_r = 4.4$ and thickness $h = 0.8$ mm, are designed to demonstrate the proposed idea. Fig. 2 shows a photograph of the practical UWB bandpass filter, which is connected with two SMA connectors for measurement.

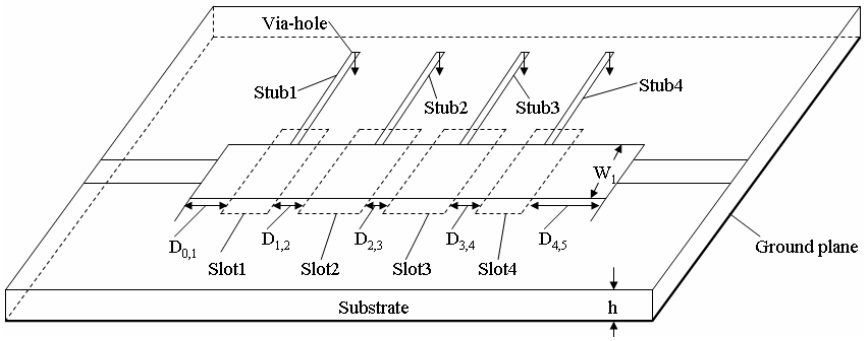

Figure 1: Structure of the novel UWB filter with DGS.

Table 1: Geometry of the UWB filter, which is fabricated on the double side FR4 substrate with $\varepsilon_r = 4.4$, and thickness $h = 0.8$ mm

Top layer	D0,1	D1,2	D2,3	D3,4	D4,5	Stub1	Stub2	Stub3	Stub4
Length (mm)	1.16	2.38	2.52	2.38	1.16	6.66	6.59	6.59	6.66
Width (mm)	W1 2.55	W1 2.55	W1 2.55	W1 2.55	W1 2.55	0.44	0.63	0.63	0.44
Back layer	Slot1		Slot2		Slot3		Slot4		
Length (mm)	2.1		2.45		2.45		2.1		
Width (mm)	3.8		3.8		3.8		3.8		

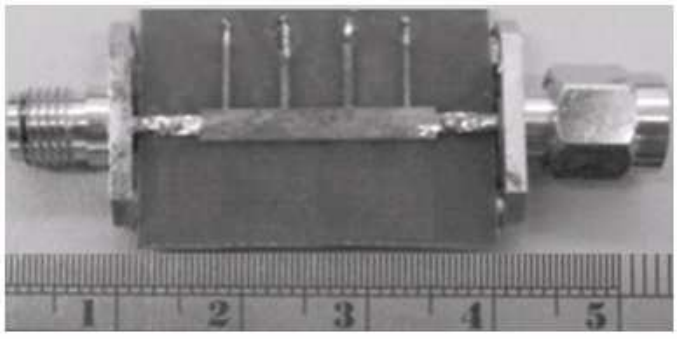

Figure 2: Photograph of the fabricated UWB filter with DGS.

3. EXPERIMENTAL VERFICATION

Simulation design for the filter is carried out on the full wave simulator. In simulation, it is found that the proposed filter in which the insertion loss $|S21|$ is less than -3 dB, return loss $|S11|$ is below -20 dB in the passband, and has an ultra-wideband passband of 3.1–10.6 GHz, respectively. This proposed BPF is conformed to ultra-wideband establishment. The fabricated filter was measured

on network analyzer HP8720C. In measurement, it is found that the proposed filter in which the insertion loss $|S21|$ is less than -3 dB, return loss $|S11|$ is near -15 dB in the passband, and has an ultra-wideband passband of 3.1–10.6 GHz, respectively.

Both the measured results and simulated results are shown in Fig. 3. For comparison, Fig. 3 shows the in-passband performance of the proposed filter that the measured results agree very well with the simulated results. Except the stopband higher than 12 GHz, the measured data have deviations from the simulation. The discrepancy may attribute to the inaccurate modeling of via holes in simulation, since each via may have a strong radiation at these frequencies, and the out-of-band rejection level of below -30 dB at high frequencies can be improved by properly designing both the DGS and the microstrip line for the transitions. Fig. 4 shows both the simulated and measured of group delay, the measured group delay varies between 0.39 and 0.51 ns with a maximum variation of 0.12 ns over its whole passband. At the same time, its out-of-band performance is significantly improved.

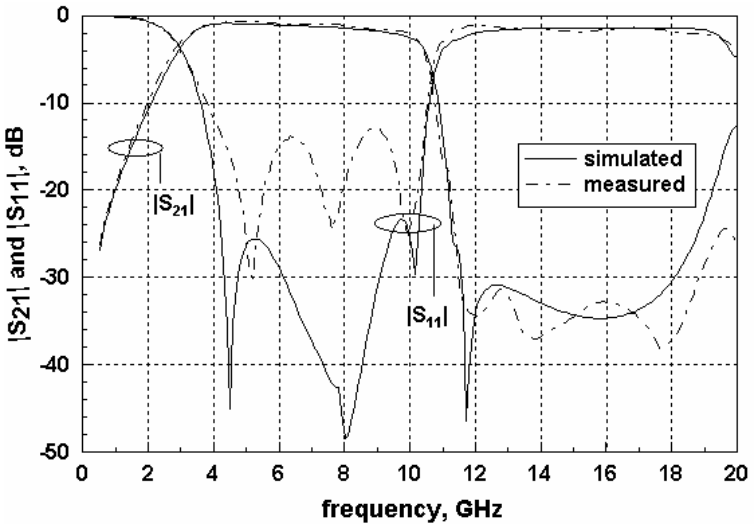

Figure 3: Simulation and measure of the UWB filter with DGS.

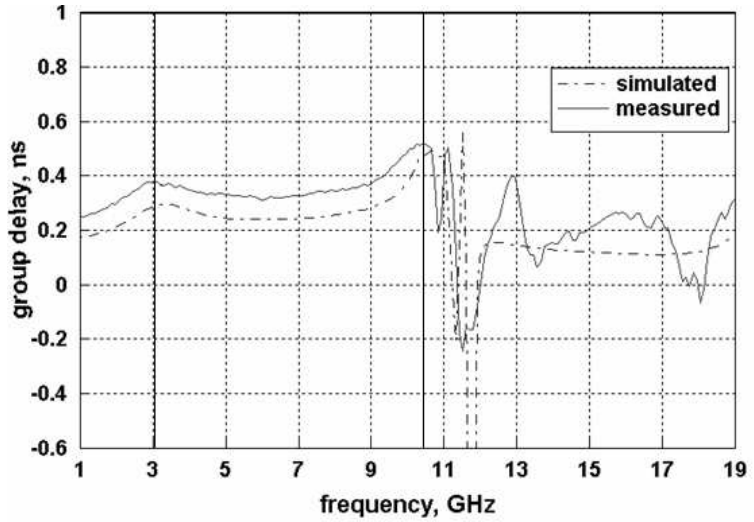

Figure 4: Group delay of the UWB filter with DGS.

4. CONCLUSIONS

A new technique for designing microstrip BPFs suitable for UWB wireless communications is proposed. The UWB BPF is designed with a shunt short-circuited stub HPF etching slots on the

ground plane. Although the high-pass using shunt short-circuited stub structure and suppression the spurious band using DGS structure by each other, the entire design shows a satisfactory band-pass characteristic over a wide bandwidth. This experimental filter is designed to have bandwidths complying with the UWB specifications. The measured data show a good passband characteristic and a good agreement with the simulated results.

ACKNOWLEDGMENT

This work was sponsored by the National Science Council under the contract number of NSC 95-2221-E-024-025.

REFERENCES

1. Federal Communications Commission, "Revision of part 15 of the commission's rules regarding ultra-wideband transmission systems," *Tech. Rep.*, ET-Docket 98-153, FCC 02-48, Apr. 2002.
2. Aiello, G. R. and G. D. Rogerson, "Ultra-wideband wireless systems," *IEEE Microw. Mag.*, Vol. 4, No. 2, 36–47, 2003.
3. Zhu, L., S. Sun, and W. Menzel, "Ultra-wideband (UWB) Bandpass filters using multiple-mode resonator," *IEEE Microw. Wireless Compon. Lett.*, Vol. 15, No. 11, 796–798, Nov. 2005.
4. Hus, C.-L., F.-C. Hus, and J.-T. Kuo, "Microstrip bandpass filters for ultra-wideband (UWB) wireless communications," *IEEE MTT-S Int. Dig.*, 679–682, Jun. 2005.
5. Kim, C. S., J. S. Lim, S. Nam, K. Y. Kang, and D. Ahn, "Equivalent circuit modeling of spiral defected ground structure for microstrip line," *Electron. Lett.*, Vol. 38, No. 19, 1109–1111, Sep. 2002.
6. Hong, J.-S. and H. Shaman, "An optimum ultra-wideband microstrip filter," *IEEE Microwave Opt. Technol. Lett.*, Vol. 47, No. 3, 230–232, 2005.

Measurement of the Dielectric Constant of Liquids Using a Hybrid Cavity-ring Resonator

M. S. Kheir[1], **H. F. Hammad**[1], **and A. S. Omar**[2]

[1]Faculty of Information Engineering and Technology
German University in Cairo, Cairo, Egypt
[2]Microwave and Communication Engineering
University of Magdeburg, Magdeburg, Germany

Abstract— A simple and efficient solution for extracting the dielectric constant of liquids utilizing microstrip ring resonators simultaneously with rectangular waveguide (RWG) cavities is presented. Employing both techniques in a single structure is a confirmation procedure rather than comparing the obtained results with any other standard method. The proposed structure is intended to be mechanically suited for holding liquid samples without enclosing any air gaps which enhances the measurement sensitivity. Since the structure is being totally enclosed, the loaded quality factor will be consequently increased due to the absence of radiation losses. The waveguide cavity acts as metallic enclosure for the ring circuit in order to maintain the design procedures as well.

1. INTRODUCTION

Material characterization is an important field in microwave engineering since it is employed in various systems and applications ranging from high-speed circuits to satellite and telemetry applications [1]. Several measurement techniques are already available nowadays and can be mainly classified into transmission-reflection, free-space, and resonance techniques. The later technique is of a great interest and wide range of application due to its higher accuracy and resolution. Among the resonant methods used in material characterization are waveguide cavities and printed-line resonators [3–11]. Rectangular and cylindrical waveguide cavities have been commonly used for a long time in characterizing low-loss materials [4–6] as they offer a high quality factor. However, performing material measurement with waveguides concurrently with another printed resonator has not been investigated yet and will be the goal of this work It is intended to use both structures simultaneously as a double-check procedure for measurement convenience and low fabrication cost. Using both methods consequently will definitely reduce measurement ambiguity. The key feature in this structure is that it is an ordinary microstrip ring resonator covered with a metallic enclosure which acts as a RWG as illustrated in Section 3. Above all, a practical solution for characterizing the electrical properties of liquids is strongly needed.

2. MEASUREMENT THEORY

Napoli and Hughes [10] introduced a simple and accurate technique for determining the dielectric constant of integrated circuit substrates. It was assumed that the substrate material forms a parallel-plate waveguide cavity if it is metallized on both sides. Using the formula below the relative dielectric constant (ε_r) can be easily obtained just by detecting the resonance frequency (f_{mn}) of this waveguide.

$$f_{mn} = \frac{c}{\sqrt{\varepsilon_r}} \sqrt{\left(\frac{m}{2w}\right)^2 + \left(\frac{n}{2l}\right)^2} \tag{1}$$

where

c is the speed of light,
m is the order of transverse resonance,
n is the order of longitudinal resonance,
w is the waveguide width,

and l is the waveguide length.
However, the resulting quality factor was not as high as expected. In a later work, Howell [7] suggested a slight modification to this method which significantly increased the quality factor and

offered a convenient way of measurement. In his work he short-circuited the ends of the parallel-plate waveguide to eliminate the losses due to end-effect and fringe fields. The resulted resonator was a simple RWG with the resonance equation

$$\varepsilon_r = \frac{c^2}{4f_{pq}}\left(\frac{p^2}{a^2} + \frac{q^2}{b^2}\right) \tag{2}$$

where p and q are the transverse and longitudinal resonance modes respectively while a and b are the transmission line length and width. By observing the resonance frequency and applying the above-mentioned formulas, the effective dielectric constant can be calculated. Nevertheless, Robinson [5] also investigated the resonant modes that result from RWG cavities partially loaded with a microstrip line. This approach still can be a good approach for representing the modes of the metallic enclosure used in our proposed design. The guided wavelength (λ_g) of this excited mode is given by

$$\lambda_g = \frac{\lambda_o}{\sqrt{\dfrac{1}{1-\left(\dfrac{h}{b}\right)\left(1-\dfrac{1}{\varepsilon_r}\right)} - \left(\dfrac{\lambda_o}{2l}\right)^2}} \tag{3}$$

where h represents the substrate thickness, b is the cavity height (including the substrate material), and λ_o is the free space wavelength.

3. THE HYBRID CAVITY-RING STRUCTURE

The detailed structure of the proposed hybrid resonator is shown in Fig. 1(a) with a separate illustration of the ring circuit structure in Fig. 1(b). It consists of three major parts; the microstrip ring resonator, the metallic enclosure and the common ground plane. This structure is made of Aluminum and is fed by an SMA coaxial-to-microstrip transition for measurement using the vector network analyzer (VNA). The details of the hybrid resonator structure are declared next.

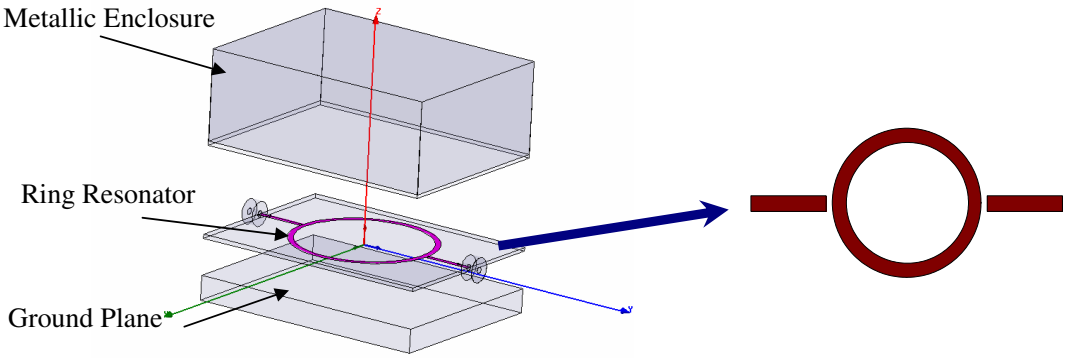

Figure 1: Exploded view of the proposed hybrid resonator (a) and top view of the used ring resonator (b).

3.1. The Microstrip Ring Resonator

A gap-coupled microstrip ring resonator with an FR4-type substrate has a dielectric constant ($\varepsilon_r = 4.4$), a loss tangent ($\tan\delta = 0.02$) and a thickness ($h = 1.5\,\text{mm}$) is used. The operation of the ring resonator is based on the well-known relation

$$n\lambda_g = 2\pi r \tag{4}$$

where r is the mean radius of the ring and n is the harmonic order of resonance. Then the effective dielectric constant (ε_{eff}) can be extracted from the above equation since

$$\lambda_g = \frac{\lambda_o}{\sqrt{\varepsilon_{eff}}} \tag{5}$$

Meanwhile, the resonance frequency can by detected by observing the peaks of the magnitude and the rapid phase variation of the insertion loss (S_{21}) of the ring. Considering that the ring is operating at its fundamental resonance.

3.2. The Waveguide Enclosure

Another way for confirming the estimated ε_{eff} is to use the metallic enclosure which acts as a waveguide cavity with L-band standard dimensions [2] operating at its dominant mode $TE_{10\delta}$. When the cavity is perturbed by the material under test (MUT) the resulting resonance frequency will be deviated from its original resonance frequency. From this frequency shift the material properties can be evaluated using the Cavity-Perturbation theory [4]. However, through the following section the details of the dielectric constant extraction procedures will be illustrated.

4. MEASUREMENT AND EXTRACTION PROCEDURES

In the simulation phase, several materials with different dielectric constants have been tested and the resulting effective dielectric constant of the substrate has been extracted using a finite-elements method simulator. The detected resonance frequency of the overall structure is used in Equations (2) and (4) to calculate the respective ε_{eff} of the cavity and ring resonators. Fig. 2(a) shows the effective dielectric constants calculated in both cases while the results are in excellent agreement. In Fig. 2(b) the relative dielectric constant extracted at different resonance frequencies is plotted where the simulation points precisely fit a fourth order polynomial function. This curve can be efficiently used to extract the dielectric constant of any MUT using the proposed structure only by measuring its resonance frequency.

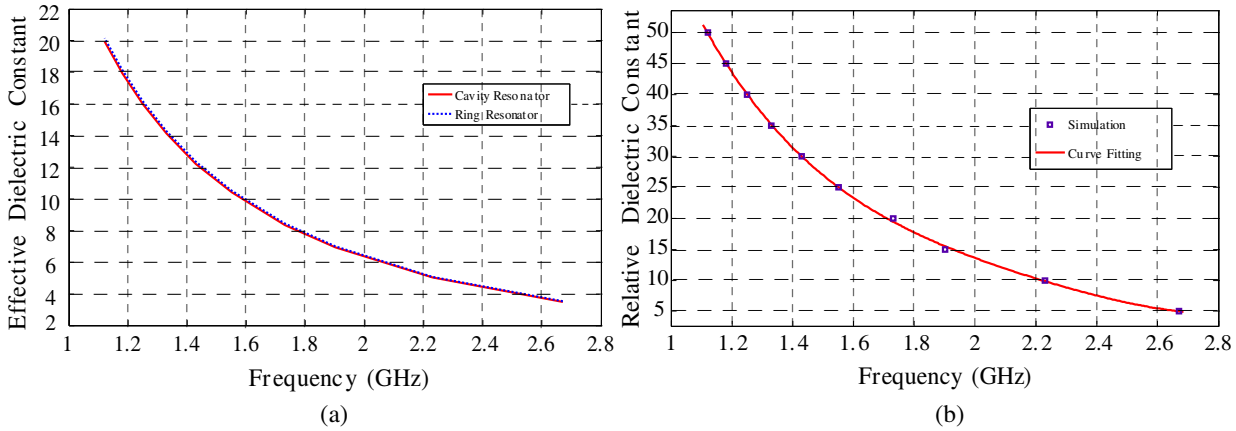

Figure 2: The extracted ε_{eff} from both resonators (a) and the estimated ε_r against frequency (b).

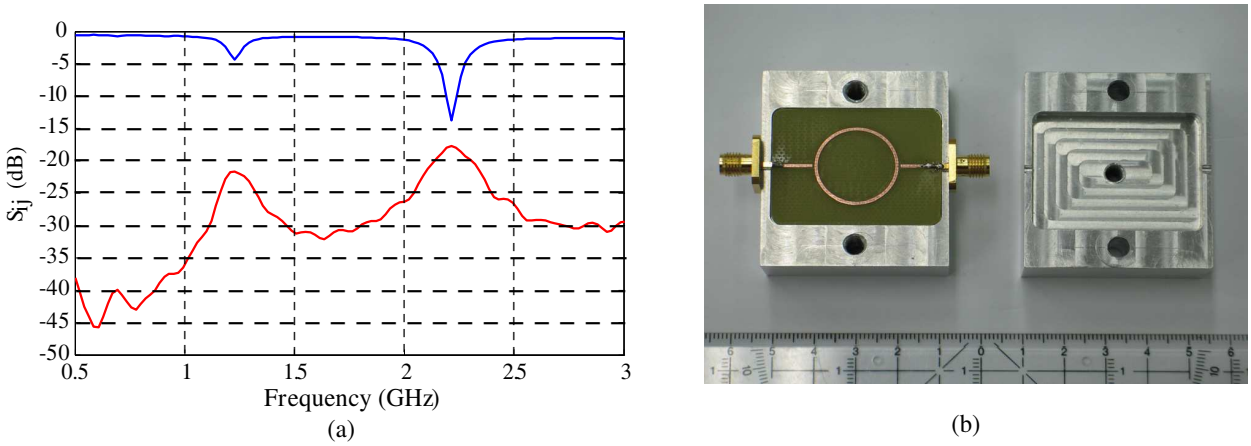

Figure 3: The measured S_{11} and S_{21} (a) and a photograph (b) of the resonator.

As a measurement example the experimental prototypes have been filled with an unknown liquid. As shown in the S-parameters curve in Fig. 3(a) that the first resonance peak appears at 1.25 GHz. Such result typically corresponds to a liquid with $\varepsilon_r = 40$ according to the previously depicted graph. The measurement was performed by the Rohde and Schwarz® ZVB-20 network analyzer.

The photograph of this prototype is shown in Fig. 3(b) where the screw-hole in the middle of the enclosure is intentionally introduced for transferring the liquid into the structure. The structure was mechanically suitable for holding such liquids due to its sealed design. A screw is then used to close this hole which completes the upper metal boundary of the waveguide.

5. CONCLUSIONS

A simple method for evaluating the dielectric constant of liquids has been proposed. It is based on using ring and RWG cavity resonators simultaneously in a single structure. By observing the resonance frequency of this hybrid resonator the effective dielectric constant can be extracted. An excellent agreement between the results extracted from both cavity and ring resonator has been achieved. Such technique can give a preliminary indication about the dielectric properties of the tested material. It can also be suitable for characterizing biological liquids such as blood or urine as a promising technique for medical diagnosis.

ACKNOWLEDGMENT

The authors are sincerely grateful to Prof. Hisham El-Sherif, the Head of Industrial Automation Dept., German University in Cairo, for his helpful consultations and efforts in fabricating the experimental prototypes.

REFERENCES

1. Chen, L. F., C. K. Ong, C. P. Neo, V. V. Varadan, and V. K. Varadan, *Microwave Electronics: Measurement and Material Characterization*, John Wiley & Sons Inc., 2004.
2. Pozar, D. M., *Microwave Engineering*, John Wiley & Sons Inc., 2005.
3. Baker-Jarvis, J., R. G. Geyer, J. H. Grosvenor, Jr., M. D. Janezic, C. A. Jones, B. Riddle, C. M. Weil, and J. Krupa, "Dielectric characterization of low-loss materials: A comparison of techniques," *IEEE Transactions on Dielectrics and Electrical Insulation*, Vol. 5, No. 4, 244–246, 1998.
4. Kumar, A., S. Sharma, and G. Singh, "Measurement of dielectric constant and loss factor of the dielectric material at microwave frequencies," *Progress In Electromagnetics Research*, PIER 69, 47–54, 2007.
5. Robinson, G. H., "Resonant frequency calculations for microstrip cavities (correspondence)," *IEEE Transactions on Microwave Theory Tech.*, Vol. 19, No. 7, 244–246, 2003.
6. Baysar, A. and J. L. Kuester, "Dielectric property measurements of materials using the cavity technique," *IEEE Transactions on Microwave Theory Tech.*, Vol. 40, No. 11, 2108–2110, 1992.
7. Howell, J. Q., "A quick accurate method to measure the dielectric constant of microwave integrated circuit substrates," *IEEE Transactions on Microwave Theory Tech.*, Vol. 51, No. 4, 142–143, 1973.
8. Ivanov, S. A. and V. N. Peshlov, "Ring-resonator method — Effective procedure for investigation of microstrip line," *IEEE Microwave and Wireless Components Letters*, Vol. 13, No. 6, 665–666, 1971.
9. Bernard, P. A. and J. M. Gautray, "Measurement of dielectric constant using a microstrip ring resonator," *IEEE Transactions on Microwave Theory Tech.*, Vol. 39, No. 3, 592–595, 1991.
10. Napoli, L. S. and J. J. Hughes, "A simple technique for the accurate determination of the microwave dielectric constant for microwave integrated circuit substrates (correspondence)," *IEEE Transactions on Microwave Theory Tech.*, Vol. 19, No. 7, 664–665, 1971.
11. Heinola, J. M., K. P. Latti, and P. Silventoinen, "Dielectric characterization of printed wiring board materials: A comparison of ring and T-resonator based measurement methods," *Proceedings of Electrical Insulation and Dielectric Phenomena Conference CEIDP'05*, 629–632, October 2005.

Microwave Assisted Processing of $Sm(Zn_{0.5}Ti_{0.5})O_3$ and ZnO-TiO_2 Dielectric Resonators

S. Roopas Kiran, V. R. K. Murthy, and V. Subramanian
Microwave Laboratory, Department of Physics
IIT Madras, Chennai 600036, India

Abstract— Dielectric resonators are widely used as components of microwave resonant cavities with high dielectric constant, high quality factor and low temperature dependent resonant frequency. Recent advances in the synthesis of materials find several methods of preparation that includes microwave processing. It is possible to use the microwave for the synthesis of materials in two ways. Once the calcination of the required material is performed with conventional furnace, the microwave assisted sintering can be used for more densification. The other way is to directly use the microwave assisted process for obtaining the densified pellets from the stoichiometrically mixed starting reagents. In this paper, we report the synthesis of $Sm(Zn_{0.5}Ti_{0.5})O_3$ and ZnO-TiO_2 using conventional sintering, microwave assisted sintering and microwave assisted synthesis. Phase formation was observed with XRD and surface morphology was observed using AFM. Microwave dielectric properties of all these systems were obtained using Hakki-Coleman method and cavity resonance method. The paper analyzes the variation between the microwave dielectric property and surface morphology of the above two systems synthesized by the three different routes.

1. INTRODUCTION

Dielectric resonators occupy a prominent position in the development of miniaturized microwave components because of their advantage of compactness and ease of matching to the microwave integrated circuit. The performance of these materials as filters and oscillators in base stations increases with increasing the dielectric constant (ε'), quality factor ($Q \times f$) and reducing the temperature coefficient of resonant frequency (τ_f). Various materials have been reported [1–3] due to their excellent microwave dielectric properties. To improve the microwave dielectric properties and to reduce the processing parameters various methods such as addition of different dopants like CuO, B_2O_3, ZnO, SiO_2, Bi_2O_3 etc. [4, 5] and variation in preparation techniques such as Pechini method [6], wet-dry combination technique [7], sol-gel and other chemical routes [8] have been followed. Application of microwave heating in ceramic processing is relatively new technique that offers significant saving of time, energy and cost compared to the existing conventional methods. Microwave processing of ceramic materials results in rapid and volumetric heating, selective heating, enhanced densification rate and improved microstructure. This technique is reported to be of much use in improving the dielectric properties of several ferrites [9], ferroelectrics [10], but much attention was not paid in processing the dielectric resonators. Dielectric resonators are low loss dielectric materials and hence it is difficult to make these materials absorb microwaves. Theoretical and experimental works have shown that the increase of dielectric properties of material with temperature can lead to uniform and enhanced microwave power absorption in the dielectric ceramics. So susceptors can be used in increasing the temperature of dielectric resonators and hence dielectric properties and microwave absorptive ability. Various microwave transparent materials such as Al_2O_3, ZrO_2 have been microwave sintered using silicon carbide based susceptors [11, 12].

In the present work, two dielectric resonator materials samarium zinc titanate and zinc titanate are processed using microwaves (hybrid microwave heating) at different temperatures. Microwave processing is done in two different ways. First one is the microwave sintering of the green pellets obtained after calcination in conventional furnace. The other one is the microwave processing of compacts of uniform mixture of starting reagents taken in the stoichiometric ratio to get the final compound. In this paper, the density and microwave dielectric properties of the samples prepared in the three different methods viz. conventional sintering (CS), microwave sintering (MS) and reaction microwave sintering (RMS) are compared. Microstructures are analyzed with the help of atomic force microscope.

2. EXPERIMENTAL METHOD

2.1. Samarium Zinc Titanate (SZT)

High pure (> 99.9%) Sm_2O_3, ZnO and TiO_2 (from Alfa Aesar) were mixed in an agate mortar stoichiometrically. Sm_2O_3 was pre-fired at 1000°C for 24 h to remove the moisture, CO_2 and other volatile compounds. The mixture was hand-milled both in dry and wet (distilled water) conditions for 2 h. The dried mixture was made into two parts. One part was calcined in a conventional furnace at 1200°C for 4 h. The calcined powder was again hand-milled in distilled water medium. The calcined powder was mixed with 2 wt.% PVA binder and compacted uniaxially to a diameter of 12 mm and thickness of 6 mm. The binder-free pellets were sintered in both conventional and microwave furnace separately at different temperatures. Conventional sintering (CS) was done at 1380–1470°C for 2 h and microwave sintering (MS) was performed at 1300 and 1350°C for 20 min. On the other hand the uniform mixture of Sm_2O_3, ZnO and TiO_2 was compacted to a diameter of 12 mm and thickness 6 mm using PVA binder. Binder evaporated green pellets were treated with microwaves (RMS) at 1300 and 1350°C for 25 min.

The microwave furnace can deliver a maximum power of 1100 watt at 2.45 GHz in a multimode applicator. Silicon carbide powder is used as susceptor to facilitate the hybrid microwave heating. The input microwave power will be controlled by Eurotherm controller to attain the set temperature and the temperature can be measured with a thermocouple.

2.2. Zinc Titanate (ZT)

ZnO and TiO_2 were mixed in 1:1 molar ratio. The mixture was hand-milled to 2 h in distilled water medium and dried in a conventional oven. The experimental procedure was done in the same manner as mentioned in the case of SZT. The calcination was performed at 800°C for 4 h. Sintering temperature of all the samples was varied between 950–1150°C. Conventional sintering was done for a soaking period of 4 h and microwave processing was performed for 25 min.

The bulk densities of the samples were measured by Archimedes technique. The phase formation was observed with XRD using Philips X'Pert Pro MPD. Microwave dielectric properties were measured using a vector network analyzer (Agilent N5230A). Dielectric constant was measured by Hakki-Colemann method modified and improved by Courtney. Quality factor was measured by reflection technique and the temperature coefficient of resonant frequency was obtained by observing the change in resonant frequency from 30–70°C.

3. RESULTS AND DISCUSSION

3.1. SZT

X ray diffractograms in Figure 1 show the phase obtained for CS, MS and RMS samples of SZT. Homogeneous $Sm(Zn_{0.5}Ti_{0.5})O_3$ phase with orthorhombic structure belonging to Pnm_{21} space group is observed in all the three cases. The densities obtained by Archimedes technique are presented in Table 1. The densification is found to be more in case of RMS. It is observed that during RMS, the samples are found to melt at temperatures beyond 1375°C, which is not the case in CS and MS. This shows that RMS results in more liquid phase, which can be responsible for higher densification. The density and microwave dielectric properties of CS samples show a maximum at 1410°C. Table 1 includes the microwave dielectric properties of CS samples sintered at 1410°C, MS and RMS samples sintered at 1350°C. The microstructures obtained from atomic force microscope are shown in Figure 2. The uniform grain structures are observed in the microwave treated samples (both MS and RMS) than conventional sintered samples. To understand the effect of microwave sintering other characterization like IR and Raman spectra are needed.

Table 1: Density and microwave dielectric properties of conventionally sintered (CS), microwave sintered (MS) and reaction microwave sintered (RMS) samples of SZT.

Sample & Sintering Temperatiure	Density (g/cc)	Dielectric Constant (ε')	Quality factor $Q \times f$ (GHz)	τ_f (ppm/°C)
CS-1410°C	7.04	30.2	3100	−23
MS-1350°C	7.08	28.6	3000	−24
RMS-1350°C	7.11	28.7	3050	−23

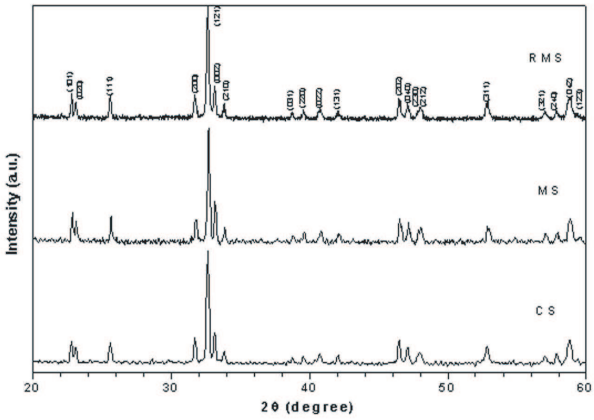

Figure 1: XRD of conventionally sintered (CS) at 1410°C, microwave sintered (MS) at 1350°C and reaction microwave sintered (RMS) at 1350°C of SZT samples.

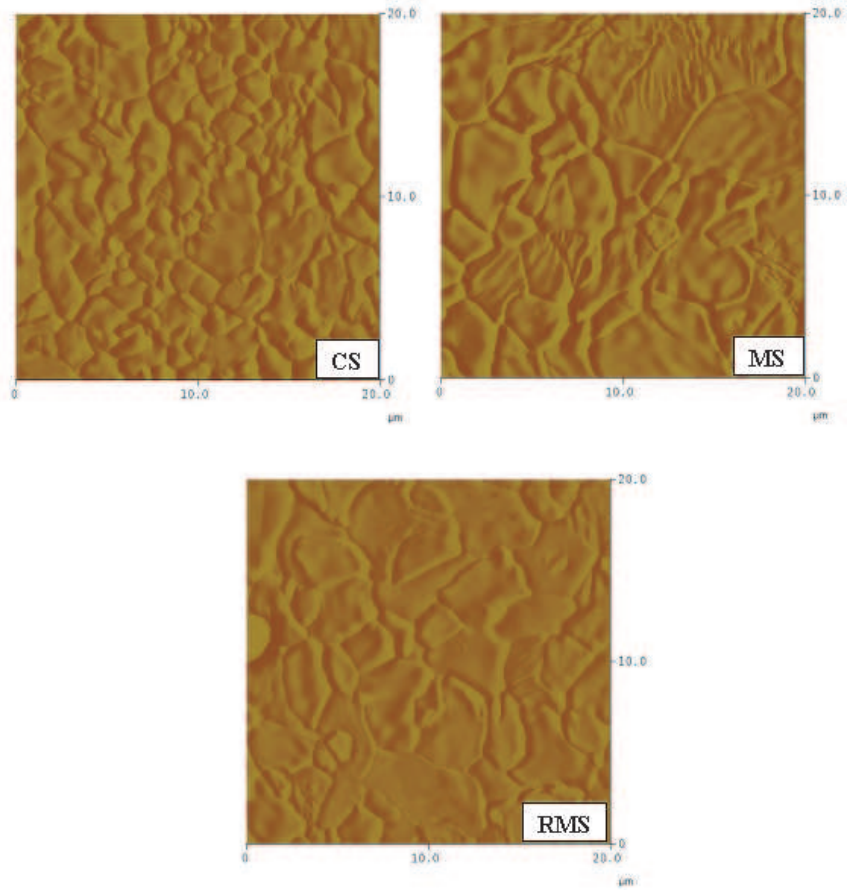

Figure 2: Atomic force micrographs of conventionally sintered (CS) at 1410°C, microwave sintered (MS) at 1350°C and reaction microwave sintered (RMS) at 1350°C of SZT samples.

3.2. Zinc Titanate

The calcined powder of ZnO and TiO_2 mixture is observed to posses all the three possible phases, $Zn_2Ti_3O_8$, $ZnTiO_3$ and Zn_2TiO_4. But all the sintered samples show Zn_2TiO_4 phase, which was obtained by the dissociation of $ZnTiO_3$ into Zn_2TiO_4 and TiO_2 at 945°C. Figure 3 represents the XRD of CS, MS and RMS samples at 1100°C. The densities of all the samples are observed to increase with sintering temperature upto 1100°C. Table 2 gives the density and microwave dielectric properties of CS, MS and RMS samples. Dielectric constant is observed to increase with temperature. This can be attributed to the increase in TiO_2, which has higher dielectric constant,

Table 2: Density and microwave dielectric properties of conventionally sinterd (CS), microwave sintered (MS) and reaction microwave sintered (RMS) samples of ZnO-TiO_2.

Temperature. (°C)	Density (g/cc)	Dielectric constant. (ε')	Quality factor $Q \times f$ (GHz)	τ_f (ppm/°C)
Conventional Sintering				
950	- - -	22.25	3265	- - -
1000	4.59	26.46	15540	52
1050	4.82	29.87	18240	75
1100	4.84	29.75	18920	80
1150	4.84	29.56	17660	73
Microwave Sintering				
950	4.48	24.38	17320	46
1000	4.63	26.23	17600	49
1050	4.74	27.70	18600	50
1100	4.80	28.20	20940	49
1150	4.78	27.93	20300	50
Reaction Microwave Sinteirng				
950	- - -	- - -	- - -	- - -
1000	4.57	26.11	10180	65
1050	4.72	27.33	19460	62
1100	4.79	28.22	21010	61
1150	4.79	26.57	21060	59

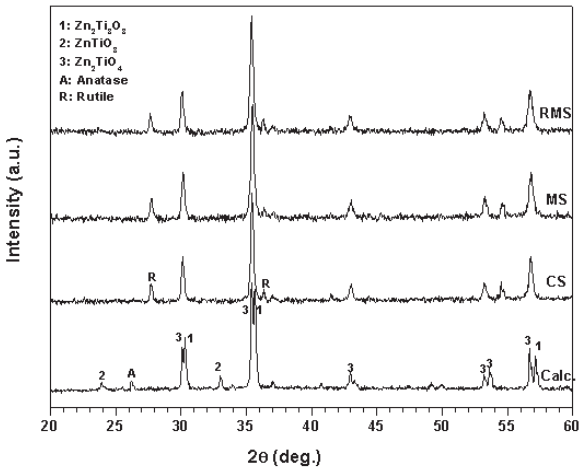

Figure 3: XRD of ZnO-TiO_2 processed by conventionally sintered (CS), microwave sintered (MS) and reaction microwave sintered (RMS) at 1100°C and calcined powder.

concentration with temperature obtained in the dissociation process. The gradual increase in quality factor and τ_f in the case of CS samples with temperature can be related to the increase in density and TiO_2 concentration. Similar trend is observed in the case of RMS samples for density, dielectric constant and quality factor. The quality factor is found to be more in RMS samples than CS. But the temperature coefficient of resonant frequency reduced slightly with temperature. The quality factor is very high for MS samples even at lower sintering temperature and the variation of quality factor with temperature is relatively small. The temperature coefficient of resonant frequency found to be almost independent on the sintering temperature for MS samples. The microstructures, obtained from AFM, of CS, MS and RMS samples sintered at 1100°C are given in Figure 4. The microstructure presents particles of two different sizes one in nano scale and other in micron scale that can be attributed to the dissociation. Uniform distribution of the two phases is observed in microwave treated samples.

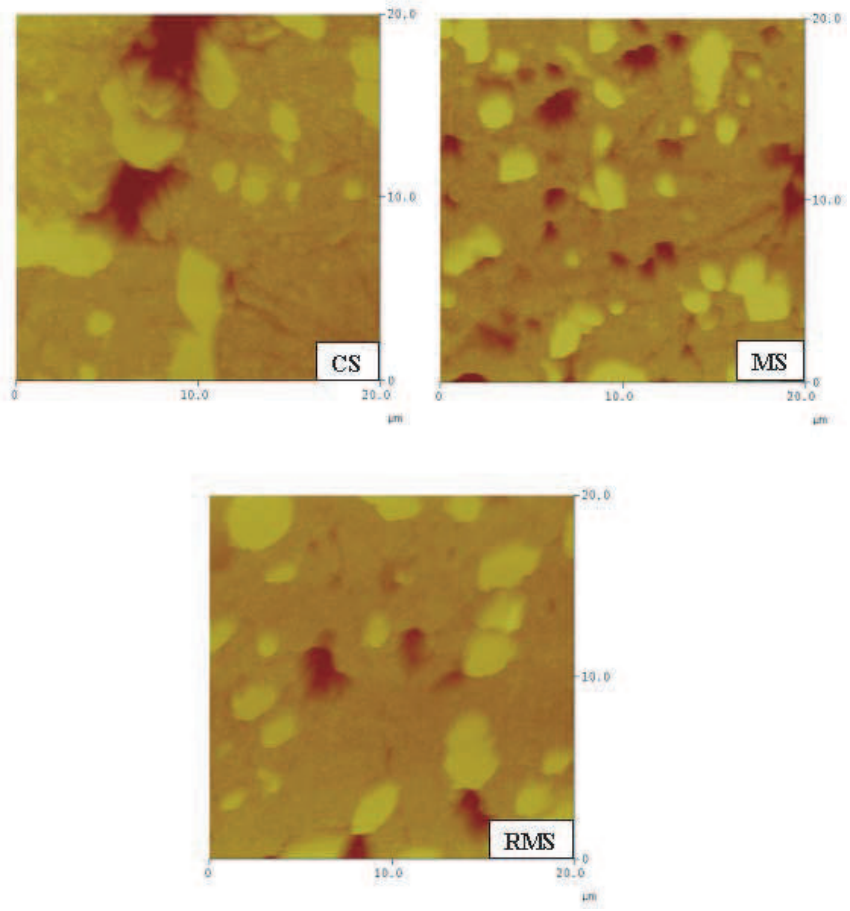

Figure 4: Atomic force micrographs of ZnO-TiO_2 processed by conventionally sintered (CS), microwave sintered (MS) and reaction microwave sintered (RMS) at 1100°C.

4. CONCLUSIONS

Two dielectric resonators samarium zinc titanate and zinc titanate are prepared using microwaves at different temperatures. Reaction microwave sintering is observed to give higher density at low processing temperatures than the conventionally sintered samples. The density and microwave dielectric properties of these samples are compared with those of conventionally sintered ones and found to be comparable. Uniform grain structures are attained with microwave processing. In the case of microwave treated samples (MS and RMS), the temperature dependent resonant frequency is less in comparison with conventionally sintered ones. Zinc titanate shows comparable density and dielectric constant in the case of CS, MS and RMS samples, but the quality factor and τ_f show much difference with microwave sintering. Application of microwaves in preparation of these dielectric resonators shows an enhancement in the microwave dielectric properties.

REFERENCES

1. Takata, M. and K. Kageyama, "Microwave characteristics of $A(B^{3+}_{1/2}B^{5+}_{1/2})O_3$ ceramics (A = Ba, Ca, Sr; B^{3+} = La, Nd, Sm, Yb; B^{5+} = Nb, Ta)," *J. Am. Ceram. Soc.*, Vol. 72, No. 10, 1955–1959, 1989.
2. Cho, S.-Y., C.-H. Kim, D.-W. Kim, K. S. Hong, and J.-H. Kim, "Dielectric properties of $Ln(Mg_{1/2}Ti_{1/2})O_3$ as substrates for high-T_c superconductor thin films," *J. Mater Res.*, Vol. 14, No. 6, 2484–2487, 1999.
3. Khalam, L. A., H. Sreemoolanathan, R. Ratheesh, P. Mohanan, and M. T. Sebastian, "Preparation, characterization and microwave dielectric properties of $Ba(B'_{1/2}Nb_{1/2})O_3$ [B′ = La, Pr, Nd, Sm, Eu, Gd, Tb, Dy, Ho, Y, Yb and In] ceramics," *Mater. Sci. & Engg. B*, Vol. 107, No. 3, 264–270, 2004.

4. Bijumon, P. V. and M. T. Sebastian, "Influence of glass additives on the microwave dielectric properties of $Ca_5Nb_2TiO_{12}$ ceramics," *Mater. Sci. & Engg. B*, Vol. 123, No. 1, 31–40, 2005.
5. Sebastian, M. T. and K. P. Surendran, "Tailoring the microwave dielectric properties of $Ba(Mg_{1/3}Ta_{2/3})O_3$ ceramics," *J. Eur. Cer. Soc.*, Vol. 26, Nos. 10–11, 1791–1799, 2006.
6. Seabra, M. P., M. Avdeev, V. M. Ferreira, R. C. Pullar, N. McN Alford, and I. M. Reaney, "Structure-property relations in xBaTiO$_3$-(1−x)La$(Mg_{1/2}Ti_{1/2})O_3$ solid solutions," *J. Am. Cer. Soc.*, Vol. 87, No. 4, 584–590, 2004.
7. Kakegawa, K., T. Wakabayashi, and Y. Sasaki, "Preparation of $Ba(Mg_{1/3}Ta_{2/3})O_3$ by using Oxine," *J. Am. Cer. Soc.*, Vol. 69, No. 4, 82–83, 1986.
8. Surendran K. P., P. C. Rajath Varma, and M. R. Verma, "Solid state and solution synthesis of $Ba(Mg_{1/3}Ta_{2/3})O_3$: A comparative study," *Mater. Res. Bull.*, Vol. 42, No. 10, 1831–1844, 2007.
9. Yadoji, P., R. Peelamedu, D. Agrawal, and R. Roy, "Microwave sintering of Ni-Zn ferrites: Comparison with conventional sintering," *Mater. Sci. & Engg. B*, Vol. 98, No. 3, 269–278, 2003.
10. Felgner, K.-H, T. Muller, H. T. Langhammer, and H.-P. Abicht, "On the formation of $BaTiO_3$ from $BaCO_3$ and TiO_2 by microwave and conventional heating," *Mater. Lett.*, Vol. 58, Nos. 12–13, 1943–1947, 2004.
11. Xie, Z., J. Yang, X. Huang, and Y. Huang, "Microwave processing and properties of ceraics with different dielectric loss," *J. Eur. Cer. Soc.*, Vol. 19, 381–387, 1999.
12. Brosnan, K. H., G. L. Messing, and D. K. Agrawal, "Microwave sintering of alumina at 2.45 GHz," *J. Am. Cer. Soc.*, Vol. 86, No. 8, 1307–1312, 2003.

Simulation of Multiscale Circuit Problems Using Equivalence Principle Algorithm

Mao-Kun Li[1], **Weng Cho Chew**[2], **and Zhi Guo Qian**[3]

[1]Schlumberger-Doll Research, Cambridge, MA, USA
[2]The University of Hong Kong, Hong Kong, China
[3]University of Illinois at Urbana-Champaign, Urbana, IL, USA

Abstract— The equivalence principle algorithm is introduced in this paper to solve multiscale problems in the electromagnetic modeling of circuit problems. In these problems, low frequency circuit physics coexists with high frequency wave physics that makes the matrix equation ill-conditioned. As a domain-decomposition based algorithm, the equivalence principle algorithm casts the entire domain into different parts based on their physical properties. Each part is solved individually by introduction of virtual equivalence surfaces. Moreover, the interactions among domains are still modeled accurately that captures the electromagnetic wave propagation. With this algorithm and powered up with multilevel fast multipole algorithm, large multiscale problems can be solved on a single computer efficiently.

1. INTRODUCTION

As technological devices become smaller, faster, and more complex, computer simulations of physical phenomena become an increasingly important part of the design process. This makes computational electromagnetic (CEM) simulations indispensable. However, many challenges arise when applying CEM solvers to microelectronic structures. Multiscale phenomena are some of them. A single device can be very tiny and dominated by circuit physics, while thousands of devices can extend to several wavelengths in high frequencies that are dominated by wave physics. The existence of both wave and circuit physics introduces large and small eigenvalues simultaneously resulting an ill-conditioned matrix equation. One kind of methods uses multi-resolution basis set to describe different physics such as [1]. The other approach separates different physics via domain decomposition such as [2]. The references here are far more from complete due to space limitation.

Equivalence principle algorithm (EPA) is essentially a domain decomposition scheme based on equivalence principle and integral equations. By the introduction of virtual equivalence surfaces to enclose the regions with fine features, low frequency physics is isolated from high frequency physics. This results in a better conditioned matrix equation with fewer unknowns. Compared with other integral-equation-based domain decomposition scheme, such as boundary element tearing and interconnecting methods, EPA still allows the interactions between any two basis functions, hence it can catch wave propagation with less dispersion error.

To model continuous current flow in and out of the equivalence surface, a tap basis scheme was introduced. This scheme avoids the computation of current singularities at the cut and can be incorporated with EPA naturally.

In the errors of EPA, a main factor is the high-frequency noise in field projection onto equivalence surfaces. This noise comes from the discretization of the equivalent currents and becomes dominant when objects are very close to the equivalence surfaces. To recover the accuracy, the high-order quadrature point-sampling scheme was used on the equivalence surfaces. This scheme samples the currents directly at points on the equivalence surfaces and integrates using high-order quadrature rules. By using this, EPA is shown to be accurate. The translation procedure in EPA can be accelerated using attached unknown accelerations when equivalence surfaces contact with each other. The current interactions on the touched regions can be computed using local interpolations instead of field integrations. This saves the time in both matrix filling and matrix-vector multiplications. Moreover, the efficiency of EPA can be further improved when accelerated using multilevel fast multipole algorithm (MLFMA). With a proper preconditioning scheme and a careful balancing of the equation, large multiscale problems of over 3 million unknowns can be computed on a personal computer.

2. EQUIVALENCE PRINCIPLE ALGORITHM

EPA is an integral equation solver derived from the equivalence principle. The basic notations and formulations can be found in [3]. There are mainly two operators used in EPA: the equivalence

principle operator and the translation operator. The first is used to compute the scattered equivalent currents given the incident currents on the equivalence surfaces. This operator characterizes the domain enclosed by equivalence surface. The other is the translation operator to calculate the radiation from one equivalence surface to another. With this two operators, we can therefore decompose the whole problem into several domains while keeping their interactions accurate.

2.1. High Order Quadrature Point Sampling Scheme

The accuracy of EPA is highly related with the accuracy of equivalent currents projected onto equivalence surfaces. Nevertheless, numerical errors exist due to the discrete description of the continuous current. We call this error as high frequency noise because it is related with the high-frequency component of the current spectrum. Detailed analysis of the origin of the high-frequency noise can be found in [4, 5]. In the worst scenario when the observation points are very close to the equivalence surface, the computed current values will possess this numerical noise. As a remedy, a high order point sampling scheme is used. The side lobes of the current spectrum are suppressed, hence the numerical noise is reduced.

In high order point sampling scheme the currents are represented by the values at the sampling points and the integrations are approximated as a weighted summation of these points. When the observation points close to one of the source points, the integrand varies rapidly that is hard to evaluate with quadrature rules. An interpolatory local correction technique is applied to this case [6] where the current on the local patch is represented by interpolations. In the current EPA, rectangular patches are used to model the equivalence surfaces, with 9 sampling points on every patch. The interpolation scheme can be found in [7]. Using the high order point sampling scheme, the field is represented more accurately than using the RWG basis set in [3].

When applying EPA, the equivalence surfaces usually enclose the parts with fine features or resonating structures. A general triangular mesh can be decomposed into different parts based on the coordinates of the equivalence surfaces, and tap basis functions are defined at the intersection. This is done automatically using Matlab scripts. From the author's experience, four points per wavelength on the equivalence surfaces usually result the errors in near field less than one percent.

2.2. Attached Unknown Accelerations

When two equivalence surfaces contact each other, the evaluation of the field integration can be accelerated using attached unknown acceleration. This comes from the field continuity and also known as the Calderon projectors [8] in integral operators. For instance, the currents on the attached interface in Figure 1 satisfy,

$$\begin{aligned} \mathbf{J}_2 &= \hat{\mathbf{n}}_2 \times \mathbf{H}_2 = -\hat{\mathbf{n}}_1 \times \mathbf{H}_1 = -\mathbf{J}_1 \\ \mathbf{M}_2 &= -\hat{\mathbf{n}}_2 \times \mathbf{E}_2 = \hat{\mathbf{n}}_1 \times \mathbf{E}_1 = -\mathbf{M}_1 \end{aligned} \tag{1}$$

The minus sign is due to the flip of the normal direction between the two equivalence surfaces.

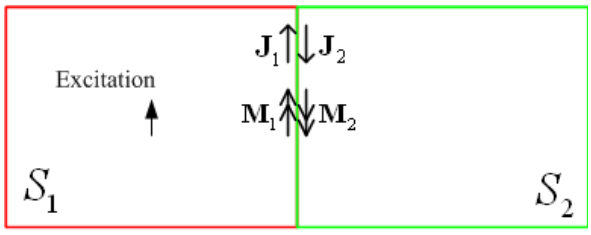

Figure 1: Two equivalence surfaces touching each other.

In high order quadrature point sampling scheme, the equivalent currents on the testing points can be evaluated from local interpolation as

$$J_{2mi,x} = -\sum_{j=1}^{9} N_j J_{1nj,x} \tag{2}$$

where $J_{2mi,x}$ is the value of the electric currents on the ith sampling point of the mth element on surface S_2. If this sampling point falls into the nth elements of surface S_1, it can be expressed as a local interpolation of the current coefficients $J_{1nj,x}$. Here N_j is the interpolation function. This

scheme substitutes field integrations with direct interpolations, saving both CPU time and memory. Moreover, this scheme is not limited to the case of two identical surfaces, but also valid if only a part of the surface touches with each other.

2.3. Acceleration of EPA Using MLFMA

Like other MOM based algorithms, the dense EPA matrix equations require many computing resources when problems get large. To improve the computational efficiency, MLFMA is used to speed up the matrixvector multiplication in the translation procedure in which all the equivalent currents radiate and interact with each other.

Assume N_p PEC surfaces, N_d dielectric objects, and N_h equivalence surfaces exist in the problem, and no connection between any two objects for simplicity. The matrix equations can be written as follows:

$$\begin{bmatrix} 0 & & \\ & 0 & \\ & & \mathcal{I} \end{bmatrix} + \begin{bmatrix} \mathcal{I} & & \\ & \mathcal{I} & \\ & & -\mathcal{S} \end{bmatrix} \cdot \begin{bmatrix} \mathcal{I} & & & \\ & \mathcal{I} & & \\ & & -\frac{1}{\eta}\hat{\mathbf{n}}\times\mathcal{I} & \hat{\mathbf{n}}\times\mathcal{I} \end{bmatrix} \cdot \begin{bmatrix} \frac{1}{\eta}\mathcal{L}_{pp} & \frac{1}{\eta}\mathcal{L}_{pd} & \frac{1}{\eta}\mathcal{L}_{ph} & \mathcal{K}_{ph} \\ \frac{1}{\eta}\mathcal{L}_{dp} & \frac{1}{\eta}(-\mathcal{I}+\mathcal{L}_{dd}) & \frac{1}{\eta}\mathcal{L}_{dh} & \mathcal{K}_{dh} \\ \frac{1}{\eta}\mathcal{L}_{hp} & \frac{1}{\eta}\mathcal{L}_{hd} & \frac{1}{\eta}\mathcal{L}_{hh} & \mathcal{K}_{hh} \\ -\mathcal{K}_{hp} & -\mathcal{K}_{hp} & -\mathcal{K}_{hh} & \frac{1}{\eta}\mathcal{L}_{hh} \end{bmatrix} \cdot \begin{bmatrix} \mathbf{J}_p \\ \mathbf{J}_d \\ \mathbf{J}_h \\ \frac{1}{\eta}\mathbf{M}_h \end{bmatrix} = \begin{bmatrix} \mathcal{I} & & \\ & \mathcal{I} & \\ & & \mathcal{S} \end{bmatrix} \cdot \begin{bmatrix} -\frac{1}{\eta}\mathbf{E}_p^{inc} \\ -\frac{1}{\eta}\mathbf{E}_d^{inc} \\ \mathbf{J}_h^{inc} \\ \frac{1}{\eta}\mathbf{M}_h^{inc} \end{bmatrix} \tag{3}$$

Here $\mathbf{J}_d$ is the set of all electric currents on PEC surfaces, similar manners for $\mathbf{J}_d$, $\mathbf{J}_h$ and $\mathbf{M}_h$. $\mathcal{L}_{pp}$ represents the set of $\mathcal{L}$ operators among PEC surfaces; other operators follow the same convention. Notice that the self interaction of equivalence boxes $\mathcal{L}_{hh}$ and $\mathcal{K}_{hh}$ contain zeros although not written explicitly. The multiplication of this matrix with the current vector can be accelerated using MLFMA.

Compared with other equations, accelerating EPA is different in several aspects. The exclusion of self interactions, the attached unknown accelerations, and the tap basis scheme all require certain interactions excluded from the matrix-vector multiplication. This is implemented in two steps: for the interactions in the near neighbor terms and computed using direct MOM, the matrix elements are set to zero; if the interactions are computed through the fast multiple expansion, they will be subtracted after matrix-vector multiplication. Both of the two procedures are carried out by sparse matrix-vector multiplications. The high order quadrature point sampling scheme requires the setup of radiation and receiving patterns in MLFMA. Every sampled field component was regarded as a dipole source polarized in the direction of this component. This is a more natural link with MLFMA because fast multipole expansions are themselves point based. Therefore, We can write the patterns in a similar form as [9]. For $\mathcal{L}$ operators, the radiation and receiving patterns share the same form as

$$\begin{aligned} \mathbf{V}_{smi}^{E}(\hat{\mathbf{k}}) &= \int_S dS e^{i\mathbf{k}\cdot(\mathbf{r}_m-\mathbf{r})}\left(\bar{\mathbf{I}}-\hat{\mathbf{k}}\hat{\mathbf{k}}\right)\cdot\hat{\mathbf{u}}\delta(\mathbf{r}-\mathbf{r}_i) \\ &= e^{i\mathbf{k}\cdot(\mathbf{r}_m-\mathbf{r}_i)}\left(\bar{\mathbf{I}}-\hat{\mathbf{k}}\hat{\mathbf{k}}\right)\cdot\hat{\mathbf{u}} \end{aligned} \tag{4}$$

where $\hat{\mathbf{u}}$ is the direction of the field component and $\mathbf{r}_i$ is the location of the sampling point. The radiation patterns for $\mathcal{K}$ operators are

$$\begin{aligned} \mathbf{V}_{smi}^{M}(\hat{\mathbf{k}}) &= i\mathbf{k}\times\int_S dS e^{i\mathbf{k}\cdot(\mathbf{r}_m-\mathbf{r})}\hat{\mathbf{u}}\delta(\mathbf{r}-\mathbf{r}_i) \\ &= i\mathbf{k}\times e^{i\mathbf{k}\cdot(\mathbf{r}_m-\mathbf{r}_i)}\hat{\mathbf{u}} \end{aligned} \tag{5}$$

Because $\mathbf{V}_{smi}^{M}$ does not contain components in $\hat{\mathbf{k}}$ direction, the receiving pattern of $\mathcal{K}$ operators can be the same as that of $\mathcal{L}$ operators.

2.4. Preconditioning and Balancing the EPA Equation

Although iterative solvers are efficient at solving large matrix equations, their rate of convergence, which is related with the eigenvalue distribution of the matrices, is not easy to predict and control.

Therefore, preconditioning techniques are usually applied side by side with iterative solvers. A good preconditioner accelerates the convergence to the correct solution by approximating the inverse of the matrix and rearranging its eigenvalue distribution.

EPA can also be considered a physics-based preconditioner in general by enclosing the specific region with equivalence surface to solve the inner part with different methods from outside. It can improve the convergence of problems where multiscale structures exist. In such cases, small features need a fine mesh that introduces singular eigenvalues in the matrix system. If the solution lies in the subspace spanned by eigenvectors of large and small eigenvalues, the iterative solver will converge very slowly. Such problems in computational electromagnetics include small radiators on large platforms, mix-frequency problems, etc.

In the current program of EPA, GMRES solver is used. Besides the preconditioning effect from EPA itself, the diagonal preconditioner is also used to improve the convergence. This preconditioner is used in the right-preconditioning scheme. It solves the matrix equation $\bar{\mathbf{A}} \cdot \mathbf{x} = \mathbf{b}$ through $\bar{\mathbf{A}} \cdot \bar{\Lambda}^{-1} \cdot (\bar{\Lambda} \cdot \mathbf{x}) = \mathbf{b}$. This preconditioning scheme can improve the convergence while still keeping the same residual norm ($\|\bar{\mathbf{A}} \cdot \mathbf{x} - \mathbf{b}\|_2$) and stop criteria in the GMRES solver. Therefore, it is immune from variation of the element size. Moreover, in multiscale radiation problems, although the field values away from the radiator are usually much smaller than the one close to it, they are still important in the calculations of many physical quantities. The same residual norm as the original equation could keep the numerical errors of field at the same level.

Besides right-preconditioning, the EPA equations are also balanced to improve the convergence. The scale of the matrix elements of the high order quadrature point sampling scheme is independent of the size of the patches due to direct sampling. However, the matrix elements in EFIE and VIE are proportional to the triangle area or tetrahedron volume of the testing functions. In order to merge this gap between point sampling scheme and Galerkin's method, the matrix elements in EFIE and VIE are normalized to its area or volume so that every row of equations is of the same scale.

With both the preconditioning and balancing techniques, large problems can be solved using EPA and GMRES solver. Some numerical examples will be shown in the following section to validate EPA.

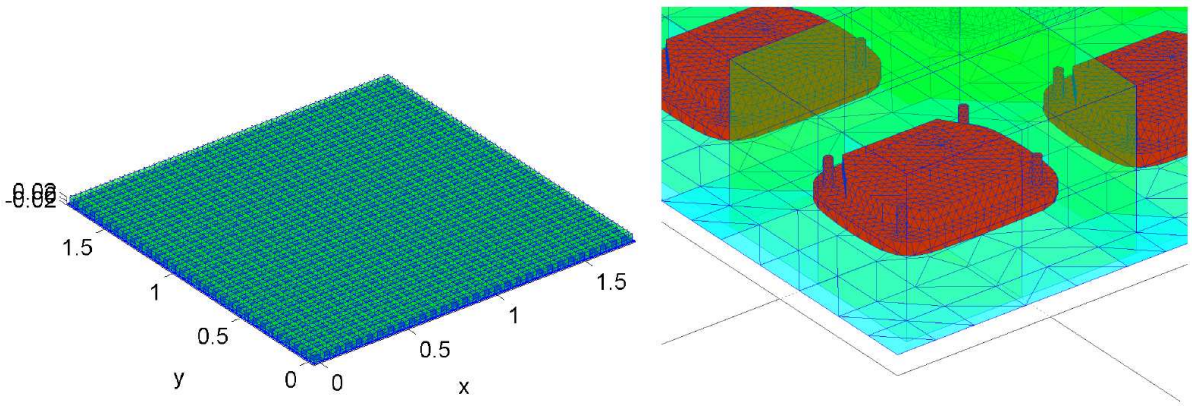

(a) (b)

Figure 2: The 30×30 antenna array on a ground plane with every element enclosed by an equivalence surface.

3. NUMERICAL EXAMPLES

An antenna array constructed from 30×30 XM antennas on a ground plane is simulated here. The antennas are arranged in the xy plane with x-distance and y-distance both 6 cm between neighboring elements as shown in Figure 2. Every antenna is excited by the multiple delta gap source in the same phase. The number of unknowns would be around 7.2 million for a MoM solver. Equivalence surfaces with mesh density of 4 points per wavelength enclose every antenna. Tap basis functions are defined at the at the intersections. The number of unknowns then decreases to 856 216, which is only about 12% of unknowns of direct solver. The simulation used six level MLFMA with attached unknown accelerations on the touched surfaces. The error converges to 2×10^{-2}

after 149 iterations with each iteration 36.9 s on a workstation. [1] Figure 3 shows the electric field in the plane of $x \in [-0.5, 1.2]$ m, $y \in [-0.5, 1.2]$ m, $z = 1.15$ m.

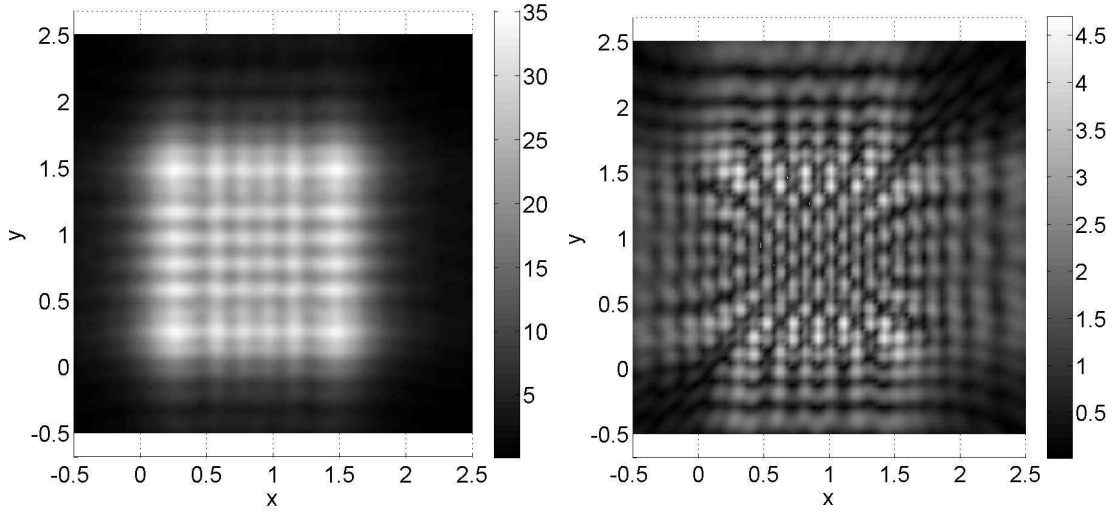

(a) $\mathbf{E}_x$ (b) $\mathbf{E}_z$

Figure 3: The electric field distribution on $x \in [-0.5, 2.5]$ m, $y \in [-0.5, 2.5]$ m, $z = 1.25$ m.

4. CONCLUSION

An enhanced EPA is introduced in this paper. Its accuracy was improved by applying high order point sampling scheme on the current representation. Moreover, the attached unknown acceleration and MLFMA help to make the algorithm more efficient. With all these techniques, large multiscale problems with over million unknowns can be solved on a single computer rapidly.

ACKNOWLEDGMENT

The authors are grateful to Intel Corporation for supporting this research through a custom SRC project. We express our gratitude to Henning Braunisch, Kemal Aygün, Kaladhar Radhakrishnan, and Alaeddin A Aydiner from Intel for insightful suggestions and discussions.

REFERENCES

1. Vipiana, F., G. Vecchi, and P. Pirinoli, "A multiresolution system of rao-wilton-glisson functions," *IEEE Trans. Antennas Propagat.*, Vol. 55, No. 3, 924–930, Mar. 2007.
2. Barka, A. and P. Caudrillier, "Domain decomposition method based on generalized scattering matrix for installed performance of antennas on aircraft," *IEEE Trans. Antennas Propagat.*, Vol. 55, No. 6, 1833–1842, Jun. 2007.
3. Li, M.-K. and W. C. Chew, "Wave-field interaction with complex structures using equivalence principle algorithm," *IEEE Trans. Antennas Propagat.*, Vol. 55, No. 1, 130–138, Jan. 2007.
4. Warnick, K. F., G. Kang, and W. C. Chew, "Regulated kernel for the electric field integral equation," *2000 IEEE Antennas and Propagation Society International Symposium*, Vol. 4, 2310–2313, Salt Lake City, UT, Jul. 2000.
5. Davis, C. P. and K. F. Warnick, "High-order convergence with a low-order discretization of the 2-D MFIE," *IEEE Antennas Wireless Propagat. Lett.*, Vol. 3, No. 1, 355–358, 2004.
6. Tong, M. S. and W. C. Chew, "Super-hyper singularity treatment for solving 3D electric field integral equations," *MOTL*, Vol. 49, No. 6, 1383–1388, Jun. 2007.
7. Ergatoudis, I., B. M. Irons, and O. C. Zienkiewicz, "Curved, isoparametric, 'quadrilateral' elements for finite element analysis," *Int. J. Solids Structures*, Vol. 4, 31–42, 1968.
8. De La Bourdonnaye, A., "Some formulations coupling finite element and integral equation methods for Helmholtz equation and electromagnetism," *Numer. Math.*, Vol. 69, No. 3, 257–268, Jan. 1995.

[1] Computer details: Dell Precision 690 with Intel Xeon 3.0 GHz CPU and 16 GB RAM, Linux OS.

9. Donepudi, K., J. Song, J. Jin, G. Kang, and W. Chew, "Point-based implementation of multilevel fast multipole algorithm for higher-order Galerkin's method," *2000 IEEE Antennas and Propagation Society International Symposium*, Vol. 1, 476–479, 2000.

A Full-wave Wide-band Surface-integral-equation-based Field Solver

N. Kurt-Karsilayan[1] and K. A. Michalski[2]

[1]Texas A&M University and Mentor Graphics Corporation, USA
[2]Texas A&M University, USA

Abstract— A full-wave, wide-band field solver based on surface integral formulation is introduced. The equivalence principle is used to derive the surface integral formulations based on the interior and the exterior electric and magnetic fields and the boundary conditions. The method of moments (MoM) is used to transform the continuous surface integrals to a discretized linear matrix system. Singularity cancellation and subtraction methods are used to address the numerical integrations of weakly and highly singular terms, respectively. The loop-star basis and testing functions are used along with the frequency scaling to address the low frequency problem. The accuracy of the field solver is analyzed for various surface integral equations as well as roof-top and loop-star basis and testing functions.

1. INTRODUCTION

The significance of parasitic extraction for integrated circuit (IC), printed circuit board (PCB) or package interconnects increases as the switching frequency, density and complexity continue to increase [1]. For the interconnect problem, integral-equation-based methods such as the method of moments (MoM), are more attractive compared to differential-equation-based methods, such as the finite difference method (FDM) or the finite element method (FEM). The former involves discretizing the conductor surfaces or volumes whereas the latter involve discretizing the whole problem domain. Earlier integral-equation-based tools, such as FastCap and FastHenry, are based on electro-quasistatic (EQS) and magneto-quasistatic (MQS) assumptions, where the electric and magnetic displacement currents are neglected, respectively [2, 3]. In [3], electromagnetoquasistatic (EMQS) approach is also applied where both capacitive and inductive effects are considered by assuming a surface charge, whereas in the MQS case, the surface charge is assumed to be zero. In [4], the EMQS method is applied so that only the conductor surfaces are discretized, whereas in [3], both volumes and surfaces of conductors are discretized. Full-wave parasitic extraction is necessary for high frequencies since the EMQS assumption becomes inaccurate when the structure's maximum size is comparable to the wavelength. The full-wave solution is obtained using the original Maxwell equations without any assumptions. Although several research groups proposed surface-integral-equation-based solutions recently, this still remains an open research area due to the frequency-dependent nature of the problem [5, 6].

In this paper, a full-wave, wide-band surface-integral-equation-based field solver is presented. In Section 2, a surface integral formulation based on the equivalence principle is introduced. In Section 3, the discretization of the surface integral formulation is explained. In Section 4, the details of the implementation is discussed. In Section 5, various experiment results are presented to show the accuracy of the field solver for canonical examples over a wide frequency range. Section 6 contains the concluding remarks.

2. SURFACE INTEGRAL FORMULATION

Any arbitrary-shaped interconnect can be considered as a homogeneous volume with permittivity ϵ_2 and permeability μ_2 residing in an unbounded exterior medium with (ϵ_1, μ_1). Dielectric and lossy conducting objects have real and complex values of ϵ_2, respectively. According to the equivalence principle, the original problem in Fig. 1(a) can be separated into two problems where the homogeneous medium Green's functions for the interior and the exterior regions can be used [7]. For the interior problem in Fig. 1(b), the exterior and the interior fields are zero and non-zero, respectively. To compensate for the difference in the interior and the exterior fields, fictitious electric and magnetic surface currents are assumed to exist over the surface. For the exterior problem in Fig. 1(c), the interior and the exterior fields are zero and non-zero, respectively and the fictitious surface currents are in the opposite direction of the interior problem. The surface normal unit vector $\hat{n}$ points outward and $(\overline{E}^{inc}, \overline{H}^{inc})$ represent the incident electric and magnetic fields.

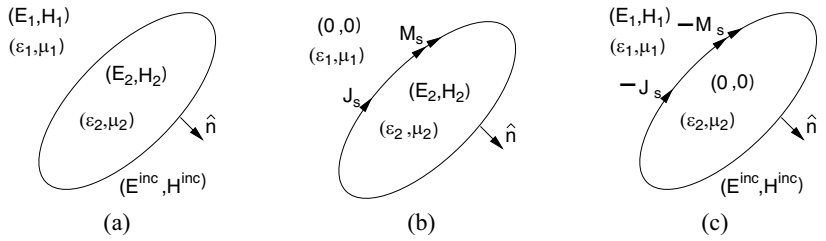

Figure 1: Equivalence principle, (a) Original problem, (b) Interior equivalence, (c) Exterior equivalence.

The interior and the exterior surface integral equations are obtained by using the Green's vector identity [9]. These equations can further be cast in a parametric form

$$\sum_{i=1}^{2}\alpha_i\left[-\sigma_i\frac{\overline{M}_s}{2}+\hat{n}\times\oint\left[j\omega\mu_i G_i\overline{J}_s+\frac{1}{j\omega\epsilon_i}\nabla'_s\cdot\overline{J}_s\nabla'G_i+\overline{M}_s\times\nabla'G_i\right]ds'\right]=\alpha_1\hat{n}\times\overline{E}^{inc} \quad (1)$$

$$\sum_{i=1}^{2}\beta_i\left[\sigma_i\frac{\overline{J}_s}{2}+\hat{n}\times\oint\left[-\overline{J}_s\times\nabla'G_i+\frac{1}{j\omega\mu_i}\nabla'_s\cdot\overline{M}_s\nabla'G_i+j\omega\epsilon_i G_i\overline{M}_s\right]ds'\right]=\beta_1\hat{n}\times\overline{H}^{inc} \quad (2)$$

where $\sigma_1=1$, $\sigma_2=-1$, $\overline{J}_s=\hat{n}\times\overline{H}_1$, $\overline{M}_s=\overline{E}_1\times\hat{n}$, $i=1,2$ represents the exterior and the interior regions, respectively.

For a perfect electric conductor (PEC), (1) and (2) reduce to electric field integral equation (EFIE) and magnetic field integral equation (MFIE), respectively. When $\alpha_1=\alpha_2$ and $\beta_1=\beta_2$, (1) and (2) represent the Poggio-Miller-Chang-Harrington-Wu-Tsai (PMCHWT) equations.

3. DISCRETIZATION

MoM is used to transform continuous surface integrals to a discretized linear matrix system [8]. Fig. 2 shows the roof-top, loop and star functions used in the discretization process along with the reference current directions for each function. Rao-Wilton-Glisson (RWG) or roof-top functions are defined as follows [10].

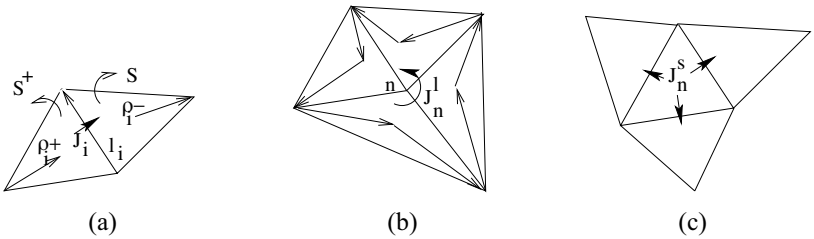

Figure 2: Basis and testing functions, (a) Roof-top or RWG function, (b) Loop function, (c) Star function.

$$\overline{\Lambda}_i\left(\overline{r}'\right)=\begin{cases} l_i\dfrac{\overline{\rho}_i^{+}}{2S^{+}}, & \overline{r}'\epsilon S^{+} \\ l_i\dfrac{\overline{\rho}_i^{-}}{2S^{-}}, & \overline{r}'\epsilon S^{-}\end{cases} \quad (3)$$

Loop and star (LS) functions simply represent divergence-free and nondivergence-free parts of the electric and magnetic currents, respectively [14].

$$\overline{L}_n=\sum_{i=1}^{N_n}\gamma_i\frac{\overline{\Lambda}_i}{l_i},\quad \overline{S}_n=\sum_{i=1}^{3}\gamma_i\frac{\overline{\Lambda}_i}{l_i} \quad (4)$$

where N_n is the number of edges for loop n and γ_i can be -1 or 1 depending on the current direction.

Surface currents can be represented by RWG and LS functions as follows,

$$\overline{J} = \sum_{i=1}^{N} \overline{\Lambda}_i J_i, \quad \overline{J} = \sum_{n=1}^{N_l} \overline{L}_n J_n^l + \sum_{n=1}^{N-N_l} \overline{S}_n J_n^s \tag{5}$$

where N is the number of independent edges, N_l is the number of internal nodes. $\overline{\Lambda}_i$, $\overline{L}_n$, $\overline{S}_n$ represent RWG, loop and star functions for edge i, node n and element n, respectively.

Testing (1), (2) and expanding currents with RWG functions, we obtain

$$\begin{bmatrix} \sum_{i=1}^{2} \alpha_i A_i & \sum_{i=1}^{2} \alpha_i B_i \\ \sum_{i=1}^{2} -\beta_i B_i & \sum_{i=1}^{2} \beta_i C_i \end{bmatrix} \begin{bmatrix} J \\ M \end{bmatrix} = \begin{bmatrix} \alpha_1 E \\ \beta_1 H \end{bmatrix} \tag{6}$$

$$A_i = j\omega\mu_i \left\langle \overline{\Lambda}_k, G_i, \overline{\Lambda}_j \right\rangle + \frac{1}{j\omega\epsilon_i} \left\langle \nabla \cdot \overline{\Lambda}_k, G_i, \nabla \cdot \overline{\Lambda}_j \right\rangle \tag{7}$$

$$B_i = \left\langle \overline{\Lambda}_k, \overline{\Lambda}_j \times \nabla' G_i \right\rangle + \frac{\sigma_i}{2} \left\langle \overline{\Lambda}_k, \hat{n} \times \overline{\Lambda}_j \right\rangle \tag{8}$$

$$C_i = j\omega\epsilon_i \left\langle \overline{\Lambda}_k, G_i, \overline{\Lambda}_j \right\rangle + \frac{1}{j\omega\mu_i} \left\langle \nabla \cdot \overline{\Lambda}_k, G_i, \nabla \cdot \overline{\Lambda}_j \right\rangle \tag{9}$$

$$E = \left\langle \overline{\Lambda}_k, \overline{E}^{inc} \right\rangle \tag{10}$$

$$H = \left\langle \overline{\Lambda}_k, \overline{H}^{inc} \right\rangle \tag{11}$$

where $\langle \overline{f}, \overline{g} \rangle = \oint \overline{f} \cdot \overline{g} ds'$.

When Equations (1), (2) are discretized with loop-star functions, each matrix component A_i, B_i and C_i in (6) is composed of four sub-matrices due to loop-loop, loop-star, star-loop, star-star interactions. Similarly, each vector, J, M, E, H is composed of two sub-vectors due to loop and star parts.

4. IMPLEMENTATION

The presented field solver is written in Fortran90 and supports triangular patches in neutral format from any outside mesher. Reference edge current direction for the first encountered edge is assumed to be outward and normal to the edge. The same edge corresponding to a latter element is assigned a negative value which implies that the current direction is inward and normal to the edge. This avoids the computation of the current direction based on the surface normal and the edge vectors. Each matrix element involves a double integration which is carried out only for element pairs where one and three Gaussian quadrature points are used for the outer and the inner integrals, respectively. For roof-top basis and testing functions, each matrix element corresponds to non-boundary testing and source edge pairs and is composed of four contributions due to the interactions between testing and source triangles connected to the edge pairs. For loop-star basis and testing functions, each matrix element corresponds to loop-loop, loop-star, star-loop or star-star pairs. Loop current orientation is counter-clockwise and patch current direction is outward. The same algorithm is used to compute integrals for each element pair and contributions for each edge pair, however each edge-pair contribution is added to sixteen matrix locations with the correct sign. In the case of excitation or right-hand-side vector, contribution from each testing edge is added to four locations with the correct sign. To address the low frequency problem, frequency scaling is used in addition to the loop star functions [6].

5. EXPERIMENT RESULTS

The EFIE and MFIE electric currents are analyzed and compared for a PEC sphere of radius 0.2λ for a z-directed, y-polarized incident electric field at 300 MHz in Fig. 3. The number of nodes, elements and edges on the discretized sphere are 1749, 1856 and 2784, respectively. The electric surface currents in Figs. 3(b) and 3(c) are consistent between EFIE and MFIE formulations based on the RWG basis and testing functions. The PMCHWT-based electric and magnetic currents are analyzed in Figs. 3(d), 3(e) for a dielectric sphere of permittivity $2\epsilon_0$. These results are consistent with [14].

The accuracy of the loop-star basis and testing functions along with frequency scaling are compared to roof-top basis and testing functions with respect to frequency. Thin plate with width and

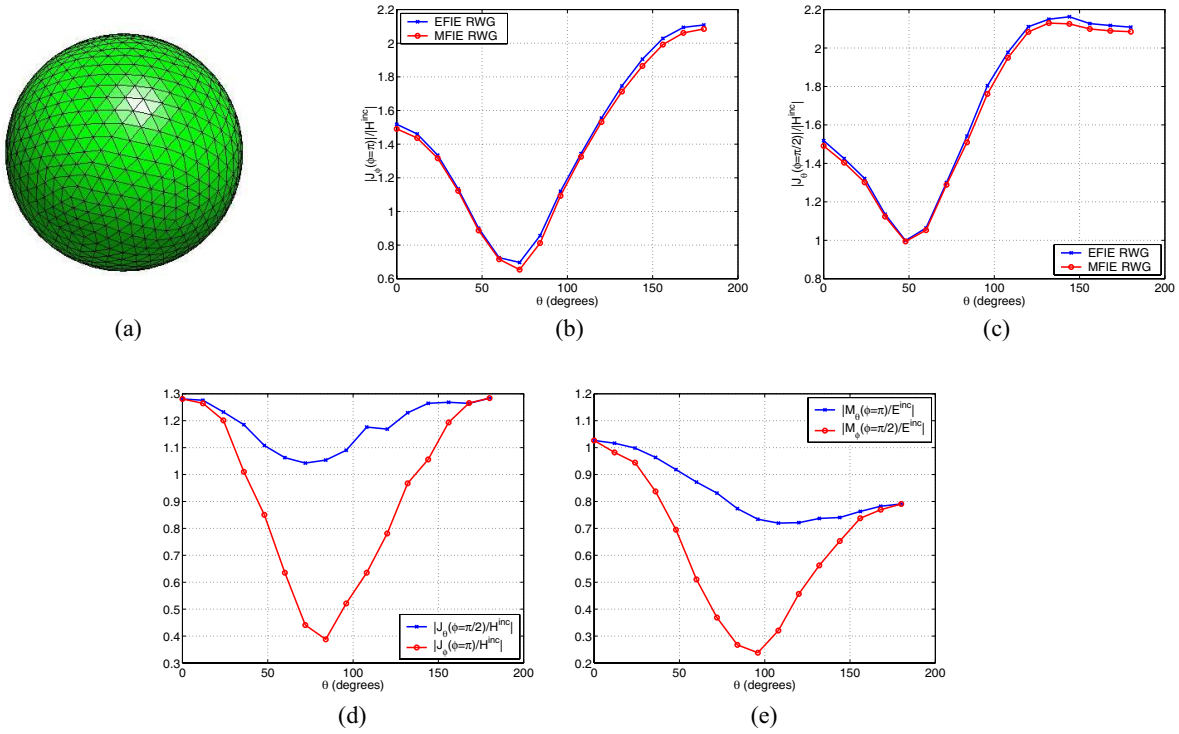

Figure 3: Normalized currents on a sphere of radius 0.2λ for a z-directed, y-polarized incident electric field, (a) Meshed sphere, (b) EFIE/MFIE solution for the PEC sphere, (c) EFIE/MFIE solution for the PEC sphere, (d) PMCHWT solution for the dielectric sphere, (e) PMCHWT solution for the dielectric sphere.

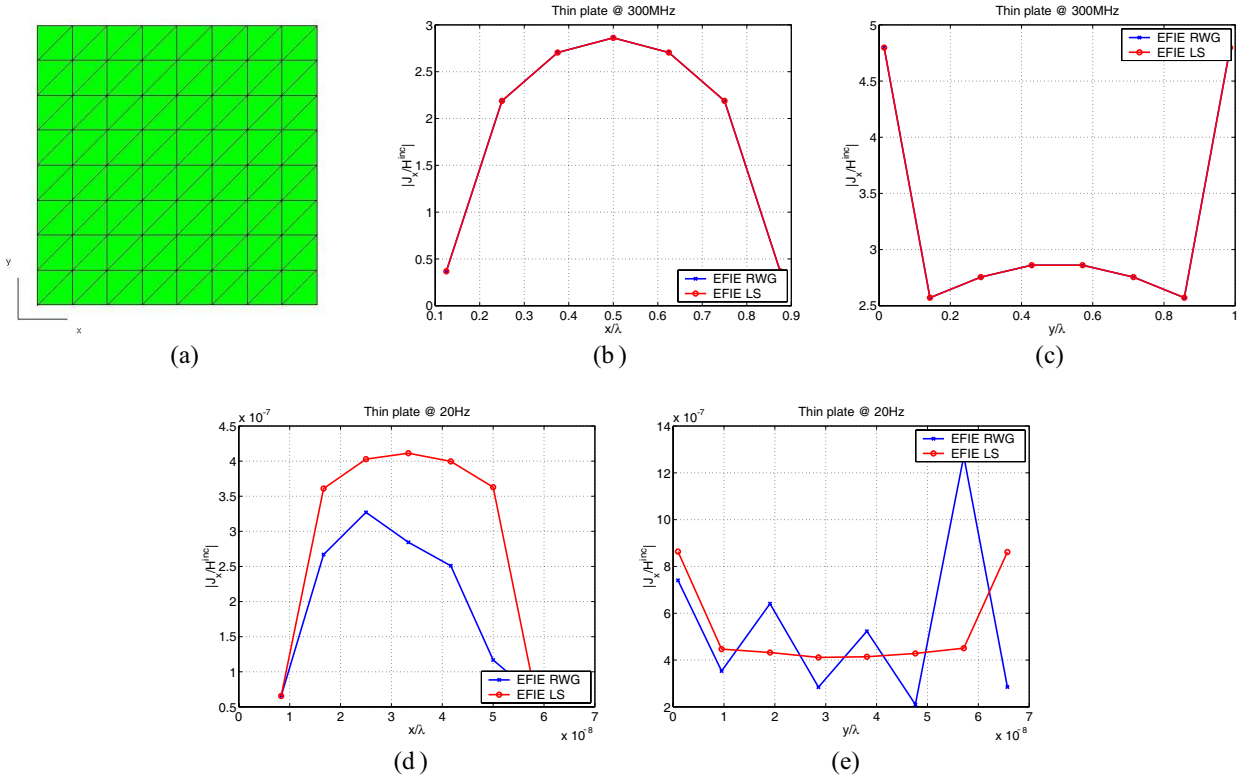

Figure 4: Normalized current vs frequency on a thin plate.

length of 1m is discretized so that there are 81 nodes, 208 edges, 128 elements. Incident electric field is z-directed and x-polarized. It is clear from Figs. 4(b)–4(e) that the RWG and the LS functions provide consistent results at 300 MHz, however the RWG approach starts to be unreliable at 20 Hz. Since double precision is used in Fortran90, RWG method can provide expected results down to 20 Hz.

Global matrices are analyzed for EFIE, MFIE, PMCHWT formulations and RWG, LS methods as shown in Fig. 5. A coarser mesh is used for the sphere in this experiment where there are 61 nodes, 174 edges and 116 elements. It can be visually observed that the global matrix is diagonally dominant in all cases, however the range of values are different based on each formulation.

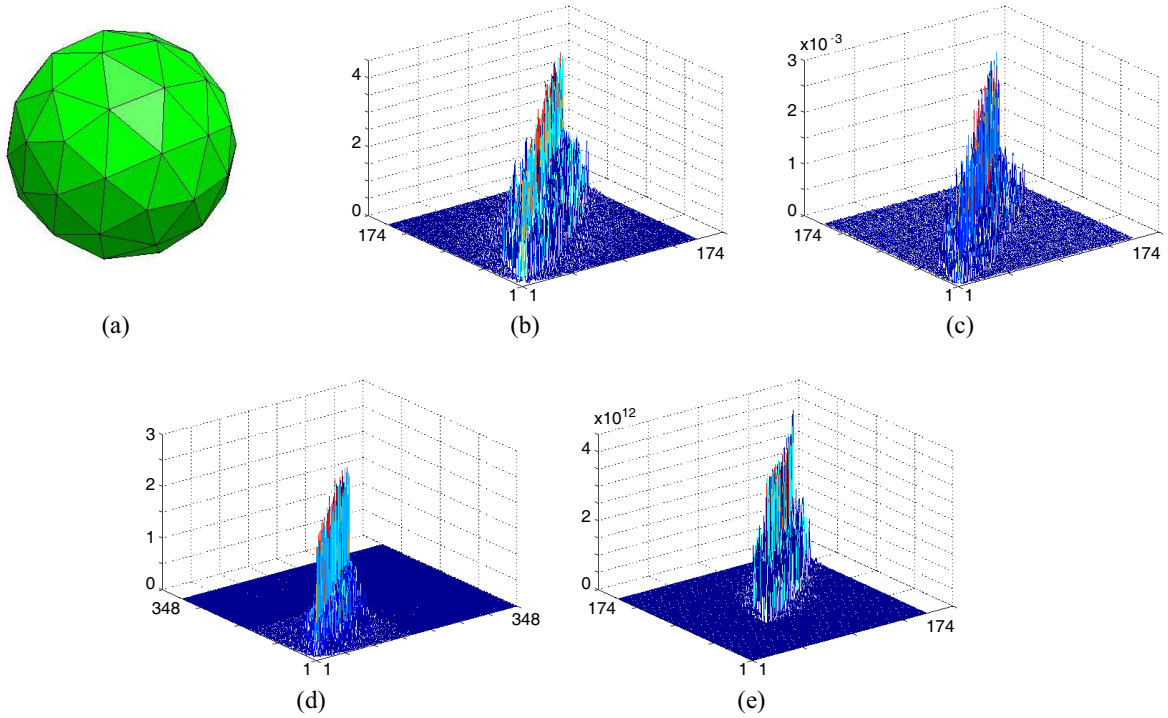

Figure 5: Magnitude of global matrices for a coarsely meshed sphere, (b) EFIE-RWG method, (c) MFIE-RWG method, (d) PMCHWT-RWG method, (e) EFIE-LS method.

6. CONCLUSION

A full-wave, wide-band surface-integral-equation-based field solver is introduced for arbitrary-shaped homogeneous objects which is applicable to interconnect parasitic extraction problem. Surface integral equation is discretized using method of moments which involves the discretization of only conducting surfaces. The tool is full-wave since it does not make any assumptions for solving the Maxwell's equations. It is wide-band since it separates divergence-free and non-divergence-free components of the electric and magnetic surface currents. The accuracy of the tool is validated using canonical objects over a wide frequency range.

REFERENCES

1. Ruehli, A. E. and A. C. Cangellaris, "Progress in the methodologies for the electrical modeling of interconnects and electronic packages," *Proceedings of the IEEE*, Vol. 89, No. 5, May 2001.
2. Nabors, K. and J. White, "FastCap: A multipole accelerated 3-D capacitance extraction program," *IEEE Transactions on Computer-Aided Design*, Vol. 10, No. 11, November 1991.
3. Kamon, M., "Fast parasitic extraction and simulation of three-dimensional interconnect via quasistatic analysis," PhD Thesis, MIT, 1998.
4. Zhu, Z., B. Song, and J. White, "Algorithms in fastImp: A fast and wideband impedance extraction program for complicated 3-D geometries," *DAC 2003*, June 2–6, 2003
5. Jandhyala, V., Y. Wong, D. Gope, and C. J. R. Shi, "A surface-based integral-equation formulation for coupled electromagnetic and circuit simulation," *Microwave and Opt. Tech. Letters*, Vol. 34, No. 2, 103–106, 2002.

6. Chew, W. C., J. Jin, E. Michielssen, and J. Song, *Fast and Efficient Algorithms in Computational Electromagnetics*, Artech House, 2001.
7. Harrington, R., *Time-harmonic Electromagnetic Fields*, IEEE Press, Wiley Interscience, 2001.
8. Harrington, R., *Field Computation by Moment Methods*, IEEE Press, 1993.
9. Poggio, A. J. and E. K. Miller, "Integral equation solutions of three-dimensional scattering problems," *Computer Techniques for Electromagnetics*, R. Mittra, editor, Chapter 4, 159–264, Hemisphere Publishing Corporation, 1987.
10. Rao, S. M., D. R. Wilton, and A. W. Glisson, "Electromagnetic scattering by surfaces of arbitrary shape," *IEEE Transactions on Antennas and Propagation*, Vol. 30, No. 3, May 1982.
11. Wilton, D. R., "Computational methods," *Scattering and Inverse Scattering in Pure and Applied Science*, R. Pike and P. Sabatier, editors, Chapter 1.5.5, 316–365, Academic Press, London, 2002.
12. Hodges, R. E. and Y. Rahmat-Samii, "The evaluation of MFIE integrals with the use of vector triangle basis functions," *Microwave and Optical Technology Letters*, Vol. 14, No. 1, January 1997.
13. Wilton, D. R., S. M. Rao, A. W. Glisson, D. H. Schaubert, O. M. Al-Bundak, and C. M. Butler, "Potential integrals for uniform and linear source distributions on polygonal and polyhedral domains," *IEEE Transactions on Antennas and Propagation*, Vol. 32, No. 3, March 1984.
14. Lim, J., "The electromagnetic scattering from arbitrarily shaped bodies at very low frequency range using triangular patch modeling," PhD Dissertation, Auburn University, March 1994.

Evolving a 3-D Model for Determining the Impact of Reference Plane Discontinuities

Richard Mellitz and Ted Ballou
Intel Corporation, Columbia, SC, USA

Abstract— Problems of return path management require accurate modeling of reference plane discontinuities when simulating board interconnects. For large structures the preferred transmission line model (w-element) is referenced to ideal ground, and this fact poses a problem for a simulation attempting to capture the effects of multiple reference planes.

Since return path in board interconnects is essentially a 3-D problem, the appropriate model must be derived from a Full Wave Finite Element Method (FEM) 3D solver such as Ansoft-HFSS. While a 3D solver provides robust modeling capability absent in 2D tools, it presents the user with a host of new issues that can make the problem unnecessarily difficult. In particular, questions of radiation boundaries, port dimensions and meshing effects may derail a straightforward effort into an exercise in discovering the peculiarities of the modeling tool. This is especially problematic for modeling topologies of the size commonly found in board interconnect signal integrity.

The work describes a study of discontinuous reference plane effects in a DDR3-1600 interconnect, with focus on how to calibrate the target problem vs. the tool details at several steps of model evolution. Emphasis is placed on nourishing an intuitive skepticism of any results that vary significantly with only modest changes in input parameters. The resulting findings show that crosstalk (rather than insertion loss) is by far the most important issue affected by reference plane discontinuity. They further show that, with good reference plane decoupling, return paths can be adequately managed even in the presence of discontinuous reference planes.

1. INTRODUCTION

With serial differential signaling now the predominant technology for high speed I/O interfaces, it may yet be premature to declare the last of the parallel, single ended bus. FSB and DDR3, for instance, have been extended past the GHz barrier and will be with us as long as cost/performance warrants. At the same time, cost consideration is driving PCB routing design to choices that previously have been ruled out as either too risky or not worth the analysis effort.

A prime example is the specification of reference plane design for management of signaling return path. Routing guidelines have typically required continuous reference on either the ground plane, power plane or both, depending on I/O buffer and package referencing design. System builders seeking cost reduction want to know the cost/benefit of each routing rule. One of the most attractive targets is PCB layer count, but fewer layers means more broken reference planes in today's multi-rail designs. This adds margin and EMI risk due to discontinuous signal return paths, and good design practice calls for appropriate analysis.

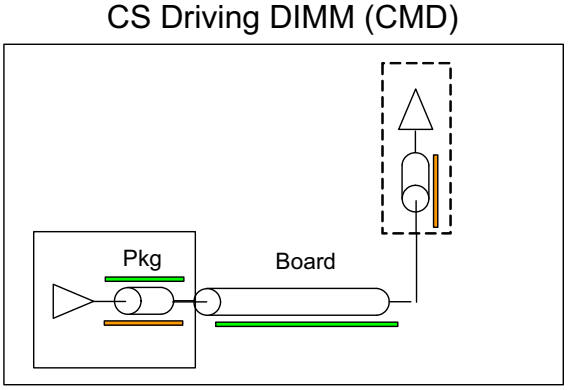

Figure 1: System configuration.

2. ANALYSIS METHODS

The example presented here in Figure 1 studies DDR3 common-clock signaling across a standard DIMM connector. Ground-referenced microstrip from the motherboard goes to being power-referenced on the DIMM; return path is through the connector pins, together with the associated vias and pads.

This configuration includes buffer, package, 12″ of 50 ohm single-ended transmission line and the connector. With no reference discontinuity, it would be modeled accurately at DDR3-1600 speed using w-elements plus assorted models for via, package and connector. But with the discontinuous return path, a basic assumption of the w-element algorithm — referencing to 0 volts — is violated, and no amount of fiddling with the reference nodes will produce accurate results. Recognizing that return current induced on the DIMM power plane must reach motherboard ground through significantly vertical pathways, we see that we have to invoke a 3-D field solver (in this study, Ansoft-HFSS).

For problems of interest in today's PCB designs, the 3-D solver is not just an option, but is in fact a required tool. It can produce s-parameter or equivalent circuit models accurate to multi-GHz frequencies, and these models complement traditional spice-based time domain simulation methods. It does, however, introduce complexity and generality into analysis that is otherwise amenable to cookbook-like procedures. In the worst scenario, working with such a tool may produce starkly incorrect results due to mistaken notions of significance and apparent accuracy.

Our thesis here is to draw helpful distinction between the viewpoint of the traditional SI method and that of the RF/microwave world, and to illustrate how using a 3-D solver effectively requires some "reality check" at key points in the model articulation. The strategy is to start simply and evolve, developing each iteration to answer a specific question of significance by testing results against comparable findings either from another method (2-D analysis) or from intuitive engineering judgment.

3. QUESTIONS OF SIGNIFICANCE

Referring to Figure 2, we outline the modeling sequence, which starts with an extremely simple tline construct (Figure 3). What does the 3-D solver have to say about a basic microstrip configuration? Does it solve the correct impedance? We already know the answer we're looking for from our 2-D tools and from measurement. This provides the first sanity-check point that will help us interpret results from more complex iterations.

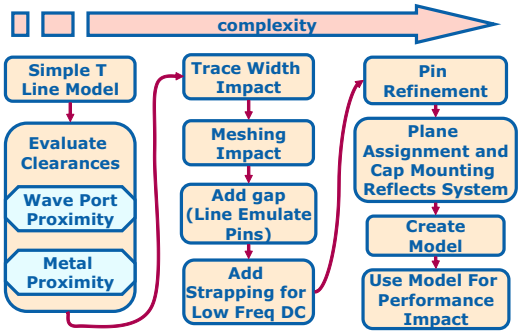

Figure 2: Model flow.

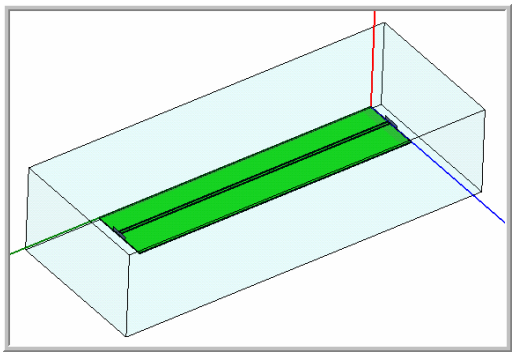

Figure 3: Basic microstrip with waveports and radiation boundary.

All simulation tools use numerical analysis based on discrete quantization. In spice the quanta could be timestep or fmax, while in field solvers we deal with meshing and finite universes. Accuracy is traded against compute time, but setting this up may or may not be an overtly made choice. It's important to do some sensitivity testing when faced with managing the quantization parameters, particularly for occasional or first-time users.

As an example of some surprising dependencies, Figure 4 illustrates the relation between radiation boundary clearance to waveports and the solved insertion loss (which indicates solved model impedance). Of course we want to see an almost perfectly flat response with a 50 ohm line and termination (and would definitely see this in an equivalent spice simulation), but with the Full Wave Finite Element Method (FEM) 3-D solver we don't have built-in model calls such as the w-element.

In contrast to the hierarchical and heterogeneous model ecosystem of spice, the 3-D solver handles every structure with the same inexorable algorithm. The good news is that all things are possible; the bad news is that, again, all things are possible, including phenomena such as shown in Figure 4.

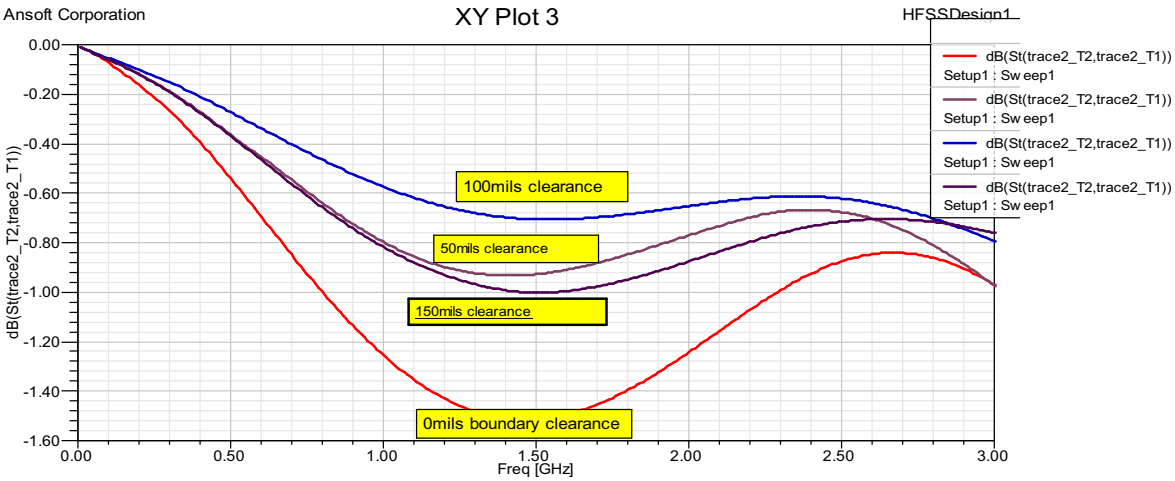

Figure 4: Radiation boundary effects: Clearance to waveport faces.

Similarly obscure insertion loss dependencies are seen from radiation boundary clearance to other structure faces, as well as from the size of the waveport itself. Even the quantization of trace width may have peculiar importance if a small change leads to a non-trivial redistribution of meshing objects (Figure 5).

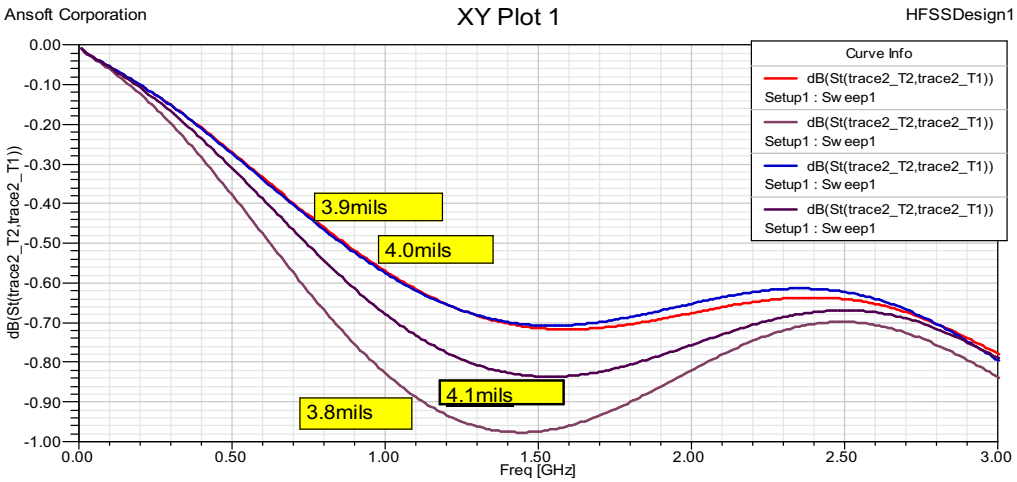

Figure 5: Trace width effects.

In practice, a 3-D structure is often sectioned (and rejoined) for drawing convenience or dimensional variation. By now we are getting enough of a sense of meshing impacts to see why, when we compare identical structures — one monolithic, the other cut in half and fit back together in full electrical contact — we get different answers (Figure 6). This source of meshing dependency is practically unavoidable.

The preceding insertion loss distortions are on the whole minor issues, but it makes sense to minimize them wherever possible by setting the 3-D tool parameters such that the simplest version of the model as accurate as it can be (i.e., as close as possible to comparable results from other tools). Going forward in the model flow, the meshing issues will have been instructive in understanding the larger effects that arise from significant changes in the design.

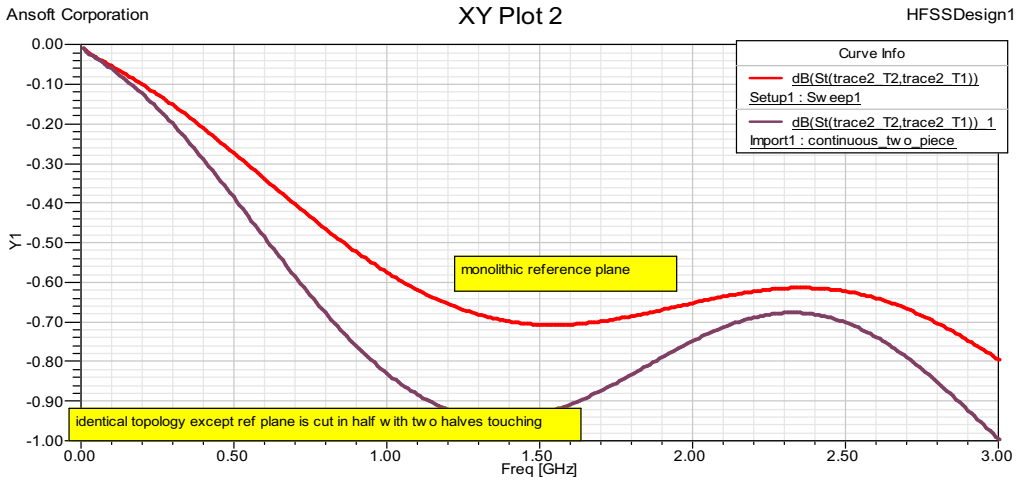

Figure 6: Other meshing effects.

4. ELABORATION

Proceeding to the problem of reference plane discontinuity, a gap is now inserted under the transmission lines (Figure 7). The gap is initially modeled as infinite, forcing complete mode conversion for single-ended signals (the second tline models a crosstalk path). Taking this step clarifies by exaggeration the effects that will be seen less dramatically when real (finite) gaps and reference discontinuities are modeled. We see in the insertion loss (Figure 8) a major resonance near 3 GHz and a huge drop at DC, and recognize these as being asymptotic limits of the real effects. In this way a very simple structure has already told much of the story we need to know.

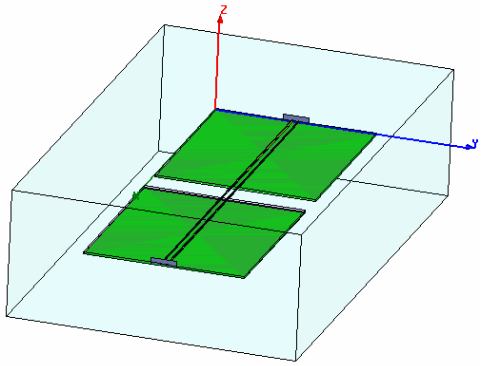

Figure 7: Modeling a gap.

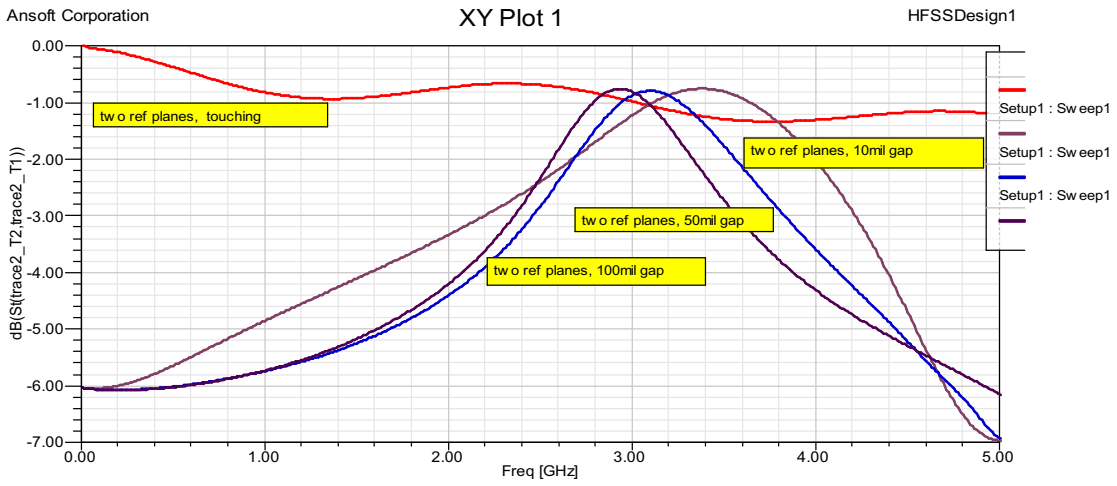

Figure 8: Gap resonance in the extreme case.

This basic (and cheaply bought) insight stands in contrast to a common situation in which a highly detailed modeling effort is attempted without any preamble. In the hands of an experienced designer this approach may bear fruit, but all too often it tends to get bogged down in unforeseen ways, from compute resource issues to software problems, and not least, from a lack of perspective. We may get some kind of answer eventually, but one without much to say about tradeoffs and what-ifs.

The gap is elaborated into a connector by establishing pin dimensions, and by crossing the gap with an arbitrarily large pair of reference straps. This is a crucial (and admittedly artificial) detail required to model low-frequency to DC continuity (Figure 9). The only alternative would be to greatly increase the size and complexity of the drawn structure by adding a large enough number of reference pins (and the result would be much the same). Insertion loss (Figure 10) is starting to look pretty realistic at this point.

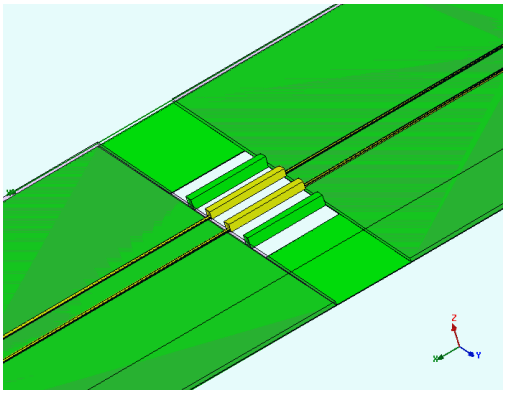

Figure 9: Proto-connector.

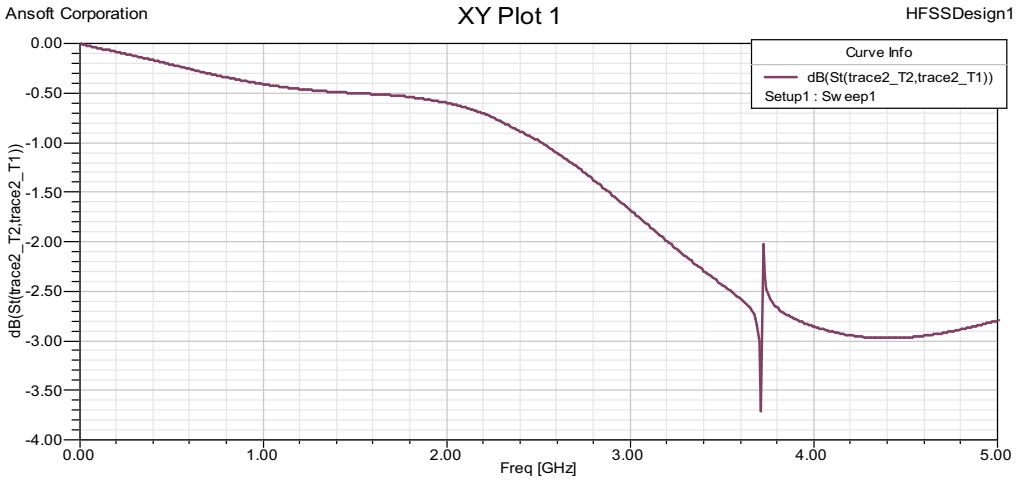

Figure 10: Insertion loss for proto-connector.

Pads and vias are added to finish a serviceable DIMM connector model accurate to above 2 GHz (provided that reference is as continuous as Figure 11 depicts). In the insertion loss for this case (Figure 12) we see a characteristic via resonance at around 3 GHz in addition to the now reduced (finite) gap resonance. But the job isn't finished yet.

5. MODELING REFERENCING DISCONTINUITY

With the basic structure finished and its characteristics well understood, we now focus on the issue of referencing. From the earlier iterations we saw a total mode conversion with the infinite gap. Return current was forced onto the second conductor, and in terms of circuit significance this would be realized as crosstalk voltage. The gross insertion loss at DC was of less practical concern since in real structures there would be some kind of return path. As stated before, the simple but extreme

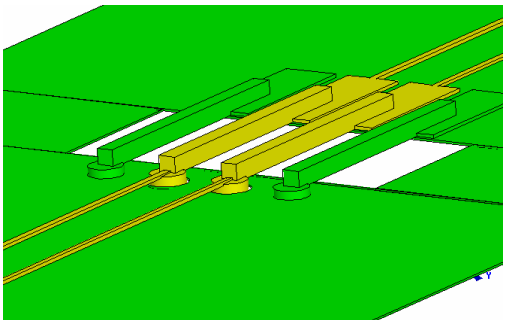

Figure 11: Fully elaborated connector structure.

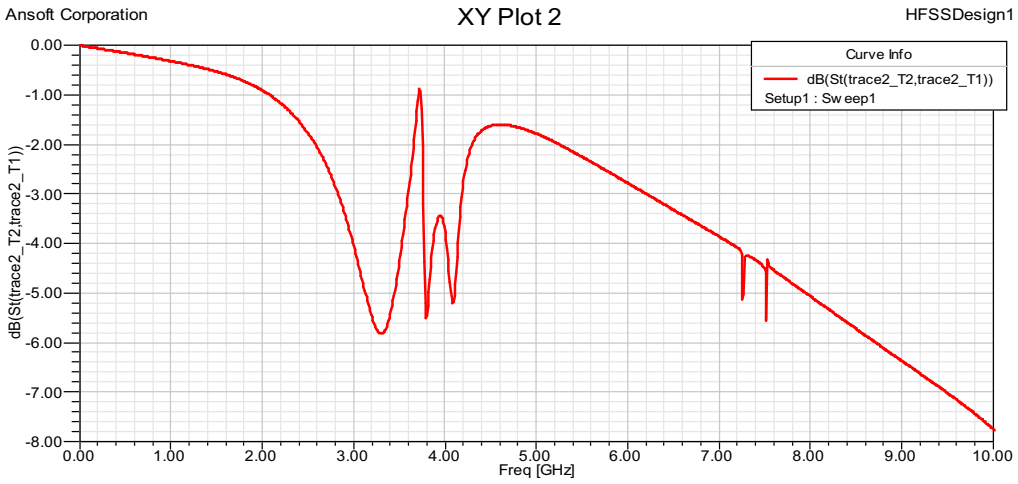

Figure 12: Connector with via insertion loss.

case (absolute reference discontinuity) is instructive, pointing at least qualitatively to the correct issue of interest, i.e., crosstalk.

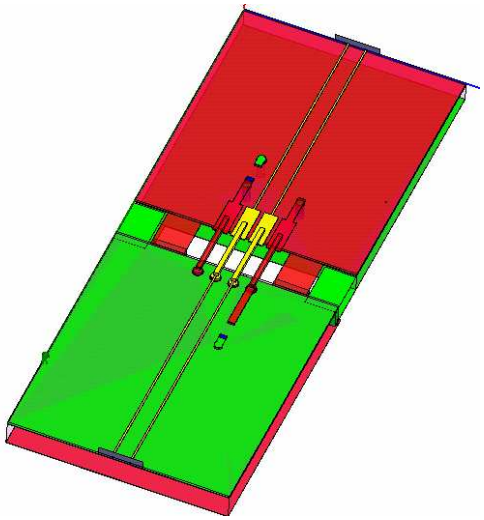

Figure 13: Fully elaborated model with reference plane discontinuity.

The model is elaborated to instantiate a realistic reference discontinuity (Figure 13). The power and ground planes are connected through decoupling capacitors and vias. For simplicity, the actual devices are omitted since a physical model of even one capacitor would be more complex than the rest of the structure combined. Instead, lumped port elements are added to the cap connections.

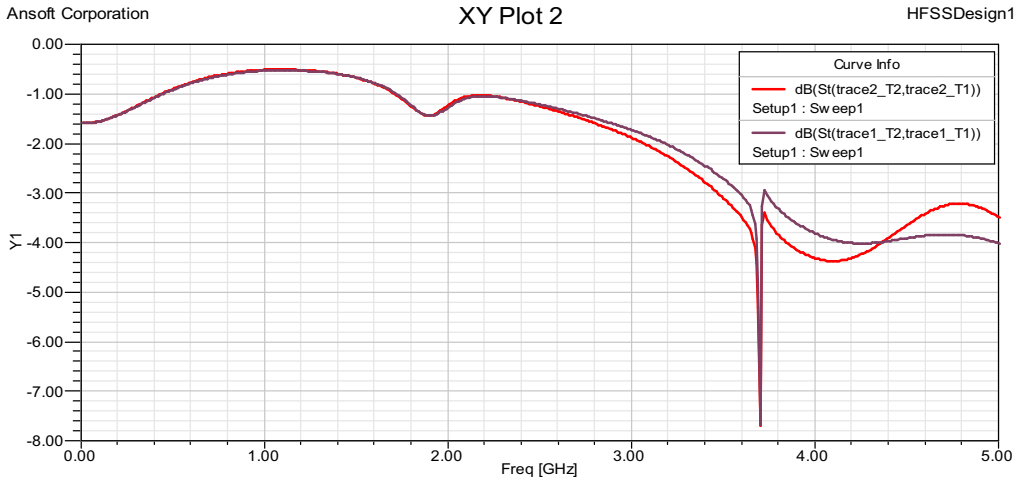

Figure 14: Insertion loss for full model with reference discontinuity.

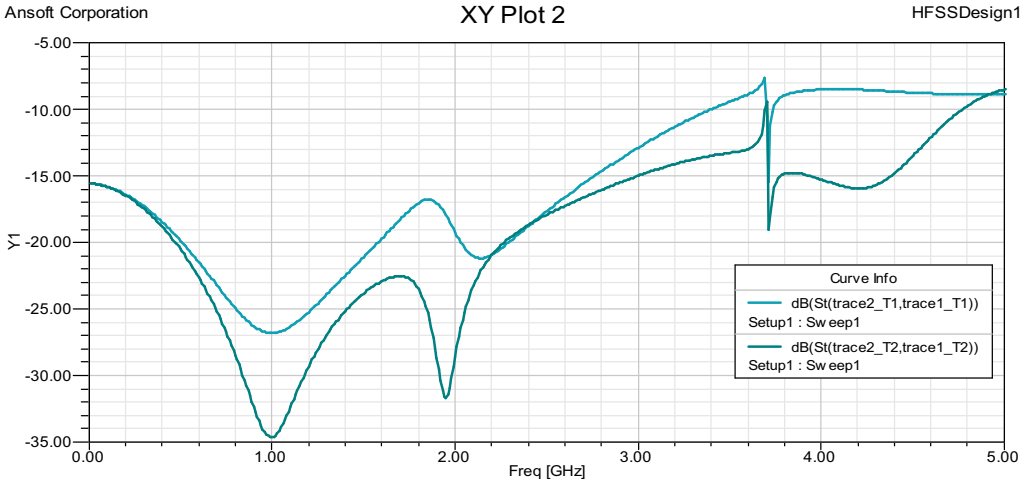

Figure 15: NEXT for full model with reference discontinuity.

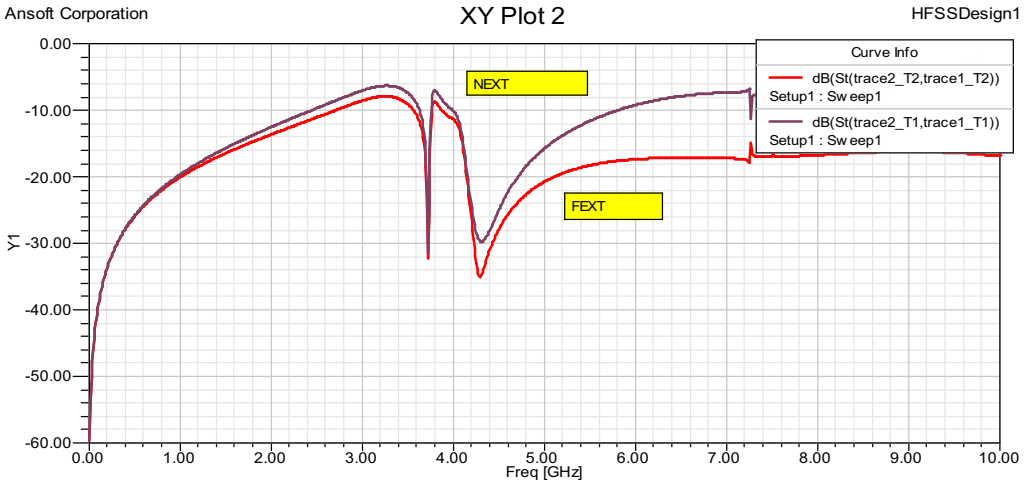

Figure 16: NEXT for full model with continuous reference.

Figure 14 shows the insertion loss. Note that this transfer function is with lumped ports at the capacitor, and will interact with any capacitor models used in a simulation. A reasonable capacitor

should improve the low frequency, but may add resonance if it has high effective series inductance.

For discontinuous reference, the crosstalk response is probably of more interest than the insertion loss. In Figure 15 we see that near end crosstalk is bad at low frequencies. Compare this to Figure 16 which shows the same response for the continuous reference case.

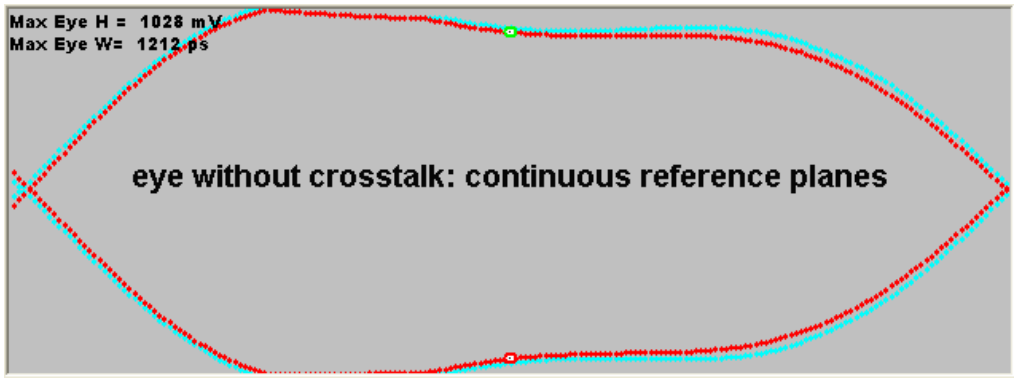

Figure 17: Simulated channel w/o crosstalk, continuous reference.

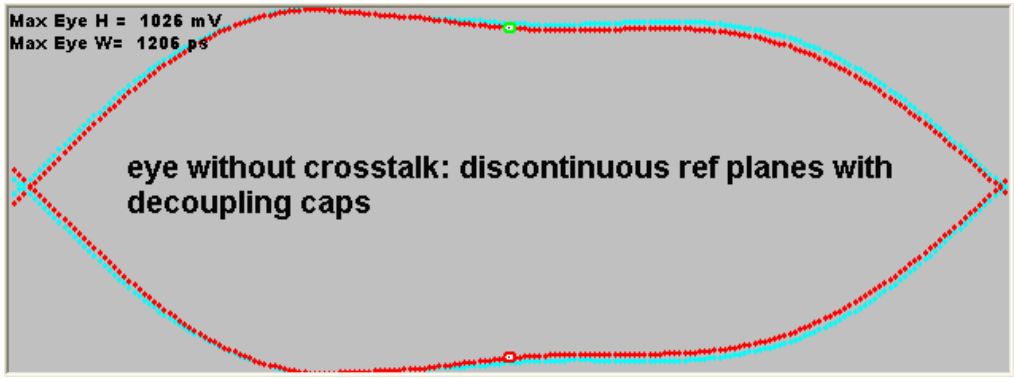

Figure 18: Simulated channel w/o crosstalk, discontinuous reference.

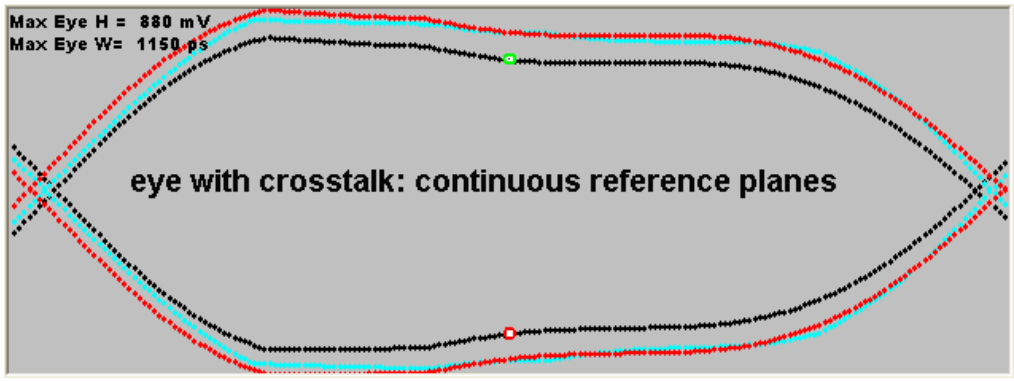

Figure 19: Simulated channel w/crosstalk, continuous reference.

6. PUTTING IT ALL TOGETHER

In simulation usage, the entire structure is represented by an 8-port s-parameter (2 signals in, signals out, 2 power, 2 ground ports). It replaces the standard connector model plus an inch of trace on either side. Decoupling capacitor models are connected to the power ports, and we're ready to simulate. Figures 17 and 18 show DDR3-1600 signal eyes (without crosstalk) through a

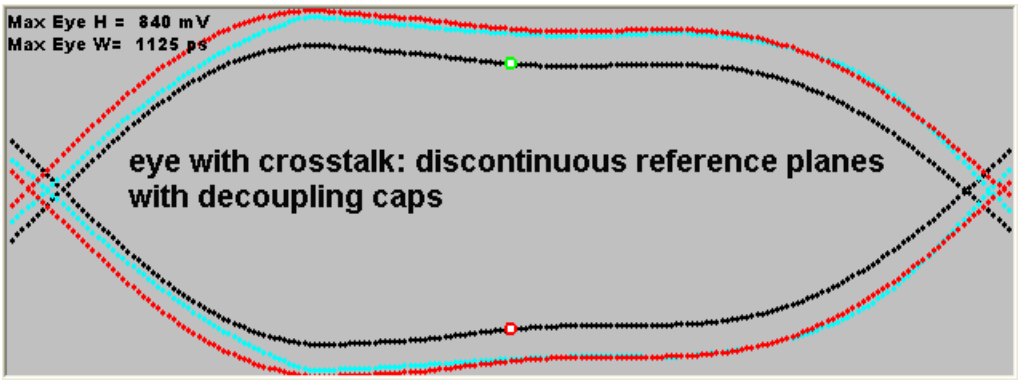

Figure 20: Simulated channel w/crosstalk, discontinuous reference.

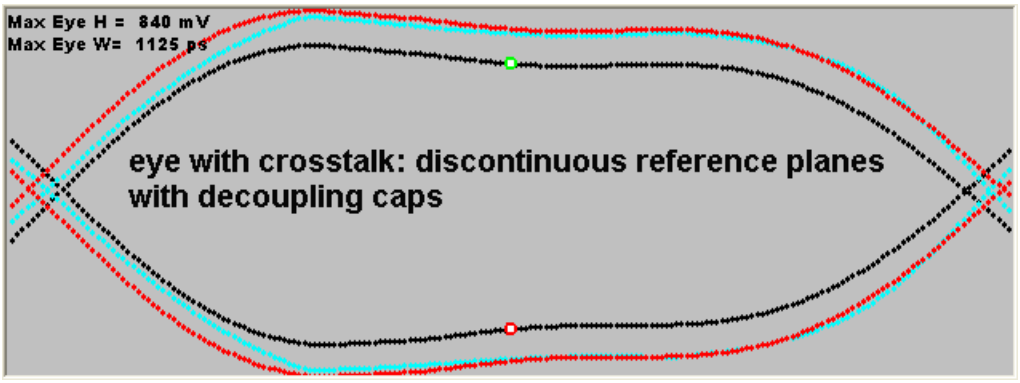

Figure 21: Simulated channel w/crosstalk, decoupling caps: continuous reference.

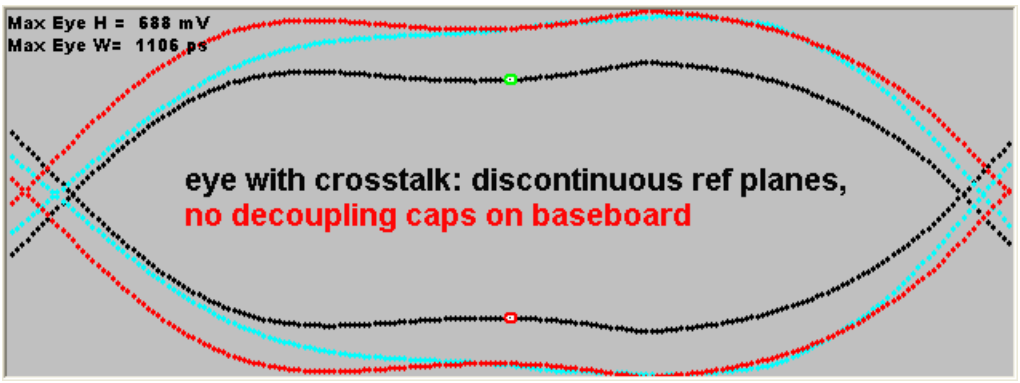

Figure 22: Simulated channel w/crosstalk, no decoupling, discontinuous reference.

simulated test correlation channel, comparing continuous planes to discontinuous reference planes. Decoupling caps provide reasonable return path and insertion losses are about the same.

When crosstalk is counted, we see a clear difference, as shown in Figures 19 and 20. With decoupling caps in place, the margin cost is 40 mV and 25 ps for the reference plane discontinuity — almost all of the margin reduction is due to crosstalk, as was hinted earlier in the gap analysis.

How important are the decoupling caps? This is easily determined by resimulating without the capacitor models. The results (Figures 21 and 22) suggest that considerable eye height margin would be lost without their contribution to return path.

Actual measurements of the simulated DDR3-1600 channel agree with the simulation prediction. Figure 23 shows a channel with continuous reference and plenty of decoupling caps.

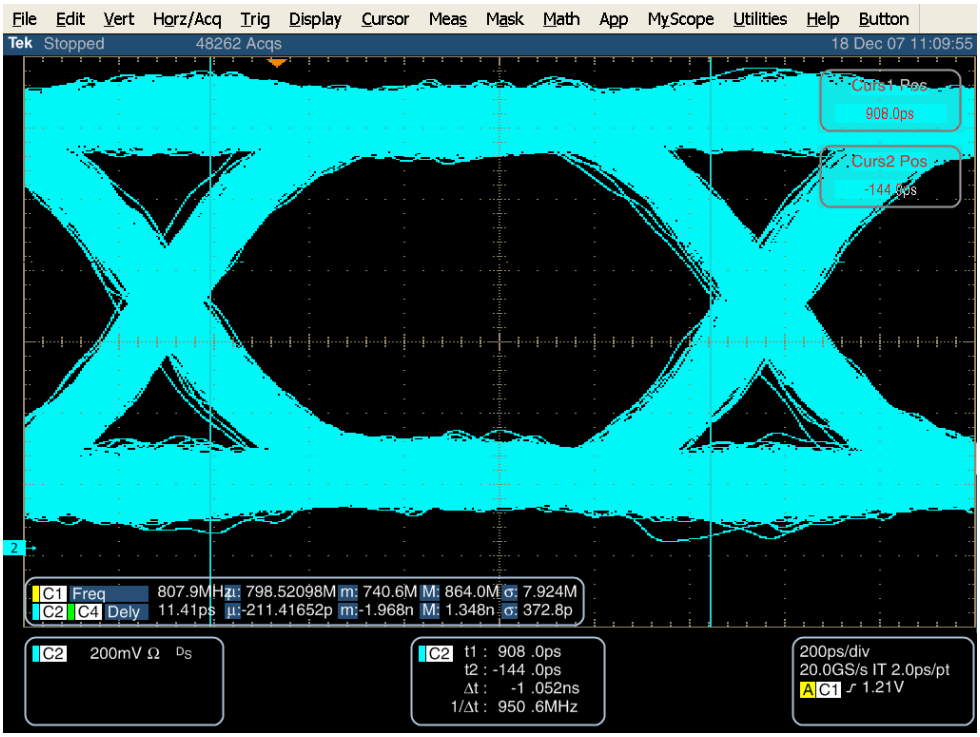

Figure 23: DDR3 channel, continuous reference.

Last, we see the waveform for an identical channel with reference plane discontinuity.

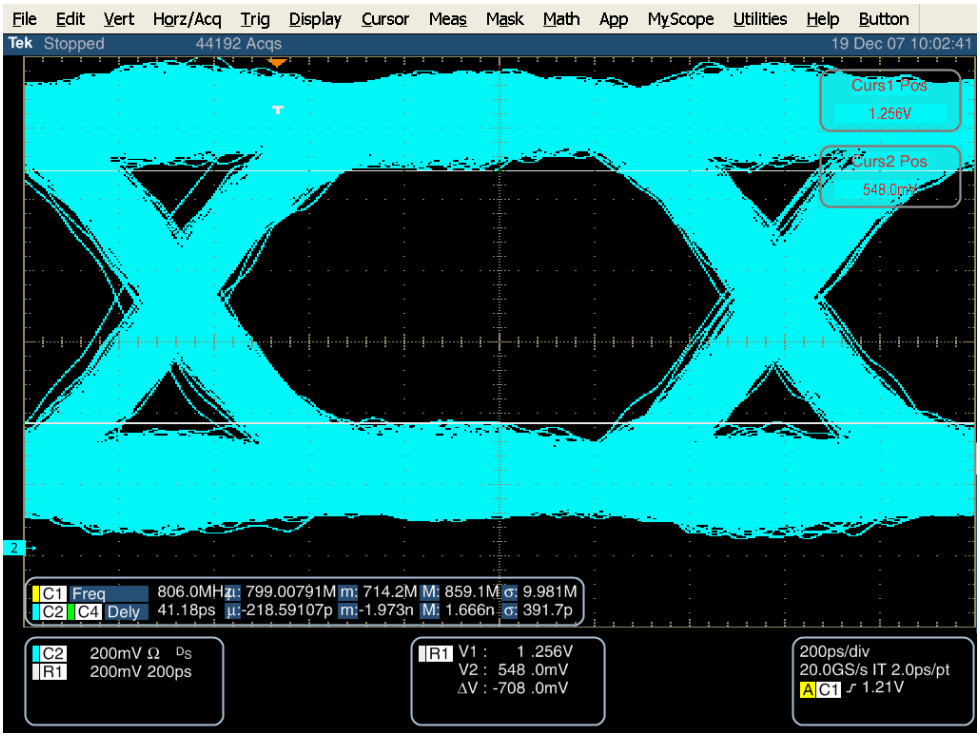

Figure 24: DDR3 channel, reference plane discontinuity (with decoupling caps).

The iterative modeling has helped to clarify 3-D modeling issues on the one hand, and the larger effects due to the connector structure and the topology of the plane references. From this outside-in approach, we gain a deeper understanding of the relative significance of the various effects, and are better equipped to make an informed engineering judgement.

Sensitivity of the Resonance Characteristics of SRR and DSRR (Double-Sided SRR) Type Metamaterials to the Changes in Substrate Parameters and the Usefulness of DSRR Structure for Reduced Electrical Size

E. Ekmekci[1,2] and G. Turhan-Sayan[1]

[1]Dept. of Electrical and Electronics Engineering, Middle East Technical University, Ankara, Turkey
[2]Dept. of Electronics and Communication Engineering, Suleyman Demirel University, Isparta, Turkey

Abstract— In this study, transmission characteristics of split-ring resonator (SRR) and double-sided SRR (DSRR) are investigated using Ansoft's HFSS software, for varying values of substrate parameters, which are thickness, the real part of relative permittivity and the dielectric loss tangent of the substrate. Simulation results have shown that resonance patterns of both SRR and DSRR are affected similarly from permittivity and loss tangent variations. However, changes in the substrate thickness affect their resonance characteristics quite differently. Resonance frequency, resonance strength, and bandwidth of the resonance curve noticeably decrease for the DSRR structure in response to decreasing substrate thickness while the resonance frequency of the SRR increases at a comparatively slower rate without any noticeable change in the bandwidth and the resonance strength. Besides, the simulation results show that doubling the SRR (i.e., using DSRR), while keeping the unit cell dimensions fixed, provides an electrically smaller structure, and thus better effective medium approach.

1. INTRODUCTION

Materials having simultaneously negative permeability and negative permittivity values over the same frequency band are called left-handed metamaterials, which show unusual properties such as negative refractive index, negative group velocity, and negative Vavilov-Cerenkov effect [1]. It is well known that all naturally existing materials show positive values of permeability since there are no free magnetic charges in the nature [1, 2]. In 1999, Pendry et al. showed that it was possible to obtain negative values of effective permeability using Swiss rolls and SRRs [2]. In 2003, Marques et al. compared the SRR with a related structure called broad-side coupled SRR (BC-SRR) that is composed of only the outer ring of the SRR, which is printed on both faces of the substrate in a reversely doubled manner. They also investigated the effects of changing SRR and BC-SRR parameters on the value of resonance frequency (f_0). Effects of changing substrate thickness and substrate permittivity on f_0 are investigated for the BC-SRR structure in the same reference [3].

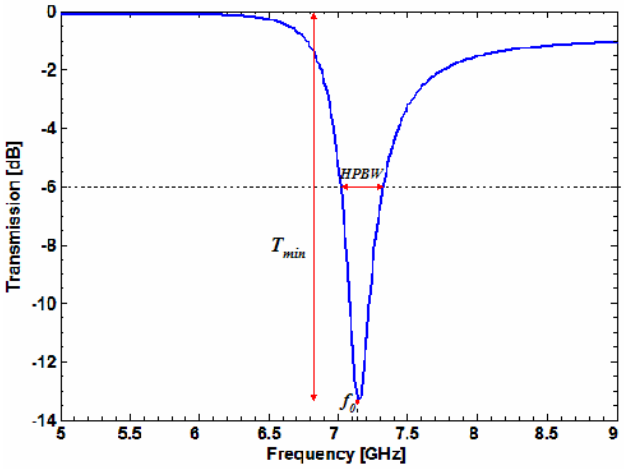

Figure 1: f_0, $HPBW$, and $T_{\min}$ defined on a transmission versus frequency curve.

In this paper, we investigate the sensitivity of the resonance characteristics of SRR and DSRR type metamaterials to the changes in substrate parameters, and we also investigate the usefulness

of DSRR to reduce electrical size. Herein, the above mentioned substrate parameters are the thickness (d), the real part of relative permittivity (ε_r) and the dielectric loss tangent ($\tan\delta_c$). On the other hand, the resonance characteristics are the value of the resonance frequency (f_0), half power bandwidth ($HPBW$) and the resonance strength that can be measured by the value of the transmission minimum ($T_{\min}$). These characteristics are indicated in Figure 1 for better visualization. The simulation results obtained for the DSRR structure are compared to those obtained for the SRR emphasizing the important differences.

2. DESIGN AND SIMULATION

In Figure 2(a), the schematic view of the SRR is given. It has the geometrical parameters of $L = 5\,\text{mm}$, $l = 4\,\text{mm}$, $h = 3\,\text{mm}$, $g = 0.5\,\text{mm}$, and $w = 0.3\,\text{mm}$. The structure is made of copper lines with the thickness of $0.03\,\text{mm}$. The relative permeability μ_r of the substrate is set to be equal to unity. All these parameters are kept constant during the simulations, while only the substrate parameters d, ε_r and $\tan\delta_c$ are all chosen to be variables. In Figure 2(b) the schematic view of the DSRR structure is given, which consists of two identical SRR structures aligned over the opposite faces of the dielectric substrate in an inverted position. The parameter values defined on Figure 2(a) are also valid for the double SRR of Figure 2(b).

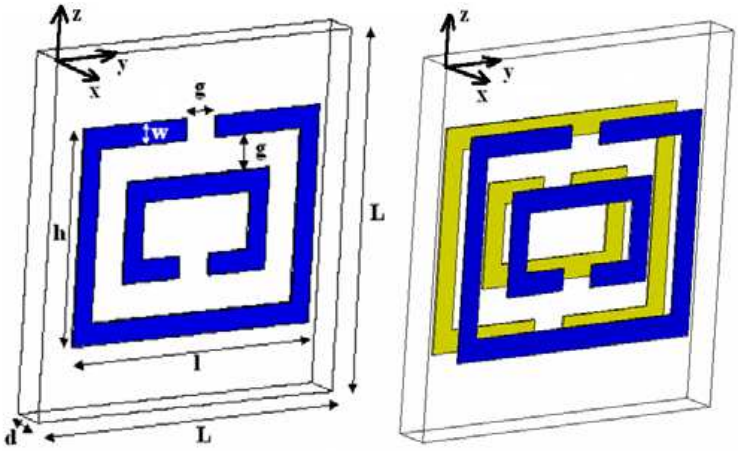

(a) SRR structure (b) DSRR structure

Figure 2: Schematic views of the unit cells for two alternative metamaterial structures.

The transmission characteristics of these SRR and DSRR cells are simulated by using the Ansoft's HFSS software to compute the scattering parameter S_{21}. This software is a numerical electromagnetic solver based on the finite element method (FEM). In the simulation setup, the given unit cell is surrounded by an air medium and the incident plane electromagnetic wave propagates along the y direction. The direction of the electric field vector is along the z axis (i.e., z-polarized plane wave excitation) and hence, the direction of the magnetic field vector is along the x axis. Perfect electric conductor (PEC) boundary conditions are applied along the boundaries perpendicular to the z axis and perfect magnetic conductor (PMC) boundary conditions are applied along the boundaries perpendicular to the x axis. Open boundary conditions are applied to the remaining two boundaries [4]. Simulations are performed with $0.02\,\text{GHz}$ incremental steps.

3. RESULTS

Herein, we investigate the effects of changing d, ε_r and $\tan\delta_c$ on f_0, $HPBW$ and $T_{\min}$ both the SRR and DSRR structures in a comparative manner.

To observe the effects of changing the substrate thickness d on the resonance pattern, the other substrate parameters are kept constant as $\varepsilon_r = 4.4$ and $\tan\delta_c = 0.02$. Transmission versus frequency curve of the SRR is computed for four different values of d as shown in Figure 3. As to be inferred from this figure, as d increases from 0.51 to $2\,\text{mm}$, f_0 decreases from 7.13 to $6.74\,\text{GHz}$ almost exponentially, being consistent with the results given in reference [5]. In the meantime, there is no noticeable change in the $HPBW$ which is about $0.3\,\text{GHz}$ and the change in the transmission minimum $T_{\min}$ negligible, less than $0.7\,\text{dB}$.

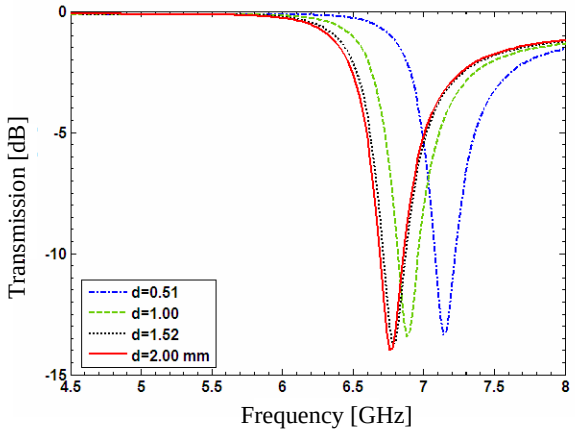

Figure 3: Simulated transmission spectra (i.e., $|S_{21}|$) of the SRR for different substrate thicknesses with $\varepsilon_r = 4.4$ and $\tan\delta_c = 0.02$.

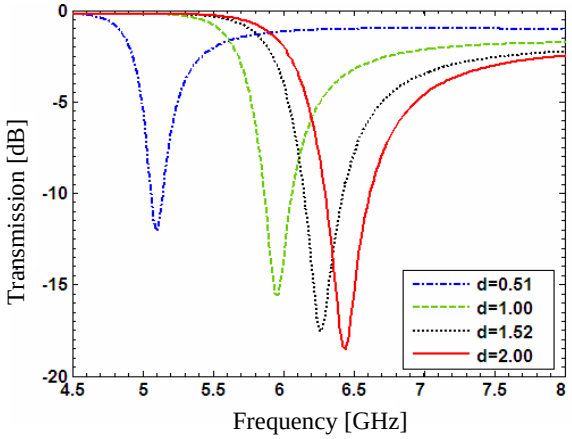

Figure 4: Simulated transmission spectra (i.e., $|S_{21}|$) of the DSRR for different substrate thicknesses with $\varepsilon_r = 4.4$ and $\tan\delta_c = 0.02$.

Next, the same simulation is run for the DSRR structure. As opposed to the SRR case, as d increases from 0.51 to 2 mm, f_0 of the DSRR increases from 5.10 to 6.43 GHz almost exponentially as shown in Figures 4 and 5. In fact, doubling the SRR causes an additional distributed capacitive effect (C_{add}) to arise due to the overlapping conducting strips printed on both faces of the substrate. Consequently, the DSRR structure resonates at lower frequencies than the comparable SRR structure for any given value of d. As d increases, however, C_{add} decreases resulting an increase in f_0 of the DSRR structure. This behavior is also consistent with the results reported for BC-SRR in [3]. It is also obvious from Figure 4 that increasing d leads to a wider resonance bandwidth ($HPBW$ increases from 0.211 to 0.621 GHz) and a stronger resonance ($T_{\min}$ changes from -12.09 to -18.56 dB). Resonance frequency versus substrate thickness curves for both SRR and DSRR structures are given in Figure 5. As d is increased from 0.51 to 2 mm for both structures, the amount of increase in f_0 of the DSRR is much larger than the amount of decrease in f_0 for the SRR structure.

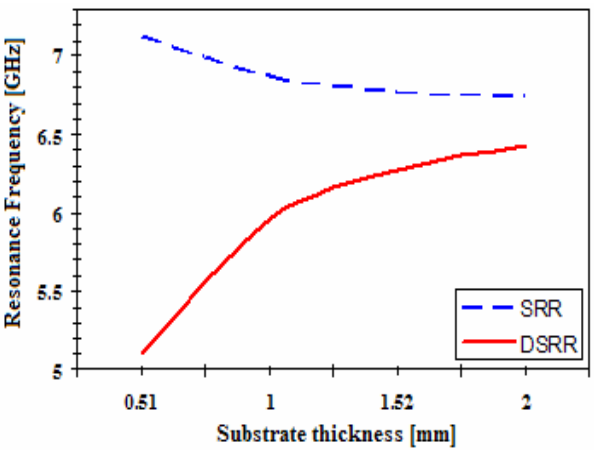

Figure 5: Resonance frequency versus substrate curve for both SRR and DSRR.

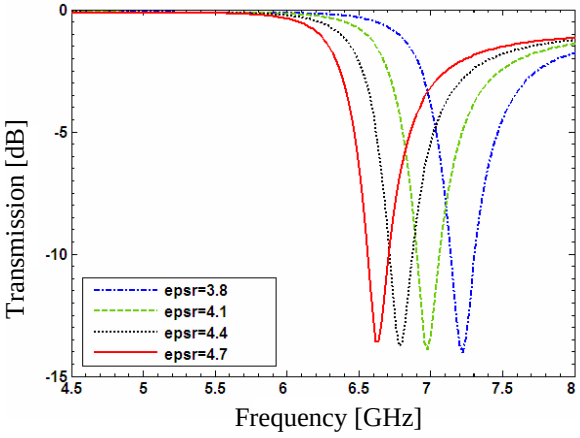

Figure 6: Simulated transmission spectra (i.e., $|S_{21}|$) of the SRR for different permittivity values with $d = 1.52$ mm, $\tan\delta_c = 0.020$.

To observe the effects of changing ε_r on the resonance pattern, the other substrate parameters are kept constant as $d = 1.52$ mm and $\tan\delta_c = 0.02$. Transmission versus frequency curves of the SRR and DSRR structures are computed for four different values of ε_r as shown in Figures 6 and 7, respectively. It can be seen that as ε_r increases, $HPBW$ and $T_{\min}$ do not change much but, f_0 decreases slightly and almost linearly for both SRR and DSRR structures. This linear behavior can also be observed in Figure 8. The results shown in Figure 6 for the SRR are also in good agreement

with those given in [5].

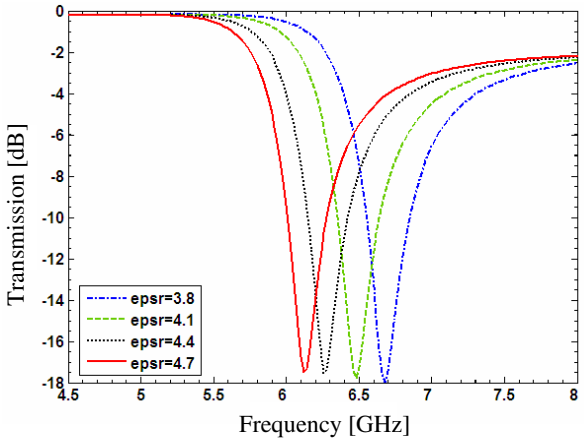

Figure 7: Simulated transmission spectra (i.e., $|S_{21}|$) of the DSRR for different permittivity values with $d = 1.52\,\text{mm}$, $\tan\delta_c = 0.020$.

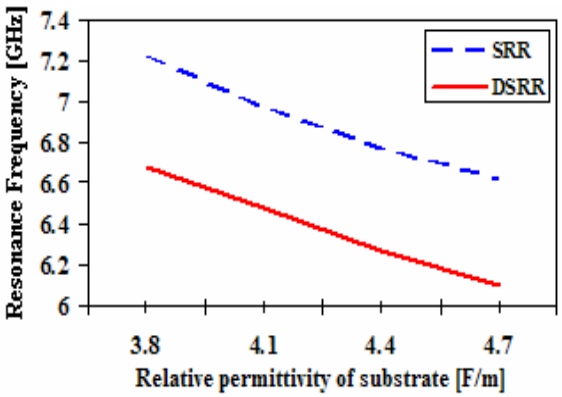

Figure 8: Resonance frequency versus relative permittivity curve for both SRR and DSRR.

To observe the effects of changing $\tan\delta_c$ on the resonance pattern, the other substrate parameters are kept constant as $d = 1.52\,\text{mm}$, $\varepsilon_r = 4.4$. Transmission versus frequency curves of the SRR and DSRR structures are computed for four different values of $\tan\delta_c$ as shown in Figures 9 and 10, respectively. It is observed for both structures that as $\tan\delta_c$ decreases from 0.020 to 0, the f_0 and the $HPBW$ values do not change much; but $T_{\min}$ decreases by about 13 dB for SRR and 12 dB for DSRR implying a stronger resonance behavior.

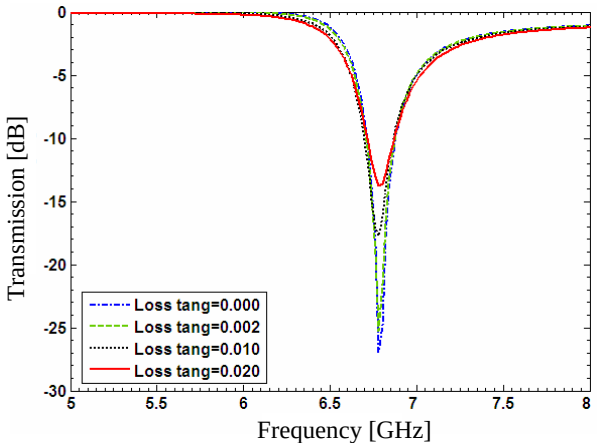

Figure 9: Simulated transmission spectra (i.e., $|S_{21}|$) for SRR structures having $d = 1.52\,\text{mm}$, $\varepsilon_r = 4.4$, and four different $\tan\delta_c$ values.

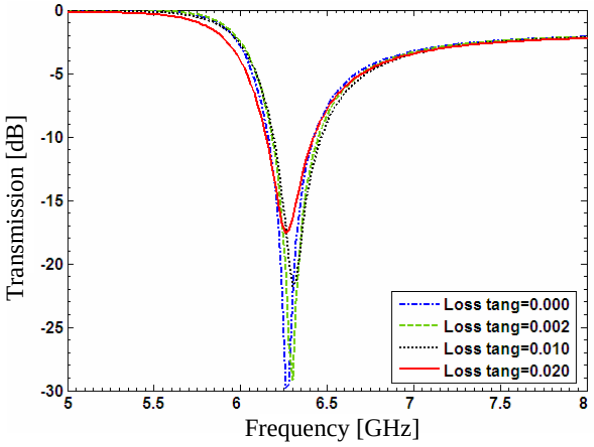

Figure 10: Simulated transmission spectra (i.e., $|S_{21}|$) for DSRR structures having $d = 1.52\,\text{mm}$, $\varepsilon_r = 4.4$, and four different $\tan\delta_c$ values.

Electrical size of the SRR and DSRR are defined to be $u = D/\lambda_0$ where D is the maximum linear dimension of the resonator, which is 5 mm for both structures, and $\lambda_0 = c/f_0$ is the free space wavelength at the resonance frequency.

In Figure 11, the electrical sizes (u) of the SRR and DSRR structures are given as a function of substrate thickness. As we decrease d from 2 mm to 0.51 mm, u of the SRR increases from 0.112 to 0.119 whereas u of the DSRR decreases from 0.107 to 0.085. As the substrate gets thicker, the electrical sizes of SRR and DSRR structures tend to converge to each other around the value of 0.11. In fact, this is an anticipated result because the DSRR structure geometrically approaches to an SRR structure in the limit as the substrate thickness d increases.

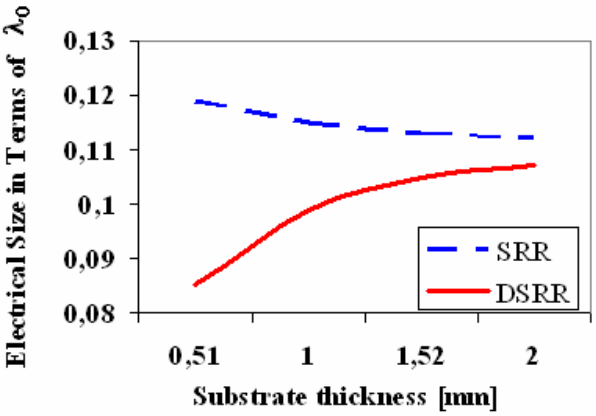

Figure 11: Electrical sizes versus substrate thickness for both SRR and DSRR.

4. CONCLUSION

In this paper, we investigated the effects of changing substrate parameters on the resonance patterns of the DSRR and SRR type metamaterials. It is demonstrated that both structures behave similarly in response to changes in ε_r and $\tan\delta_c$ of the substrate: As ε_r increases f_0 drops; and as $\tan\delta_c$ decreases both structures resonate more strongly. However, the responses of the SRR and the DSRR to the changes in d are quite different. As the d increases, f_0 of the SRR decreases slightly while the $HPBW$ and $T_{\min}$ do not change noticeably. The DSRR structure, on the other hand, experiences pronounced increases in the f_0 and $HPBW$ while having stronger resonances due to increased d. Besides, the DSRR structure provides much smaller electrical sizes than the SRR, especially for thinner substrates. In other words, for given unit cell dimensions, a DSRR structure can be used at much lower frequencies as compared to an SRR structure.

REFERENCES

1. Veselago, V. G., "The electrodynamics of substances with simultaneously negative values of ε and μ," *Sov. Phys. Usp.*, Vol. 10, 509–514, 1968.
2. Pendry, J. B., A. J. Holden, D. J. Robbins, and W. J. Stewart, "Magnetism from conductors and enhanced nonlinear phenomena," *IEEE Trans. Microwave Theory Tech.*, Vol. 47, No. 11, 2075–2084, 1999.
3. Marqués, R., F. Mesa, J. Martel, and F. Medina, "Comparative analysis of edge- and broadside-coupled split ring resonators for metamaterial design-theory and experiments," *IEEE Trans. Antennas Propag.*, Vol. 51, No. 10, 2572–2581, 2003.
4. Lubkowski, G., R. Schuhmann, and T. Weiland, "Extraction of effective metamaterial patameters by parameter fitting of dispersive models," *Microw. Opt. Technol. Lett.*, Vol. 49, No. 2, 285–288, 2007.
5. Sheng, Z. and V. V. Varadan, "Tuning the effective properties of metamaterials by changing the substrate properties," *J. Appl. Phys.*, Vol. 101, 014909 (1)–(7), 2007.

Calculation Technic of Diffracted Electromagnetic Waves by a Circular Disk of Perfect Conductor Using Multiple Precision Arithmetic

Takashi Kuroki[1], **Teruhiro Kinoshita**[2], **and Toshihiko Shibazaki**[1]

[1]Tokyo Metropolitan College of Industrial Technology, Japan
[2]Tokyo Polytechnic University, Japan

Abstract— In the case of the numerical calculation using the exact analysis method, good results up to 2.5 or 3.0 wavelengths with double precision or quadruple precision are obtained, to electromagnetic diffraction by a circular disk of a perfect conductor. The cause of it can be explained by the fact that numerical calculation is not executed with sufficient precision in its process. GMP is the library that can execute the numerical calculation by multiple precision in C and C++ language. The purpose of this study is to investigate the cause of the faulty results, and alter them to be good results using GMP while the radius of the circular disk is over 3 wavelengths. As a result, in the case of 64-bit precision, as a/λ grows large, accuracy of $g_1(p, q)$ becomes 0. While a radius of a disk is 7 wavelengths, the calculation result in 128-bit precision have a rounding accuracy of 15 decimal digits.

1. INTRODUCTION

In the case of the numerical calculation using the analysis method of Nomura and Katsura [1], good results up to 2.5 or 3.0 wavelengths with double precision or quadruple precision are obtained, to electromagnetic diffraction by a circular disk of a perfect conductor [2]. However, poor results are obtained over 3 wavelengths. The cause of it can be explained by the fact that numerical calculation is not executed with sufficient precision in its process.

We have no problem in executing more complex numerical calculation since the processing speed of computers has been progressive and memory capacity has grown in recent years. GMP (GNU Multiple Precision Arithmetic Library) [3] is a software library for arbitrary precision arithmetic in C and C++ language.

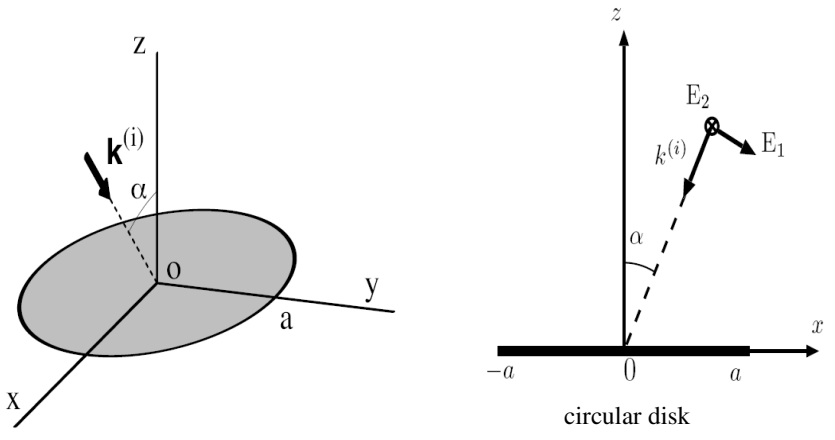

(a) Conductive Disk (radius a; thickness 0) (b) Coordinate System of Incident Plane Wave

Figure 1: A coordinate system of a conductive disk and an incident plate wave.

The purpose of this study is to investigate the cause of the faulty results, and alter them to be good results using GMP while the radius of the circular disk is over 3 wavelengths.

2. FORMULATION OF THE PROBLEM

We consider calculating a diffracted field by a circular disk of a perfect conductor for plane wave incidence. In Fig. 1(a), the rectangular coordinate system is chosen with the origin at the center of

the disk (radius a) and oriented so that the disk lies in x-y plane ($z = 0$). In Fig. 1(b), an incident wave enters from the inside of x-z plane and angle α. The wave number vector for incident wave is

$$\boldsymbol{k}^{(i)} = k(-\sin\alpha,\ 0,\ \cos\alpha).$$

In this case, having only x and y components, an electric Hertz vector $\boldsymbol{\Pi}^{(i)}$ of the incident field is expressed by

$$\boldsymbol{\Pi}^{(i)} = \left(\Pi_x^{(i)},\ \Pi_y^{(i)},\ 0\right) e^{-j\boldsymbol{k}^{(i)}\cdot\boldsymbol{r}}. \tag{1}$$

Here, the induced current on the circular disk has no z component of Hertz vector. Using the harmonic time dependence $e^{j\omega t}$ (is omitted throughout) and wave number $k(=\omega\sqrt{\mu\epsilon})$, the diffracted fields $\boldsymbol{E}^{(s)}$, $\boldsymbol{H}^{(s)}$ caused by the induced current is expressed by

$$\boldsymbol{E}^{(s)} = \nabla(\nabla\cdot\boldsymbol{\Pi}) + k^2\boldsymbol{\Pi} \tag{2}$$

$$\boldsymbol{H}^{(s)} = j\omega\varepsilon\nabla\times\boldsymbol{\Pi}. \tag{3}$$

$\boldsymbol{\Pi}$ can be expanded as follows [1]:

$$\Pi_x = \sum_{n=0}^{\infty}\sum_{m=0}^{\infty}\epsilon_n S_m^n(r,z)\left\{A_m^n\cos n\varphi + B_m^n\sin n\varphi\right\}, \tag{4}$$

$$\Pi_y = \sum_{n=0}^{\infty}\sum_{m=0}^{\infty}\epsilon_n S_m^n(r,z)\left\{C_m^n\cos n\varphi + D_m^n\sin n\varphi\right\}, \tag{5}$$

$$\Pi_z = 0, \tag{6}$$

where ϵ_n is either 1 (if $n = 0$) or 2 (if $n \neq 0$). $S_m^n(r,z)$ is an eigen function of a wave function [1] and is continuous except for the surface of a circular disk of a conductor. A_m^n, B_m^n, C_m^n, D_m^n are unknown expansion coefficients that are decided using a boundary condition and so on. In this paper, we devise the calculation of these coefficients in consideration of calculation precision.

The decision of the expansion coefficients requires to expand the electromagnetic field by a solution of a wave equation and satisfy a boundary condition, an edge condition and an outgoing radiation condition. The expansion coefficients can analytically be decided by the introduction of an arbitrary scalar function and expression of a wave equation with cylindrical coordinates. Since the result of the analysis is fully described in [5], we show only the required equation according to the procedure of the numerical calculation after this section.

3. GMP, MPFR AND NEW INTERFACE

GMP is a multiple precision library. We can specify the arbitrary binary digits for integer, rational and floating point variables in GMP.

MPFR (Multiple Precision Floating-Point Reliable Library) [4], based on GMP, is the supplementary library equipped with the mathematical library functions, such as trigonometric functions, a gamma function and so on. (As these functions are not equipped in GMP). In addition, MPFR has functions of verified numerical computation in arbitrary precision. However, GMP is useless since we must write "add(m, n)" in adding m to n and so on.

GMP++ is a library that corresponds to C++ language. In GMP++, we can use "$+-*/$" symbols and a class and do not need initialization or a closing process for variables. However, MPFR do not have C++ class interfaces.

We design new interfaces in this study. The flow of the new interfaces between GMP++ classes and MPFR functions is as follows: (1) Recieve GMP++ class. (2) Convert GMP++ class to MPFR variable. (3) Calculate MPFR function with MPFR variable. (4) Convert MPFR variable to GMP variable. (5) Convert GMP variable to GMP++ class. (MPFR variable cannot be directly converted to GMP++). (6) Return GMP++ class. The precision of variables is guaranteed since each class or variable is converted by the same precision in this process.

4. FLOW OF NUMERICAL CALCULATION

In this paper, we discuss calculaion from coefficients of a matrix equation to expansion coefficients and do not discuss calculation of a current distribution and a radiation field from a long distance. If you want to know the contents in detail, see [5].

Choosing the ratio a/λ of radius a of a circular disk to wavelength λ as a parameter, we put the value of $\gamma = ka = 2\pi \times \frac{a}{\lambda}$ and calculate expansion coefficients $n = 0, 1, 2, \cdots$. The procedure of the calculation is as follows:

1. Using Equations (7)–(9), calculate coefficients of a matrix equation and so on.

$$G^n_{\ell,m} = \frac{\Gamma(n+\ell+\frac{1}{2})\Gamma(\ell+\frac{1}{2})}{\Gamma(n+\ell+1)\Gamma(\ell+1)}\{g_1(n+m+\ell, |m-\ell|) - jg_2(m+n+\ell, |m-\ell|)\} \tag{7}$$

$$g_1(p,\, q) = \frac{\sqrt{\pi}}{2}\sum_{k=q}^{\infty}\frac{(-1)^k}{k!}\frac{\Gamma(p-k+\frac{1}{2})\Gamma(2k+1)\left(\frac{\gamma}{2}\right)^{2k}}{\Gamma(\frac{1}{2}-k)\Gamma(p+k+\frac{3}{2})\Gamma(k+q+1)\Gamma(k-q+1)} \tag{8}$$

$$g_2(p,\, q) = \frac{\sqrt{\pi}}{2}\sum_{k=0}^{\infty}\frac{(-1)^k}{k!}\frac{\Gamma(p+k+1)\Gamma(2p+2k+2)\left(\frac{\gamma}{2}\right)^{2p+2k+1}}{\Gamma(2p+k+2)\Gamma(p+k+q+\frac{3}{2})}\frac{1}{\Gamma(p+k-q+\frac{3}{2})\Gamma(p+k+\frac{3}{2})} \tag{9}$$

2. Applying an incident field $\boldsymbol{E}^{(i)}$ to Equations (10)–(11), calculate expansion coefficients of a linear Hertz vector on a circular disk.

$$\Pi_x^{(e,o)n}{}_{\ell} = -\int_0^1 \frac{t^{n/2}}{\sqrt{1-t}} u^n_\ell(t)\Pi_x^{(i)}{}^{(e,o)}_{n}\, dt \tag{10}$$

$$\Pi_y^{(e,o)n}{}_{\ell} = -\int_0^1 \frac{t^{n/2}}{\sqrt{1-t}} u^n_\ell(t)\Pi_y^{(i)}{}^{(e,o)}_{n}\, dt \tag{11}$$

$$f^n_\ell = \int_0^1 \frac{t^{n/2}}{\sqrt{1-t}} u^n_\ell(t) J_n(\gamma\sqrt{t})\, dt, \tag{12}$$

where an eigen function [1] of Equations (4)–(5) is

$$S^n_m(r,z) = \int_0^\infty \frac{\sqrt{\xi}J_n(r\xi/a)J_{n+m+\frac{1}{2}}(\xi)}{\sqrt{\xi^2-(ka)^2}}\exp\left[-\sqrt{\xi^2-(ka)^2}\frac{|z|}{a}\right]\, d\xi \tag{13}$$

For simplification, we use $ka = \gamma$, $\left(\frac{r}{a}\right)^2 = t$. we expand Equations (10)–(12) using equation

$$t^{n/2}u^n_m(t) = \int_0^\infty \frac{J_n(\xi\sqrt{t})J_{n+2m+\frac{1}{2}}(\xi)}{\sqrt{\xi}} d\xi, \tag{14}$$

that is related to Jacobi's polynominal equation, where $t = (r/a)^2$. $u^n_m(t)$ is orthogonal perfect function series in $0 < t < 1$.

An incident field is given as follows: In case of an incident plane wave, the incident fields $\boldsymbol{E}^{(i)}$ $\boldsymbol{H}^{(i)}$ are expressed by

$$\boldsymbol{E}^{(i)} = (E_2\cos\alpha,\, E_1,\, -E_2\sin\alpha)e^{jk(-x\sin\alpha+z\cos\alpha)} \tag{15}$$

$$\boldsymbol{H}^{(i)} = -\frac{1}{j\omega\mu}\nabla\times\boldsymbol{E}^{(i)}, \tag{16}$$

where α is the transmitting direction of the plane wave (see Fig. 1). The incident wave is expressed by the Hertz vector

$$\boldsymbol{\Pi}^{(i)} = (\Pi_x,\, \Pi_y,\, 0) \tag{17}$$

$$\Pi_x = -\frac{E_2}{k^2\cos\alpha}e^{jk(-x\sin\alpha+z\cos\alpha)} \tag{18}$$

$$\Pi_y = \frac{E_1}{k^2}e^{jk(-x\sin\alpha+z\cos\alpha)}. \tag{19}$$

On the circular disk,

$$\Pi_x(x,\, y,\, 0) \;=\; -\frac{E_2}{k^2\cos\alpha}e^{-jkx\sin\alpha} \tag{20}$$

$$\Pi_y(x,\, y,\, 0) \;=\; \frac{E_1}{k^2}e^{-jkx\sin\alpha}. \tag{21}$$

Using $e^{ja\cos\varphi} = \sum_{n=0}^{\infty}\epsilon_n j^n J_n(a)\cos n\varphi$,

$$e^{jkx\sin\alpha} = e^{jkr\sin\alpha\cos\varphi} = \sum_{n=0}^{\infty}\epsilon_n(-j)^n J_n(kr\sin\alpha)\cos n\varphi. \tag{22}$$

Therefore, using Equations (10)–(11) and equation (that is expansion of Bessel function)

$$I \;=\; \int_0^1 \frac{t^{n/2}}{\sqrt{1-t}}u_\ell^n(t)J_n(\gamma\sqrt{t})\,dt = \frac{\Gamma(\ell+\frac{1}{2})\Gamma(n+\ell+\frac{1}{2})}{\sqrt{2}\Gamma(\ell+1)\Gamma(n+\ell+1)}\sum_{k=0}^{\infty}\frac{(-1)^k\left(\frac{\gamma}{2}\right)^{n+2\ell+2k}}{\Gamma(k+1)\Gamma(k+n+2\ell+\frac{3}{2})}, \tag{23}$$

the incident wave can be expressed by

$$\begin{aligned}\Pi_{x\;\ell}^{(e)\,n} &= \frac{(-j)^n E_2}{k^2\cos\alpha}\int_0^1 \frac{t^{n/2}}{\sqrt{1-t}}u_\ell^n(t)J_n(\sqrt{t}\gamma\sin\alpha)\,dt \\ &= \frac{(-j)^n E_2}{\sqrt{2}k^2\cos\alpha}\frac{\Gamma(\ell+\frac{1}{2})\Gamma(n+\ell+\frac{1}{2})}{\Gamma(\ell+1)\Gamma(n+\ell+1)}\sum_{\nu=0}^{\infty}\frac{(-1)^\nu\left(\frac{1}{2}\gamma\sin\alpha\right)^{n+2\ell+2\nu}}{\Gamma(\nu+1)\Gamma(\nu+n+2\ell+\frac{3}{2})} \qquad (24)\end{aligned}$$

$$\Pi_{y\;\ell}^{(e)\,n} \;=\; -\frac{(-j)^n E_1}{\sqrt{2}k^2}\frac{\Gamma(\ell+\frac{1}{2})\Gamma(n+\ell+\frac{1}{2})}{\Gamma(\ell+1)\Gamma(n+\ell+1)}\sum_{\nu=0}^{\infty}\frac{(-1)^\nu\left(\frac{1}{2}\gamma\sin\alpha\right)^{n+2\ell+2\nu}}{\Gamma(\nu+1)\Gamma(\nu+n+2\ell+\frac{3}{2})} \tag{25}$$

$$\Pi_{x\;\ell}^{(o)\,n} \;=\; \Pi_{y\;\ell}^{(o)\,n} \;=\; 0 \tag{26}$$

3. Approximating with equations truncated by the finite terms for the infinite simultaneous linear equations, calculate the coefficient (27)–(31).

$$\left[\widetilde{A_m^n}\right] \;=\; \left[G_{\ell,\,m}^n\right]^{-1}\left[\Pi_{x\;\ell}^{(e)\,n}\right], \tag{27}$$

$$\left[\widetilde{B_m^n}\right] \;=\; \left[G_{\ell,\,m}^n\right]^{-1}\left[\Pi_{x\;\ell}^{(o)\,n}\right], \tag{28}$$

$$\left[\widetilde{C_m^n}\right] \;=\; \left[G_{\ell,\,m}^n\right]^{-1}\left[\Pi_{y\;\ell}^{(e)\,n}\right], \tag{29}$$

$$\left[\widetilde{D_m^n}\right] \;=\; \left[G_{\ell,\,m}^n\right]^{-1}\left[\Pi_{y\;\ell}^{(o)\,n}\right], \tag{30}$$

$$\left[\widetilde{f_m^n}\right] \;=\; \left[G_{\ell,m}^n\right]^{-1}\left[f_\ell^n\right], \tag{31}$$

4. To satisfy an edge condition, calculate correction coefficients using Equations (32)–(34).

$$kU_0^{(e)} = \frac{\sum_{m=0}^{\infty}(-1)^m\left(\widetilde{A_m^1}+\widetilde{D_m^1}\right)}{\sum_{m=0}^{\infty}(-1)^m\widetilde{f_m^1}} \tag{32}$$

$$kU_n^{(e)} = -\frac{\sum_{m=0}^{\infty}(-1)^m\left[\widetilde{A_m^{n-1}}+\widetilde{A_m^{n+1}}-\widetilde{D_m^{n-1}}+\widetilde{D_m^{n+1}}\right]}{\sum_{m=0}^{\infty}(-1)^m\left[\widetilde{f_m^{n-1}}-\widetilde{f_m^{n+1}}\right]}, \qquad (n\geq 1) \tag{33}$$

$$kU_n^{(o)} = -\frac{\sum_{m=0}^{\infty}(-1)^m\left[\widetilde{B_m^{n-1}}+\widetilde{B_m^{n+1}}+\widetilde{C_m^{n-1}}-\widetilde{C_m^{n+1}}\right]}{\sum_{n=0}^{\infty}(-1)^m\left[\widetilde{f_m^{n-1}}-\widetilde{f_m^{n+1}}\right]}, \qquad (n\geq 1) \tag{34}$$

where $\widetilde{B_m^0} = \widetilde{D_m^0} = 0$.

5. Calculate expansion coefficients of the Hertz vector in the diffracted (qadratic) field using Equations (35)–(39).

$$[A_m^n] = \left[\widetilde{A_m^n}\right] + \frac{k}{2}\left(U_{n+1}^{(e)} - U_{n-1}^{(e)}\right)\left[\widetilde{f_m^n}\right], \tag{35}$$

$$[B_m^n] = \left[\widetilde{B_m^n}\right] + \frac{k}{2}\left(U_{n+1}^{(o)} - U_{n-1}^{(o)}\right)\left[\widetilde{f_m^n}\right], \tag{36}$$

$$[C_m^n] = \left[\widetilde{C_m^n}\right] + \frac{k}{2}\left(U_{n+1}^{(o)} + U_{n-1}^{(o)}\right)\left[\widetilde{f_m^n}\right], \tag{37}$$

$$[D_m^n] = \left[\widetilde{D_m^n}\right] - \frac{k}{2}\left(U_{n+1}^{(e)} + U_{n-1}^{(e)}\right)\left[\widetilde{f_m^n}\right], \tag{38}$$

5. NUMERICAL CALCULATION

5.1. Problem in Numerical Calculation

We suppose that a part of the calculation process in which an error occurs is the calculation of $G_{\ell,m}^n$ or simultaneous linear equations in the calculation process of a current distribution and a radiation field. To investigate our expectation, g_1, g_2 (are the structure factors of $G_{\ell,m}^n$) and A_m^n try to be calculated in the parameters of the ratio a/λ and the calculation precision that can be set in GMP. In addition, we compare numerical results among some different calculation precision, and investigate the relation between a/λ and the set of calculation precision. The rounding mode is "round to the nearest" in all investigations.

To avoid a rounding error for calculation of the gamma function, Equations (8) and (9) are

modified to

$$g_1(p,\,q) \;=\; \sum_{k=q}^{\infty} a_k \simeq \sum_{k=q}^{q+N} a_k \frac{a_k}{a_{k-1}} = \frac{(2k-1)^2}{\left(p+k+\frac{1}{2}\right)\left(p-k+\frac{1}{2}\right)(k+q)(k-q)} \left(\frac{\gamma}{2}\right)^2 \tag{39}$$

$$a_q \;=\; \frac{(-1)^q 2^2 \gamma^{2q}}{q!} \frac{\{2(p-1)+1-2q\}\{2(p-2)+1-2q\}\cdots\{1-2q\}}{(2p+2q+1)(2p+2q)(2p+2q-1)\cdots(p+q+1)} \tag{40}$$

$$g_2(p,\,q) \;=\; \sum_{k=0}^{\infty} b_k \simeq \sum_{k=0}^{N} b_k \frac{b_k}{b_{k-1}} = \frac{4(p+k)^2\gamma^2}{k(2p+k+1)(2p+2k+2q+1)(2p+2k-2q+1)} \tag{41}$$

$$\begin{aligned} b_0 \;=\; & \frac{2^2\gamma^{2q+1}}{\pi} \frac{p(p-1)(p-2)\cdots 1}{\left(p+\frac{1}{2}\right)\left(p-\frac{1}{2}\right)\left(p-\frac{3}{2}\right)\cdots\frac{3}{2}} \frac{1}{2(p+q)+1} \frac{1}{2(p+q)-1} \cdots \frac{1}{2(p-q)+3} \\ & \times \left(\frac{1}{2(p-q)+1}\right)^2 \left(\frac{1}{2(p-q)-1}\right)^2 \cdots \left(\frac{1}{3}\right)^2. \end{aligned} \tag{42}$$

As a result, the accuracy of $G^n_{\ell,\,m}$ cannot be held in $a < 4\lambda$. However, when the calculation precision is larger, the accuracy of $G^n_{\ell,\,m}$ can be held. The accuracy of A^n_m is almost held. Refer to [5] in detail.

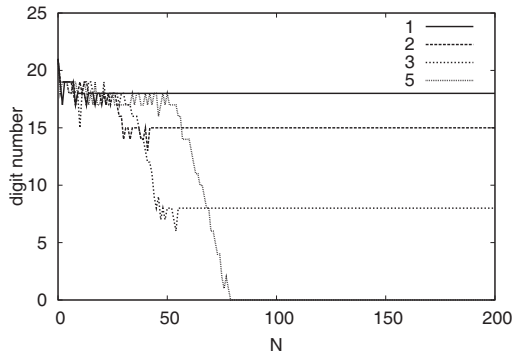

Figure 2: Digit number in which the two values, $g_1(p,\,q)$ with 64-bit precision and 512-bit, coinside with each other ($p = 0$, $q = 0$, $a/\lambda = 1,\,2,\,3,\,5$).

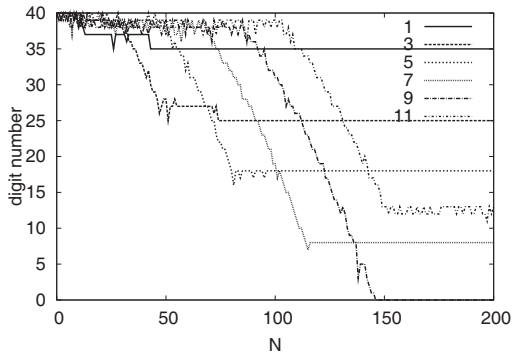

Figure 3: Digit number in which the two values, $g_1(p,\,q)$ with 128-bit precision and 512-bit, coinside with each other ($p = 0$, $q = 0$, $a/\lambda = 1,\,3,\,5,\,7,\,9,\,11$).

6. ANALYZING ACCURACY OF $G^N_{\ell,M}$

Calculation of $G^n_{\ell,m}$ is a major factor which causes poor accuracy. So, it's accuracy is discussed in detail.

Since g_1 and g_2 in Equaions (39) and (41) are infinite alternating series, it is expected that cancellation error occurs in these series. But g_1 and g_2 show similar tendency, we show the result only for g_1.

Each result in some precision is compared with that in 512-bit precision ($g_{1_{\text{512-bit}}}$). Fig. 2 shows the numerical result in 64-bit precision at $p = 0, q = 0, a/\lambda = 1, 2, 3, 5$. In this figure horizontal axis shows truncation number N, and vertical axis shows the digit number

$$-\log_{10}\left|\frac{g_{1_{\text{64-bit}}} - g_{1_{\text{512-bit}}}}{g_{1_{\text{512-bit}}}}\right|,$$

which corresponds to an accuracy. The figure shows that, as a/λ grows larger, the accuracy of $g_{1_{\text{64-bit}}}$ becomes 0 without convergence.

Figure 3 shows the results with 128-bit precision. As a result, accuracy of 15 decimal digits are obtained in 512-bit precision for $a/\lambda = 7$.

7. CONCLUSION

In this paper, we investigated the cause of the faulty result in the numerical calculation of the diffracted electromagnetic waves by a circular disk of perfect conductor using GMP library. When radius of the disk is more than 3 wavelengths, one of the reasons of the faulty results was the low precision of $G^n_{\ell,m}$. As a result, good results are obtained using the multiple precision arithmetic.

REFERENCES

1. Nomura, Y. and S. Katsura, "Diffraction of electormagnetic waves by circular plate and circular hole," *Journal of the Physical Society of Japan*, Vol. 10, No. 4, 285–304, 1955.
2. Ando, M., T. Murasaki, and T. Kinoshita, "Elimination of false singula rities in GTD equivalent edge currents," *Proc. IEEE*, Vol. H-138, No. 4, 289–296, 1991.
3. "GNU MP — The GNU multiple precision arithmetic library," Edition 4.2.1, 2006.
4. "MPFR — The multiple precision floating-point reliable library," Edition 2.2.0, 2005.
5. Kuroki, T., T. Kinoshita, T. Shibazaki, and I. Matsuda, "Numerical calculation of diffractive electromagnetic waves using circular disc of perfect conductor by mutiple precision arithmetic," *The Paper of Technical Meeting on Electormagnetic Theory*, 85–90, EMT-07-95, IEE Japan, 2007.

Comparison of Optical Pulse Propagation in Water and Acetonitrile

Marc Currie
Naval Research Laboratory, USA

Abstract— Optical propagation in water has been studied primarily by light sources that have either a constant amplitude in time or have a modulated temporal width greater than a picosecond. Attenuation of light as it propagates through water has been experimentally measured throughout the optical spectrum with these light sources. Quantities such as absorption and scattering have been thoroughly characterized as a function of wavelength of light. Yet with this wealth of measurements, a model that describes the transparency of water in the visible region still does not exist. The reason has been attributed to the complexity in understanding the hydrogen bonding that occurs in water [1].

Recently, an experimental study challenged the well established empirical knowledge of attenuation in water at near-infrared wavelengths. The study examined propagation of ultrafast optical pulses in water and demonstrated increased transmission of ultrafast light pulses as compared to longer pulses or cw light [2]. In these experiments, pulses as short as 60 fs with a center wavelength of 800 nm were propagated through as much as 6 meters of water. To explain their observations, the authors suggested the possibility of light propagation by optical precursors. The question is: How and why were the optical precursors stimulated in the water?

To better understand the propagation of ultrafast pulses of light in water, as demonstrated by Fox and Österberg [2], we will compare measurements in water with those in acetonitrile. Both water and acetonitrile are polar solvents, but water molecules exhibit hydrogen bonding while acetonitrile molecules do not. In addition, this study will compare the differences of the OH bond in water with the CH bond in acetonitrile. Harmonics of these molecular stretching frequencies in the near-infrared region are explored with a femtosecond laser system.

1. INTRODUCTION

Optical properties of water as well as optical propagation in water has been well studied. Femtosecond pulse propagation in water, however, is a field that has not been fully explored. Recent experiments by Choi and Österberg [3] and Fox and Österberg [2] have demonstrated optical pulse propagation with power transmssion in excess of the well known Beer-Lambert law (i.e., exponential decay). The authors explain their findings with a theory that exists only for sufficiently fast transients, namely optically excited Brillouin and/or Sommerfeld precursors.

Optically generated precursors is a field with a fair number of theoretic papers (for a brief review with references see Ref. [4]), but only a handful of experimental papers [2, 3, 5–7]. Of these, the works by Aaviksoo et al. [5] and by Sakai et al. [6] are in solids while that of Jeong et al. [7] is in cold potassium gas. This leaves the work of Choi and Österberg [3] and Fox and Österberg [2] as the experimental work in liquids, and more specifically, experiments in water.

Historically, the description of transient pulse propagation in dielectrics has followed two different paths. The early results by Sommerfeld and Brillouin used classical physics and a linear description of the interaction between radiation and matter [8]. Crisp investigated pulsed light propagation through resonant media revealed a new theoretical twist on Brillouin's precursors [9].

A Brillouin precursor is excited in a dielectric material whose response time is longer than the rise-time of an incident rectangular electromagnetic (EM) pulse. The EM pulse rapidly evolves into a pair of leading- and trailing-edge Brillouin precursors that increase monotonically with propagation distance [10].

Crisp's small-area pulse is short compared to the medium's dielectric dephasing time, T_2. Upon interacting with the medium the pulse will change its shape so that its pulse area decays exponentially (as predicted by Beer's law) while its energy decays more slowly due to the pulse reshaping.

One could apply Crisp's theory of small-area pulse propagation to the studies of Choi and Österberg [3] and Fox and Österberg [2]. If this is true several further questions arise: why does this depend on the repetition rate of the pulses? How are the optical precursors generated in water? Does the generation mechanism require an absorption resonance in water?

Since water is the material under study, it is possible that the effects are due to hydrogen bonding. The hydrogen bond attraction in water moves molecules closer together and forms an

electrostatic-type attraction between them (as opposed to the covalent O-H bond of the water). Water (as a liquid) is one of the densest hydrogen bonding solvents, and as such many of its properties are often attributed to its hydrogen bonding. A compendium of information on the chemistry water is maintained by Martin Chaplin (see http://www.lsbu.ac.uk/water/).

In this paper, water is compared with acetonitrile. Both are polar liquids, but while water is a protic solvent (hydrogen bonding), acetonitrile is an aprotic solvent (non-hydrogen bonding). Both structures are probed at a second harmonic absorption resonance. For water the second harmonic of the OH-stretch (1450 nm) is examined, and in acetonitrile the second harmonic of the asymmetric CH-stretch (1680 nm) is explored.

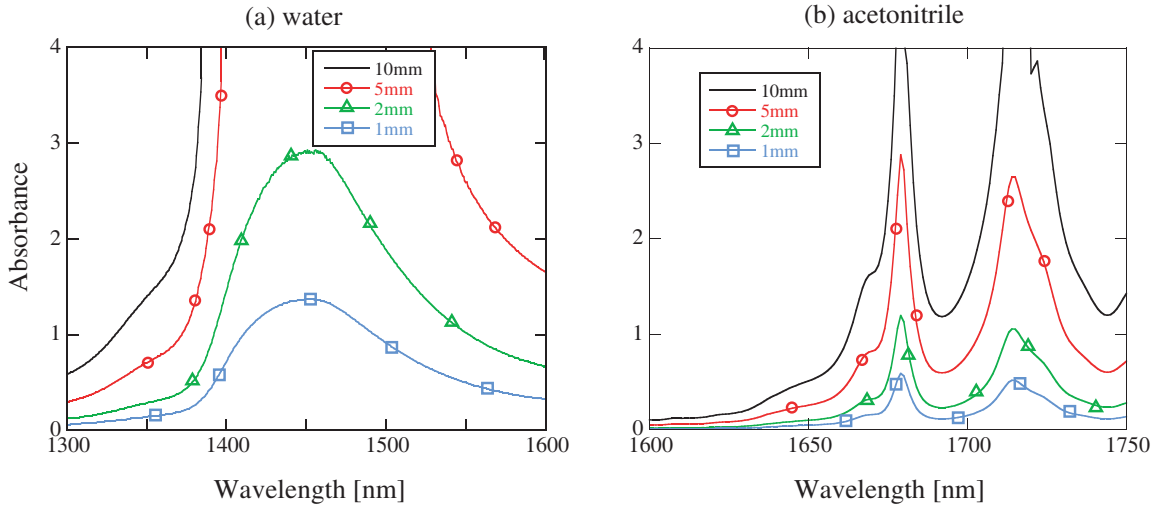

Figure 1: NIR spectra of (a) water and (b) acetonitrile.

2. EXPERIMENTS

Rectangular Spectrocell NIR cuvettes of 1, 2, 5, 10-mm widths were filled with the solvents. A Cary 5G spectrophotometer was used to characterize the cw absorption of the two liquids. Figure 1 shows the absorbance of the samples. Note the peak absorption values for the thicker cells are limited by the dynamic range of the instrument. The data show a strong OH resonance in the water centered at 1455 nm with a 73-nm full-width at half maximum (FWHM). The acetonitrile CH resonance is located at 1679 nm and has a much smaller width, < 8 nm FWHM.

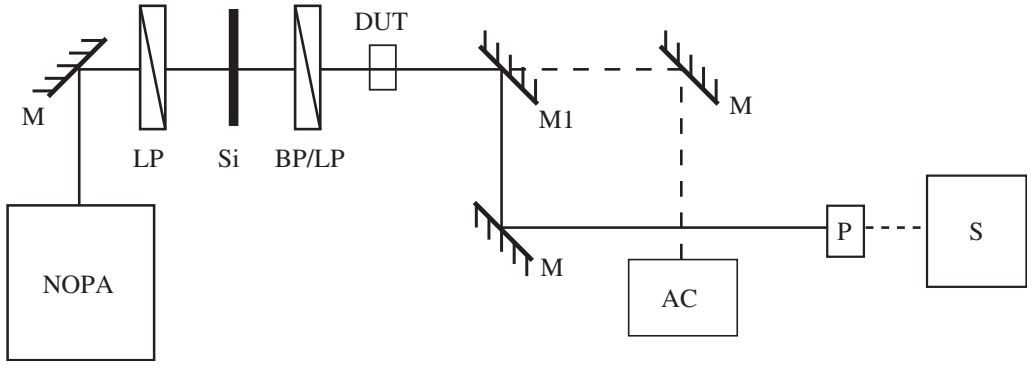

Figure 2: Experimental setup: NOPA laser with long-pass (LP) and bandpass (BP) filters, silicon wafer (Si), sample (DUT), mirrors (M, M1), autocorrelator (AC), photodetector head (P), and spectrometer (S).

An optical parametric amplification laser system (Clark NOPA) with a 970-Hz repetition rate was tuned to achieve femtosecond pulses in the NIR at 1450- and 1680-nm center wavelengths. Pulse energies of $<$0.5-μJ were incident on the cuvette samples with a 4.6-mm, $1/e^2$ beam diameter. The laser system's 771-nm fundamental tone was blocked by an RG800 long-pass filter.

The residual white-light continuum from the laser was blocked with a 0.6-mm unintentionally doped Si wafer. This was followed by either a 85-nm bandpass filter at 1460 nm for the 1450-nm OH

resonance studies, or by a 1500-nm long-pass filter for the 1680-nm CH resonance studies. Without the filters the white-light continuum was observed after 10-100x attenuation of the main pulse by the sample. The filters were measured (by the Cary 5G) to have an extinction of $> 1:1000$ outside of the passband, allowing measurements over at least 5 orders of magnitude of attenuation.

The setup, as shown in Figure 2, sends the femtosecond pulses through the samples and then to either an autocorrelator, a spectrometer, or a photodetector. Swinging the photodetector out of the way allows for a spectral measurement, while removing mirror M1 allows for an autocorrelation measurement.

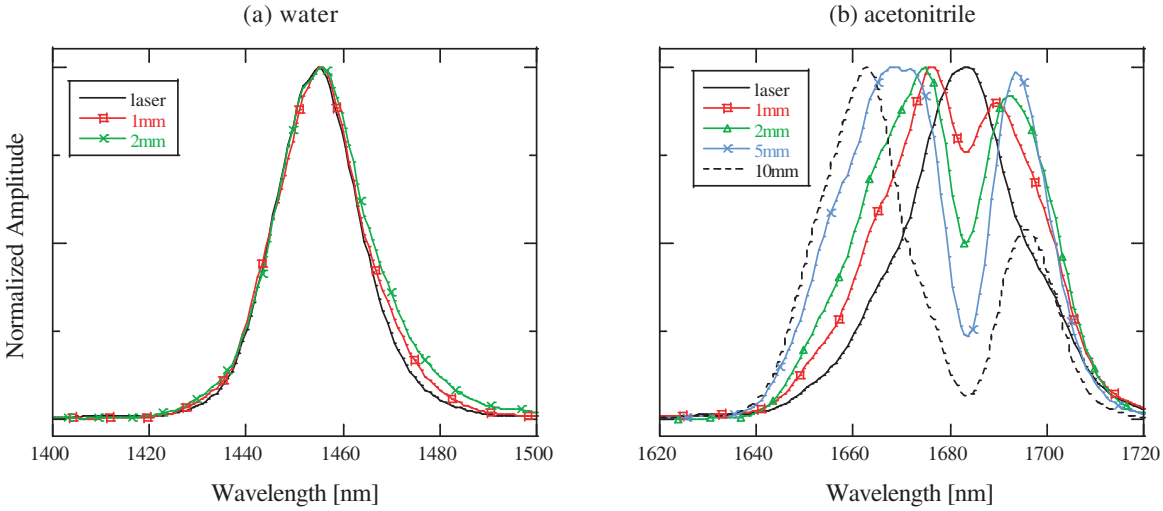

Figure 3: Spectra of the laser pulse before and after propagation in (a) water and (b) acetonitrile.

3. RESULTS

The spectra for the pulse propagation in water and acetonitrile samples are shown in Figure 3 as recorded by a StellarNet InGaAs spectrometer. The water absorption data in Figure 3(a) shows nearly identical laser spectra after propagation through the 1- and 2-mm cuvettes of water. The data are normalized to the peak to facilitate comparison. Figure 3(b) shows the effect of the narrow CH resonance compared with the laser pulse. Here the central spectral region of the laser light is attenuated much more strongly than the light in the wings producing a different spectral structure after 10-mm of propagation.

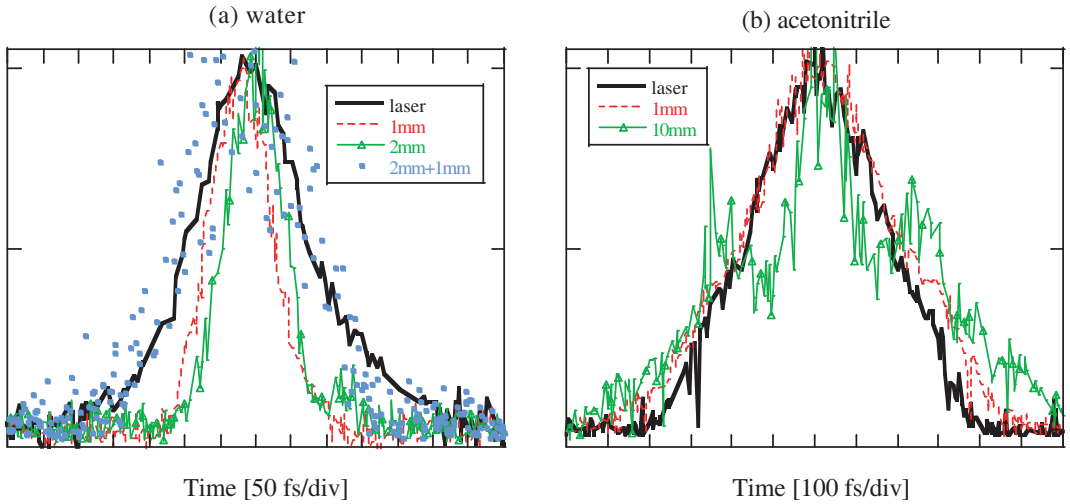

Figure 4: Autocorrelation of pulses before and after propagation in (a) water and (b) acetonitrile.

A Femtochrome FR103MN autocorrelator with a low-repetition rate option was used to record the pulse shape after propagation through the materials. Figure 4(a) shows the results for 1450-

nm pulse propagation in water. As the pulse progressed through the 1- and 2-mm water samples the pulse became shorter. The signal was too weak for a measurement after 5-mm, so the 1-mm cuvette was placed after the 2-mm cuvette to provide an additional propagation in water (labeled 2 mm+1 mm in figure). Although noisy, this quasi-3-mm propagation distance through water shows the pulse broadening to a width comparable to the laser input.

In Figure 4(b), the 1680-nm pulses probing the acetonitrile samples are wider. This is likely due to chirp from the NOPA which is tuned to the edge of its range. As the pulse propagates through more acetonitrile, the central portion narrows slightly while it broadens at its half width.

Finally, the transmitted optical power is measured with an optical power meter. The propagating pulse power spans several decades, requiring a linear detector over this range. Using carefully calibrated neutral density filters, a wide range of detectors were tested and the Ophir PD300-IR detector head was the most linear, and its range was suitable for this study. Power readings were taken with and without the input blocked. The average power along with the standard deviation of the power were recorded for each measurement. The data are plotted in Figure 5.

4. DISCUSSION

The data for both the water and acetonitrile experiments demonstrate Beer-Lambert absorption as shown in Figure 5. In water at low-light levels of 10^{-6}, the strong resonant absorption at 1450-nm with weaker off-resonance absorption allows measurement of the white-light continuum that leaks through the silicon and band-pass filters. This optical power level also coincides with the detection limit of our power meter.

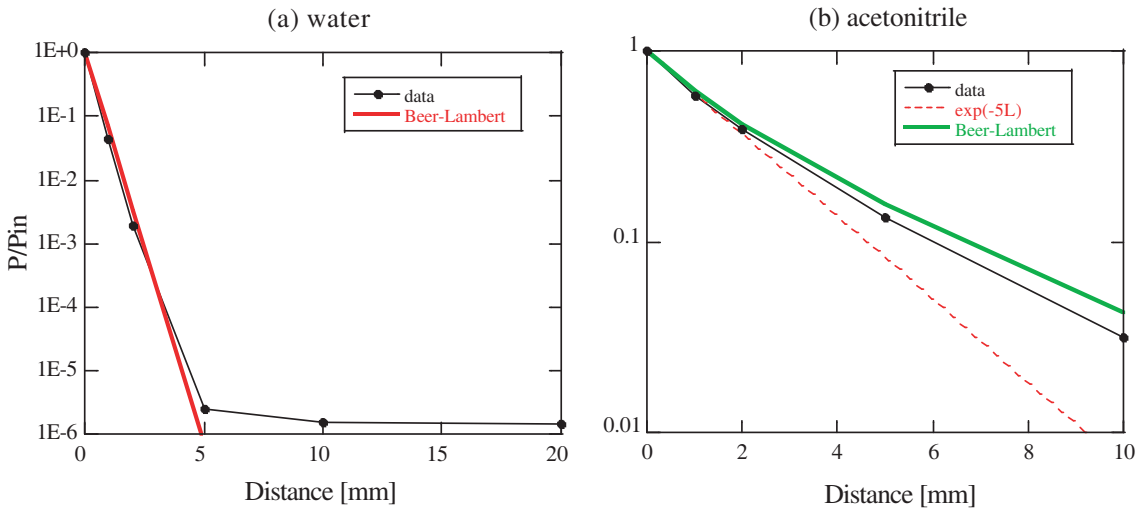

Figure 5: Optical transmitted power (normalized to the input power) after propagation in (a) water and (b) acetonitrile.

The broad optical bandwidth of the laser combined with the wavelength-dependent absorption of the media require calculation of the Beer-Lambert absorption curve in these wavelength regions, since a simple exponential function would only describe monochromatic light. These calculated Beer-Lambert curves provide a good fit the measured data.

A useful metric for comparison with other experiments in water is the ratio of the laser bandwidth to the resonance bandwidth. In the 1450 nm water experiments a ratio of $25/73 = 0.34$ is comparable to the 0.36 value of Fox and Österberg [2]. The 1680-nm acetonitrile experiments have a ratio of $25/8 = 3.13$ demonstrating a pulse spectrum that is significantly wider than the absorption resonance. Large spectral ratios match conditions in simulations of precursor generation.

The temporal width of the pulses, from the autocorrelation traces in Figure 4, are reported here as autocorrelated pulse widths, and unless otherwise stated have not been multiplied by a correction factor. Figure 4(a) shows that in water the laser pulse has an initial 175-fs pulsewidth. After propagating through 1- and 2-mm of water this pulse becomes compressed to 100 and 95 fs, respectively. Then after the quasi-3-mm propagation the pulse expands again to 200-fs.

The pulsewidths for 1- and 2-mm propagation are below the transform limit for a Gaussian pulse. The error could be due to experimental error in measuring the spectrum and the auto-

correlation. The autocorrelator time error is $\leq$10%, while the resolution of the spectrometer is 2-nm. Broadening the bandwidth and expanding the pulsewidth come close to accounting for the measurement anomaly.

The pulse compression via material dispersion does not entirely explain this effect. Several references have refractive index calculations for water and some have dispersion. However, these are either too coarsely spaced or do not include values near 1450 nm due to large absorption [11]. Using Segelstein's data [12], and fitting it in the 1450-nm region with polynomial functions provide solutions for dispersion of 0.4 fs/nm/mm. Using the same data and fitting in the 800-nm range produce a dispersion value of -0.17 fs/nm/mm, which is in good agreement with the reported values of -0.073 fs/nm/mm from Ref. [11], especially since water purity and temperature have not been taken into account. The 1450-nm calculated dispersion would not compress the pulses by nearly 100 fs, it is almost an order of magnitude too small. The glass cuvettes provide even less dispersion (by more than an order of magnitude) at these wavelengths, so they cannot account for the compression either. This demonstrates a need for better experimental dispersion characterization in this region.

The pulse temporal evolution in the acetonitrile is less dramatic. The 350-fs laser pulse is more strongly chirped, representing about a 250-fs Gaussian pulse. While not as short as the pulses in water, these pulses are shorter than that of the acetonitrile resonance, which is 270-fs wide assuming a 1679-nm Lorentzian resonance of 8-nm width (FWHM). The pulse shape remains nearly the same after 1- and 2-mm of propagation, but by 5- and 10-mm of propagation the central portion of the pulse has decreased to $<$ 200-fs but rests on a much wider pedestal which is indicative of the pulse evolution due to suppression of the central wavelengths.

5. CONCLUSION

The pulsed response of water and acetonitrile in the NIR range was investigated to explore the possibility of exciting optical precursors at absorption resonances in liquids. This study focussed on the NIR second harmonic resonances in the liquids as compared to that of Fox and Österberg [2] who operated near the fourth harmonic resonance. The laser bandwidth to water's absorption bandwidth of the two cases were similar (0.36 @800 nm [2] compared with 0.34 @1450 nm here), while that in acetonitrile was much larger (3.13 @1680 nm). While Beer-Lambert absorption was measured, the dynamic evolution of the pulse's temporal profile in water was not able to be explained at this time. This suggests the need for better measurement of water's dispersion in the 1400–1500 nm region. In addition, excitation with shorter (compressed) pulses along with better time-resolved pulse measurements will aid in better understanding of the correlation between the pulse's dynamic evolution and the material's response.

ACKNOWLEDGMENT

The author would like to thank G. Beadie, U. Österberg, A. Fox, N. Condon, J. Lou, and F. Bucholtz for valuable discussions. This work was supported by the Office of Naval Research.

REFERENCES

1. Tokmakoff, A., "Shining light on the rapidly evolving structure of water," *Science*, Vol. 317, 54–55, 2007.
2. Fox, A. E. and U. Österberg, "Observation of sub-exponential absorption of ultra-fast pulses in water," *Optics Express*, Vol. 14, 3688–3693, 2006.
3. Choi, S.-H. and U. Österberg, "Observation of optical precursors in water," *Phys. Rev. Lett.*, Vol. 92, 193903-1–193903-3, 2004.
4. Oughstun, K. E., *Electromagnetic and Optical Pulse Propagation 1*, Springer, New York, 2006.
5. Aaviksoo, J., J. Kuhl, and K. Ploog, "Observation of optical precursors at pulse propagation in GaAs," *Phys. Rev. A*, Vol. 44, R5353–R5356, 1991.
6. Sakai, M., R. Nakahara, J. Kawase, H. Kunugita, K. Ema, M. Nagai, and M. Kuwata-Gonokami, "Polariton pulse propagation at exciton resonance in CuCl: Polariton beat and optical precursor," *Phys. Rev. A*, Vol. 66, 333021–333024, 2002.
7. Jeong, H., A. M. C. Dawes, and D. J. Gauthier, "Direct observation of optical precursors in a region of anomalous dispersion," *Phys. Rev. Lett.*, Vol. 96, 143901-1–143901-4, 2006.
8. Brillouin, L., *Wave Propagation and Group Velocity*, Academic Press, New York, 1960.

9. Crisp, M. D., "Propagation of small-area pulses of coherent light through a resonant medium," *Phys. Rev. A*, Vol. 1, 1604–1611, 1970.
10. Oughstun, K. E., "Dynamical evolution of the Brillouin precursor in Rocard-Powles-Debye model dielectrics," *IEEE Transactions on Antennas and Propagation*, Vol. 53, 1582–1590, 2005.
11. Van Engen, A. G., S. A. Diddams, and T. S. Clement, "Dispersion measurements of water with white-light interferometry," *Applied Optics*, Vol. 37, 5679–5686, 1998.
12. Segelstein, D. J., "The complex refractive index of water," Ph.D. Thesis, Department of Physics, University of Missouri-Kansas City, 1981.

Precursors and Broadband Beer's Law: A Discussion on Sub-exponential Decay of Ultrafast Pulses in Water

David Lukofsky, **Heejeong Jeong**, **Jonathan Bessette**, **and Ulf Österberg**
Dartmouth College, USA

Abstract— We present a qualitative description of the precursor phenomena to place their existence in the context of a practical application. We assert that precursors are nothing more than the time-domain representation of a linear broadband Beer's law. We support this description with absorption measurements of femtosecond pulses through 7 meters of water, and suggest that further deviations from Beer's law in water may be observed due to saturation effects.

1. INTRODUCTION

The theoretical investigation launched by Brillouin and Sommerfeld in 1914 on precursor waveforms recently raised excitement about the possibility of using them for efficient radar systems or for efficient transmission of optical signals through absorptive media [1–3]. Indeed, Brillouin showed that the rate at which the energy of a monochromatic signal is absorbed in a single-resonance medium differs depending on whether the monochromatic signal is infinitely long in time or truncated with a step function. While the infinitely long signal attenuates after only a few absorption lengths, Brillouin showed that the truncated one contains a significant amount of energy even after many absorption lengths. The waveforms associated with the surviving energy were named precursors [4]. The basic requirement for exciting these precursors is for the pulse duration $\Delta\tau$ to be on the order of the inverse of the medium's linewidth.

In this paper we link the theory of precursors with their potential for use in a practical application, such as underwater communication or medical imaging. We do so by circumventing the more involved mathematics present in Brillouin's work, and instead explain their origin with a straightforward qualitative approach. We show that precursors are a manifestation of a time-domain representation of a broadband Beer's absorption law. We then support this claim by explaining experimental data of absorption measurements involving the transmission of femtosecond pulses through 7 meters of water. We conclude by presenting the opportunity for future work to suggest that deviations from Beer's absorption law may occur as a result of coherent and incoherent saturation effects.

2. THE UNDERLYING ASSUMPTION TO THE PRECURSOR DESCRIPTION

The description of precursors usually begins with the general linear wave propagation integral, Eq. (1), where $n(\omega)$ is the wavelength dependent complex refractive index of the medium. The waveform $E_{in}(0,t)$ in Brillouin's work is a sinusoidal signal with a rapidly rising edge.

$$E_{out}(z,t) = \int E_{in}(0,\omega)e^{jn(\omega)\omega z/c}e^{j\omega t}d\omega \tag{1}$$

The mathematics used to solve this integral analytically are somewhat involved, even for the case of a single-resonance medium, and different authors have resorted to different mathematical tools to find a solution. Brillouin himself in 1914 used the method of steepest descent by assuming a large propagation distance, yet it should also be possible to reach the same result with numerical methods and a computer.

Regardless of how the integral in Eq. (1) is computed, a key observation is that the equation is both linear and time-invariant with respect to the input field $E_{in}(0,t)$, which is a point that has been raised previously by Roberts [5]. In light of this, we choose not to solve the integral explicitly to avoid obscuring the physical implications of the precursor phenomena. Instead we present a qualitative description of precursors that exploits the important linear, time-invariant characteristics as effectively as the more involved mathematical methods. We will show that precursors are a result of a time-domain representation of a broadband Beer's absorption law.

3. QUALITATIVE DESCRIPTION OF PRECURSORS

Let us assume that the medium through which the pulse propagates is modeled with a single-Lorentzian function, Eq. (2)

$$n(\omega) = \left(1 + \frac{\omega_p^2}{\omega_o^2 - \omega^2 - i\omega\gamma}\right)^{1/2} \tag{2}$$

where ω_p is the plasma frequency, ω_o the resonant frequency and γ the damping factor. Fig. 1 plots the real and imaginary plot of the refractive index using the same parameters used by Brillouin in his original analysis: $\omega_p = 4.47 \times 10^{16}$ rad/s, $\omega_o = 4.0 \times 10^{16}$ rad/s and $\gamma = 0.28 \times 10^{16}$ rad/s [4].

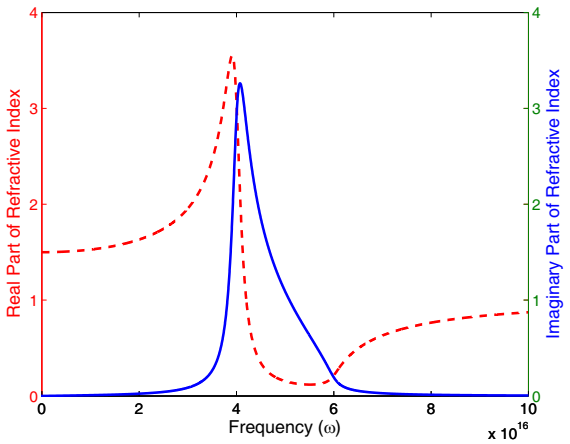

Figure 1: The line profile of the single-Lorentz medium defined by Brillouin. The solid line is related to absorption, while the dotted line is related to dispersion.

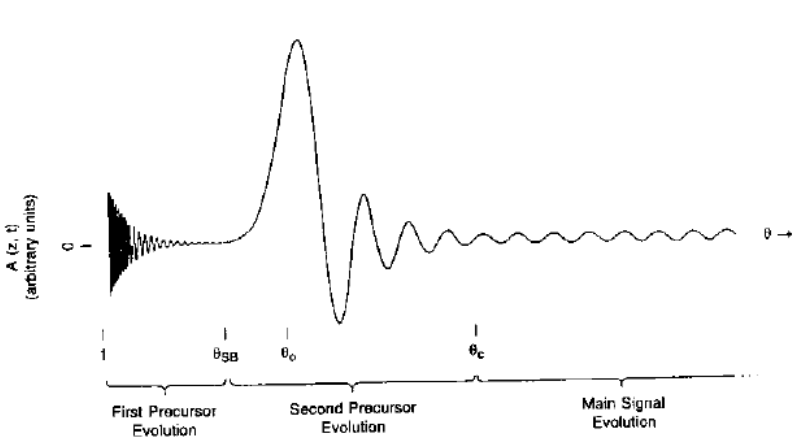

Figure 2: The location of the high frequency and low-frequency precursors in relation to the main signal [1].

Let us consider what happens when a pulsed light source has a spectrum that overlaps a large portion of the absorption profile of this medium. It is clear from the figure that the frequencies neighboring the medium resonance will be strongly absorbed (because of the large imaginary refractive index), while the off-resonance frequencies will attenuate less (because of the smaller imaginary refractive index). In addition, the off-resonance high frequency components will propagate the fastest as is indicated by the high group velocities (approaching the vacuum speed of light as frequencies approach infinity) with which they are associated. Though not as great as for high frequencies, the group velocities associated with the off-resonance low frequencies are greater than the group velocities of the on-resonance portion of the pulse spectrum, and so these low frequencies should also propagate faster than the resonant portion. After some propagation distance,

a broadband pulse whose spectrum spans the medium's resonance will break up into several distinct waveforms due to these propagation dynamics. The waveforms that arrive the quickest and attenuate the least are the precursors, Fig. 2.

It is worth commenting on the $1/z$ and $1/\sqrt{z}$ energy decay that is often interpreted as the indirect signature of the Brillouin and Sommerfeld precursor, respectively. These absorption functions arise from solving Eq. (1) for the specific case of a truncated sinusoidal function tuned to the frequency of a single-resonance medium. It should be possible to obtain different absorption functions associated with the low and high frequency precursors by considering the propagation of the same input signal in another single-resonance medium having a non-Lorentzian line profile, for example. In other words, the $1/z$ and $1/\sqrt{z}$ decay associated with precursors are nothing more than the leading terms of a power expansion of a linear broadband Beer's law discussed in more detail by Gibson and Österberg [6].

Therefore it is acceptable to extend Brillouin's precursor formalism to media having more complex resonance structures, such as water or any other inhomogeneously broadened media. The hurdle of course is to solve Eq. (1) analytically, yet precursors do exist as long as the spectral energy of a pulsed signal overlaps a medium resonance. Fig. 3 shows the absorption profile of water in the visible regime with a circle highlighting one of water's vibrational overtone resonances that could give rise to precursor behavior.

4. ABSORPTION OF FEMTOSECOND PULSES IN WATER

Path dependent absorption measurements of femtosecond pulses in water were completed to put the theory presented above in an experimental context. Length-dependant absorption measurements were done with a multipass cell based on the laser resonator geometry proposed by Herriott [8]. Two concave mirrors facing each other were separated by a distance that was varied to obtain paths of different absorption lengths, Fig. 4. The laser pulses were generated with a tunable Spectra Physics Ti: Saphire MaiTai laser unit. We scanned the 730-nm to 840-nm region in 5-nm increments, and payed extra attention to the 739-nm and 840-nm wavelengths to coincide with the vibrational overtones of water at those wavelengths [9]. The laser pulse widths ranged from 80 to 120 fs as a result of the inherent linewidth of the Ti: Saphire crystal.

The normalized Energy-vs-Distance plots from these experiments are shown in Fig. 5. The solid lines are the expected absorption function based on monochromatic Beer's law, that is the monochromatic decay stemming from absorption of the center wavelength only. The dots are the mean of the measured data. Thus, it is clear that deviations from *monochromatic* Beer's law do occur at 735-nm, 739-nm, 820-nm and 840-nm. Yet this is a result of the wavelength dependent absorption coefficient of water. Although pulses at all wavelengths have a rather large bandwidth (8–12 nm), the deviation due to the wavelength dependance of the absorption coefficient is exacerbated for wavelengths neighboring resonances because of the stronger *derivative* of the absorption coefficient of water near those wavelengths, Fig. 3.

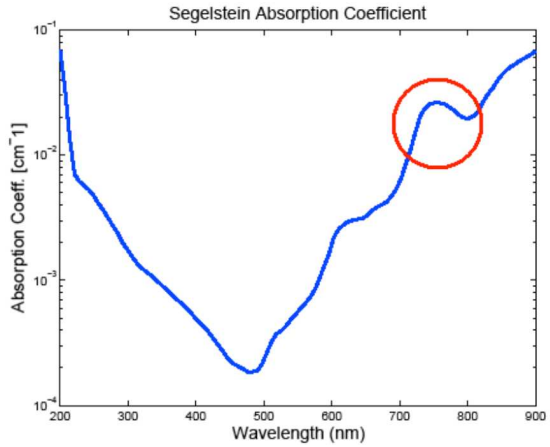

Figure 3: The absorption coefficients of water [7]. The circle indicates a region where precursors could be generated and potentially measured.

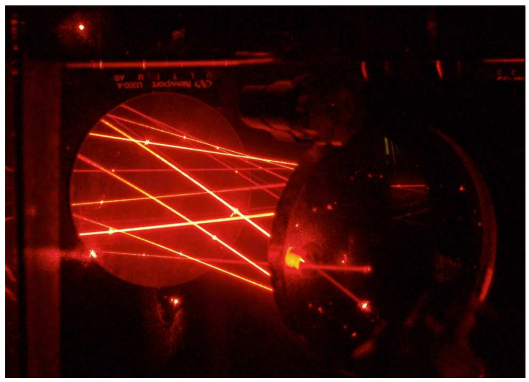

Figure 4: A long-exposure photograph of an absorption measurement with a HeNe laser to show path geometry of absorption cell.

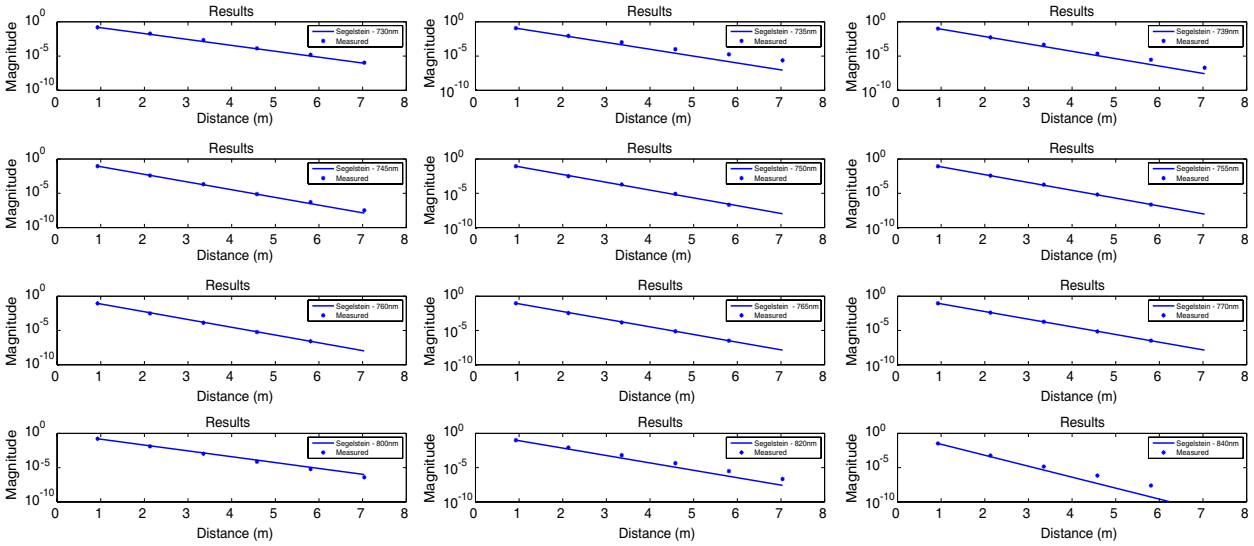

Figure 5: Absorption as a function of distance for femtosecond pulses at different wavelengths in pure water.

5. DISCUSSION AND FUTURE WORK

These results do not imply that further Beer law deviations — monochromatic or broadband — are unachievable in water since it could be possible to initiate coherent and incoherent non-linear *energy* effects in the medium. The experimental challenge in observing these is to create an input pulse with sufficient energy to initiate the energy bleaching effects, while still being below the thresholds for non-linear *intensity* effects such as Raman scattering and two-photon absorption. Preliminary calculations indicate that the threshold of incoherent bleaching is on the order of MW/cm^2 input power and that the one for coherent bleaching (the effect of self-induced transparency discussed by McCall and Hahn, [10]) is on the order of GW/cm^2. However, the onset of the effect of self-induced transparency involves rather stringent requirements concerning resonance strength and resonance placement with respect to other medium resonances. Thus, if self-induced transparency were to be observed in water, it might be most fruitful to focus on investigating the well defined absorption peak associated with the fundamental vibrational resonance at 1.3 µm. This could seem as counter-intuitive, although going to a highly-absorbing wavelength might be necessary to observe complete transparency.

6. CONCLUSION

This paper provided a qualitative understanding of the precursor phenomena, and highlighted that precursors stem from the time-domain representation of broadband Beer's law. This implies that in the linear regime, in which the phenomenom of precursors is included, optimal transmission is achieved by placing the signal's energy at the medium's least absorptive wavelength. We presented absorption measurements of femtosecond pulses propagating through 7 meters of water and showed that monochromatic Beer law deviation occurs as a result of the broad bandwidth of these pulses. We concluded by proposing that deviations from broadband Beer's law might still occur as a result of bleaching effects.

ACKNOWLEDGMENT

We gratefully acknowledge the financial support of NIST through grant # 60NANB4D1142. We are also grateful for helpful discussions with Professor Elsa Garmire at the onset of this investigation.

REFERENCES

1. Griffiths, H. D., C. J. Baker, A. Fernandez, J. B. Davies, and A. L. Cullen, "Use and application of precursor waveforms," *1st EMRS DTC Technical Conference*, 2004.
2. Olson, T., "Precursor-based HRR for foliage penetration: A 10–14 dB win," in *AFOSR Electromagnetics Workshop*, San Antonio, January 2004.
3. Choi, S. and U. L. Osterberg, "Observation of optical precursors in water," *Phys. Rev. Lett.*, Vol. 92, No. 19, 2004.

4. Brillouin, L., *Wave Propagation and Group Velocity*, Academic Press, 1960.
5. Roberts, T. M., "Radiated pulses decay exponentially in materials in the far field of antennas," *Electron. Lett.*, Vol. 38, No. 14, 2002.
6. Gibson, U. J. and U. L. Osterberg, "Optical precursors and Beer's law violations; non-exponential propagation losses in water," *Opt. Express*, Vol. 13, No. 6, 2005.
7. Segelstein, D. J., "The complex refractive index of water," Master's thesis, University of Missouri-Kansas City, 1981.
8. Herriott, D., K. Kogelnik, and R. Kompfner, "Off-axis paths in spherical mirror interferometers," *Appl. Opt.*, Vol. 3, No. 4, 1964.
9. Thomas, M. E., *Optical Propagation in Linear Media*, Oxford University Press, 2006.
10. McCall, S. L. and E. L. Hahn, "Self-induced transparency by pulsed coherent light," *Phys. Rev. Lett.*, Vol. 18, No. 908, 1967.

Ultrawideband Dispersive Pulse Propagation in Double-resonance Lorentz Model Dielectrics

K. E. Oughstun
College of Engineering & Mathematical Sciences, University of Vermont, USA

Abstract— The asymptotic description of ultrawideband electromagnetic pulse propagation in a double resonance Lorentz model dielectric is presented. Previously published results have shown that the inclusion of an additional resonance line results in the conditional appearance of an intermediate frequency precursor field in addition to the high-frequency Sommerfeld and low-frequency Brillouin precursor fields described in the classical and modern asymptotic theories. These results are extended through a careful examination of the middle saddle point dynamics and their corresponding asymptotic contribution to the middle precursor field.

1. INTRODUCTION

The propagation of an ultrawideband electromagnetic pulse through a linear, dispersive dielectric described by the Lorentz model with two isolated resonance frequencies is presented in the context of the classical [1–3] and modern asymptotic theories [4]. Previously published results [5] have shown that the inclusion of an additional resonance feature in the dispersive medium model resulted in the conditional appearance of a new, intermediate frequency precursor field in addition to the high-frequency Sommerfeld and low-frequency Brillouin precursor fields described in the classical and modern theories. A sufficient condition for the appearance of this middle precursor was also given [5] in terms of the energy transport velocity [6]. These results are extended in this paper through a careful examination of the saddle point dynamics. The importance of the middle saddle points is fully realized when the input pulse spectrum is situated in the passband between the two resonance frequencies, as typically occurs for optical pulses. In that case they provide the majority of the observed pulse distortion.

2. FORMULATION

The asymptotic theory of dispersive pulse propagation is based on the integral representation [1–4]

$$A(z,t) = \frac{1}{2\pi}\int_C \tilde{f}(\omega)e^{\frac{z}{c}\phi(\omega,\theta)}d\omega \tag{1}$$

for all $z \geq 0$, where $\tilde{f}(\omega)$ is the frequency spectrum of the initial plane wave pulse $A(0,t) = f(t)$. The contour of integration C is the path $\omega = \omega' + ia$ with a a constant greater than the abscissa of absolute convergence [4] for the function $f(t)$ and with $\omega' = \Re\{\omega\}$ varying from $-\infty$ to $+\infty$. The complex phase function $\phi(\omega,\theta)$ appearing in the integrand of Eq. (1) is given by [2–4]

$$\phi(\omega,\theta) = i\frac{c}{z}\left(\tilde{k}(\omega)z - \omega t\right) = i\omega\left(n(\omega) - \theta\right), \tag{2}$$

where $\tilde{k}(\omega) \equiv \beta(\omega) + i\alpha(\omega) \equiv (\omega/c)n(\omega)$ is the complex wave number in the linear dispersive dielectric with complex index of refraction $n(\omega) = \left(\mu\epsilon(\omega)\right)^{1/2}$ and relative magnetic permeability $\mu = 1$, and where $\theta \equiv ct/z$ is a dimensionless space-time parameter. The angular frequency dependence of the relative dielectric permittivity of a double-resonance Lorentz model dielectric is described by the causal relationship [4]

$$\epsilon(\omega) = 1 - \frac{b_0^2}{\omega^2 - \omega_0^2 + 2i\delta_0\omega} - \frac{b_2^2}{\omega^2 - \omega_2^2 + 2i\delta_2\omega}. \tag{3}$$

Here ω_j denotes the undamped angular resonance frequency, δ_j the phenomenological damping constant, and b_j the (angular) plasma frequency for the $j = 0, 2$ resonance lines.

The branch points for both $n(\omega)$ and $\phi(\omega,\theta)$ are given by the singularities of Eq. (3) as

$$\omega_\pm^{(0)} = \pm\sqrt{\omega_0^2 - \delta_0^2} - i\delta_0, \tag{4}$$

$$\omega_\pm^{(2)} = \pm\sqrt{\omega_2^2 - \delta_2^2} - i\delta_2, \tag{5}$$

and by the zeros of that equation, which are approximately given by

$$\omega_{\pm}^{(1)} \approx \pm\sqrt{\omega_1^2 - \delta_0^2 + \frac{\omega_3^4+2(\omega_1^2-\delta_0^2)\omega_3^2-b_0^2b_2^2+\delta_0^3}{\omega_1^2+\omega_3^2-2\delta_0^2}} - i\delta_0, \tag{6}$$

$$\omega_{\pm}^{(3)} \approx \pm\sqrt{\omega_3^2 - \delta_2^2 + \frac{\omega_1^4+2(\omega_3^2-\delta_2^2)\omega_3^2-b_0^2b_2^2+\delta_2^3}{\omega_1^2+\omega_3^2-2\delta_2^2}} - i\delta_2, \tag{7}$$

where $\omega_1 \equiv \sqrt{\omega_0^2 + b_0^2}$ and $\omega_3 \equiv \sqrt{\omega_2^2 + b_2^2}$. The branch cuts are then taken as the straight line segments $\omega_-^{(3)}\omega_-^{2)}$ and $\omega_-^{(1)}\omega_-^{0)}$ in the left-half plane and $\omega_+^{(0)}\omega_+^{(1)}$ and $\omega_+^{(2)}\omega_+^{(3)}$ in the right-half plane.

3. SADDLE POINT DYNAMICS AND THE ASYMPTOTIC DESCRIPTION

Consider the propagation of a rectangular envelope pulse $f(t) = u_T(t)\sin(\omega_c t)$ with pulse width T and fixed angular carrier frequency ω_c through a double resonance Lorentz model dielectric described by an infrared resonance ($\omega_0 = 1.7412 \times 10^{14} r/s$, $b_0 = 1.2155 \times 10^{14} r/s$, $\delta_0 = 4.955 \times 10^{13} r/s$) and a visible resonance ($\omega_2 = 9.1448\times10^{15} r/s$, $b_2 = 6.7198\times10^{15} r/s$, $\delta_2 = 1.434\times10^{15} r/s$). The dynamical evolution of the propagated pulse due to an initial single-cycle pulse ($T = 2\pi/\omega_c \approx 7.85 fs$) with angular carrier frequency $\omega_c = 8.0\times10^{14} r/s$ in the passband between the two resonance lines is illustrated in Fig. 1 at $z = 3z_d$ and in Fig. 2 at $z = 5z_d$, where $z_d \equiv \alpha^{-1}(\omega_c)$ is the e^{-1} absorption depth at the initial pulse carrier frequency. Each feature in the propagated pulse may then be traced back to the dynamical behavior of a particular saddle point (or points) of the complex phase function $\phi(\omega, \theta)$ [determined by the roots of $\phi'(\omega, \theta) = 0$] together with their interaction with the simple pole singularity at $\omega = \omega_c$, as described in the modern asymptotic theory [4].

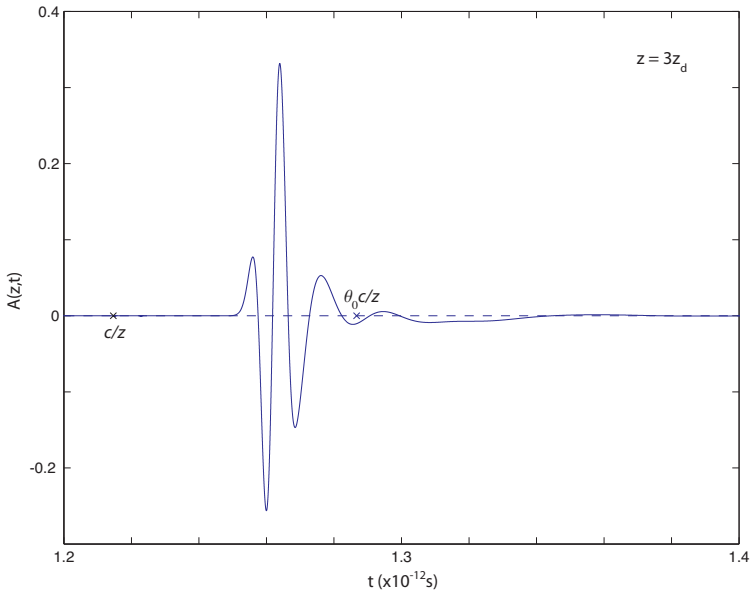

Figure 1: Single-cycle pulse evolution at 3 absorption depths with carrier frequency $\omega_c \in (\omega_1, \omega_2)$ in the passband between the infrared and visible resonance lines of a double-resonance Lorentz model dielectric. The point c/z marks the speed of light front.

Because the rectangular envelope pulse may be expressed as the time-delayed difference between two Heaviside step-function signals, the asymptotic description of the propagated wave field may be expressed as the time-delayed difference of the leading and trailing-edge wave-fields of the form

$$A(z,t) = A_s(z,t) + A_m(z,t) + A_b(z,t) + A_c(z,t), \tag{8}$$

the trailing-edge field delayed in time by the pulse width T after the leading-edge of the wave field. Here $A_c(z,t)$ describes the pole contribution, where the time-delayed difference of the leading- and trailing-edge pole contributions describe the undistorted rectangular envelope pulse with amplitude attenuated by the factor e^{-z/z_d}. The wave field component $A_s(z,t)$ is the Sommerfeld precursor

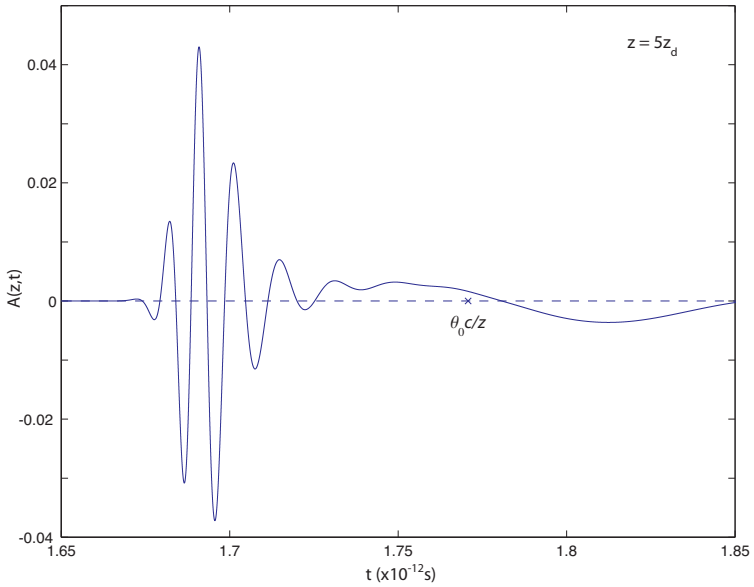

Figure 2: Single-cycle pulse evolution at 5 absorption depths in a double-resonance Lorentz model dielectric.

due to a symmetric pair of distant saddle points $SP_d^{\pm}$ whose dynamical evolution is given by

$$\omega_{SP_d^{\pm}}(\theta) \;=\; \pm\xi(\theta) - i(\delta_0+\delta_2)\big(1+\eta(\theta)\big), \tag{9}$$

$$\xi(\theta) \;\approx\; \sqrt{\omega_2^2 - \tfrac{1}{4}(\delta_0+\delta_2)^2 + \tfrac{\left(b_0^2+b_2^2\right)\theta^2}{\theta^2-1}}, \tag{10}$$

$$\eta(\theta) \;\approx\; \frac{b_0^2+b_2^2}{(\theta^2-1)\,\xi^2(\theta)}, \tag{11}$$

for all $\theta \geq 1$. These distant saddle points then move in from $\pm\infty - i(\delta_0+\delta_2)$ at $\theta = 1$ and approach the outer branch points $\omega_{\pm}^{(3)}$, respectively, as $\theta \to \infty$, giving rise to the Sommerfeld precursor's characteristic frequency down-chirp over the high-frequency domain above the upper absorption band of the medium [1–4]. The field component $A_b(z,t)$ appearing in Eq. (8) is the Brillouin precursor due to a pair of near saddle points $SP_n^{\pm}$ whose dynamical evolution is given by

$$\omega_{SP_n^{\pm}}(\theta) \;=\; \pm\psi(\theta) - \frac{2}{3}i\delta_0\zeta(\theta), \tag{12}$$

$$\psi(\theta) \;\approx\; \left[\frac{\omega_0^2(\theta^2-\theta_0^2)}{\theta^2-\theta_0^2+3\left(\frac{b_0^2}{\omega_0^2}+\frac{b_2^2\omega_0^4}{\omega_2^4}\right)} - \tfrac{4}{9}\delta_0^2\zeta^2(\theta)\right]^{1/2}, \tag{13}$$

$$\zeta(\theta) \;\approx\; \frac{3}{2}\frac{\theta^2-\theta_0^2+2\frac{b_0^2}{\omega_0^2}\left(1+\frac{\delta_2 b_2^2\omega_0^4}{\delta_0 b_0^2\omega_2^4}\right)}{\theta^2-\theta_0^2+3\frac{b_0^2}{\omega_0^2}\left(1+\frac{b_2^2\omega_0^4}{b_0^2\omega_2^4}\right)}, \tag{14}$$

for all $\theta > 1$. As θ increases over the space-time domain $(1,\theta_1]$, the pair of first-order near saddle points approach each other along the imaginary axis, coalescing into a single second-order saddle point point SP_n at

$$\omega_{SP_n}(\theta_1) \approx -i\frac{2\left(\delta_0 b_0^2\omega_2^4 + \delta_2 b_2^2\omega_0^4\right)}{3\left(b_0^2\omega_2^4 + b_2^2\omega_0^4\right)} \tag{15}$$

when $\theta = \theta_1$, where

$$\theta_1 \approx \theta_0 + \frac{2\left(\delta_0 b_0^2\omega_2^4 + \delta_2 b_2^2\omega_0^4\right)}{3\theta_0\omega_0^4\omega_2^4\left(b_0^2\omega_2^4 + b_2^2\omega_0^4\right)}, \tag{16}$$

with $\theta_0 \equiv n(0)$. The near saddle points then move apart symmetrically in the lower-half of the complex ω-plane as θ increases above θ_1, approaching the inner branch points $\omega_{\pm}^{(0)}$ as $\theta \to \infty$. This

dynamical evolution gives rise to the Brillouin precursor's characteristic frequency up-chirp over the low-frequency domain below the lower absorption band of the medium [1–4], which is clearly evident in Figs. 1–2 about the point $t = \theta_0 z/c$. Of particular importance to this field component is the zero exponential decay of the peak amplitude at $\theta = \theta_0$, the field amplitude decaying only as $z^{-1/2}$ at this space-time point [4]. Finally, the approximate dynamical evolution of the pair of middle saddle points SP^{+}_{mj} in the right-half of the complex ω-plane is found to be given by

$$\omega_{SP^{+}_{mj}}(\theta) \approx \frac{2}{3}\bar{\omega}_s + \frac{2\Omega_1}{3\Omega_2} + (-1)^j \left[\frac{(2\Omega_1 - \Omega_2\bar{\omega}_s)^2}{9\Omega_2^2} - \frac{2\bar{n}_s}{3\Omega_2}\left(\theta - \bar{\theta}_0\right) \right]^{1/2} \tag{17}$$

for $j = 1, 2$, where $\bar{\omega}_s \equiv \frac{1}{2}(\omega_0 + \omega_2)$ is the mean angular resonance frequency, $\bar{n}_s \equiv n(\bar{\omega}_s)$, and

$$\Omega_1 \equiv b_0^2 \frac{\bar{\omega}_s + i\delta_0}{\omega_\alpha^4} + b_2^2 \frac{\bar{\omega}_s + i\delta_2}{\omega_\beta^4}, \tag{18}$$

$$\Omega_2 \equiv \frac{b_0^2}{\omega_\alpha^4}\left(4\frac{(\bar{\omega}_s + i\delta_0)^2}{\omega_\alpha^2} - 1\right) + \frac{b_2^2}{\omega_\beta^4}\left(4\frac{(\bar{\omega}_s + i\delta_2)^2}{\omega_\beta^2} - 1\right) + \frac{\Omega_1^2}{\bar{n}_s}, \tag{19}$$

where $\omega_\alpha^2 \equiv \bar{\omega}_s^2 - \omega_0^2 + 2i\delta_0\bar{\omega}_s$ and $\omega_\beta^2 \equiv \bar{\omega}_s^2 - \omega_2^2 + 2i\delta_2\bar{\omega}_s$. The middle saddle point locations in the left-half plane are given by $\omega_{SP^{-}_{mj}}(\theta) = -\omega^*_{SP^{+}_{mj}}(\theta)$. Although these expressions provide just a first-order approximation of the middle saddle point dynamics in the intermediate frequency domain between the two resonance frequencies, they do show their complicated evolution with θ. Numerically determined middle saddle point dynamics show that the upper middle saddle point SP^{+}_{m1} approaches the upper branch point $\omega_+^{(1)}$ of the lower resonance line while the lower middle saddle point SP^{+}_{m2} approaches the lower branch point $\omega_+^{(2)}$ of the upper resonance line as $\theta \to \infty$. The interaction of their complicated θ-evolution with the pole contribution at $\omega = \omega_c$ produces the resultant leading- and trailing edge pulse distortion depicted in Figs. 1–2.

4. DISCUSSION

For an ultrawideband pulse with spectrum centered in the passband between two resonance lines of a Lorentz-type dielectric, the majority of the observed pulse distortion is found to be due to the middle precursor. Indeed, it is this middle precursor that is coincidentally described in the group velocity approximation. However, as the propagation distance increases, the Brillouin precursor will become increasingly important and will increasingly influence the temporal pulse structure.

ACKNOWLEDGMENT

The research presented in this paper was supported, in part, by the United States Air Force Office of Scientific Research under Grant #9550-04-1-0447.

REFERENCES

1. Sommerfeld, A., "Über die fortpflanzung des lichtes in disperdierenden medien," *Ann. Phys.*, Vol. 44, 177–202, 1914.
2. Brillouin, L., "Über die fortpflanzung des licht in disperdierenden medien," *Ann. Phys.*, Vol. 44, 203–240, 1914.
3. Brillouin, L., *Wave Propagation and Group Velocity*, Academic Press, New York, 1960.
4. Oughstun, K. E. and G. C. Sherman, *Electromagnetic Pulse Propagation in Causal Dielectrics*, Springer-Verlag, Berlin-Heidelberg, 1994.
5. Shen, S. and K. E. Oughstun, "Dispersive pulse propagation in a double-resonance Lorentz medium," *J. Opt. Soc. Am. B*, Vol. 6, No. 5, 948–963, 1989.
6. Oughstun, K. E. and S. Shen, "The velocity of energy transport for a time-harmonic field in a multiple resonance Lorentz medium," *J. Opt. Soc. Am. B*, Vol. 5, No. 11, 2395–2398, 1988.

Conception and Realization of the Manual and Programmable Command of Stimulating Electric Muscular

S. Bri[1] **and L. Zenkouar**[2]

[1]Microwave and Materials Group, ESTM, B. P. 3103, Meknès, Maroc
[2]Electronics and Telecommunications Laboratory, EMI, B. P. 765, Rabat, Maroc

Abstract— The objective of this work is to propose a reliable solution allowing restoring deficient functions of the nervous system. This solution passes by an artificial control of certain nervous information in the human body. The objective of the works presented in this paper is to propose a circuit of electric stimulation allowing the contraction of the muscle to restore its function by the generation of an electric signal. Its basic principle rests on the generation of more or less wide impulses and very specific frequency. This solution avoids a habituation of the muscle, an unwanted coetaneous ionization or a polarization of the metal prostheses.

1. INTRODUCTION

Certain disturbances, damages or damages of the chain of command (nerve centre/nerve/muscle) can pull a dysfunction of the nervous system. This last one can be the cause of numerous pathologies (Parkinson's disease, paraplegia, tetraplegia, hemiplegia, deep deafness, etc.). Most of these pathologies cannot be regrettably treated by a classic therapy (medicinal, surgical) [1–5].

However, in the case of a pathology bound to a dysfunction of the nervous system, there is an alternative solution which consists in applying an impulse of electric current to the nervous structures in cause. This technique, called Functional Electric Stimulation (FES). The basic architecture of the restoration of a function includes a block of command, a logical sequencer and a floor of exit which supplies the currents of stimulation in nerves or in muscles via electrodes.

In this paper, we present the conception and the realization of stimulating electric, based on the clock, then the assembly of the logical sequencer which allows to generate two tensions of exit moved certain values, these last ones will be amplified by means of a floor of power commanded by a circuit which allows the regulation of the amplitude with manual or programmable possibility.

2. PRINCIPE OF THE FUNCTIONAL ELECTRIC STIMULATION

One of the main problems of the diseases or the accidents getting the nervous system comes because the important hurts within GENERAL PARTNERSHIP cannot regenerate. Therefore, in the case of a modularly wound for example, any communication enters GENERAL PARTNERSHIP and muscles commanded by nerves rooted on the column below the hurt is impossible and muscles are paralyzed [6–9]. The principle of the rehabilitation by SEF thus consists in activating muscles by stimulating the driving nerves by means of stimulating one electric (Figure 1).

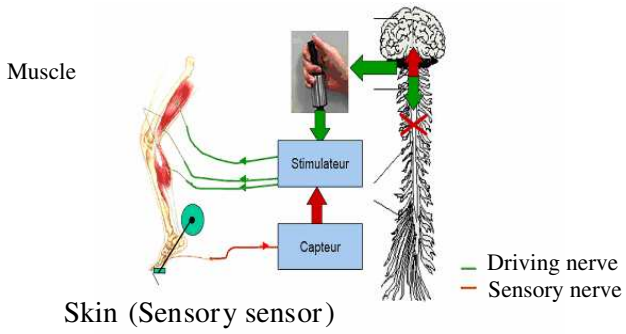

Figure 1: Rehabilitation of the driving function of lower limbs of modularly injured person.

The answer of the muscle can be then observed, either in ravers of its mechanical answer, or its electric answer because the muscular cell is an irritable cell that generates too and propagates a potential of action. By applying an impulse of current to the driving nerve of a muscle, we provoke,

after a small latent period, the release of potential of action. The muscles contracts initially and slacken thereafter. One measures the response of the muscle by measuring the force produced by the contraction. During this phase, the force grows and, then, during the phase of relaxation, it decrease.

The signals have the same form, but the width of the impulses, frequency $F = 1/T$ as well as the amplitude are different. Muscular stimulation within the framework of the medical rehabilitation has an aim completely different from magnetotherapy RF. It is a question here of contracting a muscle, most of the time member, at ends of post-traumatic rehabilitation. This electric stimulation is also used on the paraplegic ones, for the prevention of the escarres. Energy necessary to fold a leg or an arm is definitely more important than that used in magnétothérapie RF. Times Tc, MT, td and tr correspond respectively to the time of contraction, maintenance, contraction and rest of the muscle.

3. PRESENTATION OF THE FUNCTIONAL DIAGRAM OF THE ELECTRIC STIMULATION

The functional diagram of simulating is given in Figure 2.

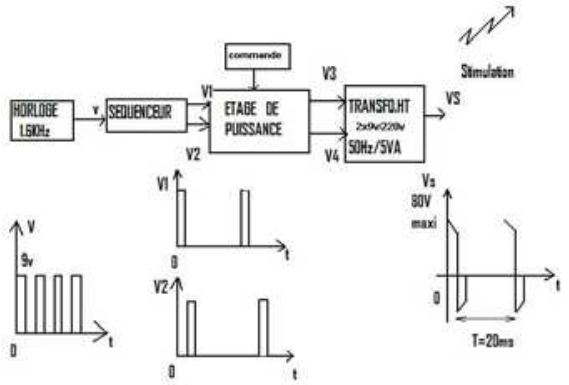

Figure 2: Functional of stimulating electric muscular.

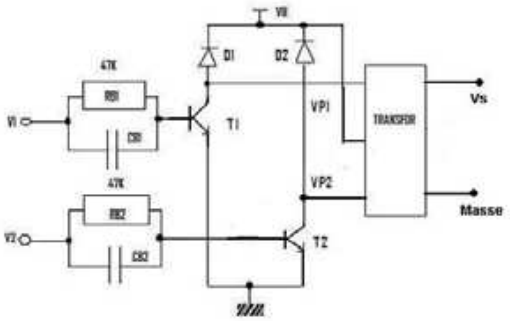

Figure 3: Plan of the floor power.

The Clock is based on the NE555 is an integrated circuit used as soon as the concept of time is important in an assembly. As it is cheap (approximately 0.5 Euro) and relatively simple of use, it is an integrated circuit "traditional" in electronics. One uses it in two basic assemblies: the monostable one and the astable. The logical sequencer allows, leaving the clock signal, to generate two signals $V1$ and $V2$ identical, but shifted in the time of period 20 ms. The bit $D0$ of the memory allows the restoring of counting when E numbers bytes of the form of wave is lower than 4.096. Seven only of the eight bits of the digitital/analogical are used. What represents 128 levels of tension ranging between 0 and 2, 56 V is increment of 20 mV. The period of the clock will be adjusted with 30 ms. The role of the stage of power and to amplify the power of stimulation output (Figure 3).

Two transistors of power, slightly erased, attack a traditional mains transformer turned over $220\,\mathrm{V}/2 * 9\,\mathrm{v}$. The exit high voltage of this transformer provides the impulses of stimulation. In sinusoidal mode, the report/ratio of transformation η with vacuum of this transformer is equal to 15. In impulse mode, this report/ratio is not any more but 10. If $VB = 8\,\mathrm{V}$ and $Vcesat = 0.2\,\mathrm{V}$, the output voltage will be equal to: $Vs = \eta.\ (VB - Vcesat)$ with $Vs\max = 10 * 7.8 \approx 80\,\mathrm{V}$. The transistors $T1$ and $T2$ function alternatively. The tensions with the primary education of transformer $VP1$ and $VP2$ are in opposition of phase, which makes it possible to obtain a signal of stimulation $Vs(t)$ of null average value. Condensers $CB1$ $CB2$ decrease the switching times of the transistors of powers. The diodes of free wheel $D1$ and $D2$ portaging these same transistors counter the tensions opposite due to the effect of self-service of the transformer. One can obviously use a transformer of lower power, in order to minimize the obstruction, but the performances of the system will be of them definitely decreased L' amplitude of the impulses of exit depends VB. To regulate the power of stimulation it is thus enough to vary VB.

4. PRACTICAL SOLUTION SUGGESTED OF ELECTRIC STIMULATION

After having presented the functional diagram of electric muscular stimulation, we will present his practical realization. This stimulation makes it possible to generate impulses of width 625 µs, period equal to 20 ms and adjustable amplitude. The clock makes it possible to regulate the frequency of the signal to the wanted value, all one fixing the values of resistances Ra and $P1$. The clock of the base of the assembly is provided by a circuit Timer NE555. The operation of the clock, in this solution of stimulation is equivalent to that of the preceding solution but here, on the outlet side of our clock we have a $V1$ signal of frequency 50 Hz and time of assembled equal to 625 µs. The period of oscillation T is equal to the sum of the duration of load of the condenser (Vc variable of 1/3 Valim with 2/3 Valim) and of the duration of discharge (Vc variable of 2/3 Valim with 1/3 Valim). $T = C\ Ln2.\ (R1 + 2\ R2)$; with T is independent of the supply voltage. The signals obtained will be following form (Figure 4).

The goal of this assembly is to provide to its exit a $V2$ signal, of the same amplitude, of the same period and especially of the same time to go up as $V1$ (Figure 5):

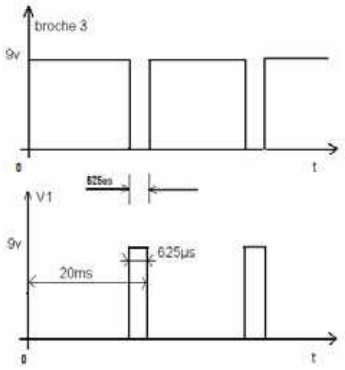

Figure 4: Signals at the output of the NE555 and $V1$.

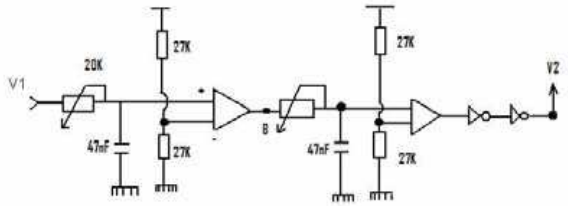

Figure 5: Logical sequencer.

The operation of the assembly is rather simple, $V1$ attacks the sequencer, when $V1$ is in a high state we have the load of the $C1$ condenser through $R1$ resistance, and when the load of the condenser reaches V, we have the swing of the first amplifier in a high state, the time of load of the condenser is thoroughly regulated by $R1$ resistance in such way to reach V with half of time of assembled of $V1$, the condenser will continue to undertake during other half of the time thus assembled until $V1$ falls to zero, there the discharge of the condenser will start, since it constant of load are, the tension has condensing will decrease until reaching V at a time equal to half time assembled. From where we will have at the point B a signal identical to $V1$ but shifted in the time of 312.5 µs which is equivalent to half of the time of assembled of $V1$. L operation is the same one for the second part of the assembly except here we will have signal at the point B which will be attacked and at the end us a $V2$ signal identical to that of the point B but will be shifted in the time of 312.5 µs, and thus the $V2$ signal will be shifted of 625 µs of $V1$ (Figure 6).

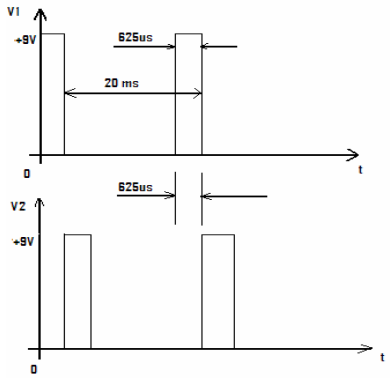

Figure 6: Tensions $V1$ and $V2$ (Input of the stimulating muscular).

The goal of the stage of power is of being able adapted the power of $V1$ and $V2$ to that necessary to inject with the transformer. By analyzing the assembly we note that each half winds transformer

can be regarded as impedances of the collectors as of the this two transistors, therefore when $V1$ or $V2$ is in a high state, that causes the saturation of the one of the transistors, by thus putting a half winds with the mass, and that produced on the outlet side of the transformer a signal of Vs stimulation of null average value and period 20 ms is the output voltage Vs of the transformer according to the report/ratio of transformation η and tension VB : $Vs = \eta\ (VB - Vcesat)$. From where, to regulate the amplitude of Vs, it is thus enough to vary VB, for that one has two possibilities, that is to say a hand drive operation or programmable.

4.1. Manual Command

One knows that the Vs tension of stimulation depends directly on VB; there therefore if one acts on VB, implicitly we act on Vs (Figure 7).

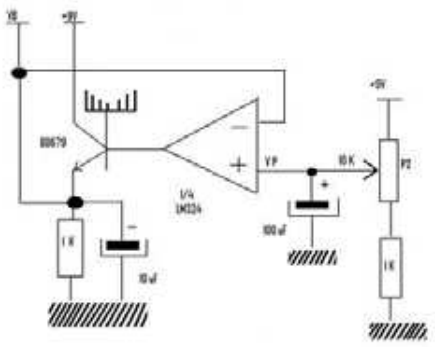

Figure 7: Floor of manual command.

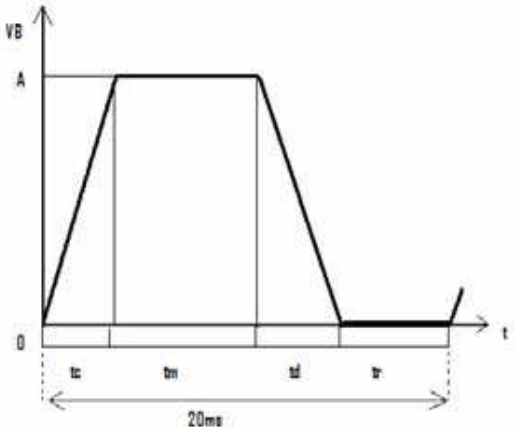

Figure 8: Shape of wave of the programmable command.

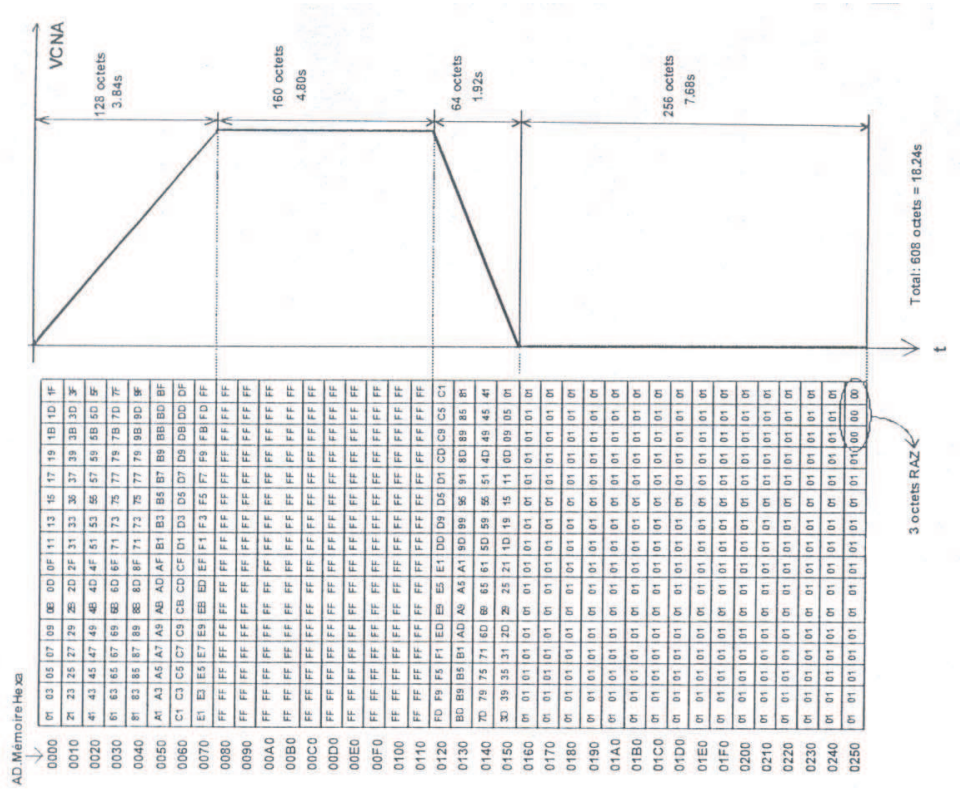

Figure 9: Programming of the shape of wave of the output signal Vs (t) given in Figure 8.

The terminal voltage of $e+$ will be varied using the potentiometer, this $V+$ tension, starting from properties of the amplifier, one can say that $V+$ equal to V, therefore equal to VB, which implies that any variation in tension of $V+$ is transmitted directly to VB, and the output current will come directly from the collector.

4.2. Programmable Command

Very often the meetings of electrotherapy are summarized with successions of muscular contractions with times of contraction (Tc), maintenance (MT), relaxation (td), and rest (tr) defined by the kinesitherapist. The number of meetings and their duration are defined by the medical profession. It is thus necessary to be able to generate a form of wave (Figure 8), whose times are programmable at will.

A clock of 33 Hz will allow, thanks to meter 12 bits, the addressing of a memory containing the bytes representing the form of desired wave. An analogical digitizer transforms these bytes into a tension which, by intermediary of a stage of power, will allow an automatic and programmable stimulation muscle. A muscular cycle of contraction will be represented to the maximum by 212 Octets is 4096 Octets. The period of the clock being of 30 µs the maximum time of a cycle will be equal to $t\max = 4096 * 30 * 10^{-3} = 124\,\text{Seconds} \approx 2\,\text{min}$. The use of a memory of 32 Ko will allow the programming of eight forms of different waves. The use of a memory of 32 KB will allow the programming of eight forms of different waves. One obtains thus the output signal VCNA on the outlet side of a numerical-analogical converter (Figure 9).

The electronic diagram of the programmable order is presented on Figure 10. The bit D0 of the memory allows the restoring of counting when the number of bytes of the form of wave is lower than 4096. Seven only of the eight bits of the analogical digitizer are used. What represents 128 niveaux tension ranging between 0 V and 2.56 V is an increment of 20 mV.

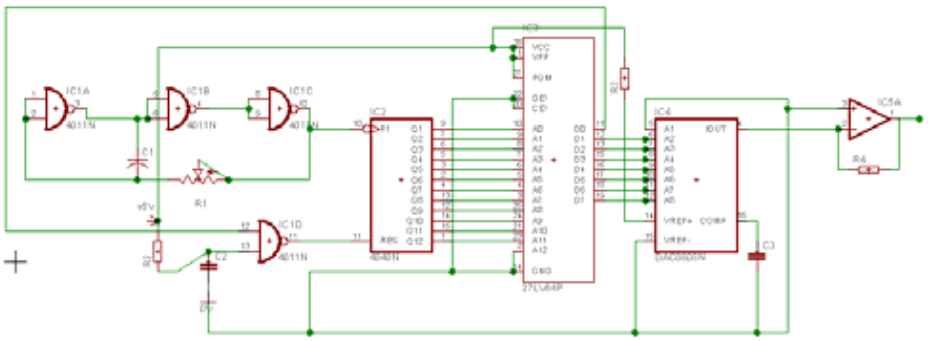

Figure 10: Electronic diagram of the programmable command.

The choice of a form of wave among eight is done by the intermediary of microphone-switches SW1. The period of the clock is adjusted with 30 ms. The maximum amplitude of stimulation remains adjustable in an analogical way by the operator using PG (Figure 11).

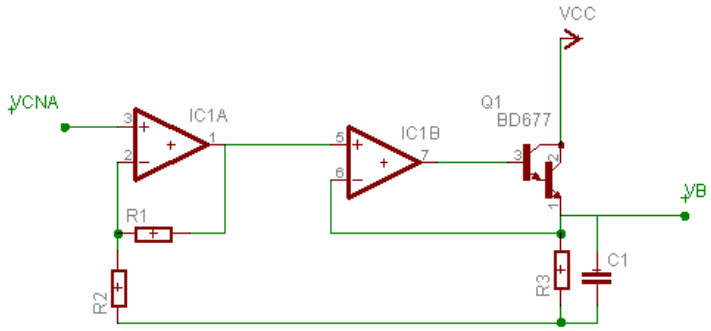

Figure 11: Stage power of programmable command.

Notice that you can never to make this stimulation on a food 220 V, but always on an autonomous food with pile or accumulator 9 V or 12 V. A system of refill must be envisaged in this case. Only an autonomous food guarantees a complete protection against electrification.

5. CONCLUSION

Functional Electric Stimulation (FES) one of the technological solutions is currently considered for the rehabilitation of certain functions among patients paraplegic. The techniques of (FES) make it possible to restore partially certain deficiencies of the nervous system due to an accident (medullar lesion) or a disease. The principle consists in emulating or inhibiting the nerve impulse on the level of the brain or the peripheral nerves. The natural nervous system is complex and it is very difficult artificially to reproduce natural functions with the same control. Indeed the stimulation electric ones become in constant evolution. A certain number of experiments on animals made it possible to validate new techniques of stimulation and to extend their field of application. There currently exists on the market or in the form of prototypes of research a rather great number of stimulation electric. Our work has as a finality to conceive the fourth class of the stimulation ones. This stimulation is based on a made up architecture: initially of a clock at base of the circuit Timer NE555 used as the clock at frequency $f = 1.6\,\mathrm{KHz}$,, the latter allows to adjust the frequency of the signal of stimulation according to the required treatment. The exit of the clock will be connected to the logical sequencer which will generate two identical signals, but shifted in the time of 625 µs and of period 20 ms and in end, so that these signals reach the high voltages one amplify them using a stage of power and a transformer in order to obtain only one signal of stimulation $Vs(t)$ of null average value.

REFERENCES

1. Crépon, F., *Electrophysiothérapie et rééducation fonctionnelle*, Third Edition, Editions Frison-Roche, 2002.
2. Faucher, J., *Pratique de l'AMDEC: Assurez la qualité et la sûreté de fonctionnement de vos produits, équipement et procédés*, Editions Dunod, 2004.
3. De Bisschop, G., E. de Bisschop, and F. Commandré, *Electrophysiothérapie*, Editions Masson, 1999.
4. Crépon, F., *Electrophysiothérapie et rééducation fonctionnelle*, Editions Frison-Roche, 2002.
5. Finn, S. M., G. E. Mann, and P. N. Taylor, "Using functional electrical stimulation (FES) in Parkinson disease," *7th Vienna International on Functional Electrical Stimulation Vienna*, Austria, September 12–15, 2001.
6. Loeb, G. E., W. Tan, N. Sachs, Q. Zou, and E. S. Kim, "A modular approach to sensing limb position in FES patients," *The 9th Annual Conference of the International Functional Electrical Stimulation*, September 2004.
7. Wong, L. S. Y., S. Hossain, A. Ta, J. Edvinsson, D. H. Rivas, and H. Nääs, "A very low-power CMOS mixed-signal IC for implantable pacemaker applications," *IEEE Journal of Solid-state Circuits*, Vol. 39, No. 12, 2446–2456, December 2004.
8. Sweeney, J. D., N. R. Crawford, and T. A. Brandon, "Neuromuscular stimulation selectivity of multiple-contact nerve cuff electrode arrays," *Medical & Biological Engineering & Computing*, 418–425, May 1995.
9. Uranga, A. and N. J. M. Rijkhoff, "A modified pulseshape for selective stimulation using anodal block," *The 8th Annual Conference of the International Functional Electrical Stimulation*, July 2003.

Wave Structure Functions of Multiply Scattered Electromagnetic Waves by Anisotropic Magnetized Turbulent Plasma Layer

G. V. Jandieri[1], **A. Ishimaru**[2], **V. G. Jandieri**[3], **A. G. Khantadze**[1]
I. B. Shirokov[1], **Yu. B. Gimpilevich**[1], **and Zh. M. Diasamidze**[1]

[1]Physics Department, Georgian Technical University, Georgia
[2]Department of Electrical Engineering, University of Washington
FT-10 Seattle, Washington 98195, USA
[3]Department of Electrical and Computer Engineering, Kumamoto University, Japan

Abstract— Wave structure functions of both phase and logarithmic relative amplitude, their mutual wave structure functions for two plane electromagnetic waves with different frequencies are studied. Besides, features of intensity of frequency fluctuations of multiply scattered radiation by finite thickness of anisotropic magnetized plasma layer are investigated in complex geometrical optics approximation. Source and receiver are assumed to be located on opposite sides with respect to turbulent plasma layer. Numerical calculations have been carried out for F-region of the ionosphere using satellite data of ionospheric plasma parameters.

1. INTRODUCTION

Wave structure functions for plane, spherical waves and Gaussian beams have been investigated in [1–4]. Evolution of the angular power spectrum of scattered electromagnetic radiation and features of its statistical characteristics, broadening and displacements of its maximum has been studied in geometrical optics approximation [5–8]. High-frequency monochromatic EM wave scattered on electron density fluctuations of ionospheric plasma lead to distortion of the observable angular power spectrum. Wave propagation in turbulent plasma with electron density fluctuations is usually accompanied by fluctuations of its parameters — amplitude, phase, intensity and so on. Investigation of peculiarities of frequency and frequency-spatial correlation functions are under the particular interest in satellite communications. It enables to define frequency band that could be transferred through statistically inhomogeneous medium without distortion of the form of signal spectrum. Determination of the frequency band demands the knowledge of frequencyspatial correlations of fluctuated field in the aperture plane of a highly directional antenna. In satellite communications, the ability to transmit a wideband data is closely related to the frequency correlation of the signal. Information about the frequency and spatial correlation of the signal is essential in designing and analyzing frequency and/or spatial diversity schemes. Therefore, in this paper, statistical characteristics: the log-amplitude and the phase wave structure functions, of frequency-spaced plane EM waves are computed. Complex geometrical optics approximation is applied taking into account multiple scattering effects. Numerical calculations have been carried out utilizing satellite data of F-region ionospheric plasma parameters.

2. CORRELATION FUNCTION OF THE PHASE

A point source, located in vacuum at a terminal distance l_1 above from the plane boundary of random magnetized plasma, irradiate high-frequency electromagnetic waves. Thickness of the scattered layer is equal to l_2, receiver is located in vacuum below the layer at a distant l_3 in the XZ plane (principle plane) and the length of line-of-sight connecting the source and the receiver is $L_0 = l_1 + l_2 + l_3$. The imposed magnetic field makes an angle θ_0 between Z axis and angle θ with the direction of a wavevector of the incident wave. The plasma concentration in the layer is: $N(\mathbf{r}) = N_0 + N_1(\mathbf{r})$; where N_0-is the constant term, $N_1(\mathbf{r})$ is a random function of the spatial coordinates describing concentration fluctuations. We shall suppose that the inequalities are satisfied for magnetized plasma: $\omega_B \gg \omega$, $\omega_B \gg \nu_{eff}$, $\omega_B \gg \omega_p$, where ω is the angular frequency, ν_{eff} is the effective collision frequency of electrons with other particles, $\omega_p = (4\pi e^2 N/m)^{1/2}$ is the plasma frequency and $\omega_B = eB_0/mc$ is the angular gyro-frequency for magnetic field; e and m are the charge and the mass of an electron, respectively, c is the speed of light in the vacuum. Plasma is considered as a uniaxial crystal having permittivity tensor components: $\tilde{\varepsilon}_{xx} = \tilde{\varepsilon}_{yy} = 1$, $\tilde{\varepsilon}_{xy} = \tilde{\varepsilon}_{yx} = \tilde{\varepsilon}_{xz} = \tilde{\varepsilon}_{zx} = \tilde{\varepsilon}_{yz} = \tilde{\varepsilon}_{zy} = 0$, $\tilde{\varepsilon}_{zz} = 1 - \omega_p^2/(\omega^2 + i\omega\nu_{eff})$ in the coordinate system, where the imposed magnetic field is directed towards Z-axis [7]. Performing geometrical optics

approximation, omitting throughout the multiplier $\exp(-i\omega t)$ together with factors describing the power and radiation pattern of the point source, at $\theta' \ll 1 (\theta' = \theta_0 - \theta)$, in a zero approximation, major contribution to the wave field at the observation point is given by one inhomogeneous plane wave, whose wave-vector projection on X axis is determined by:

$$k_x^0 \approx k_0 \left(v \frac{l_2 \sin\theta_0 \cos\theta_0}{L_0} + \frac{x}{L_0} \right) - isvk_0 \frac{l_2 \sin\theta_0 \cos\theta_0}{L_0}, \tag{1}$$

Inhomogeneity of this wave (imaginary part of k_x^0) is determined by the joint influence of both absorption and anisotropy in the plasma layer; $v = \omega_p^2/\omega^2$ and $s = \nu_{eff}/\omega$ are non-dimensional plasma parameters, $k_0 = \omega/c$.

Chaotic inhomogeneities of electron density in the plasma layer give rise to fluctuations of the wave field at the observation point. Statistical characteristics of the wave field are primarily determined by complex phase ($\tilde{\varphi}$) fluctuations of a principal plane wave in case of small-angle scattering [1, 2]. As electron density fluctuations are sufficiently small $N(\mathbf{r}) = N_0 + N_1(\mathbf{r})$, $N_1 \ll N_0$, we expand the phase characteristics into a series, $\tilde{\varphi} = \tilde{\varphi}_0 + \tilde{\varphi}_1 + \cdots$. Outside the plasma layer, the fluctuating term of a complex phase at the observation point is proportional to the small dimensionless parameter N_1/N_0:

$$\begin{aligned} \tilde{\varphi}_1(x, 0, l_1 + l_2 + l_3) \;=\; & \frac{\alpha}{k_0} \int_{-\infty}^{\infty} \int_{-\infty}^{\infty} dk_x dk_y \exp(ik_x x) \int_0^{l_2} d\zeta N_1(k_x, k_y, \zeta) \exp\left[ik_x (A - B)(l_2 - \zeta)\right] \\ & \cdot \exp\left[-ik_x \left(\tilde{k}_x/\tilde{k}_{z_1}\right) l_3\right] \exp\left[k_x \nu_{eff} A (l_2 - \zeta)/\omega\right], \end{aligned} \tag{2}$$

where: $\alpha = \frac{k_0^2}{2N_0} \frac{v \sin^2\theta_0}{(1 - v\cos^2\theta_0)^2}$, $\frac{\tilde{k}_x}{\tilde{k}_{z_1}} = v\frac{l_2}{L_0} \sin\theta_0 \cos\theta_0 + B - isv\frac{l_2}{L_0} \sin\theta_0 \cos\theta_0$, $A = v\frac{l_1 + l_3}{L_0} \sin\theta_0 \cos\theta_0$, $B = x/L_0$ is the distance between two observation points.

Transverse correlation function of complex phase fluctuations at the observation points, spaced apart at a small distance x, is given by the expression [7]:

$$\begin{aligned} W_{\tilde{\varphi}} \;=\; & \langle \tilde{\varphi}_1(x, 0, L_0) \cdot \tilde{\varphi}_1^*(0, 0, L_0) \rangle \frac{\alpha^2}{k_0^2} \int_{-\infty}^{\infty} \int_{-\infty}^{\infty} dk_x dk_y F_N(k_x, k_y, \rho) \exp\left(\frac{ik_x x l_1}{L_0}\right) \\ & \cdot \exp\left(-2svk_x l_2 \frac{l_3 \sin\theta_0 \cos\theta_0}{L_0}\right) \int_{-\infty}^{\infty} d\rho \exp\left(-iAk_x\rho + ik_x \frac{x\rho}{2L_0}\right) \\ & \int_0^{l_2} d\eta \exp\left[i\frac{x}{L_0} k_x \eta + 2Ask_x (l_2 - \eta)\right], \end{aligned} \tag{3}$$

where $\frac{1}{2\pi} \int_{-\infty}^{\infty} d\rho F_N(k_x, k_y, \rho) \exp(-ik_x\rho) = W_N(k_x, k_y, k_z)$ is a 3D power spectrum of statistically homogeneous electron density fluctuations.

3. STRUCTURE FUNCTIONS

Point source radiates two monochromatic waves with frequencies $\omega_1 = \omega_0(1-\delta)$ and $\omega_2 = \omega_0(1+\delta)$. The value $\delta = (\omega_2 - \omega_1)/2\omega_0$ characterizes the difference frequency of propagated waves. We shall calculate $<\varphi_1(\mathbf{r}_1)\varphi_1^*(\mathbf{r}_2)>$ and $<\varphi_1(\mathbf{r}_1)\varphi_2(\mathbf{r}_2)>$ in order to define the frequency structure functions of phase and logarithmic relative amplitude in a plane perpendicular to a direction of propagating waves. An asterisk '$*$' is a complex conjugate. Wave structure functions of phase and logarithmic relative amplitude, their mutual correlations for two waves with different frequencies are defined

by the following expressions:

$$
\begin{aligned}
D_{\mu_1\mu_2}(\mathbf{r}_1,\mathbf{r}_2) &= \langle[\mu_1(\mathbf{r}_1)-\mu_1(\mathbf{r}_2)][\mu_2(\mathbf{r}_1)-\mu_2(\mathbf{r}_2)]\rangle = \frac{1}{2}\mathrm{Re}\left[D_1(\mathbf{r}_1,\mathbf{r}_2)+D_2(\mathbf{r}_1,\mathbf{r}_2)\right],\\
D_{S_1S_2}(\mathbf{r}_1,\mathbf{r}_2) &= \langle[S_1(\mathbf{r}_1)-S_1(\mathbf{r}_2)][S_2(\mathbf{r}_1)-S_2(\mathbf{r}_2)]\rangle = \frac{1}{2}\mathrm{Re}\left[D_1(\mathbf{r}_1,\mathbf{r}_2)-D_2(\mathbf{r}_1,\mathbf{r}_2)\right],\\
D_{\mu_1S_2}(\mathbf{r}_1,\mathbf{r}_2) &= \langle[\mu_1(\mathbf{r}_1)-\mu_1(\mathbf{r}_2)][S_2(\mathbf{r}_1)-S_2(\mathbf{r}_2)]\rangle = \frac{1}{2}\mathrm{Im}\left[D_2(\mathbf{r}_1,\mathbf{r}_2)-D_1(\mathbf{r}_1,\mathbf{r}_2)\right],\\
D_{\mu_2S_1}(\mathbf{r}_1,\mathbf{r}_2) &= \langle[\mu_2(\mathbf{r}_1)-\mu_2(\mathbf{r}_2)][S_1(\mathbf{r}_1)-S_1(\mathbf{r}_2)]\rangle = \frac{1}{2}\mathrm{Im}\left[D_2(\mathbf{r}_1,\mathbf{r}_2)+D_1(\mathbf{r}_1,\mathbf{r}_2)\right], \qquad (4)
\end{aligned}
$$

where $D_1(\mathbf{r}_1,\mathbf{r}_2) =< [\varphi_1(\mathbf{r}_1)-\varphi_1(\mathbf{r}_2)][\varphi_2^*(\mathbf{r}_1)-\varphi_2^*(\mathbf{r}_2)] >$, $D_2(\mathbf{r}_1,\mathbf{r}_2) =< [\varphi_1(\mathbf{r}_1)-\varphi_1(\mathbf{r}_2)][\varphi_2(\mathbf{r}_1)-\varphi_2(\mathbf{r}_2)] >$, $\mathbf{r}_1$ and $\mathbf{r}_2$ are radius-vector with coordinates (x_1,y_1,z_1) and (x_2,y_2,z_2). In our case, $\mathbf{r}_1=(x,0,L_0)$, $\mathbf{r}_2=(0,0,L_0)$ and $x \ll L_0$.

First wave structure function for arbitrary correlation function of electron density fluctuations has the form:

$$
\begin{aligned}
D_1(x,0,L_0) &= M\int\limits_{-\infty}^{\infty}dk_x\int\limits_{-\infty}^{\infty}dk_yW_N\left[k_x,k_y,\left(p-B-\frac{i}{2}Amm\right)k_x\right]\exp\left[2i(m-iq)Jl_2k_x\right]\\
&\quad\cdot\left[1-2\cos\left(Bl_1k_x\right)\right]+M\int\limits_{-\infty}^{\infty}dk_x\int\limits_{-\infty}^{\infty}dk_yW_N\left[k_x,k_y,\left(p-\frac{i}{2}Amm\right)k_x\right]\\
&\quad\exp\left[2i(m-iq)Jl_2k_x\right]. \qquad (5)
\end{aligned}
$$

where

$$
M=\frac{\pi}{2}\sigma_N^2k_0^2l_2v^2\frac{(1-\delta)^5(1+\delta)^5\sin^4\theta_0}{\left[(1-\delta)^2-v\cos^2\theta_0\right]^2\left[(1+\delta)^2-v\cos^2\theta_0\right]^2},\quad p=\frac{A\left(1+\delta^2\right)}{(1-\delta)^2(1+\delta)^2},
$$

$$
m=\frac{2\delta}{(1-\delta)^2(1+\delta)^2},\quad n=\frac{s\left(3+\delta^2\right)}{(1-\delta)(1+\delta)},\quad q=\frac{s\left(3+\delta^2\right)}{(1-\delta)^3(1+\delta)^3},\quad A=v\frac{b+d}{1+b+d}\sin\theta_0\cos\theta_0,
$$

$$
J=v\frac{b}{1+b+d}\sin\theta_0\cos\theta_0,\quad \sigma_N^2=\left\langle N_1^2\right\rangle/N_0^2
$$

is the variance of electron density fluctuations, $a=\ell_\parallel/l_2$, $b=l_1/l_2$ and $d=l_3/l_2$ are nondimensional spatial parameters normalized on a thickness of plasma layer, $l_\parallel$ is a characteristic spatial scale of irregularities along the external magnetic field.

Second wave structure function is expressed as follows:

$$
\begin{aligned}
D_2(x,0,L_0) &= M\int\limits_{-\infty}^{\infty}dk_x\int\limits_{-\infty}^{\infty}dk_yW_N\left[k_x,k_y,(p-B-iAq)k_x\right]\left\{\exp\left[im(2-in)Jl_2k_x\right]\right.\\
&\quad\left.-2\exp\left[iBl_1k_x+im(2-in)Jl_2k_x\right]\right\}\\
&\quad+M\int\limits_{-\infty}^{\infty}dk_x\int\limits_{-\infty}^{\infty}dk_yW_N\left[k_x,k_y,(p-iAq)k_x\right]\exp\left[im(2-in)Jl_2k_x\right]. \qquad (6)
\end{aligned}
$$

We analyze the structure functions of scattered radiation for anisotropic Gaussian correlation function of electron density fluctuations in F-region of the ionosphere plasma [9]:

$$
\begin{aligned}
W_N(k_x,k_y,k_z) &= \frac{\ell_\perp^2\ell_\parallel}{8\pi^{3/2}}\exp\left\{-\frac{k_x^2\bar{\ell}^2}{4}\left[1+\frac{(1-\chi^2)^2}{\chi^2}\sin^2\alpha\cos^2\alpha\right]-\frac{k_y^2\ell_\perp^2}{4}\right.\\
&\quad\left.-\frac{\sin^2\alpha+\chi^2\cos^2\alpha}{4\chi^2}k_z^2\ell_\parallel^2+\frac{1-\chi^2}{2\chi^2}\sin\alpha\cos\alpha k_xk_z\ell_\parallel^2\right\}, \qquad (7)
\end{aligned}
$$

where α is an angle that the prolate inhomogeneities make with respect to the external magnetic field, $\chi=\ell_\parallel/\ell_\perp$ is the anisotropic parameter of prolate irregularities, $\bar{\ell}^2=\ell_\parallel^2(\sin^2\alpha+\chi^2\cos^2\alpha)^{-1}$.

4. NUMERICAL RESULTS

The following parameters are chosen for the numerical computation: $h = 230\,\text{km}$, $f = 40\,\text{MHz}$, plasma parameters are: $v = \omega_p^2/\omega^2 = 0.0133$, $s = \nu_{eff}/\omega = 5.87 \cdot 10^{-7}$, $l_2 = 50\,\text{km}$, $l_\parallel = 10\,\text{km}$, $\sigma_N^2 \approx 10^{-4}$, $l_1 = 100\,\text{km}$, $l_3 = 80\,\text{km}$ [10]; difference of frequencies of propagated waves is equal to $\delta = 0.02$. Variances of the phase $<\varphi_1^2>_1$ and $<\varphi_1^2>_2$ (indices 1 and 2 correspond to frequencies ω_1 and ω_2) are presented in Table below. Numerical calculations show that they are less than 1 *radian* that is in a good agreement with the results of satellite observations. This means that scattering of radiowaves on large-scale irregularities locating in a turbulent ionospheric plasma layer cause a diffraction picture on the Earth surface, where correlation radius of the phase fluctuations is equal to correlation radius of electron density fluctuations [11].

Variances of the phase								
No	α	χ	b	d	$\sqrt{<\varphi_1^2>_1}$		$\sqrt{<\varphi_1^2>_2}$	
1	$0^0, 10^0, 20^0, \ldots$	$1, 2, 3, \ldots$	$0, 1, 2, \ldots$	$0, 1, 2, \ldots$	0.050	2.94^0	0.052	3.06^0
2	10^0	2	$0, 1, 2, \ldots$	$0, 1, 2, \ldots$	0.049	2.88^0	0.051	3^0
3	10^0	10	$0, 1, 2, \ldots$	$0, 1, 2, \ldots$	0.035	2.53^0	0.037	2.18^0
4	20^0	10	$0, 1, 2, \ldots$	$0, 1, 2, \ldots$	0.026	1.53^0	0.027	1.59^0

The curves of normalized structure functions versus parameter b are presented in Figures 1–4 for different anisotropic parameter of electron density irregularities $\chi = (1 \div 10)$ if antennas are located on a lower boundary of turbulent plasma layer, $d = 0$; distance between antennas is about 30 m, angles are equal to $\theta_0 = 10^0$ and $\alpha = 10^0$. Numerical calculations show that the log-amplitude $D_{\mu_1\mu_2}$ and phase $D_{S_1S_2}$ structure functions tend to saturation at the same value of parameter b. In particular, saturation takes place for $b = 5.37 \cdot 10^3$, $b = 1.78 \cdot 10^3$ and $b = 1.0 \cdot 10^3$ at $\chi = 1$, 2 and 10, respectively. However, tendency to saturation is much smoother in isotropic case $\chi = 1$ than in anisotropic cases, when structure functions tend to saturation at small parameter b (Fig. 1.) The behavior of these structure functions is the same at a fixed anisotropy parameter ($\chi = 10$) and different angle of inclination α. Particularly, saturation takes place at $b = 495$, $b = 1.0 \cdot 10^3$ and $b = 1.8 \cdot 10^3$ at $\alpha = 0^0$, 10^0 and 20^0, respectively. Figures 3 and 4 show that the structure functions $D_{\mu_1 S_2}$ and $D_{\mu_2 S_1}$ are asymmetrical and tend to saturation at big values of the parameter b in proportion to the angle α. Structure functions reach maximum at small b with increasing parameter χ; $D_{\mu_1 S_2} > D_{\mu_2 S_1}$ (Fig. 3). From Figure 4 it follows that at fixed anisotropic parameter ($\chi = 3$), increasing the angle of inclination of prolate irregularities with respect to the geomagnetic

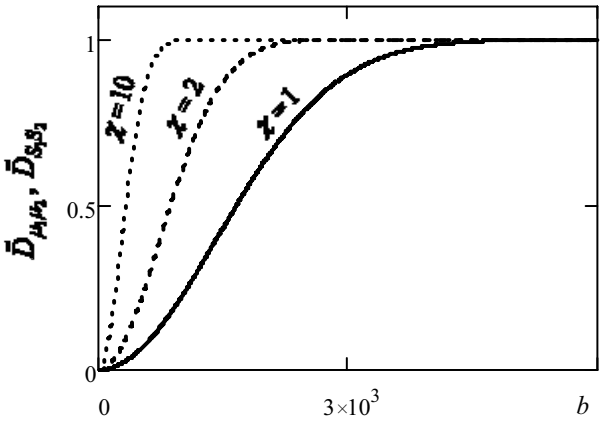

Figure 1: The dependence of normalized structure functions $\tilde{D}_{\mu_1\mu_2}$ and $\tilde{D}_{S_1S_2}$ versus nondimensional parameter b for a different anisotropy parameter χ, $\alpha = 10^0$.

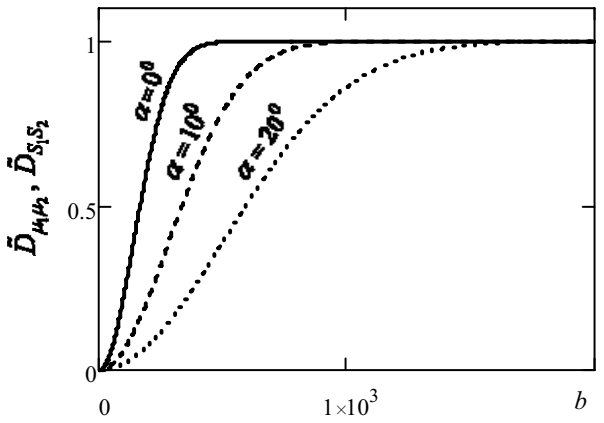

Figure 2: The dependence of normalized structure functions $\tilde{D}_{\mu_1\mu_2}$ and $\tilde{D}_{S_1S_2}$ versus nondimensional parameter b for different angle of inclination α at $\chi = 10$.

field, maximum values of structure functions $\tilde{D}_{\mu_1 S_2}$ and $\tilde{D}_{\mu_2 S_1}$ decrease. Structure functions achieve maximum values $\tilde{D}_{\mu_1 S_2} = 2.5 \cdot 10^{-10}$ and $\tilde{D}_{\mu_2 S_1} = 2.2 \cdot 10^{-10}$ at $b = 1.1 \cdot 10^3$ and $b = 1.0 \cdot 10^3$, respectively if $\alpha = 20^0$.

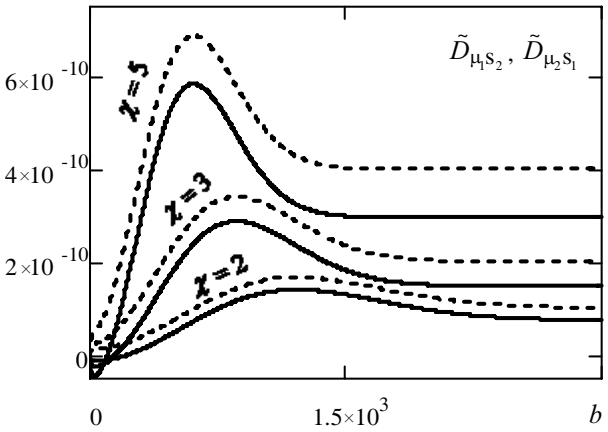

Figure 3: The dependence of normalized structure functions $\tilde{D}_{\mu_1 S_2}$ (dotted lines) and $\tilde{D}_{\mu_2 S_1}$ (solid lines) versus nondimensional parameter b for different anisotropy parameter χ, $\alpha = 10^0$.

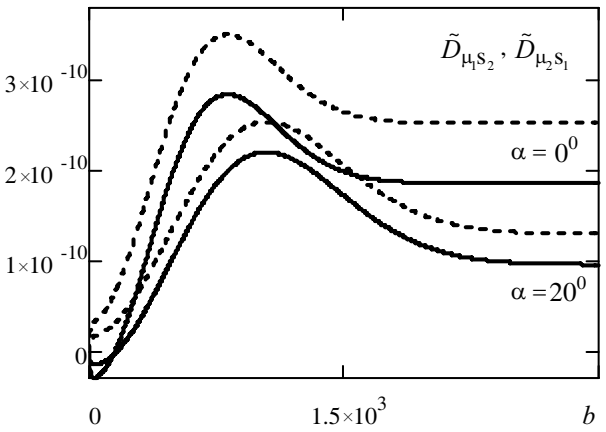

Figure 4: The dependence of normalized structure functions $\tilde{D}_{\mu_1 S_2}$ (dotted lines) and $\tilde{D}_{\mu_2 S_1}$ (solid lines) versus non-dimensional parameter b for different angle α at $\chi = 3$.

5. CONCLUSION

The phase, log-amplitude and their mutual correlation functions wave structure functions of multiply scattered radiation have been studied in complex geometrical optics approximation. The source irradiate radio waves with two different frequencies and observation points are located on opposite side with respect to anisotropic turbulent magnetized plasma layer. Numerical calculations have been carried out using satellite data of F-region ionospheric plasma parameters. From the results it follows that anisotropy and the angle of inclination of prolate irregularities with respect to the external magnetic field have a substantial influence on the behaviour of maximums and saturation levels of these functions. The results of numerical calculations are in a good agreement with satellite data.

REFERENCES

1. Ishimaru, A., *Wave Propagation and Scattering in Random Media: Multiple Scattering, Turbulence, Rough Surfaces and Remote Sensing*, Vol. 2, IEEE Press, Piscataway, New Jersey, USA, 1997.
2. Tatarskii, V. I., *Wave Propagation in a Turbulent Medium*, McGraw-Hill, New York, USA, 1961.
3. Young, C. Y., A. J. Masino, F. E. Thomas, and C. J. Subich, "The wave structure function in weak to strong fluctuations: an analytic model based on heuristic theory," *Waves Random Media*, Vol. 14, 75–96, 2004.
4. Liu, C. H. and K. C. Yeh, "Frequency and spatial correlation functions in a fading communication channel through the ionosphere," *Radio Science*, Vol. 10, No. 12, 1055–1061, 1975.
5. Jandieri, G. V., V. G. Gavrilenko, A. V. Sorokin, and V. G. Jandieri, "Some properties of the angular power distribution of electromagnetic waves multiply scattered in a collisional magnetized turbulent plasma," *Plasma Physics Report*, Vol. 31, No. 7, 655–666, 2005.
6. Jandieri, G. V., A. Ishimaru, V. G. Jandieri, A. G. Khantadze, and Zh. M. Diasamidze, "Model computations of angular power spectra for anisotropic absorptive turbulent magnetized plasma," *Progress In Electromagnetics Research*, PIER 70, 307–328, 2007.
7. Jandieri, G. V., V. G. Gavrilenko, and A. A. Semerikov, "On the effect of absorption on multiple wavescattering in a magnetized turbulent plasma," *Waves in Random Media*, Vol. 9, 427–440, 1999.
8. Jandieri, G. V., V. G. Jandieri, Zh. M. Diasamidze, I. N. Jabnidze, and I. G. Takidze, "Statistical caracteristics of scattered microwaves in gyrotropic medium with random inhomogeneities," *IJMOT*, Vol. 1, No. 2, 860–869, 2006.

9. Jandieri, G. V., A. Ishimaru, V. G. Jandieri, K. V. Kotetishvili, and T. N. Bzhalava, "A radio scintillation in the turbulent collision magnetized plasma," *Proceedings of WORLDCOMP'07*, 189–195, Las Vegas, USA., June 2007.
10. Kravtsov, Yu. A., Z. I. Feizulin, and A. G. Vinogradov, *Propagation of Radiowaves Through the Earth's Atmosphere*, Moscow, Radio and Communication, Russian, 1983.
11. Kolosov, M. A., N. A. Armand, and O. I. Yakovlev, *Propagation of Radiowaves at Cosmic Communications*, Sviaz' Moscow, Russian, 1969.

Electromagnetic Detectability of the Oil Slicks on a Sea Surface in Bistatic Configuration

A. Coatanhay and C. Gervaise
Laboratory E3I2, EA 3876, ENSIETA, 29806 Brest Cedex 9, France

Abstract— This study evaluate the influence of a polluted sea surface upon the electromagnetic scattering. More precisely, we compare this influence with the electromagnetic field scattered by a non-polluted sea surface in the same weather conditions. Using a Monte-Carlo approach and a method of moment adapted to dielectric rough surfaces (a Forward-Backward approach), we statistically estimate the detectability of the pollution in various bistatic configurations using a contrast criterion.

1. INTRODUCTION

The detection of the oil slicks on the sea surface is a very important issue for coastal pollution prevention and for the identification of illegal discharges. Then, this issue was widely studied with several approaches using several sensors (optics, infrared, microwave, ...). When microwave sensors are considered, a great part of the scientific studies analyze the detectability of oil spills in the context of synthetic aperture radar (SAR) system [1–3]. And, the issue of oil spill detection using SAR systems usually leads to evaluate the efficiency of image processing methods.

In the present paper, we focus on the scattering of a single incident electromagnetic plane wave by a polluted (oil film) sea surface in bistatic configuration (forward configuration). As a matter of fact, independently of the radar signal processing, we try to determine if this scattered field is significantly influenced by the pollution in various weather conditions.

In a first part, we present the models used to describe a sea surface without any pollution in different weather conditions (wind speed and direction) and with different physical properties (temperature, salinity, ...). In a second part, we explain how to modify these models to take into account the presence of an oil film on the sea. Then the following section describe the numerical method applied to compute the electromagnetic field scattered by an ocean-like surface. Finally, we give our statistical approach to analyze the detectability of the oil film upon the electromagnetic scattering.

2. DESCRIPTION OF A NON-POLLUTED SEA SURFACE

From a global point of view, a sea surface can be assimilated to a dielectric random rough interface. The most standard way to describe the roughness of the sea surface is to determine the sea surface spectrum $S(K, \phi)$, considering the sea surface as a random, ergodic and stationary process. In scientific literature, many papers provides fully detailed description of various sea spectra, see Pierson and Moskovitz studies [4, 5] for instance. In this paper, we considered the Elfouhaily spectrum [6], called unified spectrum, that is very consistent with actual observations and presents no discontinuity at gravity and wind driven waves.

The sea spectrum is in the form:

$$S(K, \phi) = S(K) f(K, \phi) \tag{1}$$

where $S(K)$ represents the isotropic part of the spectrum modulated by the angular function $f(K, \phi)$. K and ϕ are respectively the spatial wave number and the wind direction.

Analytically, the Elfouhaily spectrum as a function of the wave number K is given by:

$$S(K) = \frac{K^{-3}}{2c}(\alpha_p c_p F_p + \alpha_m c_m F_m) R^{\exp\left[-\frac{\left(\sqrt{\frac{K}{k_p}}-1\right)^2}{2\delta^2}\right]} \exp\left(-\frac{5k_p^2}{4K^2}\right) \tag{2}$$

where

$$F_m = \exp\left[-\frac{1}{4}\left(\frac{K}{k_m}-1\right)^2\right], \quad F_p = \exp\left[-\frac{\Omega}{\sqrt{10}\left(\sqrt{\frac{K}{k_p}}-1\right)}\right] \tag{3}$$

$$\begin{cases} R = 1.7 & 0.84 < \Omega < 1 \\ R = 1.7 + 6\ln(\Omega) & 1 < \Omega < 5 \end{cases} \tag{4}$$

with $k_p = \frac{g}{U_{10}^2}\Omega^2$, $k_m = 356\,\mathrm{rad/m}$.

$$\alpha_c = 10^2 \begin{cases} 1 + \ln\left(\dfrac{u_f}{c_m}\right) & u_f \le c_m \\ 1 + 3\ln\left(\dfrac{u_f}{c_m}\right) & u_f > c_m \end{cases} \qquad \alpha_p = 6 \times 10^3 \sqrt{\Omega} \tag{5}$$

with

$$c = c(K) = \sqrt{\frac{g}{K}\left(1 + \frac{K^2}{k_m^2}\right)} \tag{6}$$

and

$$c_p = c(k_p) = \frac{U_{10}}{\Omega}, \quad c_m = c(k_m) = \sqrt{\frac{2g}{k_m}} \tag{7}$$

As a matter of fact, the Elfouhaily spectrum only depends on the wind direction ϕ, the wind speed measured at 10 meters above the sea surface U_{10} and the variable Ω that is related to the time of interaction between the wind and the sea. In the following of the text, we assume that this interaction is medium and we let $\Omega = 0.84$. So, we can estimate the roughness spectrum of the sea as a function of the wind speed and the wind direction, see Figure 1.

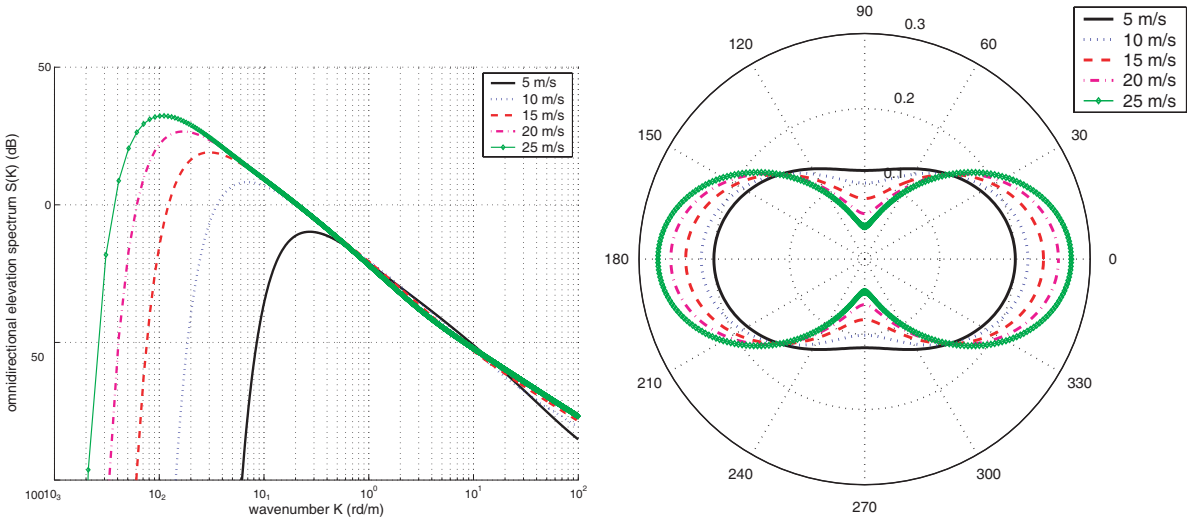

(a) Omnidirectional elevation spectrum

(b) Angular function

Figure 1: Elfouhaily sea surface spectra with different wind speeds.

In the case of a clean sea surface, the dielectric characteristic of the sea water can be modeled using the Debye theory [7] with adapted semi-empirical modifications. The so-obtained model that is a function of the frequency, can take into account the salinity and provides a good fit to the experimental data. Indeed, based on polar theory, Debye [7] gives the permittivity $\varepsilon(\varepsilon = \varepsilon' - i\varepsilon'')$ of the distilled water by the well-know expression.

$$\varepsilon = \varepsilon_\infty + \frac{\varepsilon_s - \varepsilon_\infty}{1 + j\omega\tau} \tag{8}$$

where τ is the relaxation time and ω is the circular frequency ($\omega = 2\pi f$). In the case of a saline solution, the complex permittivity is given by

$$\varepsilon = \varepsilon_\infty + \frac{\varepsilon_s - \varepsilon_\infty}{1 + (j\omega\tau)^{1-\alpha}} - j\frac{\sigma}{\omega\varepsilon_0} \tag{9}$$

where ε_0 is the vacuum electric permittivity, and σ is the ionic conductivity. This variable can be determined from the salinity and the temperature of the salt water [7]. Finally, a non-polluted sea surface can be described as a dielectric random rough interface where every parameters are known.

3. POLLUTED SEA SURFACE

With the presence of pollutant, oil for example, mechanical properties (viscosity, tension surface, ...) of the sea surface is modified and a new roughness spectrum must take into account. Letting $S_n(K)$ and $S_p(k)$, respectively, denote the non-polluted and the polluted surface spectrum, we can define a damping ratio $y(K)$ as follows:

$$y(K) = \frac{S_n(K)}{S_p(K)} \tag{10}$$

where K is the spatial wave number of the sea wave.

In low or moderate wind conditions (wind speed at 10 meters height $U_{10} < 10\,\mathrm{m/s}$), the pollutant often forms a film spreading on the ocean surface. The physicochemical-hydrodynamics theory applied in the present study can model the damping effect. Actually, this theory distinguishes two different cases: a soluble and an insoluble pollutant.

As shown in Figure 2, the film of a soluble pollutant on the sea surface induces a continuous concentration gradient interface. And, in the a similar way, an insoluble pollutant induces random precipitations on contact with sea water. In both cases, the notion of pollutant layer could lead to physical model difficulties. To avoid these difficulties, we assume, in our electromagnetic study, that the pollutant layer can be approximated by a homogeneous half-space (permittivity of the pollutant) with a rough interface whose the roughness spectrum is given by the physicochemical-hydrodynamics theory [8]. In the present paper, the pollutant is supposed to be an insoluble oil whose relative permittivity is equal to 5.

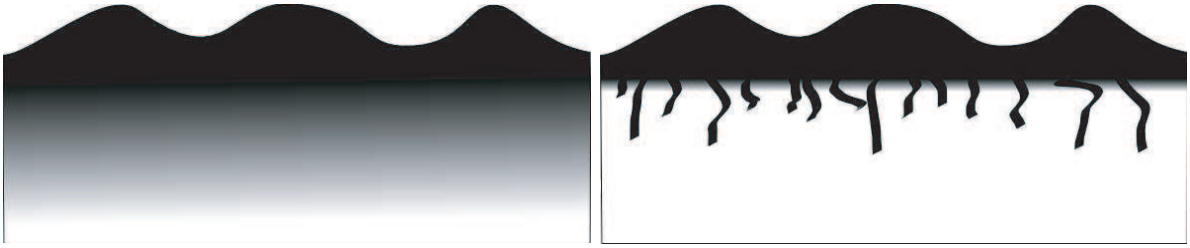

(a) Concentration gradient layer (b) Homogeneous layer with precipitations

Figure 2: Schematic presentation for two types of pollutant layers: (a) Soluble pollutant, (b) Insoluble pollutant.

For insoluble surface films, it is assumed that thermodynamic equilibrium exists within the subsurface. Below the subsurface, however, the process of precipitation is assimilate to a diffusion one characterized by a diffusional frequency ω_D. The characterization of pollutant mechanical properties can be reduced to the elasticity modulus E_0. Then, the damping ratio in this case can be expressed as follows [8]:

$$y(K) = \frac{1 - 2\tau + 2\tau^2 - X_0 + Y_0(X_0 + \tau)}{1 - 2\tau + 2\tau^2 - 2X_0 + 2X_0^2} \tag{11}$$

with

$$X_0 = \frac{E_0 K^2}{\rho_\omega \sqrt{2\nu_\omega \omega^3}} \qquad Y_0 = \frac{E_0 K}{4\rho_\omega \nu_\omega \omega} \qquad \omega = \sqrt{\zeta_\omega K^3/\rho_\omega + Gk} \qquad \tau = \sqrt{\frac{\omega_D}{2\omega}} \tag{12}$$

where ρ_ω, ν_ω and ζ_ω are respectively the sea water density, the kinematic viscosity of the sea water and the surface tension of the sea surface.

Finally with any given weather conditions, we can evaluated the roughness spectra of both a non-polluted sea surface and the corresponding surface polluted by an insoluble oil.

4. NUMERICAL ESTIMATION OF THE SCATTERED FIELD

Assuming the statistical roughness spectrum as known, the electromagnetic scattering by a dielectric random rough surface can be estimated using an asymptotic approach like Small Perturbation Method, Two scale model or Small Slope Approximation. And then, the influence of the pollutant upon the electromagnetic scattered field can be studied [9, 10]. However, the asymptotic approaches only provide the mean value of the scattered field for a given geometrical configuration. For instance, the standard deviation of the scattering remains undetermined and the detectability of the pollutant from the electromagnetic field is difficult to quantify.

In the present study, the scattering from a given rough surface (deterministic surface) is computed using a numerical algorithm based on the Method of Moment. More precisely, we apply an efficient Method of Moments (MoM) called the Forward-Backward method (FB-MOM). In its original formulation [11], the Forward-Backward method only applies to scattering from perfectly conducting surfaces. It is true that Holliday and et al. [12] introduced a more generalized algorithm that can treat imperfect conductors. However it is to be noted that this generalization assumes that the imaginary part of the complex permittivity is large. This assumption could be valid for non-polluted sea but this assumption is not applicable for pollutants like oil. More recently, Iodice [13] presented a modified version that can take into account the dielectric properties of the sea water and the pollutants.

The sea surface, denoted S, is assimilated to a one dimension height profile in the form $z = f(x)$ constant along the y direction. If the incident field is horizontally polarized $\vec{E}^{inc} = E^{inc}\hat{y}$, the electric field $\vec{E} = E\hat{y}$ above the rough surface is given by the following integral equations:

$$E(\vec{r}) = \frac{1}{2} + \int_S j\omega\mu_0 G_0(\vec{r}, \vec{r}')J_S(\vec{r}') + E(\vec{r}') \cdot [\hat{n} \cdot \nabla G_0(\vec{r}, \vec{r}')]d\vec{r}' \tag{13a}$$

$$0 = \frac{1}{2} - \int_S j\omega\mu_0 G_1(\vec{r}, \vec{r}')J_S(\vec{r}') + E(\vec{r}') \cdot [\hat{n} \cdot \nabla G_1(\vec{r}, \vec{r}')]d\vec{r}' \tag{13b}$$

where J is the electric surface current density, $\hat{n}$ is the outgoing normal to the surface and G_0 (resp. G_1) is the two dimensional Green function above the surface (resp. beneath the surface). By using rectangular pulse basis functions and the point matching method, the previous integral equations can be expressed in the form $2N \times 2N$ linear equation:

$$\begin{aligned} S_0 E_N + Z_0 J_N &= E_N^{inc} \\ S_1 E_N + Z_1 J_N &= 0 \end{aligned} \tag{14}$$

where S_0, S_1, Z_0 and Z_1 are $N \times N$ matrix. E_N and J_n are N dimensional vectors that contain the unknowns of the discretized problem. To avoid the use of time-consuming algorithms to solve this linear system, we split the electrical field and the current density in two "Forward" and "Backward" components in the same way that original Forward-Backward theory [11]:

$$E_N = E_N^f + E_N^b \qquad J_N = J_N^f + J_N^b \tag{15}$$

Letting

$$\begin{aligned} S_0 &= S_0^L + S_0^D + S_0^U \qquad S_1 = S_1^L + S_1^D + S_1^U \\ Z_0 &= Z_0^L + Z_0^D + Z_0^U \qquad Z_1 = Z_1^L + Z_1^D + Z_1^U \end{aligned} \tag{16}$$

where L, D and U respectively denote the lower part, the diagonal part and the upper part of the matrix, the linear system (14) can be decomposed into forward-propagation and backward-propagation pairs of equations:

$$\begin{aligned} S_0^D E_N^f + Z_0^D J_N^f &= E_N^{inc} - S_0^L(E_N^f + E_N^b) - Z_0^L(J_N^f + J_N^b) \\ S_1^D E_N^f + Z_1^D J_N^f &= -S_1^L(E_N^f + E_N^b) - Z_1^L(J_N^f + J_N^b) \\ S_0^D E_N^f + Z_0^D J_N^f &= -S_0^U(E_N^f + E_N^b) - Z_0^U(J_N^f + J_N^b) \\ S_1^D E_N^f + Z_1^D J_N^f &= -S_1^U(E_N^f + E_N^b) - Z_1^U(J_N^f + J_N^b) \end{aligned} \tag{17}$$

Iodice [13] show that this new linear system can be solved using a very efficient iterative algorithm ($O(N^2)$). In the case of a vertically polarized incident field, a similar method can be applied using the magnetic field.

Finally, this Forward-Backward theory can efficiently compute the electromagnetic field scattered by a given non-polluted or polluted sea surface.

5. OBSERVABILITY ANALYSIS

To realize a statistical comparison between the polluted surfaces and the non-polluted ones, we use a Monte Carlo approach and we compute the scattering from a great number of equivalent rough surfaces associated with the same sea spectrum. The convolution of a spectrum with an unitary white Gaussian random signal generates a one-dimensional profile (one realization) that represents an ocean surface for given weather conditions, see Figure 3. For fixed weather conditions and pollutant mechanical properties, the polluted and non-polluted sea spectra induce two different rough surface with the same unitary white Gaussian random signal. So, using many random signal sequences and the Forward-Backward computation of the scattering by each realization, we can estimate the statistical parameters (mean value, standard deviation, ...) of the scattered field in both polluted and non-polluted case. These parameters are functions of the incident angle θ.

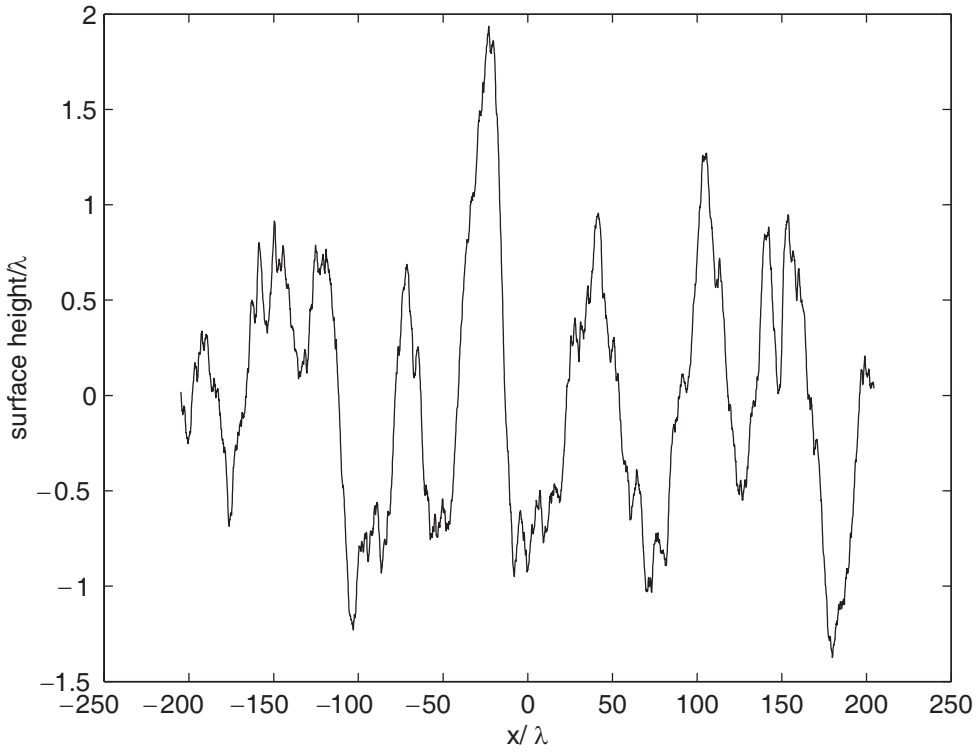

Figure 3: Realization of an ocean surface.

From a statistical viewpoint, the detectability of the pollutant become the evaluation of the similarity between two data sets. To quantify this similarity we introduce a t-value expression T (t-test) [14]:

$$T(\theta) = \frac{m_p(\theta) - m_n(\theta)}{\sigma(\theta)} \qquad \sigma(\theta) = \sqrt{[\sigma_p^2(\theta) + \sigma_n^2(\theta)]/n} \tag{18}$$

where m_p and σ_p (resp. m_n and σ_n) are the mean value and the standard deviation of the scattering by a polluted (resp. non-polluted) surface. n is the number of realizations.

6. CONCLUSION

The methodology presented is this paper enables to quantify the detectability of a pollution on an ocean surface independently of the radar signal processing. Our approach can be applied to optimize the bistatic configuration (angle of incidence) to detect a pollutant for given weather conditions.

REFERENCES

1. Franceschetti, G., A. Iodice, D. Riccio, G. Ruello, and R. Siviero, "SAR raw signal simulation of oil slicks in ocean environments," *IEEE Trans. Geoscience Remote Sensing*, Vol. 40, No. 9, 1935–1949, 2002.
2. Bertacca, M., F. Berizzi, and E. D. Mese, "A FARIMA-based technique for oil slick and low-wind areas discrimination in sea SAR imagery," *IEEE Trans. Geoscience Remote Sensing*, Vol. 43, No. 11, 2484–2493, 2005.
3. Migliaccio, M., A. Gambardella, and M. Tranfaglia, "SAR polarimetry to observe oil spills," *IEEE Trans. Geoscience Remote Sensing*, Vol. 45, No. 2, 506–511, 2007.
4. Pierson, W. and L. Moskovitz, "A proposed spectral form for fully developed wind sea based on the similarity theory of s. a. kitaigorodskii," *J. Geophys. Res.*, Vol. 69, 5181–5190, 1964.
5. Pierson, W., "The theory and applications of ocean wave measuring systems at and below the sea surface, on land, from aircraft and from spacecraft," *NASA Tech. Rep.*, 1991.
6. Elfouhaily, T., B. Chapron, K. Katsaros, and D. Vandemark, "A unified directional spectrum for long and short wind-driven waves," *Journal of Geophysical Research*, Vol. 102, No. C7, 15781–15796, 1997.
7. Debye, P., Polar Molecules, Chemical Catalog Company, NewYork, 1929.
8. Fiscella, B., P. P. Lombardini, and P. Trivero, "Ripple damping on water surface covered by a spreading film: Theory and experiment, *Il Nuovo Cimento*, Vol. 8C, No. 5, 491–500, 1985.
9. Ayari, M. Y., A. Coatanhay, and A. Khenchaf, "The influence of ripple damping on electromagnetic bistatic scattering by sea surface," *IGARSS*, Seoul, Korea, July 25–29, 2005.
10. Coatanhay, A., M. Y. Ayari, and A. Khenchaf, "Oil slick effect on electromagnetic bistatic scattering from the ocean surface in low/moderate wind conditions," (submitted).
11. Holliday, D., L. L. DeRaad, and G. C. St-Cyr, "Forward-backward: A new method for computing low-grazing angle scattering," *IEEE Trans. Antennas Propagat.*, Vol. 44, No. 5, 722–729, 1996.
12. Holliday, D., L. L. DeRaad, and G. C. St-Cyr, "Forward-backward method for scattering from imperfect conductors," *IEEE Trans. Antennas Propagat.*, Vol. 46, No. 1, 101–107, 1998.
13. Iodice, A., "Forward-backward method for scattering from dielectric rough surfaces," *IEEE Trans. Antennas Propagat.*, Vol. 50, No. 7, 901–911, 2002.
14. Press, W. H., S. A. Teukolsky, W. T. Vetterling, and B. P. Flannery, *Numerical Recipes in C: The Art of Scientific Computing*, Cambridge University Press, 2007.

Electromagnetic Waves Propagation above Rough Surface: Application to Natural Surfaces

O. Benhmammouch, L. Vaitilingom
A. Khenchaf, and N. Caouren

Laboratoire E^3I^2-EA3876 ENSIETA, Ecole Nationale Supérieure des
Ingénieurs des Etudes et Techniques de l'Armement
2 rue Franois Verny 29806, Brest cedex 9, France

Abstract— In this paper, roughness effects, in electromagnetic wave propagation above natural surfaces, are introduced using a new method based on surface generation and a roughness parameter. Different surfaces are characterized by the means of permittivity. Finally some results are presented for different surfaces (ground, sea, snow cover) and frequencies (UHF-band, X-band).

1. INTRODUCTION

Electromagnetic wave propagation above rough surfaces requires a good understanding of various interaction phenomena of the wave with the propagation medium. Numerous methods are able to predict the electromagnetic wave propagation in the troposphere. Tow kinds of methods are developed in literature, exacts methods (Mode theory [1]) and asymptotic methods (geometrical optic [2], parabolic equation [3, 4]), the most popular method is the parabolic equation. In this paper a model based on this equation has been implemented to provide a tool for electromagnetic wave propagation prediction. A new method, based on surface generation, is introduced for a better taking into account of the surface's roughness. To conclude, the surface's roughness effects, on electromagnetic wave propagation, are demonstrated threw examples where some results of simulations are showed for different configurations and different surfaces.

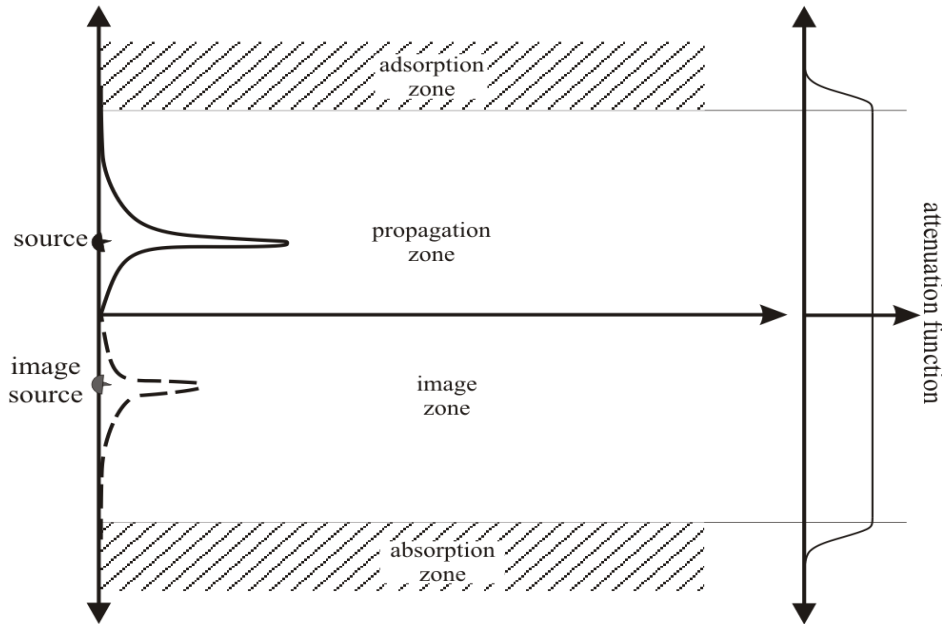

Figure 1: Image source method and attenuation function.

2. ELECTROMAGNETIC PROPAGATION METHODS

The parabolic wave equation is widely used for predicting electromagnetic wave propagation in the troposphere. To obtain this equation, some simplifications are introduced on the conventional elliptical equations propagation to obtain a parabolic equation [3, 14]. To solve this equation we use the Split Step Fourier method [3, 14, 15]. In order to take into account the reflection of waves by the surface, an image propagation domain is introduced below the propagation domain (method of

image source) (Figure 1). To satisfy Summerfield radiation conditions, towards infinity, an absorption area is added beyond maximum height, in this area the field is multiplied by an attenuation function, quick decrease towards zero.

3. PROPAGATION MEDIUM AND SURFACE CHARACTERIZATION

In our work, we are interested on electromagnetic wave propagation in the troposphere, the lowest layer of Earth's atmosphere (The mean average depth of the troposphere is about 11 km). The refraction index n is the most influent parameter in the electromagnetic wave propagation in the troposphere. It can be calculated using Smith-Weintraub model [18]: $n = 1 + 7.76 \cdot 10^{-5}\, P/T + 0.373\, e/T^2$, where P is the atmospheric pressure, T is the temperature in Kelvin and e is the partial pressure of vapour.

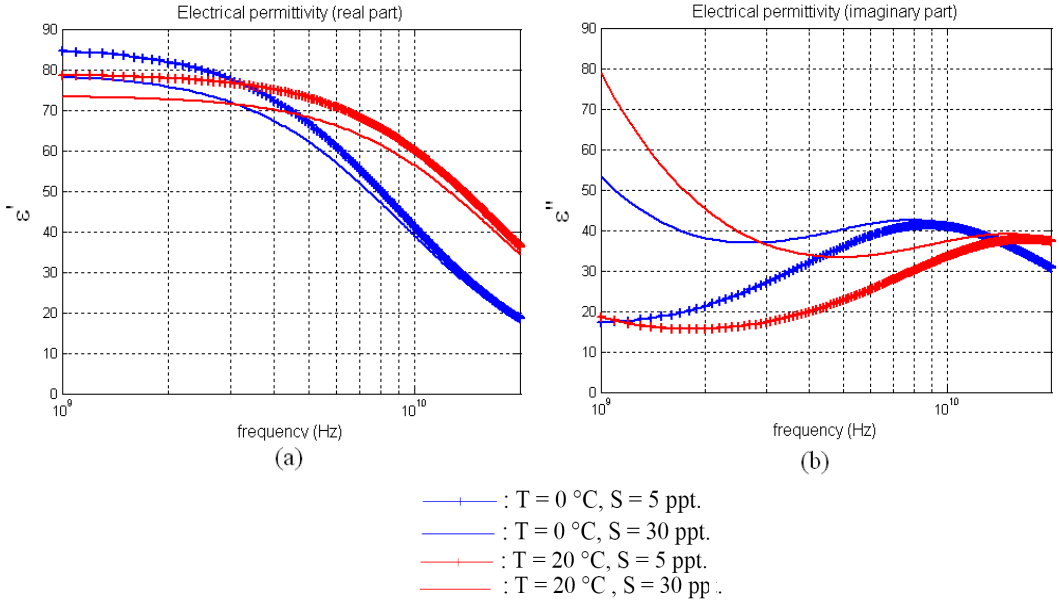

Figure 2: Debye model: (a) Real part of permittivity, (b) Imaginary part of permittivity.

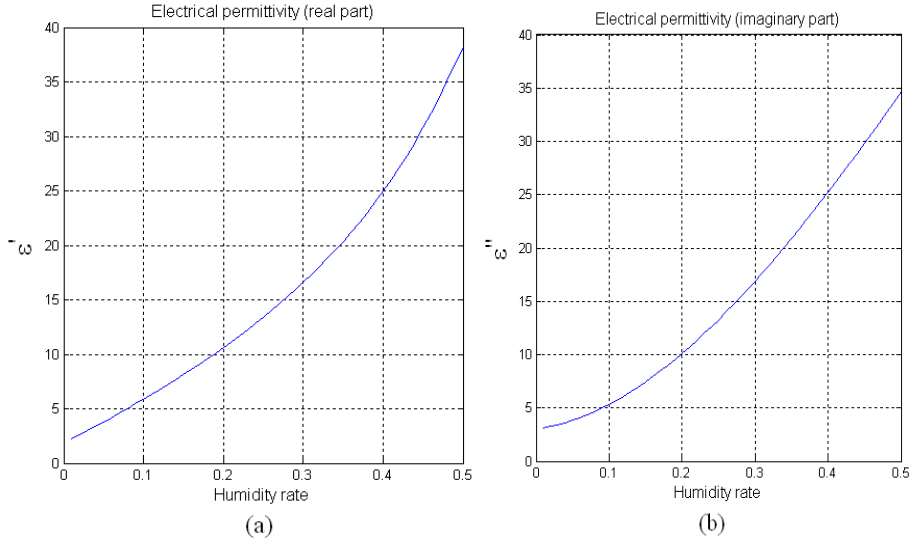

Figure 3: Topp model: (a) Real part of permittivity, (b) Imaginary part of permittivity.

To calculate the scattering properties for different kinds of surfaces, the understanding of the their dielectric proprieties is essential. These proprieties are function of complex permittivity

$\varepsilon = \varepsilon' - j\varepsilon''$ where ε' represents electrical propagation capacity and ε'' represents electrical loss. For maritime surface, we use Debye model [5] to calculate ε as a function of temperature T, salinity S of the surface and frequency of incident wave in *X-band* for a temperature between $0\,^{\circ}$C and $40\,^{\circ}$C and salinity rate between 4 ppt and 35 ppt (Figure 2).

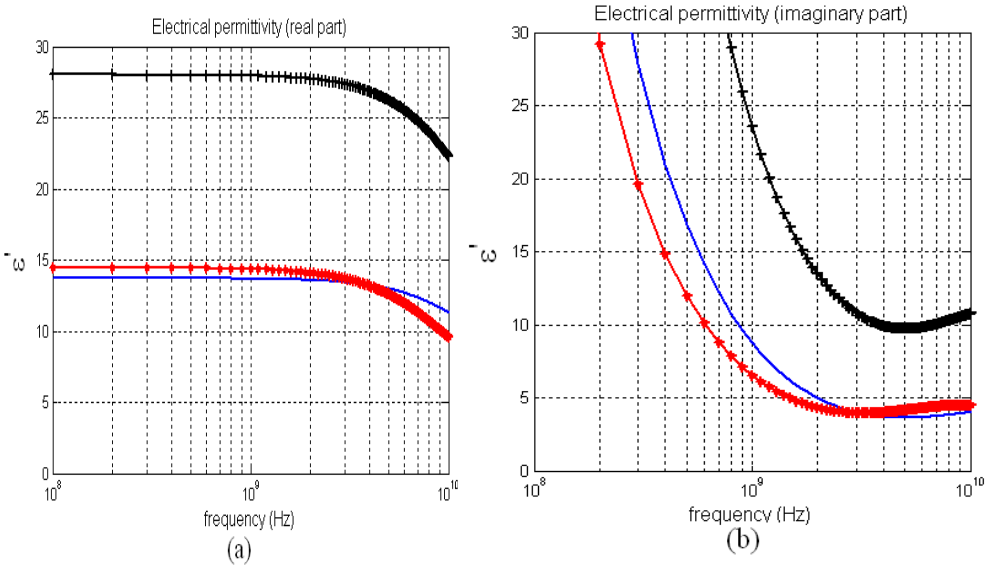

Figure 4: Dobson-Peplinsky model.

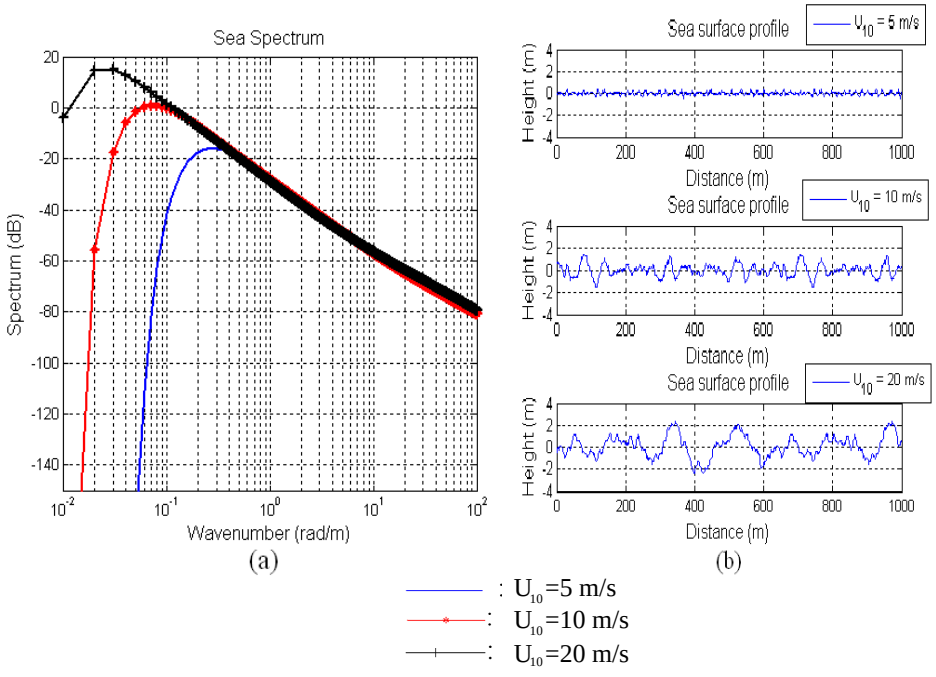

Figure 5: (a) Elfouhaily spectrum, (b) Sea profile for different wind speed.

In the case of snowy surface, we use Ozawa & Kuroiwa model [8]. The complexity of terrestrial surface impose the use of semi-empirical models like Topp model [7] or Dobson-Peplinsky model [6]. Topp quantifies permittivity of the ground in function of humidity rate for low frequency (20 MHz–1 GHz) (Figure 3). For higher frequencies, we use Dobson-Peplinsky model.

4. ROUGH SURFACES

Accurate modelling of electromagnetic wave propagation over irregular terrain is crucial for the prediction of radar performance. To observe the influence of this type of terrain, we introduce a new method which consists on generating surface using a spectrum. Once the surface created, the electromagnetic wave is propagated using the method introduced by Mac Arthur and Bebbington [11]. In literature, we find a method which consists on an introduction of a roughness parameter (Ament [16] (1953), Miller et al. [17] (1984)). In our method this parameter is used to model the influence of the low roughness that cannot be introduced in surface generation because of mesh limitation.

To generate a sea surface we use Elfouhaily spectrum [9] and a Monte-Carlo simulation [10]. This spectrum given in function of wind's speed and one-dimensional fetch.

To modeless terrestrial and snowy clutter, we employ Gaussian spectrum [13]. If we study this spectrum, we notice that the parameter σ (standard deviation) acts on vertical roughness whereas the parameter L (correlation length) acts on horizontal roughness (Figure 6).

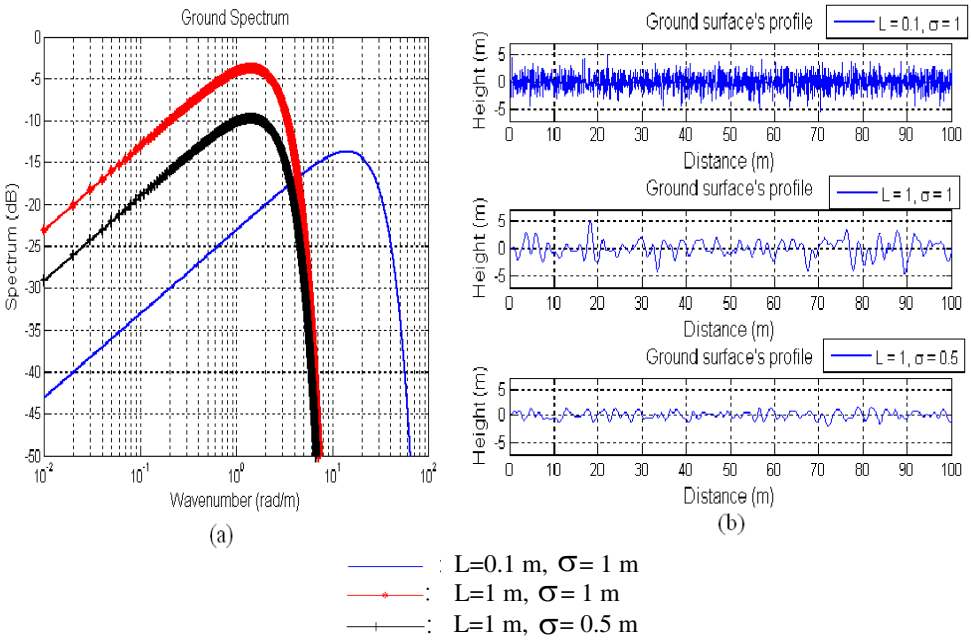

Figure 6: (a) Gaussian spectrum, (b) Ground profile for different length correlation and standard deviation.

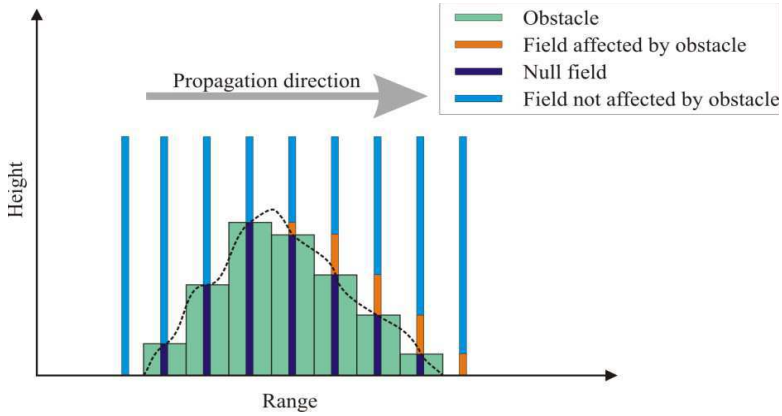

Figure 7: Propagation above staircase represented terrain.

For modelling electromagnetic wave propagation above sea or terrestrial surface, we use the method introduced by Mac Arthur and Bebbington [11]. The terrain is modelled with successive

horizontal segments as shown in Figure 7. If the terrain goes up, the field is propagated with the SSF method and the part of field which is in the obstacle is set to zero. If terrain goes down the field is merely propagated by means of SSF method.

5. NUMERICAL RESULTS

In this section, the numerical results are presented. These results are computed for different surfaces type, source's heights and different atmospheric conditions. The simulations are used to show the influence of natural surface's geometry and constitution in electromagnetic waves propagation. The results obtained coherent whit those presented by Sevgi [19].

In Figure 8, path loss is illustrated for a terrestrial surface in UHF-band (*500* MHz) the source is placed at *70* m height (a, b). The classical method consists on introduction of roughness effects using a coefficient. We can see that the new method allows a better taking into account of the surface roughness. Indeed, the interference lobes are less extended in the results obtained by the new method.

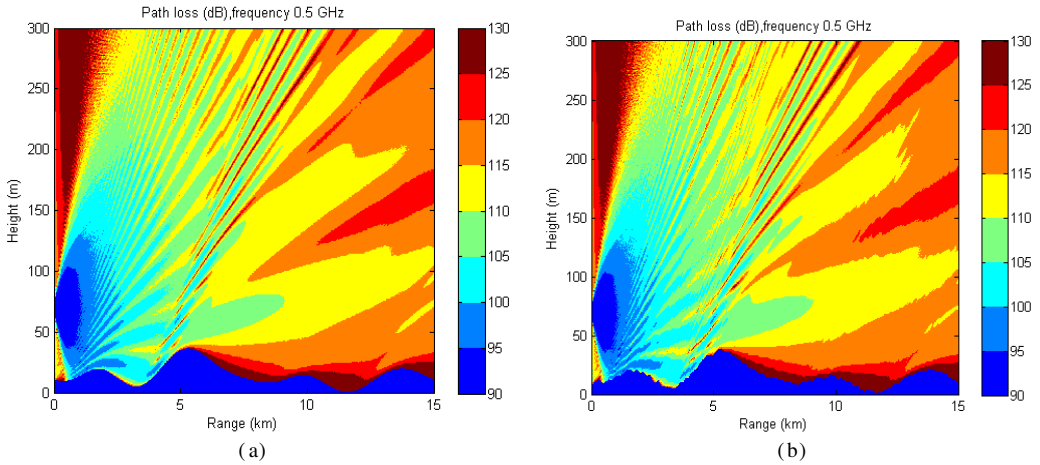

Figure 8: Path loss for a terrestrial surface, (a) Classical method, (b) Our method for 500 MHz.

In Figure 9, path loss is illustrated for a sea surface in X-band (*10* GHz) a source placed at *30* m height and a wind speed of *15* m/s. The new method allows a better of the surface's geometry, the perturbations due to roughness are more perceptible.

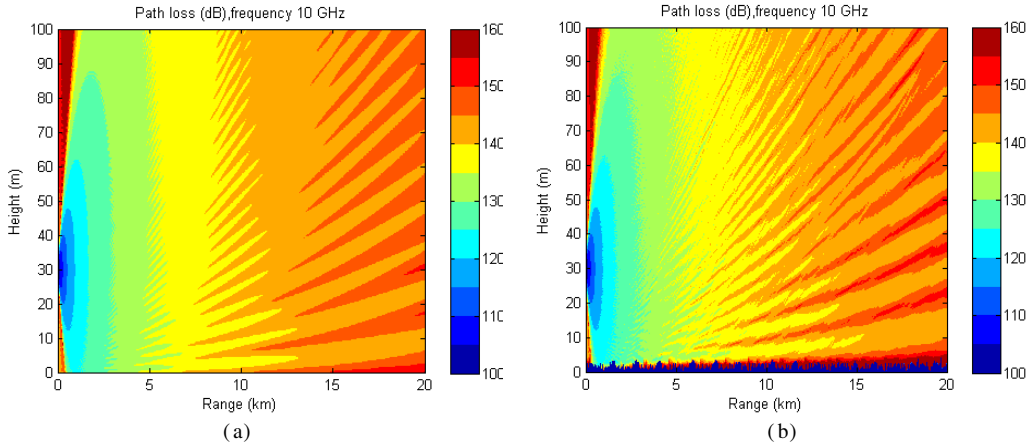

Figure 9: Path loss for 10 GHz and a sea surface, (a) Classical method, (b) Our method.

6. CONCLUSION AND PERSPECTIVES

The main purpose of this paper was the simulation of electromagnetic wave propagation, above rough natural surfaces. An original method, for a better taking into account of the surface's

roughness, was introduced. This method is based on generation of surfaces and the use of a roughness parameter to model small roughness. The results presented show an amelioration of propagation loss computation, the effects of the surface's roughness are more perceptible in the results obtained with the new method. An evolution of our work will be the implementation of this method in a tri-dimensional propagation domain in presence of different types of natural surfaces. This generalisation will require an adaptation of the propagation equation, the surface generation and roughness parameter. Another evolution can be the adaptation of Fresnel's reflection parameter to a bistatic radar configuration. This amelioration will be tested for a bi-dimensional domain and extended to a tri-dimensional.

REFERENCES

1. Durand, J. C., "Optique géométrique et diagramme de portée Radar en atmosphère satandard," *Revue Technique Thomson*, Vol. 20–21, No. 1, Mars 1989.
2. Fournier, M., "Méthodes d'évaluation de l'effet des conduits d'évaporation à la surface de la mer," *AGARD Meeting, 'Multi Mechanism Propagation Paths'*, Neuilly sur Seine, France, Octobre 1993.
3. Craig, K. H. and M. F. Levy, "Parabolic equation modelling of the effect of multipath and ducting on radar systems," *IEE Proc.*, Vol. 138, No. 2, 153–162, April 1991.
4. Douchin, N., S. Bolioli, F. Christophe, and P. Combes, "Etude théorique de la caractérisation radioélectrique du conduit d'évaporation," *49th Proc. Symposium Int. Agard Remote Sensing of the Propagation Environment*, CESME-Izmir, Turkey, December 1991.
5. Khenchaf, A., "Bistatic scattering and depolarization by randomly rough surfaces: Application to the natural rough surfaces in x-band," *Waves in Random Media*, Vol. 11, 61–89, 2001.
6. Dobson, M. C., F. T. Ulaby, M. T. Hallikainen, and M. A. El-Rayes, "Microwave dielectric behavior of wet soil — Part II — Dielectric mixing models", *IEEE Trans. GRS*, Vol. 23, No. 1, 35–46, 1985.
7. Topp, G. C., J. L. Davis, and A. P. Annan, "Electromagnetic determination of soil water content: Measurements in coaxial transmission lines," *Water Ressources Research*, Vol. 16, No. 3, 574–582, 1980.
8. Ozawa, Y. and D. Kuroiwa, "Dielectric properties of ice, snow and supercooled water microwave propagation in snowy districts," *Monograph Ser. Res. Inst. Appl. Electricity*, No. 6, 31–71, ed. Y. Asami, Hokkaido University, Sapporo, 1958.
9. Elfohaily, T., B. Chapron, K. Katsaros, and D. Vansdermark, "A unified directional spectrum for long and short wind-driven waves," *MTS/IEEE Conference Proceedings Oceans'97*, Vol. 102, No. C7, 15781–15796, July 15, 1997.
10. Bein, G. P., "Monte carlo computer techniques for one-dimensional random media," *IEEE Transactions on Antennas and Propagation*, Vol. 21, No. 1, 83–88, January 1973.
11. Mac Arthur, R. J. and D. H. O. Bebbington, "Diffraction over simple terrain obstacles by the method of parabolic equation," *ICAP91, IEE Conf. Pub.*, No. 333, 2824–2827, 1991.
12. Klein, L. and C. Swift, "An improved model for the dielectric constant of sea water at microwave frequencies," *IEEE Journal of Oceanic Engineering*, Vol. 2, No. 1, 104–111, Januaray 1977.
13. Brown, G., "Backscattering from a Gaussian-distributed perfectly conducting rough surface," *IEEE Transactions on Antennas and Propagation*, Vol. 26, No. 3, 472–482, May 1978.
14. Dockery, G. D., "Modelling electromagnetic wave propagation in the troposphere using the parabolic equation," *IEEE Transactions on Antennas and Propagation*, Vol. 36, 1464–1470, 1989.
15. Ko, H. W., J. W. Sari, M. E. Thomas, P. J. Herchenroder, and P. J. Martone, "Anomalous propagation and radar coverage through inhomogeneous atmospheres," *AGARD CP-346*, 25.1–25.14, 1984.
16. Miller, A. R. and R. M. E. Brown, "New derivation for the rough surface reflection coefficient and for the distribution of seawave elevations," *IEE Proc. IRE*, Vol. 131, Part H, 114–116, 1984.
17. Ament, W. S., "Toward a theory of reflection by a rough surface," *Proc. IRE*, Vol. 41, 142–146, 1953.
18. Smith, E. K. and S. Weintraub, "The constants in the equation for atmospheric refractive index at the radio frequencies," *Proc. IRE*, Vol. 41, 1035–1037, 1953.

19. Sevgi, L. and Ç. Uluisik, "A matlab-based visualization package for planar arrays of isotropic radiators," *IEEE Antennas and Propagation Magazine*, Vol. 47, No. 1, 156–163, February 2005.

Highly Compact Embedded Duplexer Implementation for WiMAX Dual-band Front-end Module with Organic Package Substrate

Kyungo Kim, **Taeeui Kim**, **Donghwan Lee**, **and Sung Yi**
Samsung Electro-Mechanics, Korea

Abstract— In this paper, low cost and high performance duplexers are investigated for WiMAX front-end module with multi-layered organic package substrate. This dual band FEM includes a 2.5 GHz power amplifier die with switch and has tiny PKG form factor. In addition to module size limitation, FEM requires higher gain and stringent attenuation characteristics specification. The embedded BPFs and duplexer were designed on 8 layer organic substrates by using ADS and HFSS for finding out efficient structure and verifying FEM specifications.

The dual-band FEM with embedded passive components incorporates duplexer including 2 GHz and 5 GHz BPFs. BPFs and duplexer have size of $1.65 \times 1.8 \times 0.12$ mm, $1.32 \times 1.2 \times 0.12$ mm and $2 \times 2 \times 0.6$ mm respectively. Integrated dual-band BPFs show an insertion loss of < -1.8 dB in path band and 22∼40 dB attenuation performance in rejection band. The measured results of BPFs and duplexer show good electrical performance with low insertion loss, high attenuation.

Embedded passive Packaging technology has many advantages such as improving packaging efficiency and better electrical performances for low cost and highly compact RF SOP (System on Package) applications.

1. INTRODUCTION

Nowadays wireless communication systems are getting faster and requiring smaller size which are able to operate in multi-band frequency. In addition, cost issue is very strict for time to market. Many papers have introduced two representative technologies for achieving higher integration module. One is SoC (System on Chip) technology. The other is SoP (System on Package) technology. SoC technology integrates signal collection, signal conversion, data storage, I/O functionalities into single chip. It has many advantages, such as fast, high integrity, low power, small size. However design of SoC is highly complex and cost of SoC is high. In contrast, SoP is a functional system or subsystem assembled into a single package. It contains two or more dissimilar die, typically embedded other components such as passives, filters, antennas into substrate. Therefore, SoP has mainly focused on cost reduction, high reliability and small size form factor. In particular, the embedded passive device technology in SoP provides outstanding solution for these issues. In the present, LTCC has been widely used for wireless application such as FEM, BT, and WLAN module, since LTCC is possible to integrate high Q passive components. However, LTCC materials are more expensive than organic materials. And LTCC has a limitation of size, and mismatch of CTE (coefficient of thermal expansion) between LTCC module and organic main board. In the contrast, embedded passive technology has many advantages with organic material since passive components implement low cost material with high Dk, low Df. Therefore EPD with organic dielectrics becomes replacing ceramic or silicon substrates.

This paper presents the application of embedded passive technology in a dual-mode FEM. Originally, LTCC technology is adopted in this module but it is replaced with organic substrate in this research. This dual band FEM has 1 duplexer consist of 2 GHz and 5 GHz BPFs embedded in organic substrate. Designs, organic substrate structure for embedded each BPF device and electrical characteristics of BPFs and duplexer are shown as results.

2. DUAL-BAND FEM STRUCTURE

Figure 1 illustrates WiMAX FEM system architecture. The WiMAX dual band FEM consists of power amplifier (PA), SP4T, baluns, transmit band pass filter and receiver band pass filter. This front-end module support 2.4 GHz band and 5.2 GHz band. To reduce size and cost of module, FEM was designed using embedded passive technology on organic substrate.

LTCC material is good electrical characteristics such as high dielectric of 6∼10 and low loss tangent of 0.002, but also has cost conflict. The choice of material set depends on the application, cost, performance and size. This paper introduces organic material with low cost and high electrical performance. The main material of FEM substrate is epoxy material of composite type with high Dk, low Df at microwave frequencies. The Dk value is 18 @10 GHz and Df value is 0.008 @10 GHz.

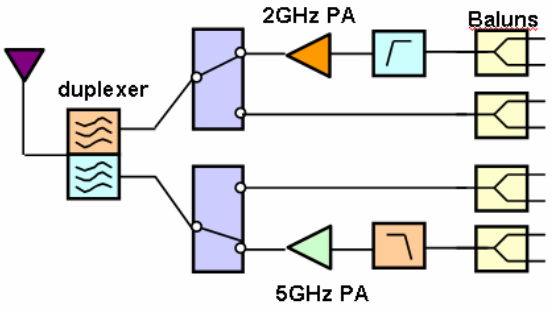

Figure 1: System architecture of dual band WiMAX FEM.

The whole process using this material is compatible with standard printed circuit board process. For the FEM device, two composite layers were laminated with BT prepregs symmetrically. Microvia drilling and Cu plating used for interconnection with each layer. Microvias were accomplished using CO_2 laser to get via size on 60∼80 µm.

Figure 2 shows 8 layer structure using this material. The composite materials used into 3-4 and 5-6 layer, so embedded passive components were designed using these layers. Capacitors can locate in 3-4 or 5-6 layers. And inductors were designed using core layers (L4, L5) that are possible to implement fine line and space with minimum 30/30 µm.

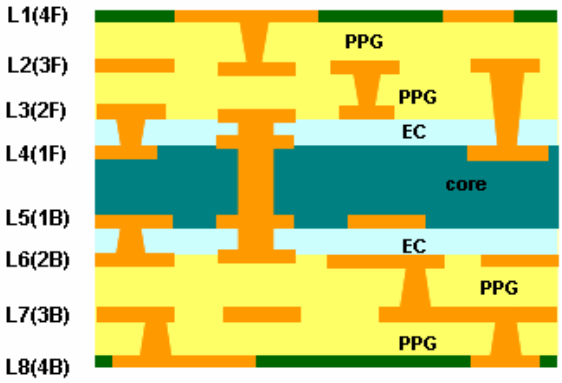

Figure 2: Multilayer stack-up structure.

3. BAND-PASS FILTER DESIGN

Figure 3 shows conventional second-order filter prototype that uses the capacitive coupling to link two LC tank resonators. The reason why it prefers capacitive coupling to inductive is because inductor Q factor is somewhat lower than LTCC. For getting additional transmission zeros, it can use either C feedback or L feedback. The prototype BPFs considered matching with other components using capacitors. Capacitors can locate in 3-4 or 5-6 layers from Fig. 2. And inductors were designed using core layers (L4, L5) that are possible to implement fine line and space.

The 2.5 GHz Band-pass filters shown in Fig. 4 can be realized by stack-up structure of Fig. 2. BPFs have size of $1.65 \times 1.625 \times 0.12$ mm, $1.32 \times 1.2 \times 0.12$ mm respectively. In order to achieve performance, these BPFs were simulated by ADS and HFSS 3D simulator. Simulation results are shown in Fig. 5. 2 GHz BPF has a low insertion loss $-1.4 \sim -1.5$ dB in pass band from 2.3 to 2.7 GHz and high rejection, -20.3 dB, required at 2 GHz band. 5 GHz BPF shows that in band insertion loss is -1.5 dB (5.15 ∼ 5.875 GHz). The out of band rejection is 30 dB at 4 GHz.

4. WIMAX FEM DUPLEXER EMBEDDED SUBSTRATE IMPLEMENTATION

This paper presents an embedded duplexer design for WiMAX dual FEM using BPFs design. To optimize the electrical performance of duplexer, additional matching network used between 2 and 5 GHZ BPF. The key to implement matching network is to make meander line inductor with fine line. Duplexer design combining 2.5 GHz BPFs is shown in Fig. 6(a). Fig. 6(b) shows the result

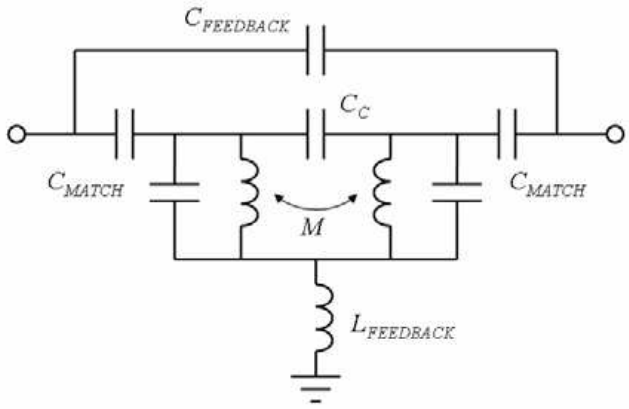

Figure 3: 2nd order BPF prototype equivalent circuit.

(a) (b)

Figure 4: (a) 2 GHz BPF 3D design, (b) 5 GHz BPF 3D design.

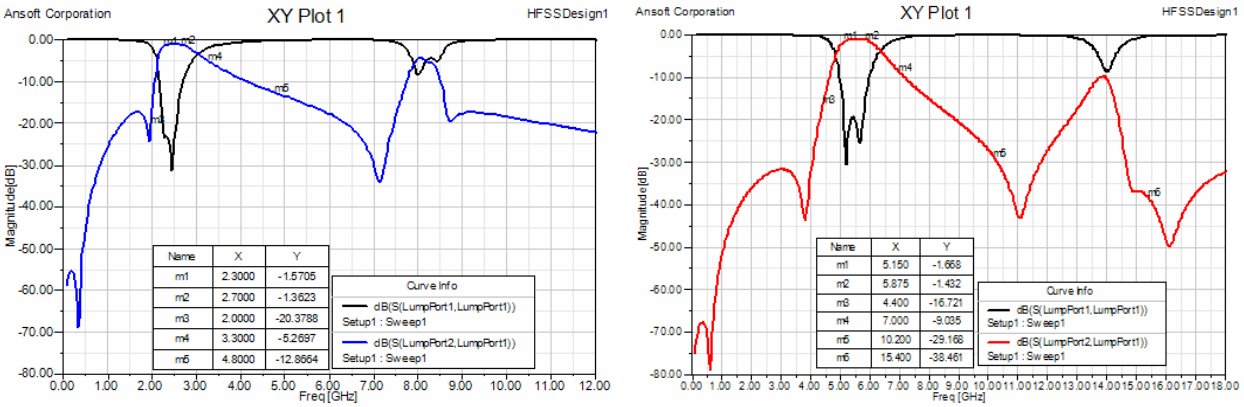

(a) (b)

Figure 5: (a) 2 GHz BPF HFSS simulation result, (b) 5 GHz BPF HFSS simulation result.

of duplexer 3D simulation. The insertion loss in pass band −1.7 dB and attenuation is less 20 dB below 2 GHz.

Figure 7 shows the sample image of WiMAX FEM embedded duplexer into organic substrate. Also this sample met the reliability condition of PKG level. The Strip has size of 105*82 mm and 144 unit. Trough hole vias used for effective thermal transfer from top and to bottom.

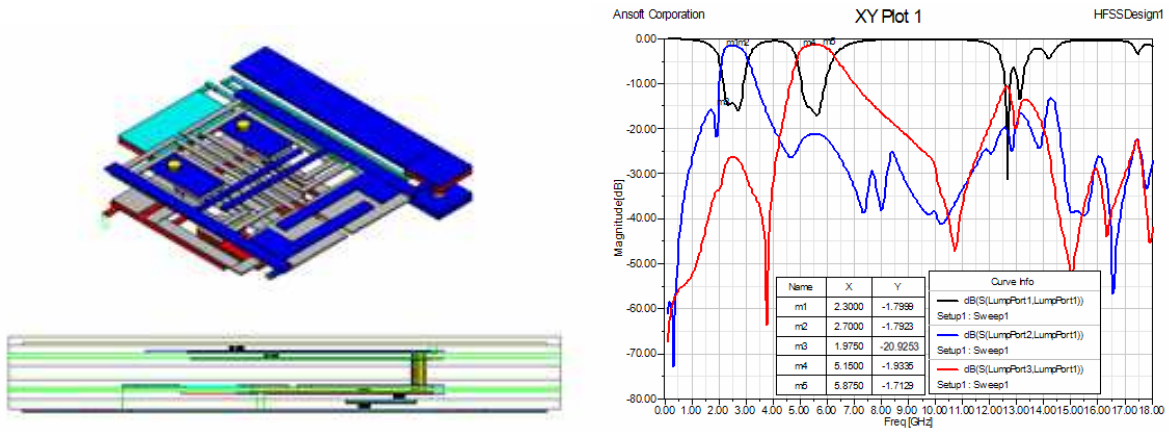

(a) (b)

Figure 6: (a) Duplexer design in substrate, (b) Duplexer simulation result.

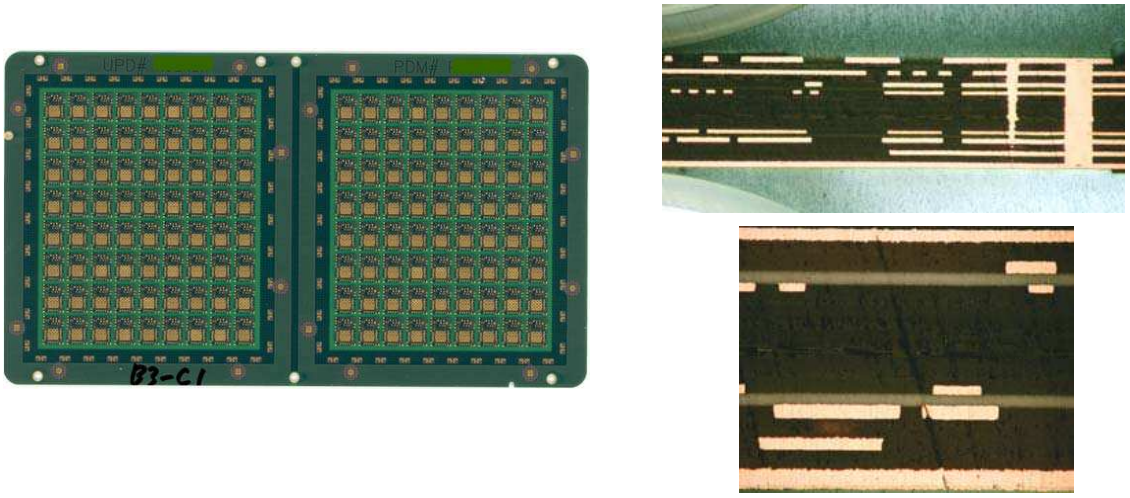

Figure 7: (a) FEM substrate embedding duplexer, (b) Cross section image.

5. CONCLUSIONS

In this paper, we presented the organic embedded passive technology using multilayer PCB process. The most important is to design complex passive components as well as to consider a limitation of size and cost. Embedded BPF and duplexer have been implemented in composite material layer. The overall size of module which includes PA and bypass capacitor is 5.4*4*1.5 mm. The duplexer and each BPFs shows the good electrical performance.

REFERENCES

1. Lee, G. A, M. Megahed, and F. D. Flaviis, "Desing of multilayer spiral inductor resonator filter and diplexer for system-in-a-package," *IEEE MTT-S Int. Microwave Symp. Dig.*, 527–530, 2003.
2. Lim, K., S. Pinel, M. Davis, A. Sutono, C.-H. Lee, D. Heo, A. Obatoynbo, J. Laskar, M. Tantzeris, and R. Tummala, *RF SOP Wireless Commun.: Microwave Mag.*, Mar. 2002.
3. Quendo, C., E. Rius, and C. Person, "Narrow bandpass filters using dual-behavior resonators," *IEEE Trans. Microwave Theory Tech.*, Vol. 51, 734–743, Mar. 2003.
4. Sturdivant, R., C. Ly, J. Benson, and J. Hauhe, "Design and performance of a high density 3D microwave module," *IEEE MTT-S Int. Microwave Symp. Dig.*, Vol. 2, 501–504, 1997.
5. Chiu, C. T., T. S. Horng, H. L. Ma, S. M. Wu, C. P. Hung, R. Chen, and C. H. Chu, "Development of high-Q embedded passive library for RF-SOP module applications," *Proc. 55th Electron. Comp. Technol. Conf.*, 1590–1593, 2005.

6. Davis, M. F., A. Sutono, K. Lim, J. Laskar, V. Sundaram, J. Hobbs, G. E. White, and R. Tummala, "High performance spiral inductors embedded on organic substrates for SOP applications," *IEEE MTT-S int. Microwave Symp. Dig.*, 2229–2232, 2002.
7. Song, H. S. and Y. S. Lee, "A miniaturized 2.4 GHz band multi-layer bandpass filter using capacitively loaded quarter-wavelenghth slow-wave resonator," *IEEE MTT-S Int. Microwave Symp. Dig.*, 515–518, 2003.
8. Gaynor, M. P., *System-in-Package RF Design and Applications*, Artech House, 92–96.
9. Li, L., P. Bowles, L. T. Hwang, and S. Plager, "Embedded passives in organic substrate for Bluetooth transceiver module," *Proc. 53rd Electron. Comp. Technol. Conf.*, 464–469, 2003.

Application of Defect Induced Microwave Band Gap Structure for Non-destructive Evaluation and the Construction of a Frequency Selector Switch

E. D. V. Nagesh, N. Yogesh, and V. Subramanian
Microwave Laboratory, Department of Physics
Indian Institute of Technology Madras, Chennai 600036, India

Abstract— The use of microwave band gap structures for the non-destructive evaluation of material property is being probed in this paper. As a first step, we studied numerically, the appearance of a point defect mode within the band gap of a microwave band gap structure for the use as a tool to evaluate the dielectric constant of the material at the defect site. The simulations were carried out using the FEMLAB software. In a pure 10×10 square lattice constructed with a material of dielectric constant (ε) 5.5 (in the form of a right circular cylinder), a point defect is created by replacing one of the rods with a geometrically similar but with different dielectric constant material. The appearance of the defect mode is governed by the refractive index contrast (defined as the ratio between the refractive index of the material at the defect site (n_d) and the material of the lattice (n_l). In this case, the refractive index contrast (n_d/n_l) was found to be between 0.85 and 1.28. Simulations were also done with the lattice material of dielectric constant 10 and the defect mode appeared for $1.18 < n_d/n_l < 0.84$. For the contrast less than 1, defect creates the fundamental mode similar to TE_{01} mode whereas for the contrast greater than 1, next higher mode similar to TE_{11} appears. Once a defect mode appears, it moves towards lower frequency as the dielectric constant of the defect site is increased. In this paper, we propose to evaluate the dielectric constant of a material using the above procedure. This paper also proposes the construction of a novel frequency selector switch that has two line defects in a 10×20 square lattice structure constructed with material of dielectric constant 10.

1. INTRODUCTION

The electromagnetic propagation through periodic structures, also called photonic crystals has attracted attention over the years [1–3] because of their potential applications [4, 5]. The periodic sites can be occupied by either dielectric and/or magnetic materials depending on the application. This is analogous to the electronic case where the propagation is because of electrons compared to photons in photonic crystals. The dielectric constant/magnetic permeability of the material at the defect site is responsible for the scattering of electromagnetic waves resulting in band gaps over a range of frequencies. In order to achieve this, the periodicity should be of the order of wavelength of source. Thus, in microwave frequencies, the periodicity will be of the order of centimeters and is of the order of micrometer in the optical frequency region. Defects can also be created in these structures and are of two types viz; acceptor type and donor type [6]. The creation of defect makes the structure acts like a resonator locally resulting in an extra mode within the band gap. The position and nature of the defect mode depends on the position as well as the dielectric constant of the material at the defect site. Similarly, line defects created in the structure act as either Fabry-Perot resonator or waveguide depending on the direction of propagation [7]. The use of these structures allows one to have control over photons in their own fashion similar to the electronic case. Since photons travel much faster than that of electrons, these structures can be exploited for communications where a faster transmission can be achieved. The applications of such structures include resonators, filters, antennas, polarizers, optical switches [8] etc. In this paper, we propose the use of these structures for non-destructive evaluation of a material property such as dielectric constant (or refractive index) and also as a frequency selective switch in the microwave frequency region. The results were based on the simulations performed using FEMLAB and few experimental results were also presented. The structure chosen was a 10×10 square lattice constructed with a material of dielectric constant 5.5 and the length and diameter of the rods were 10 and 0.414 cm respectively. The lattice spacing was chosen to be 0.9 cm. Point defect was introduced at the center of the structure in all the cases. Line defects were created at two different positions in order to demonstrate the frequency selector switch. In this case, the 10×20 lattice structure was chosen with the same set of parameters for convenience.

2. EXPERIMENTAL ARRANGEMENT

A microwave vector network analyzer (N5230A) was used to obtain the S_{21} parameter in the frequency region between 10 and 20 GHz with the help of two horn antennas kept on either side of the structure. The antennas were separated by a distance of 50 cm. The fringe effects of the electric field were assumed to be minimum. Initially, the S_{12} parameter was normalized without any structure between the antennas. For all the experiments, only E-polarized beam (with electric field parallel to the length of the rod) was used. For convenience, only the normal direction (Γ-X) was considered in the present case. In case of frequency selector switch also, the experiment was performed in a similar manner but with horn antennas placed according to the structure.

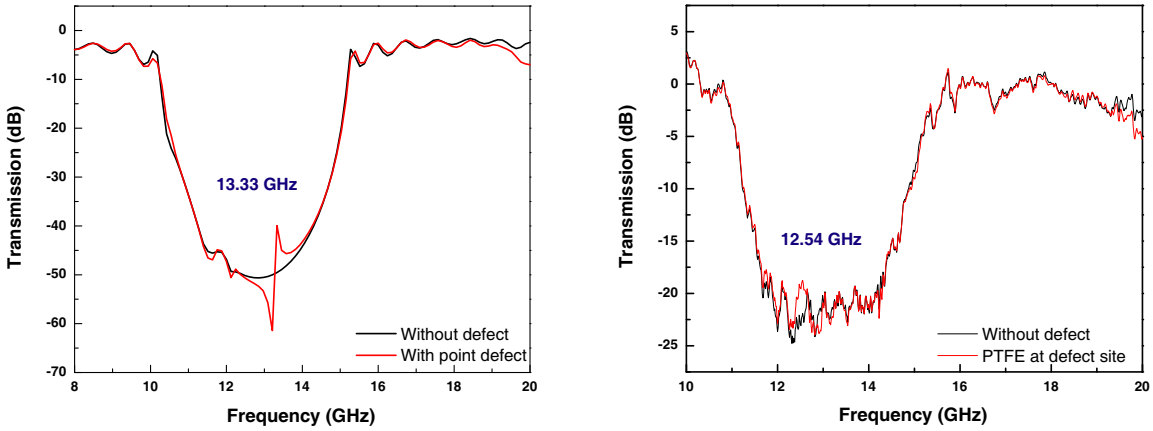

(a) (b)

Figure 1: (a) Transmission spectra obtained numerically for a pure structure and for the structure with a point defect at the center; (b) Transmission spectra obtained experimentally for a pure structure and for the structure with a point defect at the center.

3. RESULTS AND DISCUSSION

Figure 1(a) shows the transmission spectrum obtained numerically for a square lattice without any defects. It can be observed that there exists a band gap from 10.06 to 15.27 GHz with a mid-gap frequency of 12.67 GHz. The experimentally observed value was 13.30 GHz as shown in Fig. 1(b). Simulations were carried out with a point defect at the center of the structure (by inserting a geometrically similar object), but with varied dielectric constant. The dielectric constant at this particular site (ε_d) was varied from 1 to 20 in steps of 1. It was found that the resonant frequency moves towards lower frequency side as the dielectric constant at the defect site is increased from 1 to 4 indicating the resonance effect. The defect mode was again observed for a dielectric constant of 9 at the defect site. This shows that, in order for a defect structure to act as a resonator, one should have a minimum value of refractive index contrast, defined as the ratio between refractive index of the material at the defect site (n_d) and the refractive index of the material of the lattice (n_l). In the present case it was found to be 0.85 if $\varepsilon_d < \varepsilon_l$ and 1.28 if $\varepsilon_d > \varepsilon_l$. Simulations were also performed for a square lattice constructed with a material of dielectric constant 10 and the dielectric constant at the defect site was varied from 1 to 20. In this case also, the minimum refractive index contrast was observed to be 0.84 if $\varepsilon_d < \varepsilon_l$ and 1.18 if $\varepsilon_d > \varepsilon_l$. The obtained results are shown in Fig. 2. For $\varepsilon_d < \varepsilon_l$, the mode is like a fundamental mode and for $\varepsilon_d > \varepsilon_l$, it is the next higher order mode. This particular method is useful in the evaluation of dielectric constant. Suppose we have a material whose dielectric constant (or refractive index) is not known, we can insert that material at a particular defect site and observe the resonant frequency from which the dielectric constant can be found. If one couldn't observe the defect mode, it means that the refractive index contrast is not sufficient to support a resonant mode inside the band gap, in such case, changing the lattice material might help in observing a resonant mode. Thus, one can use this method effectively for non-destructive evaluation. Experiment performed by inserting a Poly Tetra Fluoro Ethylene (PTFE) sample at the center of the structure shows the resonant frequency to be 12.54 GHz as in Fig. 1(b) whereas the simulated results show a defect mode at 13.33 GHz as in Fig. 1(a). It can be observed that the position of the defect mode is towards the positive side of the mid-gap

frequency in simulated results whereas it is towards negative side of the mid-gap frequency in the experimental results.

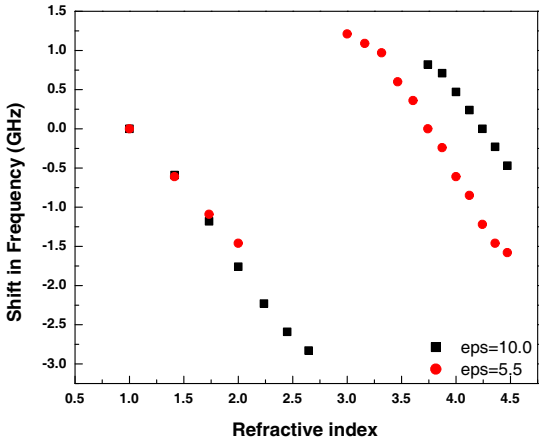

Figure 2: The shift in resonant frequency with change in refractive index of a material at the defect site.

Photonic crystals can be used for a variety of applications such as antennas, filters, switches etc. In this paper we demonstrate the frequency selector switch in which we have a 10×20 (rows $\times$ columns) square lattice constructed with a material of dielectric constant 5.5. The lattice spacing was chosen to be 0.9 cm. Line defects were created at two different positions. Along the direction of propagation, 5th and 6th columns till 5th row were removed from the structure and for convenience we labeled port 1, port 2 and port 3 at windows of the structure as shown in Figs. 3(a) to 3(c). The excitation field was at port 1 in between 5th and 6th rows of the structure and the frequency span was from 8 to 20 GHz. It was observed that for majority of the frequencies, there was output at port 2 and port 3 simultaneously as shown in Fig. 3(a). However, at 11.03 GHz, there was output only at port 3 and at 13.45 GHz there was output only at port 2 as shown in Fig. 3(b) and 3(c) respectively. This was confirmed with the experiment which was performed to obtain S_{21} and S_{31} at port 2 and port 3 respectively for the frequency range of 10–20 GHz. The parameters S_{21} and S_{31} were normalized with the background data (without structure) at port 2 and port 3. Fig. 4(a) indicates that at 14.95 GHz, S_{31} is more by 43.20 dB compared to S_{21}, whereas Fig. 4(b) indicates that at around 17.3 GHz, S_{21} is more by 26.71 dB compared to S_{31}. This gives the confirmation that line defect based photonic crystals can be used as a frequency selective switch.

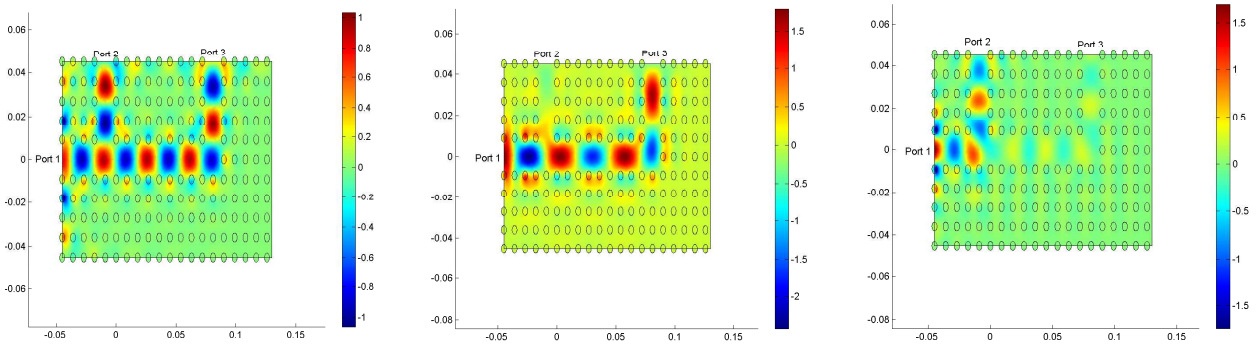

(a) (b) (c)

Figure 3: (a) Photonic crystal as a frequency selector switch with the input at port 1 and the output at the ports 2 and 3; (b) Photonic crystal as a frequency selector switch with the input at port 1 and the output at the port 3 but not at port 2; (c) Photonic crystal as a frequency selector switch with the input at port 1 and the output at the port 2 but not at port 3.

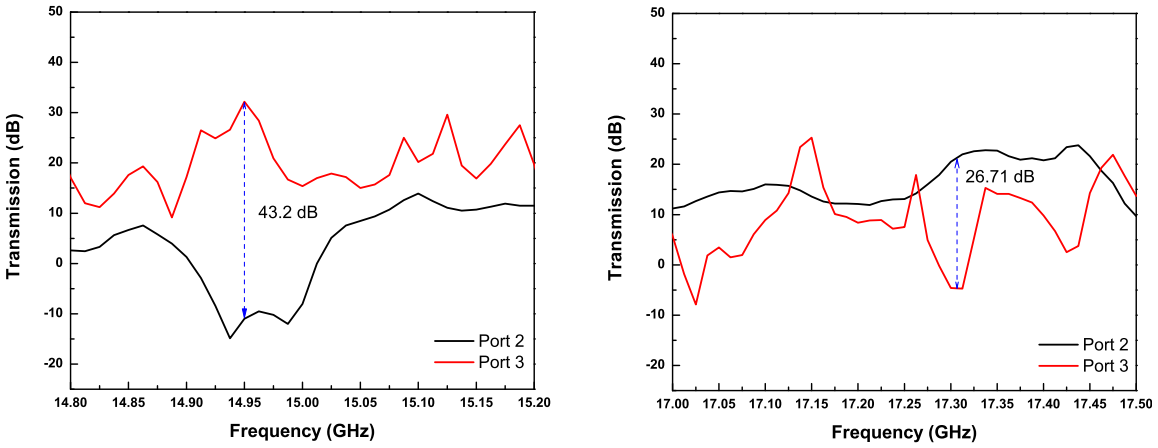

(a) (b)

Figure 4: (a) The transmission spectra obtained experimentally demonstrating frequency selection among port 2 and port 3. It can be observed that at 14.95 GHz, the output at port 3 is more by 43.20 dB compared to port 2; (b) The transmission spectra obtained experimentally demonstrating frequency selection among port 2 and port 3. It can be observed that at 17.30 GHz, the output at port 2 is more by 26.7 dB compared to port 3.

4. CONCLUSIONS

The effect of point defect in the form of varying dielectric constant shows that one can extend this to evaluate non-destructively the dielectric constant of the material at the defect site. It may be noted that to observe a defect mode, there should be some refractive index contrast depending on the lattice structure and host material. The efficient use of these structures as a frequency selector switch was also demonstrated.

REFERENCES

1. Yablanovitch, E., "Inhibited spontaneous emission in solid-state physics and electronics," *Phys. Rev. Lett.*, Vol. 58, No. 20, 2059–2062, 1987.
2. Weng, Y., Z. G. Wang, and H. Chen, "Band structure of comb-like photonic crystals containing meta-materials," *Optics Communications*, Vol. 277, 80, 2007.
3. Yang, X. L., L. Z. Cai, Y. R. Wang, G. Y. Dong, X. X. Shen, X. F. Meng, and Y. Hu, "Large complete band gaps in a two-dimensional square photonic crystal with isolated single-atom dielectric rods in air," *Nanotechnology*, Vol. 19, 025201, 2008.
4. Sirigiri, J. R., K. E. Kreischer, J. Machuzak, I. Mastovsky, M. A. Shapiro, and R. J. Temkin, "Photonic band gap resonator gyrotron," *Phys. Rev. Lett.*, Vol. 86, No. 24, 5628–5631, 2001.
5. Serpenguzel, A., "Transmission characteristics of metallodielectric photonic crystals and resonators," *IEEE Microwave and Wireless Comp. Lett.*, Vol. 12, 134–136, 2002.
6. Yablanovitch, E. and T. J. Gmitter, "Donor and acceptor modes in photonic band structure," *Phys. Rev. Lett.*, Vol. 67, No. 24, 3380–3383, 1991.
7. Temelkuran, B. and E. Ozbay, "Experimental demonstration of photonic crystal based waveguides," *Appl. Phys. Lett.*, Vol. 74, No. 4, 486–488, 1999.
8. Joannopoulos, J. D., R. D. Meade, and J. N. Winn, *Photonic Crystals: Molding the Flow of Light*, Princeton University Press, Princeton, New Jersey, 1995.

Towards R-space Bose-Einstein Condensation of Photonic Crystal Exciton Polaritons

D. L. Boiko

Sowoon Technologies S.á.r.l., 1015, Lausanne, Switzerland

Abstract— Coupled states of semiconductor quantum well (QW) excitons and photons in a two dimensional (2D) periodic lattice of microcavities are analyzed theoretically, revealing allowed bands and forbidden gaps in the energy spectrum of exciton polaritons. Photonic crystal exciton polaritons have spatially uniform excitonic constituent set by flat QWs, but exhibit periodic Bloch oscillations in the plane of QWs due to their photonic component. The envelope functions of photonic crystal exciton polaritons can be tailored via effective potential of a photonic crystal heterostructure, by using quasi-periodic lattices of microcavities. Confined envelope function states of lower and upper polaritons and the Bose-Einstein condensation of lower polaritons are analyzed here in a photonic crystal heterostructure trap with harmonic oscillator potential. This concept is numerically illustrated on example of CdTe/CdMgTe microcavities.

1. INTRODUCTION

Recently, several claims have been made on achieving the Bose-Einstein condensation (BEC) in solids [1–4]. In these experiments, semiconductor microcavities incorporating heterostructure quantum wells (QWs) sandwiched between two distributed Bragg reflectors (DBRs) are used in a strong-coupling regime, such that the coupled states of QW excitons and cavity photons represent composite (bosonic) quasiparticles. Due to photonic constituent, the cavity exciton polaritons are of light effective masses (10^{-4} of free electron mass) and allow the macroscopic quantum degeneracy to be achieved at lower density and higher temperature compared to the BEC transition in an atomic vapor. Nevertheless, the recent reports on k-space BEC and early observations of macroscopic coherence in polariton system (e.g., Refs. [5, 6]) allow one to argue that these observations may not be attributed uniquely to the BEC phase transition (e.g., Ref. [7]).

Incompleteness of experimental data and a short lifetime of the cavity exciton polaritons do not allow a thermalization and spontaneous transition to a macroscopically ordered state to be unambiguously confirmed. Thus in [1, 3, 4], a correlation function of the first order $g^{(1)}$ is measured to prove the fact of macroscopic quantum coherence. However, such phase correlations may not be attributed uniquely to a quantum coherent state, which assumes that $g^{(n)} \equiv 1$ for any order n [8]. In particular, the first order correlations can also be observed in a chaotic thermal state [9–11]. Therefore, other tests verifying the nature of a macroscopically ordered state of exciton polaritons are important.

A harmonic oscillator trap with confining potential $U{=}\frac{1}{2}\alpha_{LP}r^2$ for lower polaritons (LPs) can provide an evidence of BEC by displaying distinct spatial distributions of polaritons in the condensate and non-condensate fractions [12]. In [4], a claim is made on achieving r-space BEC of GaAs cavity exciton polaritons in a trap produced via excitonic component of polaritons, by introducing the Pikus-Bir deformation potential $U{=}\frac{1}{2}\alpha_X r^2$ for excitons (X) in GaAs QWs. The reported force constant of the trap for lower polaritons $\alpha_{LP}{=}480\,\mathrm{eV/cm^2}$ assumes that the corresponding trapping potential for excitons is of $\alpha_X{=}1150\,\mathrm{eV/cm^2}$, which improves by a factor of 30 the force constant of a trap previously reported for GaAs QW excitons [13]. However, the features of the coherent fraction of LPs, which was delocalized over a region of 8 μm size, were different from the expected point-like localization of r-space BEC condensate fraction. This discrepancy might be attributed to a negative photon-exciton energy detuning inherent to stress-induced traps, since such negative energy detuning prevents thermalization of lower polaritons [2]. These allow one to question whether the reported observations indeed might be attributed to the r-space BEC of cavity exciton polaritons and whether such traps with negative photon-exciton relative energy are suitable for BEC experiments.

In this paper, a novel concept of harmonic oscillator trap for exciton polaritons is proposed, benefiting from the light propagation features in quasi-periodic 2D arrays of optically coupled microcavities. Such photonic crystal lattices oriented in the plane of QWs are shown here to induce periodic Bloch oscillations in exciton polariton wave functions. By introducing tailored variations

of the cavity pixels across an array, an effective potential can be superimposed on these oscillations to control the envelop wave functions of photonic crystal exciton polaritons. This opens the way to trap polaritons in a harmonic oscillator potential at a positive photon-exciton detuning, by shaping the photonic constituent of polaritons. Such traps will favor thermalization of lower polaritons in experiments on r-space BEC. This concept is numerically illustrated here on example of harmonic oscillator trap implemented with array of CdTe/CdMgTe microcavities.

The paper is organized as follows. Sec. 2 details a structure of arrays of coupled microcavities treated here. In Sec. 3, the photonic crystal exciton polaritons are analyzed in a uniform-lattice arrays. In Sec. 4, a photonic crystal heterostructure trap for exciton polariton is considered. The properties of non-condensate and condensate fractions of lower polaritons in the trap are discussed in Sec. 5.

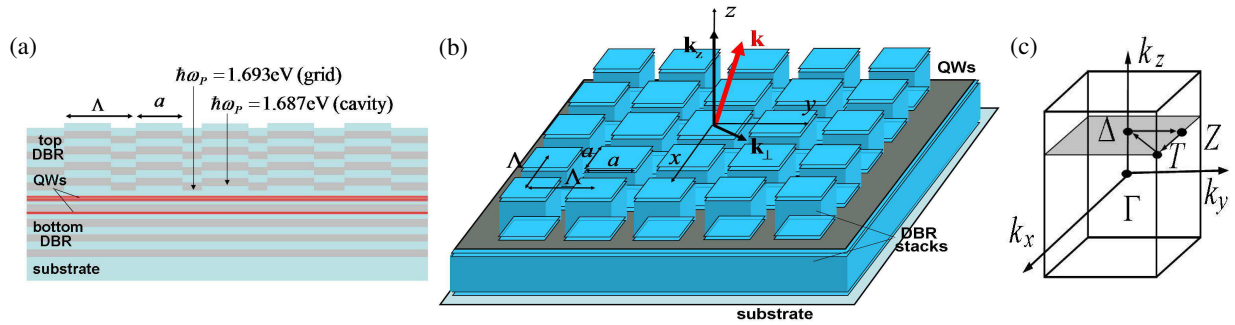

Figure 1: Photonic crystal harmonic oscillator trap implemented with quasi-periodic 2D array of coupled microcavities. (a) Schematic of the wafer structure with etched array of shallow mesa pixels at the cavity spacer layer and regrown top DBR structure. (b) Schematic of the array with parabolically varying size of microcavity pixels used to define effective potential for exciton polaritons. (c) Brillouin zone of a square lattice array of microcavities. Λ is the lattice pitch, a is the width of the cavity pixels.

2. QUASI-PERIODIC ARRAY OF COUPLED MICROCAVITIES

The microcavities discussed here are arranged in a quasi-periodic two dimensional lattice (Fig. 1). Such arrays of optically coupled microcavities belong to a particular class of paraxial photonic crystal (PhC) structures, in which the light propagates mostly normal to the periodic lattice plane [14, 15]. These structures employ lattices of periods significantly exceeding the optical wavelength. For example, the arrays of CdTe/CdMgTe microcavities treated here employ lattices of 3 μm pitch (Fig. 1) and have a vertical cavity structure (one-wavelength cavity incorporating QWs and sandwiched between two DBRs) optimized at 730 nm wavelength. In such structures, only a small transversal component of wave vector **k** of a photon undergoes periodic Bragg reflections in the optical lattice plane. The main **k**-vector component (along the cavity z-axis in Fig. 1) is fixed by the cavity roundtrip self-repetition condition.

These arrays can be fabricated by introducing intermediate processing steps during a wafer growth (e.g., shallow mesa-etching) such that microcavities share multiple QWs in the λ-cavity and in the few first periods of the bottom DBR. In this way, a periodic photonic crystal lattice can be defined in the plane of QWs, as indicated in Fig. 1. By analogy with the cavity exciton polaritons in broad-area microcavities, the coupled states of QW excitons and photons in coupled arrays of microcavities are termed here as photonic crystal exciton polaritons. (As shown in Sec. 3, their wave functions exhibit periodic Bloch oscillations in the plane of QWs.) As in the solitary microcavities utilizes in experiments on k-space BEC [1–4], there are two degrees of freedom available for photonic crystal exciton polaritons to form spontaneously a microscopically ordered state.

Lattices of CdTe/CdMgTe microcavities analyzed here theoretically are defined by etching a periodic pattern of shallow mesa structures at the cavity spacer layer and subsequently regrowing a complete top DBR structure (Fig. 1). This periodic pattern is used to define the position of cavity pixels. In the model calculations, a vertical composition of the cavity wafer is similar to the one of Ref. [1]. In particular, the cavities incorporating 16 quantum wells with exciton energy of 1.682 eV and Rabi energy splitting of 26 meV are analyzed. The vertical-cavity modes oscillate at photon energies of 1.687 and 1.693 eV at the cavity pixels and array grid separating the pixels, respectively. Such tiny variations in the resonant energy of vertical-cavity modes (∼0.3%) suffice to

define a lattice of paraxial photonic crystal [14]. As shown below, low-contrast lattices considered here allow a forbidden energy gap to be opened in the spectrum of coupled optical modes of entire array structure. Another important parameter, which impacts the photonic band structure, is the lattice cell fill factor (FF) defined as the area ratio of the cavity pixel and of the lattice cell. For square arrays treated here, the lattice period Λ is 3 μm and the lattice cell fill factor FF varies in the range of 0.5−1 (FF=a^2/Λ^2, with a being the square pixel width).

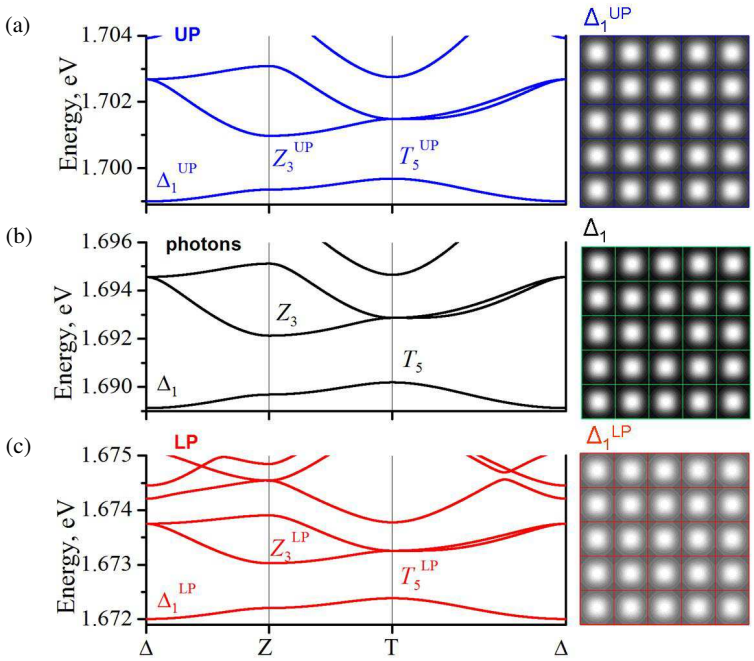

Figure 2: Energy bands (left panels) and lowest-energy state wave functions $|\psi(x,y)|^2$ (right panels) of the upper polaritons (a), photons (b) and lower polaritons (c) in a periodic lattice of coupled CdTe/CdMgTe microcavities ($FF = 0.5$, $\Lambda = 3\,\mu$m). The panels (a)–(c) are ordered according the energy scale.

3. PHOTONIC CRYSTAL EXCITON POLARITON

Figure 2(b) shows optical mode dispersion curves for a uniform array of microcavities with the lattice fill factor of FF=0.5 (2.1 μm cavity pixels arranged in a square lattice of 3 μm pitch). The photonic band structure was calculated using the paraxial Hamiltonian approach developed in Refs. [14, 15]. The energy bands are plotted along the high symmetry lines of the Brillouin zone [Fig. 1(c)]. The wave vector $\mathbf{k}$ of a photon is $(0, 0, k_z)$, $(0, \pi/\Lambda, k_z)$ and $(\pi/\Lambda, \pi/\Lambda, k_z)$ at the Δ, Z and T points of the Brillouin zone (BZ), respectively.

It can be seen that for low-contrast structures considered here, a complete 2D band gap is opened between the states in the T and Z points of the BZ [14, 15]. In Fig. 2(b), the forbidden energy gap is of 2 meV. Note that the optical modes originating from equivalent T points of the BZ show a π phase shift between adjacent lattice sites (the out-of-phase modes) while the modes located at the Z points of the BZ exhibit the out-of-phase oscillations along only one lattice direction and they oscillate in-phase at the lattice sites located along the second direction of the lattice [14, 15].

Within the framework of this study centered on photonic crystal exciton polaritons, the most important photonic state is the lowest energy state Δ_1 located at the Δ point of the BZ. In this state, the optical mode shows no phase shift at adjacent lattice sites, such that oscillations of the electromagnetic field are in-phase at all microcavities composing the lattice. The intensity distribution of the Δ_1 optical mode reveals periodic Bloch oscillations in the plane of QWs [Fig. 2(b), right panel]. As expected by the lattice fill factor considerations (FF=0.5), this mode oscillates at intermediate photon energy of 1.691 eV compared to the vertical-cavity modes at the array pixel (1.687 eV at FF=1) and at the grid (1.693 eV at FF=0). Correspondingly, the energy of the ground state Δ_1 can be modified within this range by varying the lattice cell fill factor FF. It can be then seen that a positive energy difference between a photon in the Δ_1 state and QW exciton is maintained at any FF of the lattice. [In Fig. 2, the QW exciton of 1.682 eV energy is located in

between the energy scales shown in panels (b) and (c).]

The coupled states of PhC photons and QW excitons are analyzed here using Jaynes-Cummings model that takes into account the coupling between a QW exciton and vacuum field oscillations in a PhC mode. The top and bottom panels in Fig. 2 show, respectively, the upper polariton (UP) and lower polariton (LP) energy bands as well as the coordinate probability distribution functions $|\psi(x,y)|^2$ for the upper and lower polariton states of lowest energies (the states Δ_1^{UP} and Δ_1^{LP}), calculated using the Rabi coupling constant $2\Omega_R = 26\,\text{meV}$.

It can be seen that due to a photonic constituent, the features of periodic Bragg reflections in the plane of photonic crystal lattice are transferred to exciton polaritons. Thus, the energy dispersion curves of UP and LP (Figs. 2(a) and (c), left panels) show energy bands separated by forbidden gaps. Respectively, the wave functions of exciton polaritons exhibit periodic Bloch oscillations. In the case of uniform photonic lattices, these periodic oscillations are modulated with plane wave envelope functions propagating in the plane of QWs.

As indicated by the modulation contrast of the $|\psi(x,y)|^2$ distributions, due to contribution of excitons from flat QWs, the Bloch oscillations are less pronounces in the UP and LP wave functions as compared to photons. Furthermore, in Fig. 2, the lower polariton states have higher excitonic content and they are characterized by smoother energy bands and wave function distributions, as compared to the upper polaritons. Nevertheless, the features of periodic Bloch oscillations are clearly visible in the LP wave functions and one can expect that the envelope functions of polaritons can be tailored by using photonic crystal heterostructures.

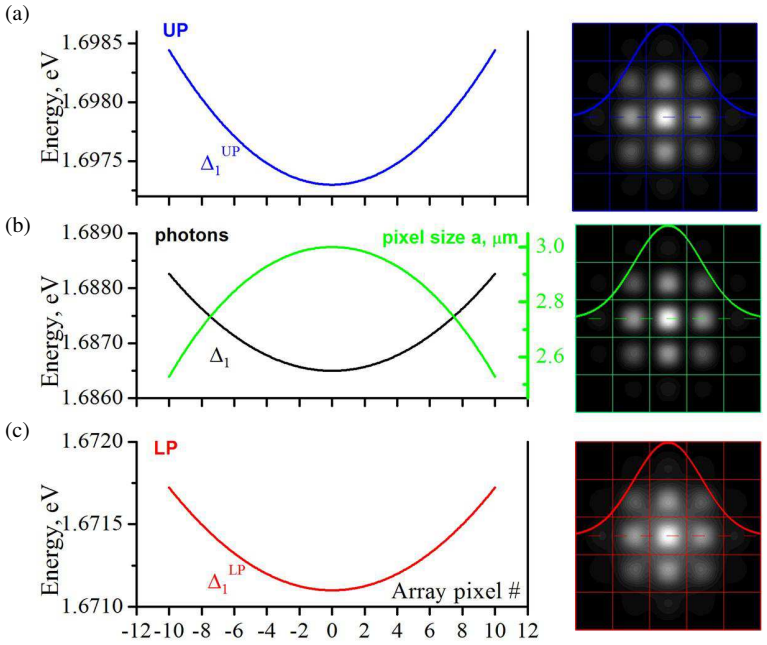

Figure 3: Parabolically graded band edges of lowest-energy bands (left panels) and ground-state probability densities $|\psi(x,y)|^2$ (right panels) of the upper polaritons (a), photons (b) and lower polaritons (c) in the trap defined by tailored pixel-size variations [green curve in (b), right axis] in a quasi-periodic 2D array of coupled CdTe/CdMgTe microcavities ($\Lambda = 3\,\mu\text{m}$). The panels (a)–(c) are ordered according the the energy scale.

4. HARMONIC OSCILLATOR TRAP FOR EXCITON POLARITONS

Trapping of exciton polaritons in a harmonic oscillator potential is accomplished here via their envelope wave functions. A photonic crystal heterostructure trap is defined by introducing tailored variations of the cavity pixel size across the array structure.

A numerical analysis shows that for the low-contrast lattices considered here and for the lattice cell fill factor FF in the range of 0.1–1, the Δ_1 photonic band edge energy decreases monotonically with increasing cavity pixel size a. Therefore, the pixel-size variations $\propto -(x^2+y^2)$ along the two lattice directions of an array produce a parabolically graded shift ($\propto r^2$) of the photonic band edge

Δ_1. Fig. 3(b) shows variations of the pixel size with the lattice position (right axis, green curve) and the resulting effective potential profile $U_P = \frac{1}{2}\alpha_P r^2$ for photons (left axis, black curve).

When an exciton from a flat QW forms a coupled state with a photon in the effective potential U_P, the upper (Δ_1^{UP}) and lower (Δ_1^{LP}) polariton bands exhibit parabolic variations of the band edge with the lattice position as well. These variations define the effective confining potentials $U_{UP}=\frac{1}{2}\alpha_{UP}r^2$ and $U_{LP}=\frac{1}{2}\alpha_{LP}r^2$ for the upper and lower polaritons (Figs. 3(a) and (c), respectively). In Fig. 3, the effective force constants of the trap are α_P=390, α_{UP}=250 and α_{LP}=140 eV/cm^2 for the photons, UP and LP states, respectively.

The confined envelope functions of exciton polaritons in the trap are analyzed here using the effective mass approximation [15] with effective masses derived from the energy dispersion curves in the vicinity of the Δ point of the BZ. The effective masses of a photon (in the plane of QWs), UP and LP are, respectively, $m_P = 0.9\cdot10^{-4}m_e$, $m_{UP} = 1.4\cdot10^{-4}m_e$ and $m_{LP} = 2.4\cdot10^{-4}m_e$, with m_e being the free electron mass. The larger mass of lower polariton is due to the higher excitonic content in LP states, in agreement with the features of periodic Bloch oscillations in probability density $|\psi(x,y)|^2$ (Fig. 2).

The calculated trap force constants and effective masses assume that the excitation energies $\hbar\omega_{osc} = \sqrt{\alpha/m^*}$ of photonic, UP and LP oscillators are of 59, 38 and 21 μeV, respectively. These energies also define a shift of corresponding ground oscillator states from the bottom of the trap.

The wave functions of photons, UPs and LPs in the ground state of the trap are indicated in Figs. 3(a)–(c) (right panels). They exhibit periodic Bloch oscillations modulated with the Gaussian envelope functions delocalized over several lattice sites. The envelope functions for the photons, UPs and LPs are almost identical to each other. The apparent difference between the spatial distributions of probability densities in Fig. 3 is caused by dissimilar Bloch functions of photons and polaritons.

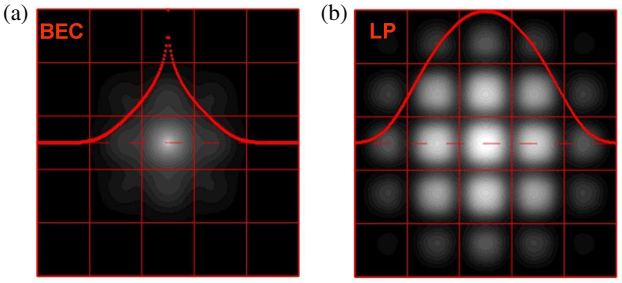

Figure 4: Probability density distributions and envelope function cross-sections for the LPs in the BEC fraction (a) and in the ground oscillator state (b) plotted across a region of 5 × 5 lattice sites of a quasi-periodic array of CdTe/CdMgTe microcavities (the array pitch is $\Lambda = 3\,\mu$m). In both cases, a logarithmic scale $\propto M\ln(1+|\psi(x,y)|^2/p_{\rm th})$ is used with the probability density threshold of $p_{\rm th} = 10^{-3}$, but different scale factors M are applied to the macroscopic wave function (a) and single-polariton wave function (b).

5. RESULTS AND DISCUSSION

In previous sections, the interactions in the LP system have not yet been taken into account and the analysis of confined states in the trap has been carried out in the effective mass approximation, using stationary Schrödinger equation. Introducing a term $\propto |\psi(x,y)|^2$, which accounts for small repulsive interactions in the polariton system, one obtains a nonlinear Gross-Pitaevskii equation for lower polaritons. Its solution at zero chemical potential represents a condensate fraction of LPs. In Fig. 3(c), this state is located at the bottom of the trap, at 21 μeV below the ground oscillator state.

The macroscopic wave function of the lower polariton condensate is shown in Fig. 4(a) (logarithmic scale). The condensate fraction is localized to a single cavity pixel at the center of the trap. The excitonic content of lower polaritons in this state is of 0.6. For comparison, Fig. 4(b) shows the LP wave function in the ground oscillator state, plotted in the logarithmic scale as well. The spatial distribution of polaritons in the condensate fraction (a) is thus significantly different from the one in the ground state of the trap (b). It even more drastically differs from the spatial distribution of polaritons in non-condensate fraction, which occupy the excited states in the trap within the k_BT energy range and are delocalized over a region of size $\sim\sqrt{2k_BT/\alpha_{LP}}$. It should be

stressed that this difference is due to the envelop function properties of lower polaritons in photonic crystal lattices with small repulsive interactions in polariton system.

For particular trap considered here, the critical threshold number of LPs needed to achieve the BEC phase transition can be estimated from expression $N_c = 1.8(k_BT)^2/(\hbar\omega_{osc})^2$ [16], yielding $Nc = 4.4 \cdot 10^3$ polaritons in the trap at a temperature of 12 K. The non-condensate fraction is delocalized over a region of 40 μm width (about 13 lattice sites), which makes it clearly distinguishable from the condensate fraction at the center cavity pixel of the trap (of ∼3 μm width). The thermal excitation energy k_BT of about 1 meV significantly exceeds the energy separation of quantized LP oscillator states in the trap (21 μeV). Taking also the positive photon-exciton energy detuning into account, one should expect that such trap favors the thermalization of LPs and spontaneous BEC phase transition in polariton system.

Finally note that the periodic photonic lattice will prevent a localization of exciton polaritons due to disorder effects in the quantum wells, observed in experiments on k-space BEC.

6. CONCLUSION

Photonic crystal heterostructures offer a powerful approach for tailoring the envelope functions of exciton polariton modes propagating in quasiperiodic arrays of microcavities. The use of this concept is illustrated here on example of photonic crystal heterostructure implementing harmonic oscillator trap for exciton polaritons. This concept should stimulate further development of novel applications of polariton-based systems for control of exciton polariton propagation and confinement, and in particular in delivering important evidence that exciton-polaritons might undergo BEC phase transition.

REFERENCES

1. Kasprzak, J., M. Richard, S. Kundermann, A. Baas, P. Jeambrun, J. M. J. Keeling, F. M. Marchetti, M. H. Szymańska, R. André, J. L. Staehli, V. Savona, P. B. Littlewood, B. Deveaud, and Le Si Dang, "Bose-Einstein condensation of exciton polaritons," *Nature*, Vol. 443, 409–414, 2006.
2. Deng, H., D. Press, S. Götzinger, G. S. Solomon, R. Hey, K. H. Ploog, and Y. Yamamoto, "Quantum degenerate exciton-polaritons in thermal equilibrium," *Phys. Rev. Lett.*, Vol. 97, 146402–4, 2006.
3. Christopoulos, S., G. Baldassarri Höger von Högersthal, A. J. D. Grundy, P. G. Lagoudakis, A. V. Kavokin, J. J. Baumberg, G. Christmann, R. Butté, E. Feltin, J.-F. Carlin, and N. Grandjean, "Room-temperature polariton lasing in semiconductor microcavities," *Phys. Rev. Lett.*, Vol. 98, 126405–4, 2007.
4. Balili, R., V. Hartwell, D. Snoke, L. Pfeiffer, and K. West, "Bose-Einstein condensation of microcavity polaritons in a trap," *Science*, Vol. 316, 1007–1010, 2007.
5. Deng, H., G. Weihs, C. Santori, J. Bloch, and Y. Yamamoto, "Condensation of semiconductor microcavity exciton polaritons," *Science*, Vol. 298, 199–202, 2002.
6. Weihs, G., H. Deng, R. Huang, M. Sugita, F. Tassone, and Y. Yamamoto, "Exciton-polariton lasing in a microcavity," *Semicond. Sci. Technol.*, Vol. 18, S386–S394, 2003.
7. Bloch, J., "Polariton quantum degeneracy in GaAs microcavities," *2008 Latsis Symposium at EPFL on Bose Einstein Condensation in Dilute Atomic Gases and in Condensed Matter*, Lausanne, Switzerland, Januarry 28–30, 2008, http://latsis2008.epfl.ch/.
8. Glauber, R. J., "Nobel lecture: One hundred years of light quanta," *Ann. Phys. (Leipzig)*, Vol. 16, 6–24, 2007.
9. Brown, R. H. and R. Q. Twiss, "Correlation between photons in two coherent beams of light," *Nature*, Vol. 177, 27–29, 1956.
10. Glauber, R. J., "The quantum theory of optical coherence," *Phys. Rev.*, Vol. 130, 2529–2539, 1963.
11. Glauber, R. J., "Coherent and incoherent states of the radiation field," *Phys. Rev.*, Vol. 131, 2766–2788, 1963.
12. Snoke, D. W., "When should we say we have observed bose condensation of excitons?" *Phys. Stat. Sol. (b)*, Vol. 238, 389–396, 2003.
13. Vörös, Z., D. W. Snoke, L. Pfeiffer, and K. West, "Trapping excitons in a two-dimensional in-plane harmonic potential: Experimental evidence for equilibration of indirect excitons," *Phys. Rev. Lett.*, Vol. 97, 016803–4, 2006.

14. Boiko, D. L., "Paraxial Hamiltonian for photons in two-dimensional photonic crystal microstructures," ArXiv 0710.5287, 1–19, 2007.
15. Boiko, D. L., "Coriolis-Zeeman effect in rotating photonic crystal," ArXiv 0705.1509, 1–12, 2007.
16. Negoita, V., et al., "Harmonic-potential traps for indirect excitons in coupled quantum wells," *Phys. Rev. B*, Vol. 60, 2661–2669, 1999.

Transmission Lines Based on Metamaterial Structures for Si-MMICs

Samir El Rai[1], **Adam Pawlikiewicz**[1], **Ralf Tempel**[2], **and Dieter Jäger**[2]

[1]ATMEL Corp., Colorado Springs, CO 80906, USA
[2]Universität Duisburg-Essen, ZHO, Duisburg 47057, Germany

Abstract— Differential transmission lines (DTL) are commonly used in Silicon Monolithic Microwave Integrated Circuits (Si-MMIC) for the electrical connections between devices and components located at different positions on a chip. In addition, these DTLs are of particular interest for devices that use travelling wave's phenomena such resonators. The flexibility of such a design and the high quality of DTLs are utterly important for this application. In classical or in standard form realized DTLs require a large chip area consumption which leads among other things to higher cost. This is obviously not very much desired. In this paper, it is proposed to use DTLs based upon the concepts of electro-magnetic-band-gap structures and metamaterials to significantly reduce the chip area occupied by the DTL. The DTLs are synthesized as a chain of identical 4-port unit cells UCs, which are discussed in detail. Experimental results are presented showing a clear benefit namely a chip area reduction as well as quality factor. Those are excellent results for Si-MMIC differential transmission lines.

1. INTRODUCTION

The functionality of differential transmission lines (DLT's) is based on coupled transmission lines (TL's) in ODD-mode operation. There is a high interest in using them as resonator circuits for oscillators or filters. But the classical form of DTL's is not suited for MMIC application because of huge area consumption. We will show a significant size reduction by using electro-magnetic-band-gap (EBG) structures.

The authors already described the theoretical background of DTL's with reduced area consumption in earlier papers [1, 2]. The proposed DTL's show much smaller areas than standard ones due to using higher specific inductances (by spirals) and cross-talk capacitances. These have been formed both inside line branches and between the two branches. Moreover, this approach allows for a significant Q-factor improvement as well.

2. PERIODIC STRUCTURE

Now lets try to decrease the size of classical TL toward a size, which is suitable for an application in MMIC design. Theoretically it is equivalent to an improvement of effective relative permittivity ($\varepsilon_{r,\,eff}$) and effective magnetic permeability ($\mu_{r,\,eff}$). The resulting TL still demonstrates classical homogeneous behavior in a wide frequency range. Papers about metamaterial structures have been published in the literature for some years. A good overview can be found in [3]. Many applications have been described during the last five years; most of the recently presented EBG structures use combinations of lumped-element inductors and capacitors on one-dimensional (1-D) or two-dimensional (2-D) TL configurations [4–6].

Until today there wasn't any work that introduced metamaterial structures onto Silicon. Only the authors of this paper have shown how to implement concentrated elements like inductors and MIM capacitors in that lines to shrink up classical TL size [1, 2]. By active usage of magnetic coupling between line sections laying face-to-face the characteristic impedance can be increased above values that can't be achieved with the classical line shapes. At the same time this increases the propagation constant of the TL, which results higher chip size efficiency. This will be achieved by forcing all adjacent line sections to carry the current in the same direction. All lines which carry current in opposite directions have been separated as far as possible. This procedure has been done for line sections of the same branch as well for both branches among each other and results in highest magnetic coupling factor. Moreover connecting several identical or similar UCs together results in a periodic structure, this will be named periodical differential transmission line PDTL now. Differently to a classical TL the new PDTL consists of an integer number of N multiplied by one UC element. That includes that only discrete values of electrical length can be adjusted. Synthesizing a new DTL the electrical length of one UC has to be adjusted accurately. Figure 1 illustrates that relationship.

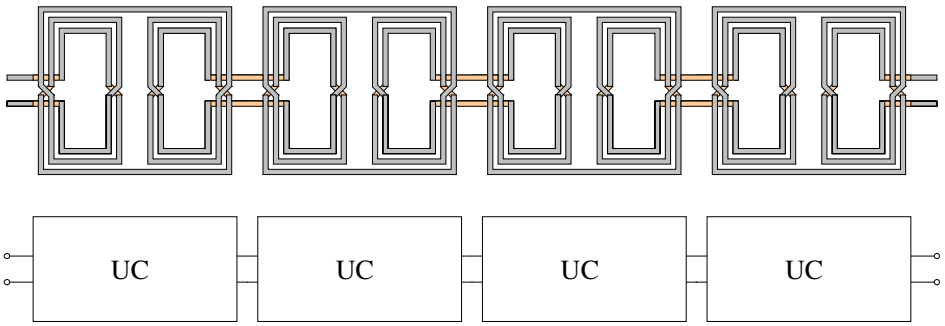

Figure 1: DTL established by several series connected UC's forming a PS: (a) Schematic, (b) Layout.

3. DESIGN

Figure 3 depicts three PDTLs which will be considered here. Each PDTL consists of four UCs. The size of each UC is 184 µm by 145 µm.

As mentioned before positive coupling for ODD-mode operation has been achieved by forcing all adjacent line sections carrying the current in the same direction. PDTL1 shows that in the proposed way and results in much better phase shift then standard TL. But it's also worth to mention that in the middle of each PDTL1 UC there is still an area with negative coupling. This lowers the overall inductivity.

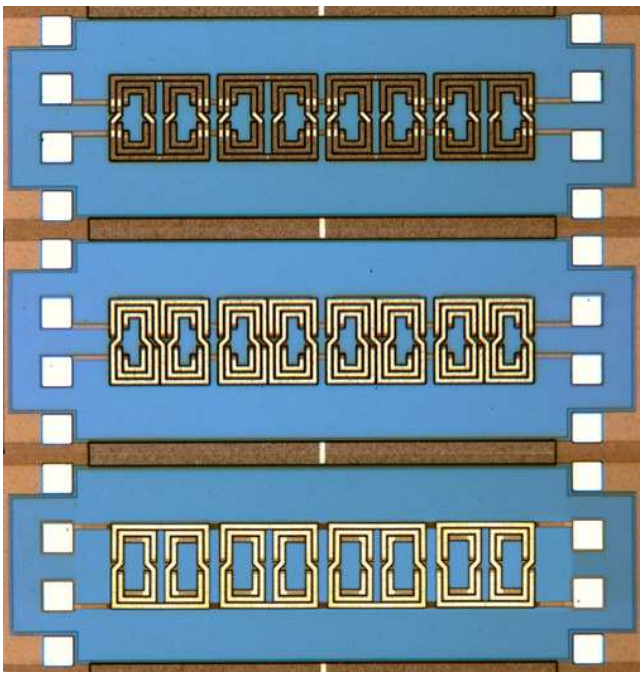

Figure 2: The three PDTL with new characteristics PDTL1 (top), PDTL2 (middle) and PDTL3 (bottom).

PDTL2 shows an additional turn after each half UC and thus enlarges the electrical line length — and an additional phase shift has been achieved too.

Up to now only two metal layer systems have been used, the first for the two line branches and the second for necessary crossings of the same. But using a third metal layer it is now possible to generate 2-turns constructions instead of former 1-turn ones. This will be double (nearly) the overall inductivity and hence the phase shift. PDTL3 has been designed in that way.

4. SIMULATION & MANUFACTURE

Because of the complex interacting of both electric and magnetic fields the simulation of only one UC is very extensively. Therefore a 3D-EM field simulator has been used for simulations — the EMPIRE simulator [7] bases on the powerful finite differences time domain method.

For the manufacture an advanced SiGe BiCMOS technology [8] from the company Atmel Corporation has been used. In standard option it's a 4-metal layer process with additional inductor layer based on a 19-Ω cm substrate.

5. MEASUREMENTS

On-wafer measurements have been performed by means of 4-port Network Analyzer N5230A in conjunction with symmetrical RF coplanar probe tips in GSSG configuration. The PDTLs exhibit a total length of four UC with dimension of 736 µm × 145 µm. The RF measurement pads possess an area of 50 µm × 50 µm with 100 µm pitch.

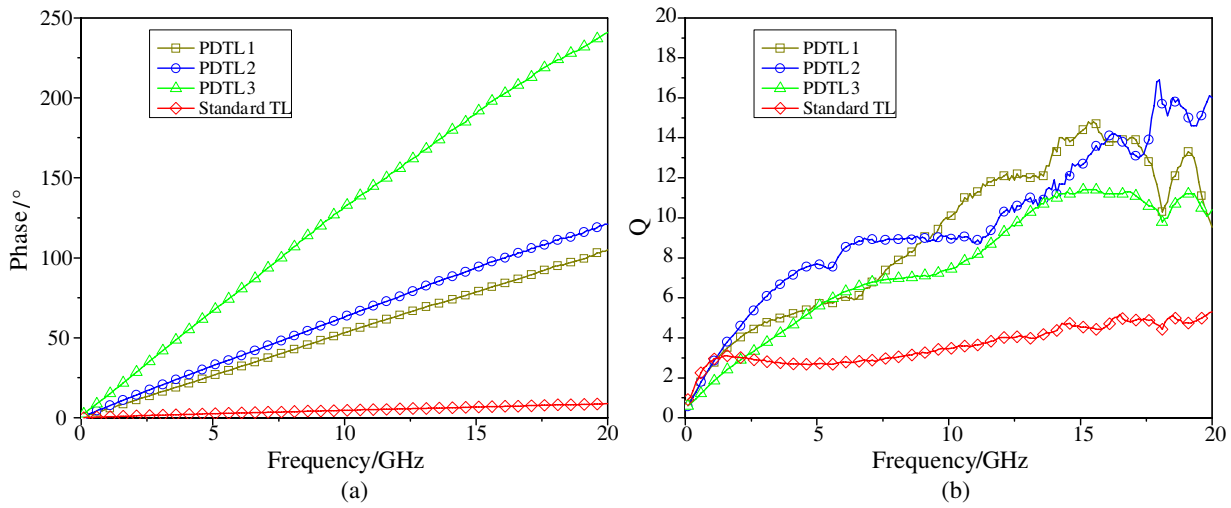

Figure 3: Measurements of the PDTLs in comparison to the standard TL. (a) Phase of the UCs, (b) Quality factor of the UCs.

6. RESULTS

The PDTLs are designed to keep the real impedance at around 100 Ohm for comparison reasons. Figure 3(a) shows the measured Phase of all UCs extracted of the measurement of the PDTLs. The procedure to extraction of the UC phase from the PDTL measurements is described in [1, 2]. The measurement of the standard TL with same size consumption like any UC is also included in Figure 3(a) for the comparison.

A drastically improved phase behavior could be achieved. PDTL 1 have has much higher phase than the standard TL. That makes the area efficiency high. At the same time the use of the technique of the PDTL 2 improve the phase by around 19%. Finally the use of additionally metal layers increases the phase of the PDTL 3 UC much more.

Figure 3(b) shows the measured quality-factor Q. The quality factor is really important for realizing resonators cause this is then the quality factor of the realized resonator self. The quality factor of all designed PDTLs is much higher (3x-4x) then in standard TL. That is an excellent result.

Table 1: Summarized measurement results for $f = 10\,\mathrm{GHz}$.

PDTL	$Z_{D,\,Real}/\Omega$	Phase/°	Q-factor
Standard TL	100	6	2.5
(a)	106	53	10
(b)	118	63	9
(c)	125	131	8

The quality factor of the PDTL 3 is lower then the other PDTLs. That is because in PDTL 3 lower metallization layers are used. This metallization layers have lower thickness therefore higher resistive loss and that causes a little lower quality factor.

Table 1 depicts the results for the frequency of 10 GHz.

7. CONCLUSION

PDTL can be synthesized by identical UC. These new PDTLs can be used as small resonators in filter or oscillator applications. This new PDTL — by using the proposed UCs — allows characteristic impedances beyond that of classical TL and in addition at much smaller size and higher Q. It is the first time that PDTL structures form a real alternative for applications in silicon MMIC design below 10 GHz. Further improvements should be possible by further optimization of the used line configurations as well as using additional metal layers.

REFERENCES

1. El Rai, S. and R. Tempel, "Differential transmission lines on silicon based on periodic photonic bandgap structures," *Radio and Wireless Symposium (RWS) 2006*, 207–210, San Diego, USA, January 14–20, 2006.
2. El Rai, S. and R. Tempel, "New design of differential transmission lines on silicon," *Silicon Monolithic Integrated Circuits in RF Systems (SiRF) 2006*, 101–102, San Diego, USA, January 18–20, 2006.
3. Lai, A., C. Caloz, and T. Itoh, "Composite right/left-handed transmission line metamaterials," *IEEE Microw. Magazine*, 34–50, September 2004.
4. Mao, S.-G., S.-L. Chen, and C.-W. Huang, "Effective electromagnetic parameters of novel distributed left-handed microstrip lines," *IEEE Trans. Microwave Theory Tech.*, Vol. 53, No. 4, 1515–1520, April 2005.
5. Falcone, F., F. Martin, J. Bonache, R. Marques, T. Lopetegi, and M. Sorolla, "Left-handed coplanar waveguide band pass filters based on bi-layer split ring resonators," *IEEE Microw. and Wireless Components Letters*, Vol. 14, No. 1, 10–12, January 2004.
6. Sanada, A., C. Caloz, and T. Itoh, "Characteristics of the composite right/left-handed transmission lines," *IEEE Microw. and Wireless Components Letters*, Vol. 14, No. 2, 68–70, February 2004.
7. 3D-FDTD Simulator EMPIRE version 5.1, IMST GmbH, Kamp-Lintfort, Germany, 2006.
8. AT46700 Rev 0.7 SiGe BiCMOS Technology, ATMEL Corp., Colorado Springs, CO, USA, 2006.

Abnormal Radiation Pattern of Metamaterial Waveguide

A. N. Lagarkov, **V. N. Semenenko**, **A. A. Basharin**, **and N. P. Balabukha**

Institute for Theoretical and Applied Electromagnetics of Russian Academy of Sciences (ITAE RAS)
Izhorskaya 13, Moscow 125412, Russia

Abstract— The idea to inverse the radiation pattern of the microwave antenna due to application of the isotropic metamaterial screen with negative refractive index in S band is demonstrated at the first time in this investigation. The electromagnetic simulation of waveguide antenna patterns by moment's methods demonstrates an agreement modeling antenna patterns with measured antenna diagrams for values of metamaterial effective parameters (permittivity and permeability) extracted from measured S-parameters of metamaterial sheet sample.

1. INTRODUCTION

The prediction of left handed materials (LHM) by V. G. Veselago in 1967 [1] can be considered as a new stage in the development of electromagnetics of continuous media. Recently a lot of papers [2, 3] related to the artificial magnetoelectric media with anomalous electromagnetic properties have been appeared. Among these papers there are ones on 2-D, 3-D media with the negative permittivity and permeability [4, 5] and, hence, negative refractive index. The abnormal antenna patterns of a rectangular open waveguide loaded by a rectangular cross-section magnetoelectric tube made of the metamaterial with the negative refractive index in S frequency band for different thicknesses of tube are demonstrated at first in this paper.

2. SCHEME OF WAVEGUIDE RADIATOR

The geometry of open waveguide loaded by the metamaterial screen having a shape of a rectangular cross-section tube (***modified open waveguide radiator***) is shown in Figs. 1–2. A standard coaxial-waveguide adapter of the S-band with the waveguide window of 50×25 mm in sizes is used in the measurements of antenna patterns of modified waveguide radiator.

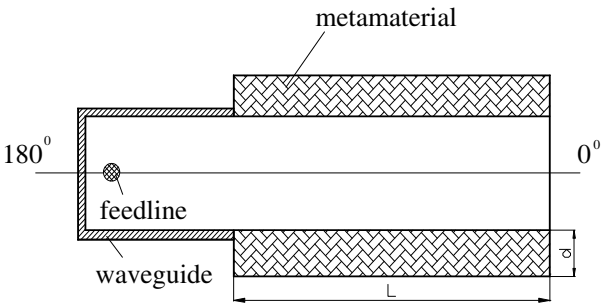

Figure 1: Schematic diagram of the waveguide radiation structure.

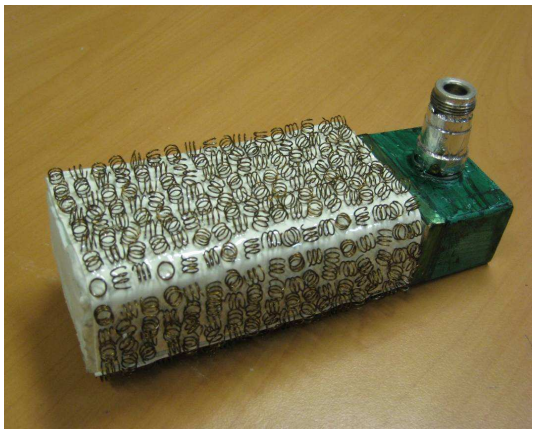

Figure 2: A view of the waveguide radiator.

The ***metamaterial*** under investigation is an isotropic 2D lattice made of nichrome spiral wires (helixes) positioned randomly on the polyurethane substrate with 0.2 mm in thickness. To exclude chiral properties of the metamaterial sample is used an identical combination of left- and right handed helixes. The helixes were wound of the 0.4 mm nichrome wire with the number of turns 3 and coil pitch 1 mm. The helix external diameter is 5 mm. In the experiments an isotropic metamaterial sheet sample named as ***LR-5I*** (see Fig. 3 — 1/3 part of helixes set is positioned along rectangular coordinate axes of x, y and z respectively) with 5.2 mm in thickness is used.

A peculiarity of the spiral elements of the metamaterial under investigation consists in revealing of the 3D-isotropic electric and magnetic properties in one and the same frequency band [4]. A helix with the non-zero coil pitch is magnetic and electric dipole simultaneously effectively excited

both by the electric and magnetic fields under the coincidence of their polarization with the helix axis.

Figure 3: A view of the metamaterial planar sample LR-5I.

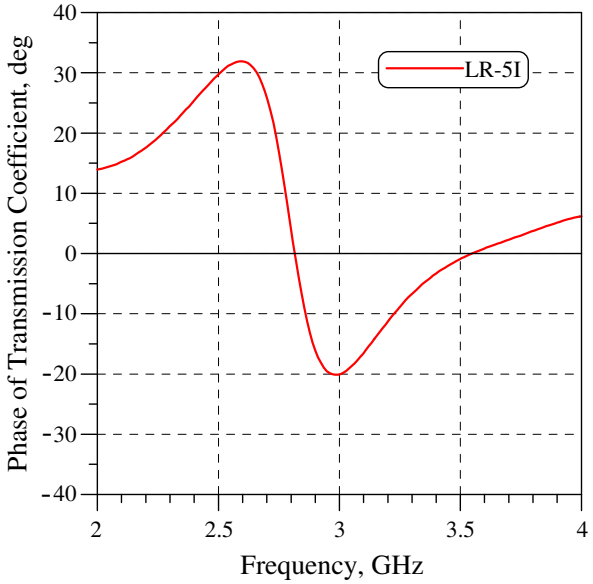

Figure 4: Phase of the metamaterial transmission coefficient in dependence on frequency.

The experimental dependence of the phase of metamaterial transmission coefficient in the dependence of frequency with the area of negative values of phase in the vicinity of frequency of 3 GHz corresponding to the negative refractive index is demonstrated in Fig. 4. Extracting values of effective material parameters of the metamaterial sheet sample recalculated by the Fresnel's formulae from the S-parameters values (complex reflection and transmission coefficients) are presented in Fig. 5. The measurements of metamaterial S-parameters are performed on R&S Vector Network Analyzer ZVA-24 with the time domain option and special calibration procedure and using wide-band horn antenna.

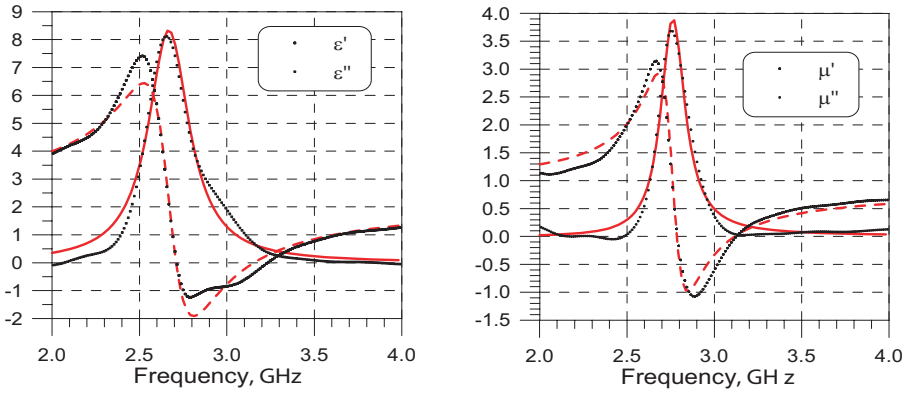

Figure 5: The effective permittivity and permeability of metamaterial LR-5I in dependence on frequency.

3. THE ANTENNA PATTERNS OF WAVEGUIDE RADIATOR LOADED BY METAMATERIAL

Based upon the numerical estimations of antenna patterns by the Method of moments (thin red lines) and experimental antenna patterns (thick black lines) for the waveguide radiator obtained in the anechoic chamber are presented in Figs. 6–11. The antenna diagrams are performed at the frequencies closed to the metamaterial resonance frequency which is equal to 3 GHz. An opportunity of obtaining a reversed antenna patterns for waveguide antenna structure loaded by the

metamaterial tube had been shown at these diagrams (in Figs. 6–11 normalized antenna patterns is represented).

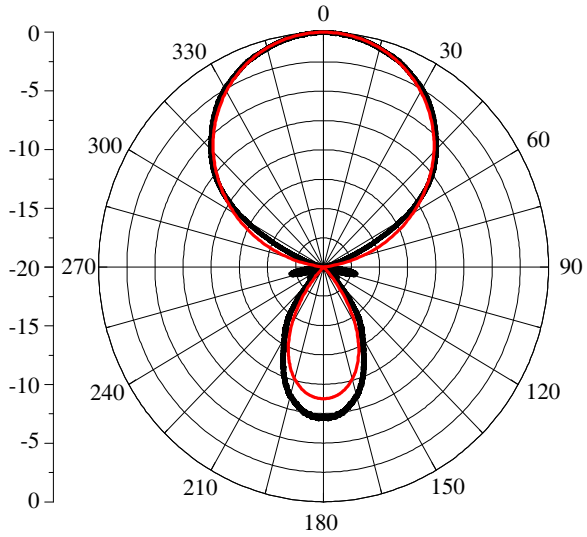

Figure 6: The antenna patterns of a waveguide radiator at the frequency 3.1 GHz.

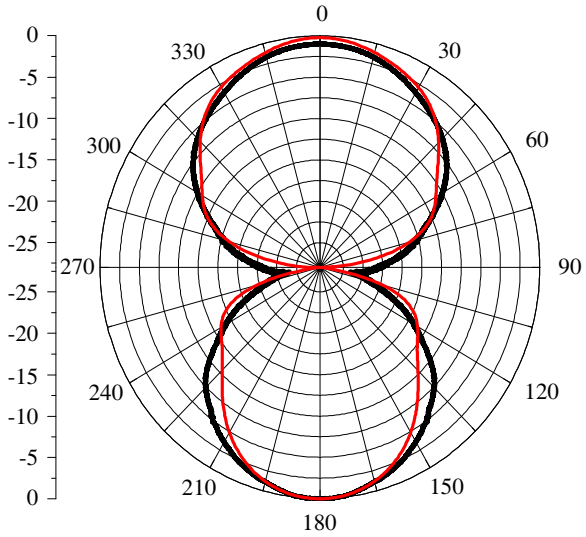

Figure 7: The antenna patterns of a waveguide radiator loaded by the metamaterial tube ($d = 5$ mm) at the frequency 3.1 GHz.

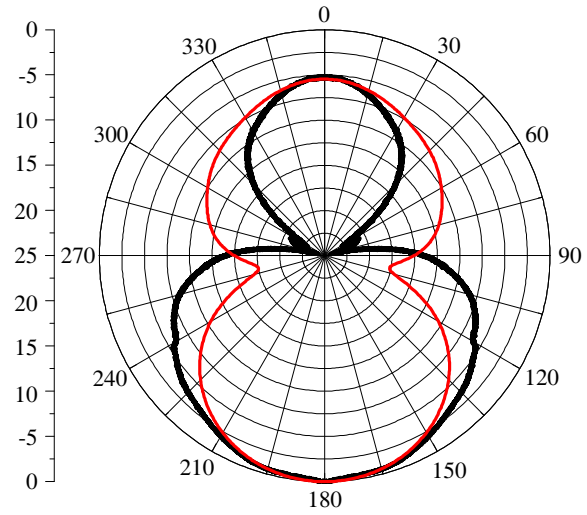

Figure 8: The antenna patterns of a waveguide radiator loaded by the metamaterial tube ($d = 10$ mm) at the frequency 3.1 GHz.

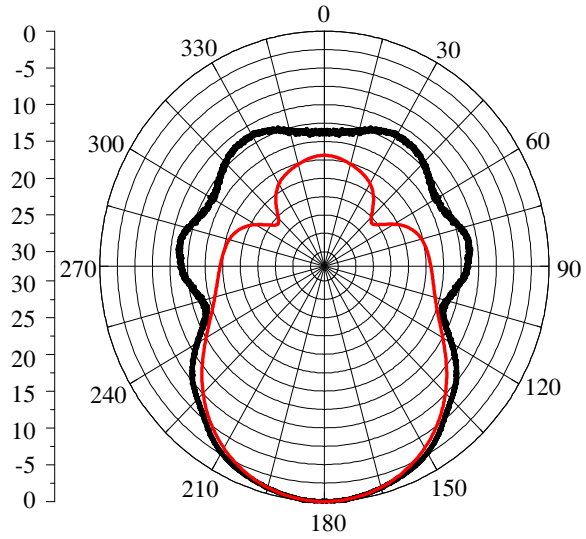

Figure 9: The antenna patterns of a waveguide radiator loaded by the metamaterial tube ($d = 20$ mm) at the frequency 3.1 GHz.

For a waveguide radiator loaded by the LR-5I metamaterial tube with the wall thickness $d = 5$ mm and length $L = 150$ mm there is a growing of the backside antenna lobe in comparison with the main antenna lobe. The difference between levels of the main and back directional lobes is approximately equal to 2 dB.

With the increasing of the tube wall thickness d, there is an abnormal antenna pattern diagram when the backside directional lobe exceeds the main one more than by 20 dB. In this case the waveguide structure radiates mainly in the backside direction of "180 deg". This effect is observed only in the case when the metamaterial reveals negative refractive index of $n = \sqrt{(\varepsilon' + i\varepsilon'')(\mu' + i\mu'')}$. To prove this fact in Fig. 11 an antenna pattern of the waveguide structure with the metamaterial tube screen at the frequency of 4 GHz is presented. At this frequency refractive index of metamaterial is $n > 0$. The antenna pattern at this frequency has an ordinary form of diagram where

the main directional lobe exceeds the backside lobe and the radiation occurs mainly in the front direction "0 deg". The physical nature of this effect may be explained by the refraction of the electromagnetic waves at the boundary (air/metamaterial tube) inside waveguide structure. At this boundary the surface waves are excited and propagated in an opposite direction towards the spatial wave propagation in the waveguide structure.

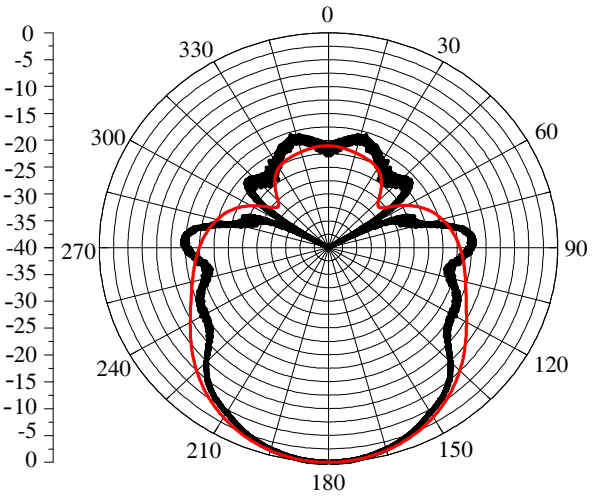

Figure 10: The antenna patterns of a waveguide radiator loaded by the metamaterial tube ($d = 30$ mm) at the frequency 3.1 GHz.

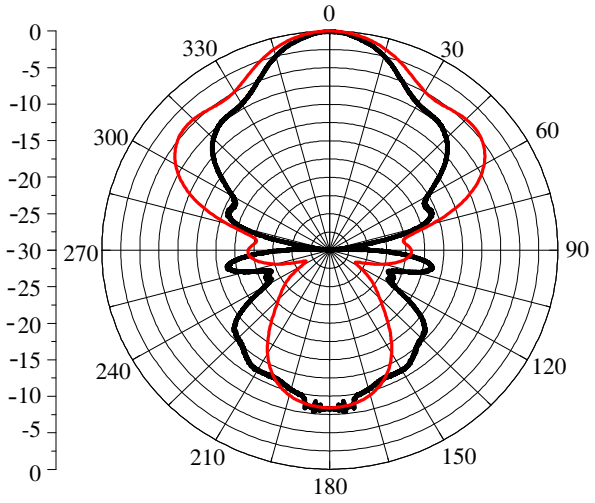

Figure 11: The antenna patterns of a waveguide radiator loaded by the metamaterial tube ($d = 20$ mm) at the frequency 4 GHz.

4. CONCLUSIONS

Therefore, at the frequencies, at which a metamaterial possess negative refractive index $n < 0$, and the metamaterial tube thickness exceed 5 mm, and abnormal antenna pattern diagram of waveguide structure with the maximal radiation in the backside direction (<<***backside radiation***>>) are observed. At the frequencies, at which $n > 0$, the antenna patterns present ordinary diagrams with the maximal radiation in the front direction for any metamaterial tube thickness.

REFERENCES

1. Veselago, V. G., "The electrodynamics of substances with simultaneously negative values of ε and μ," *Sov. Phys. Usp.*, Vol. 10, 509–514, 1968.
2. Caloz, C. and T. Itoh, *Electromagnetic Metamaterials: Transmission Line Theory and Microwave Applications*, John Wiley & Sons, Inc., 2006.
3. Lagarkov, A. N., V. N. Semenenko, D. E. Ryabov, S. A. Tretyakov, and C. R. Simovski, "Resonance properties of bi-helix media at microwaves," *Electromagnetics*, Vol. 17, No. 3, 213–237, 1997.
4. Lagarkov, A. N., V. N. Semenenko, V. N. Kisel, and V. A. Chistyaev, "Development and simulation of microwave artificial magnetic composites utilizing nonmagnetic inclusion," *Journal of Magnetism and Magnetic Materials*, Vol. 258–259, 161–166, 2003.
5. Lagarkov, A. N. and V. N. Kissel, "Near-perfect imaging in a focusing system based on a left-handed-material plate," *Phys. Rev. Lett.*, Vol. 92, 077401, 2004.

A New Bandstop Filter Based on Photonic Crystals

F. Monifi, M. Djavid, A. Ghaffari, and M. S. Abrishamian
Department of Electrical Engineering, K. N. Toosi University of Technology, Tehran, Iran

Abstract— We present a Photonic Crystal bandstop filter design based on $N \times M$ ring resonators placed beside an ordinary waveguide. Our FDTD simulations show that by choosing proper N and M we can obtain specific filter parameters.

1. INTRODUCTION

The photonic crystal (PC) is attracting much attention, because it has photonic band gaps (PBG) where no propagating electromagnetic mode exists. Among various devices based on PCs, optical filters receiving great consideration because they can act as a demultiplexer to select or reject a particular channel or multiple channels in dense wavelength-division-multiplexed (DWDM) optical communication systems [2]. A possible design for bandstop filters is to use a photonic crystal ring resonator beside a waveguide. Based on this configuration we discuss several bandstop filter structures using photonic crystal ring resonators. The response of these structures is simulated using a finite-difference time-domain (FDTD) approach.

Optical filters are key components receiving great consideration because they can act as a demultiplexer to reject a particular channel or multiple channels in dense wavelength-division-multiplexed (DWDM) optical communication systems. A possible design for bandstop filters is to use a photonic crystal ring resonator inside a waveguide [1]. Based on this configuration we discuss several bandstop filter structures using photonic crystal ring resonators. The response of these structures is simulated using a finite-difference time-domain (FDTD) approach.

2. OPTICAL RESONATORS

In photonic crystal structures many kinds of optical resonators can be constructed. Changing the size or dielectric constant of each rod causes the consequent defect to behave as a resonator. In fact creating a defect in the structures, the periodicity and completeness of the bandgap are broken and light can be localized at the defect region with the frequency corresponding to the defect frequency inside the gap [3]. Another group of optical resonators are ring resonators. If we remove some rods in order to have a ring shape, we have a ring resonator. For these structures, the choice of the ring size is determined by the desired resonant wavelength, and the tradeoff between the cavity Q and the modal volume V [1]. Compared to point-defect or line-defect PC cavities, PCRRs offer scalability in size and flexibility in mode design due to their multi-mode nature [4]. The ring resonator used in this research is depicted in Figure 1. Four scatterers are placed at the corners of the ring for higher quality factor [5]. The design parameters for a ring resonator can be the radius of the scatterers, the radius of coupling rods as well as the dielectric constant of the structure.

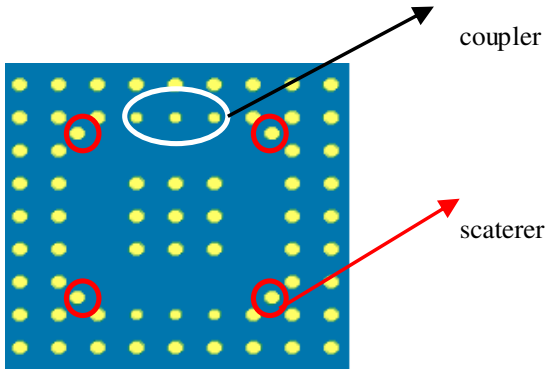

Figure 1: A photonic crystal ring resonator (PCRR) the scatteres are specified in circles and the coupling rods in the oval.

3. A SINGLE RING PHOTONIC CRYSTAL BANDPASS FILTER

Figure 2 shows a structure of a ring resonator side-coupled to a waveguide, where both the ring resonator and the waveguide can support only one mode in the frequency range of interest. The structure is a square lattice of dielectric rods in air host, where the lattice constant is a, and the radius of rods is $0.185a$, and the dielectric constant ε is 12, which corresponds to Si at 1550 nanometer).

By choosing the lattice constant $a = 540\,\text{nm}$ and therefore the rods' radii $r = 99.9\,\text{nm}$ we will have a broadband bandgap with a guided single-mode spans from 1270 to 1740 nm in our waveguide. Also the $N \times M$ ring used in this research depends on the value of N and M may support one or more modes about 1550 nm.

During an optimization process the radius of the couplers is chosen to be $Rc = 0.8$ for more coupling and the radius of scaterers is chosen to be $Rs = 1$ [6] (See Figure 2(a)).

When the ring resonator resonates, energy couples in the ring and it will be sent back through the input port, so the output will receive no energy. It should be noted that when the ring mode is such that energy rotates clockwise in the ring, energy will again propagate through the output port, so we are interested in mode configuration in which energy propagates counter clockwise in the ring resonator. In such situation we can obtain a bandstop filter, where will reject the frequencies correspond with the ring's resonant frequency.

First a 6×4 Ring resonator is investigated. As illustrated in Figure 2(b) there is a notch at wavelength $\lambda = 1564$ nm at which the output power drops to 2%.

Finite Difference Time Domain (FDTD) method is used to simulate the structure and Perfect Matched Layers (PML) are placed as absorbing boundary conditions.

An adequately broadband Gaussian pulse is launched into input port and power is calculated over output port. Then the power spectral density of each port is normalized to the power spectral density of the input port. Figure 2(b) illustrates the transmission spectra for the structure.

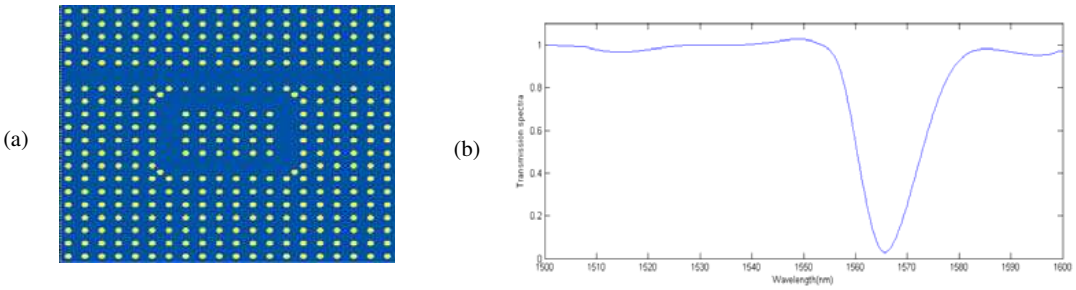

Figure 2: (a) A 6×4 single-ring photonic crystal ring resonator bandpass filter, (b) Normalized transmission spectra at output ports for photonic crystal ring resonators (PCRRs) with $\varepsilon_r = 12$ (at the wavelength $\lambda = 1566$ the normalized power spectra drops to 2%.

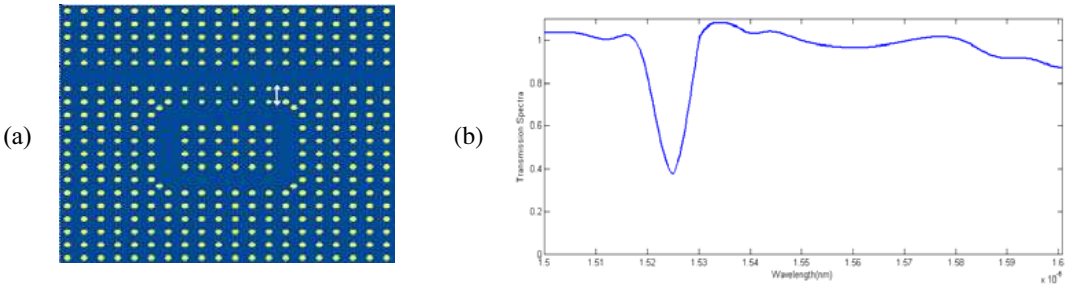

Figure 3: A 6×4 single-ring photonic crystal ring resonator with two coupling periods between waveguide and PCRR cavity, (b) Normalized transmission spectra at output ports for photonic crystal ring resonators (at the wavelength $\lambda = 1566$ the normalized power spectra drops to 2%.

4. TUNABILITY OF RING RESONATOR BANDSTOP FILTERS

Because we always need to change the filter parameters depends on its applications, we prefer the structure to be designable. Here, the central frequency and the width of the stop band can be regulated by changing the size of the ring and the distant between the ring and the waveguide. As it is shown in Figure 3(a) when the ring is located 2 rods apart from the waveguide the stop band will be narrower and the drop efficiency will be less.

The resonant frequency changed due to change in size of the coupling rods. As another example when the size of the ring is changed, the resonant frequency of the ring will be changed. Figure 4 depicts the filter spectra for three different ring sizes. Using these two techniques we can easily design a filter with desirable parameters, we suggest the structure can be improved by adding more ring resonators for instant in both side of the waveguide.

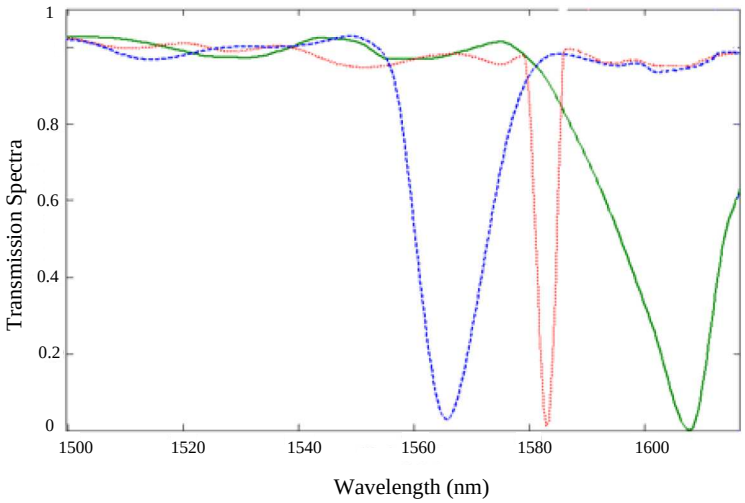

Figure 4: The filter characteristic of three different ring size, the green curve relates to a 3×3 ring, the stop wavelength is 1608 nm and 99.2% drop efficiency, the red curve relates to a 6×5 ring, he stop wavelength is 1583 nm and 98.5% drop efficiency and the blue curve relates to a 6×4 ring, the stop wavelength is 1566 nm and 98% drop efficiency.

Snapshots of the electric field distribution in the filter for pass and stop wavelengths are shown Figure 5.

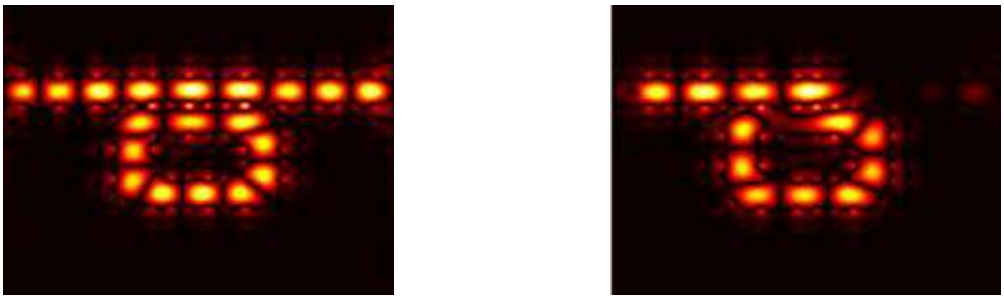

(a) in the pass region (b) in the stop region

Figure 5: The electric field patterns of the filter.

5. CONCLUSION

In this paper, we investigated a photonic crystal bandstop filter with a single ring resonator side coupled to a waveguide we demonstrated that in some configurations more than 98% drop efficiency is achievable. We showed that by choosing a proper ring size we can obtain a desire central frequency for the filter, and the band width of the filter can be adjusted by changing the distance between the ring and waveguide.

ACKNOWLEDGMENT

This paper was supported by Iran Telecommunication Research Center.

REFERENCES

1. Qiang, Z., W. Zhou, and R. A. Soref, "Optical add-drop filters based on photonic crystal ring resonators," *Opt. Express*, 1823, 2007.
2. Chen, C., X. Li, H. Li, K. Xu, J. Wu, and J. Lin, "Bandpass filters based on phase-shifted photonic crystal waveguide gratings," *Opt Express*, Vol. 15, No. 18, 11278, 2007.
3. Villeneuve, P. R., S. Fan, and J. D. Joannopoulos, "Microcavities in photonic crystals: Mode symmetry, tunability, and coupling efficiency," *Phys. Rev. B*, Vol. 54, 7837–7842, 1996.
4. Manolatou, C., M. J. Khan, S. Fan, P. R. Villeneuve, H. A. Haus, and J. D. Joannopoulos, "Coupling of modes analysis of resonant channel add-drop filters," *IEEE J. Quantum Electron.*, Vol. 35, 1322–1331, 1999.
5. Dinesh Kumar, V., T. Srinivas, and A. Selvarajan, "Investigation of ring resonators in photonic crystal circuits," *Photonics and Nanostructures*, Vol. 2, 199–206, 2004.
6. Ghafari, A., M. Javid, F. Monifi, and M. S. Abrishamian, "A numeric analysis of photonic crystal tunable add-drop filters based on ring resonators," *IEEE/LEOS Annual Meeting*, Florida, USA, 2007.

Power Splitters with Different Output Power Levels Based on Directional Coupling

A. Ghaffari, M. Djavid, F. Monifi, and M. S. Abrishamian
Department of Electrical Engineering, K. N. Toosi University of Technology, Tehran, Iran

Abstract— Here, properties of two dimensional photonic crystal power divider based on directional coupling are investigated. Different output power levels are achieved by changing the coupling length and the distance between parallel waveguides. Total transmission up to 96% is achieved in power splitter with two branches.

1. INTRODUCTION

Power splitters are key building blocks in integrated photonic devices. There are different ways to equally split the power of incoming signal into two output ports: for example using directional coupler (DC) or a Y-junction structure .However typical power splitters built on Photonic crystal (PC) with Y-junction structure has poor transmission. In the first approach the relative phase shift between outputs is 90° whereas in Y-junction outputs signals are in phase. Directional coupling has been used to design high efficient power splitters [1–3]. Here we investigate a power splitter based on PC waveguide directional coupling. The dependence of the transmission on the length of directional coupling region as well as distance between parallel waveguides is investigated.

2. NUMERICAL ANALYSIS OF A POWER SPLITTER BASED ON DIRECTIONAL COUPLING

First we investigate a power splitter with two branches as shown in Fig. 1(a). There is a bend waveguide beside a straight one. The bend must be low loss one because back reflection has intensive impact on directional coupling, such as bend in Ref. [1] or novel L-shaped bend which we have recently proposed [4]. By using optimized bends, total transmission up to 0.96 is achieved. The 2D FDTD method with perfectly matched layers is applied to evaluate the performance of the structure which is a dielectric rod photonic crystal structure with rectangular lattice and dielectric constant $\varepsilon_r = 8.9$. The ratio of rod radius to lattice constant is set to be 0.23. A Gaussian wave at the input entrance with narrow width at the normalized frequency $a/\lambda = 0.34$ is launched.

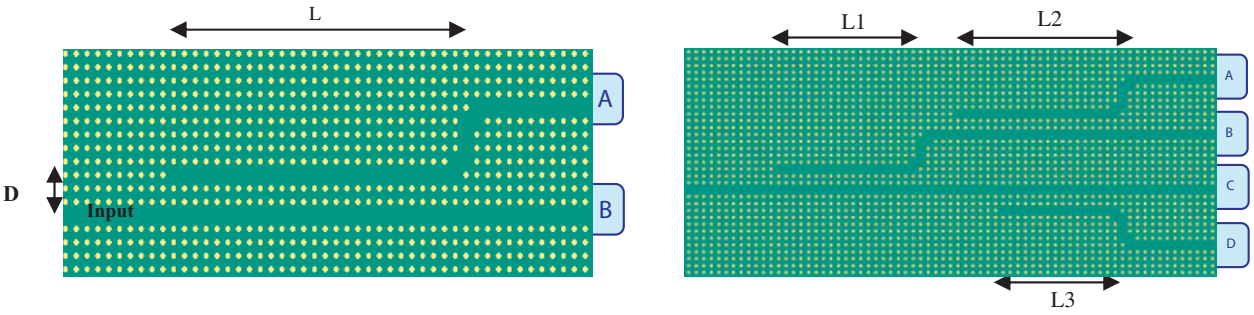

Figure 1: (a) Power splitter based on directional coupling with two branch and $D = 2$. (b) 4 output branches and different coupling lengths ($L1$, $L2$, $L3$).

Directional coupling between parallel waveguide occurs. The input single mode splits to odd and even mode. There is a phase difference between these modes and the wave function in the upper waveguide is the sum of the odd and even mode wave functions. So by changing the coupling length (L) and distance of parallel waveguide (D) we can obtain different output power levels. Our power splitter can be designed to have more branches.

2.1. Changing Coupling Length of Parallel Waveguides

Due to the presence of the second waveguide, the W1 modes couple with each other and split up into two DC modes with different propagation constants k. Their splitting Δk of the two coupler

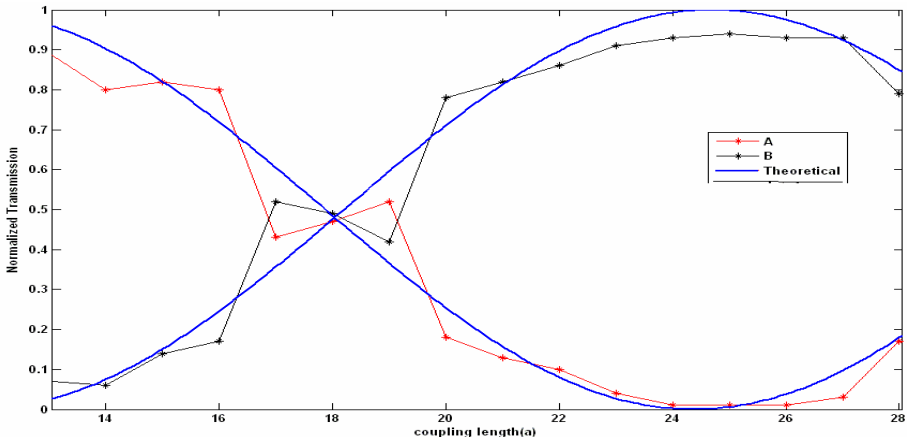

Figure 2: Normalized Transmission at normalized frequency $a/\lambda = 0.337$ versus coupling lengths for $D = 2$, $L = 13a$ ($A = 89\% - B = 7\%$), $L = 18a$ ($A = B = 48\%$), $L = 25a$ ($A = 94\% - B = 1\%$).

modes relates to the coupling length by $L_c = 2\pi/\Delta k$. L_c is defined to be the distance required for the light to couple once to the second waveguide and back and is related to the coupling constantc κ as $\kappa = \pi/L_c$ [5].

By changing coupling lengths different output power ratios can be obtained. It is shown that transmission of the output port A and B can be calculated by following formulas [3]:

$$T_A(\mathrm{L}) = \sin^2\left[\pi L/\left(2L_c\right)\right], \quad T_B(\mathrm{L}) = \cos^2\left[\pi L/\left(2L_c\right)\right]$$

Because of the discrete structure of photonic crystal L should be integral times of a. In Fig. 2 L_c is approximately $13a$. Relation between different coupling lengths ($13a$ to $28a$) and transmission of each port is obtained.

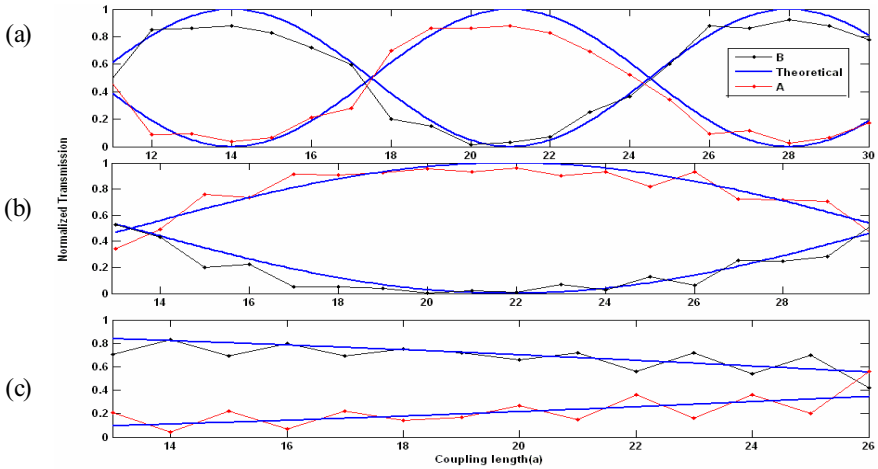

Figure 3: Normalized Transmission at wavelength 1516 nm versus coupling lengths for different distances (D) (a) $D = 1$; (b) $D = 2$; (c) $D = 3$.

Simulation results using FDTD code confirms theoretical results as shown in Fig. 2. The slight disagreements between FDTD and theoretical results are due to influence of the discrete structure of PC which can be reduced by using larger L_c [3]. For $L = 18a$ we have equal power splitting while for $L = 13a$ or $L = 25a$ we can switch power to output ports A and B respectively.

2.2. Changing Distance of Parallel Waveguides

Now we change the distance between parallel waveguides. Figure 3 shows the normalized transmissions of the two ports structure for three different values of D (distance of parallel waveguide). Effect of changing D between a to $3a$ for wavelength 1516 nm over the different coupling lengths $10a$ to $30a$ is investigated.

Our FDTD simulations show that L_c increases rapidly as the D increases which is in accordance with above theoretical formula.

2.3. 1×4 Power Dividers with Different Output Power Levels

The number of output ports can be improved by splitting power in each branch. Fig. 4 shows the electric field pattern in a splitter with 4 output port for different coupling lengths.It is seen that different output power levels can be obtained by changing the coupling lengths ($L1$, $L2$, $L3$) based on previous results in Fig 2. For example in order to have equal power splitting between 4 output ports, $L1 = L2 = L3 = 18a$ is chosen as shown in Fig. 4(c). High total transmission ($\sim 92\%$) is achieved throughout the calculated coupling lengths.

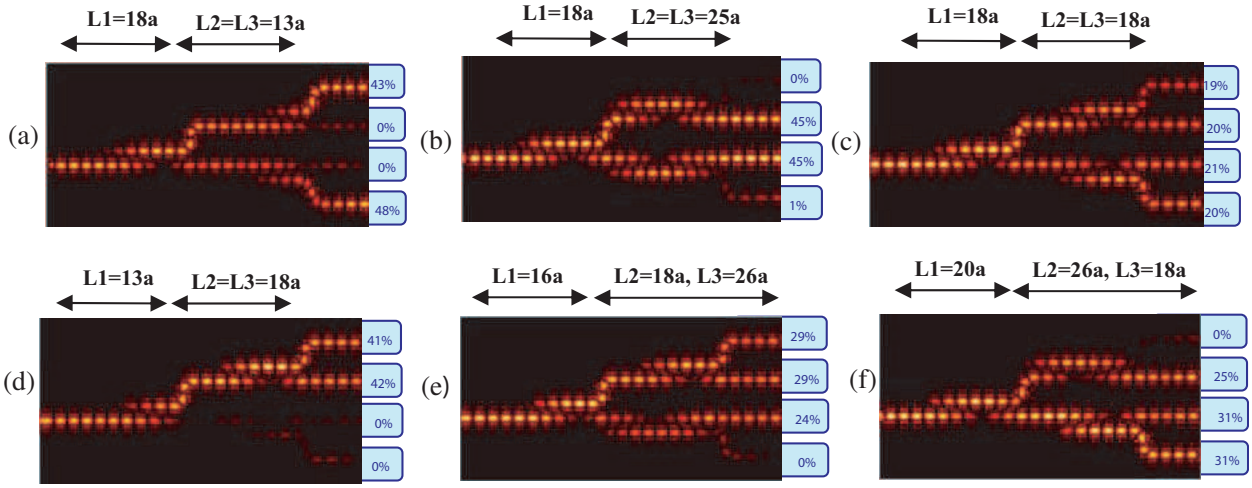

Figure 4: Electric field intensity of a power splitter with 4 output branches and different coupling lengths.

3. CONCLUSIONS

In this paper, we have investigated a power splitter based on PC waveguide directional coupling. The effects of coupling parameters such as coupling length and distance between parallel waveguides on the coupling characteristics have been investigated. Different output power levels can be obtained by changing these parameters. FDTD simulations are in accordance with theoretical results. Based on achieved results a power splitter with two or four output branches with different output power level can be designed. A total transmission up to 0.96 and 0.92 is obtained for two and four output branches respectively throughout the calculated coupling lengths.

ACKNOWLEDGMENT

This paper was supported by Iran Telecommunication Research Center.

REFERENCES

1. Mekis, A., J. C. Chen, I. Kurland, S. H. Fan, P. R. Villeneuve, and J. D. Joannopoulos, "High transmission through sharp bends in photonic crystal waveguides," *Phys. Rev. Lett.*, Vol. 77, No. 18, 3787–3790, 1996.
2. Park, I., H.-S. Lee, H.-J. Kim, K.-M. Moon, S.-G. Lee, B.-H. O, S.-G. Park, and E.-H. Lee, "Photonic crystal power-splitter based on directional coupling," *Opt. Express*, Vol. 12, No. 15, 3599–3604, 2004.
3. Huang, S., J. Shi, D. Wang, and W. Li, "Power splitters with different output power levels built with two-dimensional photonic crystals," *Opt. Engineering*, February 2006.
4. Javid, M., F. Monifi, A. Ghafari, and M. S. Abrishamian, "A new broadband L-shaped bend based on photonic crystal ring resonators," *PIERS Proceedings*, 1097–1099, Hangzhou, China, March 24–28, 2008.
5. Strasser, P., R. Flückiger, R. Wüest, F. Robin, and H. Jäckel, "InP-based compact photonic crystal directional coupler with large operation range," *Optics Express*, 8472, 2007.

A New Bi-periodic Photonic Crystal Y-splitter

A. Ghaffari, F. Monifi, M. Djavid, and M. S. Abrishamian

Department of Electrical Engineering, K. N. Toosi University of Technology, Tehran, Iran

Abstract— We investigate the properties of bi-periodic photonic crystal structures. We show that these structures have significantly better performances. A new bi-periodic Y splitter is presented which its normalized transmission is widened and increased in amplitude in comparison with conventional Y splitters.

1. INTRODUCTION

Photonic crystals (PCs) are artificially engineered materials with periodic arrangement of dielectric constants. They prohibit propagation of light for frequencies within the photonic band gaps. Many optical devices based on PCs have been proposed. Optical power splitters or dividers are essential components in integrated photonic devices used in fiber optic networks. The most straightforward Y-splitter design consists of three single-defect ('W1') waveguides joined together at 120°, which leads to strong reflections and narrow-bandwidth operation [1]. Ideally, the splitters should divide an input power equally into output ports without significant reflection or radiation losses, and should be small in size [2]. Having a perturbation in the period of the two rows next to the guiding region by considering a new periodicity (a') results in biperiodic photonic crystal waveguide (PCW) as shown in Fig. 1(a). Bi-periodic PCW can have very small loss coefficient. It has previously shown that nonlinear dispersion and modegap of PCWs can be overcome by use of bi-periodic structures [3–5]. If we generalize the application of bi-periodic structures other bi-periodic structures such as bends and couplers can also be implemented.

2. TRANSMISSION OF BI-PERIODIC STRAIGHT WAVEGUIDES

The PC under study has a triangular lattice photonic crystal with a radius of $r = 0.3a$ and an effective permittivity of 7.9, and is excited with TM polarization. The spectrum of the power transmission is obtained with a finite difference time domain method (FDTD) code. A perfect matched layer (PML) is put around the whole structure. Now the effect of changing the period (a) and radius (r) of the holes next to the guiding region is investigated.

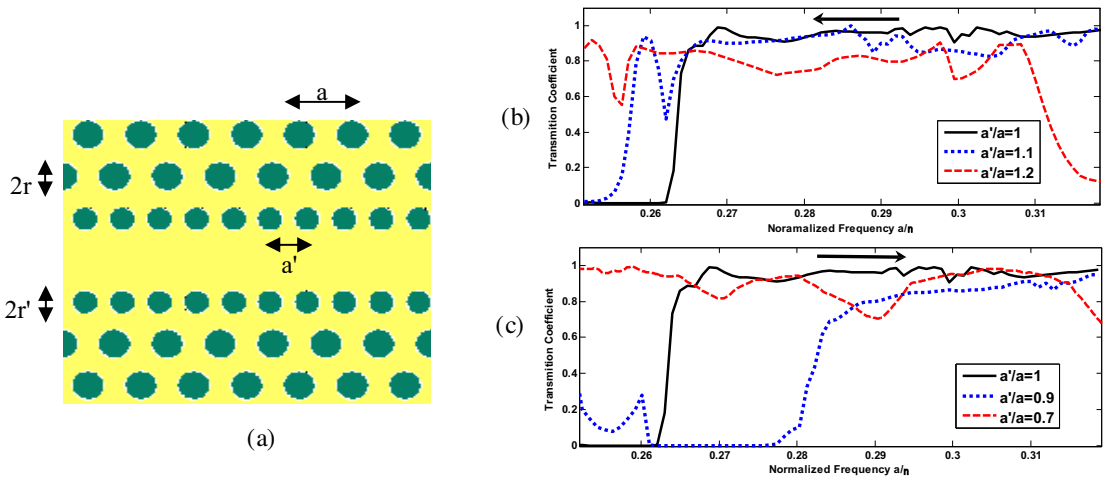

Figure 1: (a) Bi-periodic photonic crystal waveguide. r' and a' are radius and period of the air holes next to the guiding region, (b) The evolution of Normalized transmission when a' changes, increased periods ($a'/a = 1.1, 1.2$), (c) Decreased periods ($a'/a = 0.7, 0.9$).

Figure 1(b) and Fig. 1(c) shows the power transmission spectra for five PCWs with different values of a' while its radius remains unchanged. It is seen that decreasing (increasing) the periodicity shift the edge of modegap toward higher (lower) frequencies.

Also effect of changing the radius (r) of the holes next to the guiding region is depicted in Fig. 2. It shows the power transmission spectra for five different values of r' while its lattice constant remains unchanged. It is clear that an increase (decrease) in the radius of holes shifts the edge of modegap toward higher (lower) frequencies and increases (decrease) the amplitude of transmission coefficient.

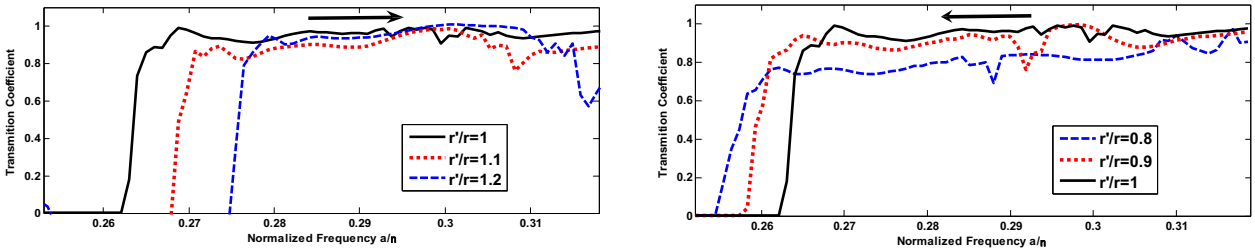

(a) (b)

Figure 2: The evolution of Normalized transmission as the period of the air holes in the rows next to the guiding region changes. (a) Increased radius ($r'/r = 1.1, 1.2$), (b) Decreased radius ($r'/r = 0.8, 0.9$).

3. TRANSMISSION OF BI-PERIODIC BENT WAVEGUIDES

Based on previous section results, by selecting $a'/a = 0.7$ (where (a) represents the lattice constant of the original PCW) it is possible to have guiding with high transmission coefficient and linear dispersion diagram over the whole Photonic bandgap.

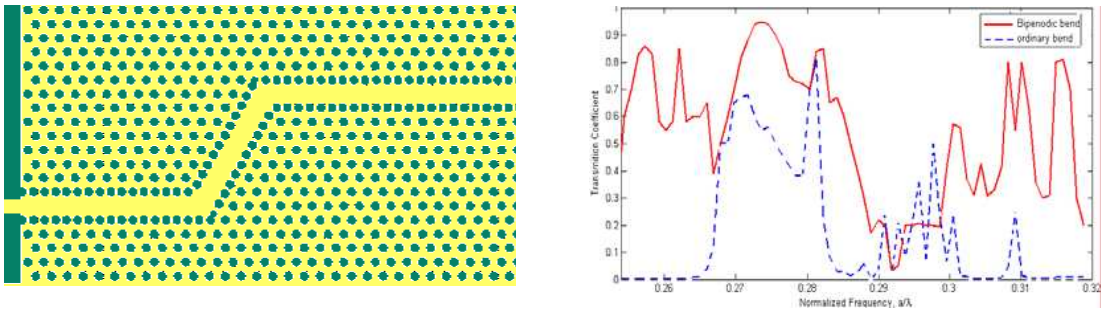

(a) (b)

Figure 3: (a) A biperiodic bend, (b) The transmission coefficient of the biperiodic and conventional bends.

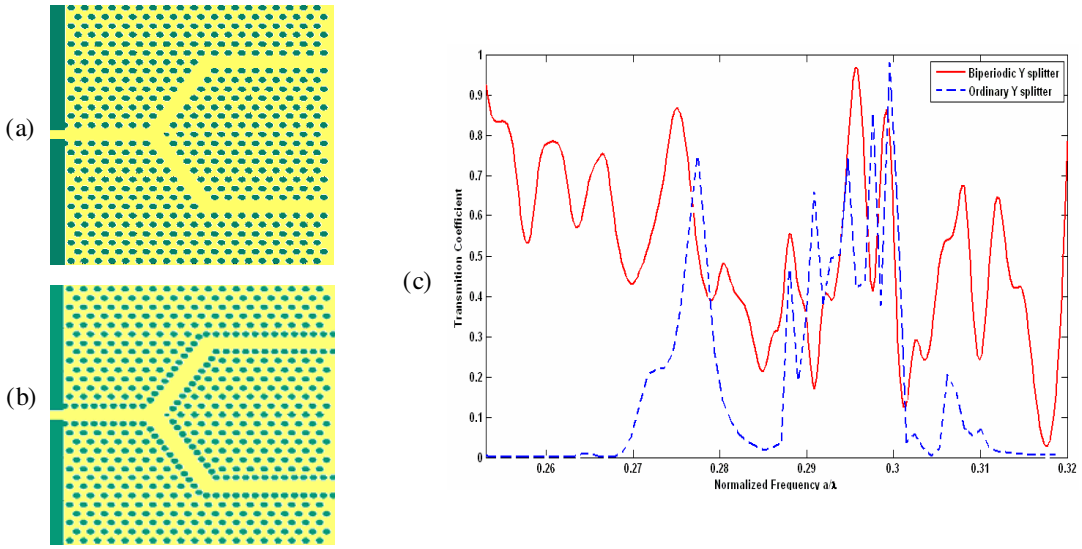

Figure 4: (a) Conventional Y splitter, (b) Bi-periodic Y splitter, (c) Associated transmittance spectra of the biperiodic and conventional Y splitter.

It has previously shown that bi-periodic photonic crystal bends can have much better performances compared to conventional bends [3]. First we simulate two cascading 120° biperiodic bends. Normalized transmission of a biperiodic and conventional bend are depicted in Fig. 3. This is in accordance with Ref. [3]. It shows that the transmission has been widened, and increased in amplitude.

4. BI-PERIODIC Y SPLITTER

Now as a result of previous section we anticipate same results for a biperiodic Y splitter. So we propose a new bi-periodic Y splitter and show that photonic crystal Y splitter can have much better performance compared to their conventional counterparts. To best of our knowledge, this article presents the first comparison between biperiodic and conventional Y splitter.

As shown in Fig. 4(c) high transmission window corresponding to the conventional Y splitter has been widened and increased in amplitude in the corresponding biperiodic Y. Besides, conventional Y has zero transmission for normalized frequency below 0.27 but there is a new high transmission window in the spectrum of the biperiodic Y at this lower part of the PBG.

5. CONCLUSIONS

In this paper, first we investigated transmission properties of the guided mode in a biperiodic PCW and we showed that changing the periodicity and radius of two rows of air holes that are adjacent to guiding region affects the transmission spectra. Based on this results we chosen best value for r', a' to have highest guiding bandwidth, linear dispersion within the PBG. Then we generalized application of biperiodic structures to two 120° bends. Based on its promising results finally we have developed a new biperiodic Y splitter. Transmission window of this new Y splitter has been widened and flattened. Also it has higher transmission amplitude as a result of low loss biperiodic structure.

ACKNOWLEDGMENT

This paper was supported by Iran Telecommunication Research Center.

REFERENCES

1. Sugimoto, Y., N. Ikeda, N. Carlsson, K. Asakawa, N. Kawai, and K. Inoue, "Light-propagation characteristics of Y-branch defect waveguides in AlGaAs-based air-bridge-type two-dimensional photonic crystal slabs," *Opt. Lett.*, 27388–90, 2002.
2. Boscolo, S., M. Midrio, and T. F. Krauss, "Y junctions in photonic crystal channel waveguides: High transmission and impedance matching," *Opt. Lett.*, Vol. 27, 1001–3, 2002.
3. Jafarpour, A., et al., "Large-bandwidth ultra-low-loss guiding in bi-periodic photonic crystal waveguides," *Applied Physics B*, Vol. 79, 409–414, 2004.
4. Jafarpour, A., A. Adibi, Y. Xu, and R. K. Lee, "Mode dispersion in bi-periodic photonic crystal waveguides," *Physical Review B*, Vol. 68, 233102–233105, 2003.
5. Jafaipour, A., et al., "Calculating the dispersion of an arbitrary photonic crystal waveguide," *IEEE Journal of Quantum Electronics*, Vol. 40, 1060–1067, 2004.

Full Wave Analysis for Finlines and Antennas with Metamaterial

Humberto César Chaves Fernandes

Department of Electrical Engineering, Federal University of Rio Grande do Norte
Natal-RN, 59078-970, P. O. Box 1583, Brazil

Abstract— Metamaterials are defined as artificial effectively non-homogeneous electromagnetic structures with desired anisotropic dielectric and magnetic characteristics. In this paper the bilateral fin line and planar antennas with EBG — Electromagnetic Band Gap — metamaterial substrate are analyzed using the full wave TTL — Transverse Transmission Line, method. In order to analyze these structures the effective dielectric constant, the attenuation constant and the pattern fields are determined. The results obtained for these applications and the conclusions are presented.

1. METAMATERIAL STRUCTURE

A metamaterial (MTM) is defined as artificial non-homogeneous electromagnetic structure not readily available in nature [1–4]. One characteristic of this material shown in Fig. 1, is the negative permittivity, ε, and permeability, μ.

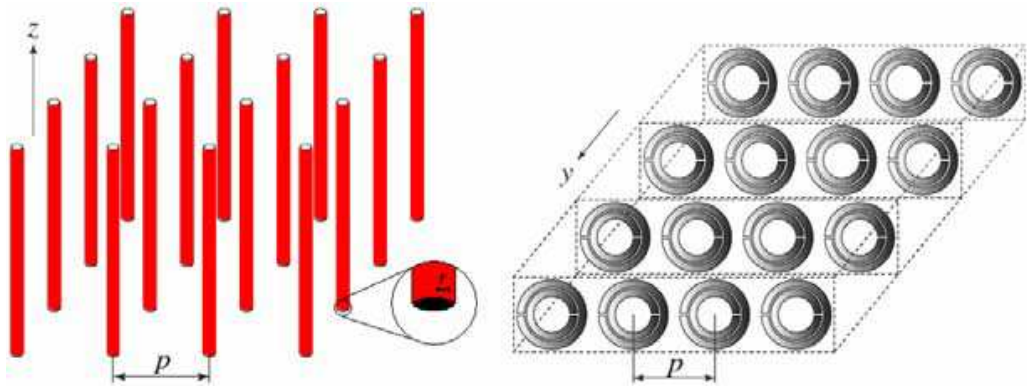

(a) (b)

Figure 1: (a) Thin-wires (TW), with negative-ε/positive-μ if $\vec{E}\|y$, (b) Split-ring resonator (SRR) positive-ε/negative-μ, if $\vec{H} \perp Z$.

If the excitation electric field $\vec{E}$ is parallel to the "y" axis in the MTM thin-wire shown in Fig. 1(a) so to induces a current along them, and generates equivalent electric dipole moment, this MTM can be characterized by plasmonic-type permittivity frequency function of the form [2],

$$\varepsilon_r(\omega) = 1 - \frac{\omega_{pe}^2}{\omega^2 + \zeta^2} + j\frac{\zeta\omega_{pe}^2}{\omega(\omega^2 + \zeta^2)}; \tag{1}$$

$\omega_{pe} = \sqrt{\frac{2\pi c^2}{p^2 \ln\left(\frac{p}{a}\right)}}$ (c: light speed, a: radius of the wires, p: period) is the electric plasma frequency. $\zeta = \varepsilon_0(p\omega_{pe}/a)^2/\pi\sigma$, is the dumping factor due to metal loss.

Analyzing the Equation (1),

$$\mathrm{Re}(\varepsilon_r) < 0, \quad \text{for} \quad \omega^2 < \omega_{pe}^2 - \zeta^2; \tag{2}$$

If consider $\zeta = 0$, results:

$$\varepsilon_r < 0 \Leftrightarrow \omega^2 < \omega_{pe}^2 \tag{3}$$

If the excitation magnetic field $\vec{H}$ is perpendicular to the "z" axis in the MTM split-ring resonator shown in Fig. 1(b) so to induce a current in the loop of the ring, and generates equivalent magnetic

dipole moment, this MTM can be characterized by plasmonic-type permeability frequency function of the form [2],

$$\mu_r(\omega) = 1 - \frac{F\omega^2(\omega^2 - \omega_{0m}^2)}{(\omega^2 - \omega_{0m}^2)^2 + (\omega\zeta)^2} + j\frac{F\omega^2\zeta}{(\omega^2 - \omega_{0m}^2)^2 + (\omega\zeta)^2}; \tag{4}$$

$F = \pi(a/p)^2$, $\omega_{0m} = c\sqrt{\frac{3p}{\pi \ln(2\omega a^3/\delta)}}$ (w: width of the rings, δ: radial spacing between the rings) is a magnetic resonance frequency. The Equation (4) analyze, reveals the range of frequency where the permeability is negative: $\mu_r < 0$, for $\omega_{0m} < \omega < \frac{\omega_{0m}}{\sqrt{1-F}} = \omega_{pm}$; ω_{pm} is the magnetic plasma frequency.

The structure described in the Fig. 1(b) is a LH bidimensional, so $\vec{E}$ has to be directed along the axis of the wires, and two directions are possible for $\vec{H}$, then we have the following conditions: $\varepsilon_{xx}(\omega < \omega_{pe}) < 0$, $\varepsilon_{yy} = \varepsilon_{zz} > 0$; $\mu_{xx} < 0$ for $\omega_{0m} < \omega < \omega_{pm}$ and μ_{yy}, $\mu_{zz} > 0$.

The paper discusses the effect of the metamaterial double anisotropy by utilizing the tensor properties, which are expressed as [1–3]:

$$\mu = \mu_0 \begin{pmatrix} \mu_{xx} & 0 & 0 \\ 0 & \mu_{yy} & 0 \\ 0 & 0 & \mu_{zz} \end{pmatrix} \tag{5}$$

$$\varepsilon = \varepsilon_0 \begin{pmatrix} \varepsilon_{xx} & 0 & 0 \\ 0 & \varepsilon_{yy} & 0 \\ 0 & 0 & \varepsilon_{zz} \end{pmatrix} \tag{6}$$

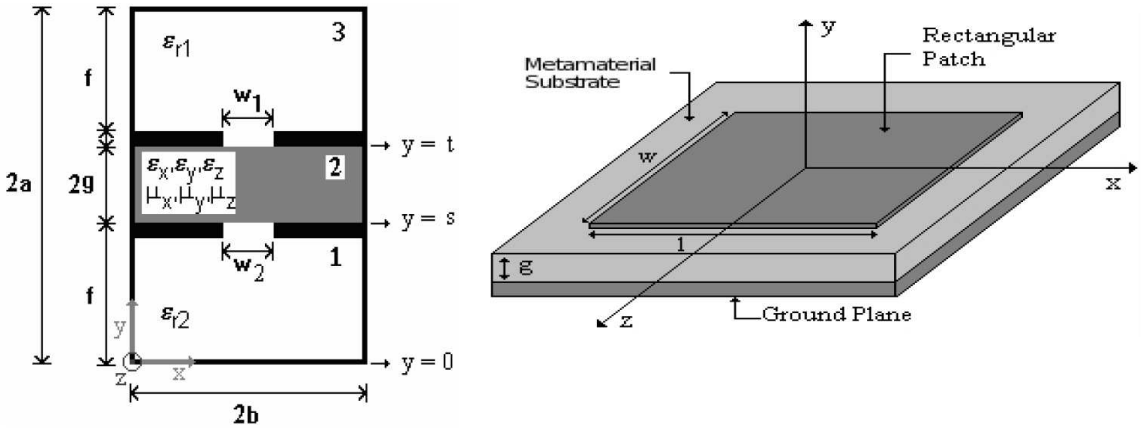

Figure 2: (a) Transversal cut of a bilateral fin line structure with metamaterial substrate, (b) Microstrip resonator antenna with metamaterial.

2. FINLINES AND ANTENNAS APPLICATIONS

Fin lines are widely used as a millimeter wave components, due to its various advantages such as reducing size, weight, cost and because it interfaces easily with other millimeter wave devices. The metamaterial bilateral fin line is shown in Fig. 2(a). In this analysis the concise full wave TTL method, making possible a significant algebraic simplification of the equations and reducing the computational time [1].

The general equations of the fields in the TTL method are obtained after using the Maxwell's equations. The characteristic equation for determining the complex propagation constant Γ, is obtained by setting the determinant of the system matrix equal to zero. The effective dielectric constant is determined after numerical solutions of the matrix determinant by the relation between the phase constant and the free space wave number, $\varepsilon_{ef} = (\beta/ko)^2$.

This microstrip antenna is composed of a rectangular patch, metamaterial substrate and a ground plane. The MTM impedes the propagation of electromagnetic waves in some frequency, which can be used to made devices most efficient, and eliminate unwanted frequencies. The analysis

is made using the TTL method, with efficient bases function in both x and z direction, as is shown in the Fig. 2(b) [1]. In order to analyze this structure the resonant frequency and pattern fields are obtained [4–8].

The metamaterial substrate shown in Region 1 of Fig. 2(b) is modeled by using bi anisotropic tensor properties Equations (5) and (6), together with wave equations which are expressed as [4, 5]:

$$\frac{\partial^2 \tilde{E}y}{\partial y^2} - \gamma^2 \tilde{E}y = 0 \tag{7.1}$$

$$\frac{\partial^2 \tilde{H}y}{\partial y^2} - \gamma^2 \tilde{H}y = 0 \tag{7.2}$$

After using the Maxwell's equations in the spectral domain, the general equations of the electric and magnetic fields to the metamaterial resonator are obtained as:

$$\tilde{E}_{xi} = \frac{1}{\gamma_i^2 + k_0^2 \varepsilon_{ri}} \left[-j\alpha_n \frac{\partial}{\partial y} \tilde{E}_{yi} + \omega\mu_0\mu_{xi}\beta_k H_{yi} + \omega\mu_0\mu_{zi}\beta_k \tilde{H}_{yi} \right] \tag{8.1}$$

$$\tilde{E}_{zi} = \frac{1}{\gamma_{yi}^2 + k_0^2 \varepsilon_{ri}} \left[-j\beta_k \frac{\partial}{\partial y} E_{yi} - \omega\mu_0\mu_{xi}\alpha_n H_{yi} - \omega\mu_0\mu_{zi}\alpha_n H_{yi} \right] \tag{8.2}$$

$$H_{xi} = \frac{1}{\gamma_{yi}^2 + k_0^2 \varepsilon_{ri}} \left[-j\alpha_n \frac{\partial}{\partial y} H_{yi} - \omega\varepsilon_0\varepsilon_{xi}\beta_k E_{yi} - \omega\varepsilon_0\varepsilon_{zi}\beta_k E_{yi} \right] \tag{8.3}$$

$$\tilde{H}_{zi} = \frac{1}{\gamma_{yi}^2 + k_0^2 \varepsilon_{ri}} \left[-j\beta_k \frac{\partial}{\partial y} H_{yi} + \omega\varepsilon_0\varepsilon_{xi}\alpha_n E_{yi} + \omega\varepsilon_0\varepsilon_{zi}\alpha_n E_{yi} \right] \tag{8.4}$$

where: $i = 1$, 2 represent the dielectric regions of the structure; $\gamma_i^2 = \alpha_n^2 + \beta_k^2 - k_i^2$ is the propagation constant in y direction; α_n is the spectral variable in "x" direction and β_k is the spectral variable in "z" direction; $k_i^2 = \omega^2\mu\varepsilon = k_0^2\varepsilon_{ri}^*$ is the wave number of the ith dielectric region; $\varepsilon_{ri}^* = \varepsilon_{ri} - j\frac{\sigma_i}{\omega\varepsilon_0}$ is the relative dielectric constant of the metamaterial with losses; $k_1^2 = \omega^2\mu_0\mu_{yy}\varepsilon_0\varepsilon_{yy}$. $\omega = \omega_r + j\omega_i$ is the complex angular frequency; $\varepsilon_i = \varepsilon_{ri}^* \cdot \varepsilon_0$ is the dielectric constant of the metamaterial.

The equations above are applied to Helmohltz equations in the spectral domain (7.1) and (7.2), [4, 5] to determine the field's equations to the structure. The solutions of these equations to the Regions 1 and 2 are:

$$\tilde{E}_{y1} = A_{1e} \cdot \cos h(\gamma_1 y); \tag{9.1}$$

$$\tilde{H}_{y1} = A_{1h} \cdot \sin h(\gamma_1 y); \tag{9.2}$$

$$\tilde{E}_{y2} = A_{2e} \cdot e^{-\gamma_2 y}; \tag{9.3}$$

$$\tilde{H}_{y2} = A_{2h} \cdot e^{-\gamma_2 y} \tag{9.4}$$

Substituting these solutions in the Equations (8.1) to (8.4), as functions of the unknown constants A_{1e}, A_{1h}, A_{2e} and A_{2h}, and applying the boundary conditions in the interface $y = g$, relating the current densities in the sheets ($\tilde{J}_{xt}$ and $\tilde{J}_{zt}$) and the magnetic fields, the impedance matrix will be obtained.

$$\tilde{H}_{x1} - \tilde{H}_{x2} = \tilde{J}_{zt}; \tag{10.1}$$

$$\tilde{H}_{z1} - \tilde{H}_{z2} = -\tilde{J}_{xt} \tag{10.2}$$

Substituting the Equations (8.3) and (8.4), into the Equations (10.1) and (10.2), the admittance matrix is obtained:

$$\begin{bmatrix} Y_{xx} & Y_{xz} \\ Y_{xz} & Y_{zz} \end{bmatrix} \begin{bmatrix} \tilde{E}_{xg} \\ \tilde{E}_{zg} \end{bmatrix} = \begin{bmatrix} \tilde{J}_{zg} \\ \tilde{J}_{xg} \end{bmatrix} \tag{11.1}$$

For example,

$$Y_{xx} = \frac{j}{\omega\mu_0\gamma_1\gamma_2} \left\{ \frac{\gamma_2 \mathrm{cotg} h(\gamma_1 g) \left[-\beta_k^2\gamma_1^2 + \omega^2\alpha n^2\varepsilon_0\mu_0(\varepsilon_{x1} + \varepsilon_{z1})(\mu_{x1} + \mu_{z1}) \right]}{(\gamma_1^2 + k_1^2)(\mu_{x1} + \mu_{z1})} \right.$$
$$\left. + \frac{\gamma_1 \left(-\beta_k^2\gamma_2^2 + \omega^2\alpha n^2\mu_2\varepsilon_2 \right)}{\left(\gamma_2^2 + k_2^2 \right)\mu_{r2}} \right\} \tag{11.2}$$

The matrix inversion is used to obtain the impedance matrix, and the current densities in the interface are expanded using base functions [4, 5]. The Galerkin method is applied to (11.1), to eliminate the electric fields and then, the complex resonant frequency is obtained numerically.

3. NUMERICAL RESULTS

To calculate the numerical results computational programs in Fortran PowerStation language and Scilab were developed, according to the previous theoretical analyses. As illustrated in the previous section the metamaterial present negative permeability and permittivity constants. Fig. 3 shows the metamaterial waveforms. The fin line uses a WR-28 millimeter wave guide, and at 27.0 GHz (resonance frequency) occurs the threshold conditions to both curves.

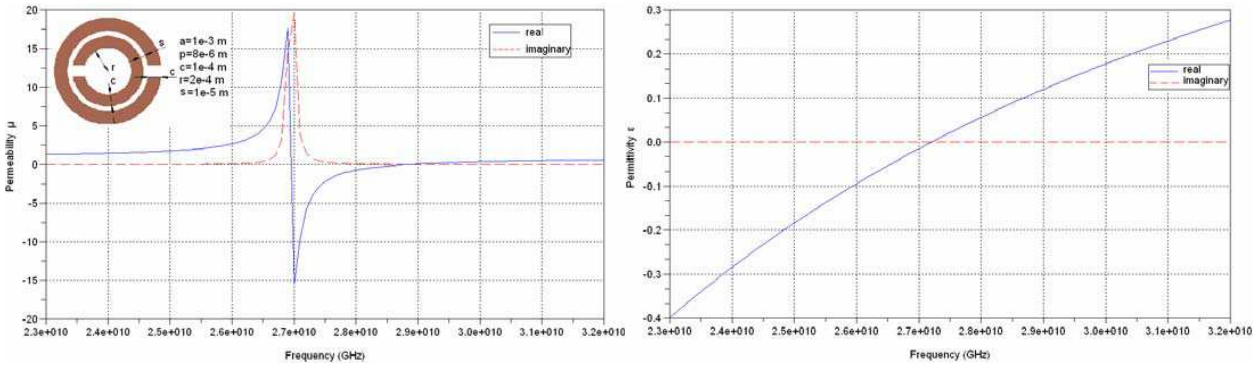

(a) (b)

Figure 3: (a) Permeability for the SRR structure, (b) Permittivity for the TW configuration.

The new results for the bilateral fin line with metamaterial substrate, in a WR-28 millimeter wave guide, according to Fig. 2(a), with $2g = 0.125\,\text{mm}$, $f = 3.4935\,\text{mm}$, $w_1 = w_2 = 0.15\,\text{mm}$ and $\varepsilon_{r1} = \varepsilon_{r3} = 1$, ε_{r2} and μ_{r2}, given by Figs. 3(a) and (b), are shown in Figs. 4(a) and (b).

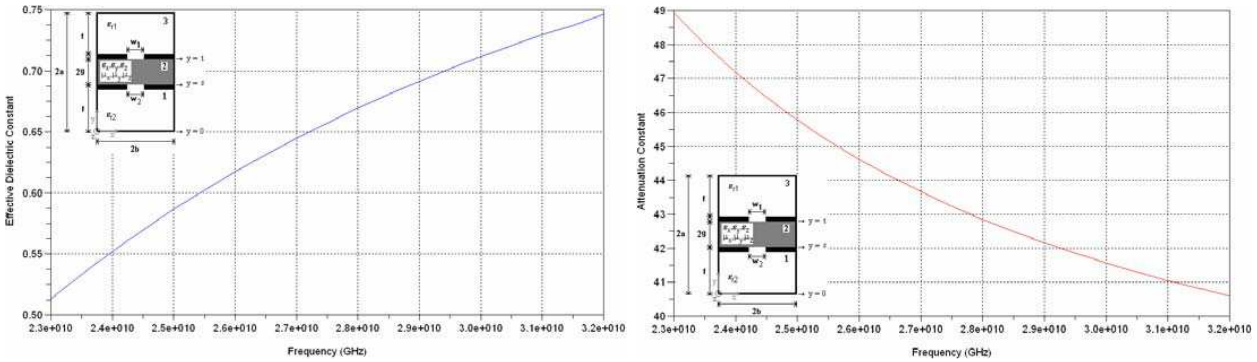

(a) (b)

Figure 4: (a) Effective dielectric constant vs. frequency, (b) Attenuation constant vs. frequency; for a bilateral fin line in a WR-28 millimeter wave guide with metamaterial substrate.

The Figs. 5(a) and (b) show the waveforms permeability and permittivity constants, to the structure TW-SRR, used in the antenna results. At 1.34 GHz (resonance frequency) occurs the threshold conditions to both curves. These characteristics are very important because a range of values available to devices project is increased around the resonance frequency point. It's also shown the far fields comportment to operate in two different ranges (negative μ-ε and positive μ-ε). Here can be seen that the radiation patterns characteristic can change just varying the operation frequency.

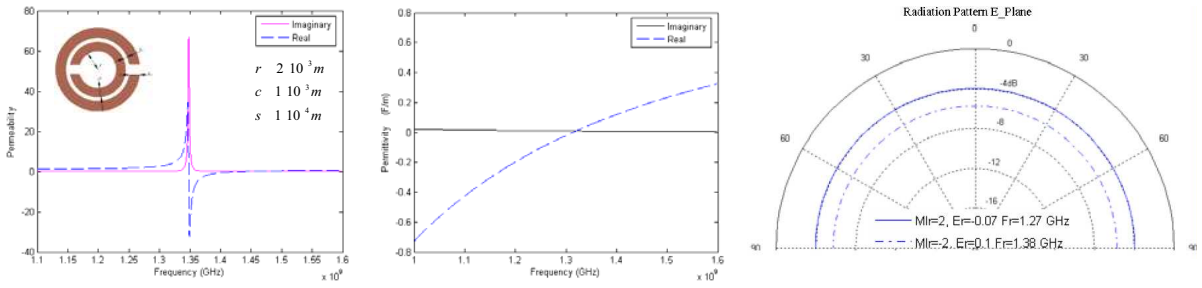

(a) (b) (c)

Figure 5: (a) Permeability for the SRR structure, (b) Permittivity for the TW configuration, and (c), E-plane radiation pattern.

4. CONCLUSIONS

Theoretical and numerical results have been presented for the bilateral fin line and rectangular antenna resonator with metamaterial substrate, using the TTL method. The field's equations were shown to a wide range of permeability and permittivity values, by varying the structure parameters. These characteristics are very important to improve the design of the antenna devices. It was observed a considerable reduction in the algebraic development using the TTL method and a performance improvement using the metamaterial substrate. New results were shown for permeability and permittivity parameters in the GHz range, for the attenuation and effective dielectric constants for the fin line structure, as well as the far fields and resonance frequency of metamaterial antenna.

ACKNOWLEDGMENT

The author acknowledges the support of CNPQ, Brazilian Agency.

REFERENCES

1. Fernandes, H. C. C. and G. D. F. Alves, "Meta-material multilayer substrate planar resonators with superconductive patch," *Progress In Electromagnetics Research Symposium Abstracts*, 382, Praha, Czech Republic, Ago. 2007.
2. Smith, D. R., P. Rye, D. C. Vier, A. F. Starr, J. J. Mock, and T. Perram, "Design and measurement of anisotropic metamaterial that exhibit negative refraction," *IEICE Trans. Electron.*, Vol. E87-C, No. 3, Mar. 3, 2004.
3. Caloz, C. and T. Itoh, *Electromagnetic Metamaterials: Transmission Line Theory and Microwave Applications*, John Wiley & Sons, 2006.
4. Fernandes, H. C. C, M. B. L. Aquino, and D. B. Brito, "Rectangular slot resonator with four dielectrics layers," *PIERS Proceedings*, 2121–2126, Beijing, China, Mar. 26–30, 2007.
5. Fernandes, H. C. C. and D. B. Brito, "Unilateral fin line directional coupler," *International Journal of Infrared and Millimeter Waves*, Vol. 28, No. 8, 651–661, USA, Ago. 2007.
6. Fernandes, H. C. C., J. L. G. Medeiros, I. M. Araujo, Jr., and D. B. Brito, "Photonic crystal at millimeter waves applications," *PIERS Online*, Vol. 3, No. 5, 689–694, 2007.
7. Bhat, B. and S. K. Koul, *Analysis, Design and Applications of Fin Lines*, 383–471, Artech House, Inc., Norwood, MA, USA, 1987.
8. Wiersma, D. S., P. Bartolini, A. Lagendijk, and R. Righini, "Localization of light in a dimensional medium," *Letters to Nature*, Vol. 390, 18/25, Dec. 1997.